TECHNICAL REPORT
NATICK/TR-90/039

AD A230 832

US ARMY
TROOP
SUPPORT COMMAND
NATICK RD&E CENTER

PROCEEDINGS OF THE THIRD NATICK SCIENCE SYMPOSIUM 5 - 6 JUNE 1990

Editors

Matthew L. Herz

Thomas A. Sklarsky

August 1990

Office of the Technical Director
United States Army Natick Research, Development and Engineering Center
Natick, Massachusetts

APPROVED FOR PUBLIC RELEASE; DISTRIBUTION UNLIMITED

DISCLAIMERS

The findings contained in this report are not to be construed as an official Department of the Army position unless so designated by other authorized documents.

Citation of trade names in this report does not constitute an official endorsement or approval of the use of such items.

DESTRUCTION NOTICE

For Classified Documents:

Follow the procedures in DoD 5200.22-M, Industrial Security Manual, Section II-19 or DoD 5200.1-R, Information Security Program Regulation, Chapter IX.

For Unclassified/Limited Distribution Documents:

Destroy by any method that prevents disclosure of contents or reconstruction of the document.

REPORT DOCUMENTATION PAGE

Form Approved
OMB No. 0704-0188

1. AGENCY USE ONLY *(Leave blank)*	2. REPORT DATE	3. REPORT TYPE AND DATES COVERED
	August 1990	Proceedings, 5-6 June 1990

4. TITLE AND SUBTITLE
PROCEEDINGS OF THE THIRD NATICK SCIENCE SYMPOSIUM, 5-6 JUNE 1990

5. FUNDING NUMBERS
Program Element No: 1L162786
Project No: CARRIER

6. AUTHOR(S)
Matthew L. Herz, Scientific Editor
Thomas A. Sklarsky, Managing Editor

7. PERFORMING ORGANIZATION NAME(S) AND ADDRESS(ES)
U.S. Army Natick Research, Development and Engineering Center, ATTN: STRNC-T, Kansas Street, Natick, MA 01760-5000

8. PERFORMING ORGANIZATION REPORT NUMBER
NATICK/TR-90/039

9. SPONSORING/MONITORING AGENCY NAME(S) AND ADDRESS(ES)

10. SPONSORING/MONITORING AGENCY REPORT NUMBER

11. SUPPLEMENTARY NOTES
Third Natick Science Symposium, 5-6 June 1990. Held at the U.S. Army Natick RD&E Center, Natick, MA. Symposium Director: Dr. Robert W. Lewis, Technical Director; (continued)

12a. DISTRIBUTION/AVAILABILITY STATEMENT
Approved for public release; distribution unlimited

12b. DISTRIBUTION CODE

13. ABSTRACT *(Maximum 200 words)*
This proceedings incorporates 25 papers presented at the Third Natick Science Symposium, held 5-6 June 1990 at the U.S. Army Natick RD&E Center, Natick, MA. The papers are included under the headings: Chemical Biological Protection, Military Materials, Ration Design and Food Science, and General Topics.

14. SUBJECT TERMS

Chemical Protection	Food
Biological Protection	Materials
Rations	Mathematical Modeling (contd)

15. NUMBER OF PAGES
392

16. PRICE CODE

17. SECURITY CLASSIFICATION OF REPORT	18. SECURITY CLASSIFICATION OF THIS PAGE	19. SECURITY CLASSIFICATION OF ABSTRACT	20. LIMITATION OF ABSTRACT
UNCLASSIFIED	UNCLASSIFIED	UNCLASSIFIED	SAR

Report Documentation Page
(continued)

11. Symposium Moderator: Dr. Matthew L. Herz, Associate Technical Director for Technology; Symposium Coordinator: Mr. Thomas A. Sklarsky, Scientific and Technical Information Manager.

14.
Food Storage
Shelters
Bread
Polymers
Fabrics
Ballistic Impact
Soman
Blast Protection
G-agent
Thermal Food Processing
Chemical Markers
Listeria
Time Zone
Liquid Crystals
Composites
Diet Countermeasures
Bright Light Countermeasures
Jet Lag
Spider Silk
Silk Proteins
Maillard Browning
Ascorbic Acid
Fruit
Vapor
Laser
Laminates
Nonlinear Optical Materials
Contaminants
Conductive Fibers

DEPARTMENT OF THE ARMY

U.S. ARMY TROOP SUPPORT COMMAND
NATICK RESEARCH, DEVELOPMENT AND ENGINEERING CENTER
NATICK, MA
01760-5001

REPLY TO ATTENTION OF

STRNC-T

June 1990

MEMORANDUM FOR SEE DISTRIBUTION

SUBJECT: Proceedings of the Third Natick Science Symposium, 5-6 June 1990

1. The U.S. Army Natick Research, Development and Engineering Center held its third science symposium on 5-6 June 1990. Natick's programs emphasize a broad range of scientific and technical efforts to protect, sustain, and shelter the soldier on the battlefield.

2. This year, 25 papers were presented by Natick scientists, engineers, and mathematicians, including eight Army Science Conference papers. The general topical areas covered were:

Chemical Biological Protection
Military Materials
Ration Design and Food Science
General Topics

3. The Natick Science Symposium, established in 1986, has a threefold purpose:

a. To recognize and encourage scientific and engineering talent.

b. To demonstrate excellence in research and development.

c. To stimulate the exchange of ideas among researchers at Natick, as well as among attendees from other Army commands and universities.

4. The symposium included papers and presenters from five Natick Directorates:

Advanced Systems Concepts
Aero-Mechanical Engineering
Food Engineering
Individual Protection
Soldier Science

The symposium also included papers, coauthors, and presenters from universities. The 25 papers represent the outstanding efforts of 56 researchers. This year's symposium was highly

STRNC-T
SUBJECT: Proceedings of the Third Natick Science Symposium, 5-6 June 1990

successful, providing a lively scientific exchange amoung Natick researchers and numerous outside attendees. The Fourth Natick Science Symposium will be held in June 1992.

5. This volume is of value to attendees and other professionals interested in Natick's R&D efforts; it is approved for public release. -- The Soldiers' Command

FOR THE COMMANDER:

Robert W. Lewis
ROBERT W. LEWIS
Technical Director

DISTRIBUTION:
Commander,
U.S. Army Armament RD&E Center, ATTN: SMCAR-CO/SMCAR-TD, Dover, NJ 07801-5000
U.S. Army Chemical RD&E Center, ATTN: SMCCR-TD, APG, MD 21010-5423
U.S. Army Communications-Electronics RD&E Center, ATTN: AMSEL-DCGD/AMSEL-TDD, Fort Monmouth, NJ 07703-5000
U.S. Army Belvoir RD&E Center, ATTN: STRBE-Z/STRBE-ZT, Fort Belvoir, VA 21005-5066
U.S. Army Aviation RD&E Center, ATTN: AMSAV-GRD/AMSAV-GTD, 4300 Goodfellow Blvd, St. Louis, MO 63120-1798
U.S. Army Atmospheric Sciences Laboratory, ATTN: SLCAS-D, White Sands Missile Range, NM 88002-5501
U.S. Army Electronic Warfare Vulnerability Assessment Laboratory, ATTN: SLCEV-M-D, White Sands Missile Range, NM 88002-5513
U.S. Army Vulnerability Assessment Laboratory, ATTN: SLCVA-D, White Sands Missile Range, NM 88002-5513
U.S. Army Missile RD&E Center, ATTN: AMSMI-R, Redstone Arsenal, AL 35898-5000
U.S. Army Tank Automotive RD&E Center, ATTN: AMSTA-CF/AMSTA-CR, Warren, MI 48397-5000
U.S. Army Ballistic Research Laboratory, ATTN: SLCBR-D, APG, MD 21005-5066
U.S. Army Electronics Technology and Devices Laboratory, ATTN: SLCET-D, Fort Monmouth, NJ 07703-5302
U.S. Army Harry Diamond Laboratories, ATTN: SLCHD-D, 2800 Powder Mill Road, Adelphi, MD 20783-1145

STRNC-T
SUBJECT: Proceedings of the Third Natick Science Symposium, 5-6 June 1990

DISTRIBUTION (CONT'D):
Commander,
U.S. Army Troop Support Command, ATTN: AMSTR-E, 4300 Goodfellow Blvd, St. Louis, MO 63120-1798
U.S. Army Materiel Command, ATTN: AMCDE, 5001 Eisenhower Avenue, Alexandria, VA 22333-0001
U.S. Army Human Engineering Laboratory, ATTN: SLCHE-D, APG, MD 21005-5001
U.S. Army Materials Technology Laboratory, ATTN: SLCMT-D, Watertown, MA 02172-0001
U.S. Army Materiel Systems Analysis Activity, ATTN: AMXSY-D, Aberdeen Proving Ground, MD 21005-5071
U.S. Army Armament, Munitions and Chemical Command, ATTN: AMSMC-CG, Rock Island, IL 61299-6000
U.S. Army Aviation Research and Technology Activity, ATTN: SAVDL-D, Ames Research Center, Moffett, CA 94035-1099
U.S. Army Laboratory Command, ATTN: AMSLC-TD/AMSLC-TP-PO, 2800 Powder Mill Road, Adelphi, MD 20783-1145
U.S. Army Research Office, ATTN: SLCRO-ZC, Research Triangle Park, NC 27709-2211
U.S. Army Test and Evaluation Command, ATTN: AMSTE-TD, Aberdeen Proving Ground, MD 21005-5055

TABLE OF CONTENTS

I. CHEMICAL BIOLOGICAL PROTECTION

II. MILITARY MATERIALS

* *Army Science Conference paper*

* *Army Science Conference paper*

CONTENTS

IV. GENERAL TOPICS

**Army Science Conference paper*

TITLE: Induction of Enhanced Strains of a Thermophile That Synthesize an OPA Anhydrase Effective in Hydrolyzing 4-Nitrophenyl Esters of Phenylphosphinate

*Benedict J. Gallo, Dr., Paula M. Scotland, Ms., and David A. Gowenlock, Mr.

ABSTRACT:

A strain of Bacillus stearothermophilus JD100 previously reported to synthesize intracellular organophosphorus acid anhydrase was genetically altered in order to increase the synthesis of this enzyme. The approach involves traditional genetic methods of improving enzyme titers. The multistep process includes mutagenesis of parental strain I5D with UV light and subsequent screening of the surviving population for enhanced activity against p-nitrophenyl ethyl(phenyl)phosphinate. Several putative mutants have been isolated with enhanced synthesis of this organophosphorus acid anhydrase.

*BIOGRAPHY: Benedict J. Gallo, Ph.D.
PRESENT ASSIGNMENT: Research Microbiologist in the Biological Sciences Division of the Soldier Science Directorate, U. S. Army Natick Research, Development and Engineering Center, Natick, MA.
PAST EXPERIENCE: Conducted research in fungal genetics and microbiology as a National Research Council Research Associate at U. S. Army Natick Research, Development and Engineering Center, Natick, MA.
DEGREES HELD: B.A. University of Connecticut, 1958; M.S., University of Michigan 1962 and Eastern Michigan University 1970; Ph.D., University of Michigan, 1976.

Induction of Enhanced Strains of a Thermophile That Synthesize an OPA Anhydrase Effective in Hydrolyzing 4-Nitrophenyl Esters of Phenylphosphinate

Benedict J. Gallo, Dr., Paula M. Scotland, Ms., and David A. Gowenlock, Mr.

Introduction

The bacterial thermophile JD100, a soil microbe, was identified as a strain of *Bacillus stearothermophilus* and has been reported to synthesize a unique endogenous organophosphorus acid anhydrase (OPA anhydrase), which cannot hydrolyze diisopropylfluorophosphate (DFP) but is very active in hydrolyzing 4-nitrophenyl esters of phenylphosphinate.[1] The use of this and other similar OPA anhydrases in hydrolyzing organophosphorus esters and pesticides has been suggested by a number of authors[2]. In order to make enzyme from this strain of *B. stearothermophilus* more available for research and development, we conducted a program to produce hyperproducing mutants. This paper describes the methodology and results from our studies.

Experimental methods

Organisms - *Bacillus stearothermophilus* JD100, JD200 and JD300 were obtained from Dr. J. DeFrank, U. S. Army Chemical Research, Development and Engineering Center (CRDEC). They were maintained on LB (Lennox) agar slants at 55°C for 24-36 hours before storage at refrigerator temperatures. The streptomycin resistant (*strE*) strains of *Bacillus stearothermophilus* reported in this paper were put on the above medium but with the addition of 250 ug to 500 ug of streptomycin per mL medium.

Mutation and Mutant Screening - Log phase cells of *Bacillus stearothermophilus* grown at 45°C were mutagenized with UV light at room temperatures at a kill rate in excess of 99.99%. Immediately after irradiation survivors were protected from light, cooled and stored at 4°C for 18 to 36 hours prior to use. The mutagenized cells were put on agar plates to a average colony density of 100 per plate and incubated to maturity at 55°C. The screening protocol is described in the text.

Submerged Culture - The medium used for the growth of submerged cultures for enzyme synthesis was either that of Cook or Lennox basic broth with 0 - 0.5% dextrose and 125 ug streptomycin (minimum)/mL medium when required.[3,4] The growth vessels included 2 mL microfuge tubes, standard glass culture tubes, 300 mL culture flasks, 2800 mL Fernbach flasks and 14 liter stirred tank reactor (fermentor) with working volumes of 1.25 mL, 7 mL, 50 mL, 500 mL, and 10 liter, respectively.

Harvest and Pre-assay Processing - Ten liter cultures were harvested by cartridge flow filtration and centrifugation. For cultures of less volume, centrifugation at 12,000 rpm was used. The cell suspensions were washed free of medium by 1-3 centrifugations using normal saline without Mn++, or with bis-tris propane - KCl - NaCl buffer, pH 7.15, with Mn++ (standard buffer).[5] Final pellets were resuspended in the standard buffer and immediately frozen to -30°C. Cells for dry weight measurements were most commonly made from nonwashed centrifugation pellets after drying at 80°C for 24 or more hours.

Enzyme Activity Estimations - OPA anhydrase activity estimations were made of washed whole cells ruptured by either 1 or 6 cycles of freezing and thawing in standard buffer.[5] The assay reaction mixture consisted of 5 uL of ruptured cell suspension and 47 uL of standard buffer made 0.2 mM with respect to 4-nitrophenyl methyl(phenyl)phosphinate (MPP).[6] The assay temperature was set at or about 28°C and optical density read at 400 or 405 nm. The extinction coefficient of p-nitrophenol used in computing activity was at pH 7.15, 11.85 X 10^3.[7] Activity is expressed as uM of substrate hydrolyzed/min·mg dry weight^{-1} or mL^{-1} culture at 28°C. Spectrophotometric readings were made either with LKB Ultrospec spectrophotometer or a Molecular Devices Thermomax microplate reader and the reaction mixture volumes used with each instrument were 2600 uL/tube and 260 uL/well, respectively.

Results

In 1984 three thermophilic strains (JD100, JD200 and JD300) were isolated at U. S. Army Chemical Research, Development and Engineering Center, whose whole cells had low hydrolytic activity against DFP (personal communication J. De Frank, CRDEC). Upon further investigation the isolates were found to be different strains of *Bacillus stearothermophilus*. Table 1 shows the major species-determining traits, and dissimilar strain-differentiating traits. The strains remain as originally designated JD100, JD200 and JD300. Fifty-two different traits were determined for these three different strains of *B. stearothermophilus*.

Strain JD100 was then mutagenized for the purpose of inducing two antibiotic markers on the chromosomal genome, resistance to streptomycin and resistance to ampicillin. Antibiotic markers are useful in growth and genetic studies as an aid in maintaining strain purity and for use as a parental stock for mutation studies. In addition it was determined earlier that the development of resistance to streptomycin in *B. stearothermophilus* resulted in curing the bacterium

Table 1. Diagnostic Taxonomic Traits of Bacillus stearothermophilus strains JD100, JD200 and JD300

TAXONOMIC TRAIT	JD100	JD200	JD300
Respiration			
Obligate Aerobic	+	+	+
Endospore formation	+	+	+
Gram Strain	+	+	+
Rod Morphology	+	+	+
Growth Limits, °C			
Maximum Temperature	‹73	‹75	‹75
Minimum Temperature	40	40	35
Indole Production	+	-	-
D Xylose Oxidation	+	-	-
Nitrate Reductase	-	-	+
Growth with 5% NaCl	-	-	+
Gas Production			
Arabinose	-	+	+
L Xylose	-	-	+
Lactose	-	+	+
β-galactosidase	-	+	-

of plasmids.[8] In this study several streptomycin-resistant strains of JD100 were induced by UV mutagenesis. However one strain, I5D, arose spontaneously and was chosen as the strain for further use because of the lack of any UV treatment. Mutants with resistance to ampicillin could not be obtained via UV irradiation. Figure 1 shows the geneology of strE I5D and the derived hyperproducing OPA anhydrase strE mutants. The mutagenized spores were spread on agar medium plates with streptomycin at a target concentration of 100 colonies per plate and incubated at 55°C for 24 to 36 hours or whenever the plate seemed ready for accurate replica plating. The protocol for primary plate

FIGURE 1. GENEOLOGY OF THE ENHANCED OPA ANHYDRASE MUTANTS OF BACILLUS STEAROTHERMOPHILUS

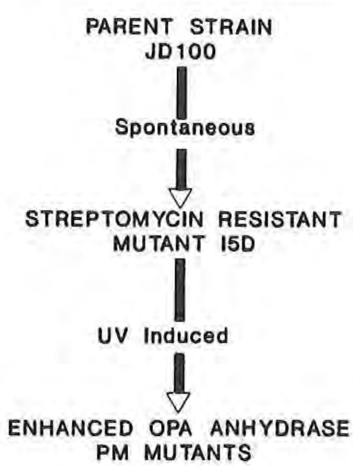

screening for enhanced OPA anhydrase strains is shown and described in Figure 2. Approximately 14,000 colonies were screened in this manner. Initially replicate filter lifts were individually tested with the 4-nitrophenyl methyl(phenyl)phosphinate, 4-nitrophenyl ethyl(phenyl)phosphinate and 4-nitrophenyl isopropyl(phenyl)phosphinate. Use of 4-nitrophenyl methyl(phenyl)phosphinate was discontinued in the plate screening because of the very rapid hydrolysis (color development time) rate at room temperature, which would make hyperproducers and nonhyperproducers indistinguishable. The bioassay overlays of 4-nitrophenyl isopropyl(phenyl)phosphinate had to be incubated at 37°C to 45°C in order to be developed but the development was poor in most cases. The 4-nitrophenyl ester of ethyl(phenyl)phosphinate was most suitable for the plate screening and its overlays generally developed within a few minutes. The substrate enzyme hydrolysis/color development controls were replicate bacteria-charged disk lifts of the experimental ones, which were denatured by heat sterilization temperatures. The selection process was strictly qualitative in nature and color development was compared within and among the combination development overlays. Three main phenotypes were selected for further testing: those that developed a strong yellow color rapidly, those that showed strong color development after a period of time, and those which showed no color development. Initially colonies that exhibited good agreement in color development on the different esters of the phosphinates were selected for further testing but this was not a prerequisite to selection for additional screening.

The primary plate screening was followed by the secondary plate screening, which involved the same plate bioassay except that eight putative mutants were grown on a plate with I5D control. Using the same qualitative process we selected 75 putative hyperproducing OPA anhydrase mutants for submerged culture testing for OPA anhydrase synthesis. The primary plate screening was discontinued after these putative mutants were obtained. A few strains found to lack activity were spurious and no negative strains were found.

The putative mutants were then tested for enhanced synthesis by growth in shaken culture in tubes containing 7 mL of medium at 55°C. After 18 to 24 hours and 44 to 48 hours the cultures were harvested for enzyme synthesis and for dry weights measurements. The amount of OPA anhydrase synthesized was computed against the dry weight of the sample. Twelve strains which showed a 25% or higher enzyme synthesis than I5D were again tested in culture tubes but samples were measured after 7 and 48 hours. In the final testing in submerged culture 8 enhanced mutants were tested for synthesis after 12, 18 and 36 hours. Figure 3 shows the putative mutants with enhanced synthesis 50% or higher than that of the control strains (JD100 and I5D). The other 4 mutants included in this testing showed enhanced activities greater than 25% but less than 50% over the controls (data not shown).

The production of OPA anhydrase synthesis by the parental strain I5D

FIGURE 2

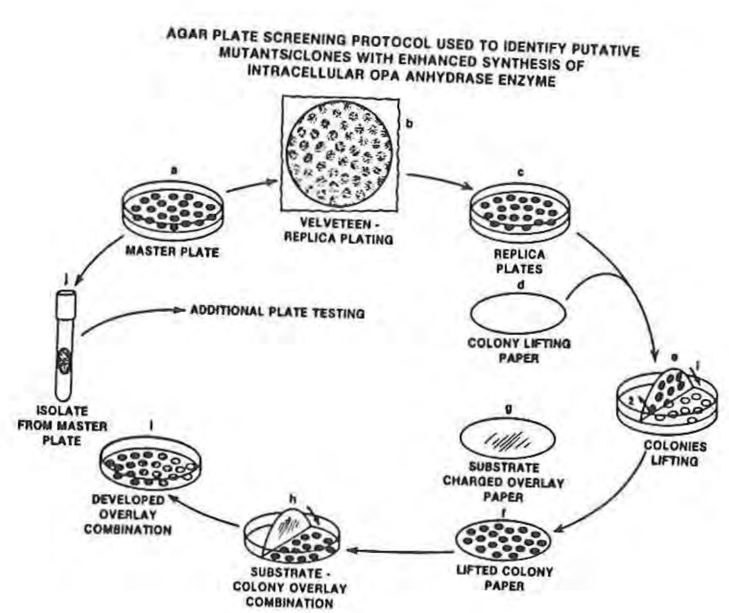

Explanation of Figure 2. a) About 100 viable, mutated bacteria are spread on a master plate and incubated until mature; b) 2 - 5 agar medium plates are inoculated with surface colonies from the master plate using short nap velveteen; and master plate is reincubated until colonies imaged and then stored at refrigerator temperatures; c) the replica plates are incubated for growth; d) heat-sterilized filter paper disks are cut to loosely fit into the lower plate; e) when mature, the colonies on the agar surface of the replicate are overlaid (1) with the prepared lift paper to which we apply gentle pressure to insure good contact between paper and colonies; after the disk is wetted from plate moisture it is carefully removed by lifting (2) and f) placed in a sterile petri plate and rapidly frozen to at least -20°C; g) sized paper disks are charged with substrate by solution impregnation and allowed to dry; h) the frozen test colony disk is placed in a petri plate, colonies face up, and moistened with a fine mist of buffer until saturated and then overlaid with a substrate-impregnated disk, moistened again and the disk-sandwiched colonies incubated for catalysis and color development at room temperature; i) during incubation the plates are observed periodically and noted for color development; j) bacterial isolates of promising reactions are transferred from the corresponding colonies on the master plate to agar slant and/or another master plate and incubated for growth and continued testing.

FIGURE 3

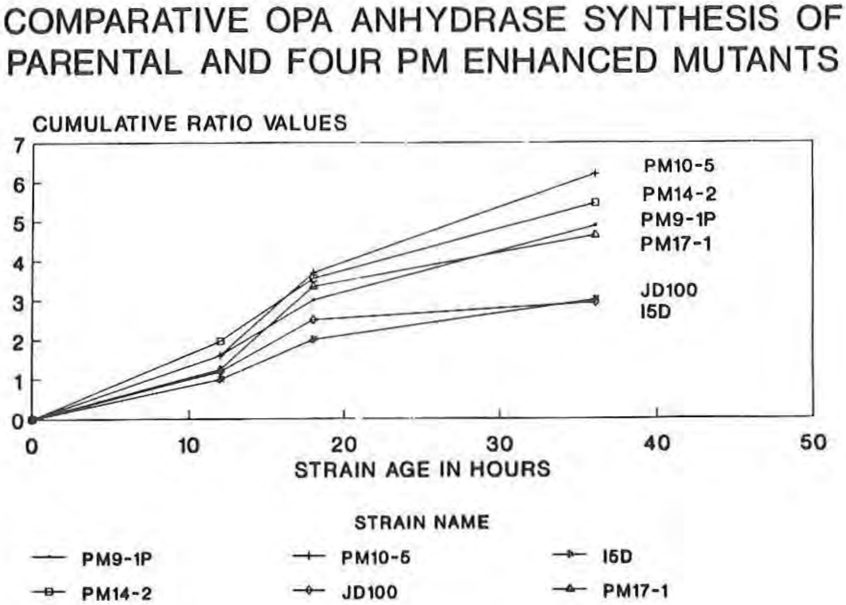

Explanation of Figure 3.
Graph showing the respective cumulative ratio values of 6 strains of B. stearothermophilus where each point represents the ratio of OPA anhydrase activity of tested strain :: OPA anhydrase activity of I5D in OD of nitrophenol formed per min for cultures harvested after shaken incubation at 55°C. Each point represents the average duplicate assay value of cultures grown in triplicate. Parent strain B. stearothermophilus JD100 is also included for comparative purposes. The cumulative ratio values assigned to the control I5D are 1, 2 and 3, corresponding to 12, 18 and 36 hour cultures, respectively. The four other putative enhanced mutants are not shown but they all have a ratio at 36 hours that lies below that of PM17-1 and a value 25% greater than that of the standard strain I5D.

---

was scaled up to 10 liters by growing it in a stirred tank reactor and under constant temperature of 55°C and the pH was controlled at 6.8 with 1N KOH. Figure 4 shows the growth kinetics and OPA anhydrase synthesis during this fermentation. The fermentation was stopped upon the rise in pH to 7. The OPA anhydrase synthesis per gram dry weight follows the same pattern as that based on turbidity in Klett Units, an increase in OPA anhydrase synthesis with an increase in dry weight. The fermentation had an approximate OPA anhydrase productivity of 0.45 units per liter per hour. This fermentation and the postharvest measurement of activity were not optimized and represent preliminary yields and productivities.

FIGURE 4

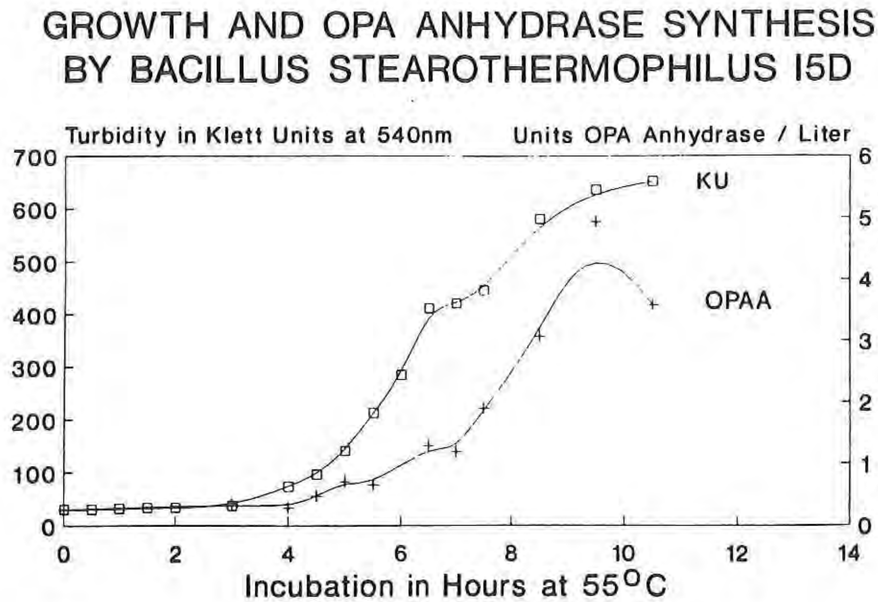

Explanation of Figure 4 - This figure describes the growth of B. stearothermophilus in a 10 liter fermentation and accompanying OPA anhydrase synthesis. Each liter of LB broth was supplemented with 5 g glucose and 250 mg of streptomycin. A 10% inoculum with an age of 12 hours was used to seed the fermentation. The pH was not allowed to drop lower than pH 6.8 by 1N KOH titration. The culture was sparged with air at 5 L/min, agitated at 250 rpm and had a head pressure of 5 psi. Growth temperatures were controlled at 55°C. Washed, once frozen-thawed cells were used in estimating enzyme activity expressed as uM of methyl-O-nitrophenyl(phenyl)phosphinate hydrolyzed/min·L culture^{-1}

Discussion and Conclusions

This study describes an effective but qualitative protocol for screening for mutants/strains with enhanced synthesis of intracellular OPA anhydrase. The protocol's use is not restricted to strains of the genus Bacillus and has been used with other bacteria including strains of Escherichia and Flavobacterium. The protocol should be applicable to other intracellular enzymes/proteins synthesized in cells whose activity or presence can be detected through some color-forming product, for example, intracellular protein. This simple protocol should also be usable with any colony-forming bacteria possessing moist, sticky surface that will adhere to filter paper. The process easily lends itself for use in robotization and computerization for large-scale screening for endogenous enzymes. The protocol also allows the testing of bacterial strains with different growth and substrate requirements on the same paper through the use of replica plating and multiple plate colony lifting.

Several forms of evidence indicate that the gene for this OPA anhydrase in B. stearothermophilus I5D has a chromosomal locus and not an extrachromosomal one. Preliminary but not exhaustive plasmid screening of its parental strain JD100 did not provide positive results for the presence of plasmids (unpublished results). Other evidence comes from the unsuccessful attempts to induce ampicillin resistance in this thermophile although spontaneous and UV-induced streptomycin resistance is obtained with relative ease. Streptomycin resistance in Bacillus can have a chromosomal origin.[9] It has been reported that induced streptomycin resistance in B. stearothermophilus clears the species of plasmids. The gene for a similar OPA anhydrase from unidentified bacterial halophilic strains was also reported to be chromosomal because of the failure to find any plasmids.[10]

Although this OPA anhydrase is unique in its properties, other similar OPA anhydrases are quite common among living things but their function and exact location in the cell remain unverified. No OPA anhydrase negative mutants were found, a fact that suggests that this OPA anhydrase plays an essential role in B. stearothermophilus. Its synthesis in B. stearothermophilus is associated with rapidly growing cultures (see Figure 4) and suggests a role in DNA replication or in protein synthesis. What further complicates the picture is that I5D is a spore former, and no attempt has yet been made to associate enzyme synthesis with sporulation.

Since the number of submerged culture samples that required testing was so large, the bacterial cells were ruptured by simple freezing to $^{-}30°C$ and thawing instead of using sound irradiation. The number of freeze and thaw cycles used in each study was either 6 or 1. Some studies show a decay of activity with repeated cycles of freezing and thawing. Even after mutant development, enzyme synthesis optimization and sound irradiation cell rupture pretreatment, the amount of OPA anhydrase synthesis is small as compared to other enzyme yields from other industrial microbes[11]. In order to continue to reduce the cost of producing this unique and militarily important enzyme it must be available in larger amounts and be made more easily recoverable than at present. To accomplish this goal the gene from strain I5D is also being cloned and inserted into multicopy expression vectors for use in extracellular enzyme production.

REFERENCES

1. Chettur, G., J. J. DeFrank, B. J. Gallo, F. C. G. Hoskin, S. Mainer, F. M. Robbins, K. E. Steinmann, and J. E. Walker. "Soman Hydrolyzing and Detoxifying Properties of an Enzyme from a Thermophilic Bacterium". Fundam. Appl. Toxicol. 11, pp. 373-380, 1988.

2. Hoskin, F. C. G., G. Chettur, S. Mainer, K. E. Steinmann, J. J. DeFrank, B. J. Gallo, F. M. Robbins, and J. E. Walker. "Soman Hydrolysis and Detoxication Properties by a Thermophilic Bacterial Enzyme" in Enzymes Hydrolyzing Organophosphorus Compounds, Chapter 5, Ellis Horwood Publishing Ltd., Chichester, Eng., 1989.

3. Cook, A.M. and Brown, M. R. W. "The Relationship Between Heat Activation and Colony Formation for the Spores of Bacillus stearothermophilus". J. Pharm. Pharmacol. 16, 725-732, 1964.

4. Lennox, E. S., "Transduction of Linked Genetic Characters of the Host by Bacteriophage P1". Virology 1, 190, 1955.

5. Hoskin, F. C. G.,and Roush, A. H. "Hydrolysis of Nerve Gas by Squid Type Diisopropylphosphorofluoridate Hydrolyzing Enzyme on Agarose Resin. Science 215, 1255-1257, 1982.

6. Lieske, C. N., J. H. Clark, H. G. Meyer, M. A. Lawson, J. R. Lowe, P. Blumbergs, and M. A. Priest, "Inhibition of Two Acetylcholinesterases by the 4-Nitrophenyl Esters of Methyl-, Ethyl-, and Isopropyl(phenyl) phosphinic Acid. Pest. Biochem. Physiol. 17, 142-148, 1982.

7. Martin, C. C., J. Golubow, and A. E. Axelrod. "A Rapid and Sensitive Spectrophotometric Method for the Assay of Chymotrypsin". J. Biol. Chem. 234, 294-298, 1959.

8. Imanaka, T., M. Fujii, I. Amamori, I., and S. Aiba, "Transformation of Bacillus stearothermophilus with plasmid and characterization of shuttle vector plasmids Between Bacillus stearothermophilus and Bacillus subtilis". J. Bacteriol. 149, 824-830, 1982.

9. Staal, S. P. and J. A. Hoch, "Conditional Dihydrostreptomycin Resistance in Bacillus subtilis", J. Bacteriol. 110, 202-207, 1972.

10. Cheng, T. C., and J. J. DeFrank, "Screening for Plasmids in Halophiles". Technical Paper CRDEC-TR-094, 13 pp., US Army Chemical Research, Development and Engineering Center, Aberdeen Proving Ground, MD. 1989.

11. U.S. Patent No. 4,472,504, September 18, 1984. Benedict J. Gallo Inventor. "Cellulase-Producing Microorganism".

Acknowledgments

We thank Dr. David Alabran and Mr. John Walker for their synthesis and purification of 4-nitrophenyl methyl(phenyl)phosphinate used in this study and Mr. E. Powers for assistance in taxonomic identification. We also thank Dr. E. Reese, Dr. N. McCormick, and Dr. D. Ball for their editorial comments.

TITLE: Stereospecificity of Microbial Enzymes for G-Agent Detoxification
*Diane M. Steeves, Ms., John E. Walker, Mr., James J. Connolly, SP4, Francis C.G. Hoskin, Dr., and Benedict J. Gallo, Dr.

ABSTRACT: Catalytic degradation by enzymes capable of hydrolyzing organophosphate (OP) agents could be the most efficient and advantageous method available for the destruction of OP agents. The reactions involved take place at neutral pH and are specific for certain labile ligands at phosphorous. Fundamental questions pertaining to the molecular aspects of catalysis by these enzymes, such as characterization of the active site and interactions between enzyme and substrate, have not been addressed. We have examined OP hydrolyzing enzymes from strains of E. coli, Flavobacterium, Tetrahymena, and Bacillus stearothermophilus for their ability to hydrolyze a series of OP surrogates (4-Nitrophenyl esters of methyl-, ethyl-, and isopropyl (phenyl) phosphinic acid). Their ability to degrade the toxic and nontoxic isomers of soman (GD) was also studied. Initial rates as well as pseudo first order rate constants were determined for the hydrolysis reactions. Also included was the OP hydrolyzing enzyme from squid (EC 3.1.8.1). A comparison was made between the phosphinate hydrolysis and the ability of these enzymes to detoxify soman. Results are discussed with regard to cofactor requirements and structure of the active sites of the agent-hydrolyzing enzymes.

*BIOGRAPHY OF PRESENTER: Diane M. Steeves

PRESENT ASSIGNMENT: Research Chemist, Special Projects Branch, Physical Sciences Division, Soldier Science Directorate, U.S. Army Natick Research, Development and Engineering Center.

PAST EXPERIENCE: N/A

DEGREES HELD: B.A., Regis College, 1988.

Stereospecificity of Microbial Enzymes for G-agent Detoxification

Diane M. Steeves, Ms., John E. Walker, Mr., James J. Connolly, SP4, Francis C.G. Hoskin, Dr., and Benedict J. Gallo, Dr.

INTRODUCTION

Enzymes from microbacteria capable of hydrolyzing a wide variety of organophosphates have been found both in procaryotic and eukaryotic organisms (1-7). In the past, these enzymes were called DFPases, somanases, paraoxonases or parathion hydrolases, based on their substrate specificity. The new name for these enzymes is organophosphorous acid (OPA) anhydrases, which was selected during the First DFPase Workshop (Marine Biological Laboratory, Woods Hole, Massachusetts, June 1987) and relates to their basic activity. Fundamental questions pertaining to the molecular aspects of catalysis by these enzymes, such as the nature and sequence of chemical and perhaps other steps involved in organophosphate agent (OP) hydrolysis, character of the active site, and interactions between enzyme and substrate have been partially addressed by Dr. James Wild of Texas A and M (8-12), whose group has cloned the gene (Opd) which codes for an OPA Anhydrase that hydrolyzed diisopropyl fluorophosphate (DFP), isopropyl methylphosphonofluoridate (sarin) and 1,2,2-trimethylpropylmethylphosphonofluoridate (soman). A mechanism for a general base catalysis having a single in-line displacement at the phosphorous center with an activated water molecule was proposed. The enzyme has a molecular weight of 39,000 daltons, an isoelectric point of 8.3 and a requirement of zinc for reactivity. It is not known if the function of zinc is structural or catalytic. Mipafox was shown to be a competitive inhibitor.

An OPA anhydrase from the thermophile Bacillus stearothermophilus (JD-100) has been found to possess a different substrate specificity towards OP hydrolysis (5). The enzyme does not hydrolyze DFP but readily breaks down soman and sarin. The enzyme was manganous (Mn) ion requiring, as are most of the microbial OPA anhydrases, but was not inhibited by mipafox. The enzyme can be covalently attached to cotton fabric with retention of its catalytic activity to hydrolyze soman (13). These properties have placed this enzyme in a separate category (Table 1) in the classification of OPA anhydrases (14).

In this paper we will report on (i) the specificity of the OPA anhydrase from Bacillus stearothermophilus in hydrolyzing a series of OP agent surrogates [p-nitro-phenyl alkyl(phenyl)phosphinates]; (ii) the effect of cations alone and in combination on the enzyme's reactivity to the OP surrogate and (iii) the ability of the enzyme to detoxify soman. A comparison will be made with other microbial OPA anhydrases (E.coli, Tetrahymena thermophilia, Flavobacterium B4079) and also with the OPA anhydrase from squid hepatopancreas.

TABLE 1

CHARACTERISTICS OF OPA ANHYDRASES

SQUID TYPE

CEPHALOPOD NERVE, HEPATOPANCREAS, AND SALIVA ONLY
MOLECULAR WEIGHT, 30,000
HYDROLYZES DFP 4-5 TIMES FASTER THAN SOMAN AT 3 mM
Mn^{2+} INDIFFERENT OR SLIGHTLY INHIBITED
STRONGLY INHIBITED BY 10^{-4} M EDTA, EGTA; INDIFFERENT TO 1, 10-PHENANTHROLINE AND 8-HYDROXYQUINOLINE-5-SULFONATE
STABEL IN 60-65% SATURATED AMMONIUM SULFATE
MIPAFOX INDIFFERENT
HYDROLYZES ALL ISOMERS OF SOMAN, SOME STEREOSELECTIVITY

OT TYPE

ONE SUBSPECIES OF *BACILLUS STEAROTHERMOPHILUS*
MOLECULAR WEIGHT, 82-84,000
HYDROLYZES SOMAN; DOES *NOT* HYDROLYZE DFP *AT ALL*
Mn^{2+} STIMULATED 80-FOLD AT 10^{3} M
STRONGLY INHIBITED BY EDTA, EGTA, 1, 10-PHENANTHROLINE, AND 8-HYDROXYQUINOLINE-5-SULFONATE
STABLE IN AMMONIUM SULFATE
MIPAFOX INDIFFERENT
HYDROLYZES ALL ISOMERS OF SOMAN

MAZUR TYPE

UBIQUITOUS; EVEN IN OTHER CEPHALOPOD TISSUES
MOLECULAR WEIGHTS VARY, 45-90,000, PROBABLY SPECIES SPECIFIC
HYDROLYZES SOMAN 5-50 TIMES FASTER THAN DFP AT 3 mM
Mn^{2+} STIMULATED 2- TO 20-FOLD
AMMONIUM SULFATE LABILE
MIPAFOX INHIBITED

MATERIALS AND METHODS

Culture and Growth Conditions of the Test Microorganisms.

1. Bacillus stearothermophilus strain I5B: The original strain (JD-100) was supplied by Dr. Joseph DeFrank, Chemical Research, Development and Engineering Center, Edgewood, Maryland. It was grown as a submerged culture in multiple 2800 mL Fernbach flasks containing 500 mL of LB broth (15) with streptomycin. They were started with 50 mL of 24-hour-old seed cultures, shaken at 75 to 80 strokes per minute at 55°C and usually harvested after 24 hours.

2. Flavobacterium SP. strain B4079: The strain was grown as a submerged culture using Cook's medium (16). The cultures were shaken in Fernbach flasks at 29°C.

3. Tetrahymena thermophilia, strain "brynat": The culture was grown in a 14 liter stirred tank reactor (fermentor) with a working volume of 10 liters using Modified Cook's Medium (16) with chelated iron and streptomycin, at 29°C.

4. E.coli, strain ATCC25922: The culture was grown in a stirred fermentor using LB Basic Broth (15) at 37°C.

Extraction of OPA Anhydrase from Cultured Cells.

The harvested cells were concentrated by centrifugation and washed two times with cold sonicate buffer (400 mM potassium chloride (KCL), 50 mM sodium chloride (NaCL) and 5 mM in 1,3-bis(tris(hydroxymethyl)-methylamino) propane (Bis-Tris-Propane), pH7.2. A 20% (w/v suspension of packed cells in the sonicate buffer was sonicated with a 19 mm probe, 80% output, 50% duty, in 10 one-minute periods alternating with one-minute rest periods. The temperature was held at or below 10°C with an ice bath. The sonicate was centrifuged at 90,000 X g and the clarified supernatant used as the source material for further enzyme purification.

Assays of OPA Anhydrase from Cultured Cells.

1. Synthesis of substrates: 4-nitrophenyl methyl(phenyl)phosphinate (PNPMPP) was synthesized by the Method of Horton (17). 4-nitrophenyl ethyl(phenyl)phosphinate (PNPEPP) was obtained commercially (Ash Stevens, Inc.) and 4-nitrophenyl isopropyl(phenyl)phosphinate (PNPiPPP) was a gift from E.Durst of CRDEC. Soman was synthesized essentially according to the Method of Larsson (18). Diisopropylfluorophosphate (DFP) was obtained commercially (Sigma).

2. Assay procedures: In the typical assay, 50 microliters (uL) of a solution containing the OPA anhydrase was added to 2.5 mL of sonicate buffer. The hydrolysis reaction was initiated by the addition of 50 uL of a 3 x 10^{-3}M solution of the 4-nitrophenyl phosphinate substrate (PNPMPP, PNPEPP or PNPiPP) in acetonitrile. The rate of hydrolysis of the substrate was monitored by the release of p-nitrophenyl anion as measured by absorbance at 400nm. Quantitation was made by reference to a calibration curve of known concentrations of p-nitrophenol released per minute. The hydrolysis of the fluorophosphonate substrated Soman and DFP were monitored with a fluoride-sensitive electrode after the method of Hoskin (19). Determination of the loss of acetylcholinesterase (AChE) inhibitory activity was performed as described by Hoskin (20).

Pseudo first order rate constants (k') were obtained by fitting the hydrolysis rate data to the equation: $A_t = A+(A_o-A)E^{-k't}$ where A_o, A_t and A are the p-nitrophenolate anion concentrations at times zero, t, and infinity. Best fit values of k' and A were obtained using a computerized least squares method (KORE).

<u>Purification of OPA Anhydrase from Cultured Cells.</u>

The supernatant from the high speed centrifugation of the cultured cells was concentrated by ultrafiltration over a PM-10 membrane (Amicon Corp). The concentrated supernatant was applied to a G150 sephadex (Pharmacia) column 2.5 x 90 cm and eluted with the sonicate buffer. The protein content of the effluent was monitored by absorbance at 280nm and the OPA anhydrase was measured by the PNPMPP assay method. The chromatographic fractions exhibiting OPA anhydrase activity were pooled and dialyzed against Tris buffer, pH7.5. The fraction was applied to a DEAE A-50 (Pharmacia) column, 1.5 x 30 cm. The OPA anhydrase was eluted after the breakthrough peak by means of a linear gradient with a limit buffer of 20 mM Tris, 0.5 MNaCL, pH7.5. In the final stage of purification, the DEAE gradient fraction containing OPA anhydrase activity after dialysis against 20 mM Tris, pH7.5 was applied to a 1 x 50 cm column of Phenyl-CL Sepharose 4B (Pharmacia) previously equilibrated in 1.7 M ammonium sulfate, $(NH_4)_2SO_4$ in 20 mM Tris pH7.5. The column was developed with a linear gradient of 400 mL using a starting buffer of 1.7M $(NH_4)_2SO_4$ in 20 mM Tris pH7.5 and a limit buffer of 20 mM Tris, pH7.5. The purified enzymes were assayed for activity against the p-nitrophenylalkylphenylphosphinates as well as against soman and DFP. Protein concentration was determined by the Coomassie dye binding assay of Bradford (21). The molecular weights of the purified OPA anhydrases were determined by SDS polyacrylamide gel electrophoresis using the discontinuous buffer method of Laemmli (22). The OPA anhydrases were also run under <u>non</u>denaturing conditions using linear gradient precast polyacrylamide gels (Jule Inc.).

<u>Addition of Metal ions and Metal ion Chelators to OPA anhydrase.</u>

Metal ions and chelators were made up in 25mM HEPES buffer pH7.2 at 100mM concentrations. Suitable additions were made to the enzyme solutions to give a range of concentrations from 1mM to 0.1mM. The reaction proceeded at room temperature for 30 minutes and changes in OPA anhydrase activity were monitored by the PNPMPP assay method.

RESULTS

The separation of the OPA anhydrase from <u>Bacillus</u> <u>stearothermophilus</u> I5B was performed by gel filtration with G150 (Figure 1) followed by hydrophobic chromatography using phenyl-sepharose CL-4B (Figure 2).

FIGURE 1
CHROMATOGRAPHIC SEPARATION OF I5B ON G-150

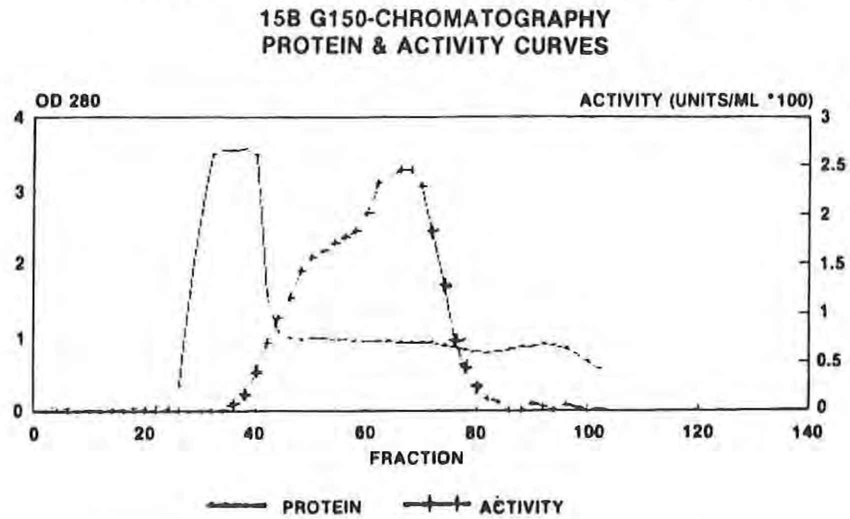

FIGURE 2
CHROMATOGRAPHIC SEPARATION OF I5B ON PHENYL-SEPHAROSE CL-4B

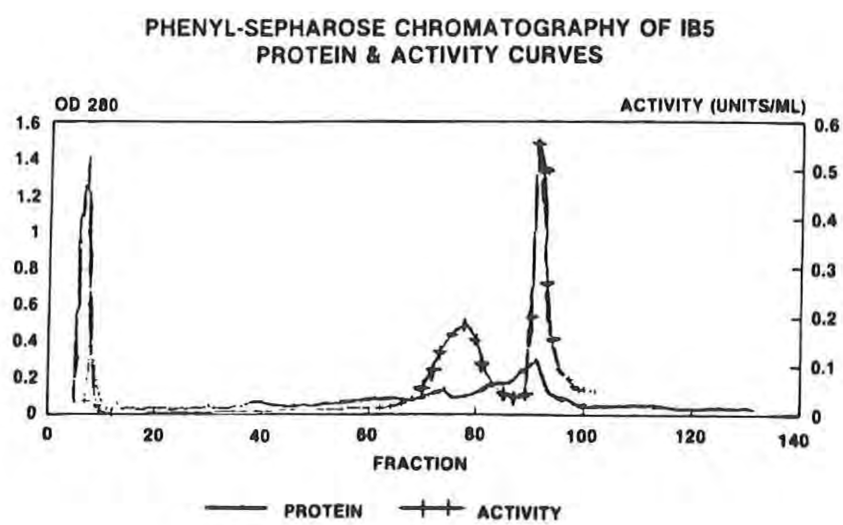

This separation methodology was followed for the enzyme isolation from the other microbial organisms. All the OPA anhydrases appeared to have a high degree of hydrophobicity since their separation from the phenyl-sepharose column was at the end of the elution gradient in every case. The molecular weights of the OPA anhydrases are shown in Table 2.

TABLE 2
MOLECULAR WEIGHTS OF THE OPA ANHYDRASES BY SDS ELECTROPHORESIS

MOLECULAR WEIGHTS OF MICROBIAL OPA ANHYDRASES

SOURCE OF OPA ANHYDRASE		MOLECULAR WEIGHT (DALTONS)
Bacillus stearothermophilus		62,000 40,000 36,000
Flavobacterium SP 4079		62,000 68,000
Tetrahymena Thermophilia		45,000
E. coli ATCC 25922		
	F-1	53,000
	F-2	38,000

A proposed model for the enzymatic hydrolysis of p-nitrophenyl methyl (phenyl)phosphinate by microbial OPA anhydrases is shown in Figure 3.

FIGURE 3
MECHANISM FOR HYDROLYSIS OF PNPMPP BY MICROBIAL OPA ANHYDRASE

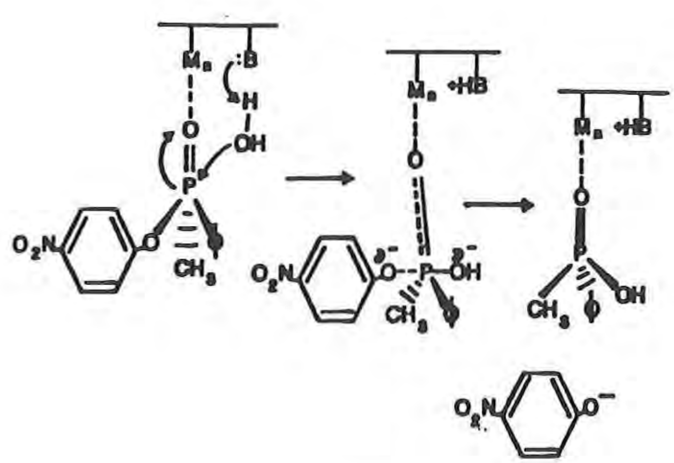

The model, which is based on a similar model for phosphotriesterase (II), postulates a single base with a Pk_a of 6.1 in the enzyme's active site that abstracts a proton from water. The activated water molecule attacks directly at the phosphorous center with the overall stereochemical outcome of inversion of configuration. Table 3 shows the organophosphorous AChE inhibitors, which were used as substrates in the study.

TABLE 3

ORGANOPHOSPHOROUS AChE INHIBITORS

4-NITROPHENYL METHYL (PHENYL) PHOSPHINATE   4-NITROPHENYL ETHYL (PHENYL) PHOSPHINATE

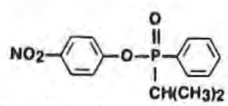

4-NITROPHENYL IPROPYL (PHENYL) PHOSPHINATE

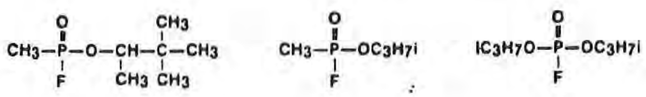

SOMAN (GD)   SARIN (GB)   DFP

The initial and pseudo-first order rate constants for the enzymatic hydrolysis of p-nitrophenyl alkyl(phenyl)phosphinates are given in Table 4.

TABLE 4

INITIAL AND PSEUDO-FIRST ORDER RATE CONSTANTS FOR THE HYDROLYSIS OF P-NITROPHENYL AKLYL(PHENYL) PHOSPHINATES

ENZYME SOURCE		PNPMPP	PNPEPP	PNPIPP
BACILLUS STEAROTHERMOPHILUS				
JD-100				
	k'	3.77E-01	4.50E-02	N.R
	K'	2.40E-03	2.80E-04	N.R
JD-200				
	k'	3.32E-01	3.00E-02	N.R
	K'	2.10E-03	2.20E-04	N.R
JD-300				
	k'	1.81E-01	N.R	N.R
	K'	1.30E-03	1.50E-04	N.R
15B				
	F-1 k'	5.40E-02	1.20E-02	N.R
	K'	1.70E-03	2.10E-04	N.R
	F-2 k'	1.51E-01	1.80E-02	N.R
	K'	4.00E-03	8.10E-04	N.R
B4079 FLAVOBACTERIUM				
	F-1 k'	1.57E-01	9.00E-02	6.00E-03
	K'	4.60E-03	3.80E-03	1.90E-04
	F-2 k'	5.40E-02	2.40E-02	6.00E-03
	K	1.90E-03	1.28E-03	1.50E-04
ATCC25922 E. COLI				
	F-1 k'	2.70E-02	1.50E-02	3.00E-03
	K'	1.60E-03	9.50*E-04	1.20E-04
	F-2 k'	1.80E-02	3.00E-03	N.R
	K'	1.00E-03	4.30E-04	5.00E-05
SQUID OPA ANHYDRASE				
	k'	4.30E-02	5.00E-03	3.00E-03
	K'	3.00E-03	9.10E-04	3.80E-05

The effect of metal cations on the reactivity of microbial OPA anhydrases is shown in Table 5.

TABLE 5

RECOVERY OF OPA ANHYDRASE ACTIVITY AFTER CHELATION INHIBITION

ENZYME SOURCE		Mn2+	Mg2+	Ca2+	Mg2+/ Mn2+	Ca2+/ Mn2+
BACILLUS STEAROTHERMOPHILUS						
JD-100		+	-	-	+/-	+/-
JD-200		+	-	-	+/-	+/-
JD-300		+	-	-	+/-	+/-
15B						
	F-1	+/-	-	-	+/-	+/-
	F-2	+/-	-	-	+/-	+/-
B4079 FLAVOBACTERIUM						
	F-1	-	-	-	-	-
	F-2	+	-	-	+	+
E. COLI						
	F-1	+	-	-	+	+
	F-2	+	-	-	+	+
SQUID						
		+	-	-	+	+

The ability of the microbial OPA anhydrases to hydrolyze and detoxify soman is shown in Table 6.

TABLE 6
RELATIVE RATES OF HYDROLYSIS OF SOMAN BY MICROBIAL OPA ANHYDRASES

CHARACTERIZATION OF ENZYME SAMPLES WITH RESPECT TO THEIR ACTIVITY (HYDROLYSIS AND DETOXIFICATION) AGAINST SOMAN

SAMPLES			PERCENT ACTIVITY HYDROLYSIS	PERCENT ACTIVITY DETOXIFICATION
Bacillus stearothermophilus		JD-100	53	49
		JD-200	40	13
		15B	53	45
Tetrahymena			50	39
Flavobacterium		B4079	47	7
E. coli	FI		50	50
E. coli	FII		55	20

DISCUSSION

All of the OPA anhydrases from the microbacteria eluted from the hydrophobic chromatographic separation step at the end of the elution gradient similarly to the I5B separation shown in Figure 2. This fact indicates that these proteins tended to possess a high degree of hydrophobicity on their exterior structure. Since sonication was needed to release them from the microorganisms, they are probably compartmentalized in the bacterial cell wall. The OPA anhydrases from Bacillus stearothermophilus showed discrimination between the methyl and ethyl homologues of the phenyl phosphinates but the OPA anhydrases from the other strains hydrolyzed the methyl or ethyl derivatives at essentially the same rate as seen in Table 4. All of the enzymes were manganous ion requiring, as is shown in Table 5. Magnesium or calcium ions could not reactivate the activity of the enzyme after EDTA inhibition. There was no evidence that calcium or magnesium bound to the manganous ion binding site in the OPA anhydrases. It was found that the level of EDTA concentration to inhibit the activity of E.coli OPA anhydrase was an order of magnitude higher than was necessary to inhibit the other enzymes, which may indicate cofactor status for Mn^{+2} in the active site of the E.coli enzyme. Table 6 shows that of the OPA anhydrases tested for their ability to both hydrolyze and detoxify soman, JD-200, B4079 and f_{II} of E.coli preferentially hydrolyzed the nontoxic soman isomers. This differential activity was not predicted from initial and pseudo first order rate constants shown in Table 4. The 4-nitrophenyl alkyl(phenyl)phosphinates were racemic mixtures and this probably prevented a discrimination in their reactivity to the microbial OPA anhydrases.

CONCLUSIONS

1. OPA anhydrases from microbacteria possess a high order of hydrophobicity.

2. OPA anhydrase from Bacillus stearothermophilus was the most selective in the hydrolysis of the soman surrogates.

3. The OPA anhydrase from E. coli may require a specific binding site for manganous ion for reactivity.

REFERENCES

1. Mazur, A. An Enzyme in Aminal Tissue Capable of Hydrolyzing the Phosphorous-fluorine Bond of Alkyl Fluorophosphates. J. Biol. Chem. 164:271 (1946).

2. Mounter, L.A., Baxter, R.F. and Chautin, A. Dialkylfluorophosphatases of Microorganisms. J. Biol. Chem. 215:699 (1955).

3. Zech, R. and Wigand, K.D. Organophosphate-detoxifying Enzymes in E. coli, Gel Filtration and Isoelectric Focusing of DFPase, Paroxonase and Unspecified Phosphohydrolases. Experimentia 31:157 (1975).

4. Landis, W.G., Savage R.E. Jr., and Hoskin, F.C.G. An Organofluorophosphate-hydrolyzing Activity in Tetrahymena Thermophilia. J. Protozool. 32:517 (1985).

5. Chettur, G., DeFrank, J.J., Gallo, B.J., Hoskin, F.C.G., Mainer, S., Robbins, F.M., Steinmann, K.E. and Walker, J.E. Soman Hydrolyzing and Detoxifying Properties of an Enzyme From a Thermophillic Bacterium. Fund. Appl. Tox. 11:127 (1988).

REFERENCES (CONT'D)

6. Cheng, F.C., Deas, R.A., DeFrank, J.J. and Elashvili, I. Purification Procedures for OPA Anhydrase-2 From Halophile JD 6.5. 1989 U.S. Army Chemical Research, Development and Engineering Center Scientific Conference on Chemical Defense Research, Aberdeen Proving Ground, Maryland.

7. Dumas, D.P., Wild, J.R. and Raushel, F.M. Diisopropylfluorophosphate Hydrolysis by an Organophosphate Anhydrase From Pseudomonas diminuta. Biotech. and Appl. Biochem. 11:235 (1989).

8. McDaniel, C.S., Harper, L.L. and Wild, J.R. Cloning and Sequencing of a Plasmid-Borne Gene (opd) Encoding a Phosphotriesterase. J. Bact. 170:2306 (1988).

9. Lewis, V.E., Donarski, W.J., Wild, J.R. and Raushel, F.M. Mechanism and Stereochemical Course at Phosphorous of the Reaction Catalyzed by a Bacterial Phosphotriesterase. Bioch. 27:1591 (1988).

10. Donarski, W.J., Dumas, D.P., Heitmeyer, D.P., Lewis, V.E. and Raushel, F.M. Structure-Activity Relationships in the Hydrolysis of Substrates by the Phosphotriesterase From Pseudomonas diminuta ibid. 28:4650 (1989).

11. Dumas, D.P., Caldwell, S.R., Wild, J.R., and Raushel, F.M. Purification and Properties of the Phosphotriesterase from Pseudomonas diminuta J. Biol. Chem. 264:19659 (1989).

12. Dumas, D.P., Durst, H.D., Landis, W.G., Raushel, F.M. and Wild, J.R. Inactivation of Organophosphorous Nerve Agents by the Phosphotriesterase from Pseudomonas diminuta Arch. Biochem. Biophys. 277:155 (1990).

13. Walker, J.E., Gallo, B.J., Starcher, B., Robbins, F.M., and Hoskin, F.C.G. Soman Hydrolyzing and Detoxifying Properties of an Enzyme from a Thermophilic Bacterium. 1988 Army Science Conference, Fort Monroe, Virginia.

14. Hoskin, F.C.G., Kirkish, M.A., and Steinmann, K.E. Two Enzymes for the Detoxification of Organophosphorous Compounds-Sources, Similarities and Significance. Fund. Appl. Tox. 4:S165 (1984).

REFERENCES (CONT'D)

15. Lennox, E.S. Transduction of Linked Genetic Characters of the Host by Bacteriophage P1. Virology 1:190 (1955).

16. Cook, A.M. and Brown, M.R.W. The Relationship Between Heat Activation and Colony Formation for the Spores of Bacillus stearothermophilus. J. Pharm. Pharmacol. 16:725 (1964).

17. Horton, G.L., Lieske, C.N., and Lowe, J.R. Phosphinate Inhibition Studies of Cholinesterases. Pestic. Sci. 9:135 (1978).

18. Larsson, L. Alkaline Hydrolysis of Isopropoxymethyl-phosphoryl fluoride (Sarin) and Some Analogues. Acta. Chem. Scand. 11:1131 (1957).

19. Hoskin, F.C.G. Inhibition of a Soman and Diisopropylphosphorofluoridate (DFP) Hydrolyzing Enzyme by Mipafox. Biochem. Pharmacol 34:2069 (1985).

20. ibid. An Organophosphorous Detoxifying Enzyme Unique to Squid in Squid as Experimental Animals; Gilbert, D.L., Adelman, W.J. Jr., and Arnold, J.M., editors, Plenum, New York, Chap. 21, 1990.

21. Bradford, M. A Rapid Sensitive Method for the Quantitation of Microgram Quantities of Protein Utilizing the Principle of Protein-dye Binding. Anal. BioCh. 72:248 (1976).

22. Laemmli, U.K. Cleavage of Structure l Proteins During the Assembly of the Head of Bacteriophage T4. Nature 227:680 (1970).

TITLE: Molecular Topography of Squid OPA Anhydrase (EC 3.1.8.1)
As Revealed By Spectroscopic Studies
*John E. Walker, Mr., James J. Connolly, SP4, Diane M. Steeves,
Ms., Francis C.G. Hoskin, Dr., and Krishma S. Rajan, Dr.

ABSTRACT: An enzyme (EC 3.1.8.1) isolated from nerve, hepatopancreas and saliva of squid (Loligo pealei) has been shown to hydrolyze the P-F bond of G-agents, resulting in the detoxification of the nerve agent. The molecular weight of the enzyme is 26,000 daltons and amino acid analysis shows that the protein contains 6 tryptophans and 11 cysteine residues. Studies involving the quenching of tryptophan fluorescence revealed that in the native enzyme 2 tryptophans are exposed on the molecular surface and 4 tryptophans are buried. Titration with 5,5'dithio bis-(2-nitro benzoic acid), DTNB, showed one available -SH and 5 S-S bridges. Ca^{+2} is required for enzymatic activity, but the enzyme's resistance to denaturation (6M urea) and disulfide reduction (dithiothreitol) indicates that maintenance of secondary and tertiary protein structure is not needed for active site functionality. A model is postulated in which Ca^{+2} forms an intramolecular bridge in the region near the enzyme's active site and is unaffected by changes in secondary or tertiary protein structure.

* BIOGRAPHY OF PRESENTER: John E. Walker

PRESENT ASSIGNMENT: Research Chemist, Special Projects Branch, Physical Sciences Division, Soldier Science Directorate, U.S. Army Natick Research, Development and Engineering Center.

PAST EXPERIENCE: Food Sciences and Physical Sciences Laboratory, Natick.

DEGREES HELD: B.S., M.S., and M.A.

Molecular Topography of Squid OPA Anhydrase (EC 3.1.8.1) As Revealed By Spectroscopic Studies

John E. Walker, Mr., James J. Connolly, SP4, Diane M. Steeves Ms., Francis, C.G. Hoskin, Dr., and Krishma S. Rajan, Dr.

INTRODUCTION

Squid OPA Anhydrase EC 3.1.8.1 (formerly Squid DFPase) is a single chain protein of molecular weight 26,000 daltons (1) and an isoelectric point of 5.5 (2). In a series of papers from 1965 to 1983, F.C.G. Hoskin and coworkers established that the enzyme is found in all tissues of cephalopods and not in members of other phyla, or even in other classes of this same phylum (3,4,5,6). The enzyme was found to hydrolyze the nerve agents Soman (1,2,2-trimethyl propylmethylphosphonofluoridate) and Sarin (isopropyl methylphosphonofluoridate) and could be covalently attached to agarose without loss of its catalytic activity (7). Military applications of the squid enzyme in a decon formulation to detoxify G-agents have been investigated by K.S. Rajan and coworkers at the Illinois Institute of Technology Research Institute (IITRI). They have shown that a phosphate buffered solution of the enzyme (100 units in 100 MLs) could decontaminate 200-250 mg Soman/square inch material surface. The enzyme retained > 96% of its initial activity after each decontamination experiment, indicating its recovery and reuse potential (8). The stability characteristics of the enzyme indicate plausible field deployment (9).

In this paper we report on studies of the secondary and tertiary structure of squid OPA anhydrase relating to the enzyme's stability.

MATERIALS AND METHODS

Isolation of Squid OPA Anhydrase from the Hepatopancreas of Squid.

The procedure followed was that of Garden et al. (2) as modified by Rajan (10). The molecular weight of the purified OPA anhydrase was determined by SDS polyacrylamide gel electrophoresis using the discontinuous buffer method of Laemelli (12).

Assay for Enzyme Activity.

Squid OPA anhydrase activity was assayed using diisopropyl fluorophosphate (DFP) as the substrate (1). The release of fluoride ion was monitored with a fluoride sensitive electrode(11) and monitored with an Orion Research Microprocessor ion analyzer 901 (Orion Research).

Circular Dichroism.

Circular dichroism spectra of the purified OPA anhydrase were recorded in the wavelength range of 240 to 190 nm on an AVIV 61DS solid-state instrument (AVIV Associates, Lakewood, NJ). The instrument is equipped with a 50 kH_z photoelastic modulator and an end-on photomultiplier. The instrument is interfaced with an AT&T computer, which is used for all mathematical calculations. Secondary structure determinations were made using the computer method of Yang (13), which was supplied with the AVIV 61DS.

Fluorescence Quenching.

Fluorescence measurements were performed using an SLM 4800S spectrofluorometer (SLM Instruments). Quenching experiments were carried out according to the method of Holmes and Robbins (14). Solutions were excited at 305 nm and the emission spectra recorded from 320 nm to 450 nm. The quenchers were reagent grade and were used without further purification; acrylamide (Eastman), N-methyl nicotinamide chloride (Sigma), and potassium iodide (Eastman). The calculations were performed by the method of Lehrer (15) and are given in Table 1.

TABLE 1

FLUORESCENCE QUENCHING OF TRYPTOPHENYL RESIDUES IN SQUID OPA ANHYDRASE

- **Quenchers: N'-Methylnicotinamide Chloride, Acrylamide, and Potassium Iodide**
- **Calculations:**

$$F_0/F = 1 + K_Q\,[Q]$$

with $K_Q = K^* \tau$

$$F_0/\Delta F = 1/[Q]f aKQ = 1/f a$$

where F_0 and F are the fluorescent intensities in the absence and presence of quencher. K_Q is the Stern-Volmer quenching constant, K* is the biomolecular rate constant for quenching, τ is the average fluorescent life time in the absence of quencher. [Q] is the concentration of the quencher, fa is the fractional accessibility of tryptophyl residues, and K_Q is their effective quenching constant.

Interfilter effects were corrected by the method of Lakowicz (16).

Amino Acid Analysis.

Amino acid analyses were performed by the Pico-Tag method (Waters) (17).

Determination of Free SH Groups.

The method of Potter et al. (18) was used.

Addition of Metal Ions and Metal Ion Chelators to Squid OPA Anhydrase.

Metal ions and chelators were made up in 25 mM HEPES buffer pH 7.2 at 100 mM concentrations. Suitable additions were made to the enzyme solutions to give a range of concentrations from 1 mM to 0.1 mM. The reaction proceeded at room temperature for 30 minutes and changes in OPA anhydrase were monitored using the DFP assay method.

RESULTS

The amino acid analysis of squid OPA anhydrase is given in Table 2.

TABLE 2

AMINO ACID COMPOSITIONAL ANALYSIS OF SQUID HEPATOPANCREASE OPAase

amino acid	average pmol	mole percent	percent SD	residue number
cys acid	169.51	5.39	.53	10.8 (11.0)
asx	409.78	13.03	.46	26.0
thru	257.06	8.12	.73	16.0
ser	118.82	3.75	.53	7.0
glx	353.87	10.93	1.07	21.8 (22.0)
pro	121.4	3.84	.32	7.6 (8.0)
gly	373.27	11.65	.95	23.2 (23.0)
ala	224.63	6.74	1.12	13.4 (13.0)
val	230.25	7.38	.35	14.6 (15.0)
met	3.20	0.07	.11	0.02 (0.0)
ile	142.41	4.56	.28	9.0
leu	203.67	6.35	.25	12.6 (13.0)
tyr	32.48	0.94	.99	1.8 (2.0)
phe	5.27	5.27	1.81	10.4 (10.0)
his	73.79	2.41	.27	4.8 (5.0)
lys	171.40	5.50	.39	11.0
arg	130.92	4.09	.27	8.2 (8.0)
trp	nd	nd	nd	(6.0)*

*calculated from extinction coefficient and number of tyrosines

Ellman reagent titration for reactive -SH groups by Potter's method (18) gave 0.7 mole SH/mole of enzyme indicating that all but one of the 11 cysteine residues in the protein exist in disulfide bridging.

The effect of N-methylnicotinamide chloride (NMNCL) on tryptophan fluorescence of squid OPA anhydrase in the presence and absence of guanidine hydrochloride (GdHCL) is shown in Figure 1.

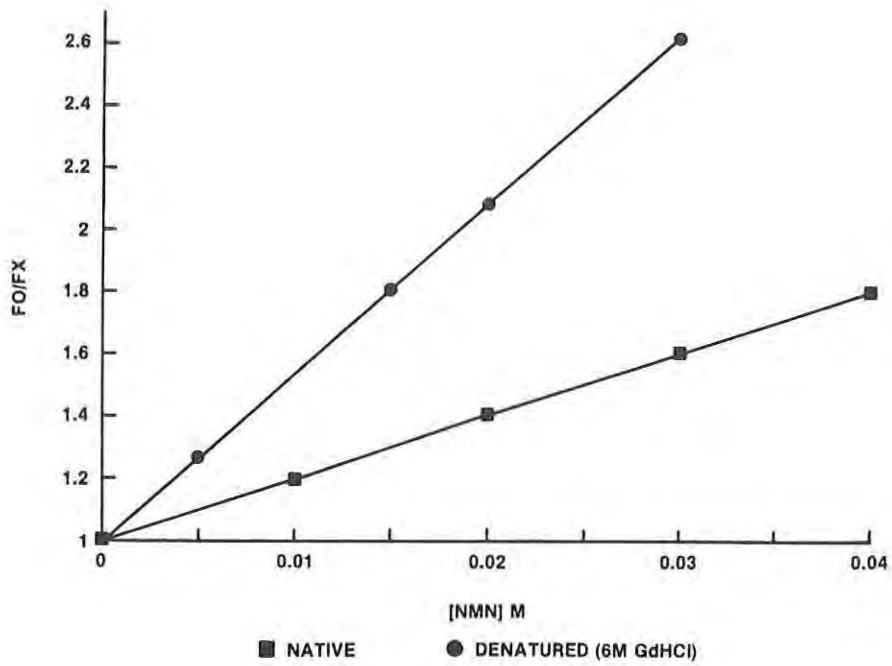

FIGURE 1 STERN-VOLMER PLOT OF .05 MG/ML SQUID .025M TRIS .10M NaCl QUENCH=NMN

The fluorescence data are plotted by the Stern-Volmer relationship as modified by Lehrer (15). Quenching data for acrylamide and KI obeyed the Stern-Volmer relationship (data not shown). The accessibility of the tryptophyl residues of the native protein was estimated by comparing the K_q value to that of the K_q value for a model compound in the presence of N-acetyl-L-tryptophan ethylester NATEE (data not shown). The quenching constants (K_q) were obtained from the slope of the Stern-Volmer plots. The K_q values determined in this manner are apparently a function of the accessibility of the tryptophyl residues in the protein. The number of tryptophan residues for the squid enzyme that are accessible was calculated from the expression

$$\frac{K_q \text{ (enzyme)}}{K_q \text{ (NATEE)}} \times N_p = N_E$$

where N_p is the number of tryptophans in the enzyme and N_E is the number of exposed tryptophans. The results show that of the six tryptophans only two are accessible in the native squid enzyme.

The effects of metal ions and chelators on OPA anhydrase are given in Tables 3 and 4.

TABLE 3

EFFECTS OF 10^{-4} M CHELATORS ON OPA ANHYDRASES (% STIMULATION [+] OR INHIBITION [-])

Chelator	Squid Enzyme (Purified or Axoplasm) (DFP or Soman)
EDTA	-92
EGTA	-75
1, 10-o-Phenanthroline	-5
8-OHQ-5-SA	-2

TABLE 4

RECOVERY OF SQUID-TYPE OPA ANHYDRASE ACTIVITY AFTER CHELATOR INHIBITION

First Treatment Chelator (Conc., Time)	Followed By Cation (Conc., Time)	% Recovery (±Std. dev., n)
EGTA	Ca^{2+}	84
(10^{-4}M, 30 min.)	(10^{-3}M, 30 min.)	(±20, 8)
EGTA	Mg^{2+}	20
(10^{-4}M, 30 min.)	(10^{-3}M, 30 min.)	(±10, 8)

The results in Table 3 indicate that squid OPA anhydrase may have a Ca^{+2} requirement. Addition of Ca^{+2} in millimolar quantities to the enzyme without prior treatment of EDTA or EGTA is slightly inhibitory (data not shown). At this time no conclusions can be made as to whether or not Ca^{+2} functions as a cofactor.

Secondary structure changes in squid OPA anhydrase in the presence or absence of EDTA are shown in Figures 2 and 3.

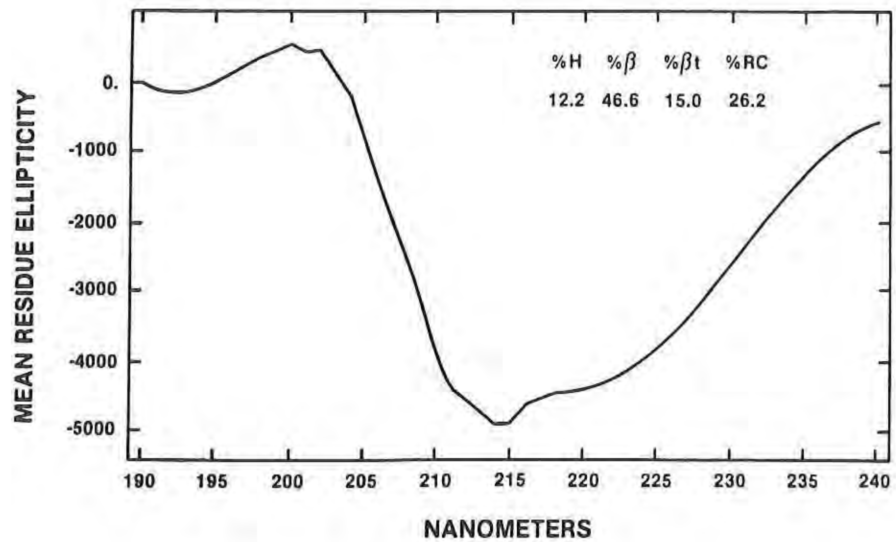

FIGURE 2 FAR UV CD SPECTRA OF SQUID OPA ANHYDRASE IN THE PRESENCE OF EDTA

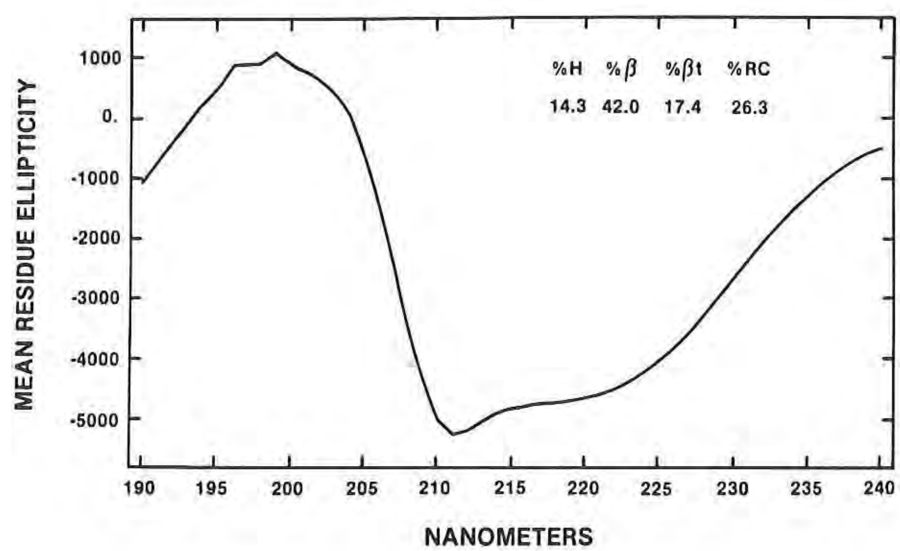

FIGURE 3 FAR UV CD SPECTRA OF SQUID OPA ANHYDRASE

The results shown in Figures 2 and 3 indicate that there is no change in the enzyme's secondary structure when Ca^{+2} is removed.

An unexpected result was obtained when squid OPA anhydrase was denatured by urea and then the disulfide bridges were reduced by dithiothreitol (DTT). As is shown in Table 5, the enzyme retained 85% of its activity.

TABLE 5

EFFECTS OF DENATURANTS ON SQUID OPA ANHYDRASE

Denaturant	% Loss of Activity
6M UREA	10
6M UREA & DTT	15
4M Gd-HCL	100

In 4M guanidine hydrochloride Gd-HCL there was complete loss of enzymatic activity, indicating that hydrogen bonding may be essential for active site stability. The fluorescence spectra for tryptophan in the presence of urea or guanidine hydrochloride are shown in Figure 4.

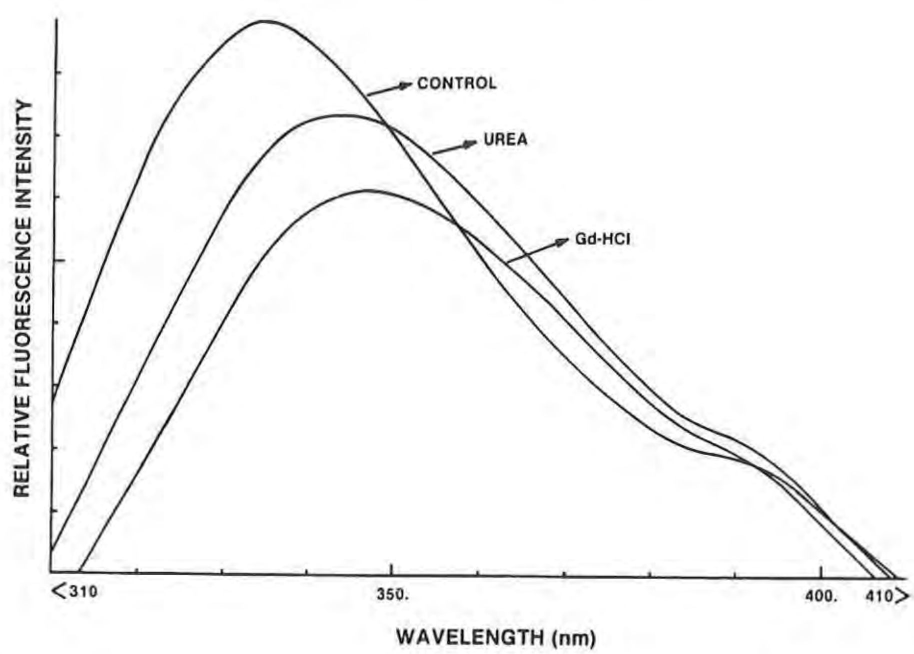

FIGURE 4 TRYPTOPHAN FLUORESCENCE OF SQUID OPA ANHYDRASE

The shifting of the tryptophan fluorescence emission to higher wavelengths indicated an opening up (denaturation) of the enzyme structure (19).

DISCUSSION

Table 6 gives the properties of squid OPA Anhydrase.

TABLE 6

PHYSICO-CHEMICAL PROPERTIES
OF SQUID OPA ANHYDRASE

- Narrow Distribution: Squid nerve, saliva, hepatopancrease
- Molecular Weight: 26,000
- Isoelectric Point, 5.5
- Soman/DFP = 0.25
- Km 2.5×10^{-3M}
- Hydrolyzes all isomers of Soman
- Ca^{+2} requiring, not Ca^{+2} stimulated. Ca^{+2} may be involved in intramolecular bonding
- Mipafox indifferent
- $E_M^{280} = 38,500$
- Disulfide bridges not essential for enzyme activity
- 2 of the 6 TRP residues are exposed to the microenvironment

Ca^{+2} may be envisioned as intramolecularly binding two portions of the peptide chain and possible configuration of the active site by interacting with glutamic acid and aspartic residues. In addition to two folds of the peptide chain being linked by Ca^{+2}, intramolecular hydrogen bonds may play an active role since enzymatic activity is lost on exposure to 4M guanidine hydrochloride. Such a model is likened to the Ca^{+2} binding region (EF-hand) of troponin C (20), but no sequencing of the squid OPA anhydrase has been reported to support such a binding region near the active site. Our results show that a certain degree of secondary and tertiary structure disruption can be tolerated by the enzyme (e.g., retention of activity in 8M urea under reducing conditions), but that a divalent cation, probably Ca^{+2}, is an essential requirement. Finally, disulfide bridging may not be in the active site domain of the enzyme. A possible model for the enzyme is shown in Figure 5.

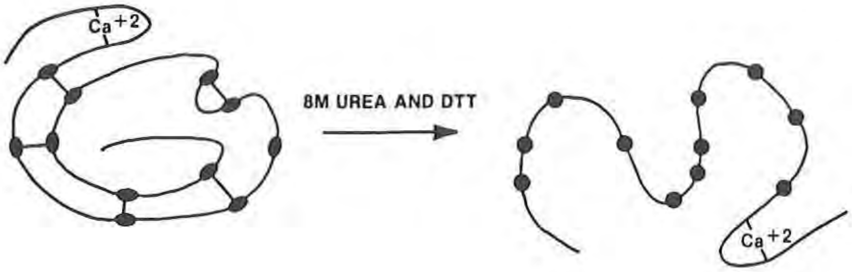

FIGURE 5 SQUID OPA ANHYDRASE

CONCLUSIONS

Squid OPA anhydrase is the first "decon" enzyme that has been demonstrated to have both specificity toward CW agent (Soman and Sarin) and good stability characteristics. Research on this enzyme should be extended toward isolating the peptide region containing the active site. Since the molecular weight of the native enzyme is low (26,000 daltons), the resulting "active site" peptide may be of such a size that it could be synthesized.

REFERENCES

1. Steinmann, K.E., "Purification and Properties of an Organophosphorous Hydrolyzing Enzyme from Squid", Ph.D. Thesis, Illinois Institute of Technology, 1989.

2. Garden, J.M., Hause, S.K., Hoskin, F.C.G., and Roush, A.H., "Comparison of DFP Hydrolyzing Enzyme Purified from Head Ganglia and Hepatopancreas of Squid (Loligo pealei) by Means of Isoelectric Focusing", Comp. Biochem. Physiol., 52C:95-98, 1975.

3. Hoskin, F.C.G., Rosenberg, P., and Brzin, M., "Re-examination of the Effect of DFP on Electrical and Cholinesterase Activity of Squid Giant Axon", Proc. Nat. Acad. Sci. USA, 55:1231-1235, 1966.

4. Hoskin, F.C.G., and Long, R.J., "Purification of a DFP-hydrolyzing Enzyme from Squid Head Ganlion", Arch. Biochem. Biophys. 150:548-555, 1972.

5. Hoskin, F.C.G., and Brande, M., "An Improved Sulfur Assay Applied to a Problem of Isethionate Metabolism in Squid Axon and Other Nerves", J. Neurochem. 20:1317-1327, 1973.

6. Hoskin, F.C.G., and Prusch, R.D., "Characterization of a DFP-hydrolyzing Enzyme in Squid Posterior Salivary Gland by Use of Soman, DFP, and Manganous Ion", Comp. Biochem. Physiol. 75C:17-20, 1983.

7. Hoskin, F.C.G., and Roush, "Hydrolysis of Nerve Gas by Squid Type Diisopropylphosphofluoridate Hydrolyzing Enzyme on Agarose Resin", Science 215:1255-1257, 1982.

8. Rajan, K.S., Mainer, S., Steinmann, K.E., and Hoskin, F.C.G., "Stability of Squid-Type DFPase and Its Recovery in CW-Agent Decontamination Application", Proceedings of the U.S. Army CRDEC Scientific Conference on Chemical Defense Research, Aberdeen Proving Ground, Maryland, Nov 15-18, 1988.

9. Rajan, K.S., "Enzymatic Detoxification of CW Agents: Immobilization of the Enzymes on Material Surfaces", Contract NO. N0014-85-K-0054-ONR.

10. Rajan, K.S., Mainer, S., Steinmann, K.E., and Hoskin, F.C.G., "The Purification and Characterization of DFPases for Detoxifying Organophosphate-Type AChE Inhibitors", Pharmacol. 29:179, 1987.

11. Frank, M.S., and Ross, J.W., Jr., "Electrode for Sensing Fluoride Ion Activity in Solution", Science 154:1553-1555, 1966.

12. Laemmli, U.K., "Cleavage of Structural Proteins During the Assembly of the Head of Bacteriophage T4", Nature 227:680-685, 1970.

13. Yang, J.T., Wu, C-S, and Martinez, H.M., "Calculation of Protein Conformation from Circular Dichroism", Methods in Enzymology 130:PtK, 208-269, 1986.

14. Holmes, L.G., and Robbins, F.M., "Quenching of Tryptophyl Fluorescence in Proteins by N'-Methylnicotinamide Chloride", Photochem. Photobiology 19:361-366, 1974.

15. Lehrer, S.S., "Solute Perturbation of Protein Fluorescence", Bioch. 10:3254-3263, 1971.

16. Lakowicz, J.R., "Principles of Fluorescence Spectroscopy", Plenum Press, New York, 1983.

17. Cohen, S.A., Meys, M., and Tarvin, T.L., "The Pico-Tag Method: A Manual for Advanced Techniques for Amino Acid Analysis", Waters Co. Tech Bulletin WM02, Rev 1, 1988.

18. Potter, J.D. Seidel, J.C., Leavis, P., Lehrer, S.S., and Gerely, J., "Effect of Ca^{+2} Binding on Troponin C", J. Biol. Chem 251:7551-7556, 1976.

19. Kronman, M.J., and Holmes, L.G., "The Fluorescence of Native, Denatured and Reduced-Denatured Proteins", PhotoChem. Photobiol. 14:113-134, 1971.

20. Zot, A.S., and Potter, J.D., "Structural Aspects of Troponin-Tropomyosin Regulation of Skeletal Muscle Contraction", Ann. Rev. Biophys. Biophy. Chem. 16:535-559, 1987.

TITLE: Catalytic Decomposition of CW-Agents by Ternary Chelates of Copper (II)

*John E. Walker, Mr., David E. Remy, Dr., and Krishma S. Rajan, Dr.

ABSTRACT: The formation and structure of Cu(II)-glucosamine (GA) 1:1 and 1:2 chelates involving coordination with aminonitrogen and C-1 hydroxyl groups with stability constants, i.e., $LogK_1 = 9.88 \pm 0.02$ and $LogK_2 = 17.96 \pm 0.02$, respectively, were determined. The hydrolysis and disproportionation of the 1:1 chelate are eliminated through its additional coordination with an equimolar amount of each of the bidentate amines, viz., dipyridyl (DP), ethylenediamine (EN), 1,3-diaminopropane (DAP), N,N,N',N'-diethylethylenediamine (DEEN), N,N,N',N'-tetraethylethylenediamine (TEEN), and N,N,N',N'-tetramethylethylenediamine (TMEN) with overall stabilities (Log_{LA}) respectively, 15.94 ± 0.09, 19.37 ± 0.02, 18.57 ± 0.02, 17.80 ± 0.01, 10.24 ± 0.03 and 16.34 ± 0.02. The rates of decomposition of Sarin and Soman in aqueous 0.02M pipes buffer (pH 7.2) by the chelates decreased in the order: Cu-TMEN (1:1) > Cu-TMEN-GA (1:1:1) > Cu-DEEN (1:1) > Cu-DP (1:1) > Cu-GA (1:1) > Cu-GA (1:2) > Cu-DP-GA (1:1:1) > Cu-DAP (1:1). Data on the catalytic activity of the chelates are examined in the light of their stabilities and structures with a view to delineate a possible mechanism.

*BIOGRAPHY OF PRESENTER: John E. Walker

PRESENT ASSIGNMENT: Research Chemist, Special Projects Branch, Physical Sciences Division, Soldier Science Directorate, U.S. Army Natick Research, Development and Engineering Center.

PAST EXPERIENCE: Food Sciences and Physical Sciences Laboratory, Natick.

DEGREES HELD: B.S., M.S., and M.A.

Catalytic Decomposition of CW-Agents by Ternary Chelates of Copper (II)

John E. Walker, Mr., David E. Remy, Dr., and Krishma S. Rajan, Dr.

INTRODUCTION

The problem of characterization of the biopolymeric metal chelate catalyst (involving chitosan) and its stability in aqueous media has become of considerable importance in connection with the on-going efforts of the Special Projects Branch, Physical Sciences Division, Soldier Science Directorate, U.S. Army Natick RD&E Center [1,2]. Questions regarding improved stability and enhancement of catalytic reactivity of the polymer system can be best addressed by working with monomeric systems. The objectives of this research were; (i) to investigate the interactions of copper (II) with glucosamine and methoxyglucosamine in the absence and presence of a number of bidentate nitrogen donor ligands and (ii) to study the homogeneous catalytic activity of the chelates for the decomposition of the toxic organophosphorous compounds; diisopropylphosphorofluoridate (DFP) and (Soman).

EXPERIMENTAL

Aqueous stock solutions (0.02M) of D-glucosamine and the other bidentate nitrogen donor amines (see Table 1) were prepared by dissolving appropriate quantities of the respective (reagent grade) amine hydrochlorides in CO_2-free distilled water, standardized by potentiometric titration and stored in the refrigerator. Aqueous stock solution (0.02M) of copper (II) was prepared by using reagent grade copper nitrate and standardized by complexometric titration (3) against ethylenediamine tetraacetic acid (EDTA).

The potentiometric equilibrium pH method was used in this investigation. The method consists in determining the proton association equilibria of the different amines (hydrochlorides) in the presence and in the absence of Cu(II) ion in equimolar or higher molar concentrations by means of a glass-calomel electrode system in a thermostatted electrometric cell. All the titrations were carried out at $25.0 \pm 0.1^{o}C$ and ionic strength of 1.0 (1.0M KNO_3). Possible metal-binding reactions occurring in solutions were then postulated on the basis of an analysis of the potentiometric equilibrium curves. The reactions thus assumed constituted the basis for appropriate mathematical treatments and the determination of the metal chelate formation constants. The magnitude of the binding constant is a measure of the strength of metal-ligand binding. Details of the potentiometric equilibrium pH method were reported in an earlier publication (4).

The calculations of the metal chelate stability constants and the distribution of the different chelate species over the pH range 2-12 were carried out with a computer program (BEST) provided by Dr. R.J. Motekitis and Dr. A.E. Martell, Texas A&M University, College Station Texas.

TABLE 1. SECONDARY LIGANDS EXAMINED

	Donor Atom	Ligand Character
Methylamine	Nitrogen	Monodentate
Dipyridyl	Nitrogen	Bidentate
Ethylenediamine	Nitrogen	Bidentate
1,3-propanediamine	Nitrogen	Bidentate
1,6-hexanediamine	Nitrogen	Bidentate
Tetramethylethylenediamine	Nitrogen	Bidentate
Diethylethylenediamine	Nitrogen	Bidentate
Tetraethylethylenediamine	Nitrogen	Bidentate

Circular dichroism spectra of the metal-chelates were recorded in the wavelength range of 800-240 nm on an AVIV 60DS solid state instrument (AVIV Associates, Lakewood, NJ). The instrument is equiped with a 50 KH_Z photoelastic modulator and an end-on photomultiplier. The instrument was calibrated with (+)d-10-camphorsulfonic acid. The instrument was interfaced with an AT&T computer, which was used for all mathematical calculations.

RESULTS

For purpose of clarity brief descriptions are given of (i) the acid-base equilibria of the ligands (ii) the equilibria involved in the metal chelate formation (iii) the stepwise or successive formation of metal chelates, (iv) the thermodynamic stability constants of the metal chelates and (v) the overall stability constants.

The reactions of a metal ion M with one or more number of moles (per mole of the metal ion) of a ligand (L) are illustrated in Figure 1.

$$M + L \xrightleftharpoons{K_{ML}} ML$$

$$ML + L \xrightleftharpoons{K_{ML_2}} ML_2$$

$$M + 2L \xrightleftharpoons{\beta_2} ML_2$$

(CHELATE FORMATION CONSTANT, STABILITY CONSTANT)

$$K_{ML} = \frac{[M\,L]}{[M]\,[L]}$$

$$K_{ML_2} = \frac{[ML_2]}{[ML]\,[L]}$$

(OVERALL STABILITY CONSTANT)

$$\beta_2 = \frac{[ML_2]}{[M]\,[L]^2} = K_{ML} \cdot K_{ML_2}$$

FIGURE 1. METAL CHELATE EQUILIBRIA

In the present study "L" is used to represent the primary ligand, i.e., glucosamine and A is used to represent the secondary ligand having bidentate character. The chelate formation (stability) constant and the overall stability constant are given by the equations shown in Figure 1, where K_{mL} representing the equilibrium constant for the respective metal-ligand interactions is known as the formation constant (or stability constant). K_{mL2} is the equilibrium constant for the binding of the 1:1 metal chelate with a second mole of the same ligand, L, and is called the "stepwise" (or successive) formation constant. β_n is known as the overall formation constant. It represents the equilibrium constant for the interaction of the metal ion with 'n' number of ligands. It is calculated by determining the product of the stepwise formation constants.

Whenever an aquo metal ion is only partially coordinated or weakly bound on all its coordination sites, it tends to undergo hydrolysis through an interaction with hydroxide ions from the aqueous medium resulting in the formation of hydroxometal chelate. This process could lead, in several instances, to the formation of stable, and homogeneous polymeric species or, alternately, to the separation of metal hydroxide precipitates. This type of strong solvolytic (hydrolytic) tendency on the part of the chelate often underlies the cause for the lability (or the instability) of the chelates. The hydrolysis and polymerization reactions are illustrated in Figure 2.

$$M + L \xrightleftharpoons{K_{ML}} ML$$

$$ML + H_2O \xrightleftharpoons{K_{HYD}} ML(OH) + H^+$$

$$2ML(OH) \rightleftharpoons M_2L_2(OH)_2$$

$$ML + A \xrightleftharpoons{K_{MLA}} MLA$$

FIGURE 2. HYDROLYSIS OF METAL CHELATE AND TERNARY CHELATE FORMATION

It is possible to overcome this kind of lability tendency by bringing in a secondary ligand (with affinity to coordinate the metal ion greater then that of the hydroxide ion) and enabling the formation of a stable mixed-ligand (or a ternary) chelate, as illustrated by the reaction shown in Figure 2. An examination of the potentiometric equilibrium curves (i.e., $-\log [H^+]$ versus m, where m represents the number of equivalents of base added per mole of the total metal ion present in the metal-ligand system) will reveal any possible hydrolysis of the partially chelated metal ion, the formation of mono-, di-, or higher hydroxo-chelates and leads ultimately to the polymerization or disproportionation of the chelate.

The binding of a hydrated metal ion with a ligand takes place through an equilibrium displacement of one or more protons already bound to the ligand. Therefore, for a quantitative determination of the metal chelate equilibria, it is necessary to know the proton association equilibrium constants of the ligands' values of the negative logarithm of the equilibrium constant representing the acid dissociation of the ligand, i.e., pK are thus determined on the basis of the reactions given in Figure 3.

$$H_2L \xrightleftharpoons{K_1} HL^- + H^+$$

$$HL^- \xrightleftharpoons{K_2} L^{2-} + H^+$$

$$K_1 = \frac{[HL^-]\,[H^+]}{[H_2L]}$$

$$K_2 = \frac{[L^{2-}]\,[H^+]}{[HL^-]}$$

$$pK = -\log K$$

FIGURE 3. DISSOCIATION EQUILIBRIA OF THE LIGAND ACID

The titration curve for the free ligand, glucosamine (GA) and those for the Cu(II)-GA (1:1), (1:2) and (1:3) system are shown in Figure 4 in which the number of moles of base added per mole of total ligand or total metal (i.e., m) are plotted against the corresponding measure values of $-\log\,[H^+]$.

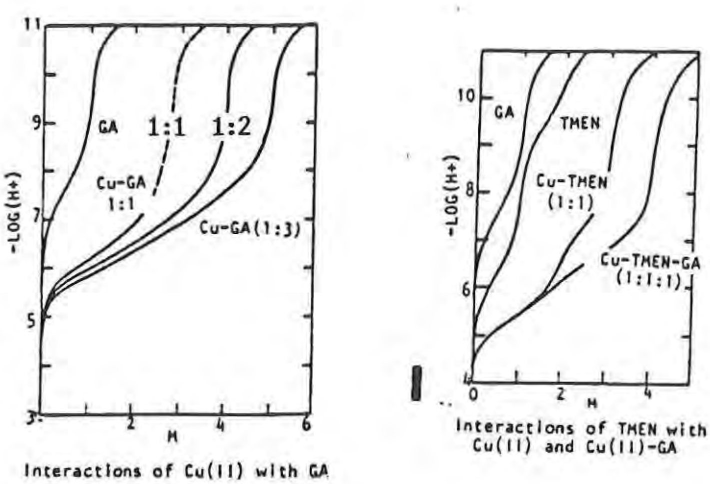

FIGURE 4. INTERACTIONS OF CU(II) WITH GLUCOSAMINE AND TETRAMETHYLETHYLENE DIAMINE.

The Cu(II)-GA (1:1) curve shows an inflection at m = 2.5 to 3.0 with precipitation occurring at m = 2.5 (as shown by the dash line). This could be taken to indicate the interaction of Cu(II) with GA involving the $-NH_3^+$ and the -(OH) groups of the glucosamine molecule. The curve further indicates that the partially coordinated Cu(II)-GA chelate undergoes hydrolysis followed by disproportionation, resulting in the separation of solid phase (precipitate). It is noted that the destabilization associated with Cu(II)-glucosamine (1:1) chelate has been obviated through its interaction with a second mole of either the glucosamine or the other bidentate amines (Table 1). Among the secondary ligands examined, tetramethylethylene- diamine (TMEN), diethylenediamine (DEEN), tetraethylethylenediamine (TEEN), ethylenediamine (EN), and dipyridyl (DP) exhibit additional coordination with Cu-GA resulting in the formation of a ternary chelate each. TMEN interacts with Cu(II) forming a 1:1 chelate in the buffer region m = 0 to m = 2 (Figure 4) followed by hydrolysis and formation of a stable Cu(II)-TMEN-monohydroxo chelate in the second buffer region, i.e., m = 2 to m = 3. The formation of a Cu(II)-TMEN-GA (1:1:1) ternary chelate is indicated by a single strong inflection at m = 4 proceeded by a buffer region between m = 0 and m = 4.

The equilibrium interactions occurring in the different systems along with the corresponding stability constants determined are summarized in Table 2.

TABLE 2. EQUILIBRIUM INTERACTIONS AND THE CORRESPONDING STABILITY CONSTANTS

M	Reaction	Log K	Sigma
	Glucosamine HCl (H_2A^+)		
0-1	$HA + H^+ \rightleftharpoons H_2A^+$	7.67	0.01
0-2	$A^- + H^+ \rightleftharpoons HA$	11.92	0.02
	Cu-Glucosamine.HCl (1:2)		
0-4	$Cu^{2+} + A^- \rightleftharpoons Cu\,A^+$	9.88	0.02
	$Cu\,A^+ + A^- \rightleftharpoons Cu\,A_2$	8.08	0.02
	Ethylenediamine 2HCl (H_2L^{2+})		
0-1	$HL^+ + H^+ \rightleftharpoons H_2L^{2+}$	7.41	0.01
1-2	$L + H^+ \rightleftharpoons HL^+$	10.04	0.01
	Cu-Ethylenediamine.2 HCl (1:1)		
0-2	$Cu^{2+} + L \rightleftharpoons CuL^{2+}$	10.60	0.005
	$CuL^{2+} + L \rightleftharpoons CuL_2^{2+}$	9.26	0.005
	Cu-Ethylenediamine.2HCl-Glucosamine.HCl (1:1:1)		
0-2	$Cu^{2+} + L \rightleftharpoons CuL^{2+}$	10.68	0.04
2-4	$CuL^{2+} + A^- \rightleftharpoons CuLA^+$	8.85	0.06
	$Cu^{2+} + L + A^- \rightleftharpoons CuLA^+$	19.37	0.02
	1,3-Propanediamine.2 HCl (H_2L^{2+})		
0-2	$HL^+ + H^+ \rightleftharpoons H_2L^{2+}$	9.05	0.01
	$L + H^+ \rightleftharpoons HL^+$	10.67	0.01
	Cu-Glucosamine.HCl-1,3-propanediamine.2 HCl (1:1:1)		
0-4	$Cu^{2+} + A^- + L \rightleftharpoons CuAL^+$	18.57	0.02
	1,6 - hexanediamine 2HCl (H_2L^{2+})		
0-2	$HL^+ + H^+ \rightleftharpoons H_2L^{2+}$	10.32	0.01
	$L + H^+ \rightleftharpoons HL^+$	11.02	0.01
	Cu(II)-1,6-hexanediamine.2HCl (1:1)	No chelation formation	
	N,N,N',N' tetramethylethylenediamine.2 HCL (H_2L^{2+})		
0-1	$HL^+ + H^+ \rightleftharpoons H_2L^{2+}$	6.31	0.01
1-2	$L + H^+ \rightleftharpoons HL^+$	9.42	0.01
	Cu-tetramethylethylenediamine 2 HCl (1:1)		
0-2	$Cu^{2+} + L \rightleftharpoons CuL^{2+}$	7.57	0.02
2-4	$CuL^{2+} + L \rightleftharpoons CuL_2^{2+}$	4.70	0.02
	Cu-Glucosamine HCl-tetramethylethylenediamine. 2HCl (1:1:1)		
0-4	$Cu^{2+} + A^- + L \rightleftharpoons Cu\,AL^+$	16.34	0.02
	N,N,N',N'-tetraethylethylenediamine 2 HCl (H_2L^{2+})		
0-1	$HL^+ + H^+ \rightleftharpoons H_2L^{2+}$	6.81	0.01
1-2	$L + H^+ \rightleftharpoons HL^+$	9.99	0.01

(Continued)

TABLE 2. (CONT'D)

M	Reaction	Log K	Sigma
	Cu(II)-tetraethyl thylenediamine.2HCL	No chelation formation	
	Cu-Glucosamine HC,-tetraethylethylenediamine 2 HCl (1:1:1)		
0-4	$Cu^{2+} + A^- + L^+ \rightleftharpoons CuAL^+$	10.24	0.03
	N,N'-diethylethylenediamine.2 HCl (H_2L^{2+})		
0-1	$HL^+ + H^+ \rightleftharpoons H_2L^{2+}$	7.63	0.02
1-2	$L + H^+ \rightleftharpoons HL^+$	10.35	0.01
	Cu-diethylethylenediamine.2 HCl (1:1)		
0-2	$Cu^{2+} + L \rightleftharpoons CuL^{2+}$	9.05	0.01
	$CuL^{2+} + L \rightleftharpoons CuL_2^{2+}$	6.09	0.01
	Cu-Glucosamine HCl-diethylethylenediamine.2HCl (1:1:1)		
0-4	$Cu^{+2} + A^- + L \rightleftharpoons Cu\ AL^+$	17.80	0.01
	2,2' dipyrdyl.2HCl (H_2L^{2+})		
0-1	$HL^+ + H^+ \rightleftharpoons H_2L^{2+}$	2.40	0.01
1-2	$L + H^+ \rightleftharpoons HL^+$	4.91	0.04
	Cu-dipyridyl.2 HCl (1:2)		
0-2	$Cu^{2+} + L \rightleftharpoons CuL^{+2}$	7.11	0.01
	$CuL^{2+} + L \rightleftharpoons CuL_2^{2+}$	6.88	0.01
	Cu-dipyridyl.2 HCl-glucosamine HCl (1:1:1)		
0-2	$Cu^{2+} + L \rightleftharpoons CuL^{2+}$	4.75	0.08
2-4	$CuL^{2+} + A^- \rightleftharpoons CuLA^+$	8.97	0.01
	$Cu^{2+} + L + A^- \rightleftharpoons CuLA^+$	15.94	0.09
	Bistrispropane.2HCl (H_2L^{2+})		
0-1	$HL^+ + H^+ \rightleftharpoons H_2L^{2+}$	7.11	0.03
1-2	$H^+ + L \rightleftharpoons HL^+$	9.19	0.02
	Cu(II)-Bistrispropane.2HCl (1:1)		
0-2	$Cu^{2+} + L \rightleftharpoons CuL^{2+}$	11.01	0.02
	$CuL + H_2O \rightleftharpoons CuL(OH)^+ + H^+$	5.89	0.07
	$CuL(OH) \rightleftharpoons CuL(OH)_2 + H^+$	8.57	0.04
	Cu(II)-Bistrispropane.2HCl (1:2)		
0-2	$Cu^{2+} + L \rightleftharpoons CuL^{2+}$	10.80	0.10
2-4	$CuL^{2+} + L \rightleftharpoons CuL_2^{2+}$	5.90	0.10
	Cu(II)-Bistrispropane.2HCl.Glucosamine.HCl (1:1:1)		
0-4	$Cu^{2+} + L + A^- \rightleftharpoons CuLA^+$	20.07	0.20

On the basis of an examination of the values of the stability constants of the different chelate systems (Table 2), the following trends are noted. The 1:1 chelates of Cu(II) with the different amines decrease in the order: Cu(II)-EN > Cu(II)-GA   Cu(II)-DAP > Cu(II)-DEEN > Cu(II)-TMEN > Cu(II)-DP. With respect to the 1:2 chelates, the order is: Cu(II)-EN > Cu(II)-GA > Cu(II)-DAP > Cu(II)-DEEN > Cu(II)-DP > Cu(II)-TMEN. In regard to the formation of a ternary chelate of Cu(II)-GA with each of the amines, the decreasing order is: Cu(II)-GA-EN > Cu(II)-GA-DAP > Cu(II)-GA-DEEN > Cu(II)-GA-TMEN > > Cu(II)-GA-DP.

If the molecular structure and nature of the donor groups (along with their pK's) of the glucosamine molecule as well as the established coordination geometry of the aquo Cu(II) ion are considered along with the magnitude of the chelate stability constant determined in this research, it is possible to visualize the involvement of the amine nitrogen and one of the hydroxyl groups (of the ligand molecule) in the coordination of the metal ion leading to the formation of a (1:1) chelate as illustrated in Structure I, Figure 5.

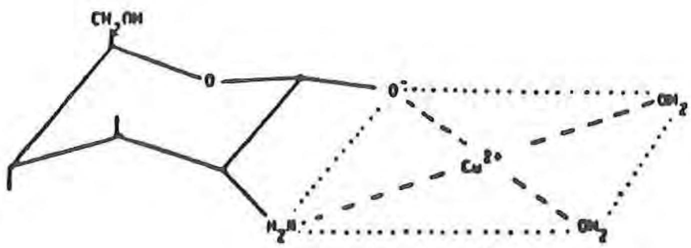

Structure I: Cu(II)-Glucosamine (1:1) Chelate

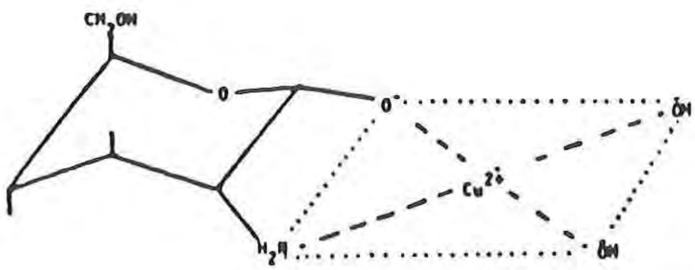

Structure II: Hydrolysis of Cu(II)-Glucosamine Chelate

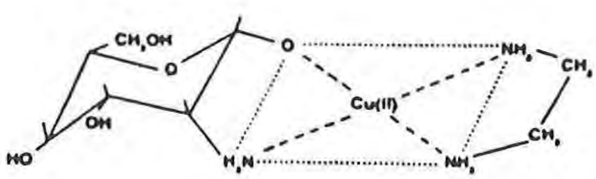

Structure III: Cu(II)-Glucosamine-Ethylenediamine (1:1:1) Chelate (C, -OH bound to Cu(II)

FIGURE 5. STRUCTURES OF Cu(II) CHELATES

The ligand hydroxyl could be either from the C-1 or the C-3 position of the glucosamine molecule. This observation is consistent with literature reports.[5-7] In order to gain further insight into this, a C-1-methoxy derivative was prepared and included in this research and its mode of chelation with Cu(II) was investigated.

Further, an examination of the titration curve of the Cu(II)-glucosamine (1:1) system (Figure 1) indicates that the 1:1 chelate undergoes hydrolysis (see Structure II, Figure 5) and disproportionation, leading to the separation of a solid phase. However, in the presence of either a second mole of glucosamine (i.e., 1:2) or an equimolar amount of a secondary ligand (i.e., 1:1:1), such a "destabilizing" tendency of the Cu(II)-chelate is obviated. In either case, the Cu(II) chelate formed involves both the amine nitrogen and the hydroxyl donor groups of the glucosamine molecule. Structure III (Figure 5) illustrates the possible mode of coordination in a Cu(II) ternary chelate system by which hydrolysis of the Cu(II) chelate is overcome.

The titration curves for 1-methyoxyglucosamine (MGA), Cu(II)-MGA (1:1) and (1:2), Cu-EN-MGA, Cu-DP-MGA, and Cu-TMEN-MGA (1:1:1) are shown in Figure 6. The inflection at m=3 in the Cu(II)-MGA 1:1 curve can be taken to indicate the formation of a hydrolyzed Cu(II)-MGA chelate involving the coordination of the NH_2 group of methoxyglucosamine and the C-3 hydroxyl group followed by the dissociation of a proton from a Cu(II) coordinated water molecule. The Cu(II)-MGA (1:2) system exhibits an inflection point at M=4 (Figure 6) indicating the displacement of the protons from both the protonated amine group and the C-3 hydroxyl group on each of the MGA molecules to form a 1:2 chelate. All three of the (1:1:1) ternary systems, viz., Cu(II)-TMEN-MGA, Cu(II)-EN-MGA, and Cu(II)-DP-MGA show inflection points at m=2 and m=4 indicating the formation of the 1:1 chelate of Cu(II) with each of the diamines followed by their interaction with a mole of MGA resulting in the formation of the 1:1:1 ternary chelate at a slightly high pH (i.e., 6-8:5). The equilibrium constants for the postulated reactions are given in Table 3 along with the values for the corresponding reactions with glucosamine. A possible mode of binding of 1-methoxy glucosamine with Cu(II) and the attachment of a secondary ligand (i.e., ethylenediamine) are shown in structure IV (Figure 7).

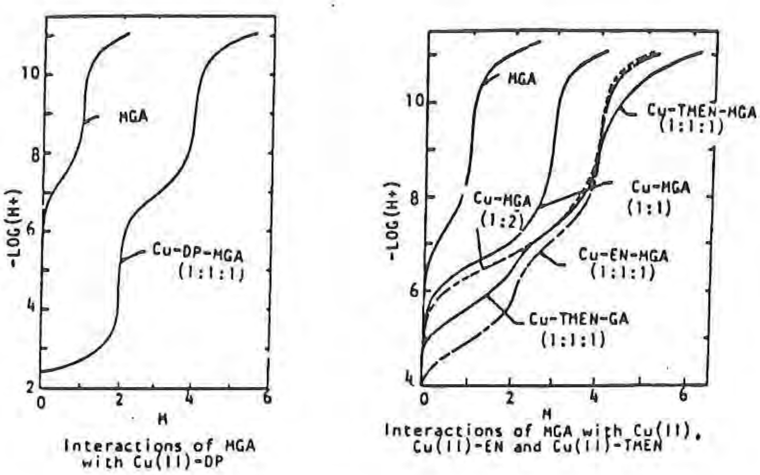

FIGURE 6. INTERACTIONS OF Cu(II) WITH 1-METHOXY GLUCOSAMINE, DIPYRIDYL ETHYLENEDIAMINE AND TETRAMETHYL ETHYLENE DIAMINE

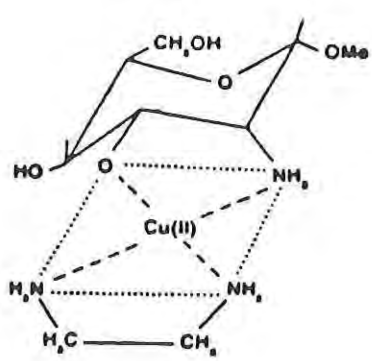

Structure IV: Cu(II)-Methoxy Glucosamine-Ethylenediamine (1:1:1) Chelate (C_3-OH bound to Cu(II))

FIGURE 7. STRUCTURE OF CU(II) TERNARY CHELATE

On the basis of the stability constants of the different chelates, their equilibrium concentrations over the pH range 2-12 were computed and the corresponding distribution profiles were plotted, a few of which are shown in Figure 8 and the remaining ones are compiled in Appendix 1 of reference 8. Data on the nature and extent of distribution of the Cu(II) chelate species were generated in order to develop a proper mechanistic insight into the catalytic activity of the Cu(II) chelates for decomposition of toxic phosphonofluoridates. In Tables 4 and 5 are summarized the percent distribution of the aquo Cu(II) ion and the different Cu(II)-chelates at pH 7.2 in the different chelate systems being examined in this research for their agent-decomposing activity.

The data obtained for the hydrolysis of diisopropylfluorophosphate (DFP) by a number of Cu(II)-chelates at pH 7.2 are reported in Table 6. The equilibrium constants for the formation of the corresponding Cu(II) chelates are also included.

TABLE 3. REACTIONS OF 1-METHOXYGLUCOSAMINE (MGA) WITH Cu(II) AND Cu(II) AMINE CHELATES

With m	Reaction	Log K	Sigma	β Values Glucosamine
	1-methoxyglucosamine-HCl (H_2A^+)			
0-1	$HA + H^+ \rightleftharpoons H_2A^+$	7.39	0.01	7.67
1-2	$A^- + H^+ \rightleftharpoons HA$	12.30	0.01	11.92
	$(A^+ + 2H^+ \rightleftharpoons H_2A^+)$	19.69		19.59
	Cu-MGA HCl (1:2)			
0-4	$Cu^{2+} + A^- \rightleftharpoons CuA^+$	9.61	0.03	9.88
	$CuA^+ + A^- \rightleftharpoons CuA_2$	7.92	0.03	8.08
	$(Cu^{2+} + 2A \rightleftharpoons CuA_2$	17.53	0.03	17.96
	Cu-Dipyridyl HCl-MGA-MCl			
0-4	$Cu^{2+} + A^- + L \rightleftharpoons CuAL^+$	15.85	0.03	15.94
	Cu^{2+} - EN.2HCl - MGA - HCl			
0-4	$Cu^{2+} + A^- + L \rightleftharpoons CuAL^+$	18.77	0.03	19.37
	Cu-TMEN.2HCl-MGA-HCl			
0-4	$Cu^{2+} + A^- + L \rightleftharpoons CuAL^+$	15.39	0.08	16.34
	Cu-MGA.HCl (1:1)			
0-3	$Cu^{2+} + A^- \rightleftharpoons CuA^+$	9.46	0.01	9.88
	$CuA^+ + OH^- \rightleftharpoons CuA(OH)$	2.29	0.01	

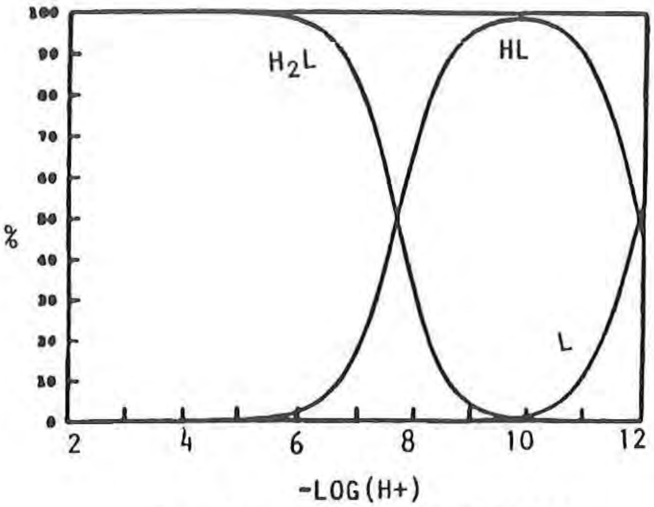

3a. Protonated Glucosamine.

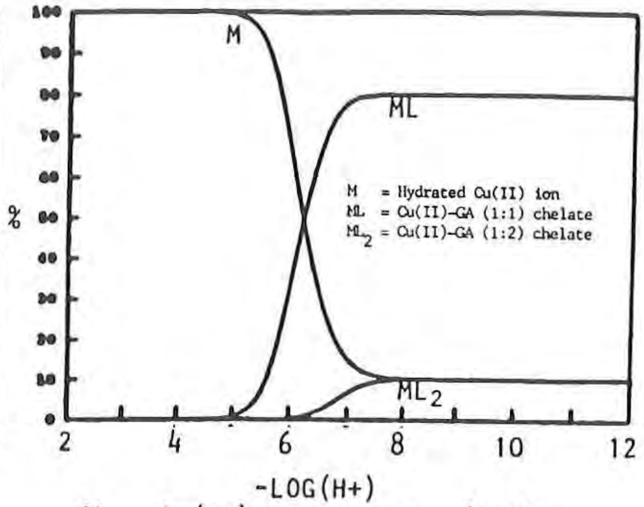

3b. Cu(II)-Glucosamine (1:1).

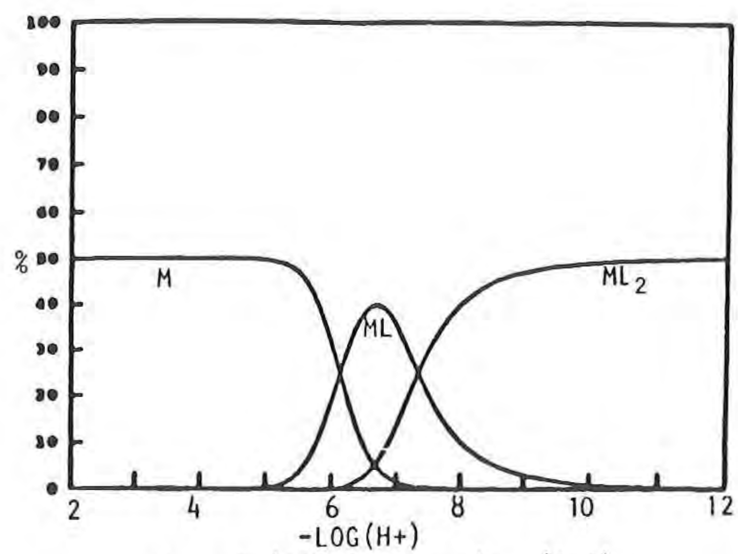

3c. Cu(II)-Glucosamine (1:2).

FIGURE 8. SPECIES DISTRIBUTION IN (A) GLUCOSAMINE, (B) CU(II)-GLUCOSAMINE (1:1), (C) Cu(II)-GLUCOSAMINE (1:2), AND (D) Cu(II)-ETHYLENEDIAMINE-GLUCOSAMINE SYSTEMS

(Continued)

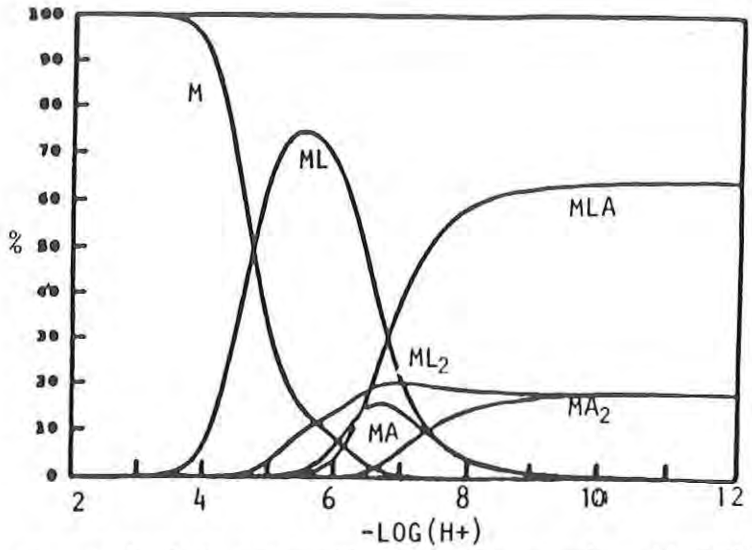

3d. Cu(II)-Ethylenediamine Glucosamine (1:1:1).

FIGURE 8. (CONT'D)

TABLE 4. Cu(II) CHELATE SPECIES DISTRIBUTION AT pH 7.2

System	Chelate Stability β_2	Stoichiometry	% of Total Cu(II) in the Respective Chelate Forms
Cu-TMEN (1:1)		1:0	4.8
	7.57	1:1	92.8
		1:2	2.4
Cu-TMEN-GA (1:1:1)		1:0:0	0.3
		1:1:0	23.3
		1:2:0	2.7
		1:0:1	8.8.
		1:0:2	4.4
	16.34	1:1:1	60.5
Cu-DEEN (1:1)		1:0	4.5
	9.05	1:1	93.4
		1:2	2.1
Cu-GA (1:1)		1:0	12.4
	9.88	1:1	79.4
		1:2	8.1
Cu-DP (1:1)		1:0	30.3
	7.11	1:1	39.4
		1:2	30.3
Cu-GA (1:2)		1:0	0.6
		1:1	46.9
	17.96	1:2	52.5
Cu-DP-GA (1:1:1)		1:0:0	0.5
		1:1:0	5.7
		1:2:0	36.6
		1:0:1	21.7
		1:0:2	14.3
	15.94	1:1:1	21.2
Cu-DAP (1:1)		1:0	9.3
	9.90	1:1	87.8
		1:2	2.9
Cu-BTP		1:0	0.3
	10.86	1:1	99.4
		1:2	0.3

TABLE 5. SPECIES DISTRIBUTION OF Cu(II)-MGA CHELATES AT pH 7.2

	Log β	Stoichiometry			% of Total Cu(II) In The Respective Chelate Forms
Cu-MGA (1:1)			Cu	MGA	
	-		1	0	18.0
	9.61		1	1	82.0
Cu-MGA (1:2)			Cu	MGA	
	-		1	0	3.6
	9.61		1	1	69.1
	17.53		1	2	27.3
Cu-TMEN-MGA (1:1:1)		TMEN	Cu	MGA	
	-	0	1	0	1.0
	7.57	1	1	0	59.6
	12.27	2	1	0	5.0
	9.61	0	1	1	14.9
	17.53	0	1	2	4.7
	15.39	1	1	1	14.9
Cu-EN-MGA (1:1:1)		EN	Cu	MGA	
	-	0	1	0	1.5
	10.60	1	1	0	30.1
	19.86	2	1	0	27.5
	9.61	0	1	1	20.4
	17.53	0	1	2	5.7
	18.77	1	1	1	14.8
Cu-DP-MGA (1:1:1)		DP	Cu	MGA	
	-	0	1	0	2.4
	7.11	1	1	0	12.0
	13.99	2	1	0	35.1
	9.61	0	1	1	26.7
	17.53	0	1	2	6.0
	15.85	1	1	1	17.9

TABLE 6. HYDROLYSIS OF DFP BY Cu(II) CHELATES

Chelate System	Log K ML or Log K MAL	Hydrolysis (μmoles/min) DFP
Cu-TMEN (1:1)	7.57	2.53
Cu-TMEN-GA (1:1:1)	16.34	1.67
Cu-DEEN (1:1)	9.05	1.57
Cu-GA (1:1)	9.88	1.04
Cu-DP (1:1)	7.11	1.64
Cu-GA (1:2)	17.96	0.44
Cu-DP-GA (1:1:1)	15.94	0.73
Cu-DAP (1:1)	9.90	0.04
Cu-BTP (1:1)	10.86	0

Initial concentration of agent and Cu(II) chelate is $4x10^{-3}M$
Buffer: 0.02M pH 7.2 pipes with 0.4M KCl
Temperature 25°C

DISCUSSION

It should be noted that from a consideration of the overall thermodynamic stabilities of the chelates and their agent-hydrolyzing activities, a simple correlation between the two is not possible. In order to determine the nature of the catalyst species that might be predominantly involved in the hydrolysis of the agents, it is of interest to consider and compare the rank order of the above-hydrolysis activity with those of the percent distribution of the different species, i.e., aquo-Cu(II) ion, Cu(II)-ligand (1:1 and 1:2) chelates and the ternary chelates of Cu(II)-glucosamine (1:1:1) at pH 7.2, at which the agent-hydrolysis reactions were carried out (see Tables 4 and 5).

For the aquo Cu(II)-ion, the order is:

Cu-DP > Cu-GA > Cu-DAP > Cu-TMEN > Cu-DEEN
> Cu-GA > Cu-DP-GA > Cu-TMEN-GA.

For Cu(II)-Ligand (1:1) chelates:

Cu-DEEN, Cu-TMEN > Cu-DAP > Cu-GA > Cu-GA (1:2)
> Cu-DP > Cu-TMEN-GA > Cu-DP-GA.

For Cu(II)-Ligand (1:2) chelates:

Cu-GA (1:2) > Cu-DP-GA (Cu-DP) > Cu-DP >
Cu-DP-GA (Cu-GA) > Cu-GA (1:1) > Cu-TMEN-GA (Cu-GA)
> Cu-DAP > Cu-TMEN-GA (Cu-TMEN) > Cu-TMEN > Cu-DEEN.

For the ternary chelates:

Cu-TMEN-GA > Cu-DP-GA.

A critical examination of the above would indicate that neither the aquo-Cu(II) ion nor the different Cu(II)-chelates (i.e., 1:1, 1:2, or the 1:1:1) could be considered to be the predominant moiety solely responsible for the catalytic activity.

Alternatively, on the basis of a critical examination of the structure and steric factors associated with the different chelate systems, it seems reasonable to state that bidentate chelation of Cu(II) with alkyl substitution on the amine nitrogens favors catalytic activity. While ternary chelation helps overcome the destabilizing tendency of a number of the partially coordinated Cu(II)-chelates (i.e., having 1:1 stoichiometry), it does not constitute a sufficient or necessary criterion for conferring maximal catalytic activity on the Cu(II)-chelate moiety. It seems important to have as one of the Cu(II)-coordinating ligands, di- or tetra-N,N,N',N'-substituted diamines (bidentates) in order to confer maximal agent-hydrolysis activity. This, as Courtney et al.[9] have pointed out, helps stabilize the catalyst chelates (1:1) against their disproportionation tendency, while at the same time enabling them to perform their catalytic function.

Thus, in order to overcome such a destabilizing tendency on the part of the Cu(II)-glucosamine (1:1) system and to confer maximal catalytic activity, the attachment of a secondary ligand such as TMEN is found to help. It is possible to consider two alternate mechanisms for the catalytic action of such a ternary chelate moiety along the lines proposed by Courtney et al.[9], viz., (i) combination of the metal chelate with the agent being hydrolyzed followed by attack of this complex with hydroxide ion, and (ii) an analogous push-pull mechanism of Swain.[10] In order to consider both mechanisms, we have to invoke a distorted hexa-coordination geometry for Cu(II) in the ternary chelate catalysts, as illustrated in mechanisms I and II (Figure 9).

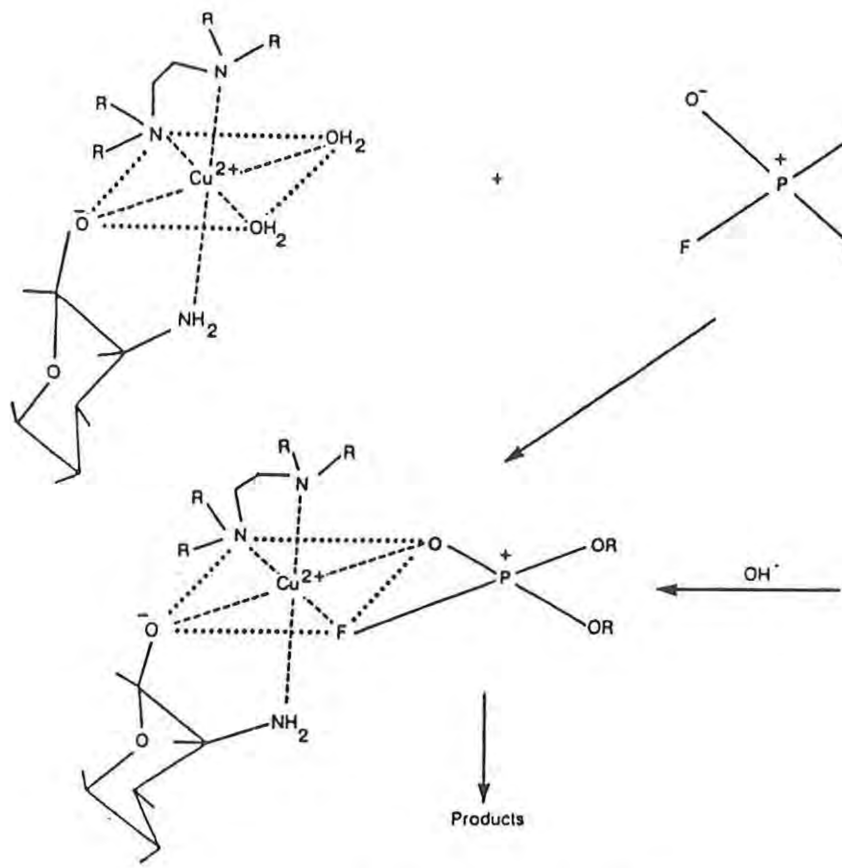

Mechanism - 1 For Catalysis by Ternary Cu (II) Chelate.

FIGURE 9. MECHANISMS FOR CATALYSIS BY TERNARY Cu(II) CHELATE

(Continued)

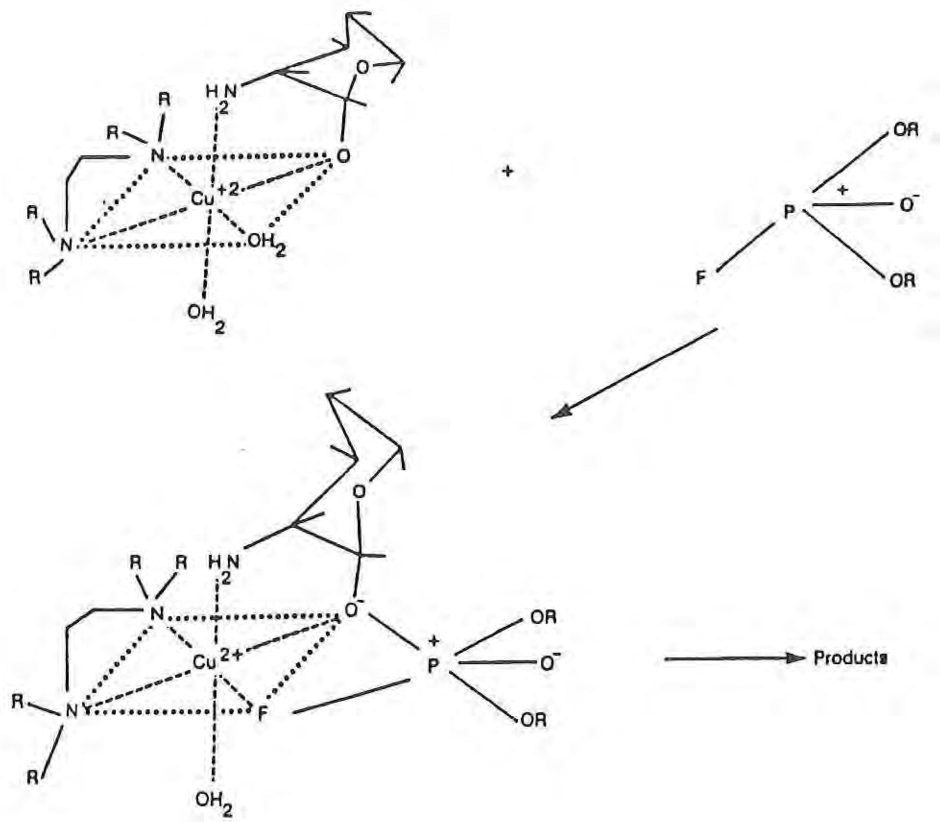

Mechanism - 2 For Catalysis by Ternary Cu (II) Chelate.

FIGURE 9. (CONT'D) MECHANISMS FOR CATALYSIS BY TERNARY Cu(II) CHELATE

CONCLUSIONS

1. Copper(II) Glucosamine and Copper(II) Methoxyl-glucosamine are able to form ternary chelates with a number of bidentate ligands.

2. Ternary chelate formation acts to stabilize the Copper(II) against disproportionation.

3. Mechanisms for catalytic reactivity of the Copper(II) ternary must invoke a distorted hexa-coordinated geometry.

REFERENCES

1. Robbins, F.M., Andreotti, R.E., Walker, J.E., and Remy, D.E., 1988 "Preparation and Properties of a Metal-Coordinated Polymer-Complex ", Natick/TR-88/003L

2. Robbins, F.M., Andreotti, R.E., Walker, J.E., Evans, G., and Woodbury, C., 1988 "Metal-Coordinated Polymers for Chemical Protection", Natick/TR-89/004L.

3. Schwarzenbach, G.V., and Flaschka, H., "Complexometric Titrations", Methuen and Co., Ltd., (London) 1969.

4. Rajan, K.S., and Martel, A.E., 1965 "Equilbrium Complexes of Uranyl Complexes Part III Interaction of Uranyl ion with Citric Acid", Inorg. Chem. 4:462-469.

5. Micera, G., Deiana, S., DeCock, P., DuBois, B., and Kozlowski, H., 1985 "Copper(II) Complexation by D-Glucosamine Spectrophotometric and Potentiometric Studies", Inorg. Chim. Acta. 107:45-48.

6. Lerivry, J., DuBois, B., DeCock, P., Micera, G., Urbanska, J., and Kozlowski, H., 1986 "Formation of D-Glucosamine Complexes with Cu(II), Ni(II) and Co(II) Ions", ibid 125:187-190.

7. Pusino, A., Droma, D., DeCock, P., and Kozlowski, H., 1987 "Potentiometric and Spectroscopic Study of Copper(II), Nickel(II), and Cobalt(II) Complexation by Methoxy-D-Glucosamine", ibid 138:5-8.

8. Rajan, K.S., 1989 "Detoxification of Chemical Warfare Agents By Biopolymer Catalysts", Contract No. DAAL03-86-D-0001, Final Progress Report, August 1989 - December 1989.

9. Courtney, R.C., Gustafson, R.L., Westerback, S.J., Hyytiainen, H., Chaberek, S.C., Jr., and Martel, 1957 "Metal Chelate Compounds as Catalysts in the Hydrolysis of Isopropyl Methylphosphonofluoridate and Diisopropylphosphorofluoridate", J. Amer. Chem. Soc. 79:3030-3036.

10. Swain, C.G., and Lupton, E.C., Jr., 1968 "Field and Resonance Components of Substitution Effects", ibid 90:4328-4337.

TITLE: **Characterization of the Catalytic Site for G-Agent Hydrolysis Using Electron Paramagnetic Resonance**

*John W. Halliday, Mr., John E. Walker, Mr., and Krishma S. Rajan, Dr.

ABSTRACT: Coordinated metal ions are becoming increasingly important as reactive centers in the catalytic hydrolysis of chemical warfare agents for protection and decontamination applications. Both the chemical and physical nature of the bonding in these complexes in large part determine their reactivity and characterize the catalytic site. For many systems the coordinated metal ion contains an unpaired electron in its outer shell and thus is an *in situ* paramagnetic probe responsive to the chemical and physical characteristics of the site. Divalent copper complexes, the experimental focus of the present study, catalyze the hydrolysis of phosphonates - the functional group that is responsible for G-agent toxicity. Electron paramagnetic resonance (EPR) techniques can be advantageously employed to characterize such reaction sites.

Cu(II) is a hexacoordinated $3d^9$ system whose EPR spectra reflect an axial symmetry. The anisotropy of the spectroscopic *g* factor and the associated Cu hyperfine coupling constant, A, are reduced to parallel and perpendicular components. In practice the EPR spectra are characterized only by $g_{\parallel}$ and $A_{\parallel}$.

A series of complexes was prepared with various ligands, including glucosamine (GA), 1-methoxyglucosamine (MGA), and N,N,N',N'-tetramethyl ethylenediamine (TMEN), chosen to model Cu(II) binding sites. Values of $g_{\parallel}$ and $A_{\parallel}$ for each coordination complex were extracted from EPR spectra taken at 150°K.

The correlation between the measured EPR parameters and the nature of the Cu-ligand interaction was based on the approach of Peisach and Blumberg (Archives of Biochemistry and Biophysics 165, 691 (1974)). Plots of $g_{\parallel}$ versus $A_{\parallel}$ revealed the data clustered in three $g_{\parallel}$ value regions: $g_{\parallel} = 2.24\text{-}2.25$, $g_{\parallel} = 2.30$, and $g_{\parallel} = 2.40\text{-}2.42$. These results were interpreted in terms of chelate structures involving various nitrogen and oxygen donor sets using the ratio $g_{\parallel} / A_{\parallel}$ as an index of structural distortion. The contribution of species identified at pH=7.2 to the effectiveness of G-agent hydrolysis by Cu(II) - ligand systems was determined.

*BIOGRAPHY OF PRESENTER: John W. Halliday

PRESENT ASSIGNMENT: Research Chemist, Physical Sciences Division, Soldier Science Directorate, U.S. Army Natick Research, Development and Engineering Center, Natick, MA 01760-5020

DEGREES HELD: B.S., Ohio State University, 1960; M.S., Northeastern University, 1970.

Characterization of the Catalytic Site for G Agent Hydrolysis Using Electron Paramagnetic Resonance

John W. Halliday, Mr., John E. Walker, Mr., and Krishma S. Rajan, Dr.

INTRODUCTION

The exploration of several new technologies will provide the technical basis to augment the protection of the soldier, both individually and collectively, from the diverse hazards of operation in a chemical agent contaminated environment. These technologies seek to complement and supplement the current reliance on the barrier properties and sorptive capabilities of materials used in protective device construction. Prominent among these new systems are those based on reactive and catalytic materials - especially those employing metal complexes. In the research and, to a more limited extent, the developmental phases, the reactivity of such systems towards chemical agents and their reaction surrogates is studied in solution. To be of practical use, however, these systems must be immobilized by, for example, inclusion in a bio- or synthetic-polymer matrix. The challenge is to relate the reactivities and associated mechanisms between these two dissimilar physical conditions.

Metal-ligand systems are an appropriate model for study in approaching the structure surrounding the metal center in a polymer matrix. Divalent copper chelate systems, the subject of the present study, are accessible to several types of spectroscopic investigation - electron paramagnetic resonance (EPR) techniques being especially useful. The copper center is an *in situ* paramagnetic probe sensitive to various types of relevant perturbations. Divalent copper, Cu(II), is a $3d^9$ system with one unpaired electron in the valence shell. Cu(II) is a hexacoordinated system with six ligand molecules arranged around the copper center in a basically octahedral symmetry. The five-fold degeneracy of the 3d electron orbital manifold (holding a maximum of 10 electrons) is lifted by the field of these six ligands. Two orbital subsets result, t_{2g} and e_g; the unpaired electron is in the latter set. The energy states of Cu(II) and how these states are perturbed by the various ligands can be approached using the constructs of crystal field, ligand field and molecular orbital theory.

In most practical cases the symmetry of the coordinated Cu(II) is reduced to axial symmetry by distortion along a C_3 axis perpendicular to a plane containing the Cu center and four ligand electron donor sets. The minimal effect of the apically coordinated ligands (usually H_2O) on the spectroscopy of Cu(II)[1] results in the familiar square planar representation for the coordination configuration.

EPR spectra are quantitatively characterized (Figure 1) by the spectroscopic factor, g, and the hyperfine coupling constant, A. For axial symmetry, the spectroscopic g factor and the hyperfine coupling constant, A, are anisotropic with $g_x = g_y = g_\perp$, $A_x = A_y = A_\perp$ and $g_z = g_\parallel$, $A_z = A_\parallel$. Thus, the EPR spectrum experimentally observed (Figure 1) is characterized by a *perpendicular* portion and a *parallel* portion. The paramagnetism of Cu(II) systems is best observed at low temperatures, e.g. < 160°K; thus, the EPR spectra obtained in this study are powder-type spectra, i.e., the paramagnetic centers are randomly oriented (spatially) and are relatively immobile.

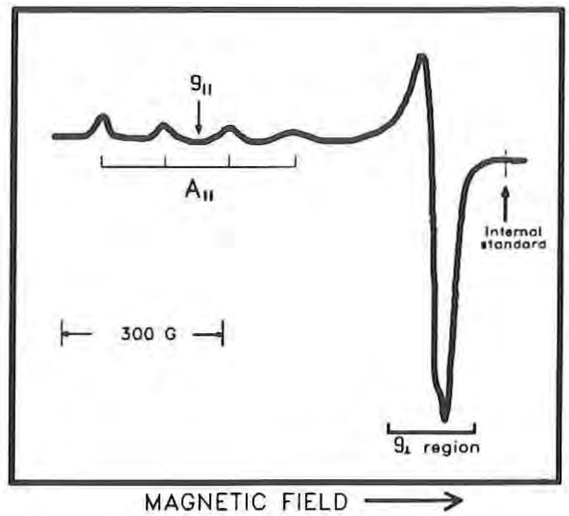

Figure 1. EPR spectrum of Cu(II) aquo complex in an ethylene glycol glass at 150°K

The line widths expected for powder spectra are further broadened by the unresolved contributions of the ^{63}Cu and ^{65}Cu isotopes in their natural abundance (69.2% and 30.8%, respectively). Due to the broad lines and small $A_\perp$ values, the perpendicular portion of the spectrum is unresolved. The occurrence of extra artifact lines at high field [2] makes even the determination of $g_\perp$ problematical. For these reasons, interpretation of the EPR spectra is based on the parallel portion.

The interaction between the ligand and the Cu(II) is manifested in both the g values and the hyperfine coupling constants. Deviation of the g value from the free electron value (g=2.0023) is effected by a spin orbital contribution from the ligand donor atoms. Thus, the nature of the ligand affects the g value, i.e., the "position" of the spectrum on the magnetic field axis. Information bearing on the type and "strength" of the Cu(II) - ligand bond is evidenced in the magnitude of the hyperfine coupling constant, the interaction of the unpaired electron with a nucleus having a net moment. In the present case, only the hyperfine interaction of the unpaired electron with the ^{63}Cu and ^{65}Cu nuclei (both nuclear spin 3/2 systems) is observed. The broadness of the lines precludes observation of superhyperfine interactions from, for example, ^{14}N. Although the magnetogyric ratios of the two copper isotopes differ by about 7%, separate contributions from each isotope could not be resolved and the observed lines are thus averages.

The ligands included in this study are N,N,N',N'-tetramethyl ethylenediamine (TMEN), glucosamine (GA), and 1-methoxy glucosamine (MGA). The structures of these ligands are:

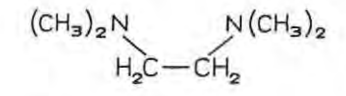

N,N,N',N'-tetramethyl
ethylenediamine
TMEN

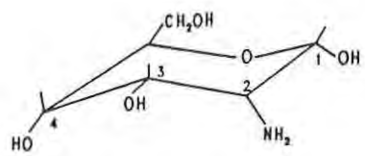

glucosamine
GA

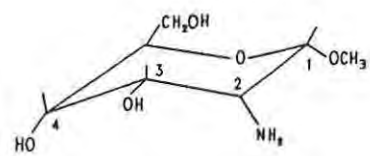

1-methoxy glucosamine
MGA

EXPERIMENTAL

EPR spectra were taken using a Bruker Model ER 200 D-SPC Electron Spin Resonance Spectrometer equipped with an ESP 1600 data system, an ER041MR microwave bridge and a BVT-1000 Variable Temperature controller. An ER 4103 TM X-Band Microwave Resonator, a flat cylindrical cavity resonating in the TM $_{110}$ mode with a nominal 9.8 GHz center frequency, was used. The magnet was equipped with 10-inch diameter pole faces with specially contoured caps to correct field inhomogeneities resulting from the presence of 1 cm diameter axial holes. Scans of ± 750 gauss centered at 3000 gauss (with a field resolution of 0.18 gauss) were normally made at a scan rate of 1.1 gauss/second (a nominal 20-minute scan). Longer scan times were occasionally required to achieve adequate signal/noise ratios. The normal 100 kHz modulation frequency was used with a modulation amplitude of 2 gauss (occasionally 5 gauss was used for extremely weak signals). Power saturation effects were not observed; consequently, a 20 mW excitation level was used throughout.

EPR measurements were made at two temperatures: 77°K and 150°K. The lower temperature was achieved using a special liquid nitrogen (LN_2) dewar. For the higher one, the BVT-1000 Variable Temperature system, which generates a stream of cold nitrogen gas by controlled boil-off from a reservoir of LN_2, was used. This cold gas stream is conveyed by a series of transfer dewars to an open ended sample-holding dewar situated in the microwave cavity. Temperatures in the range 145-150°K were the lowest that could be achieved and reliably maintained using this technique.

The EPR investigation of the binary Cu(II) chelate systems tetramethylethylenediamine (TMEN), glucosamine (GA), and 1-methoxyglucosamine (MGA) and the ternary systems Cu(II):TMEN:GA and Cu(II):TMEN:MGA was carried out in both a glassy matrix at 150°K and in a polycrystalline aqueous matrix at 77°K. Gradual freezing of sample solution maintained in a piece of thin quartz tubing (ca. 3mm internal diameter) using cold vapors from LN_2 produced a poly-microcrystalline sample. Rapid freezing of the dilute aqueous solutions by submersion in LN_2 resulted in highly fractured samples (due to the wide discrepancies in the expansion coefficients) which were useless for EPR analysis. Samples in a glassy matrix were produced from a 1:1 dilution of the aqueous sample with ethylene glycol. In this case, rapid submersion in LN_2 produced a glassy, transparent sample of near optical quality.

The EPR spectra obtained in the glassy system were in all cases dramatically better resolved (Figure 2) than corresponding spectra in a polycrystalline matrix.

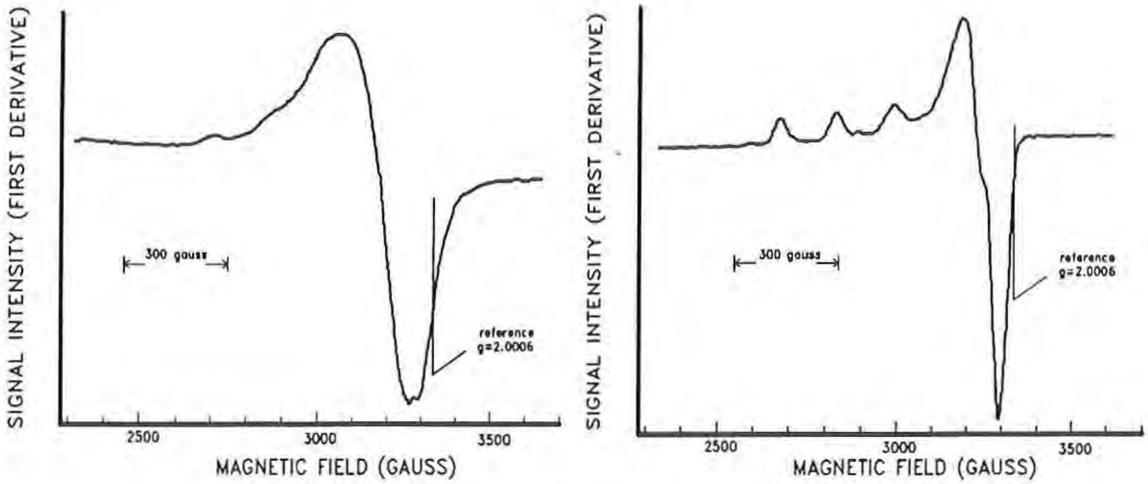

Figure 2. EPR spectra for Cu:TMEN:MGA, 1:1:1 at pH=6.5 in a polycrystalline matrix at 77°K (left) and in a 1:1 ethylene glycol glass matrix at 150°K (right).

An internal g-value standard was used in all measurements - a color center produced in the quartz tube by exposure to ionizing radiation (high energy (10 MeV) electrons or ^{60}Co γ-rays). The positive going lobe was used as the reference point. The g-value for this feature (g=2.0006) was determined by direct comparison (Figure 3) with the commonly used g-value standard 2,2-diphenyl-1-picrylhydrazyl free radical (DPPH), g=2.0037 [3].

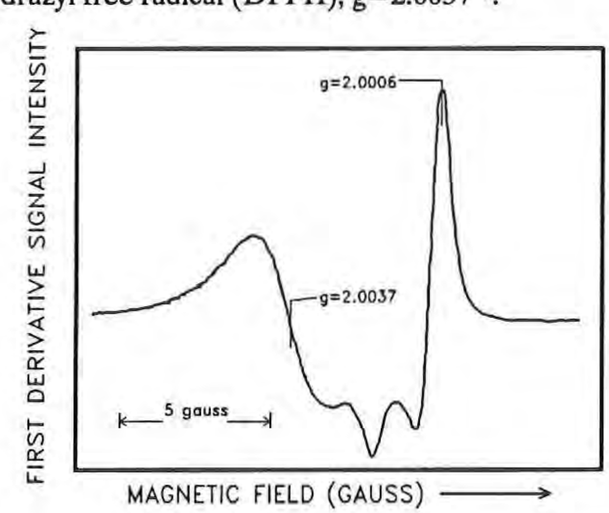

Figure 3. EPR spectrum of the color center in γ-irradiated quartz. The correction in g-value between DPPH (g=2.0037) and the positive lobe of the color center (g=2.0006) is illustrated. The DPPH contribution to the spectrum is at lower field and the asymmetric quartz color center part is at higher field.

The position of hyperfine features relative to this internal standard for the parallel portion of the experimental spectra was determined using spectrum manipulation features of the Bruker ESP 1600 data system. Features were assigned to groups or patterns based on comparison and contrast with selected basis spectra, e.g., $Cu^{+2}(aq)_6$ and TMEN 1:1 (pH=6.0 and pH=7.2).

The relative positioning of these patterns is shown in Figure 4. The value of $A_{\parallel}$ for each group was based on the two lowest field hyperfine features. Splittings between higher field features (when resolution permitted) was used as confirmatory data. From these measurements the center of the parallel region of the spectrum for that group was located and a simple algorithm calculated the g-value, $g_{\parallel}$, for this position. Figure 1 illustrates, graphically, the positioning of $g_{\parallel}$ for an uncomplicated spectrum in which only one species is present. As indicated previously, little useful quantitative information can be gleaned from the perpendicular (high field) part of the spectrum.

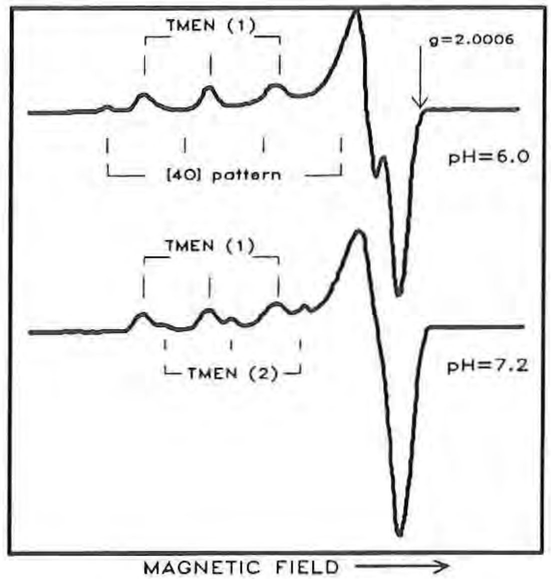

Figure 4. EPR spectra of TMEN 1:1 pH=6.0 & pH=7.2 in an ethylene glycol glass at 150°K. Base patterns TMEN (1) and TMEN (2) as well as the superposition of the Cu(II) aquo ([40] pattern) line positions are illustrated.

Solutions of the variously coordinated Cu(II) species were prepared using copper salts with the naturally occurring isotopic distribution: ^{63}Cu (69.2%) and ^{65}Cu (30.8%). Copper and ligands were mixed in the appropriate molar ratios, i.e., 1:1 or 1:2 for the binary chelates and 1:1:1 for the ternary, and the pH adjusted to the desired value.

RESULTS

The basic agreement of averaged $A_{\parallel}$ and $g_{\parallel}$ values derived from the EPR spectra obtained for both the polycrystalline matrix at 77°K and the 1:1 ethylene glycol glass matrix at 150°K confirm the absence of significant matrix effects. Consequently, the better resolved and more revealing spectra obtained for the glassy matrix at 150°K will form the basis for the ensuing analysis.

The several combinations of pH and metal:ligand molar ratios resulted in 10 binary systems and six ternary systems for EPR investigation. The results are summarized in Table 1. The ratio $g_{\parallel} / A_{\parallel}$ is cited as an indicator of the amount of tetragonal distortion[2]. Complexes with ratios > 135 cm are believed to exhibit such distortion. In our case (Table 1 and Figure 5) these are limited to the aquo-type species.

Table 1. Values of the EPR parameters $g_{\parallel}$ and $A_{\parallel}$ derived for the discernible species in binary and ternary Cu chelate systems involving TMEN, GA, and MGA at various pHs and molar ratios. $A_{\parallel}$ is in mK (10^{-3} cm^{-1}); the ratio $g_{\parallel}$ / $A_{\parallel}$ has units of cm.

Ligands	Ratio	pH	Peak	$A_{\parallel}$ (mK)	$g_{\parallel}$	$g_{\parallel}/A_{\parallel}$ (cm)
TMEN	1:1	6.0	-	17.9	2.298	128
TMEN	1:1	7.2	1	18.3	2.297	126
			2	19.0	2.247	118
GA	1:1	6.0	-	14.1	2.420	171
GA	1:2	6.5	1	18.7	2.308	123
			2	14.4	2.418	168
GA	1:2	7.0	1	19.3	2.303	119
			2	17.6	2.409	137
MGA	1:1	6.0	-	14.3	2.418	169
MGA	1:1	6.5	-	14.3	2.418	169
MGA	1:2	6.5	1	19.4	2.298	119
			2	15.0	2.410	161
MGA	1:2	7.2	-	17.6	2.299	131
MGA	1:2	8.0	-	20.8	2.255	109
TMEN-GA	1:1:1	6.5	1	18.2	2.298	126
			2	19.1	2.246	117
TMEN-GA	1:1:1	7.2	1	19.0	2.294	121
			2	19.7	2.241	114
TMEN-GA	1:1:1	8.0	1	18.7	2.302	123
			2	19.8	2.241	113
TMEN-MGA	1:1:1	6.5	-	18.1	2.297	127
TMEN-MGA	1:1:1	7.5	1	17.6	2.298	131
			2	19.6	2.247	114
TMEN-MGA	1:1:1	8.0	1	17.7	2.296	130
			2	19.1	2.250	118

Ideally, the EPR results would be used to determine parameters appropriate to crystal field or ligand field models and thereby provide a quantitative measure of the Cu-ligand interaction. Powder-type data, such as our spectra provide, do not have sufficient resolution or detail to support this approach[4]. The most productive treatment is that of J. Peisach and W.E. Blumberg[1]. Their empirical approach based on an extensive survey of copper complexes uses plots of $g_{\parallel}$ versus $A_{\parallel}$ to relate the independent changes in $g_{\parallel}$ and $A_{\parallel}$ to changes in the nature of the complexation.

A summary of all the data, both binary and ternary systems, in a Peisach/Blumberg style plot (Figure 5) of $g_{\parallel}$ versus $A_{\parallel}$ reveals clustering in three g value regions - $g_{\parallel} = 2.24\text{-}2.25$, $g_{\parallel} = 2.30$, and $g_{\parallel} = 2.40\text{-}2.42$. The Cu(II)aquo complex is in this last cluster. This clustering would, at first glance, indicate three basic types of complexation. A more detailed analysis of each group as well as the significance of the intergroup differences requires several interpretative guidelines. A shift in the g factor towards a lower value indicates increased contribution from a more "electron rich" donor set, such as nitrogen, to the Cu-ligand interaction. The effect of decreasing charge within a given donor set is to shift the g value downward and to increase the hyperfine coupling energy - an upward and to the left offset on the plot.

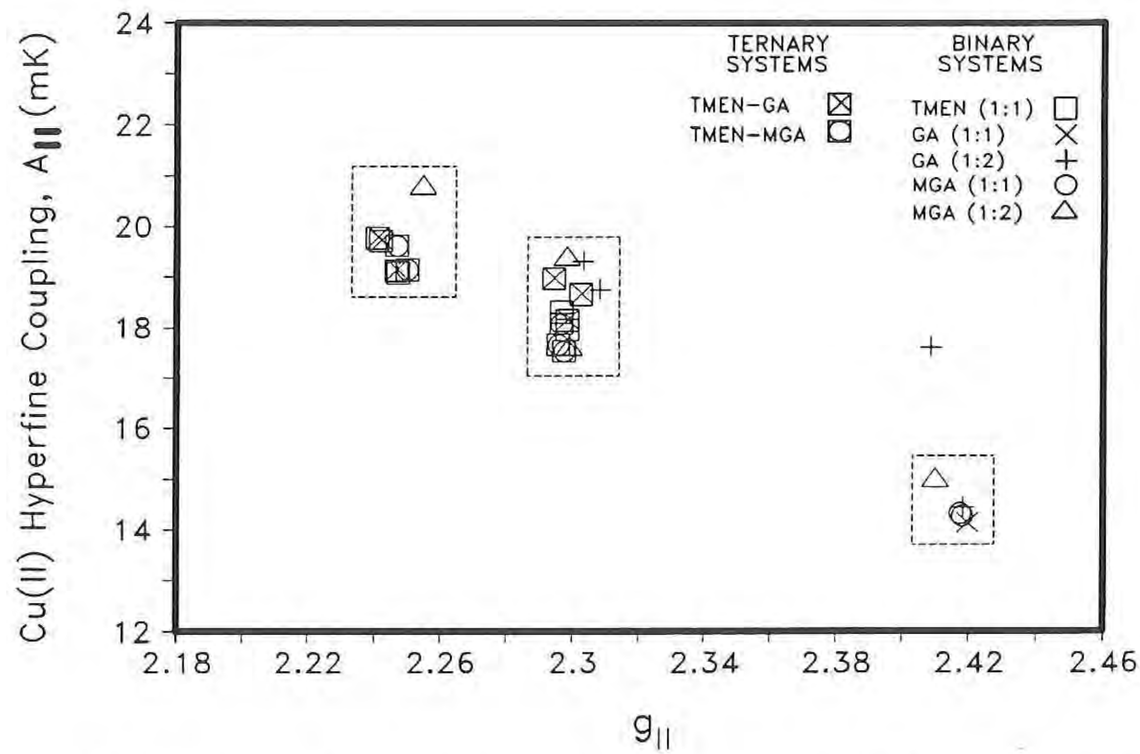

Figure 5. Plot of $g_{\parallel}$ versus $A_{\parallel}$ for all the binary and ternary systems studied. The hyperfine coupling constant is in mK (10^{-3} cm^{-1}) .

The Binary Systems. The results for the binary systems Cu:TMEN (1:1), Cu:GA (1:1), Cu:GA (1:2), Cu:MGA (1:1), and Cu:MGA (1:2) are summarized as a Peisach/Blumberg style plot in Figure 7. With the pH variants, there are 10 such systems approximately 50 percent of whose EPR spectra indicate more than a single species present. The ligands are all bidentate; that is, each ligand molecule has two atoms that can serve as potential electron donors to the copper-ligand interaction - two nitrogens for TMEN and a nitrogen and oxygen for GA and MGA. The inclusion of MGA as a ligand provides the opportunity to distinguish between hydroxyls in the C-1 and in the C-3, C-4 positions and their involvement in the ligation. Free of the constraints imposed by consideration of pH and metal to ligand ratio, there are a multitude of bonding possibilities depending on which ligand molecules can be involved in the bonding and which donor atoms can contribute.

The scheme in Figure 6 identifies structures for some of the potential complexes [5,6,7] as the pH of the system increases. While the pH and molar ratio regimes used restrict the number of possibilities for a given chelate system, a distribution of species exists under most experimental conditions. These different species are reflected in the EPR spectra as distinctive patterns.

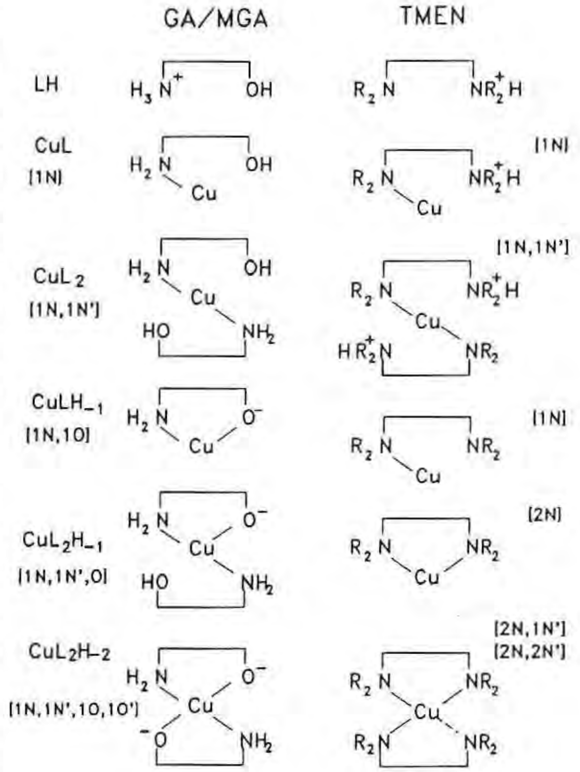

Figure 6. Some chelate structures for binary Cu:GA, Cu:MGA, and Cu:TMEN systems. The designation in the brackets ([1N]) is the donor set.

The cluster in the $g_{\parallel}$ =2.42, $A_{\parallel}$ =14-16 mK region for the pH=6.0 and 6.5 is due to the aquo-type complexes. These complexes are observed for several systems - Cu:GA(1:1), Cu:GA(1:2), Cu:MGA(1:1), and Cu:MGA(1:2). For the Cu:GA(1:1) and Cu:MGA(1:1) these are the sole species observed. Species distribution data based on potentiometric titration techniques [5,6,7,8] indicate that from 50-90% of the metal is present in an unchelated form, i.e., the aquo complex in this pH range. Even for the TMEN system at pH 6.0, H_2O is able to compete for the Cu(II) and the aquo complex is observed (Figure 4).

For TMEN (1:1) at pH=7.2, only nonaquo species are observed - two species, in fact. The pattern for one species is the same as observed at pH=6.0. At this lower pH, the species is predominantly due to the donor set [1N,1N'], i.e., coordination with two TMEN molecules through the [NH_2] donor set. At the higher pH (7.2) contributions from a mixture of species, including the donor set [2N,1N'], are possible. The EPR parameters do not allow us to distinguish among these species. The second species at pH=7.2, however, is consistent with the [2N,2N'] donor set. The offset towards both lower g-value and higher hyperfine coupling energy indicates involvement of four nitrogens.

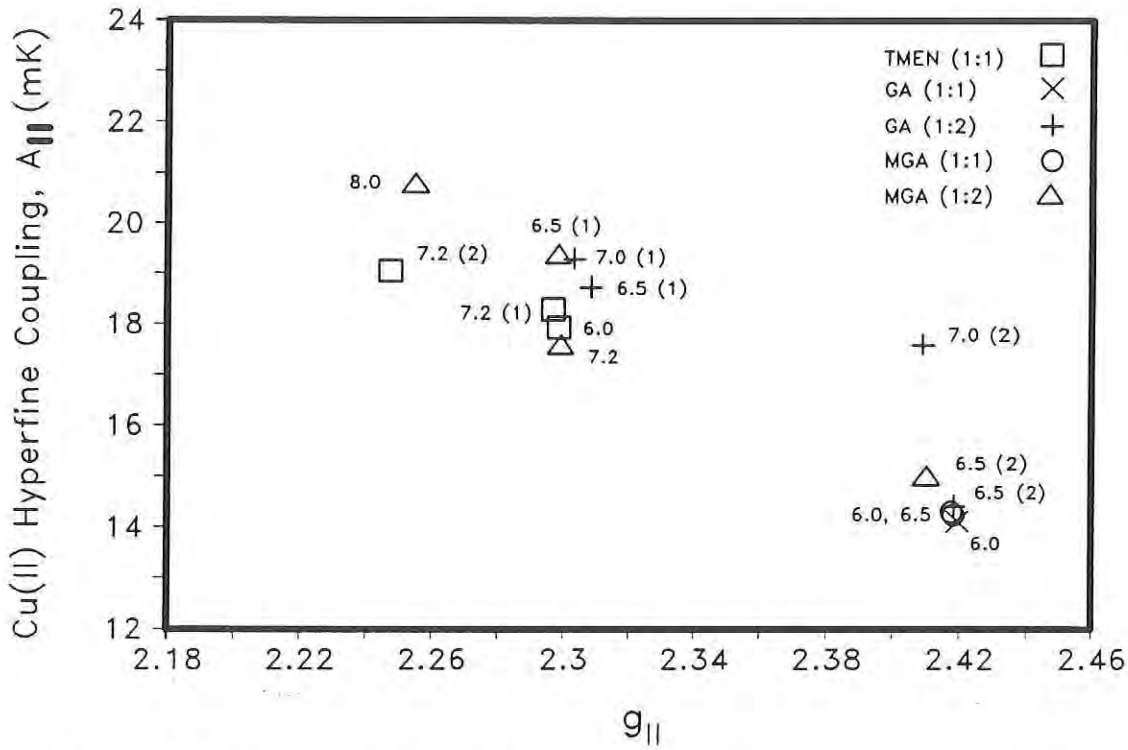

Figure 7. Plot of $g_{\parallel}$ versus $A_{\parallel}$ for the binary systems. The hyperfine coupling constant is in mK (10^{-3} cm^{-1}). Each entry has been annotated with its pH and EPR pattern (in parentheses) as designated in Table 1.

For GA(1:2) at the higher pHs (6.5 -7.0) there is a second species present. The $g_{\parallel}$ =2.308, $A_{\parallel}$ =18.7 mK (pH=6.5) and $g_{\parallel}$ =2.303, $A_{\parallel}$ =19.3 mK (pH=7.0) are consistent with the EPR parameters reported by Micera et al.[6] for the CuL_2 species. The [NH_2] donor sets are from different GA molecules. The species distribution data differ on the exact amounts of these species present. The other possibility is the $CuLH_{-1}$ species - a [1N,1O] donor set. Whether the slightly higher $g_{\parallel}$ and $A_{\parallel}$ values (compared to those for TMEN) support this interpretation is problematic. The parameters from the Peisach/Blumberg plots for these two donor sets[1] predict little difference in either the value for $g_{\parallel}$ or the interaction energy. While CuL_2 is the major contributor in this general pH range[6], CuL_2H_{-2} may also present at the higher end of the range (pH 7.0). Our results do not, however, show the shift in $g_{\parallel}$ predicted for this species. A small contribution from this species may account for the slightly higher $A_{\parallel}$ at pH 7.0. It should be noted and emphasized that two species with different $g_{\parallel}$ values but present in disproportionate amounts may be manifested in the EPR spectrum as slightly broader, but unresolved lines.

Results for the MGA systems qualitatively parallel those for GA. At the lower pHs (6.0 and 6.5), the MGA(1:1) spectra are attributable solely to the aquo species. For the MGA(1:2) system at pH 6.5, the aquo is one contributing species; the other is probably CuL. The spectra of the MGA(1:2) series are considerably less intense and resolved than for any of the other systems. This situation is a caveat with regard to the precision and accuracy of the $g_{\parallel}$ and $A_{\parallel}$ determinations.

At the higher pHs (7.2 and 8.0), only one species can be clearly discerned. The resolution is, however, so poor that pursuing an interpretation based on the $g_{\parallel}$ and $A_{\parallel}$ shifts is not merited.

__The ternary systems.__ The results for the two ternary systems Cu:TMEN:GA (1:1:1) and Cu:TMEN:MGA (1:1:1) are summarized in the Peisach/Blumberg style plot in Figure 8. The data cluster in two fairly narrow regions around $g_{\parallel} = 2.3$ and $g_{\parallel} = 2.25$. The $A_{\parallel}$ values are also fairly narrowly clustered.

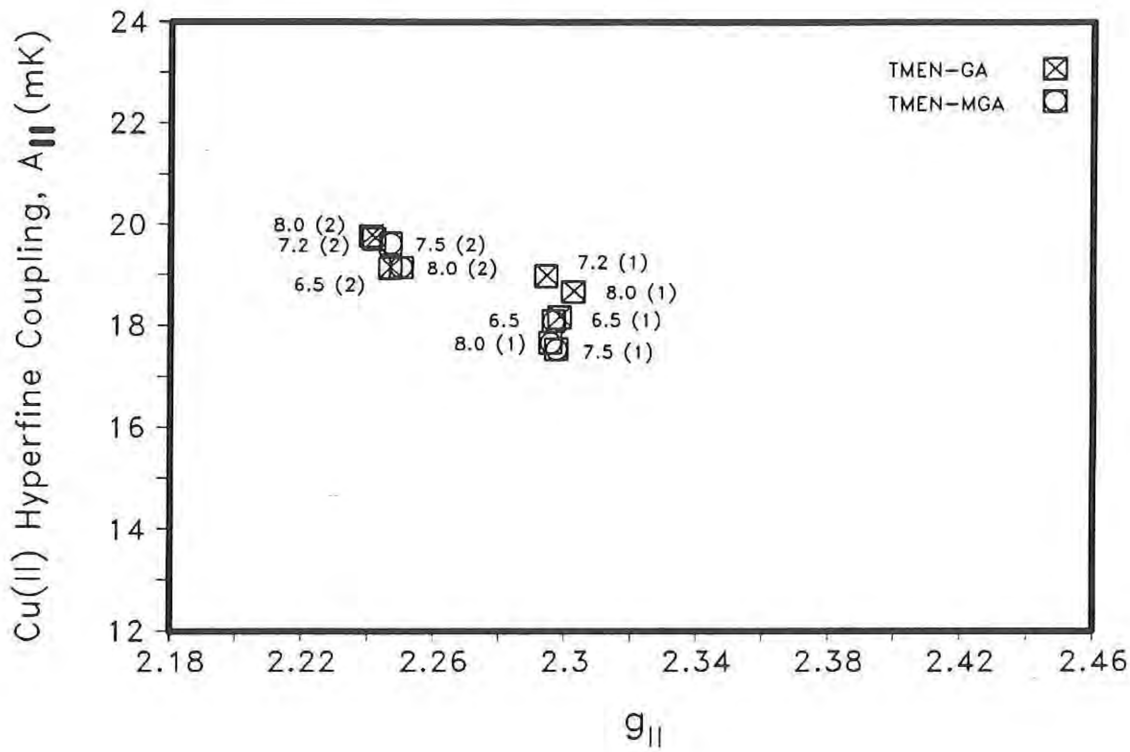

Figure 8. Plot of $g_{\parallel}$ versus $A_{\parallel}$ for the ternary systems. The hyperfine coupling constant is in mK (10^{-3} cm^{-1}). Each entry has been annotated with its pH and EPR pattern (in parentheses) as designated in Table 1.

Both ternary systems are characterized by two species; or, to be more precise, by two collections of species with comparable EPR parameters. The relative amount of each species is pH dependent. As shown in Figure 9, pattern (1) with $g_{\parallel} = 2.294 - 2.302$ and $A_{\parallel} = 17.6 - 19.0$ mK predominates at low pH. As the pH increases, pattern (2) ($g_{\parallel} = 2.241 - 2.250$, $A_{\parallel} = 19.1 - 19.8$ mK) assumes dominance. The shift in the average $g_{\parallel}$ from the 2.30 to the 2.25

region and the slight increase in the average $A_{\parallel}$ is consistent with a change in donor sets from [2N]/[3N] to [4N]. The involvement of a [2N,2O] donor set from CuL_2H_{-2} is also consistent. Except for the aquo complexes, the contributing species at the lower pHs may, in principle, be any combination of those discussed for the binary systems. The completely coordinated mixed ligand case, i.e., one TMEN molecule ([2N]) and one GA molecule ([1N,1O]), a [3N,1O] donor set, would also be in the ensemble of species at $g_{\parallel} = 2.30$. The effect of increasing pH favors both the involvement of more nitrogen donor sets from TMEN and the aforementioned potential contribution from CuL_2H_{-2}. The ternary system may be, in a simplistic view, a source of nitrogen donor sets. The species distribution data [5,8] (obtained, again, by potentiometric titration methods) indicates a shift from a primarily TMEN-dominated ligation at lower pH to a mixed ligand complex at the higher pHs.

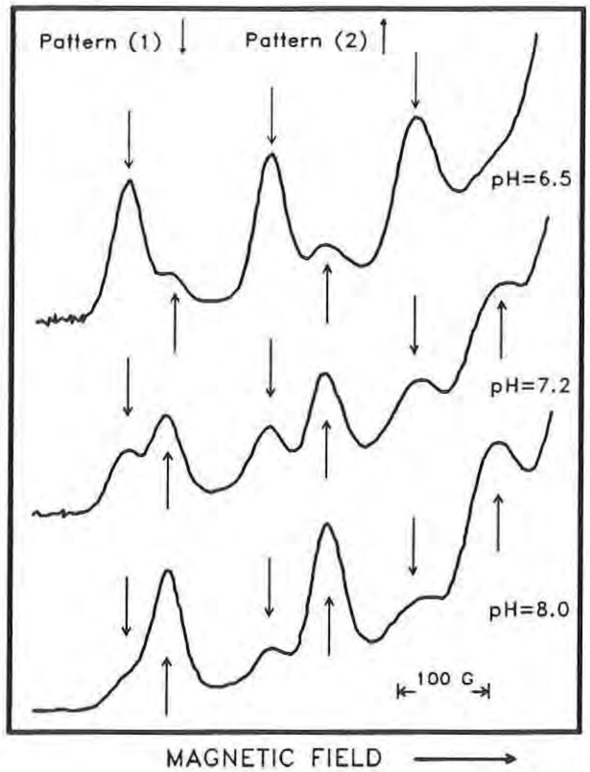

Figure 9. The change in the species distribution with pH for the ternary system Cu:TMEN:GA as reflected in the EPR spectra. This figure shows only the low field ($g_{\parallel}$) part of the spectrum. Pattern (1) is indicated by ↓, pattern (2) by ↑.

The distribution among the two EPR pattern types (based on peak height measurements) for both Cu:TMEN:GA and Cu:TMEN:MGA is given in Table 2.

Table 2. Distribution of species for the Cu:TMEN:GA and Cu:TMEN:MGA ternary systems as derived from the EPR spectra.

	TMEN:GA		TMEN:MGA	
pH	% pattern 1	% pattern 2	% pattern 1	% pattern 2
6.5	80	20	95	5
7.2	40	60	-	-
7.5	-	-	46	54
8.0	18	82	34	66

In contrast to the binary system Cu:MGA(1:2), EPR spectra for the ternary system involving MGA (Cu:TMEN:MGA) were of similar good intensity and quality to those involving GA.

DISCUSSION

The spectroscopic identification and characterization of specific species are relevant to a consideration of the reactivity of Cu(II) chelate systems only to the degree that identification and characterization illuminate our understanding of the factors controlling that reactivity. The hydrolysis/detoxification of phosphonate chemical agents by Cu(II) complexes, even in solution, undoubtedly depends on many factors. One of the authors (K.S. Rajan) has reported [5,8] thermodynamic stability constants for a number of Cu(II) chelates and the rates of hydrolysis of chemical agents by them. The relative hydrolysis rates of GB at pH=7.2 by the systems considered in this study are reported as:

Chelate system	Normalized Hydrolysis Rate
Cu:TMEN:MGA (1:1:1)	1.0
Cu:TMEN (1:1)	0.79
Cu:TMEN:GA (1:1:1)	0.73
Cu:GA (1:1)	0.31
Cu:MGA (1:1)	0.24
Cu:MGA (1:2)	0.22
Cu:GA (1:2)	0.22

Except for TMEN (1:1) there is a marked contrast in rates between the binary and ternary systems. The order of reactivity between the two ternary systems is in the same direction as contribution of the pattern (1) species to the total distribution (Table 2). At pH=7.2 the

Cu:TMEN:MGA pattern (1) contribution is estimated at 57% of the total. This is 42% greater than the pattern (1) content in the Cu:TMEN:GA system (40%). The hydrolysis rates differ by 37%. It would thus seem that the transition from the [2N]/[3N] donor set cluster to the fully coordinated [4N] is a factor. TMEN, it will be recalled (Figure 4), exhibited the partition between patterns (1) and (2) as a function of pH. At pH=7.2 the predominant species was pattern (1). The pattern (1) species in both TMEN and the ternary systems is characterized by an average $g_{\parallel} / A_{\parallel}$ ratio of 126 cm. The average ratio for the pattern (2) species is slightly, but consistently, lower - 115 cm. Thus, there also appears to be a slight difference in distortion between the two species.

The complexation site for Cu(II) in the biopolymer chitosan is characterized[2] by $g_{\parallel} = 2.244$ and $A_{\parallel} = 18.5$ mK ($g_{\parallel} / A_{\parallel} = 121$ cm). These values are very close to our pattern (2) and consistent with a [4N] donor set. That our pattern (1) type species exhibit the enhanced reactivity would indicate the need for an unencumbered coordination site to support the transition state.

Most of the questions associated with the correlation of species (or ensemble of species) with the observed EPR parameters have already been discussed and will receive no additional discussion. Other spectroscopies can be used to augment and further illuminate the characterization offered here. However, EPR spectroscopy is in a unique position to be able to study the Cu(II) centers in all their divergent physical environments. Thus, the present characterization is a basis with which to compare and contrast the behavior of Cu(II) in these more relevant matrices.

REFERENCES

1. J. Peisach and W. E. Blumberg, Arch. Biochem. & Biophy., 165, 691-708, 1974.
2. S. Schlick, Macromolecules, 19 (1), 192-195, 1986.
3. J. E. Wertz and J. R. Bolton, ***Electron Spin Resonance***, 1972, McGraw-Hill, Inc.
4. J. F. Boas, J. R. Pilbrow, and T. D. Smith, ***Biological Magnetic Resonance*** (ed. L. J. Berliner & J. Reuben), Chapter 7, 1978, Plenum Press.
5. K.S. Rajan, S. Mainer, J.E. Walker, *et al.*, ***Proceedings of the 1989 Conference on Chemical Defense Research***, Chemical Research, Development and Engineering Command, in preparation.
6. G. Micera, S. Deiana, A. Dessi, *et al.*, Inorganica Chimica Acta, 107, 45-48, 1985.
7. A. Pusino, D. Droma, P. Decock, *et al.*, Inorganica Chimica Acta, 138, 5-8, 1987.
8. K.S. Rajan, private communication.

TITLE: Effect of Faults on Organic Vapor Permeation Through Fabric
* Donald Rivin, Dr., Cyrus E. Kendrick, Mr., and Martin Katz, Mr.

ABSTRACT: For Chemical Protective Fabric (CPF) to quantitatively scavenge agent or simulant vapor from a moving air stream, intralayer rates of diffusion and adsorption must be significantly faster than the vapor transport rate as determined by the transverse linear velocity of entrained vapor molecules. This requirement is satisfied for intact CPF layers under a wide range of use and test conditions.

Adequate protection is attained even in the presence of faults (e.g. holes, tears, loose or open seams) provided that the smallest dimension of the fault does not exceed a minimum size determined by the effective rate of the adsorption process. The limits of this critical dimension are explored via mass-transport and kinetic analyses of dynamic simulant sorption for CPF samples containing predetermined fault arrays. Test samples include polyurethane foam laminate impregnated with activated carbon (mean diameter ca. 4 μm), and protective fabric containing clusters of porous carbon spheroids (mean diameter ca. 500 μm) bonded in a repeating pattern to a textile support.

* BIOGRAPHY OF PRESENTER: Donald Rivin

PRESENT ASSIGNMENT: Chief, Materials Section, Materials Research and Engineering Division, Individual Protection Directorate, Natick Research, Development and Engineering Center, Natick, MA

PAST EXPERIENCE: Corporate Research Fellow, Cabot Corporation, Billerica, MA

DEGREES HELD: B.A., M.A., Ph.D. (Chemistry), Columbia University, New York, NY

Effect of Faults on Organic Vapor Permeation Through Fabric

Donald Rivin, Dr., Cyrus Kendrick, Mr., and Martin Katz, Mr.

Introduction

At present, all permeable fabrics which provide protection against exposure to toxic agents contain activated carbon as a nonselective, high capacity adsorbent of organic vapors. The carbon is distributed uniformly throughout the fabric by impregnation or surface coating techniques. Under conditions of use, the rate of adsorption is fast compared to the velocity of vapor transport, so that no premature breakthrough occurs if the fabric is intact and free of faults; e.g., tears, punctures and open seams. Even when such faults are present, toxic vapor penetration will not occur provided that the opening does not exceed a critical dimension determined by the adsorption properties of the carbon, fabric construction, vapor concentration, and air speed.

Dynamic adsorption of a toxic vapor or simulant from an air or nitrogen carrier stream is used for laboratory evaluation of chemical protective fabrics. For example, in the standard method (1) described in MIL-C-43858B, a low concentration of carbon tetrachloride in nitrogen is pulled through 100 cm^2 of fabric at a rate of 1 L/min until breakthrough of the simulant is observed. Newer, improved dynamic adsorption procedures employ different methods for vapor delivery, control, and detection, but retain similar flow conditions (2,3). Although a linear velocity of 10 cm/min (0.004 mph) impinging on the fabric surface is much less than wind speeds encountered in the field, the laboratory conditions are more severe in that all of the gas is forced through the fabric, whereas the resistance due to the wearer's body and multiple layers of fabric substantially reduces wind penetration in use. Furthermore, the gas velocity through openings in the fabric would be expected to be quite high at the constant flow (variable pressure differential) conditions in the laboratory.

In order to test the effect of faults on vapor penetration, samples of a carbon impregnated, polyurethane foam fabric containing well-characterized perforation arrays were exposed to a simulant/air stream over a three-fold range of flow rates. In addition, two experimental fabrics which have a relatively large separation between adsorption units were also examined.

Materials and Methods

Fabrics

Type III chemical protective fabric manufactured commercially as described in MIL-C-43858B is a polyester polyurethane open-cell foam laminated to a nylon tricot backing and impregnated with Calgon Type PCB-G powdered activated carbon (100 g/m^2) in an acrylic latex binder. Three lots of fabric differing mainly in resistance to air flow are used in this study. Perforated samples were produced by first drilling the desired array of holes ($d \leq 3.1$ mm) in a solid template then penetrating through the fabric into the template using a rod having a diameter almost equal to the hole size in the template. Larger diameter openings were cut with a cork borer. Perforation arrays used in this study are illustrated in Figure 1, and described quantitatively in Table 1. Single perforations of 7.6, 8.0, and 8.8 mm are situated in the center of the 100 cm^2 fabric disk.

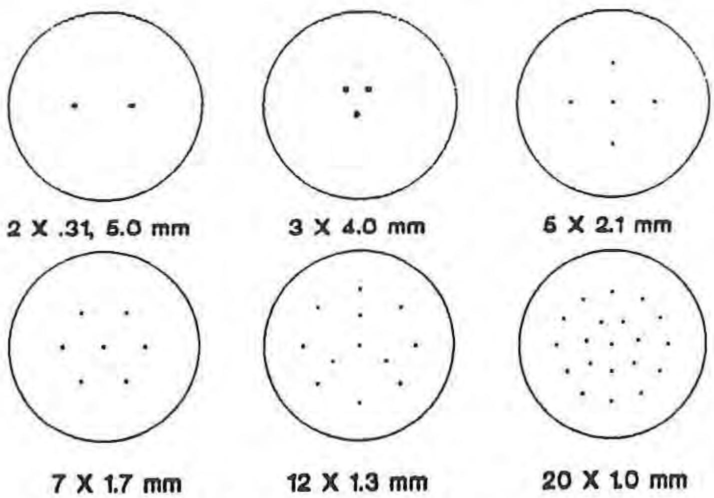

FIGURE 1. Perforation Arrays in Type III Fabric

Table 1
Perforation Arrays in Type III Fabric

Array ID	Diameter, mm	Perforations	Total Area, cm^2
1	1.0	20	0.16
2	1.3	12	0.16
3	1.7	7	0.16
4	2.1	5	0.17
5	3.1	2	0.15
6	4.0	3	0.38
7	5.0	2	0.40
8	7.6	1	0.45
9	8.0	1	0.51
10	8.8	1	0.61

An experimental Saratoga(r) fabric obtained from Blucher GmbH contains a layer of activated carbon spheroids sandwiched between layers of cotton knit. In the sample designated Saratoga V941, 0.4-0.7 mm diameter carbon beads are adhesively bonded to the textile backing, in a repeating ABAB sequence of 1.6 mm diameter clusters with an average edge-to-edge spacing of 0.86 mm. This array and that produced by physically removing alternate clusters after softening the adhesive by heating with a soldering iron, are shown in Figure 2. The adsorbent layer in the original composite fabric consists of carbon spheroids (120 g/m^2) partially embedded in islands of adhesive (130 g/m^2). Removal of alternate clusters left the adhesive intact with visible residual carbon in most adhesive regions. Total activated carbon on the modified fabric is 87 g/m^2. Based on cluster size and geometry, open area between adsorbent clusters constitutes about one-third of the exposed surface for the original fabric and less than two-thirds of the surface after removal of half of the clusters. However, this modification causes an almost four-fold change in cluster spacing, with the intercluster distance of 0.86 mm increasing to a separation of 3.3 mm between linear staggered cluster groups.

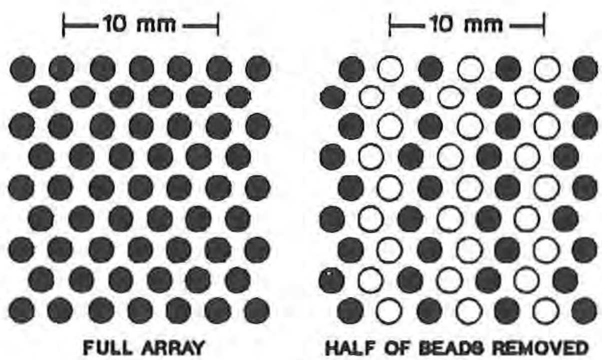

FIGURE 2. Carbon Spheroid Cluster Arrays

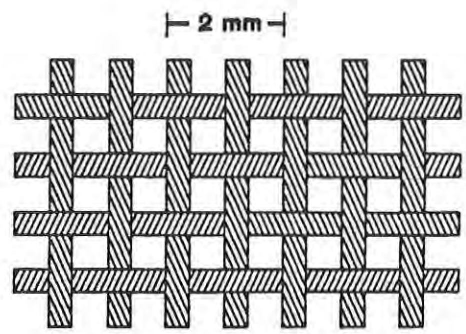

FIGURE 3. Activated Carbon Fabric

An experimental Toyobo fabric woven from activated carbon fibers was also investigated. As seen in Figure 3, this fabric consists of 0.4 mm yarn in a plain weave with 0.6 mm X 0.6 mm interstices. Each strand of yarn is made up of a twisted bundle of 10 µm activated carbon fibers, leaving many free ends projecting into the interstitial area.

Vapor Challenge System

Die-cut fabric disks (100 cm^2) were exposed to trichloroethylene (TCE) vapor in dry air at 32°C in the dynamic adsorption system (DAS) outlined in Figure 4. Volumetric flow rates ranged from 0.67 to 2.0 L/min, with TCE concentrations of 10-12 mg/L. Effluent TCE was monitored continuously with a photoionization detector. Details of the DAS and the adsorption procedure were presented recently (4).

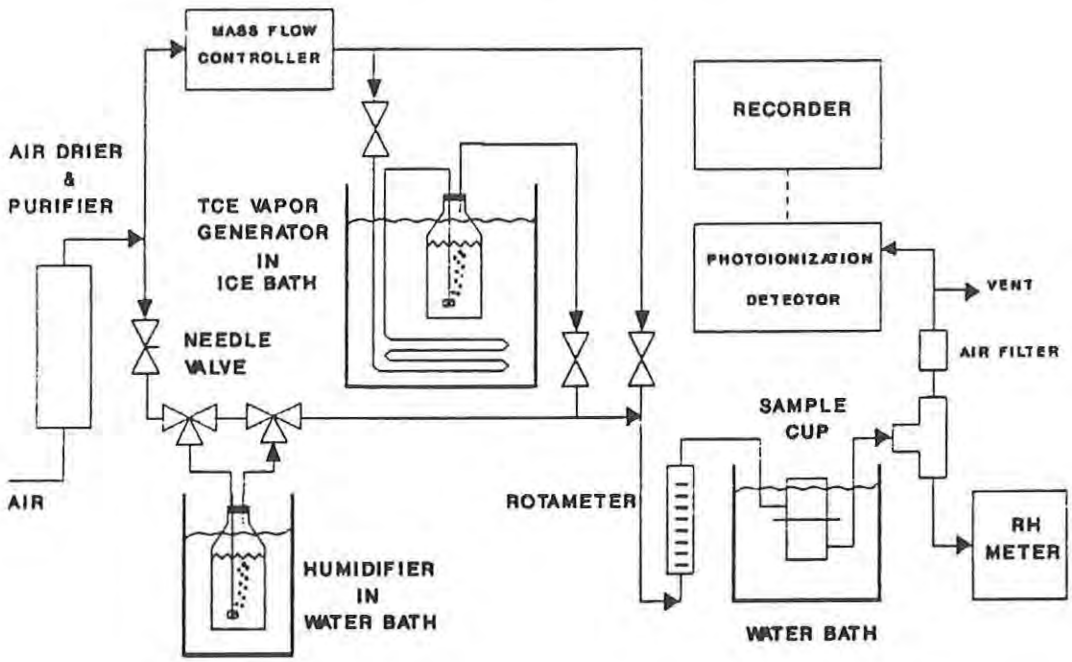

FIGURE 4. Dynamic Adsorption System

Measurement of Air Permeation Rates

Precise determination of the total open area in perforated fabrics is difficult for small and irregularly shaped openings. For this reason air permeability was investigated as a means of determining the area of low air resistance faults. The rate of air flow through a perforated fabric is

$$Q = Q_f + Q_p = U_f A_f + U_p A_p \qquad (1)$$

where Q, U, and A are the flow rate, linear velocity and area associated with fabric, f, and perforations, p. Flow additivity was confirmed by comparing the permeability of perforated and intact fabric specimens, to that of cardboard templates containing identical perforation arrays. All air permeation determinations were carried out in accordance with ASTM Standard Test Method D737-75. In separate experiments with fabric and with templates, it was shown that air permeation conforms to the well-known orifice equation, with flow rate, directly proportional to test area and to the square root of the pressure differential. Thus air permeation velocity for a perforated fabric at manometer reading, R, is given by

$$U = (C_f A_f + C_p A_p)\ R^{1/2} \qquad (2)$$

Permeation constants for a test area of 38.5 cm^2 at 0.5 inch water are C_p = 37.6 for open areas, based on the mean air rate (cm^3/sec cm^2 or cm/sec) through templates, and for lots A, B and C of Type III fabric, C_f = 2.59, 2.45 and 2.05, which correspond to air permeation rates of 70.5, 66.8 and 55.9 cm/sec, respectively. When air permeation rates calculated from eq.2 are compared to measured rates for perforated specimens in Table 2, the agreement is sufficient to support the visual measurement of A_p, but shows deviations which are probably due to variation in C_f between specimens. Air permeation constants for the fabrics were obtained for specimens cut from fabric areas adjacent to those which were perforated, and may differ slightly in air resistance.

Table 2
Air Permeation of Perforated Type III Fabric

Array ID	Fabric	Permeation, cm/sec	
		Calc.	Obs.
1	A	74.7	75.2
5	A	74.2	72.6
6	B	76.2	75.7
7	B	76.7	77.2
9	A	83.3	83.8
9a	C	68.6	69.1
10	C	71.1	71.6

For the constant flow conditions of the dynamic adsorption experiments, the pressure drop across the exposed fabric area (100 cm^2) in the DAS specimen holder was determined using a Dwyer Microtector, which is sensitive to pressure differences of one milli-inch water. Even so, no pressure differential could be detected for a volumetric flow of one liter per minute. However, when the exposed area was reduced to 6.6 cm^2, pressure drops of 6.0, 9.4, 14 and 19 milli-inches water at 0.67,1.0,1.5 and 2.0 L/min were obtained for a nonperforated fabric. It follows that for the same flow range under normal DAS operating conditions, the 100 cm^2 fabric area is subjected to a pressure differential of only 0.4 to 1.2 milli-inches.

Characteristic Breakthrough Curves

When a chemical protective fabric is challenged with an organic vapor in an inert carrier gas, no vapor is detected in the effluent stream for

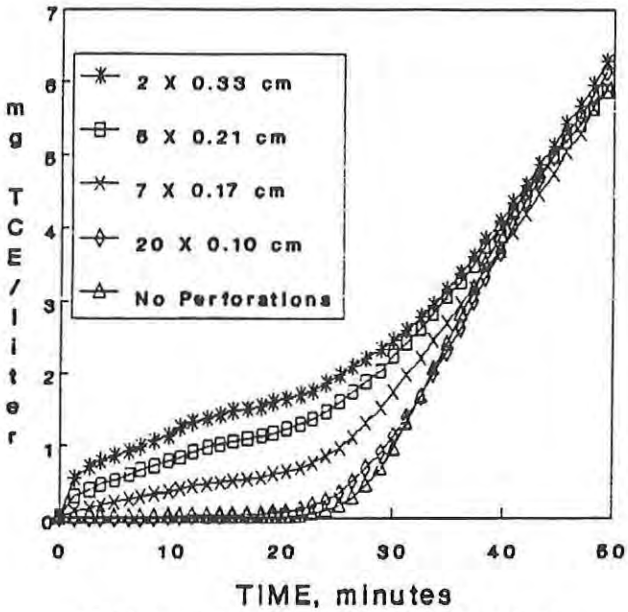

FIGURE 5. BTC for Perforated Type III Fabric at 1 l/min

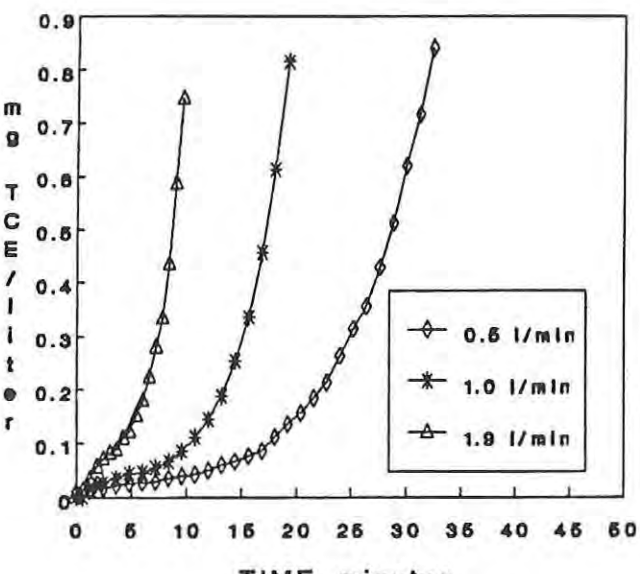

FIGURE 6. BTC for Activated Carbon Fabric

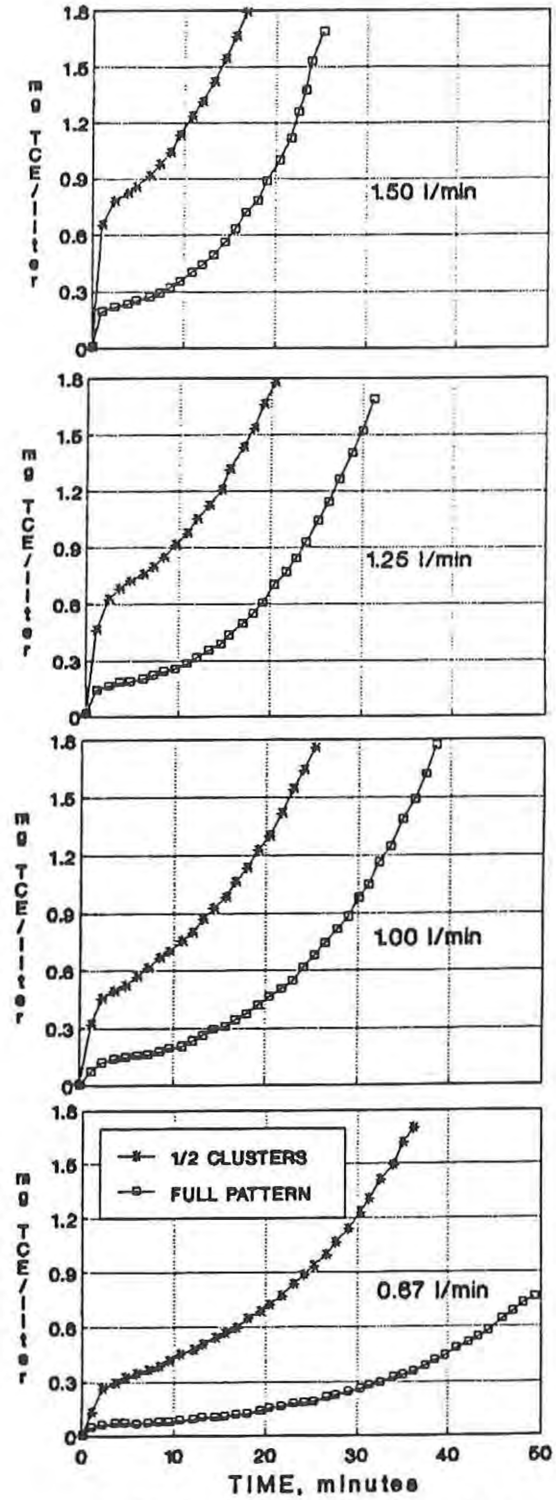

FIGURE 7. BTC for Carbon Spheroid Cluster Fabric

the period of time required for the adsorption wave to emerge from the opposite surface of the fabric (5). The resultant sigmoid breakthrough curve (BTC) is characterized by a breakthrough time, t_b, at a preselected effluent vapor concentration, and by kinetic rate and capacity parameters.

If sufficiently large openings or equivalent faults are present in a generally homogeneous adsorbent fabric, an initial step occurs in the BTC followed by an intermediate period of moderately increasing concentration, which precedes emergence of the isotropic adsorption wave. This behavior is demonstrated in Figure 5 for a series of constant area (15-17 mm^2) perforation arrays composed of 1.0 to 3.1 mm openings in Type III fabric.

A stepped BTC is also observed for fabrics containing adsorbent-free regions inherent in their structure. This is shown as a function of volumetric flow rate in Figure 6 for a plain weave activated carbon fiber fabric, and in Figure 7 for a Saratoga fabric constructed of clusters of activated carbon spheroids in a symmetrical array with a uniform separation distance of 0.86 mm. The effect on the BTC of increasing adsorbent separation by removing alternate clusters from the surface also is shown in Figure 7.

Mechanism For Premature Breakthrough

Although a similar mechanism is responsible for premature vapor penetration with all three materials, we will discuss this phenomenon in detail for Type III fabric, because of its importance and the complexity of its stepped BTC. Stages in the dynamic adsorption process in the vicinity of a fabric fault are keyed to the corresponding points on a representative BTC for perforated Type III fabric, in Figure 8. The diagrams on the right hand side of Figure 8 illustrate the status of vapor transport and adsorption processes in the vicinity of the perforation, in relation to the BTC. Arrows represent vapor flow vectors, and the shaded area denotes areas of the fabric in which the vapor loading of the activated carbon is at or near its adsorption capacity.

Upon initial exposure of the fabric to the challenge stream t_o, vapor impinges on the face of the fabric and on the walls of the perforation. For relatively narrow openings, all of the vapor enters the fabric matrix via molecular diffusion and no vapor is found in the effluent. As the perforation diameter increases, mass transfer to the walls is essentially unchanged but an increasing amount of vapor escapes adsorption and produces a step increase to concentration C_i at time t_i. The lag of 1-2 minutes between t_o and t_i is due mainly to the time required for the gas to flow from the sample cell to the photoionization detector. Continued diffusion of vapor through the wall of the perforation creates a circumferentially expanding area in which adsorbent particles become saturated with vapor. A region forms behind this transverse adsorption front through which challenge vapor can pass from the face to back of the fabric with only partial loss to adsorption. During this phase, which is

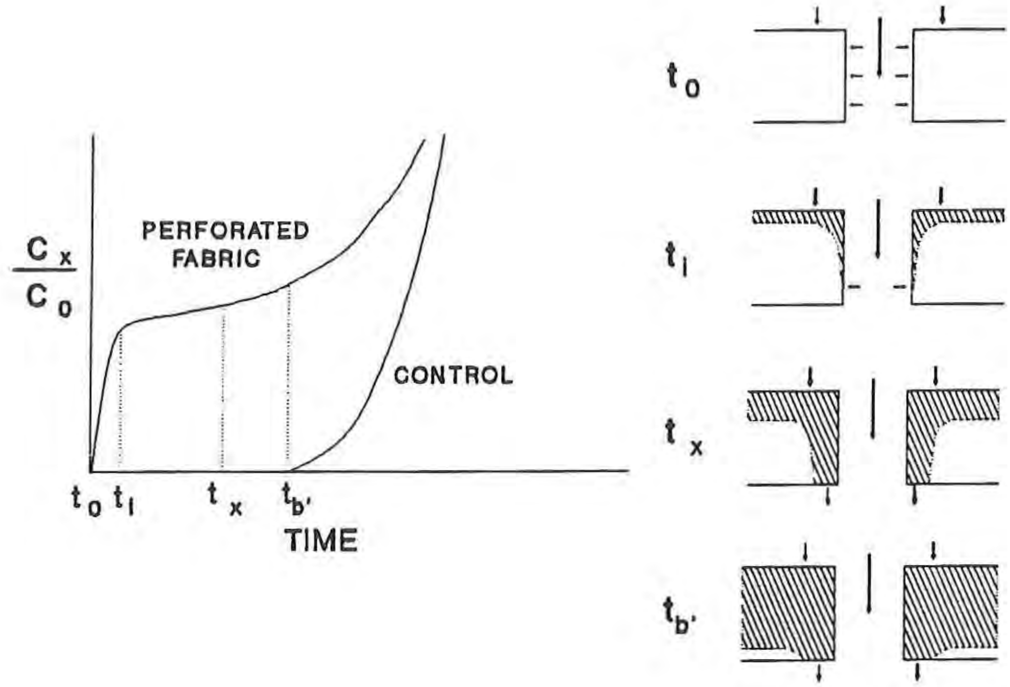

FIGURE 8. Breakthrough Mechanism

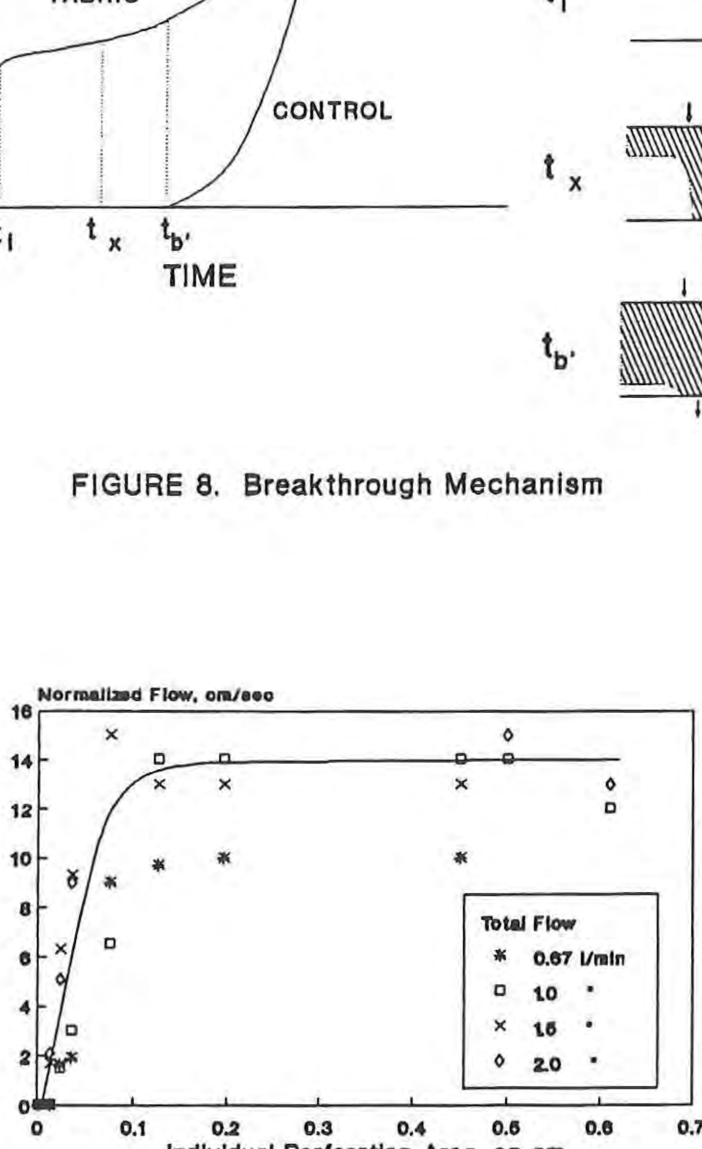

FIGURE 9. Effect Of Perforation Size on Linear Velocity

denoted by t_x in the corresponding region of the BTC, mass transfer through the perforation wall ceases due to the disappearance of the vapor concentration (partial pressure) gradient between the gas phase and the fabric, while the transverse adsorption front continues to move as a result of vapor diffusion from the stream passing through the fabric in the normal direction. The area of this saturated region, its rate of growth and the resultant slope of the BTC are, of course, directly determined by the diameter of the perforation. Time t_b, in Figure 8, describes the last point at which effluent vapor passes exclusively through the perforation and surrounding zone of saturated adsorbent, before emergence of the normal adsorption wave. In the following sections, quantitative support for this mechanism is provided, with emphasis on the t_i portion of the BTC.

Mass-Transfer Characteristics

Molecular diffusion per unit cross-sectional area in the direction of a partial pressure gradient is given by

$$-dn/dt = k_g \; (P_i - P_f) \tag{3}$$

Equation 3 is a first-order rate expression with k_g an empirical mass-transfer rate constant, and P_i and P_f, the initial and final partial pressures of the diffusing gas. At steady-state in the absence of axial gas flow, the rate of mass-transfer, dn/dt, denoted by N_a, can be calculated for one component (e.g., TCE) of a binary mixture from

$$N_a = DPM \; (P_i - P_f) \; / \; RTxP_{bm} \tag{4}$$

where D is the molecular diffusivity in cm^2/sec, P is total pressure in atm, M is the weight of the diffusing species per mole in g/mole, R is the gas constant in cm^3 atm / mole ^oK, T is absolute temperature, x is the diffusion path length, and P_{bm} is the logarithmic mean pressure of the second component. At one atmosphere pressure, in the presence of a large excess of diluent gas and no net flow in the direction of diffusion, eq. 4 simplifies to

$$N_a = DM\Delta P/RTx \tag{5}$$

Taking $P_f = 0$, so $\Delta P = P_i = 2.2 \times 10^{-3}$ atm (12mg TCE/liter), M = 131 g/mole, and D = 0.088 cm^2/sec at 32^0C (6), eq. 5 becomes

$$X \text{ (mm)} = 1.01 \times 10^{-5} \; / \; N_a \; (g/cm^2 \text{ sec}) \tag{6}$$

The effective path length for TCE diffusion from the gas-phase to the surface of the fabric should be less than the steady-state x due to the effect of axial gas flow, $P_f \neq 0$, and limited contact time. Nevertheless, the effective path length can be estimated from the extent of TCE mass-transfer deduced from the attenuation of effluent TCE concentration as a function of perforation dimensions and flow rate.

If the diffusion path is of the same magnitude as the perforation radius, then for a decrease in flow rate or radius, proportionately more vapor is lost from the vapor phase as is reflected by a reduced simulant concentration at t_i. A minimum fault size exists for each gas velocity below which all simulant vapor is adsorbed by activated carbon within the fabric, and none emerges from the opening.

Conversely, as the size of the fault increases, the quantity of vapor diffusing into the fabric becomes an insignificant fraction of the total flow. Therefore, U_p approaches an upper limit, which is determined by the true gas velocity in the perforation. Apparent flow velocity in faults can be calculated from the effluent concentration C_i, at t_i, by

$$U_p = Q\ (C_i/C_o)/A_p \tag{7}$$

whereas, the flow velocity through the fabric is obtained by combination of eq. 7 and eq. 1 with $A_t = A_f + A_p$, to give

$$U_f = Q\ (1-C_i/C_o)/(A_t - A_p) \tag{8}$$

If $A_t >> A_p$, then from eqs. 7 and 8 it follows that

$$U_p/U_f = (A_t/A_p)(C_i/C_o)/(1-C_i/C_o) \tag{9}$$

The velocity ratio, U_p/U_f, should reach a maximum limiting value in parallel with U_p as axial vapor transport becomes much greater than radial diffusion.

Effluent ratios at t_i, as well as U_p, and U_p/U_f are summarized for Type III fabric perforation arrays in Table 3. No instantaneous breakthrough is observed for < 1.7 mm openings at the two lowest volumetric flow rates, and for < 1.3 mm openings at the higher flows. At the other extreme, U_p and U_p/U_f attain their maximum value at $d \geq 4.0$ mm. The dependence of apparent velocity (normalized to a volumetric rate of 1 L/min) on the cross-sectional area per fault is illustrated graphically in Figure 9. Limiting velocity is ca. 14 cm/sec at all flow rates except 0.67 L/m which plateaus about 25% lower, possibly due to kinetic limitations (see below).

An experimental mass-transfer rate is derived from the data in Table 3 via the following relationship

$$N_a = U_{pmax}\ A_p\ C_o/A_{px} \tag{10}$$

where the total open area $A_p = 0.25n\,\pi\,d_{min}^2$, the perforation wall area $A_{px} = n\,\pi\,l d_{min}$, d_{min} is the perforation diameter at which $C_i \rightarrow 0$, and U_{pmax} is the limiting velocity. For a fabric thickness of 0.24 cm, eq. 10 becomes

$$N_a = 1.04\ U_{pmax}\ d_{min}\ C_o \tag{11}$$

TABLE 3

Breakthrough Parameters for Perforated Type III Fabric*

Array ID	Q = 0.67 L/m			Q = 1.0 L/m			Q = 1.5 L/m			Q = 2.0 L/m		
	C_i/C_o	U_p, cm/sec	U_p/U_f	C_i/C_o	U_p, cm/sec	U_p/U_f	C_i/C_o	U_p, cm/sec	U_p/U_f	C_i/C_o	U_p, cm/sec	U_p/U_f
1	0	—	—	0	—	—	—	—	—	—	—	—
2	0	—	—	0	—	—	0.016	2.5	10	0.020	4.2	10
3	0.016	1.1	10	0.014	1.5	10	0.061	9.5	40	0.049[c]	9.7	30
	0.033[a]	2.3	20									
4	0.020	1.3	10	0.031	3.0	20	0.096	14	60	0.090	18	60
	0.062[a]	4.0	40									
5	0.082	6.0	60	0.058	6.5	40	0.13	22	100	—	—	—
	0.097[a]	7.2	70									
6	0.22	6.5	75	0.310	14	120	0.30	20	115	—	—	—
	0.25[a]	7.3	90									
7	0.25	7.0	85	0.33	14	125	0.33	20	125	—	—	—
	0.25[a]	7.0	85									
8	0.28	7.0	85	0.38	14	135	0.38	20	135	—	—	—
	0.30[a]	7.5	95									
9	—	—	—	0.43[b]	14	150	—	—	—	0.45[c]	28	160
10	—	—	—	0.45[b]	12	135	—	—	—	0.47[c]	24	145

* Except as noted in a–c, the TCE challenge concentration (mg/L) at each flow rate (l/m) is: 12.3 at 0.67, 11.3 at 1.0, 11.3 at 1.5, and 10.9 at 2.0.

a. 11.8 mg/L
b. 11.8 mg/L

Mass-transfer rates from eq. 11, and effective diffusion path lengths from eqs. 6 and 11 are given in Table 4.

Table 4
Mass-Transfer Rate and Distance

Q, L/m	U_p, cm/sec	N_a, µg/sec cm^2	x, mm
0.67	7.2	15	>0.67
1.0	14	27	>0.37
1.5	20	30	>0.34
2.0	26	39	>0.26

Kinetic Analysis

In order to estimate the rate of vapor adsorption during passage through fabric openings, it is convenient to consider the perforations as miniature flow reactors of length l, and volume $\pi r^2 l$, where l is the fabric thickness (2.4mm) and r the radius of the perforation. For viscous flow*, a steady-state expression is obtained by equating the rate of vapor entry into the reactor to the sum of the rates of molecular diffusion to the wall and volumetric flow transport of vapor through the exit of the reactor. The result is

$$Q_p C\,dt = Q_p (C+dC)dt + k_p C^n dV dt \qquad (12)$$

Integrating eq. 12 over the volume of the reactor; at the entrance V=0 and $C=C_o$, while at the exit V=V and $C=C_p$. For a first-order diffusion process, the rate constant, k_p, obtained by integration is

$$k_p = (Q_p/V)\ \ln\,(C_p/C_o) \qquad (13)$$

The volume rate of flow through perforations in any array is estimated from the limiting velocity at each challenge flow rate and the total open area. Thus

$$Q_p = U_{pmax}\,A_p = n\pi r^2 U_{pmax} \qquad (14)$$

When Q_p and V in eq. 13 are replaced by eq. 14 and the geometric equivalent of V, we obtain

$$k_p = (U_{pmax}/l)\ \ln\,(C_p/C_o) \qquad (15)$$

Note that the quantity U_p/l is the reciprocal of the residence time (t_{res}), which is the average time a vapor molecule takes to pass through the perforation.

The Reynolds number, R_e, is < 150 for all air velocities and perforation diameters investigated. This is well below the value of 2100 at which viscous (streamline) flow begins to transform into turbulent flow. For example, R_e for air at 32°C flowing at 26 cm/sec through a 0.88 cm perforation is
$R_e = dU\rho/\mu = (0.88\ cm)(26\ cm/sec)(1.16\times10^{-3}\ g/cm^3)/1.9\times10^{-4}\ g/cm\ sec$
$= 140$

To apply eq. 15, the exit vapor concentration, C_p must be determined. Conside passage through perforations, the continuity equation of mass balance gives

$$QC_i = Q_p C_p \qquad (16a)$$

or

$$C_p = QC_i / U_{pmax} A_p \qquad (16b)$$

Calculated values for C_p and k_p from eqs. 16b and 15 are summarized in Table 5 for arrays 2-4. It is not possible to determine k_p for the larger diameter perforations in arrays 5-10 because $C_p \approx C_o$ (except at Q = 11 cm^3/sec), and also for array 1 where $C_p = 0$ for the flow rates examined.

Table 5
Flow Reactor Analysis of Type III Fabric

	Sample 2		Sample 3		Sample 4	
Q, cm^3/sec^{-1}	C_p, mg/L	k_p, sec^{-1}	C_p, mg/L	k_p, sec^{-1}	C_p mg/L	k_p sec^{-1}
11	0	—	3.0	40	4.6	30
17	0	—	1.2	130	2.5	90
25	1.4	170	5.4	60	8.0	30
33	1.7	200	4.5	110	7.4	40

It appears that k_p is relatively insensitive to flow rate, but shows an inverse dependence on perforation diameter which may be due to nonattainment of steady-state conditions, particularly in the larger diameter perforations.

Analogous behavior was observed in the dependence of the adsorption rate constant for dimethylphosphonate vapor/granular activated carbon on particle size and linear flow velocity (7). At a velocity of 60 cm/sec, the rate constant increased over seven-fold as the mean carbon particle diameter was decreased from 1.4 mm to 0.2 mm. The rate constant was independent of flow velocity for 0.2 mm particles but increased nonlinearly with velocity for the larger particles. This phenomenon was ascribed to diffusion control across a stagnant air film surrounding each adsorbent particle; however, no independent verification of this mechanism was obtained.

Analysis of the kinetics of mass-transfer for the Saratoga fabric is similar to that for the Type III fabric, in spite of the difference in morphology. The appropriate rate expression is equivalent to eq. 15, with U_{pmax}/l replaced by t'_{res} the time required for the vapor to traverse the spheroidal carbon monolayer (0.50 mm).

$$k_s = (t'_{res})^{-1} \ln (C_o/C_i) \qquad (17)$$

The fraction of the fabric surface not obscured by adhesive was determined by air permeation at R = 0.5 in water. Air velocity through the original and modified fabrics is 29% and 32%, respectively, that of the cotton layer alone. The lower value for open area (29 cm^2) is considered more reliable in that thermal-mechanical removal of the carbon clusters created a few tiny holes which penetrate the adhesive/fabric layer.

Mass-transfer rate constants in Table 6 are obtained from initial TCE breakthrough concentrations for the original and modified carbon cluster fabrics (Figure 7) at a challenge rate of 11.6 mg/L, and volumetric flows of 0.67-1.50 L/min (U = 0.39 - 0.86 cm/min). Partial removal of the clusters has no significant effect on TCE uptake per unit weight of carbon. This is probably a consequence of the relatively long contact time in this system, whereby t'_{res} is 4.5 to 6.5-fold the apparent half life for the mass-transfer process. In general, the diffusion rate constant is similar to that for Type III fabric, especially for perforation diameters > 0.17 cm.

Table 6
Initial TCE Permeation Rate for Carbon Spheroid Cluster Fabric

Q, cm^3/sec	C_i, mg/L original	C_i, mg/L modified	t'_{res}, ms	k_s, $sec^{-1}\ g^{-1}$ original	k_s, $sec^{-1}\ g^{-1}$ modified
11	0.05	0.26	130	35	34
17	0.12	0.45	87	44	43
21	0.14	0.58	70	53	49
25	0.19	0.76	58	59	54

The half life for vapor disappearance derived from the first-order rate constants in Table 5 ranges from 3.5 ms to 23 ms, and in Table 6 from 12 ms to 20 ms. With half lives of this magnitude, it is possible that premature breakthrough is dependent not only on the dimensions of the fault which controls the extent of molecular diffusion, but also on the overall rate of adsorption. A series of dynamic adsorption experiments were carried out to test this possibility.

Several models are available for evaluating kinetic parameters for adsorption of chemical agents or simulants by fabrics containing activated carbon (8-12). In this work, the rate constant for adsorption is determined from the relationship between the time to achieve 1% breakthrough and sample weight at fixed challenge and flow rates, according to the Wheeler equation (8,9).

$$t_b = [W_e/C_oQ][W-(F_cQ\ln(C_o/C_x)/k_v)] \qquad (18)$$

From a plot of breaktime, t_b, vs. sample weight, W, one obtains the kinetic adsorption capacity, W_e, from the linear slope and the kinetic rate constant, k_v, from the slope and intercept. Kinetic parameters for Type III and Saratoga fabrics are given in Table 7, for carbon loading density, F_c, of 0.042 g/cm^3 and 0.24 g/cm^3, respectively.

Table 7
Kinetic Adsorption Parameters

Fabric	W_e, g TCE/g carbon	k_v, sec^{-1}	$t_{1/2}$, ms
Type III	0.34	9.8	71
Saratoga V941	0.62	20	35

From the magnitude of the k_v's in Table 7, it would seem that the overall adsorption rate for Type III fabric is not strongly controlled by molecular diffusion external to the absorbent particles; however, k_v is sufficiently close to k_p so that factors which alter the fabric's adsorption properties will have a significant effect on penetration through small openings in the fabric. In the case of the carbon cluster fabric, there is a closer correspondence between the rate of external diffusion and the overall rate of adsorption.

Summary

A mechanism for vapor leakage through faults in chemical protective fabric is proposed and supported by mass-tranfer and adsorption kinetics arguments. The existence of a minimum fault dimension, below which no leakage occurs, is demonstrated for Type III foam laminate fabric.

Acknowledgements

We would like to thank Mr. Randall Natches for fabrication of the perforated Type III fabric samples, and Mrs. Madeline Piccioli for assistance in preparation of the manuscript.

References

1. P.B. Dawson and M.F. Gilchrist, Edgewood Arsenal Technical Memo EATM 311-3, Dec 1967
2. D.E. Cagliostro, W. Changtal and J.M. Smith, Ind. Eng. Chem. Process Des. Dev., 24, 377-381 (1985)
3. D.M. Baars, D.B. Eagles and J.A. Emond, ASTM STP900, R.L. Barker and G.C. Coletta, Eds., American Society for Testing Materials, Phila. 1986, pg 39-50
4. C.E. Kendrick and D. Rivin, Proc. Fourth International Simulant Workshop, G.R. Famini, Ed., CRDEC, Aberdeen Proving Ground, 1990
5. I.M. Klotz, Chem. Rev., 39, 241-268 (1946)
6. G.O. Nelson and C.A. Harder, Am. Ind. Hyg. Assoc. J., 35, 391-410 (1974)
7. J.A. Rehrmann and L.A. Jonas, Carbon, 6, 47-51 (1978)
8. A. Wheeler and A.J. Robell, J. Catal., 13, 299-305 (1969)
9. L.A. Jonas and W.J. Svirbely, J. Catal., 24, 446-459 (1972)
10. J.K. Ferrell, R.W. Rousseau and M.R. Branscome, Ind. Eng. Chem. Process Des. Dev., 15, 114-122 (1976)
11. O. Grubner and W.A. Burgess, Environ. Sci. Technol., 15, 1346-1351 (1981)
12. L. A. Graceffo, S.G. Chatterjee, H. Moon and C. Tien, Carbon, 27, 441-456 (1989)

TITLE: Nephila Clavipes Major Ampullate Gland Silk Proteins: Amino Acid Composition Analysis, Protein Sequencing, Construction and Screening of Recombinant Genomic and cDNA Libraries

*Stephen J. Lombardi, Mr.

ABSTRACT: Spider silks form an extremely diverse group of naturally occurring fibers, particularly with respect to their mechanoelastic/physiochemical properties. Amino acid composition of major ampullate gland silk (dragline) produced by the mature, female, golden orb-weaving spider, Nephila clavipes (ARANEAE, ARANEIDAE) was determined. Several solvents were applied in order to dissolve the spider silk. The results show that the major ampullate gland secretion is characterized by a high degree of small side chain amino acids (Ala, Gly, and Ser) and polar residues (Glx and Arg), comprising almost 75% of the total amino acids present. The composition of major ampullate gland silk appears to be uniform within the species and when multiple samples are taken from an individual spider during both single and multiple silkings.

Protein isolated from the major ampullate gland shows a molecular weight of ~350,000 Daltons by polyacrylamide gel electrophoresis analysis. High molecular weight genomic DNA was isolated, partially digested and cloned into lambda phage vector (EMBL 3) generating a genomic library of Nephila clavipes. Major ampullate gland mRNA was isolated and reverse transcribed to generate a cDNA library for dragline silk. Synthetic oligonucleotide probes were constructed from dragline silk protein sequences to screen recombinant DNA libraries. The purified major ampullate gland cDNA was expressed and the expression product identified by immunological techniques to be a recombinant silk protein. Sequencing of the major ampullate gland silk gene is currently underway. The composition of the secretion is discussed in relation to the known and implied functions of the major ampullate gland as well as in relation to the mechanical properties of the silk produced by orb-web building spiders.

*BIOGRAPHY OF PRESENTER: Stephen J. Lombardi

PRESENT ASSIGNMENT: Research Microbiologist in the Biological Sciences Division of the Soldier Science Directorate, U.S. Army Natick Research, Development and Engineering Center, Natick, MA.

PAST EXPERIENCE: Conducted research in Bacillus spore heat and UV resistance at Syracuse University, Department of Biology, Syracuse, NY, and research fungal enzyme kinetics and nucleic acid cloning at Dartmouth College, Department of Molecular Genetics, Hanover, NH.

DEGREES HELD: B.S., Microbiology, Syracuse University, 1985; B.A., Biopsychology, Syracuse University, 1985; M.S., Molecular Biology, Dartmouth College, 1987; Ph.D. candidate, Chemistry, Clark University.

Nephila Clavipes Major Ampullate Gland Silk Proteins: Amino Acid Composition Analysis, Protein Sequencing, Construction and Sequencing of Recombinant Genomic and cDNA Libraries (U)

Stephen J. Lombardi

INTRODUCTION

Silks represent an unusual class of fibers generally considered to be protein in composition. Unlike enzymes which are termed globular proteins, silks belong to the structural fibrous protein class which also includes keratin and collagen. Silk proteins exhibit a high degree of crystallinity which is derived from the anti-parallel beta sheet secondary structure. This crystalline array is stabilized by a combination of hydrogen bonding between anti-parallel chains, and hydrophobic interactions between the sheets or layers. These interactions result in a class of fibers with unusual and interesting properties, including high tensile strength and extensibility. The unique properties of silk, and the possibility of genetically engineering controls over fiber structure, greatly expand the availability of biologically-derived materials.

In addition, there is evidence for noncrystalline or amorphous regions in the secondary structure of the silk and it is believed that these regions give rise to extensibility of the fiber and the resulting property of high energy absorption to break. It is the unusual combination of high strength and high extensibility that drives much of the interest in this class of fiber.

In natural systems, the two common sources of silks are the domesticated silkworm, Bombyx mori, and the orb weaving spiders. The silkworm produces one type of silk used in spinning its cocoon during one stage in its life cycle. For domestic silk production the cocoon silk is boiled to remove the soluble sticky sericin protein, and the remaining fibroin portion of the silk is then unwound and used as silk fiber. Orb weaving spiders have the capability to produce many different silks, each of which is synthesized in a separate set of silk secreting glands in the abdomen. In addition some of the silks, such as the dragline, are produced continuously throughout the lifecycle of the spider. Each of the different silks exhibits different physical properties and functions. These differences are reflected in the amino acid composition of the silk. Some of the silks function in web construction/engineering, in egg cocoon structures, as adhesives, and in prey capture.

There has been some data collected on the physical properties of spider silks. Zemlin [8] and Work and Emerson [7] published data on the amino acid composition and mechanoelastic performance data of different spider silks. Dragline silk from N. clavipes has been reported to have a modulus of 1 X 10^{10} N/m^2, tensile strength of 1 X 10^9 N/m^2, and energy absorbed to break value of 1 X 10^5 J/kg. This compares with the silk worm which exhibits a modulus of 1 X 10^{10} and a tensile strength of 7.4 X 10^8. Both fibers exhibit about 18% elongation. Spider silks are of interest because the physical properties of the fibers appear superior to the silkworm silks.

For the silkworm, part of the fibroin gene has been mapped and partial sequencing of the 5' end of the gene was completed [2, 5, 6]. This information, in combination with X-ray data has provided the basic information on the protein structure which indicates discrete crystalline and amorphous regions as reflected in discrete coding regions in the silk gene. Genetic information on the silk worm is extensive because of the commercial interest in this material and in the translational controls over silk expression. No data on the organization of spider silk genes are available.

As in the silk worm, X-ray diffraction data on spider silk implies the presence of crystalline regions dispersed in a matrix of amorphous protein [3]. Additional data on conformation is being developed to further understand the relationships between primary and secondary structures for this class of proteins.

It can be assumed that the mechanoelastic and functional properties of silk fibers correlate closely with their chemical composition and molecular conformation. In addition, the capability of spiders to produce a multitude of silks with very different functions through changes in amino acid composition dictates this system as useful for genetic manipulation for fiber production. The first goal is to clone silk coding genes from the spider into a more useful expression system to increase available amounts of silk. The dragline silk, because of its high tensile strength, was chosen for cloning.

RESULTS AND DISCUSSION

To accomplish the goal of increased silk production the silk gene was cloned. First, genetic libraries were constructed from the spider. High molecular weight genomic DNA was isolated and purified from N. clavipes and then partially digested with restriction enzymes to yield 25 kb fragments. These fragments were cloned into a Lambda phage vector to generate a genomic library. RNA was purified from the major ampullate gland of the spiders. The major ampullate gland is the site of dragline silk production. The mRNA was isolated by density gradient centrifugation and oligo (dT) column chromatography and then reverse transcribed to generate a cDNA library.

To screen these libraries, the native silk protein had to be solubilized, partially hydrolyzed, and sequenced [4]. This was accomplished and the sequence data developed was used to construct DNA probes. The protein composition data confirmed the high percent of short side chain amino acids (glycine, alanine, serine) which permits the close packing density of the beta sheets. The amino acid composition for major ampullate gland silk was determined and glycine, alanine, serine, glutamic acid/glutamine, and arginine were the most abundant amino acids, together comprising over 75% of the total amino acids present. The genomic and cDNA libraries were then screened with these probes. The probes were radiolabelled by the 5' end labelling method and hybridization was determined using autoradiography. Positive clones were then subcloned and expressed in a bacterial host system. Recombinant silk protein was produced and both the clones and the silk are being analyzed. This first phase of work provides the means to produce larger quantities of silk materials for study.

The second phase of the work which is also underway involves selective modification of the natural gene sequence to tailor silk structure and properties to specific functions. To accomplish this goal, molecular modeling studies are being conducted on silk protein sequences to understand the influence of primary sequence on secondary structure. The predicted secondary structure data must then be extrapolated to predicted functional properties of the fibers spun from these sequences. This extrapolation will be validated using protein engineering techniques to enact the sequence changes in the gene, expressing the modified silk proteins, spinning fibers, and then studying fiber properties from the modified proteins.

In general, fiber spinning from recombinant silk proteins will involve mimicking the natural process used by the spider which can be correlated to spinning lyotropic liquid crystals. In the silk gland, the translated product is present in a metastable state. As the material is processed and then spun at the spinerette, there is a loss of water and the silk protein becomes highly ordered and crystalline. Physical processing appears to effect the major changes in the silk structure and there is no evidence for post-translational chemical modification of the protein. Of interest, based on the amino acid composition data collected, is the fact that spider silk fibers, despite containing a lower percentage of short side chain amino acids, exhibit superior strength properties. This would not be expected and therefore implies a significant role for the processing/spinning steps on resulting fiber properties.

Silk proteins may find application in a number of areas including structural fibers and composite materials. From a composites perspective, a high strength fiber such as silk with its ability to self-assemble into its secondary structure and its reactive functional groups, may provide some unique opportunities in processing and design. In addition, the environmental resistance of natural silks, presumably due to the high degree of crystallinity, would indicate that environmentally stable composite systems incorporating these materials could be considered. Illustrative of the resistance of silk fibers is the fact that proteolytic enzymes are not active in degrading silk proteins. Whether these fibers could also be incorporated into composites for biomedical implants remains to be demonstrated. Work on immobilized enzyme systems using silks for biosensor applications has already been reported [1].

Through genetic engineering we can now consider large scale production of fibrous proteins such as silk. The increased availability of this material will lead to many material applications in the future. In addition, the ability to tailor these structures at the genetic level to meet specific functional requirements further amplifies the potential utility of this approach to materials science.

REFERENCES

1. Demura, M., Asakura, T., Nakamura, E., Tamura, H., J. Biotech. 10, 113-120, 1989.
2. Gage, L. P., Manning, R. F., J. Biol. Chem. 255 (19), 9444-9450, 1980.
3. Gosline, J. M., Danny, M. W. DeMont, M. E. Nature 309, 551-552, 1984.
4. Lombardi, S. J., Kaplan, D. L., J. Arachnol. In Press.
5. Tsujimoto, Y. Suzuki, Y. Cell 16, 425-436, 1979.
6. Tsujimoto, Y., Suzuki, Y. Cell 18, 591-600, 1979.
7. Work, R. W., Emerson, P. D., J. Arachnol. 10, 1-10, 1982.
8. Zemlin, J. C. Technical Report 69-29-CM, AD684333, U. S. Army Natick Laboratories, Natick, MA, 1968.

TITLE: **A General Synthesis of Side Chain Liquid Crystalline Polymers**

*John H. Cornell, Dr., and Charles A. Lovelette, Dr.

ABSTRACT: A simple synthetic method has been created permitting the preparation of side chain liquid crystalline polymers with the following structural variation: polymer, backbone, restricted or unrestricted rotation at the site of side chain attachment to the backbone, the length and flexibility of the spacer segment and the type of mesogen incorporated. The title synthetic method starts with acrylic acid or one of its homologs and/or derivatives, e.g., methylacrylate. A bifunctional spacer group comprising methylene and aromatic units terminating with amino and/or hydroxy groups is attached by esterification or amination of the acrylate carboxyl group. A mesogenic group, e.g., cyanophenol, is then fixed to the terminal end of the spacer. Finally the modified acrylate monomer is polymerized using conventional catalyst systems to give a side chain polymer having the structural variation that is needed. Another synthetic route that involves chemical modification of preformed acrylate polymers has been developed.

Progress in the synthesis of liquid crystal side chain polymers via these methods is discussed and their potential use as nonlinear optical polymers.

*BIOGRAPHY OF PRESENTER: John H. Cornell

PRESENT ASSIGNMENT: Physical Sciences Division, Soldier Science Directorate, U.S. Army Natick Research, Development and Engineering Center, Natick, MA 01760-5020.

PAST EXPERIENCE: Monsanto Research Corp., Everett, MA (1959-1964); Nitrogen Division, Allied Chemical Corporation, Hopewell, VA (1952-1959).

DEGREES HELD: B.S., Harvard University, 1948; M.S., Stanford University, 1950; Ph.D., Stanford University, 1952.

A General Synthesis of Side Chain Liquid Crystalline Polymers

John H. Cornell, Dr., and Charles A. Lovelette, Dr.

INTRODUCTION

The objective of this project is to develop eye protection media which will defend the soldier against low energy laser threats such as laser range finders and target designators. Recently a new battlefield threat has emerged through the potential use of tunable laser weapons systems. Coherent radiation from these sources even at low energy levels is capable of inflicting severe damage to the retina of the eye. One mode of protecting against such threats involves the development of nonlinear optical polymers, which permit the transmission of visible light at ambient intensities but will reversibly block visible and near infrared radiation at intensities harmful to the eye.

There has been great interest recently in nonlinear optical materials because of the growing need in the telecommunication and computer industries for high speed, wide-bandwidth optical switching and processing devices. Nonlinear optics involves the interaction of incident electromagnetic radiation with various media to produce emergent radiation altered in phase, frequency, amplitude or other characteristics from the incident radiation. In principle it should be possible to design devices that make use of one or more of those changes in the transmission characteristics of the nonlinear optical media to secure the desired eye protection. To attain this objective, optical materials that give nonlinear effects, such as a change in refractive index of the media, are required. Successful candidate materials must produce such effects with sufficient magnitude and speed to block the incident laser pulse. Devices comprising nonlinear optical components for individual eye protection should result in reduction of pulse intensity equivalent to an optical density of four within one nanosecond.

In recent years organic and polymeric materials have emerged as promising classes of nonlinear optical media because in these materials the nonlinear polarization originates from purely electronic effects.[1] This leads to ultrafast (subpicosecond) response, broadband operation, and large nonresonant optical nonlinearities due to electron delocalization. In addition these materials possess excellent chemical and structural stability and do not require ei vironmental protection or cryogenic operation. Polymers of pyrrole, thiophene, benzene, aniline, benzoxazole, and benzothiazole can be fabricated as self-supporting films, filters, coatings, monolayers, liquid crystalline polymers, etc.[2-6] They are susceptible to structural variation by chemical synthesis or processing and possess a high potential for larger scale production through existing polymer manufacturing techniques.

At Natick RD&E Center a program for the development of nonlinear optical polymers that can be incorporated into devices for laser eye protection is in progress. The nonlinear polymer should pass visible light at ambient intensities but reversibly block laser radiation at intensities harmful to the eye. The program for the development of nonlinear optical polymer for use in eye protective devices is divided into two phases (a) selection and synthesis of polymers that potentially have suitable nonlinear optical properties and (b) evaluation of the nonlinear optical properties of candidate polymers. A facility for the measurement of $\chi^{(3)}$ is being constructed at Natick, Research Development and Engineering Center. A neodymium dye laser will be used and $\chi^{(3)}$ determinations carried out using the degenerate four wave mixing technique. When feedback is available from this facility, it will of course be used to explore the relationship between $\chi^{(3)}$activity and polymer structure. This data in turn will be employed for the design and synthesis of polymers that will display the highest third order nonlinear optical effects.

Current out-of-house efforts center on polybithiophenebenzylidene and substituted polybithiopheneacetoxybenzylidene [7].

Prior to discussing the selection of candidates for nonlinear optical polymers for laser eye protection, the principles involved in providing the type of protection will be outlined.

BACKGROUND

The minimum performance requirements for laser eye protection are a pulse intensity reduction of at least 10^4 times with a response time of 1 nanosecond or less. Normal chemical reactions involving the movement of atoms cannot be expected to yield a sufficiently rapid response. On the other hand response times as short as 10^{-15} seconds are possible where only the movement of electrons is involved. Large classes of conjugated molecules and polymer structures exist whose nonlinear optical responses of this type occur by lossless excitation of the pi-electron states, especially those containing large charge correlations.

When an electromagnetic impulse is propagated through a medium, the polarization (P) of the medium is expressed in terms of the field strength E:

$$P = \chi^{(1)}E + \chi^{(2)}E^2 + \chi^{(3)}E^3 + \ldots..$$

The first order term ($\chi^{(1)}$) is associated with linear transmission at ordinary light intensities. As light intensities increase, nonlinear effects associated with the second order ($\chi^{(2)}$) and third order ($\chi^{(3)}$) terms become more significant.

The higher order nonlinear effects are associated with certain symmetry requirements. Thus $\chi^{(2)}$ is observed only with non-centrosymmetric systems while $\chi^{(3)}$ is characteristic of centrosymmetry. The higher orders also produce different physical effects on incident radiation. $\chi^{(2)}$results in frequency doubling (second harmonic generation) and $\chi^{(3)}$in frequency tripling and changes in the refractive index. It is this last property that is considered most significant from the standpoint of individual laser eye protection.

An initial selection of candidate nonlinear optical polymers was made on the basis of the molecular structures of compounds that have exhibited nonlinear optical properties. These structures include extended pi-electron systems, permanent dipoles, and anisotropic structures.

Moieties containing these structural features may be distributed in various ways throughout the polymer chain, giving rise to different types of nonlinear optical polymers. These optical polymers comprise polymers in which the main chain is fully conjugated, or in which the centers of unsaturation are still in the main polymer chain but are broken up into segments by saturated moieties interspersed along the chain. Finally, the centers of unsaturation may be in the form of pendent groups suspended from the main chain by saturated spacer groups.

RESULTS AND DISCUSSION

The synthetic methods developed in this program will facilitate the preparation of side chain liquid crystal polymers with the following structural variations: polymer, backbone, restricted and unrestricted rotation at the site of side chain attachment to the backbone, length and flexibility of the spacer segment, and the type of mesogen incorporated. Systematic variation of the polymer structure in this manner will permit a detailed evaluation of the effect of such variation on the nonlinear optical properties for that type of polymer.

One method, Scheme 1, starts with acrylic acid and one of its homologs and/or derivatives, e.g., methyl acrylate or methyl methacrylate. A bifunctional spacer group comprising methylene and aryl units terminating with amino and/or hydroxy groups is attached by esterification or amination of the acrylate carboxyl function. A mesogenic group, e.g., cyanophenol, is then fixed to the terminal end of the spacer. Finally the modified acrylate monomer is polymerized using conventional catalyst systems to give a side chain polymer having the structural variation that is required.

Starting with readily available monomeric vinyl acids or methyl esters (1) represented an attractive beginning and formed the basis of the entire synthetic approach. Initial experiments centered on an attempt to accomplish ester interchange reactions with the appropriate methyl esters and terminal diols using type A molecular sieves [8]. This procedure appeared quite attractive in the context of experimental simplicity allowing the conversion to be accomplished without any special equipment. However, the procedure was unsuccessful, affording only clear, highly viscous liquid products whose infrared spectra contained OH and aliphatic CH stretching as well as C=O stretching but lacked the all important C=C stretching frequency. Proton nuclear magnetic resonance confirmed the absence of the double bond and failed to exhibit any vinyl proton resonances. Further attempts to characterize these materials were unsuccessful and the method was abandoned.

SCHEME 1

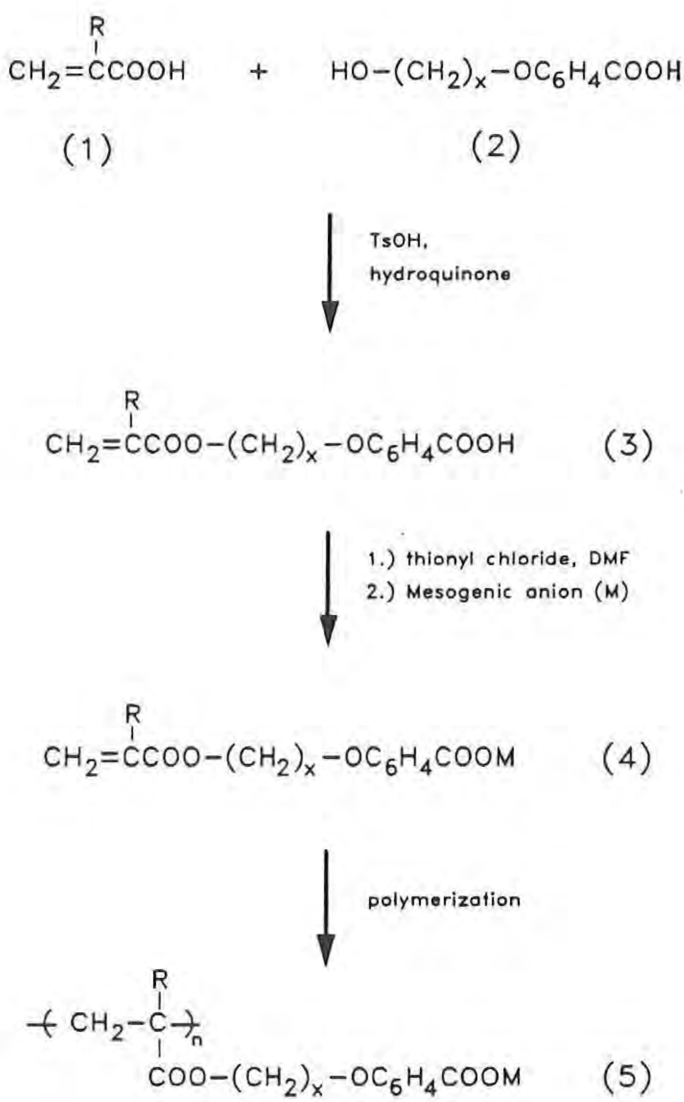

Next, standard Fischer esterification procedures were employed using the protocol described by Ringsdorf [9]. This method using the corresponding acids was successful, affording a series of esters whose structures are illustrated by (3): $R=H,CH_3$ and $X=2,3,6$. The presence of the aryl carboxy group served two purposes: its acidic nature made purification simple and it served as a site for attachment of the mesogenic group. This was most readily accomplished by conversion into the acid chloride with thionyl chloride, followed immediately by the addition of the appropriate nucleophile, e.g., p-cyanophenol. As is readily apparent, mesogenic group variability is, in theory, very extensive using this approach.

Finally this general approach affords a convenient pathway for the introduction of an amide-type functional group linking the main-chain backbone and the spacer functionality. This linkage serves the purpose of introduction of restricted rotation about the C(=O)NH bond. This is accomplished from the commercially available acid chlorides (1) where $R=H,CH_3$. Treatment of the acid chlorides with hydroxyamines gives the desired amide bond. The hydroxy group is then converted to the tosyl ester and treated with the dianion of p-hydroxybenzoic acid, allowing the preparation of a completely analogous series of monomers with the property of spacer rigidity.

Further rigidity is possible by treating (1) with diamines of varying length. Also, one could employ a cyclohexane ring spacer by utilizing 1, 4-cyclohexanediol. The basic goal of establishing a simple method for the synthesis of side chain liquid crystals having a wide variety of controlled variables was accomplished. This establishes the framework for an extensive program in this area with the goal of discovery of nonlinear optical activity in such systems.

Another synthetic route that involves the chemical modification of preformed acrylate polymers has been developed, Scheme 2. In this case polymethyl methacrylate is treated with a bifunctional amine such as ethanolamine or ethylenediamine, resulting in the displacement of the methoxy group and the formation of an amide linkage. Attachment of a mesogenic group to the reactive terminal end of the spacer group will give the desired side chain nonlinear candidate polymers. Polymers obtained in this way will be compared to those prepared according to Scheme 1, which have the same structure.

SCHEME 2

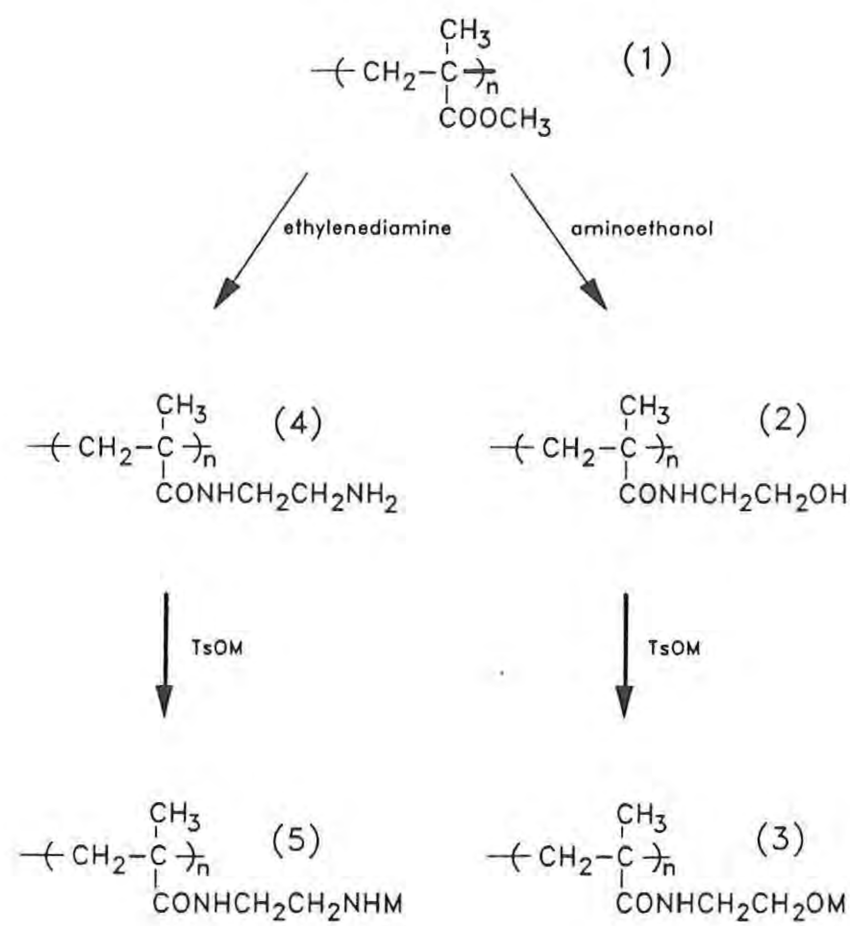

EXPERIMENTAL

Preparation of Compounds (2): (Scheme 1)

In a typical experiment, 4-hydroxbenzoic acid (13.8g, 0.1 mole) was dissolved in ethanol (100mL) and potassium hydroxide (15g, 0.3 mole) was added along with a catalytic amount of potassium iodide. The solution was heated and stirred while the chloro alcohol (0.1 mole) was added dropwise. The mixture was refluxed for 15 hours, then cooled to room temperature and the solvent removed under reduced pressure. The semisolid residue was dissolved in water (250mL) and the aqueous solution made acidic with hydrochloric acid (6M). The precipitate was collected and recrystallized from ethanol. (See Table 1.)

Preparation of Compounds (3): (Scheme 1)

A mixture of the 4-hydroxybenzoic acid (0.25 mole), acrylic, or methacrylic acid (1 mole), dichloromethane (200mL), p-toluenesulfonic acid (1g) and hydroquinonone (10g) was refluxed overnight in a Dean-Stark apparatus. If the theoretical amount of water had not been collected the reflux was continued until sufficient water was collected. The cooled reaction mixture was diluted with diethyl ether (1500mL), washed with warm water and dried over magnesium sulfate. Removal of the solvent followed by recrystallization from isopropanol afforded the final product.

Preparation of Compounds (4): (Scheme 1)

Compounds 3a-c (0.03 mole), dimethylformamide (1mL), 2,6-di-t-butyl-4-methylphenol (0.5mL) and thionyl chloride (20 mL) were stirred for 30 minutes at room temperature. After the reaction period the thionyl chloride was removed, first at the water aspirator and finally under high vacuum (1-1.5h). The residue was dissolved in dry ether (50mL) and added to a solution of the mesogen (0.03 mole) and triethylamine (5mL) in dry tetrahydrofuran (100mL) at 0°C. After warming to room temperature, the solvent was removed and the solid residue was dissolved in dichloromethane, washed with water and dried over magnesium sulfate. Final purification was effected by silica gel column chromatography using dichloromethane as the mobile phase. Removal of the solvent afforded 4a-c (Scheme 1).

Preparation of Compound (2): (Scheme 2)

PMMA (med. MW, Aldrich 18,224-9), 3.0g (0.03 mole) was refluxed and stirred for 21 hours with 10mL 95% ethanolamine (0.16 mole). The resulting thick liquid was dissolved in methanol and transferred to a distilling apparatus fitted with a Dean and Stark trap. Excess toluene was added and the mixture stirred and refluxed until the formation of a second layer in the Dean and Stark trap ceased (ca. 20 h). The toluene was decanted from the pot and the glassy residue washed several times with toluene.

The product was dissolved in refluxing methanol and was clarified by centrifugation. Excess tetrahydrofuran (THF) was added to the stirred supernatant, which resulted in the precipitation of a white solid. The product was decanted and stirred with THF several times and collected by vacuum filtration. It reached constant weight after drying in air for two weeks, 2.5g (64.6% yield).

The appearance of strong IR absorption at 1625 cm^{-1} (amide CO) and 3320 cm^{-1} (OH) and the weakening of the 1725 cm^{-1} band (ester CO) in the product indicated that the reaction had proceeded as shown in Scheme 2.

The foregoing experiment was repeated with low MW PMMA (Aldrich 18,223-0) to yield (2) (80.1 % yield). When this preparation was repeated with high MW PMMA (Aldrich 18,226-5), the immediate product was a solid insoluble in refluxing methanol, dimethylformamide and tetrachloroethylene.

Preparation of Compound (4): (Scheme 2)

PMMA (med. MW) was treated with ethylenediamine using the same procedure as for ethanolamine. The product (2) was obtained as two fractions: (2a) soluble in refluxing methanol (33.8% yield), and (2b) soluble in refluxing tetrachloroethylene (15.6% yield).

TABLE 1. Synthesis of Acrylate Monomers

Compound Scheme 1	Substituent	Monomer Chain Length	Mesogenic Group	Percent Yield	IR Bands (KBr, cm^{-1})
2a		x=2		51	3350, 1680, 1610, 1440, 1255, 775, 650
b		x=3		57	3380, 3290, 2980, 2890, 1680, 1610, 780
c		x=6		73	3400, 2940, 1690, 1610, 1360, 780, 645
3a	R=H	x=2		52	3010, 1725, 1690, 1610, 1410, 1360, 1270
		x=3		51	
		x=6		60	3010, 2940, 1720, 1690, 1610, 1360, 1270
3b	R=CH_3	x=2			3320, 1685, 780, 645
		x=3			3410, 1690, 780, 650
		x=6			3350, 1700, 790, 670
4a	R=H	x=2	M_1	35	2230
4b		x=3	M_1	42	2230
4c		x=6	M_1	40	2230
4d		x=2	M_2	45	1690
4e		x=3	M_2	33	1690
4f		x=6	M_2	38	1690

M_1 = p-HOC_6H_4CN
M_2 = p-HOC_6H_4COOH

SUMMARY AND CONCLUSION

A simple synthetic method has been created permitting the preparation of side chain liquid crystalline polymers with the following structural variations: polymer, backbone, restricted or unrestricted rotation at the site of the side chain attachment to the backbone, the length and flexibility of the spacer segment, and the type of mesogen incorporated. This method permits a detailed evalu tion of chemical structure-liquid crystal properties for this type of polymeric system.

The synthetic method starts with acrylic acid or one of its homologs and/or derivatives, e.g., methyl acrylate or methyl methacrylate. A bifunctional spacer group comprising methylene and aryl units terminating with amino and/or hydroxy groups is attached by esterification or amination of the acrylate carboxyl group. A mesogenic group, e.g., p-cyanophenol, is then fixed to the terminal end of the spacer. Finally the modified acrylate monomer is polymerized using conventional catalyst systems to give a side chain polymer having the structural variation that is needed.

Another synthetic route that involves chemical modification of preformed acrylate polymers has been developed. Polymers obtained in this way will be compared with those prepared by the first route having the same molecular structure.

REFERENCES

1. William, D.J., Angew. Chemie, Intl. Ed. 23, 690-703. (1984)
2. Sato, M., Tanaka S. and Kaeriyama K., J. Chem. Soc., Chem. Commun. 1985, 713-714.
3. Bjorklund, R. and Lindberg, B., J. Chem. Soc., Chem. Commun. 1986 1293-1295.
4. Bianco, P., and Musiani, M., J. Appl. Poly. Sci. 26, 4247-4257 (1981).
5. Tourillon, G. and Garnier, F., J. Electroanal, Chem. 135, 173-178 (1982).
6. Feinberg R., Optical Engineering Report, Soc. Photooptical Instrumentation Engineers, July 1987, 5A-7A.
7. Contract DAAK60-84-C-0044, Honeywell Systems Res. Center, Minneapolis, Minnesota.
8. Roelofsen, D.P., Hagendoorn, J.A., van Bekkum, H., Chemistry and Industry, 1622 (1966).
9. Portugall, M., Ringsdorf, H., Zentel, R. Makromol. Chem., 183, 2311 (1982)

TITLE: Synthesis and Preliminary Characterization of Novel Liquid Crystalline Polycarbonates

Michelle M. Gauthier, Dr., Jo Ann Ratto, Ms., and * Heidi L. Schreuder-Gibson, Dr.

ABSTRACT: There are two possible forms of liquid crystallinity: lyotropic, where a transition between the isotropic liquid and the crystalline state exists at a specific concentration in a solvent and at an appropriate temperature; and thermotropic, where the liquid crystalline "mesophase" exists in a melt of the compound at an intermediate temperature between the liquid and crystalline phases. Thermotropic liquid crystalline (LC) polymers have distinct advantages over the lyotropic type; conventional plastic and fiber processing equipment can be used to form the material without the use of corrosive acid solutions necessary to process the currently available lyotropic fibers. We report progress on a series of polycarbonates with structures that exhibit thermotropic LC phases. Described here are polymers with repeating units of rigid groups alternating with flexible methylene spacer groups connected with carbonate links. Specifically, the first rigid moiety is α-methyl stilbene, reported to produce liquid crystalline polymers when ester and ether linkages are employed. Evidence of the presence of liquid crystallinity in these stilbene polymers and on the second type of polycarbonate based upon a rigid benzoate repeating unit is present in thermal and polarized microscopy. Specific chemical variations have been introduced into the polymer backbone and the effect of these chemical changes, such as length of the flexible spacer and molecular weight, are interpreted with respect to structural changes in the liquid crystalline phase. Reported here are the preliminary results of the synthesis of three polymers and evidence of their thermotropic liquid crystallinity.

*BIOGRAPHY OF PRESENTER: Heidi L. Schreuder-Gibson

PRESENT ASSIGNMENT: Polymer Chemist in the Soldier Science Directorate of the U.S. Army Natick Research, Development and Engineering Center.

PAST EXPERIENCE: Research Physical Chemist, Propellant Development, U.S. Air Force Astronautics Laboratory, Edwards AFB, CA.

DEGREES HELD: B.S. Chemistry, University of California, Irvine. Ph.D. Polymer Science, the University of Akron.

Synthesis and Preliminary Characterization of Novel Liquid Crystalline Polycarbonates

* Michelle M. Gauthier, Dr., Jo Ann Ratto, Ms.,
and Heidi L. Schreuder-Gibson, Dr.

INTRODUCTION

Today in high performance fiber technology, nearly all of the super strong filaments are spun from lyotropic liquid crystalline polymers (LLCP), two examples of which are shown below.

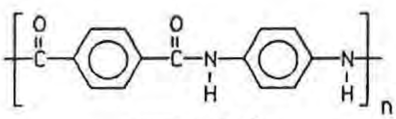

KEVLAR®
Poly(p-phenyleneterephthalamide)

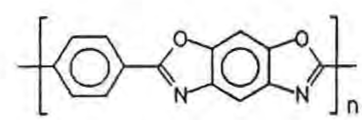

PBO
Poly(p-phenylenebenzobisoxazole)

LLCP fiber strength is due to the ability of these rigid, rod-like molecules to adopt an extended chain conformation due to their highly aromatic backbones. Their processability is due to the formation of the liquid crystal phase in solution, without which they would be intractable up to the temperature of decomposition. The lyotropic materials shown above can form their liquid crystal phase only in the presence of a concentrated inorganic acid.[1,2]

In contrast, thermotropic liquid crystalline polymers (TLCPs) present several differences compared to LLCPs. A major advantage of the TLCPs over the lyotropic type is that processing without solvents can be accomplished using conventional plastics processing equipment. The thermotropic type of polymer can attain a highly ordered liquid crystal phase; as the temperature is increased, the solid semicrystalline polymer passes through its liquid crystalline phase to an isotropic liquid state.

---

* Current address: Raytheon Corporation, Tewksbury, MA

Additional advantages of the thermotropic class of polymers are that their molecular structures can be subtly altered to fit processing requirements, and final properties of the polymers can be adjusted through chemical variations in their backbones or side groups. Therefore, these polymers are easily tailored to meet specific requirements, such as military protection devices and garments. Shown here are a few representative examples of TLCPs.

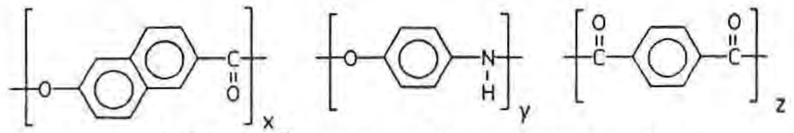

VECTRA®, a commercial copolyester amide
(Hoechst-Celanese Corp.)

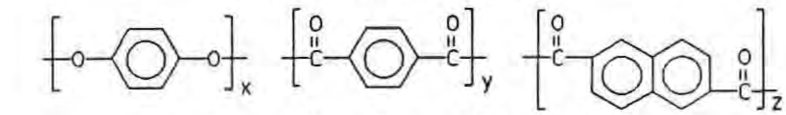

A patented copolyester (Kodak)[3]

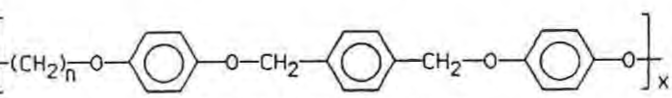

A main chain polyether[4]

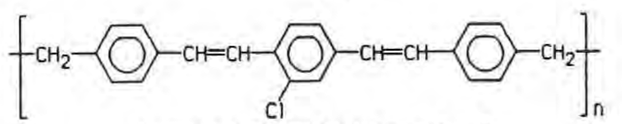

A main chain polyhydrocarbon[5]

Shown in the above polymers are a few structural features which can be used to transform a rigid aromatic polymer into a processable TLCP. The rigidity or the crystallinity of the polymer may be interrupted in three ways: by inhibiting crystallization with a crankshaft-like structure, as in the VECTRA and copolyester examples; by making the main chain flexible through the introduction of spacer groups, such as extended methylene links in between the rigid aromatic units (referred to as mesogens), as in the case of the main chain polyether; and by introducing an "impurity" into the rigid aromatic structure by ring substitution or main chain irregularity, as in the example of a main chain polyhydrocarbon.

Research is proceeding in both industry and academia to synthesize stronger, cheaper and process-tailored TLCPs. Relationships are being established, at least on the empirical level, between the polymer molecular structure (involving linkage type, flexible spacer length, substituent type, and mesogen type) and the physical properties of the product (such as thermal transitions, morphology, rheology, and tensile properties). To date, the most heavily researched families of TLCPs appear to be the ester, the amide, and the ether-linked polymers, while less data are available for wholly hydrocarbon polymers, which are difficult to synthesize, for urethane-linked polymers, and for carbonate-linked polymers. Only a few research groups have worked on polycarbonate thermotropic liquid crystalline polymers. Roviello and colleagues [6,7,8] have synthesized and studied such TLCPs:

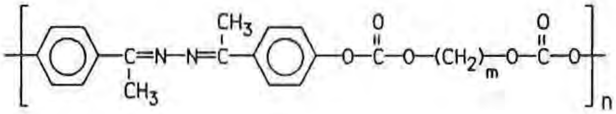

m = 6, 8, 10, 12

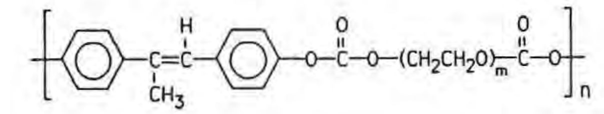

m = 2, 3, 4

In studies of the first polymer shown above, Roviello[6] has found that the polycarbonates exhibit lower melting points and that their liquid crystal phases have greater thermal stability than their polyester counterparts. It has also been found that the temperature of full isotropization (melting to the liquid state) decreases as the length of the flexible spacer -(CH_2)- increases. Also, the thermal stability range of the liquid crystalline phase decreases as the methylene chain segment increases. These last two features are not exclusive to the polycarbonates but have also been observed in polyester-based TLCPs.

More recently, Sato[9] and colleagues have successfully synthesized a polycarbonate,

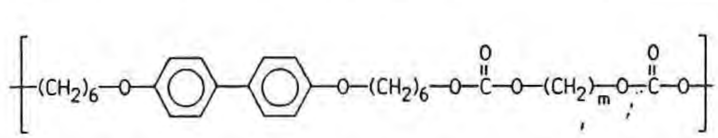

m = 4, 6, 8

which shows evidence of two forms of liquid crystalline phases: nematic and smectic. Schematically, these types of liquid crystal ordering are depicted in the following manner:

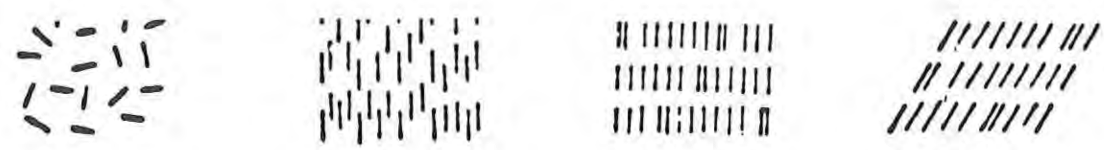

Liquid Nematic Smectic A Smectic C

Sato has found that a wide distribution in polymer molecular weights leads to a wide melting range and also can affect the liquid crystalline transition temperature. Of interest to us is Sato's thermal characterization of his polymers. Typically, the melting temperature of the crystalline to liquid crystalline phase, T_m, and the isotropization temperature of the liquid crystal to isotropic liquid, T_i, are key measurements confirming the presence of liquid crystallinity. As Sato's polycarbonates are heated, two distinct thermal transitions are observed by differential scanning calorimetry (DSC). On subsequent cooling, only one exothermic peak can be seen by DSC. As will be mentioned later, we are reporting similar phenomena. This makes phase identification of the experimental polymers difficult, and other experimental methods, such as hot-stage optical polarized microscopy diffraction, must be used to verify the liquid crystalline transitions. These latter two techniques are also particularly useful in identifying the type of liquid crystallinity present (nematic or smectic).

The polycarbonates reported by our research group are similar to Roviello's stilbene mesogen having flexible methylene spacer groups,

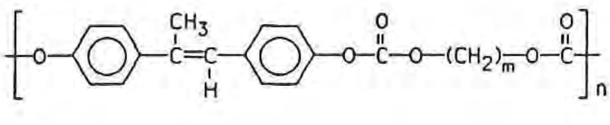

m = 5, 10

We have also examined a polymer based upon a benzoate rigid unit bonded with the carbonate linkage to the flexible methylene spacer group:

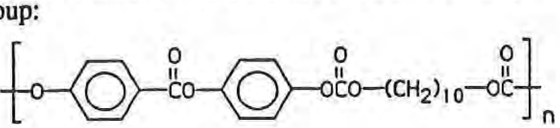

Stilbene and benzoate mesogens have developed thermotropic liquid crystallinity when synthesized with flexible methylene spacers to produce polyethers and polyesters. Recently, Percec[10] has shown that ether linkages are much more thermally stable, more soluble, more hydrolytically stable, and have lower thermal transitions than polymers containing ester linkages. It is expected that carbonate-linked mesogens will also produce very thermally stable polymers. In addition to Roviello and Sirigu's work, polycarbonates based upon other mesogens and exhibiting liquid crystallinity have recently been reported.[11,12]

In this work, flexible methylene units are incorporated into the fairly rigid main chain with carbonate linkages in order to synthesize polymers having a liquid crystal phase between approximately 200 and 300°C, the temperature range where conventional thermoplastics are processed. Discussed herein are our preliminary findings of three liquid crystalline polycarbonates.

EXPERIMENTAL

Three polymers have been synthesized, using the following procedures, which exhibit thermotropic liquid crystallinity.

Trans 4,4'-dihydroxy-α–methyl stilbene synthesis is a straightforward procedure involving acid-catalyzed addition of phenol to chloroacetone:

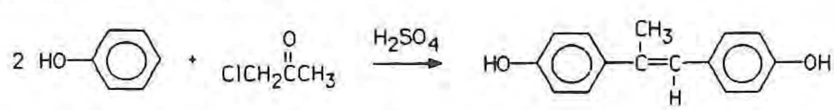

(Eq. 1)

Product 1

Following this reaction and using the procedure of Zaheer et al.,[13] the crude stilbene monomer was produced in 55% yield. However, it was found necessary to freshly distill the chloroacetone and to purify the phenol by Draper and Pollard's procedure.[14] An effective method reported by Percec[15] was used for monomer purification. The crude stilbene monomer was dissolved in a minimal amount of ethanol:water solution, followed by two 24-hour Soxhlet extractions in benzene.

The second monomer for the synthesis of the final TLCP was a diphenyl carbonate. Decanylene diphenyl carbonate was prepared as in Equation 2, and pentyl diphenyl carbonate was synthesized by the same method.

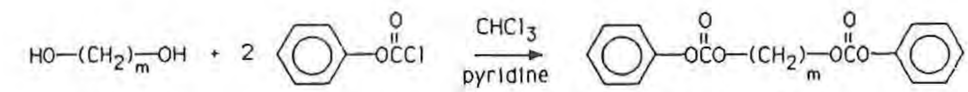

(Eq. 2)

m = 10, Product 2
m = 5, Product 3

In both syntheses, the resulting diphenyl carbonates were passed through silica gel columns with chloroform eluent to produce a final yield of 97-98%.

Polymerization to produce the final TLCPs was a condensation reaction. Again, the procedures of Sato[9] were followed using Product 1 monomer reacted with either Product 2 or Product 3 monomers:

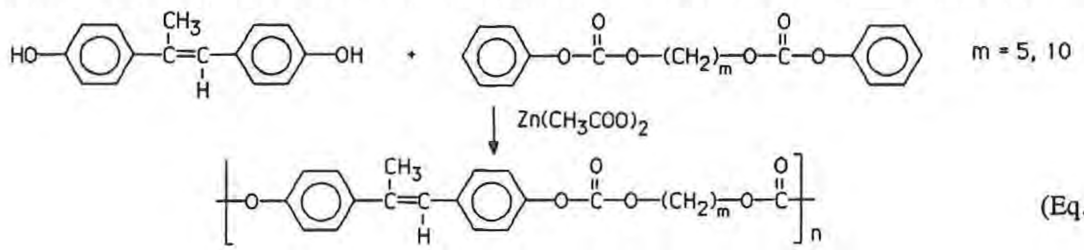

(Eq. 3)

Equimolar amounts of the two monomers were heated to 190-200°C for 2.5 hours under nitrogen atmosphere with a catalytic amount of zinc acetate. The pressure was reduced and temperature was increased to 200-210°C for an additional 2 hours. The final remaining product was a brown glassy solid for both pentyl and decanyl cases.

The second type of TLCP considered in this work is based upon the mono-(4-hydroxy benzoate) of hydroquinone mesogen with a 10-methylene spacer group. This was prepared according to the method of Krigbaum et al.[16]

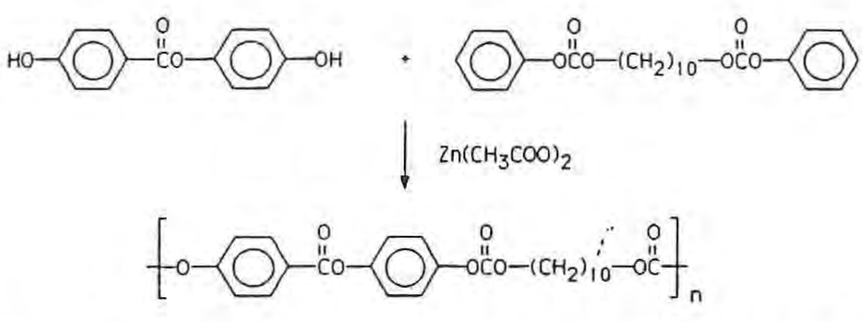

(Eq. 4)

Polymerization took place by Equation 4 in a reaction setup identical to that for the preparation of the stilbene-containing polymers. Reaction times and temperatures were respectively: 2.5 hours at atmospheric pressure under nitrogen flow at 250-260°C followed by 2 hours at reduced pressure under a nitrogen atmosphere at 260-270°C. A glassy brown solid was obtained.

CHARACTERIZATION

Elemental analysis for carbon, hydrogen and oxygen was performed on each polymer by Midwest Microlabs. Structures of the polymers were verified by carbon-13 NMR, while the structure of trans-4,4'-dihydroxy-α-methyl stilbene was verified by proton NMR using a Varian XL-200. Purity of monomers was determined by high pressure liquid chromatography (HPLC) using a Waters liquid chromatograph with a reversed phase C-18 Radial Pak cartridge column at 600 psi and a methanol carrier solvent. An HP 1040A HPLC diode array detection system monitored eluting peaks.

The soluble products from Equation 2 were analyzed by size exclusion chromatography using Waters Associates Ultrastyragel columns (500, 1,000, and 10,000 angstroms) with chloroform carrier solvent and a Hitachi UV detector at 250 nanometers.

A DuPont 951 differential scanning calorimeter (DSC) equipped with a DuPont 1090 thermal analyzer data station was used to obtain transition temperatures for heating scans only. A DuPont 2910 DSC with a 2000 analyzer was used for heating with controlled cooling experiments. A Perkin Elmer DSC-2C with a TADS-3600 microprocessor data station was also used for this purpose. Subambient analysis was performed by means of cooling by liquid nitrogen. All samples were run at a scan rate of 10°C/min in a nitrogen atmosphere. The system was calibrated with indium and tin standards.

A DuPont 951 thermogravimetric analyzer (TGA) equipped with a DuPont 1090 thermal analyzer was used to obtain information on decomposition temperatures. All samples were run at a scan rate of 10°C/min in a nitrogen atmosphere.

Thermal transition temperatures were verified by corresponding heating and cooling scans under a polarized optical microscope equipped with a programmable Mettler heating stage.

RESULTS

HPLC confirms the purity of the stilbene monomer. The recrystallized stilbene monomer shown in figure 1 exhibits a high molecular weight shoulder, which corresponds to the chromatogram for the insoluble extraction residue from the Soxhlet thimble. The once- and the twice-extracted products exhibit no shoulder, but a slight shift to longer retention times is evident.

Proton NMR of the extracted product clearly verifies the structure of the trans 4,4'-dihydroxy-α-methyl stilbene, showing no presence of the cis isomer, figure 2. Also, results from elemental analysis show no unexpected products in Table 1.

DSC traces of the stilbene monomer are also a very sensitive indicator of purity. The melting endotherms for the product show a lowering of the melting point and a sharpening of the endotherm in figure 3, as well as loss of the high melting shoulder in figure 4, as the recrystallized but impure stilbene is further purified by extraction.

The stilbene decanylene carbonate polymer produced both a chloroform-soluble and an insoluble fraction. Both the filtrate and the insoluble portion were worked up to what appeared to be a powdery low and fibrous high molecular weight polymer, respectively. Total yield of these materials was 33% for the low molecular weight and 38% for the high molecular weight polymers.

In the case of the stilbene pentylene carbonate polymer, the glassy brown solid resulting from this synthesis also incompletely dissolved in chloroform. The low (183°C) melting temperature of the soluble fraction indicated that this product was unreacted monomer. The high molecular weight fraction resulted in a 44% yield of the yellow fibrous solid.

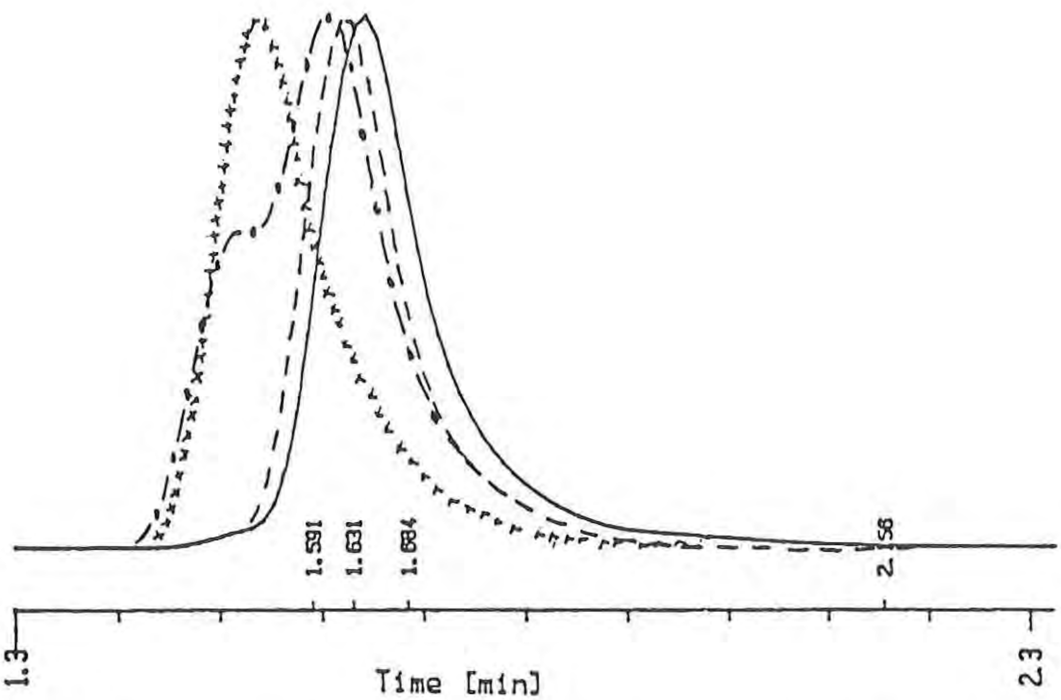

Figure 1. HPLC of recrystallized stilbene (.....), extracted stilbene (—), twice extracted stilbene (_), and extraction residue (xxx). Injection volume, 5μL; mobile phase, MeOH at 2 mL/min; detection wavelength, 210 nm.

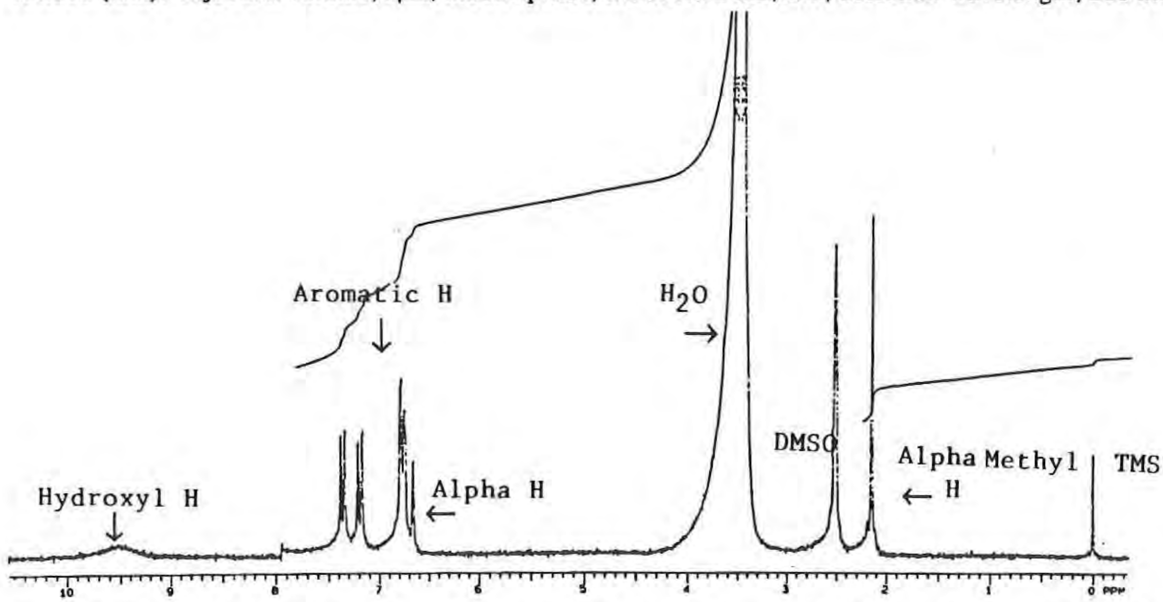

Figure 2. Proton NMR of twice extracted trans-4,4'-dihydroxy-α-methyl stilbene in deuterated DMSO.

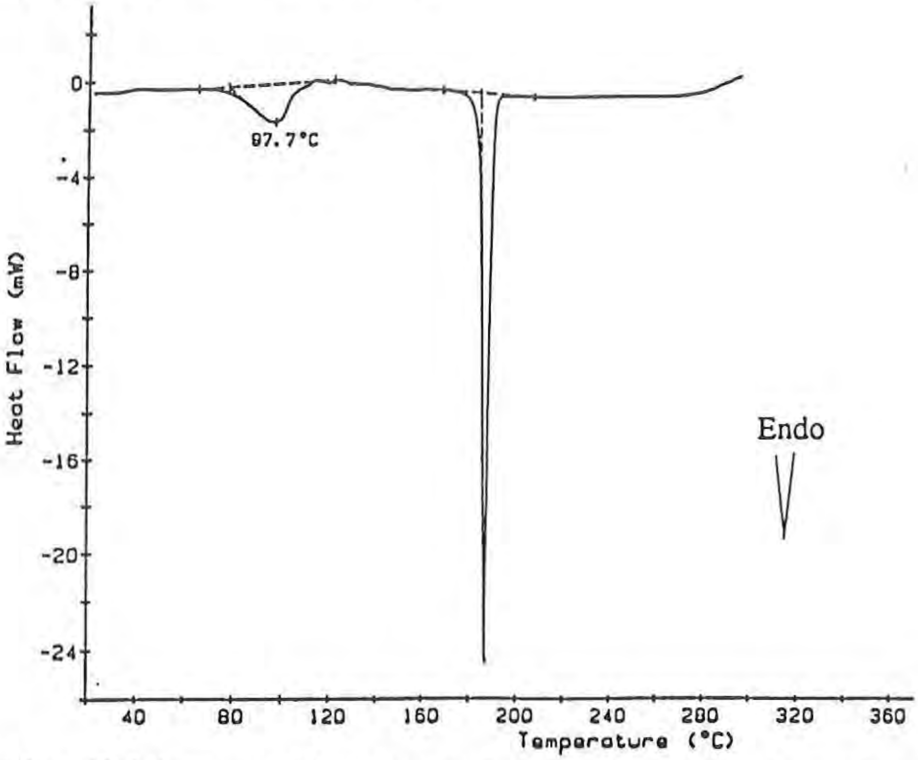

Figure 3. DuPont 1090 thermogram of twice extracted stilbene. Melting endotherm at 187°C. No impurity present. H_2O at 97.7°C. Rate, 10°C/min.

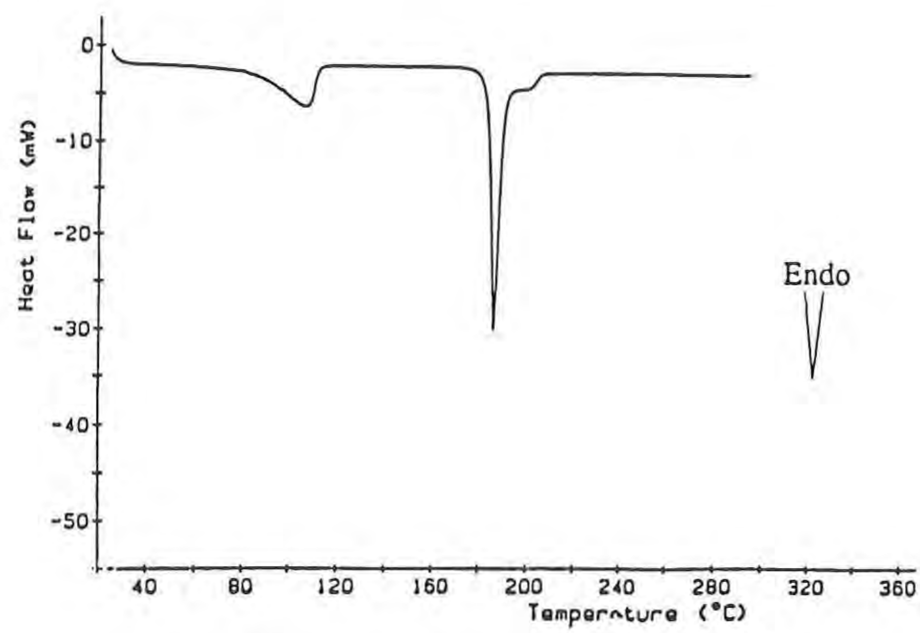

Figure 4. DuPont 1090 thermogram of recrystallized stilbene showing melting endotherm at 186°C with higher shoulder of impurity. H_2O endotherm at 100°C. Rate, 10°C/min.

Molecular weight was determined only for the soluble powdery stilbene decanylene polymer. The fibrous products were insoluble in all common solvents. The soluble polymer showed a broad molecular weight distribution with a number average of approximately 3,000 amu. Molecular weight distribution for other polymers could not be measured by solution techniques or chromatography, but for purposes of general comparison, it is assumed that fibrous polymers are high while powdery products are low molecular weight materials.

As a result of these stilbene diphenyl carbonate reactions, three main products were available for liquid crystal characterization: HMS-10H, HMS-10L, and HMS-5H, where HMS represents an acronym for hydroxy methyl stilbene polymer, 10 and 5 refer to the methylene spacer length, and H or L refer to high or low molecular weight products.

The glassy, brown solid obtained upon cooling to room temperature was dissolved in chloroform, filtered to remove insolubles and then precipitated with methanol. A tan solid having a stringy texture was obtained by filtration. Washing the precipitate several times with methanol followed by drying resulted in a gray solid in a 61% yield. This polymer is designated HBPC-10 for hydroxy benzoate polycarbonate with a 10 methylene spacer length, and was found to be soluble in chloroform.

Shown in Table 2 are thermal transitions obtained from differential scanning calorimetry (DSC). These transitions occur well below the temperatures of decomposition, which were determined by TGA and are indicated in part C of Table 2. Thermal data were collected on fresh raw products as well as on HMS-10H (aged for 2.5 years at 25°C) and on HMS-10L and HPBC (which could be purified by reprecipitation). Of the transitions in this table, T_{lc} is the liquid-to-liquid crystallization temperature and T_k is the liquid crystal-to-crystal transition; T_m and T_i have been described earlier. ΔH_m and ΔH_i are the entropies of melting and isotropization, respectively.

Complexities of the transitions listed in this Table are exemplified in figures 5 and 6, which can be compared to the melting of the corresponding simple monomeric compound of trans-4,4'-dihydroxy-α-methyl stilbene in figure 3. The polymer's thermal response involves a changing baseline, broad endotherms and exotherms due to a broad molecular weight distribution, multiple endotherms due to polymorphism, and slope discontinuities, one of which is the second-order glass transition.

Table 1.

Elemental Analysis

	Theoretical (%)			Actual (%)			
Sample	C	O	H	C	H	O	Ash
HMS-5	69.0	5.7	25.0	65.73	5.57	25.78	1.7
HMS-10L	71.6	7.07	21.2	70.4	7.17	19.8	- -
HMS-10H	71.6	7.07	21.2	67.18	6.78	16.6	4.8
HBPC-10	65.8	6.1	28.1	70.02	6.88	20.25	- -

Table 2.
Summary of Thermal Transitions

A. Differential Scanning Calorimetry of Unpurified Products

	First Heat				First Cool		Second Heat	
	T_m (°C)	T_i (°C)	ΔH_m (J/g)	ΔH_i (J/g)	T_k (°C)	T_{lc} (°C)	T_m (°C)	T_i (°C)
HMS-5H	158	184	2.7	1.0	—	—	—	—
HMS-10H	84	149	16	2.6	—	—	—	—
HMS-10H (aged)	110	157	- -	- -	72	- -	80	- -
HMS-10L	—	105	—	20	—	—	—	—
HBPC-10	81	102	—	—	—	—	—	—

B. Differential Scanning Calorimetry of Purified Products

	First Heat				First Cool		Second Heat	
	T_m (°C)	T_i (°C)	ΔH_m (J/g)	ΔH_i (J/g)	T_k (°C)	T_{lc} (°C)	T_m (°C)	T_i (°C)
HMS-10L	73	105	2.1	8.8	84	—	—	107
HBPC-10	—	76	—	1.7	—	—	—	—

C. Thermogravimetric Analysis

	Decomposition Temperature (°C)	Total Weight Loss (%)
HMS-5H	355-465	78.9
HMS-10H	390	77.3
HMS-10L	——	——
HBPC-10	455	84.9

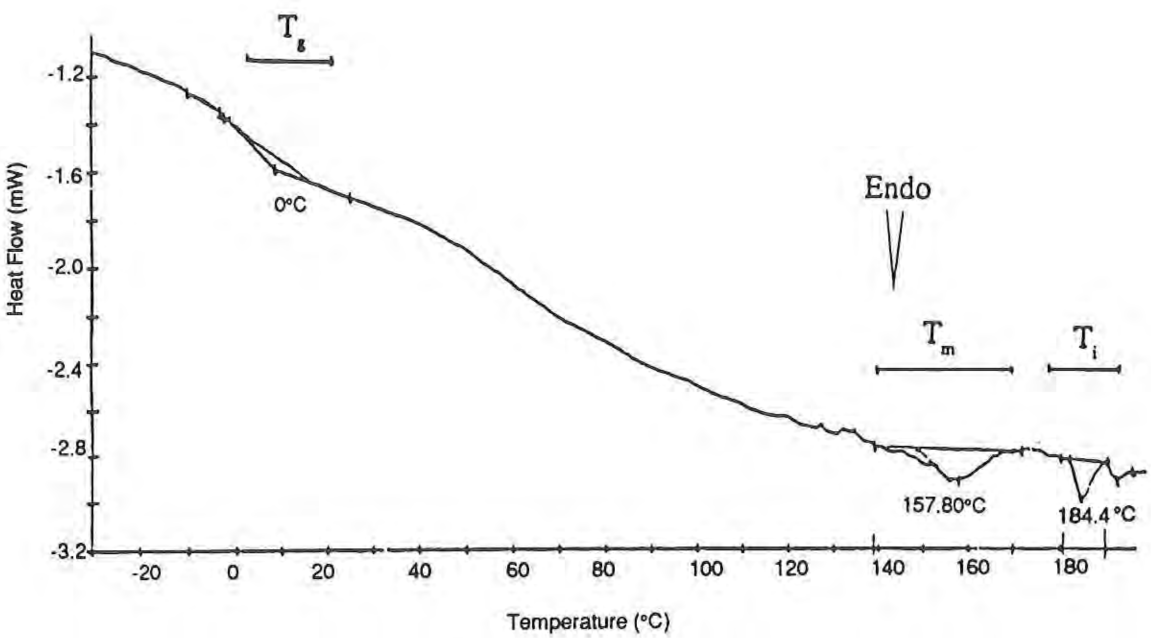

Figure 5. DuPont 1090 thermogram of HMS-5H. Rate, 10°C/min.

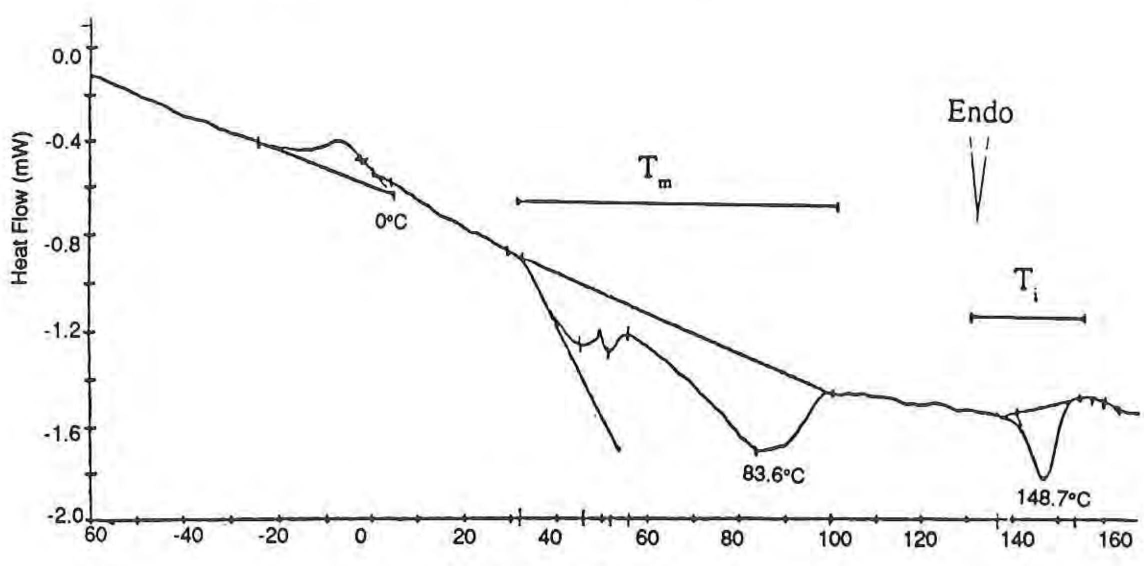

Figure 6. DuPont 1090 thermogram of HMS-10H. Rate, 10°C/min.

DISCUSSION

The structural differences between our three polymers are in the length of the spacer group and the nature of the mesogenic unit. We can observe the role that each of these structural features plays. We have also obtained both a high and a low molecular weight fraction of the HMS-10, so molecular weight effects can be assessed in this case. Shown below, the mesogen in each case is highlighted in brackets.

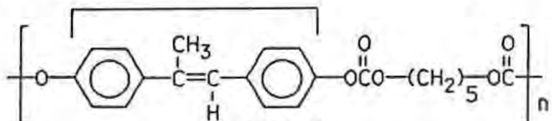

HMS-5

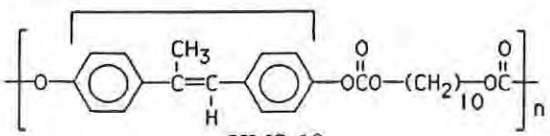

HMS-10

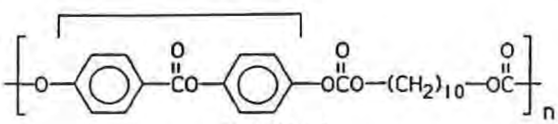

HBPC-10

Determinations of structural effects upon liquid crystallinity are limited to the measurement of thermal transitions in this preliminary work. The values we have listed in Table 2 appear to be real transitions in almost every case, as opposed to baseline fluctuations, particularly for the first heating of these samples.

Heating curves for our raw polymers (HBPC-10, HMS-10H, HMS-5H, and HMS-10L) are indicated in figures 5-8. HMS-10H and 5H are liquid crystalline. Based upon the enthalpies of the liquid crystal to isotropic transitions of the HMS-10H and 5H polymers, it is likely that a nematic phase is present, since nematic isotropic transitions have been reported in the literature with enthalpies in the range of approximately 0.5 to 3.0 J/g. [17,18] This has been verified by polarized optical microscopy, where the highlighted crystals in the darkened isotropic background arrange in a characteristic threadlike pattern at the appropriate temperature on the hot stage.

Comparing the HMS-10H with HMS-5H, the effect of longer spacer groups is to lower the transition temperatures T_m and T_i and to broaden the range of liquid crystallinity. The lower transition temperatures of HMS-10H are a result of its longer flexible spacer length. Liquid crystal to isotropic enthalpies of 0.95 J/g for HMS-5H and 2.57 J/g for HMS-10H are in agreement with the odd/even effect reported for other liquid crystalline polymers consisting of alternating rigid and flexible units. [17,19] Temperature transitions for TLCPs have shown a sensitivity to the number, m, of repeat units in a flexible spacer group. This is seen in an odd/even effect whereby ΔHi values appear normal for m-odd, but increase with increasing m-even up to a limiting value.[20,21] This behavior is thought to be due to a more highly ordered nematic phase for the m-even polymers.[22]

Investigating the effect of mesogen type, it is found that the benzoate mesogen in HBPC-10 has lowered the crystal-liquid crystal and liquid crystal-liquid transition temperatures significantly, versus those based upon a stilbene mesogen. HBPC-10 has an almost indistinguishably small LC region, as shown in figure 7.

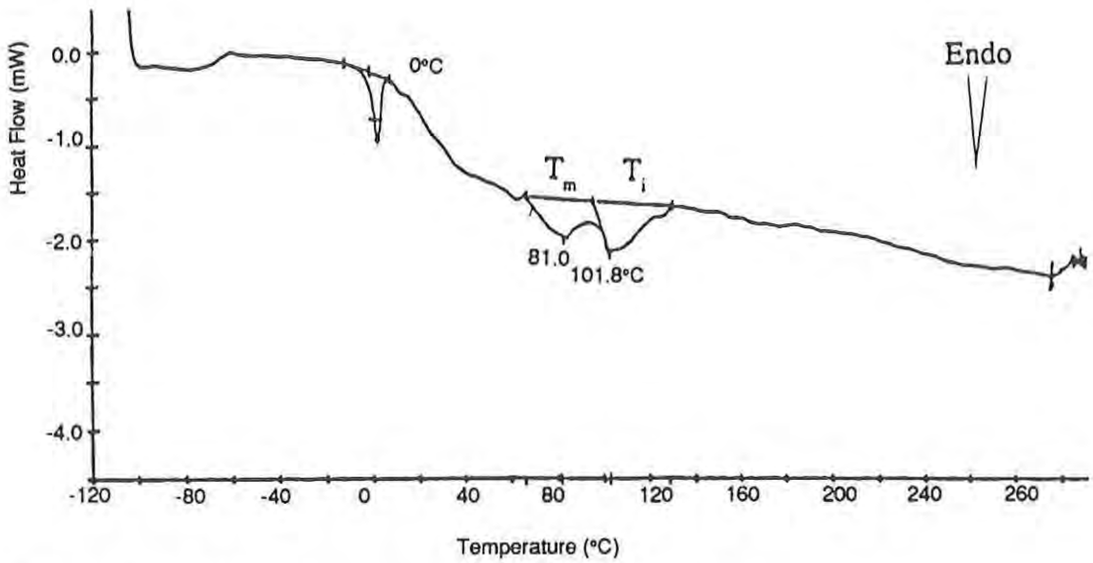

Figure 7. DuPont 1090 thermogram of HBPC-10. Rate, 10°C/min.

It is difficult to determine the effect of impurities on liquid crystallinity, but it is expected that impurities can disrupt the ordered phases. HMS-10L was examined by DSC before and after purification. Data in Table 2 and figures 8 and 9 show that liquid crystalline behavior for the low molecular weight HMS-10L occurs after purification. HMS-10 was resynthesized and characterized to determine the reproducibility of our measurements on our first material. Again, a chloroform soluble product was obtained, which we designated HMS-10L(2). After structural verification by NMR, thermal transition temperatures were obtained by DSC. These transitions, shown in figure 10, are reproducible in repeated heating and cooling scans, and are in good agreement with the first cool and second heat thermal transitions for HMS-10L, shown in figure 9.

We attempted to verify the presence of the crystalline transitions by repeated heating and cooling scans, expecting to see a purely thermodynamic response of the polymers to temperature changes. However, the liquid crystalline transitions reduce to what appears to be a single crystalline melt after repeated coolings (figures 9, 10, and 11). There was no reversibility of the phase changes — endotherms of melting during heating do not correspond to similar exotherms during crystallization of the same undisturbed sample. These observations confirm the previously mentioned behavior of Sato's[9] polycarbonates under cooling conditions.

Emerging data in the literature point to evidence that the formation of liquid crystallinity is a kinetic process. This means that one must ensure that measurements are being made on a system that is in equilibrium. It is believed that this behavior is related to the dynamics of the disclinations present in these semi- or fully rigid polymers.[23] Data show in many cases that equilibrium is achieved much faster in flexible systems such as copolymers, than in rigid homopolymers. "Equilibrium" means that the polymer chains have time to arrange themselves into crystal structures that are thermodynamically favorable. This condition can be achieved by annealing the polymers at a point 10°C above their melting temperature, T_m. The length of annealing time required for equilibrium depends on the rigidity of the polymer. These variables will be studied in the continuation of this work.

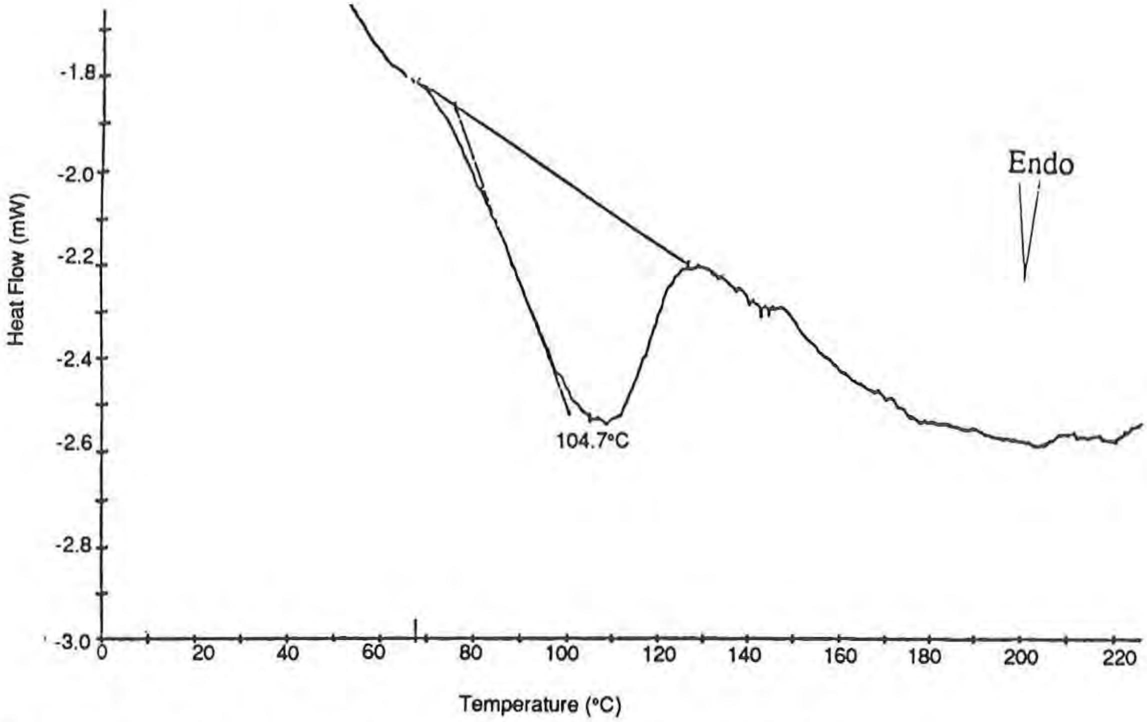

Figure 8. DuPont 1090 thermogram of unpurified HMS-10L. Rate, 10°C/min.

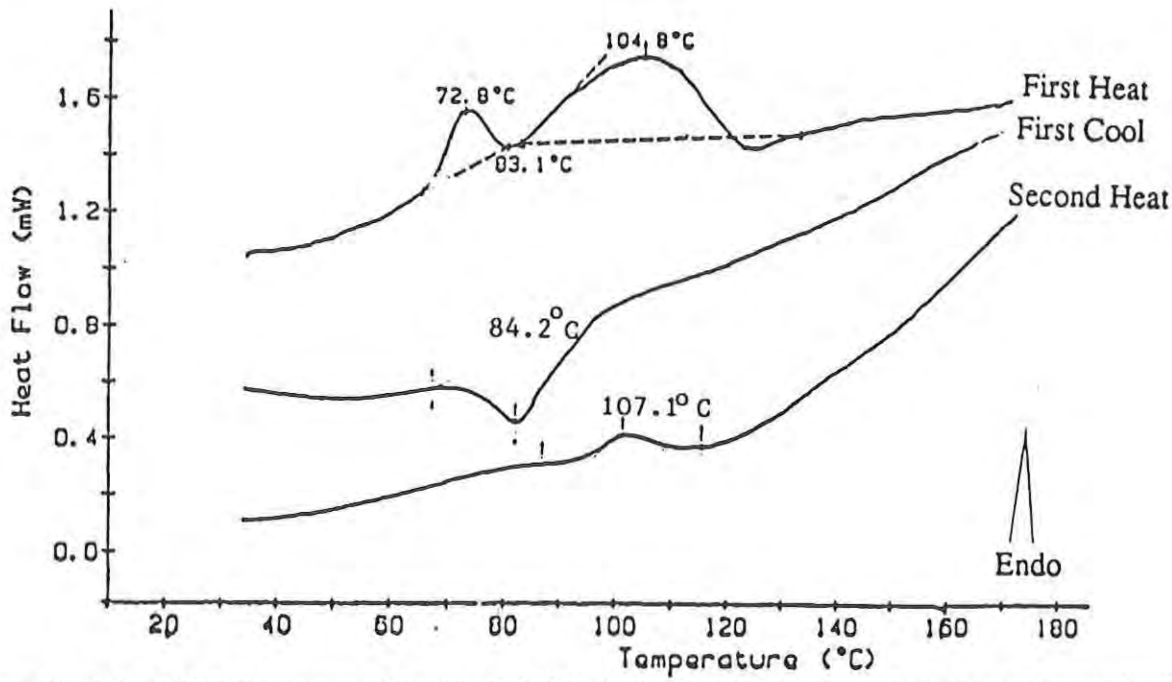

Figure 9. DuPont 2000 thermogram of purified HMS-10L with repeated heating and cooling cycles, no dwell-time between cycles. First cool and second heat are superimposed on first heat scale and are not to scale. Rate: 10°C/min.

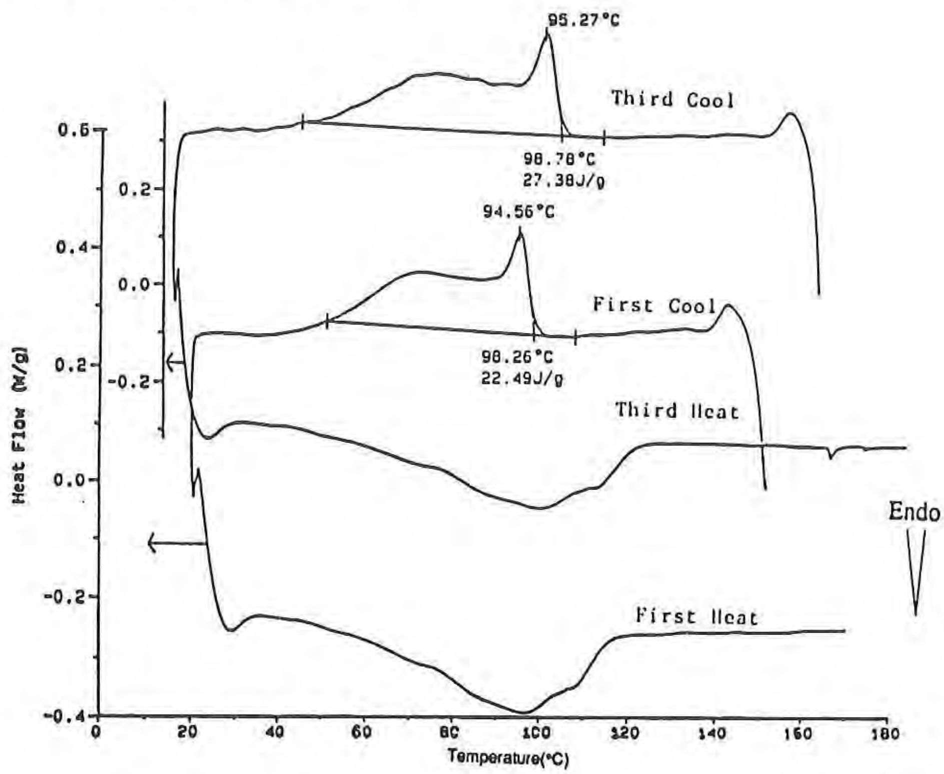

Figure 10. DuPont 2000 thermogram of resynthesized HMS-10L(2) with repeated heating and cooling cycles; no dwell-time between cycles. Third heat and cool superimposed on first heat scale.

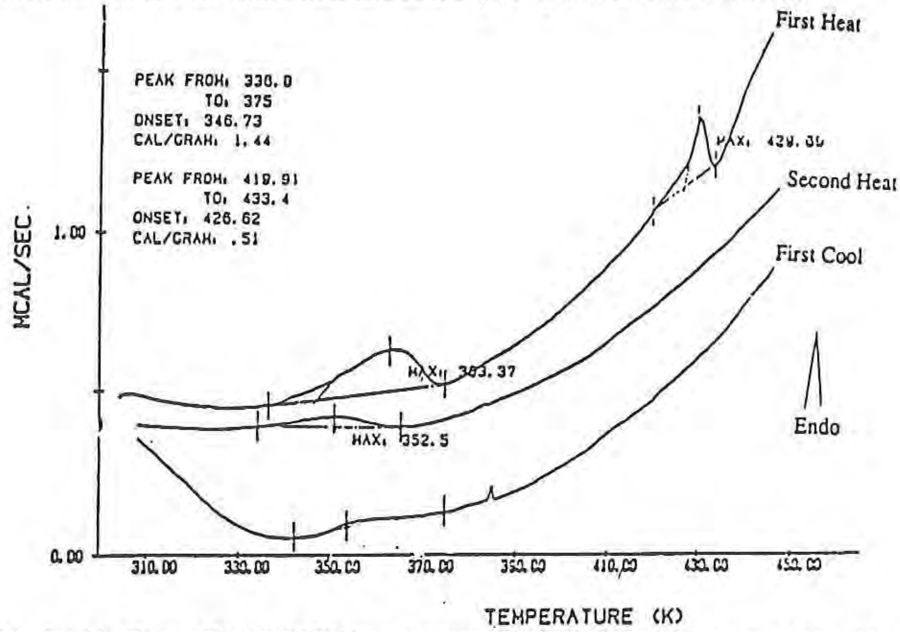

Figure 11. Perkin Elmer TADS-3600 thermogram of HMS-10H with repeated heating and cooling cycles, no dwell-time between cycles. First cool and second heat are superimposed on first heat scale and are not to scale. Rate, 10°C/min.

CONCLUSIONS

Our preliminary results suggest the following:

1. Polymers based upon the trans-4,4'-dihydroxy-α-methyl stilbene mesogen with flexible spacer lengths having 5 and 10 methylene groups appear to be liquid crystalline.

2. The polymer based upon the mono-(4-hydroxybenzoate) of hydroquinone mesogen with a flexible spacer length of 10 may be liquid crystalline.

3. High molecular weight polymers or low molecular weight purified polymers are needed to produce thermotropic liquid crystallinity.

4. Impurities suppress liquid crystallinity in low molecular weight polymers.

REFERENCES

1. M.G. Dobb, "The Production, Properties and Structure of High-Performance Poly(p-Phenylene Terephthalamide) Fibers" in Handbook of Composites - Strong Fibers, Vol. 1, W. Watt and B.V. Perov, Eds., Elsevier Science Publishing Co., NY (1988).

2. F.E. Arnold, "The Birth of Ordered Polymer Technology for Air Force Applications," in The Materials Science and Engineering of Rigid-Rod Polymers, Symposium Proceedings, Vol. 134, W. W. Adams, R. K. Eby, and D. E. McLemore, Materials Research Society, PA (1989).

3. W. J. Jackson, The British Polymer Journal, 12, 154(1980).

4. H. Jonsson, P. E. Werner, U. W. Gedde, and A. Hult, Macromolecules, 22, 1683(1989).

5. W. Memeger, Macromolecules, 22,1577 (1989).

6. A. Roviello and A. Sirigu, European Polymer Journal, 15, 423, (1979).

7. A. Roviello and A. Sirigu, European Polymer Journal, 15, 61 (1979).

8. A. Roviello and A. Sirigu, Gazz. Chim. Ital, 110, 403 (1980).

9. M. Sato, K. Nakatsuchi and Y. Ohkatsu, Macromol. Chem., Rap. Comm., 7, 231 (1986).

10. V. Percec, "Liquid Crystalline Polyethers," ONR-TR-18, Contract N0014-86-K-0284, August 1987.

11. U.S. Pat. 4,398,018 (1983), inv.: M.K. Akhapeddi, B.T. DeBend, V.C. Lai, and D.C. Prevonsek; Chem. Abstr., 99, 176482s (1983).

12. Y.C. Lai, B.T. DeBend, D.C. Prevonsek, J. Appl. Polym. Sci., 36, 819 (1988).

13. S.H. Zaheer, B. Singh, B. Bhushan, P.M. Bhargava, I.K. Kacker, K. Ramachandran, V.D.N. Sastri and N.S. Rao, J. Chem. Soc., Lond., 1954, 3360 (1954).

14. Draper and Pollard, Science, 109, 448 (1949), also in "Purification of Laboratory Chemicals," D.D. Perrin, W.L.F. Armarego, and D.R. Perrin, Pergamon Press, Ltd, NY, 235(1966).

15. V. Percec, H. Nava, and H. Jonsson, J. Polym. Sci: A, 25, 1943 (1987).

16. W.R. Krigbaum, R. Kotek, I. Ishikawa, H. Hakemi, and J. Preston, Europ. Polym. J., 20 (3), 225 (1984).

17. A. Blumstein, M.M. Gauthier, O. Thomas and R.B. Blumstein, Farad. Disc. Chem. Soc., 19, 33(1985).

18. C. Ober, J.-I. Jin and R.W. Lenz, Polym. J., 14(1), 9 (1982).

19. O. Thomas, PhD Dissertation, University of Lowell, 1984.

20. W. R. Krigbaum, J.Appl. Polym. Sci.: Applied Polymer Symp., 41, 105 (1985).

21. A. Blumstein and O. Thomas, Macromolecules, 15, 1264 (1982).

22. A. Blumstein, O. Thomas, J. Asrar, P. Makris, S.B. Clough, and R.B. Blumstein, J. Polym. Sci., Polym. Litt. Ed., 22, 13 (1984).

23. V. Percec, and K. Asami, Polymer Preprints, 29 (2), 290 (1988).

Title: Mechanistic Study of the Response of Nonlinear Optical Materials to Intense Laser Beams

*Mr. Joseph F. Roach and Dr. Edward M. Healy

ABSTRACT: The protection of the individual soldier from tunable laser sources is of considerable interest and has application to all branches of the services. The project represents a giant step up in protection from discrete line emitting lasers. A major effort in this arena centers on the interplay of nonlinear optical materials with devices and their ability to divert damaging laser light from the eyes.

The mechanisms by which laser light is modified by nonlinear effects are the object of this study. Measurements are not trivial, generally occurring in the picosecond time frame. This paper reports the establishment of a test bed set up to characterize and measure the magnitude of nonlinear coefficients using optical phase conjugation techniques. The initial test data are consistent with published data verifying the validity of the measurement technique. Data obtained from measurements will provide a basis from which interpretation of the nonlinear characteristics can be accomplished. This first step, measurement, is necessary to verify the "nonlinearity" of materials and their subsequent applicability to eye protection. Few laboratories have this special measuring capability.

* BIOGRAPHY: Present Assignment; Chief, Directed Energy Protection Branch, Physical Sciences Division, Soldier Science Directorate. Bachelor of Science Degree, Northeastern University, 1960.

Mechanistic Study of the Response of Nonlinear Optical Materials to Intense Laser Beams

Mr Joseph F. Roach and Dr Edward M. Healy

Introduction

Nonlinear optical material studies are currently being pursued by industry, the academic community and government in the interests of new and novel applications. Nonlinear materials, in general, are distinguished from linear materials by the effects generated from the interaction of intense electric fields with dipole (polarization) orientation. This interaction gives rise to a number of interesting phenomena that include electro-optic effects, frequency multiplexing, the Kerr effect (nonlinear index change), stimulated Brillouin and Raman scattering and others. The interest of this study centers on developing eye protection against tunable lasers and focuses on the Kerr effect as the most promising method by which this task can be successful. The Kerr effect, a third-order, nonlinear optical process, is characterized by the measurement of Chi-3 ($X^{(3)}$) that translates into an intensity dependent refractive index effect. To be useful, the effect must modify the incoming laser beam energy incident on the eye to acceptably safe levels (delineated in Army medical publications). Chi-3 characterizes the third-order, nonlinear susceptibility of materials arising from the relationship between polarization and electric field interactions according to the following equation:

$$P(E)=X^{(1)}E+X^{(2)}E^2+X^{(3)}E^3 \tag{1}$$

where

E is the electric field
$X^{(1)}$ is the linear susceptibility
$X^{(n)}$ is the n^{th} order nonlinear susceptibility.

The $X^{(n)}$ values are constants that can be accurately measured. It is interesting to note that classical linear optics ignores the higher order

X (Chi) terms because of their small overall polarizations at low field intensities. At higher field intensities, however, $X^{(2)}$ and $X^{(3)}$ contribute significantly to the polarization aberrations. The change in the linear index of refraction due to intensity considerations can be expressed by the following:

$$(2) \qquad n = n_o + n_2 E^2$$

where

n_o is the linear refractive index

and

n_2 is the nonlinear refractive index.

It is important to point out that n_2 depends directly on $X^{(3)}$. Therefore materials developed to maximize $X^{(3)}$ will have, as a consequence, a large value for n_2 and will provide a promising approach to solving the tunable laser eye protection problem.

The purpose of this study is to examine the relevant mathematical relationships and experimental approaches that lead to the characterization of third-order, nonlinear susceptibilities of materials being developed for laser protective eyewear.

Measurement Techniques

One important technique used in Kerr effect application is the use of degenerate 4-wave mixing (DFWM), often referred to as optical phase conjugation. As the name implies, 4-wave mixing involves the coupling or the interaction of four waves in a nonlinear medium; these are the pump beams (I_B and I_F), the probe beam (I_P) and the conjugate beam (I_S). Just as a hologram is produced by the interference between a probe and reference beam in a photographic emulsion and is read by projecting the same reference wave at the hologram, so the pump beams form a transient inteference pattern (grating) in the nonlinear material that is read by the probe beam. Since the refractive index change depends on the square of the electric fields (eqn 2) and the nonlinearity of the material, a series of high and low refractive index regions develops corresponding to the peaks and valleys of the interference pattern. The interaction of the probe beam with the transient grating produces the conjugate beam. By knowing the relevant material parameters and the power in each of the four beams used in the 4-wave mixing scheme, we can determine $X^{(3)}$ values using the formula given in the paper by Acioli, Gomes and Leite[1]:

$$(3) \qquad \left|X^3_{eff}\right| = \left(I_S / I_B\right)^{1/2} \left(I_F I_P\right)^{-1/2} \frac{n_o^2\, c\, \lambda}{32\, \pi^3 L}$$

where c is the speed of light
L is the sample thickness
λ is the wavelength of light
$I_{(n)}$ are the 4-wave mixing beams.

Once the $X^{(3)}$ values are measured, the index of refraction can be obtained from the following expression:

$$(4) \qquad n_2 = \frac{0.0395}{n_o^2} \left| X^3_{eff} \right| .$$

The experimental setup used to measure the conjugate beam from 4-wave mixing is shown in figure 1.

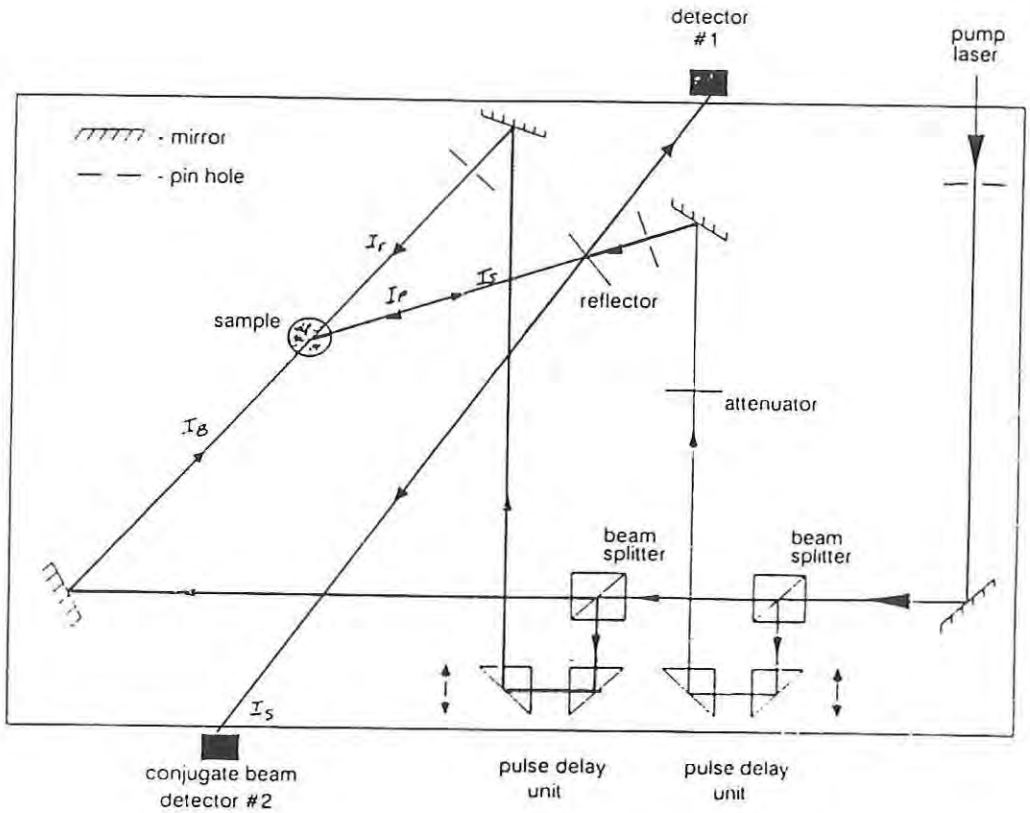

Figure 1. Experimental setup to measure phase conjugate beam via 4-wave mixing.

The pump laser originates from a doubled modelocked Nd:YAG laser operating at 10 Hertz (single pulses of 532 nm light with 17 picosecond FWHM and average energy of 25 millijoules). It is split into three beams I_F, I_B, and I_P by means of cube beam splitters. The temporal and spatial overlapping of the three beams in a nonlinear sample generates a phase conjugate intensity, I_S. The two pump beams are adjusted to be equal in energy and all four beam energies are measured to provide the data needed in eqn 3 to calculate $X^{(3)}$ values. However to make the system work, very precise timing of the arrival of the beams at the sample is required. The generation of a transient grating by the

the forward and backward beams is contingent upon those beams arriving at the sample coincidently. Additionally, the probe beam must interact with the transient grating during the time it remains viable. For the materials of interest, gratings are generally formed in picoseconds (10^{-12}s) making the task of measurement very difficult. To be successful in this measuring scheme, all four beams must be synchronized so as to arrive at the sample together. It is precisely this control that the delay units provide (see fig 1).

Investigation

Instruments for measuring $X^{(3)}$ are not readily available and hence no standard technique has been established that could be used as a bench mark for accuracy. However, one material that has been studied in depth for its nonlinear properties is carbon disulfide (CS_2). Various experimental setups were used and values of $X^{(3)}$ calculated that ranged from 6.8×10^{-13} to 1.9×10^{-12} electrostatic unit (esu), (ref. 2 and 3).

Our first measurement attempt was to obtain a value of $X^{(3)}$ for CS_2 using our experimental setup. The four beams used in the experiment were measured using power meters (Laser Precision Inc), and used to calculate the $X^{(3)}$ value according to Eqn 3. The other parameters used in the calculation were:

sample length (L) =1 cm
index of refraction n_o =1.65
wavelength =532 nanometers (nm)

The energy of the conjugate signal obtained with a Laser Precision Energy Probe was an average of 10 shots. The value obtained was 0.012×10^{-4} joule for CS_2. The calculated value for $X^{(3)}$ was 4.85×10^{-12} esu and is consistent with the range of values as published.

To avoid the complicated calculations involved with $X^{(3)}$ expressions, we used an accepted technique where $X^{(3)}$ values for materials are determined by comparison with values obtained from identical experiments using CS_2 whose $X^{(3)}$ value is assumed to be known[2,4]. The expression for this calculation is shown in Eqn 5 (from Eqn 2 in ref 2).

$$5 \qquad |\chi^{(3)}_{sample}| \doteq |\chi^{(3)}_{ref}| \left(\frac{C^{(3)}_{sample}}{C^{(3)}_{ref}}\right)^{1/2} \left(\frac{n_{sample}}{n_{ref}}\right)^2 \times \left(\frac{L_{ref}\alpha_{sample}}{(1-e^{-\alpha L})e^{-\alpha L/2}}\right).$$

The sample label refers to the material being measured and the ref to CS_2. The Ls are the absorption coefficient and length of the sample. We have used this technique to investigate the nonlinear properties of organic molecules, "Disperse Red" in a polymethylmethacrylate (PMMA) polymer matrix. This molecule has been studied in other laboratories (U. of California at Irvine, U. of Lowell MA) and relatively high nonlinearity has been observed. The mechanisms of the nonlinearity are currently under investigation by Dr. P.M. Rentzepis (U of C at Irvine), but no publication has appeared at this time. We have begun preliminary studies to measure $X^{(3)}$ values for this material with different concentrations of the "Disperse red" in PMMA. Calculated values ranged from 1.41×10^{-8} to 4.36×10^{-11} esu. The magnitude of the effect appears to be related to the concentration of the dye in the PMMA host. The results are shown in Table 1 where the optical density, measured at 532 nm, reflects the measure of the concentration of the dye.

TABLE 1

$X^{(3)}$ Values for "Disperse" Red Dye

Optical Density	$X^{(3)}$ (esu)
0.10	4.36×10^{-11}
0.10	3.08×10^{-11}
0.30	1.30×10^{-10}
0.34	1.09×10^{-10}
0.74	2.89×10^{-10}
1.02	5.75×10^{-10}
1.20	7.79×10^{-10}
1.34	1.05×10^{-9}
2.09	2.64×10^{-9}
2.18	2.20×10^{-9}
3.06	7.38×10^{-9}
3.26	1.27×10^{-8}

This study is in the preliminary stages and work to understand the mechanisms continues.

Nonlinear optical properties of semiconductor glasses have also been extensively investigated because of their relatively high $X^{(3)}$ values. In particular, the reported $X^{(3)}$ values of CdS_xSe_{1-x} doped glasses vary from 10^{-10} to 10^{-9} esu.[5] We have measured the nonlinear response of a semiconductor glass, CS 3-68 and calculated a $X^{(3)}$ value of 3.06×10^{-10} esu. In a recent communication, values of $X^{(3)}$ have been calculated to be 5.1×10^{-8} esu,[6] very different from the value we measured. In the communication it was pointed out that photodarkening in the glass was evident and after irradiation with more than $2 kJ/cm^2$ (532 nm) light, phase conjugate efficiency decreased. Photodarkening has been observed in other studies[7] on other semiconductor glasses and has a significant effect on nonlinear properties. Since our values are based on the average of 10 shots, it is likely that photodarkening was occurring and could partially account for the different values of $X^{(3)}$. This aspect of the study is currently under investigation.

Conclusions

We have established a working experimental setup to measure the nonlinear properties of optical materials, specifically $X^{(3)}$ values that relate to refractive index changes. This property could be important in the design of protective eyewear for use against tunable lasers. Most measurements using this technique reside in private laboratories and the test results appear in the open literature. Instruments are not readily available that can perform the necessary measurements since most of the experiments operate in the picosecond time frame. The preliminary results we have obtained in measuring $X^{(3)}$ values for materials that other researchers have studied appear to be reasonable, being consistent with the range of values obtained. We now have confidence that we can accurately measure $X^{(3)}$ values and determine refractive index changes that can lead to a prediction of eye protection enhancement against tunable lasers.

REFERENCES

1. L.H. Acioli, A.S.L Gomes, and J.R. Leite, Appl.Phys.Lett.,53, 1788, 1988.
2. S.A. Jenekhe, S.K. Lo, and S.R. Flom, Appl.Phy.Lett.,54, 2524, 1989.
3. R.W. Boyd (unpublished),1989.
4. N.P. Xuan, J.L.Ferrier, J.Gazengel and G.Riviore, Opt.Commun.,51,433, 1984.
5. S.M. Saltiel, B.Van Wonterghem, T.E. Dutton and P.M. Rentzepis, IEEE J.Quant.Electr. QE-24, 2302, 1988
6. B.Van Wonterghem, S.M. Saltiel and P.M. Rentzepis (unpublished).
7. B.Van Wonterghem, S.M. Saltiel, T.E. Dutton and P.M. Rentzepis, J.Appl.Phys., 66, 4935, 1989.

TITLE: Techniques for Measuring Electrostatic Properties of Fabrics Containing Conductive Fibers

* Michelle L. Sutphin, Ms., Sharyn L. Seasholtz, Ms., and David J. Manseau, Mr.

ABSTRACT: Materials containing conductive fibers are being investigated for use by the Army for wear in electrostatic sensitive operations, such as fuel and munitions handling. The presence of conductive fibers increases the electrical conductivity of the fabric, resulting in a fabric with more desirable electrostatic properties. These fibers provide more permanent protection, as opposed to topical antistatic finishes currently in use which are removed after repeated launderings.

Previously, no reliable method for measuring the electrostatic resistivity of conductive fabrics was available. For this reason, test instrumentation has been purchased and modified and a test method developed to measure the electrostatic properties of fabrics containing conductive fibers.

The new test method determines the static decay rate of fabrics containing conductive fibers. Static decay rate is a measure of the length of time it takes for the fabric to dissipate its charge, and is applicable to all fabrics, whether the fabric contains conductive fibers or is topically treated. The test method involves mounting a sample across a set of parallel electrodes and charging towards 5000 volts for a period of 20 seconds. Upon completion of the charging period, the sample is grounded and the resulting voltage behavior, an exponential decay curve, recorded. From this curve, the decay time can be measured. The shorter the decay time, the faster the fabric will dissipate its charge and the safer it will be in electrostatic sensitive environments. Fabrics containing stainless steel fibers, as well as fabrics treated with a topical antistat, were tested and reveal the effectiveness and repeatability of the test methodology and instrumentation.

*BIOGRAPHY OF PRESENTER: Michelle L. Sutphin
PRESENT ASSIGNMENT: Electrical Engineer, Materials Research and Engineering Division, Individual Protection Directorate.
DEGREES HELD: B.S., Electrical Engineering, University of New Hampshire

TECHNIQUES FOR MEASURING ELECTROSTATIC PROPERTIES OF FABRICS CONTAINING CONDUCTIVE FIBERS

MICHELLE L. SUTPHIN, SHARYN L. SEASHOLTZ AND DAVID J. MANSEAU

INTRODUCTION: Static electricity is a well known phenomena. However, many do not realize the potential for this phenomena to be a safety hazard. Hospitals, for example, have long been concerned with the possibility of electrostatic discharge (ESD) igniting fumes from anesthetics in the air during surgery. More recently, industry has been affected by the increased sensitivity of components, such as transistors and integrated circuits, to ESD. Handling such components, or circuit boards containing sensitive components, when not grounded can easily cause component failures.

Static electricity in an environment can be controlled by grounding personnel and equipment, and by wearing static-dissipative clothing. In humid environments, cotton garments may be worn, for they absorb moisture from the air. The moisture content of the fabric, in turn, conducts electricity and helps to dissipate any surface charge which may develop. The humidity levels in hospitals and clean rooms are maintained at a high level for this reason. Metallic grids may be incorporated into the fabric of garments to aid in dissipating a surface charge.

The individual soldier may be exposed to the hazards of static electricity as well, and under more hazardous and less controllable conditions. For instance, soldiers handle munitions sensitive to ESD, such as electric blasting caps, and refuel aircraft where volatile fumes may be present in the air. Static discharge during such operations could cause an explosion. Safety regulations call for special grounding procedures and cotton clothing to be worn. However, humidity levels cannot be controlled when the soldier is in the field, nor is cotton practical for wear in cold regions. The soldier requires static protection independent of humidity and without sacrificing other clothing properties. Garments for the individual soldier must be durable, provide adequate camouflage protection, be flexible, launderable, and, in some cases, flame resistant as well. Many of these properties are not concerns of either hospitals or industry, and so have not been addressed.

One method of minimizing the static electricity generation and accumulation on military uniforms is by applying a topical antistat to the uniform material. These antistats increase the ability of the material to retain moisture from the air. Though these treatments work well, they wash away after repeated launderings, and require reapplication. The reapplication method requires that an antistatic treatment be added to the home or field laundry periodically. It also appears that the antistat treatments on printed fabrics, such as Nomex^{R} Battle Dress Uniforms (BDUs), wash out more quickly than when applied to nonprinted fabrics.[1] Furthermore, antistat treatments tend to interfere with the addition of other topical treatments to the fabric, such as water repellents and flame retardants. Thus, a more permanent solution is sought. Presently, the integration of conductive fibers into the fabric is being investigated. One such fabric involves mixing stainless steel fibers with staple fibers, and forming an intimate blend from which the yarn can be made. This yarn is then woven into fabric. In another type of fabric, the fibers consist of a conductive carbon core wrapped in a nylon sheath.

Incorporation of conductive fibers allows electrically insulative materials, such as Nomex^{R}, Gore-Tex^{R} and other nylon materials which are static prone, to be utilized in garments. Many of these fabrics have other desirable qualities. For example, Nomex^{R} is inherently flame-resistant. Without the addition of conductive fibers or a topical antistat, this material would be a static hazard. The addition of conductive fibers makes the material more dissipative and will prove useful in applications such as Aircrew uniforms, which require both electrostatic and flame-resistant protection. Test methods for determining the electrostatic properties of materials, as well as typical results, are reported in this paper.

THEORY BEHIND CONDUCTIVE FIBERS: Electrostatic discharge occurs when the electric field between a charged object and a conductor becomes intense enough to cause air ionization, which allows for the travel of charge across the air gap between the two objects. Volatile fumes, sensitive powders and other explosives can be ignited by the heat generated by such a spark. Thus, for human safety in electrostatic environments, the goal is to reduce the electric fields generated by the body and by clothing. This can be accomplished by grounding personnel and having them wear conductive clothing. Fabrics containing conductive fibers rid the fabric of accumulated charge in two ways: by conduction and by ionization. Conduction distributes the charge evenly over the surface of the garment. When grounded, the conductive fibers allow accumulated charge on the fabric to dissipate to ground. Dissipating the charge to ground, or even just distributing the charge over the fabric surface, reduces the intensity of the electric field. Conductive fibers aid in neutralizing surface charge on a material by way of ionization. The convergence of the immediate electric field onto the conductive fiber increases the intensity of the field at the fiber. When this field is strong enough, air ionization occurs at the conductive fiber, creating ions in the air to allow for neutralization of charge residing on the fabric surface. For example, a positively charged fiber residing within an area of negatively charged material will, when the electric field at the fiber is intense enough, attract negative ions. Positive ions are attracted to the negatively charged material, and therefore contribute toward neutralizing the surface charge.[2]

PREVIOUS TEST METHOD: One method of determining the electrostatic properties of a fabric is by measuring its surface resistivity. Until recently, this method had been the primary means of evaluating the electrostatic properties of topically treated fabrics. Surface resistivity is indicative of how readily charge moves across the surface of a fabric. The more resistant a fabric is to the flow of charge, the more likely surface charge will accumulate. A less resistant fabric will dissipate charge more easily, making charge buildup less likely. To measure this property of a fabric, a voltage source, electrometer, and parallel or concentric ring electrodes may be used (see Figures 1 and 2). The sample is mounted across the electrodes (see Figure 3) and a known voltage applied for a given period of time. At the end of this period, the current across the surface of the material is measured. The surface resistivity of the fabric is proportional to the voltage applied divided by the measured current, and can thus be calculated.[3]

This method provides useful data on fabrics that contain no conductive materials. However, where conductive fibers, conductive coatings, or fibers with conductive cores have been integrated into the fabric, the test results are often erratic and unreliable. Reasons for this include:

1. The fabric is too highly conductive and the measurements to be made are out of range of the equipment.[4]

2. The core of the fabric is conductive and, being a surface measurement, the results indicate only the properties of the outer surface of the material.[1]

3. If a small percentage (e.g., 1%) of conductive fiber is used, a continuous conductive path may or may not be present when mounted across the electrodes. This produces erratic resistivity results, both low and high in value.[5]

ALTERNATIVE TEST METHODS: Since the surface resistivity test was found unreliable for conductive fabrics, a new method of test was sought. The U.S. Army Natick Research, Development and Engineering Center (Natick), purchased and modified static test equipment and evaluated test

BLOCK DIAGRAM: SURFACE RESISTIVITY

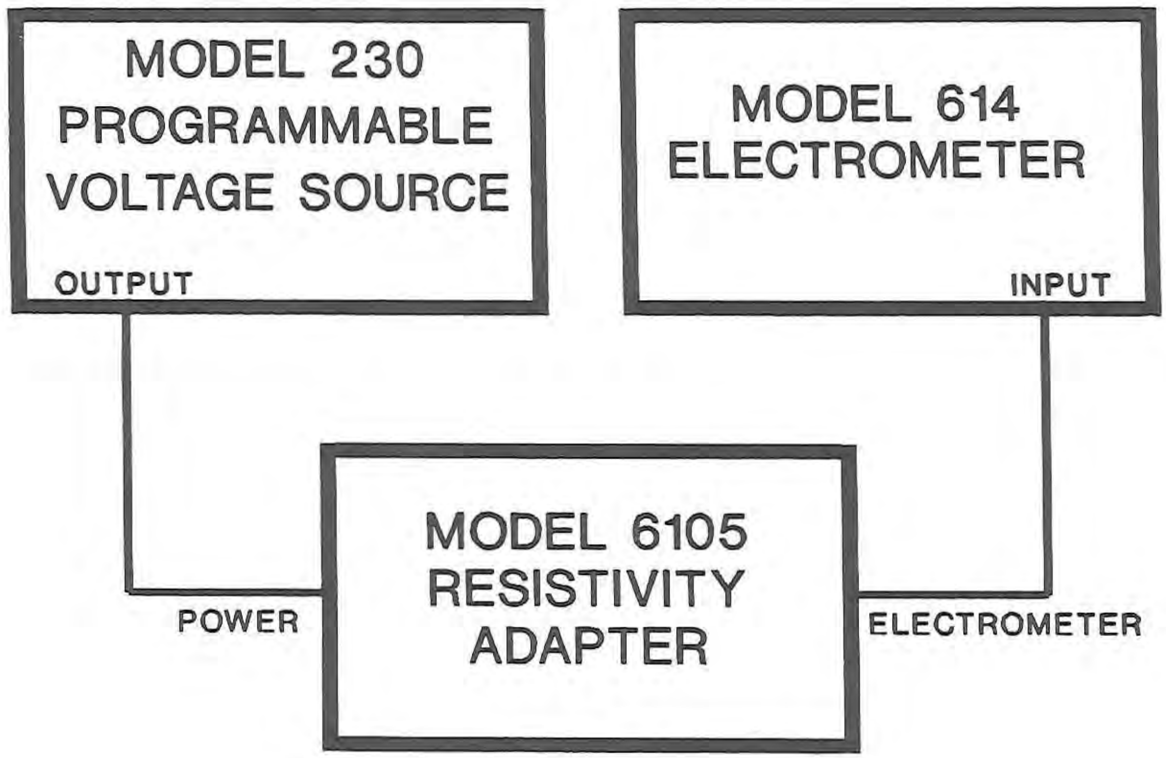

FIGURE 1

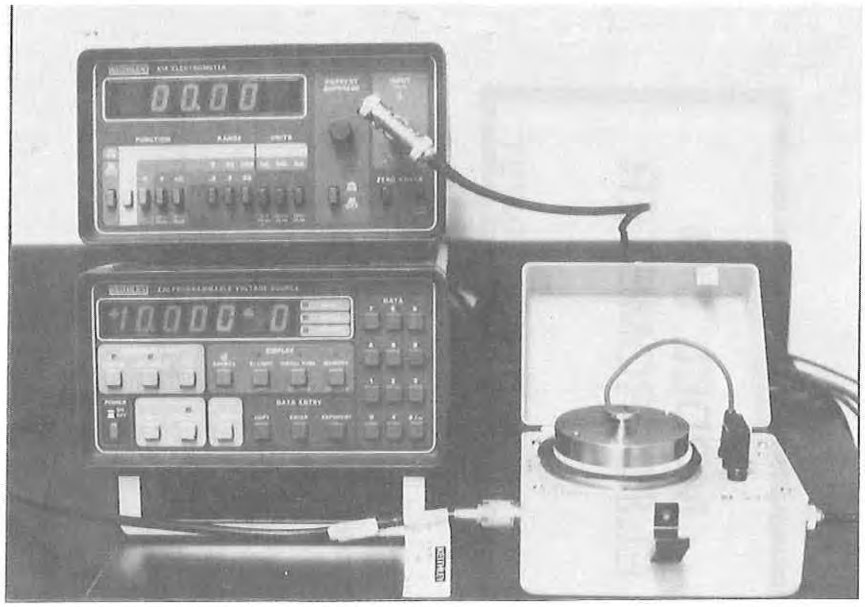

FIGURE 2

SURFACE RESISTIVITY TEST EQUIPMENT

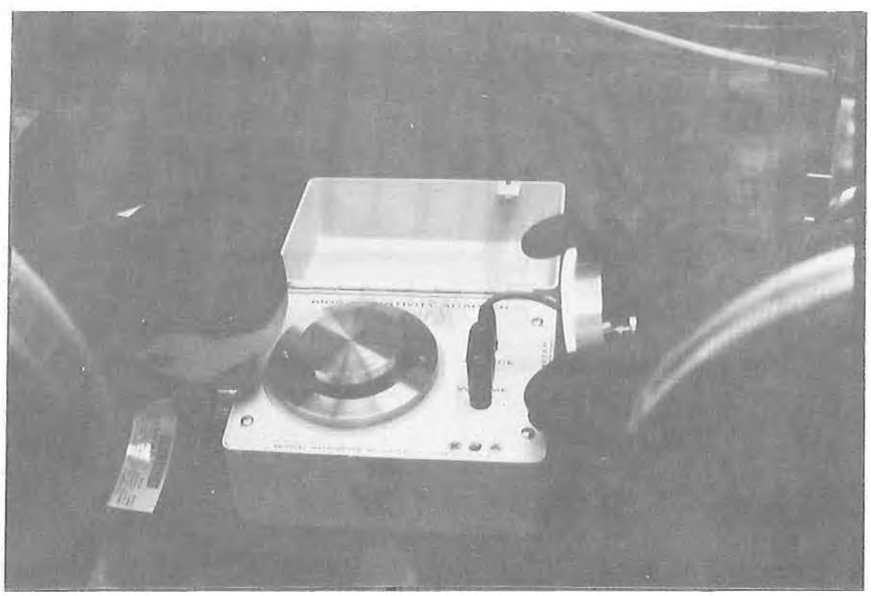

FIGURE 3

RESISTIVITY ADAPTER

procedures. Three methods for measuring the electrostatic properties of fabrics were examined to overcome the shortcoming of existing equipment in evaluating fabrics containing conductive fibers. These methods included tests for electrostatic decay rate, field suppression, and triboelectric charge generation. The feasibility of each test was then evaluated.

The triboelectric test is a measure of the amount of charge generated on a material surface after having been rubbed and separated from a second material surface. Natick found that this method yielded inconsistent results. It is believed this is due to changes in the material surface caused by the rubbing process, such as changes in smoothness, and possibly contamination of the subject material by the material with which it was rubbed. Triboelectric methods that create charge by way of separation of materials only, no rubbing, will be investigated further.

The field suppression test method is a measure of the direct current (DC) shielding ability of the material. A material with high field suppression, worn as an outer layer of clothing, will suppress any electric field caused by charges on the inner layers of clothing. Charge levels on inner layers of clothing are of little concern since most of the charge is neutralized by opposite charges residing on the layers alongside.[2] Additionally, materials which meet the requirements of the electrostatic decay method described below will also exhibit good field suppression characteristics.[1] It is therefore not deemed necessary to perform this test in addition to the electrostatic decay test. Further use for the method is not required at this time.

The electrostatic decay method has been found to be the most appropriate of the three methods evaluated for testing materials containing conductive fibers. This method is a measure of how quickly a material dissipates a charge when grounded, after having been allowed to accumulate a charge in an ungrounded state. The method has been refined so as to achieve reasonably consistent results when any one set of samples is retested under similar conditions.

THEORY BEHIND ELECTROSTATIC DECAY: Electrostatic decay is a measure of how quickly charge dissipates from sample to ground. Ideally, decay time would be determined by directly measuring the initial charge on a sample and the time it takes for the charge to decay to a certain point, such as 10% of the initial charge. Realistically, the charge on a sample cannot be measured directly, and thus another method of measurement must be utilized. This may be accomplished by measuring the electric field (volts/meter) of the charged sample at a given distance and noting the time required for the voltage level at this distance to decay from its initial value to a given level.

The time rate of charge dissipation is represented by a decay curve which is exponential. A typical exponential decay curve is written as:

(1) $X(t) = Xo \exp(-t/RC)$

where Xo = initial value, a constant (value at time t=0)
X(t) = value at time t
t = decay time (seconds)
R = effective resistance (ohms)
C = effective capacitance (farads)

The decay curve for charge is therefore written:

(2) $Q(t) = Qo \exp(-t/RC)$

where Qo = initial charge (coulombs)
Q(t) = charge at time t (coulombs)

Similarly, the decay curve for voltage is written as:

(3) $V(t) = Vo \exp(-t/RC)$

where Vo = initial voltage (volts)
V(t) = voltage at time t (volts)

It can be shown that the decay curve for voltage and the decay curve for charge are alike, since voltage is related to charge by the following equation (4).

(4) $V = Q/C$

where V = voltage (volts)
Q = charge (coulombs)
C = capacitance (farads)

Thus, substituting equation (4) into equation (3)

$V(t) = Vo \exp(-t/RC)$
$V(t) = Q(t)/C$ (capacitance is kept constant)
$Q(t)/C = Qo/C \exp(-t/RC)$
(5) $Q(t) = Qo \exp(-t/RC)$

Since equations (2) and (5) are the same, the decay curve for the voltage and for the charge of the sample are alike and will yield identical decay times. Thus, measuring the voltage behavior at a given distance from the sample is an acceptable method for measuring charge decay. Voltage measurements are taken at a one-inch distance from the fabric face.

THEORY BEHIND ELECTROSTATIC DECAY AND ELECTRIC FIELDS: Charged objects produce an electric field about them which radiates outward or inward, depending on whether the object is positively or negatively charged. An uncharged object placed in this field will acquire an induced charge opposite in polarity to that on the charged object.[2] The electrostatic decay test equipment uses this concept as a method of measuring the strength of the electric field and, thus, is indicative of charge levels on a sample.

A sample is mounted across parallel electrodes such that the sample is located one inch away from and parallel to a grounded metal plate with a hole at its center. Behind the center of this plate is a circular, metallic sensor plate. The purpose of the grounded plate is to prevent the electric field from converging onto the sensor plate, which would create a more intense field at the sensor plate. When the sample is charged, the plates attain an induced charge due to the electric field of the charged sample, and a "parallel plate capacitor" is formed. The charged sensor plate is connected to the gate of a Metal-Oxide-Semiconductor Field Effect Transistor (MOSFET).[6] The current in an FET is governed by an electric field, thus changes in charge level on the sensor plate generate current flow changes in the FET.[7] With the aid of amplifiers and additional circuitry, these changes are interpreted and ultimately displayed as voltage levels on the fabric surface.

APPARATUS AND TEST PROCEDURE: The apparatus for measuring the electrostatic decay properties of materials includes a static decay meter, faraday cage, chart recorder, digital multimeter and humidity test chamber (see Figures 4 and 5). Within the faraday cage are two parallel electrodes, and a sensor head positioned evenly between the electrodes. The sample to be tested is placed across the electrodes in front of the sensor head, and held in place with magnets[8] (see Figure 6). Descriptions of some of the materials tested are given in Table 1.

Samples, along with the faraday cage, are maintained at a constant temperature and humidity within the humidity test chamber. Circuitry contained within the faraday cage is connected to the static decay meter by way of feed-throughs in the wall of the humidity test chamber.

Six samples are cut from a fabric piece for test, three in the warp direction and three in the fill direction. These are cut such that no two samples share the same warp or filling yarns. Prior to testing, samples are preconditioned overnight at a relative humidity (RH) of 10% $\pm$ 2% RH,

BLOCK DIAGRAM: STATIC DECAY

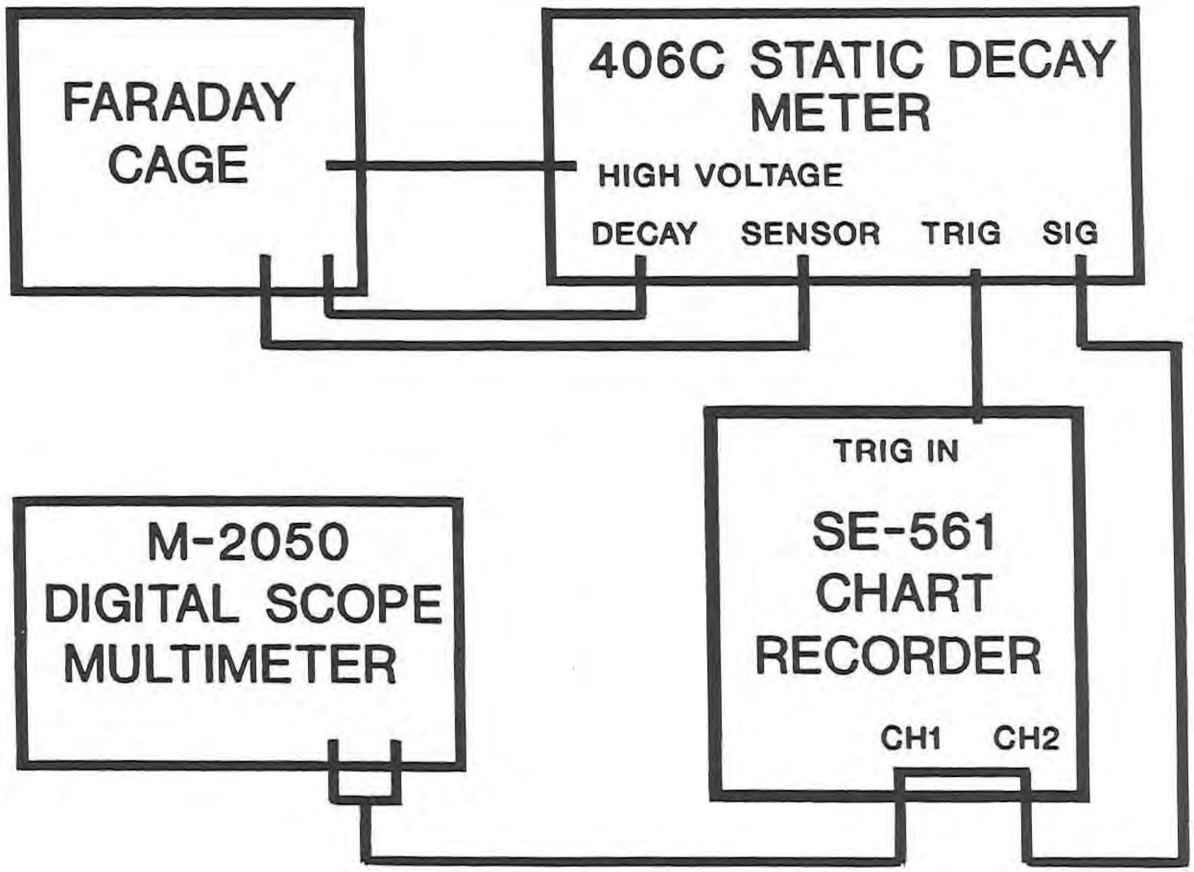

FIGURE 4

FIGURE 5
STATIC DECAY TEST EQUIPMENT

FIGURE 6
FARADAY CAGE

TABLE 1
MATERIALS DISPLAYED IN FIGURES 9 AND 10

IDENTIFIER	MATERIAL
A	Standard Sage Green, 95/5 Nomex^R/Kevlar^R, Plain Weave, MIL-C-83429, topical antistat Aston #123, No Laundering
B	Standard Sage Green, 95/5 Nomex^R/Kevlar^R, Plain Weave, MIL-C-83429, topical antistat Aston #123, Laundered 5x according to test method 5556
C	Standard Olive Green, 95/5 Nomex^R/Kevlar^R, Oxford Weave, MIL-C-43842, topical antistat Aston #123, No Laundering
D	Standard Olive Green, 95/5 Nomex^R/Kevlar^R, Oxford Weave, MIL-C-43842, topical antistat Aston #123, Laundered 5x according to test method 5556
E	Woodland Print, 99% 95/5 Nomex^R/Kevlar^R, 1% Stainless Steel, Plain Weave, MIL-C-83429, DAAK60-88-C-0064, No Laundering
F	Woodland Print, 99% 95/5 Nomex^R/Kevlar^R, 1% Stainless Steel, Plain Weave, MIL-C-83429, DAAK60-88-C-0064, Laundered 5x according to test method 5556
G	Woodland Print, 99% 95/5 Nomex^R/Kevlar^R, 1% Stainless Steel, Plain Weave, MIL-C-83429, DAAK60-87-C-0004, No Laundering
H	Woodland Print, 99% 95/5 Nomex^R/Kevlar^R, 1% Stainless Steel, Plain Weave, MIL-C-83429, DAAK60-87-C-0004, Laundered 5x according to test method 5556

(Results given in figures 9 and 10 are from references 1 and 5) then conditioned at 20% ± 2% RH for a minimum of 24 hours. The materials are tested at 20% ± 2% RH. Each sample is mounted across the electrodes and charged toward 5000 volts for 20 seconds, then grounded (see Figure 7). The voltage behavior is recorded on the chart recorder as the charge on the fabric dissipates to ground. The resulting plot takes the form of a decay curve, voltage vs time (see Figure 8). Both front and back of each sample is tested, and the mean computed.[5]

From the decay curve, the electrostatic properties of the material can be determined. A fabric with desirable static properties will approach the 5000 volt level with ease and, upon being grounded, dissipate 90% of the accumulated charge within half of a second. Fabrics which do not attain a level of at least 4000 volts and/or do not dissipate 90% of the charge within a period of one half second are considered to have insulative properties and are not safe for wear in electrostatic sensitive environments.[5]

RESULTS: Typical results on fabrics treated with a topical antistat, as well as fabrics containing stainless steel fibers, are shown in Figures 9 and 10. These fabrics were tested at 20% relative humidity and 75 degrees Fahrenheit, and correspond to those described in Table 1. It should be noted that a 100% cotton sample (Bleached Army Cotton Sateen, Style #428) with no antistatic treatment and tested at the same relative humidity yields an average Vmax of approximately 4900 volts, and an average decay time of approximately nine seconds.[5] Material consisting of 100% 95/5 Nomex[R]/Kevlar[R] yields an average Vmax of approximately 2000 volts and takes more than 20 seconds to dissipate the charge.[1] Figure 9 displays the results of two materials, A and C, treated with a topical antistat. Results before (A and C) and after five launderings (B and D) are shown. As can be seen, the antistat treatment is removed during the laundering process, for the decay time increases by a factor of five after laundering. Figure 10 shows the results of materials containing stainless steel. Again, results before (E and G) and after laundering (F and H) are shown. Here, laundering affects the materials' ability to accept a charge, for a noticeable decrease in Vmax is evident after laundering, particularly in the first material (E, F).[1] The cause of this is currently under investigation, although it is believed this may be due to a less even distribution of stainless steel after laundering. The stainless steel fibers in laundered samples appear to have migrated together when observed with an electron microscope and X-Ray equipment.[9]

Each set of samples was reconditioned and retested at a later date. The results of each retest are labeled with a "2" after the letter representing the fabric set. Results of retested samples are comparable to the initial results, indicating test repeatability. The static decay results are much more reliable than the previous surface resistivity test

ELECTRICAL CONFIGURATION OF STATIC DECAY FIXTURE

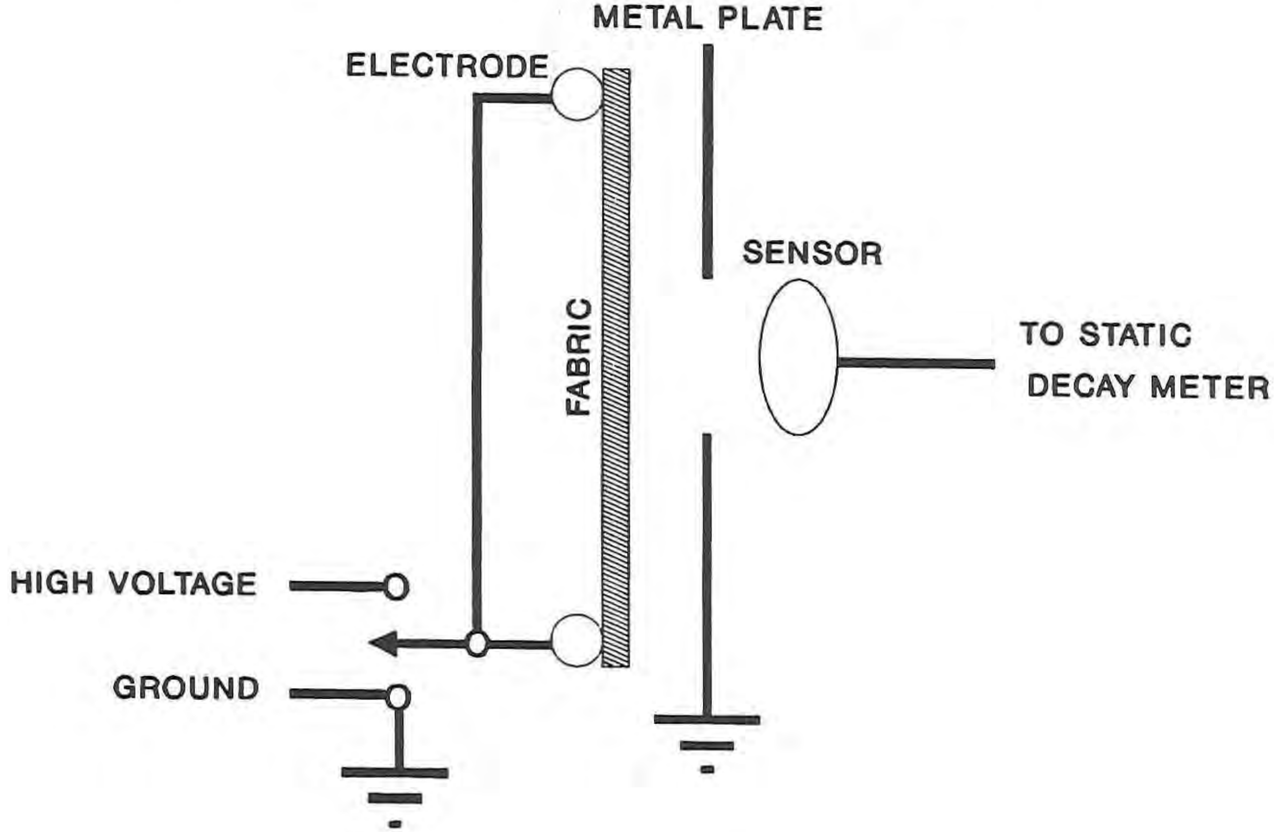

FIGURE 7

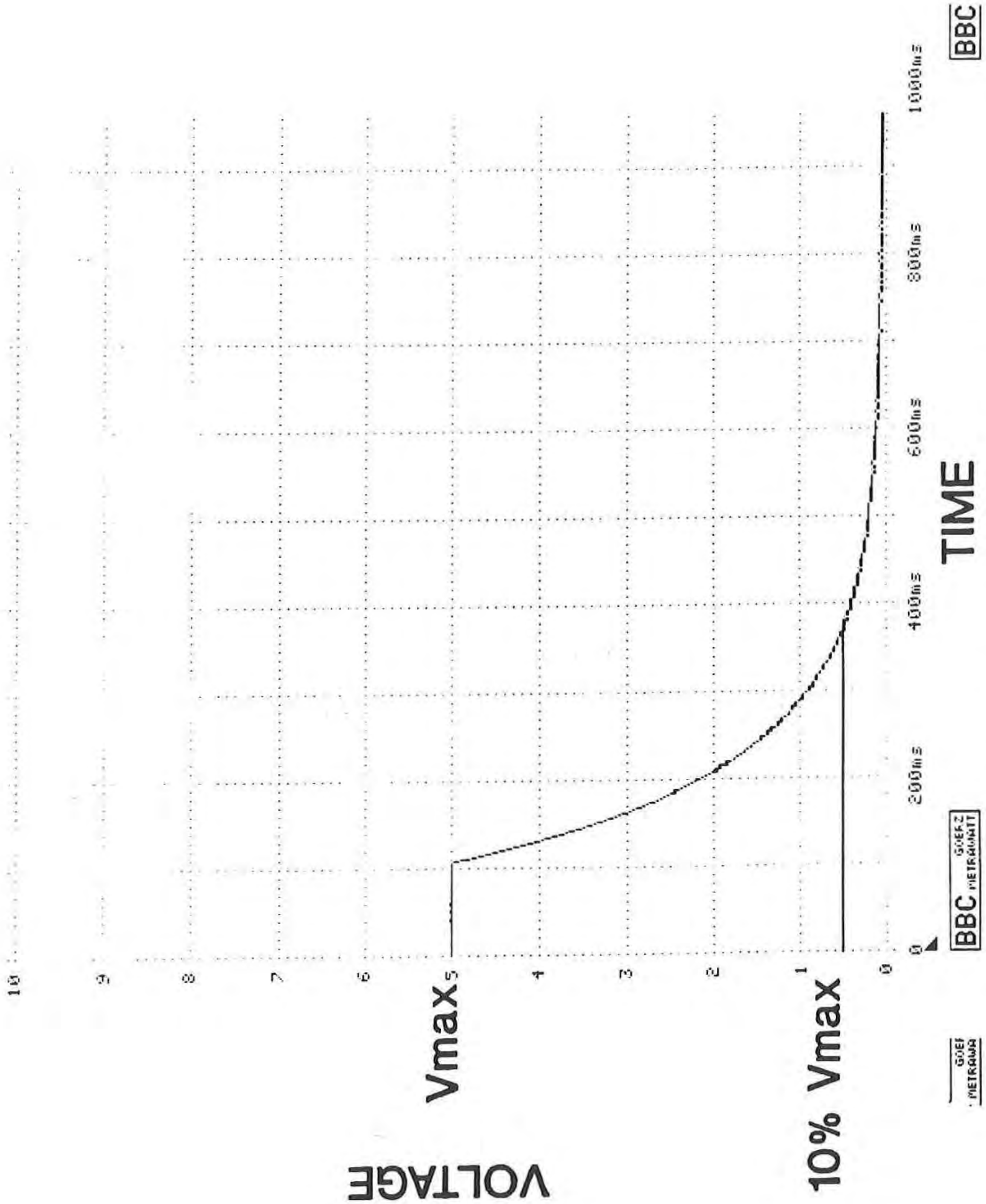

FIGURE 8 DECAY CURVE

FIGURE 9

STATIC DECAY RESULTS

ANTISTAT TREATED FABRICS

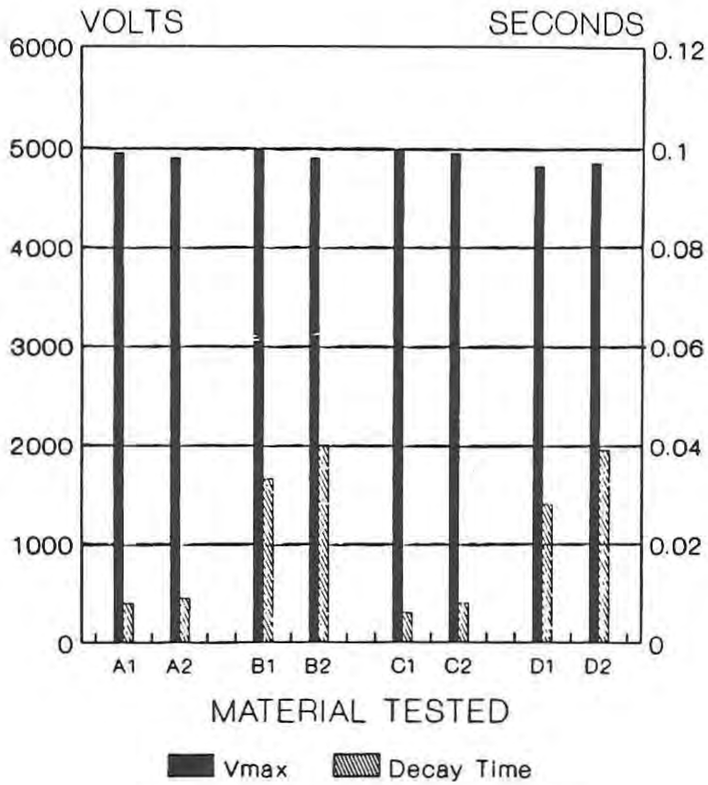

A-C BEFORE LAUNDERING

B-D AFTER 5 LAUNDERINGS

FIGURE 10

STATIC DECAY RESULTS

FABRICS CONTAINING STAINLESS STEEL

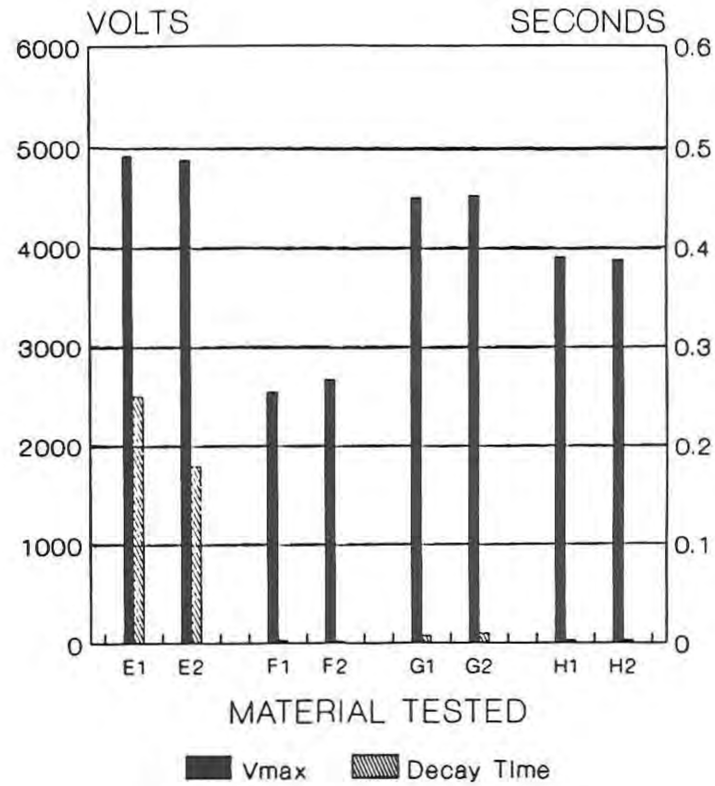

E-G BEFORE LAUNDERING

F-H AFTER 5 LAUNDERINGS

method. Results indicative of the uncertainty of the surface resistivity method when testing conductive materials are shown in Table 2. These results tend to be erratic and do not always indicate the presence of conductive fibers.

CONCLUDING REMARKS: The electrostatic decay test method for determining the electrostatic characteristics of a material has been found to be a useful and more reliable method than the surface resistivity method previously used when testing fabrics containing conductive fibers. The electrostatic decay method is capable of handling both homogeneous and nonhomogeneous materials, whereas the previous method was only reliable for homogeneous materials. The new test method is being coordinated with industry before inclusion in Federal Test Standard 101A and will replace surface resistivity as a method of test for future contracts. Natick will also investigate the natural accumulation and dissipation of charge on uniforms worn by human subjects. The results of this testing will be compared to samples of the same materials tested by the static decay method.

REFERENCES:

1. U.S. Army Natick Research, Development and Engineering Center laboratory notebook #8649, pages 35, 36, 38, 52, 98-100, 103-104, 107-108, and 110-112.

2. Wilson, Norman. "Effects of Static Electricity on Clothing and Furnishings." Shirley Institute Report.

3. Keithley "Model 6105 Instruction Manual", Document Number 31415, October 1972.

4. U.S. Army Natick Research, Development and Engineering Center laboratory notebook #8602, page 132.

5. U.S. Army Natick Research, Development and Engineering Center laboratory notebook #8719, pages 4-6, 27, 30, 46-47, 51 and 96.

6. Rupe, Bader I. (I.K.E. Associates, Inc.), Development Of Test Methods For The Electrostatic Properties Of Nonhomogeneous Fabrics: Phase II, Technical Report Natick/TR-88/010, December 1987.

7. Ghausi, Mohammed S., "Electronic Devices and Circuits: Discrete and Integrated." CBS College Publishing, New York, 1985.

8. Electro-Tech Systems, Inc., "Instruction Manual Static Decay Meter Model 406C".

TABLE 2
TYPICAL SURFACE RESISTIVITY RESULTS FOR CONDUCTIVE FABRICS

MATERIAL	SAMPLE NUMBER	SURFACE RESISTIVITY (OHMS/SQUARE)	COMMENTS
Plain Weave	1-F	$9.02x10^{3}$	Results fluctuate
99% 95/5 Nomex/Kevlar	1-B	$2.23x10^{4}$	from low to high
1% Stainless Steel	2-F	$3.51x10^{4}$	in value.
DAAK60-87-C-0004	2-B	$6.68x10^{12}$	(Reference 1)
	3-F	$1.01x10^{4}$	
	3-B	$4.77x10^{3}$	
Oxford Weave	1-F	$7.08x10^{3}$	Results fluctuate
99% 95/5 Nomex/Kevlar	1-B	$4.65x10^{3}$	from low to high
1% Stainless Steel	2-F	$2.30x10^{4}$	in value.
DAAK60-87-C-0004	2-B	$1.21x10^{11}$	(Reference 1)
	3-F	$1.16x10^{11}$	
	3-B	$2.88x10^{3}$	
Plain Weave	1-F	$9.87x10^{12}$	Results are not
99% 95/5 Nomex/Kevlar	1-B	$1.47x10^{13}$	indicative of
1% Stainless Steel	2-F	$9.96x10^{12}$	stainless steel
DAAK60-88-C-0064	2-B	$9.62x10^{12}$	content in fabric.
	3-F	$1.00x10^{13}$	(Reference 5)
	3-B	$1.67x10^{13}$	
Oxford Weave	1-F	$2.05x10^{12}$	Results are not
99% 95/5 Nomex/Kevlar	1-B	$1.67x10^{13}$	indicative of
1% Stainless Steel	2-F	$2.22x10^{13}$	stainless steel
DAAK60-88-C-0064	2-B	$1.91x10^{13}$	content in fabric.
	3-F	$1.78x10^{13}$	(Reference 1)
	3-B	$1.57x10^{13}$	
Plain Weave	1-F	$2.70x10^{14}$	Results erratic.
99% 95/5 Nomex/Kevlar	1-B	short	Stainless steel
1% Stainless Steel	2-F	short	appears to be
DAAK60-87-C-0007	2-B	$1.80x10^{14}$	"shorting"
	3-F	short	equipment.
	3-B	$3.80x10^{9}$	(measurements out
			of range at low
			end of equipment)
			(Reference 4)

(Results from references 1, 4 and 5)

9. Goode, Peggy. "Identification Of Stainless Steel Fibers In Blended Fabrics." Natick Report (reference Natick notebooks #8817, pages 11-12, and #8672, pages 120-121, 141-144), 1990.

TITLE: A Shock Tube Study of Various Textile Materials with Applications to Personnel Blast Protection

*Phillip W. Gibson, Mr.

ABSTRACT: Certain clothing items, in particular the Personnel Armor System for Ground Troops (PASGT) ballistic protection vest, seem to increase the risk of direct air-blast injury. Some textile materials apparently transform air shock waves into a form which couples more efficiently with the human chest-lung system. The response of fabric materials to air shock waves needs to be understood, particularly as direct air-blast weapons (Fuel-Air Explosives) become more prevalent on the modern battlefield.

Various materials were exposed to shock waves generated in an air-driven shock tube. Pressure transducers allowed recording of the incident shock wave, the transformed pressure pulse under the fabric, and the unattenuated reflected shock wave. The materials included ballistic protective fabrics of various weaves such as Kevlar® 49 and 29, Spectra® 1000, and nylon. Other materials, including polyurethane foam, cotton cloth, Nomex®, etc., were also tested to help evaluate the usefulness of analytical relations between material bulk density, material shock wave speed, and shock transmission properties.

A numerical model of the chest-lung system was adapted for evaluating the effects of different materials covering the chest. The shock tube results were input to the computer model of the human chest to allow a comparison between the different materials. The model allowed the internal lung pressure, which correlates with lung injury, to be determined for each material for a given blast load.

*BIOGRAPHY OF PRESENTER: Phillip W. Gibson

PRESENT ASSIGNMENT: Materials Research Engineer, Materials Research and Engineering Division, Individual Protection Directorate, U.S. Army Natick Research, Development and Engineering Center, Natick, Massachusetts.

PAST EXPERIENCE: Senior Rocket Propulsion Engineer, U.S. Air Force Astronautics Laboratory, Edwards AFB, California.

DEGREES HELD: M.S. Mechanical Engineering, University of Washington; M.S. Systems Management (R&D Option), University of Southern California; B.S. Engineering Science and Mechanics, Tennessee Tech.

A SHOCK TUBE STUDY OF VARIOUS TEXTILE MATERIALS WITH APPLICATIONS TO PERSONNEL BLAST PROTECTION

PHILLIP GIBSON, MR.

INTRODUCTION

There is evidence that soldiers wearing fibrous body armor are more vulnerable to injury from blast waves than personnel not wearing the armor. Fibrous body armor materials, such as Kevlar®, apparently cause the blast wave to couple more efficiently with the soldier's chest-lung system, thus increasing the risk of lung injury. The "blast amplification" effect is likely a consequence of the layered construction and fiber properties of the present body armor. It's important to determine what factors influence how body armor materials transform blast wave loads on the human body.

Fibrous body armor is designed to protect soldiers from the most common battlefield threat -- fragmenting munitions. The current body-armor vest, part of the Personnel Armor System, Ground Troops (PASGT), is constructed of 13 layers of Kevlar® 29 cloth sandwiched between an inner and outer nylon shell fabric. The PASGT vest provides a high level of ballistic protection without greatly hindering the soldier's mobility and effectiveness. However, the PASGT vest was not designed to protect against direct blast effects.

Some battlefield threats to the soldier do involve direct blast. Aside from conventional bomb blasts, the increased presence of fuel-air explosives on the modern battlefield constitutes a threat which may become more important in the future[1,2]. There has also been some concern that repeated exposure of personnel to high intensity gun muzzle blast waves could produce cumulative-damage injuries to large gun operators. Operators wearing the PASGT vest might be even more vulnerable to cumulative-damage effects if their body armor amplifies the blast wave. Finally, tank crews are usually well protected from fragments but may be exposed to blast waves in certain situations. Blast waves can diffract into a crew compartment through open hatches and will be intensified through reflection off walls and floors[3]. Crew members exposed to such complex shock waves could thus also be vulnerable to body armor blast wave amplification. If the PASGT vest increases the risk of blast injury, then the magnitude of the increased risk for these various cases needs to be known.

BACKGROUND

Blast intensity is usually reported in terms of overpressure, which refers to the pressure above atmospheric pressure (usually assumed to 14.7 psi). Blast overpressure damages the body most where large density differences are present. Disregarding the eardrums, the lungs and the intestines are the vital organs most susceptible to blast overpressure[4]. The chest wall is rapidly compressed during the passage of a blast wave. The sudden acceleration, deceleration, and oscillations due to chest wall compression, combined with direct shock wave transmission, reflection, and focusing in the body tissues, are the causes of blast tissue injury. The most important factors in direct blast injury are the ambient pressure, peak overpressure, pressure rise rate, pressure pulse shape, duration of the positive phase of the blast wave, and the orientation of the body with respect to the blast[5]. Peak overpressures of 10 to 20 psi can cause lung damage if the shock wave's positive phase lasts 5 milliseconds or more. The human body is better able to cope with shock waves of shorter duration, so that the threshold of lung damage rises to 50 psi overpressure for shock waves with a positive phase of 1 millisecond[6].

People can be protected from blast effects if they are behind rigid walls or within enclosures. Rigid vests enclosing the chest have also been shown to be a good way to protect people against blast waves[7].

Soft materials do not have a similar protective effect. It seems obvious that foam rubber would cushion a blast wave and reduce blast injuries. On the contrary, workers in Sweden found that layers of sponge rubber covering rabbits and anthropometric mannikins significantly increased blast-wave effects over the unprotected condition[8]. Soft materials do not offer much protection from blast and often seem to increase the damage. This is worrisome since the PASGT vest is also fairly soft and non-rigid.

The Walter Reed Army Institute of Research (WRAIR) clearly demonstrated the blast-enhancing qualities of ballistic vests in work conducted over the past few years. In one study, human volunteers were exposed to low-level blast waves[9]. The volunteers' internal lung pressure was measured during tests in which the volunteers wore different types of protective clothing. The study showed that the PASGT ballistic vest caused the greatest increase in internal lung pressure. This implies the ballistic protection vest would increase the risk of lung damage at higher blast levels.

WRAIR extended this study to cover higher blast overpressures[10]. Sheep were exposed to various blast levels. Half of them were fitted with actual PASGT vests. The sheep wearing ballistic protection vests showed significantly more lung damage and higher mortality rates than sheep not wearing the vests. The authors of this study estimated that the use of the PASGT vest reduced the overpressure necessary to obtain a given level of mortality by 25%.

There is evidence that under pressure loading the human chest-lung system behaves like a damped oscillator. The natural frequency of the human chest-lung system has been determined to be in the range of 40 to 60 cycles per second[11]. This means that blast waves with a duration comparable to the natural period of the human chest are able to couple more efficiently with the chest and lungs, thus causing a higher internal lung pressure, which correlates with an increasing chance of injury.

Compressible and porous materials transform steeply rising blast waves to a more rounded and longer duration pressure pulse. These materials apparently convert air shock waves into a shape which more easily couples to the human chest-lung system, thereby increasing the chance of injury.

The materials in the PASGT vest are also compressible and porous. Is this the reason the PASGT vest apparently amplifies blast wave effects? Is the Kevlar® contained in the vest especially efficient at transforming blast waves, or would the same be true of other fabrics? The behavior of textile materials under shock wave loading is the focus of this study.

APPROACH

The approach relied on both modeling and experiment. Various textile materials were exposed to shock waves generated in an air-driven shock tube. Pressure transducers allowed recording of the incident shock wave, the transformed pressure pulse under the fabric, and the unattenuated reflected shock wave. The experimental data generated in the testing effort provided the loading function for input into a numerical chest-lung model. The human chest model was used to evaluate the effect of different chest coverings on chest response to a given blast wave.

Short descriptions of both the shock tube test arrangement and the parameters of the numerical chest-lung model are given in the next two sections.

Shock Tube Experiments

Textile materials were tested in the 12-inch diameter shock tube at Walter Reed Army Institute of Research (WRAIR). The shock tube and sample arrangement are shown schematically in Figure 1.

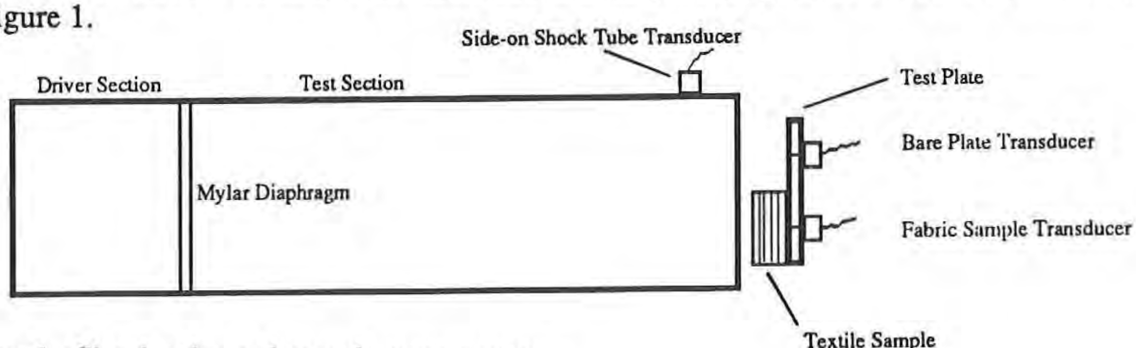

Figure 1. Shock tube and sample arrangement.

Shocks of known strength were created in the test section of the shock tube by pumping the driver section up and rupturing Mylar® diaphragms of various thicknesses. The long test section of the shock tube assured uniformity of the shock front at the end of the tube. A piezoelectric pressure transducer allowed the side-on shock wave profile near the exit to be recorded. Fabric test samples were mounted at the exit of the shock tube. Two pressure transducers were mounted side-by-side at the shock tube exit. The fabric sample only covered one of these transducers. This allowed the shock wave load on the bare plate to be recorded at the same time as the shock wave load under the plate covered by the fabric sample. Since these two pressure transducers were mounted face-on to the shock wave, they recorded the reflected shock pressure at the plate surface, rather than the side-on pressures recorded by the transducer inside the tube .

For air shock waves of known strength, the relationship between the measured side-on pressure and the reflected pressure at a rigid plate is given by[12] :

$$p_r = 2p_s + \frac{(\gamma+1)p_s^2}{(\gamma-1)p_s+2\gamma p_0} \qquad (1)$$

where p_r is the reflected peak pressure, p_s is the measured side-on pressure, p_0 is the ambient pressure, and γ is the specific heat ratio of the fluid medium. For air, γ=1.4.

This relation allowed a check of the incident shock pressure value for each test since the output of the bare plate face-on pressure transducer and the side-on shock tube transducer could be compared.

Test Conditions and Materials

Four side-on shock/blast levels of 8.0 psi, 12.5 psi, 20.0 psi, and 25.0 psi were used to load the textile samples. The positive phase duration of each shock wave was about 5 milliseconds. The positive phase duration varied some according to the shock strength, but depends mostly on the length of the shock tube test section. For positive phase durations of 5 milliseconds, the threshold of lung damage is 20 psi overpressure, so the test conditions spanned the human injury threshold level.

Test conditions also included varying the number of fabric layers for the textile materials. Fabric stacks of 4, 8, 12, 16, and 20 layers were tested at each of the four blast levels. Ballistic protection vests usually contain 10 to 20 layers, so it's important to determine if the number of layers influences the shock wave transmission process.

A variety of fabric materials were tested in the shock tube. Five types of Kevlar® 29 and Kevlar® 49 fabrics have been tested. These Kevlar® fabrics included the material used in the PASGT vest[13] as well as more exotic materials, such as titanium-coated Kevlar® fabric. Other test fabrics included three types of Spectra® high-strength polyethylene fabric, Nomex® triaxial weave cloth, ballistic nylon cloth[14], cotton/nylon Battle Dress Uniform (BDU) fabric[15], and two types of plastic foam, Ensolite®, and polyurethane foam. To date, only the test results for the ballistic nylon, the Nomex®, the nylon/cotton BDU , and the PASGT Kevlar® materials have been fully analyzed. The three materials of most interest are the nylon/cotton BDU fabric, the ballistic nylon fabric, and the PASGT Kevlar® fabrics. Only the results for these materials are presented in this paper. Results for all of the materials will be available in a technical report to be published later.

An example of a typical shock tube test result on a fabric sample is shown in Figure 2. The output from both the bare plate transducer and the transducer under a fabric sample is shown below.

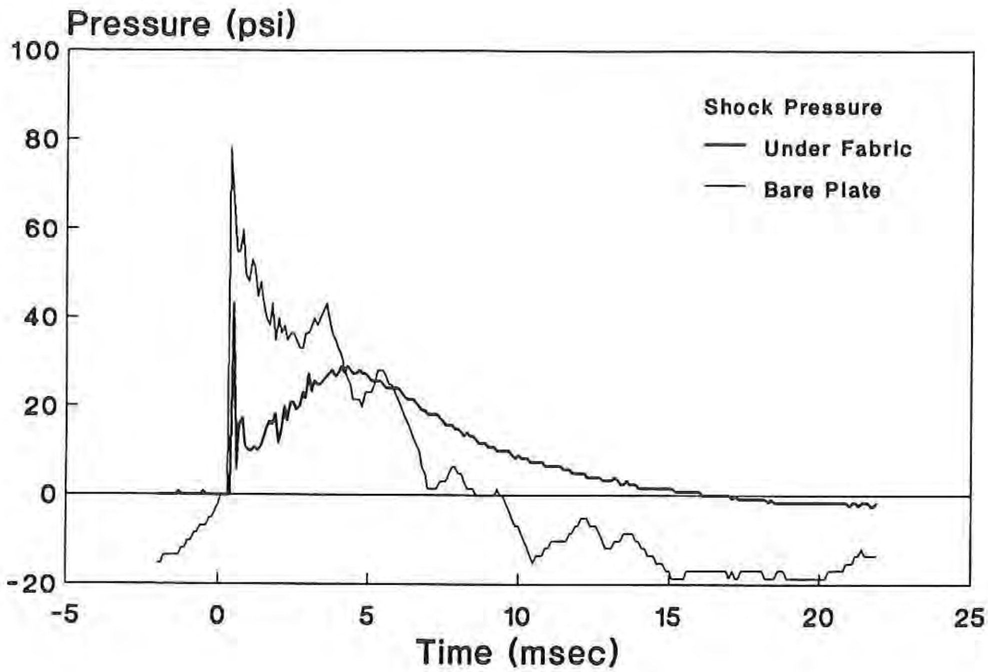

Figure 2. Face-on pressure-time profiles for one transducer mounted under a fabric sample and the other mounted on a bare plate.

The parameters of most interest for these pressure-time traces are the peak reflected overpressures, and the reflected specific impulse, I_r. I_r is defined as the integral of the positive reflected blast overpressure curve, $p_r(t)$.

$$I_r = \int_{t_0}^{t_0+t_d} [p_r(t)-p_0]dt \qquad (2)$$

where t_0 is the inital arrival time of the shock front and t_d is the positive pulse duration.

Numerical Chest-Lung Model

A lumped-parameter chest model was used to determine the response of the human chest-lung system to the loading functions measured experimentally in the shock tube tests. This model was developed by the Lovelace Foundation[16], and simplified somewhat by Bolt, Beranek, and Newman, Inc. under a previous Natick project[7]. A more complete description of the model, as well as a listing of the computer program, may be found in Reference 17. The model's schematic is shown in Figure 3.

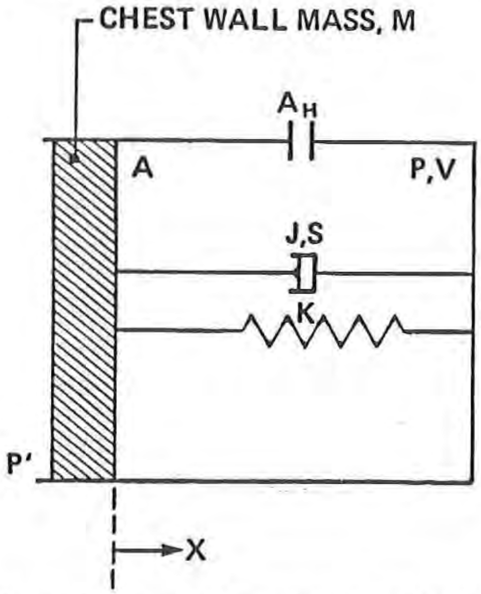

A	effective area of chest
A_H	effective air flow area of throat
M	effective mass of chest piston
K	spring constant for ribcage stiffness
J	dashpot damping coefficient for viscous resistance
S	power of velocity to which damping force is proportional
P'	external air pressure
P	internal lung pressure
V	gas volume of lungs
X	chest wall piston displacement

Figure 3. Lumped-parameter model of chest and lungs.

The lung is a gas-filled chamber connected to the outside atmosphere by an orifice of area A_H, which simulates the throat passage. A movable chest wall mass acts as a piston which compresses the gas in the lung cavity when acted upon by a force. The elastic resistance and viscous damping of the chest tissues are provided by the spring and dashpot connected to the chest wall mass. Additional compression resistance is provided by the gas in the lung cavity. The constants in the system of equations which make up the model were obtained through extensive animal experimentation on many different sizes of mammals and extrapolated to humans. The model allows the chest wall displacement, internal lung pressure, and the internal lung volume to be determined over time in response to an external load on the chest.

The lumped-parameter model proved to be sufficient for the purposes of this study, although more accurate models of the chest-lung system have been developed. In particular, finite element models, which include the important structural elements of the chest and lungs, together with appropriate tissue properties, have proven to be very useful[18].

The model was used to determine how the chest responds to the blast loads measured under the fabric samples tested in the shock tube. In the simplest case, the person is assumed to be standing face-on to the blast source. The loading on the chest is given by the measured pressure-time curve from the face-on transducers. The reflected pressure curve $p_r(t)$ is thus equivalent to the pressure P' in the chest-lung model.

Examples of applying the measured shock tube loads to the model are shown in Figures 4 and 5. In both cases the side-on blast overpressure level was 20 psi. Figure 4 shows the lung model response to the measured reflected pressure on a bare plate. Figure 5 shows the model response under 12 layers of Kevlar®. In this case the internal lung pressure was higher for the unprotected plate than it was for the plate underneath the Kevlar®.

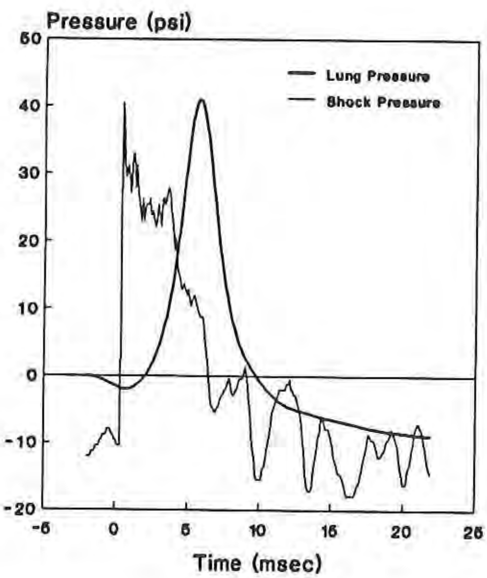

Figure 4. Lung model response to measured shock pressure at bare plate surface.

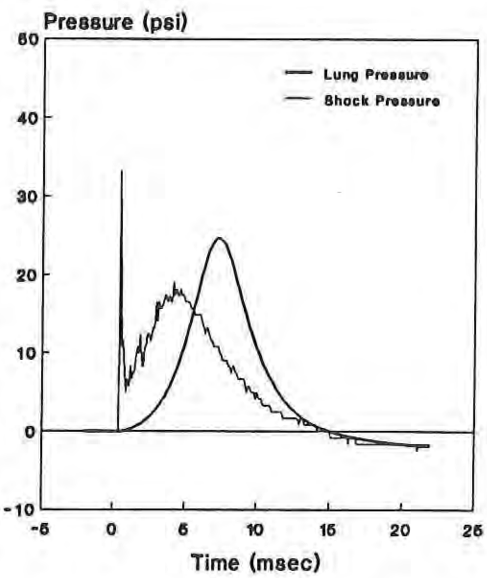

Figure 5. Lung model response to measured reflected shock pressure under 12 layers of Kevlar®.

RESULTS AND DISCUSSION

The discussion of results will concentrate on the nylon/cotton BDU fabric, the nylon fabric, and the PASGT Kevlar® fabric.

The shock tube test results do not show that Kevlar® has any unique properties with respect to the transmission of shock waves.

For example, Figure 6 shows the peak shock pressure measured under the three fabrics for a variety of blast levels and number of fabric layers. The blast level refers to the measured peak side-on overpressure of the shock wave near the tube exit. The face-on overpressure is defined as the peak overpressure measured by the face-on gage under the fabric sample.

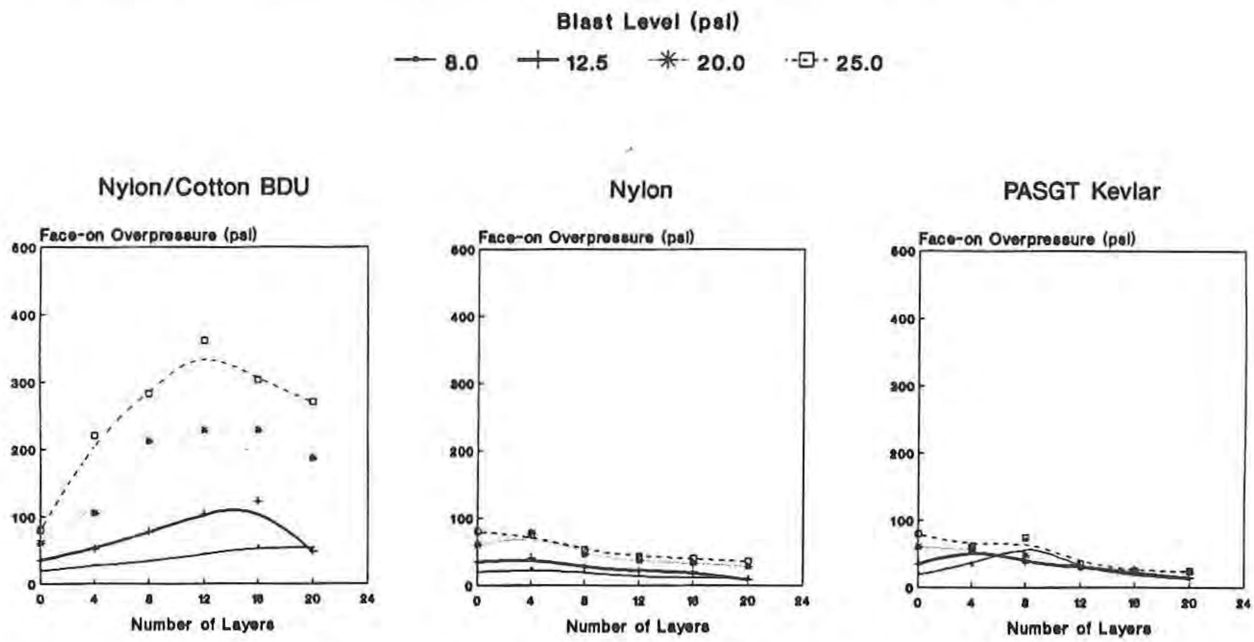

Figure 6. Peak shock pressures measured under three textile materials.

Both the nylon and the Kevlar® actually seem to reduce the reflected shock pressure. The nylon/cotton BDU fabric, on the other hand, seems to transmit a higher shock pressure than either the nylon or Kevlar®. The effect of layering is also different between the nylon/cotton BDU fabric and the other materials. For the BDU fabric, the peak pressure rises as the number of layers of fabric increases until 12 to 16 layers are over the plate. As more layers are added the peak pressure begins to fall again. The Kevlar® displays a much smaller layering effect, peaking at around eight layers, and the nylon shows no layering effect at all. For the nylon fabric, more layers simply means less shock pressure is transmitted to the plate.

This behavior can also be seen in plots of the reflected impulse, I_r, under each fabric sample.

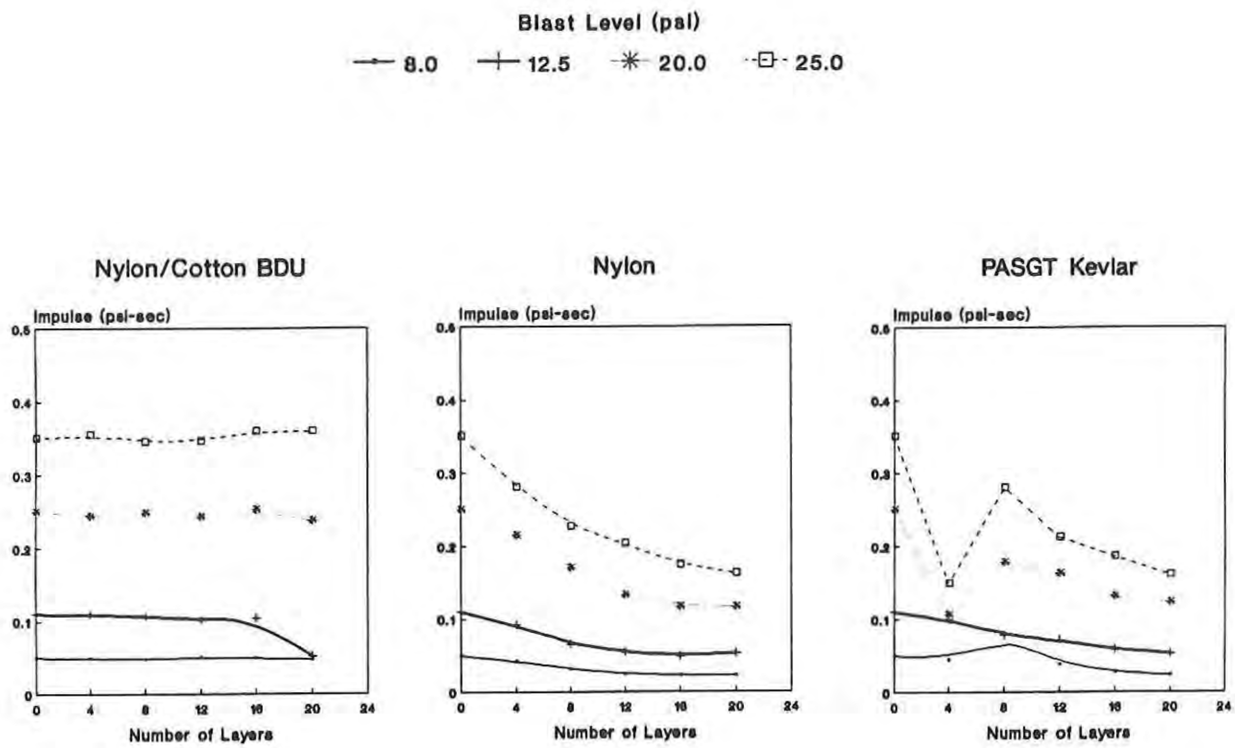

Figure 7. Reflected impulse measured under three textile materials.

Figure 7 shows the nylon/cotton fabric again behaves quite differently from the other two materials. The impulse measured under the nylon/cotton BDU fabric is nearly constant, no matter how many layers are over the test plate. This means the energy content of the incident shock wave is not being modified by the presence of up to 20 layers of the BDU fabric. In contrast, nylon fabric and the Kevlar® fabric reduce the energy content of the shock wave significantly as more fabric layers are added.

The pressure-time curves measured under the fabric samples can be used to load the numerical chest-lung model to obtain internal lung pressures as a function of time. Figure 8 shows calculated internal lung pressures for the three materials.

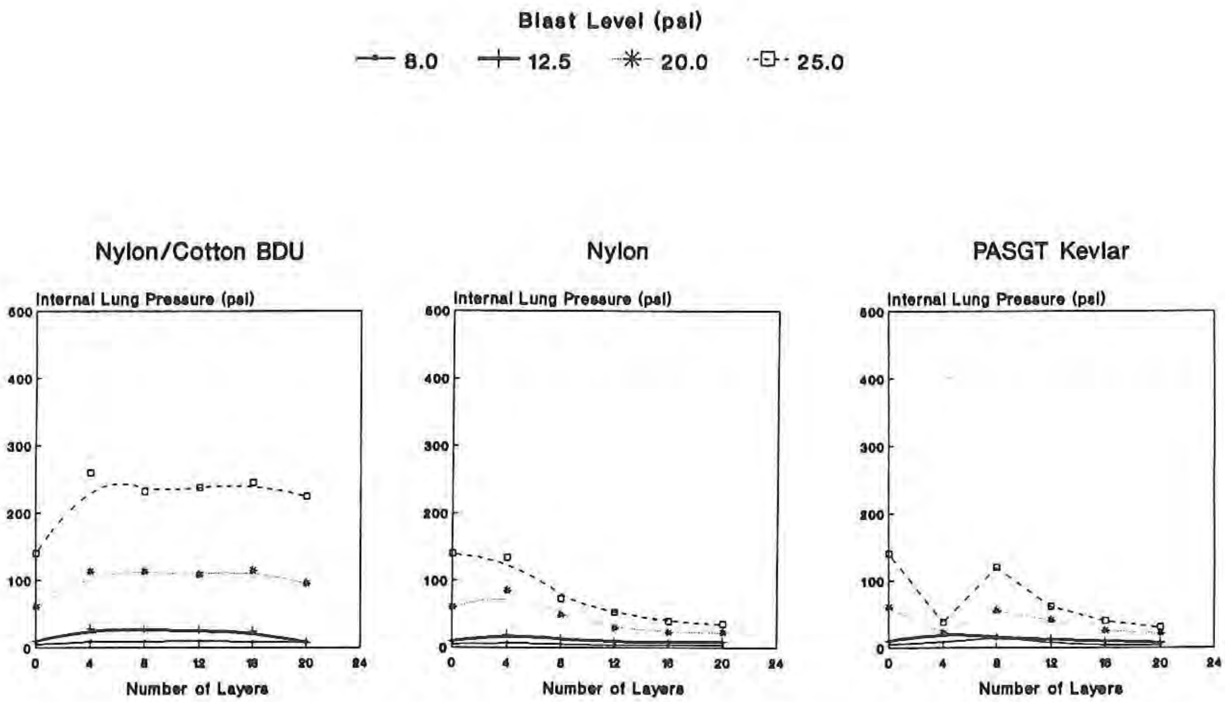

Figure 8. Internal lung pressure due to reflected shock pressures under three textile materials.

Figure 8 again shows a sharp distinction between the two ballistic protective materials and the nylon/cotton BDU fabric. The calculated internal lung pressure, in response to an external blast load, remained constant up to 20 layers thickness for the BDU fabric. The Kevlar® fabric showed a small peak at eight fabric layers. The internal lung pressure for the nylon fabric always declined as the number of fabric layers increased.

Figures 6, 7, and 8 seem to indicate that rather than "amplifying" blast waves, Kevlar® is actually pretty effective at attenuating the shock wave, especially if there are many layers.

The lung model may also be used to provide an estimate of the actual increase in lung pressure due to fabric layers over the chest. Since each blast test in the shock tube used two face-on transducers — one covered with fabric and the other bare — the lung model can be used to directly compare the two cases. The lung model was used to calculate the peak internal lung pressure from both the bare plate pressure trace and the pressure trace under the fabric sample. The percent lung pressure increase due to the presence of the fabric was then calculated based on the bare plate pressure and the fabric-covered plate pressure.

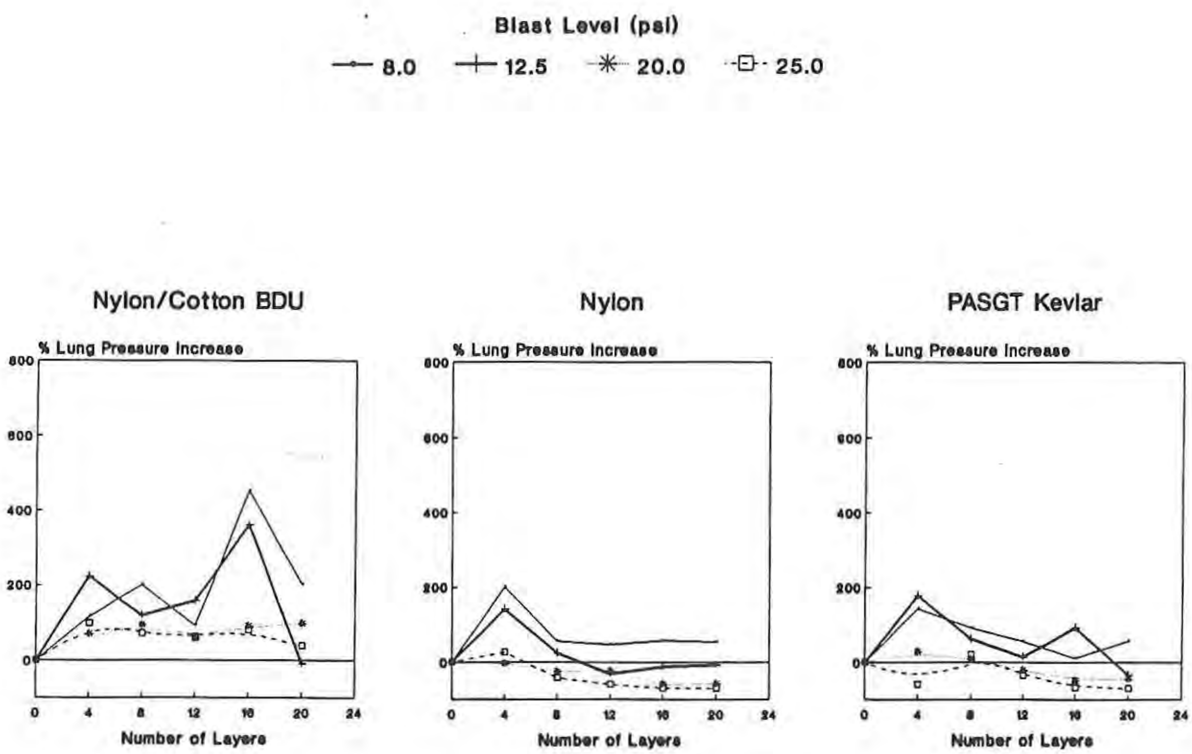

Figure 9. Percentage lung pressure increase caused by the presence of fabric covering the chest.

Figure 9 shows that the Kevlar® and nylon do cause an enhancement of lung pressure, especially when there are only a few layers of fabric. However, these two materials show negative percentage lung pressure increases when more layers of fabric are added, which means that rather than increasing the risk of injury these materials are actually providing some protection from the blast wave. The nylon/cotton BDU fabric shows a much greater enhancement of lung pressure. There again seems to be some sort of maximum layering effect around 16 layers, after which the values of percent lung pressure increase begin to fall off .

The tensile properties of the fibers in these fabrics are relatively unimportant to the shock transmission process. Since the fibers are oriented parallel to the plane of the shock wave, the high strength and moduli of the ballistic protective fibers have little influence on how layered fabrics respond to shock waves.

The material property of most importance is the bulk density (ρ_b) of the layered fabric. The bulk density includes the air trapped in the fabric. The importance of material bulk density to shock transmission properties is clearly illustrated in Figure 10. These plots are data taken for fabric stacks of 20 layers. The values for a Nomex® fabric (ρ_b=.021 lb/in^3) are included along with the values for the nylon/cotton BDU fabric (ρ_b=.019 lb/in^3), nylon (ρ_b=.025 lb/in^3), and Kevlar® (ρ_b=.028 lb/in^3).

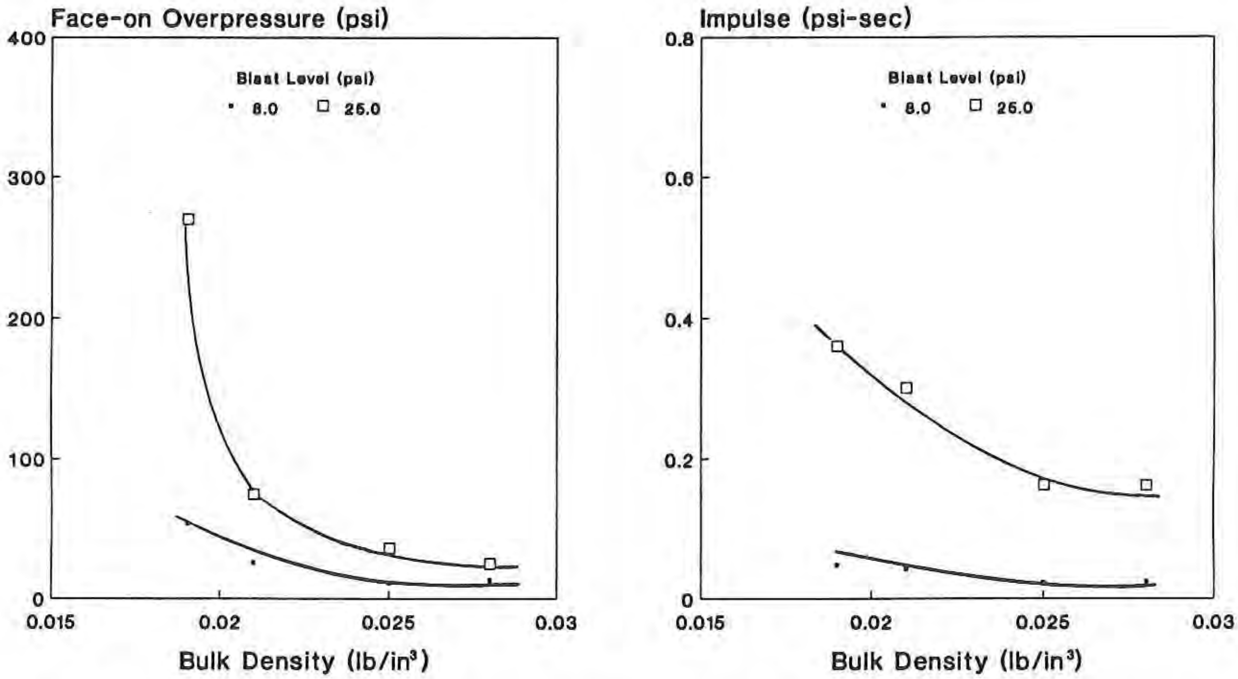

Figure 10. Influence of material bulk density on textile shock wave transmission properties.

The strong dependence of shock transmission properties on bulk density for these textile materials is similar to that exhibited by polymeric foams in experiments conducted by workers in the U.S.S.R.[19] Their modeling predicted the peak pressure and wave form under the foam materials to a high degree of accuracy. Their work was based on modeling the material as a "pseudogas" by a method developed in the U.S.[20] The Soviet method might also be applicable to layered fabrics. The only properties required are the volume fraction of fiber, the apparent density of the fabric, and the specific heat of the solid polymer.

CONCLUSIONS

The shock response of the Kevlar® fabric used in the PASGT ballistic protection vest is not qualitatively different from the shock response of other fabric materials. Kevlar® is not any worse than comparable materials, such as nylon, and may even be better at attenuating the shock wave.

The values of peak shock pressure and transmitted impulse under a textile material seem to be directly related to fabric bulk density. Materials with higher bulk density tend to decrease both the peak reflected pressure measured against a flat plate and the total impulse delivered to the plate.

The test results for the remaining materials, including the four other types of Kevlar® (which have different bulk densities), will help clarify the relationship between bulk density and shock transmission properties. The material test results may be incorporated into an existing numerical model which describes how porous and compressible materials respond to air shock waves.

The results reported here for Kevlar® seem to differ with the experimental results obtained from human and animal test subjects wearing the PASGT ballistic protection vest. It is possible that for blast loading effects, the most important property of the PASGT vest is simply its bulk density, rather than any unique properties of the Kevlar® fabric itself. If the material property shock tube tests are valid, then a vest made from 13 layers of the nylon/cotton BDU fabric in place of the 13 Kevlar® layers should cause a greater blast enhancement than the present PASGT vest. It would be interesting to test PASGT vests which contain different materials with the same bulk density as Kevlar® to see if they also cause the same degree of blast enhancement.

ACKNOWLEDGEMENTS

The assistance and guidance of Dr. Kenneth Dodd and Ms. Jennifer Morris in the shock tube testing effort at Walter Reed Army Institute of Research were much appreciated.

REFERENCES

1. Bowen. J., "Hazard Considerations Relating to Fuel-Air Explosive Weapons," *Minutes of the Fourteenth Explosives Safety Seminar*, New Orleans, Louisiana, November, 1972, pp. 27-55.

2. Robinson, C., Jr., "Special Report: Fuel Air Explosives. Services Ready Joint Development Plan," *Aviation Week and Space Technology*, February 19, 1973, pp. 42-46.

3. Richmond, D., Fletcher, E., Saunders, K., Yelverton, J., "Injuries Produced by the Propagation of Airblast Waves Through Orifices," Lovelace Biomedical and Environmental Research Institute, Defense Nuclear Agency Report DNA 5618T, 1980 (AD A106146).

4. White, C., "The Scope of Blast and Shock Biology and Problem Areas in Relating Physical and Biological Parameters," *Annals of the New York Academy of Sciences*, 152, October 1968, p. 90.

5. Richmond, D., Damon, E., Fletcher, E., Bowen, I., White, C., "The Relationship Between Selected Blast Wave Parameters and the Response of Mammals Exposed to Air Blast," *Annals of the New York Academy of Sciences*, 152, October 1968, pp. 103-121.

6. Bowen, I., Fletcher, E., Richmond, D., "Estimate of Man's Tolerance to the Direct Effects of Air Blast," Technical Progress Report, DASA-2113, Defense Atomic Support Agency, October 1968.

7. Galaitsis, A., Theobald, M., Figucia, F., "Fibrous Material System Concepts for Protecting Personnel from Blast Waves," U.S. Army Natick R,D,&E Center Technical Report TR-86/016L, April 1984. (AD B100442L)

8. Jonsson, A., Clemedson, C., Arvebo, E., "An Anthropometric Dummy for Blast Research," *Proceedings 1983: International Conference on Protective Clothing Systems*, Stockholm, Sweden, August 23-27, 1981, pp. 89-97.

9. Young, A., Jaeger, J., Phillips, Y., Yelverton, J., Richmond, D., "The Influence of Clothing on Human Intrathoracic Pressure During Airblast," *Aviation, Space, and Environmental Medicine*, , 56, January, 1985, pp. 49-53.

10. Phillips, Y., Mundie, T., Yelverton, J., Richmond, D., "Cloth Ballistic Vest Alters Response to Blast," *The Journal of Trauma*, (1st Supplement), Vol. 28, no. 1, January 1988, pp. S149-S152.

11. Von Gierke, H., "Biodynamic Response of the Human Body," *Applied Mechanics Reviews*, Vol. 17, no. 12, December 1964.

12. Baker, W., *Explosions in Air*, University of Texas Press, Austin, Texas, 1973, p. 137.

13. Military Specification MIL-C-44050A, Cloth, Ballistic, Aramid, Type I, 18 August 1987.

14. Military Specification MIL-C-44043(GL), Cloth, Ballistic, Nylon, Lightweight, Water-Repellent Treated, Class 1, 30 March 1981.

15. Military Specification MIL-C-44031D, Cloth, Camouflage Pattern: Woodland, Cotton and Nylon, Class 1, 2 September 1987.

16. Bowen, I., Fletcher, E., Richmond, D., Hirsch, F., White, C., "Biophysical Mechanisms and Scaling Procedures Applicable in Assessing Responses of the Thorax Energized by Air-Blast Overpressures or by Nonpenetrating Missiles," *Annals of the New York Academy of Sciences*, 152, October 1968, pp. 122-146.

17. Gibson, P., "Response of Clothing Materials to Air Shock Waves," U.S. Army Natick R,D,&E Center Technical Report TR-89/043, September 1989. (AD 212798)

18. Stuhmiller, J., Chuong, C., Phillips, Y., Dodd, K., "Computer Modeling of Thoracic Response to Blast," *The Journal of Trauma*, (1st Supplement), 28, January 1988, pp. S132-S139.

19. Gvozdeva, L., Lyakhov, V., Raevskii, D., Faresov, Y., "Shock Wave Propagation in a Gas and a Porous Medium," translated from *Fizika Goreniya i Vzryva*, Vol. 23, No. 4, July-August 1987, pp. 125-129.

20. Rudinger, G., "Some Effects of Finite Particle Volume on the Dynamics of Gas-Particle Mixtures," *AIAA Journal*, Volume 3, July 1965, pp. 1217-1222.

TITLE: **Fiber Orientation Effect on Dynamic Mechanical and Ballistic Properties of Spectrashield® Composites**

*John W. Song, Mr. and Janet E. Ward, Ms.

ABSTRACT: The effect of fiber orientation in ultra-high strength Spectra® polyethylene fiber-reinforced composites was examined through the correlation of dynamic mechanical properties to the ballistic impact resistance efficiency of those composites. Spectra® fabric-based composites and Spectrashield® angle-plied laminates were included in the study. Based on the findings of this evaluation, fiber orientation significantly affected the flexural moduli and damping properties measured at the glass transition temperature (T_g) of polyethylene and at room temperature. Among the Spectrashield® angle-plied composites examined, the [0/±60] laminate showed the highest ballistic resistance capability, marginally ahead of the [0/90] samples.

At very low areal density, all Spectra®-based composite systems demonstrated similar ballistic limits. However, at higher areal densities, the Spectrashield® angle-plied materials surpassed the performance levels of the fabric-based composites. In both composite systems, the ballistic impact resistance efficiency reduced as areal density increased. The rate of reduction was more severe in the fabric-based composites than in the Spectrashield® angle-plied laminates.

An energy dissipation factor, η, obtained from the relationship of flexural storage and flexural loss moduli at the T_g of polyethylene (-125 °C) showed reasonably good agreement with ballistic kinetic energy absorption efficiencies for each laminate. This suggested that the low temperature transition (γ-transition) which is the T_g of polyethylene is an important parameter contributing to the high toughness and excellent ballistic impact resistance of the Spectra® composites.

Through optical and scanning electron microscopy, multiple modes of failure resulting from the ballistic impact event were identified in the Spectra® composites. Variations in the delamination at the impact point were observed in the two composite systems. Additional differences were also seen, not only between the fabric-based system and the angle-plied laminates but also between the angle-plied materials due to fiber orientation or ply layup.

*BIOGRAPHY: John W. Song

PRESENT ASSIGNMENT: Materials Research Engineer in the Materials Research and Engineering Division of the Individual Protection Directorate, U.S. Army Natick Research, Development and Engineering Center, Natick, Massachusetts.

PAST EXPERIENCE: Textile Engineer, Dai-nong Textile Company, Seoul, Korea, 1972-1974.

DEGREES HELD: Master of Science, Polymers, Massachusetts Institute of Technology - 1986; Master of Science, Textiles, Georgia Institute of Technology - 1981; Bachelor of Science, Textile Engineering, Yeung Nam University - 1973

Fiber Orientation Effect on Dynamic Mechanical and Ballistic Properties of Spectrashield®Composites

John W. Song, Mr. and Janet E. Ward, Ms.

INTRODUCTION

Because of its excellent mechanical properties and low density, Spectra®, an ultra-high molecular weight polyethylene fiber commercially available from Allied-Signal, Inc., is a high-potential candidate for ballistic protective applications. Research and development is ongoing both at U.S. Army Natick Research, Development and Engineering Center (Natick) and in the private sector to optimize the ballistic-resistance capabilities of this high-strength fiber.

Traditionally, ballistic protection offered to the individual soldier in personnel armor is accomplished through the use of orthogonally woven fabric and fabric-based composites. In an attempt to exploit the outstanding properties of the Spectra® fiber, Allied developed a new composite technology identified by U.S. Patent No. 4,748,064.[1] The technology consists of a fibrous nonwoven-type material with polymer-impregnated Spectra® fibers formed into a unidirectional web.[2] Allied registered this technology as Spectrashield®. The Spectrashield® materials can be formed into soft armor systems, much like woven fabrics, or multiple layers of the Spectrashield®material may be molded to form composites.

Recent studies indicate that orthogonally stacked Spectrashield®unidirectional laminates show better ballistic impact resistance than orthogonally woven fabric-based composites.[2,3] With the Spectrashield® material, it is possible to alter the fiber orientation from the typical 0/90 degrees found in many fabric-based composites. Altering the fiber orientation of laminates with Spectrashield® unidirectional material produces a structural element capable of resisting load in several directions. The stiffness and damping properties of such a composite configuration are important parameters since both directly affect penetration resistance as well as deformation upon ballistic impact.

When a viscoelastic material is subjected to high frequency or high strain rates, such as a ballistic impact event, the material displays substantial stiffness, which resembles the behavior of polymeric materials at low temperatures. That is, the damping behavior associated with the amorphous region in a viscoelastic material appears negligible at low temperature or at high strain rates; thus the material behaves as if it were a glassy solid. For this reason, upon ballistic impact, its ability to elongate will be reduced and the amount of energy absorbed mainly depends on the stiffness of the polymeric material.

On the other hand, ultra-high molecular weight polyethylene has, in addition to high tensile strength and modulus, damping behavior observable at approximately -125°C. This low temperature is identified as the glass transition temperature (T_g) associated with its amorphous relaxation, which indicates that upon ballistic impact, polyethylene has the capacity to strain and the potential for amorphous reorientation.[4-8] This indication suggests that ultra-high modulus polyethylene has the capability for good ballistic impact resistance.[3,9,10]

Although some preliminary work has been completed on angle-ply effects during the developmental stage of Spectrashield®, limited information is available on this material. In this study, an analysis of fiber orientation effects on dynamic mechanical properties of Spectrashield® laminates is undertaken to assist in better understanding the failure and energy absorption mechanisms demonstrated upon ballistic impact. The damping properties of Spectrashield® laminates with various angle-plied configurations are examined in an attempt to show the correlation between these properties and ballistic impact resistance. The paper focuses on the work completed to date in assessing that relationship.

EXPERIMENTAL

TEST SAMPLES

Materials

The unidirectional Spectrashield® base material used in this study was obtained from Allied Signal, Inc., Morristown, New Jersey and was based on the Spectra® 1000 fiber. The resin matrix for the Spectrashield® prepreg consisted of a one-phase vinyl ester and polyurethane blend. The resin content represented approximately 25% by weight.

The second Spectra®-based prepreg included in this analysis consisted of a Spectra® 900, 21 x 21 plain weave fabric with a two-phase vinyl ester and polyurethane resin system. The resin add-on of this system was also approximately 25% by weight.

Molding of Laminates

Five angle-plied laminate configurations with varying angle components were fabricated from the Spectrashield® unidirectional-base materials. Due to difficulties incurred in handling the Spectrashield® product, two layers of the unidirectional prepreg were combined and treated as one layer. For example, the actual construction of a [0/90] sample was $[0_2/90_2]$. In an effort to equalize areal densities as closely as possible and to eliminate data collection difficulties, the final laminate configurations examined in the study included $[0]_4$, $[0/90]_2$, [0/±45/90], [0/±30/±60/90], and [0±60].

The Spectra®fabric-based composites samples were assembled by layering single plies of the fabric prepregs in a manner to ensure that the yarn orientation was approximately biaxial (0/90 degrees). The biaxial orientation was represented by one-ply (each direction) and two-ply (alternating directions) configurations in the fabric-based laminates. Those samples were identified as $[0/90]_{F1}$ and $[0/90]_{F2}$, respectively.

All laminates were prepared by molding the prepregs in a hydraulic press with 6.9×10^6 Pa (1000 psi) pressure for 30 minutes at 120 ± 3°C. One-foot square samples were used in the ballistic evaluation. Appropriate-sized samples for the dynamic mechanical analysis were also constructed as described above.

EVALUATION PROCEDURES

Dynamic Mechanical Analysis

A DuPont Dynamic Mechanical Analyzer (DMA-983) was used to observe the effect of the fiber orientation on the dynamic mechanical properties of the laminates, especially, at low temperature. All samples were measured using low mass clamps at a fixed frequency of 1 Hz with oscillation amplitude of 0.5 mm and 2°C/min heating rate. Dynamic mechanical measurements were made in several different directions i.e. $(\pm 45)_4$, (±30/90).

Ballistic Evaluation

Kinetic energy absorption during the ballistic penetration was measured using the high speed impact apparatus located at Natick.[11] All low areal density samples were impacted at velocities of approximately 300 m/s. The sample holder used for the low areal density sample evaluation was that described by Song and Allen.[11] Data collected at the higher areal densities was in accordance with Military Standard, MIL-STD-662E, V_{50} Ballistic Test For Armor.[13]

Assuming the projectile mass was constant during the penetration of the laminated target, kinetic energy (KE) absorbed by the laminate is:

$$KE = 1/2\, m(V_s^2 - V_r^2) \qquad (1)$$

where KE is kinetic energy (J), m is projectile mass (Kg), V_s and V_r are striking and residual velocities (m/s) respectively.

In this study, the ballistic limit (BL) is considered to be the single highest striking velocity where the residual velocity equals zero and can be estimated with:[12]

$$BL = (2KE/m)^{1/2} \tag{2}$$

Failure Mechanism Analysis

Scanning electron microscopy was used to observe the mode of failure resulting from the ballistic impact event. Small pieces (ca. 13 mm x 13 mm) of impacted laminates were mounted on specimen studs. The samples were coated in a sputter coater with a thin layer of gold palladium. The fracture patterns of the coated samples were examined in an AMRAY Model 1000A Scanning Electron Microscope using the secondary electron mode.

RESULTS AND DISCUSSION

DYNAMIC MECHANICAL ANALYSIS

Typical dynamic mechanical properties obtained during this study are represented by the plot shown in Figure 1. Four transitions are apparent. The transitions at near +140°C, +75°C, and -125°C are α', α and γ–transitions of polyethylene, respectively.[4] The α' and α-transitions are associated with motion within the crystalline regions whereas the γ transition is associated with the amorphous region hence the glass transition in the noncrystalline regions of polyethylene. The transition seen between -75°C and 0°C is considered to be the glass transition region of the polyurethane (resin matrix).[14]

The effect of fiber orientation on the flexural storage modulus (E') of the materials evaluated are shown in Table 1 and Figure 2. As indicated, the flexural storage moduli at low temperatures (T_g) are significantly higher than those at room temperature (20 °C). The laminates with more fibers aligned along the test direction demonstrated higher flexural storage modulus than the laminated samples with fibers aligned at angles to and away from the testing direction. For example, the $[0]_4$ sample which had all four (4) component fibers aligned in the test direction showed the highest values for flexural storage modulus; whereas the $[0/90]_2$ laminate with only two (2) components aligned in the test direction gave the second highest value. Those samples are followed, in descending order, by the configurations [0/±45/90], [0/±60], [0/±30/±60/90].

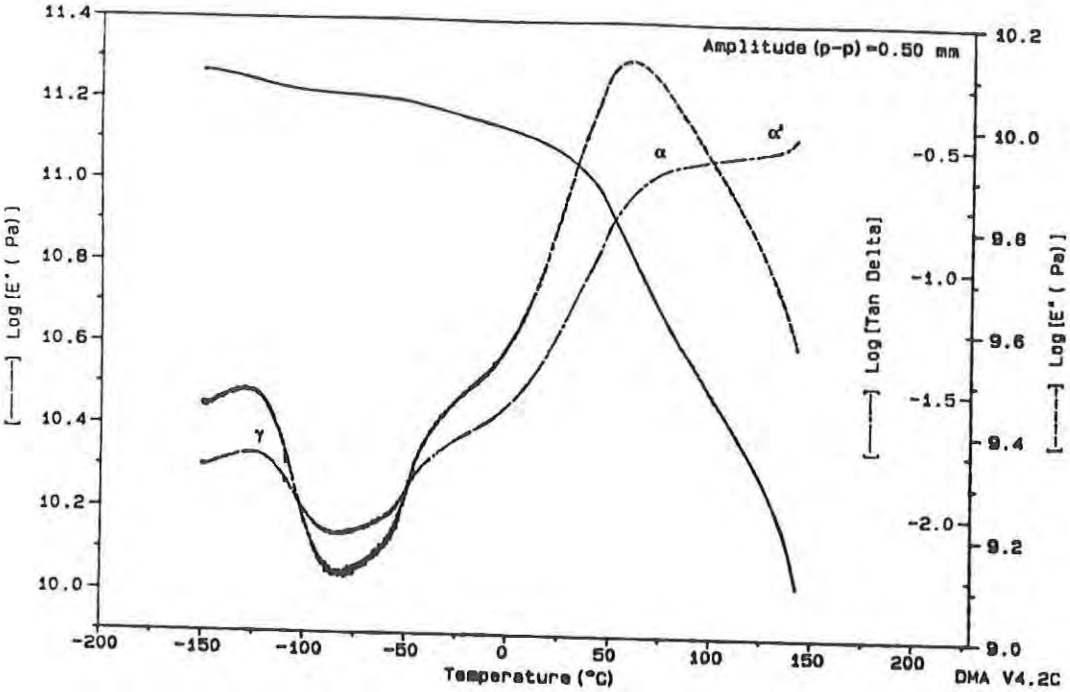

Figure 1. Typical scan of dynamic mechanical properties of Spectra®polyethylene laminate with blended matrix system of polyurethane and vinyl ester .

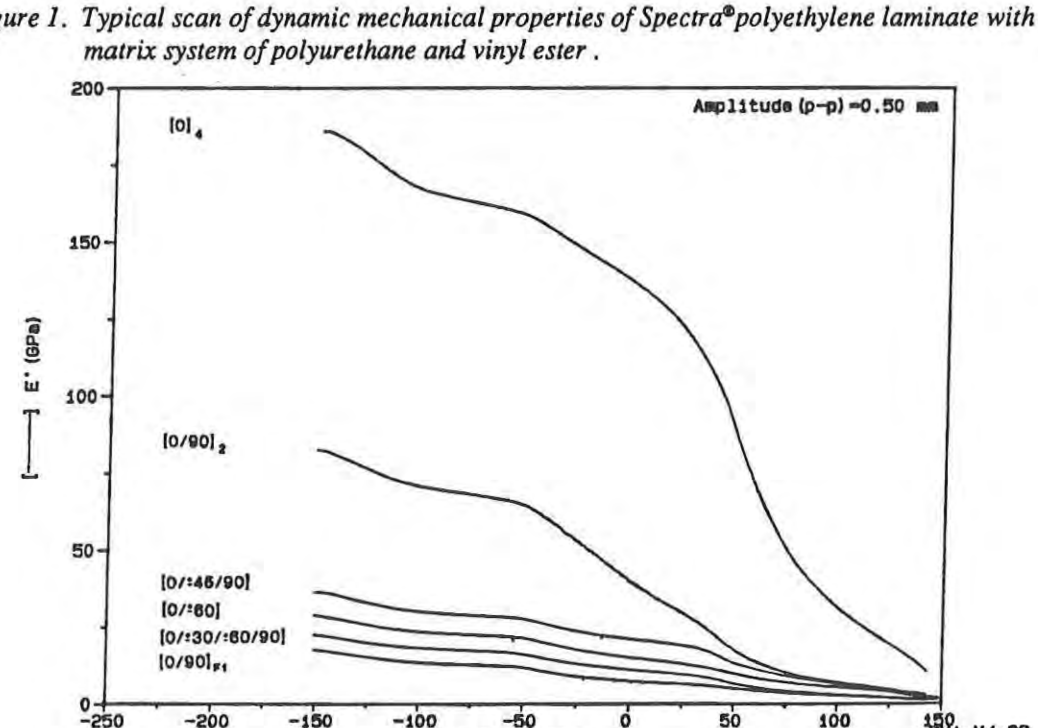

Figure 2. Flexural storage modulus (E') of Spectra®laminates as a function of temperature.

*Table 1. Dynamic mechanical properties of Spectra®laminates. **

Sample ** [Ply Angle]	T_g *** (°C)	tan δ_{Tg} ($x10^3$)	E'_{Tg} (GPa)	E''_{Tg} (GPa)	E'_{20} (GPa)
$[0]_4$	-126.4	16.51	177.20	2.93	125.30
$(90)_4$	-122.5	63.10	7.19	0.45	1.36
$[0/90]_2$	-127.8	26.11	76.83	2.01	31.61
$(\pm45)_2$	-127.9	31.13	26.12	0.81	13.58
[0/±45/90]	-124.6	39.29	32.87	1.29	19.60
(45/0/90/-45)	-124.8	53.09	14.28	0.76	8.05
(±22.5/±67.5)	-125.2	39.75	26.31	1.05	14.16
[0/±60]	-123.0	58.33	25.51	1.49	13.55
(60/0/-60)	-122.2	60.48	17.09	1.03	11.73
(±30/90)	-120.6	57.14	18.52	1.06	11.59
[0/±30/±60/90]	-127.1	32.38	20.21	0.07	10.01
(30/0/60/-30/90/60)	-124.0	31.67	21.79	0.07	7.37
(30/60/0/90/-30/-60)	-127.1	37.62	11.56	0.43	5.47
$[0/90]_{F1}$	-116.7	85.71	14.65	1.26	6.77
$(\pm45)_{F1}$	-117.8	85.24	12.52	1.07	5.90
$(\pm45)_4$	-129.6	27.81	16.91	0.47	6.12
$[0/\pm60]_2$	-127.1	52.61	15.94	0.84	5.50
$(60/0/-60)_2$	-128.2	62.38	13.61	0.85	4.90
$(\pm30/90)_2$	-129.2	58.57	12.06	0.71	3.20
$(30/90/-30)_2$	-127.8	50.48	23.05	1.16	5.98
$[0/90]_{F2}$	-123.6	44.76	22.65	1.01	10.63
$(\pm45)_{F2}$	-122.2	42.86	15.21	0.65	6.60

NOTES: * Subscripts Tg and 20 are properties at Tg and at 20 °C, respectively.
** Sample in ( ) indicate alternate test direction for preceding laminate configuration in [ ].
*** Measured by Dynamic Mechanical Analyzer.

The smallest value is demonstrated by the $[90]_4$ laminated sample where the performance appeared to be more influenced by matrix properties than fiber properties. The flexural storage moduli of the fabric laminates are significantly lower than angle-plied laminates. As was expected, the tan δ at T_g is nearly inversely proportional to the flexural storage modulus (Figure 3).

As indicated earlier, the dynamic mechanical properties within a laminate are different depending on test direction, and the final performance of the laminate is a result of the contributions of these varying properties. The relationship of the flexural loss modulus (E") versus the flexural storage modulus (E') for each laminate is plotted in Figure 4. For those configurations where three or more data points (different test directions) are available, the relationship appears linear as was expected based on fundmental viscoelastic behavior of polymeric materials.[4] By

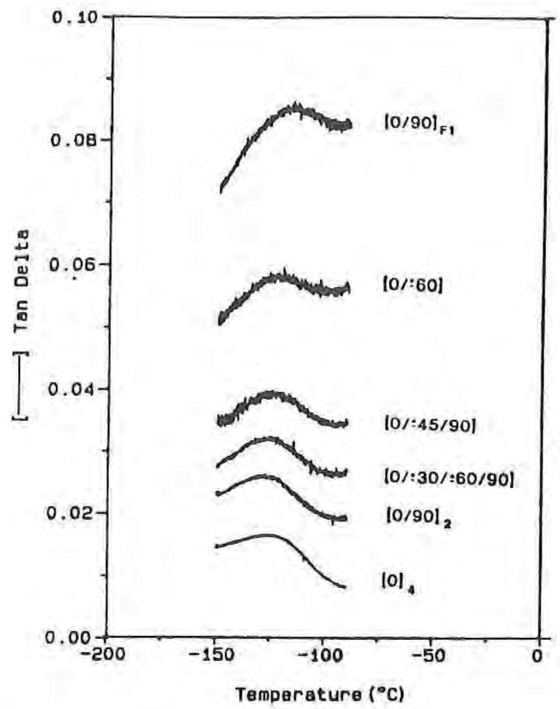

Figure 3. Tan δ at T_g of Spectra® laminates as a function of temperature.

assuming that the linear relationship is true for all laminates examined in this study, average generalized properties are calculated by the following empirical relationship obtained from Figure 4.

$$E'' = \eta E' + C \tag{3}$$

where η is the slope of the E"/E' relationship for each laminate, which represents the average damping behavior. Therefore, η is conveniently termed the energy dissipation factor of the respective laminates and is listed in Table 2.

BALLISTIC RESISTANCE ANALYSIS

Reasonably significant effects were observed in the ballistic performance of each low areal density angle-plied laminate examined in this study. However, due to classification restrictions on ballistic data at the higher areal densities, the low areal density data are combined with the high areal density data for discussion of the angle-plied laminates represented by Figures 5, 6, and 7. The significance in ballistic performance of the Spectra® composites at the low areal densities are examined later in Figure 8.

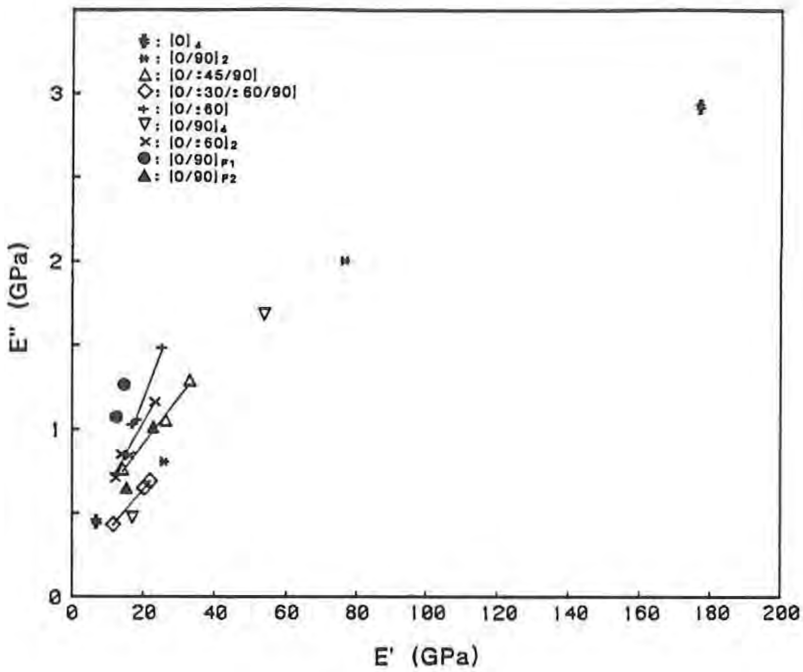

Figure 4. Flexural loss modulus (E") vs flexural storage modulus (E') at T_g of Spectra®laminates. Slopes of each laminate are energy dissipation factor of represented laminates.

Table 2. Relation Between Energy Dissipation Factor, η, Obtained From Equation 7 and Kinetic Energy Absorption Efficiency (KE/AD) of Spectra®Laminates Upon Ballistic Impact.

Sample Identification	η	KE/AD
$[0]_4$	0.0146	17.95
$[0/90]_2$	0.0237	21.16
$[0/\pm45/90]$	0.0280	18.09
$[0/\pm60]$	0.0568	22.31
$[0/\pm30/\pm60/90]$	0.0233	16.23
$[0/90]_4$	0.0329	20.39
$[0/\pm60]_2$	0.0383	21.83
$[0/90]_{F1}$	0.0892	30.14
$[0/90]_{F2}$	0.0481	26.43

The ballistic limits (BL) as a function of areal densities (AD) are plotted in Figure 5 using an empirical relationship as follows:

$$BL = a\ (AD)^b \tag{4}$$

A similar relationship was reported by Song et al. for Kevlar®and S-2® glass laminate studies.[12] In this case, both a and b are constants and are included in Figure 5. An interesting observation in this figure is that at low areal density, both Spectra®-based laminates demonstrate similar ballistic limits. However, as areal density increases, differences in ballistic limits become more apparent, with the Spectrashield®-based composites showing higher results. This trend is supported by ballistic test data generated at areal densities typical of personnel armor applications, which show Spectrashield®-based composites demonstrating significantly better ballistic impact penetration resistance than the Spectra®fabric-based composites.[3]

The specific ballistic resistance efficiency, described as BL/AD, are plotted as a function of areal density in Figures 6 and 7. As illustrated, the ballistic resistance efficiency decreased as areal density increased (Figure 6). As indicated in Figure 7, the rate of reduction of ballistic resistance efficiency is greater on fabric-based laminates than on the Spectrashield®-based composite. The relation obtained from data plotted in Figure 7 is represented by:

$$\ln (BL/AD) = \ln c - d \ln (AD) \tag{5}$$

where c and d are constants.[12]

Figure 8 is a plot of the energy dissipation factor, η, against kinetic energy absorption efficiency of the laminates (KE/AD). Although some scatter in the data is shown, proportionality between KE/AD and η is observed. This result suggests that the damping properties at the low temperature (-125 °C) transition, which happens to be the T_g of polyethylene, can be useful in predicting the potential for high-speed impact resistance capabilities in laminated composites.

FAILURE MECHANISM ANALYSIS

As indicated by Laible and others, the mode of failure can be diverse in composites materials.[15-18] Failure may occur through one mechanism acting alone or through a combination of different mechanisms, such as shear or fiber cutting, tension or fiber breaking, fiber debonding, fiber pull out, delamination and matrix failure. Visual examination of the ballistically impacted Spectra®composites suggests a variety of failure mechanisms occurred in the

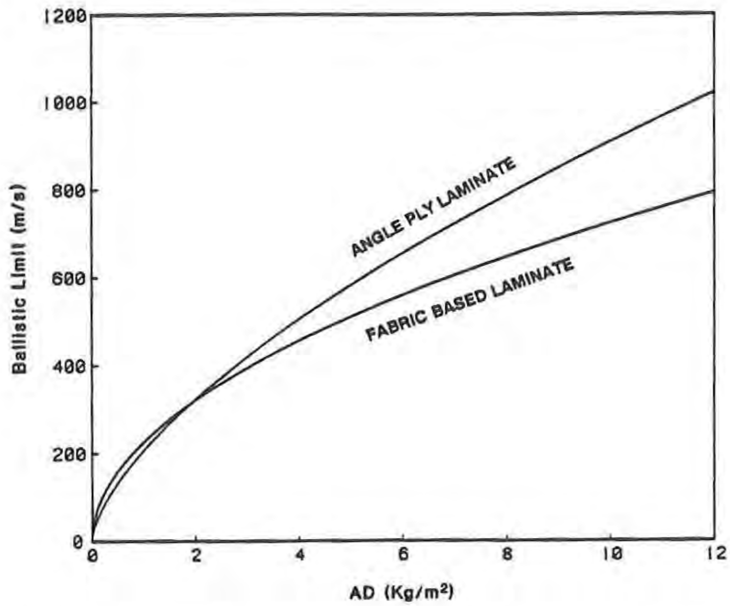

Figure 5. Ballistic limit of Spectra®laminates as a function of areal density. Constants a and b for angle plied and fabric-based laminates are 205.36, 0.65 and 226.36, 0.51 respectively.

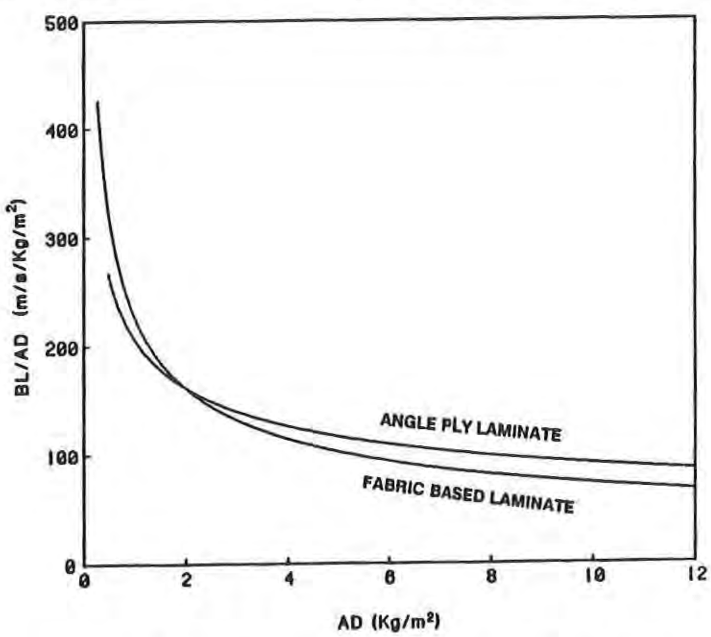

Figure 6. BL/AD vs areal density of Spectra® laminates.

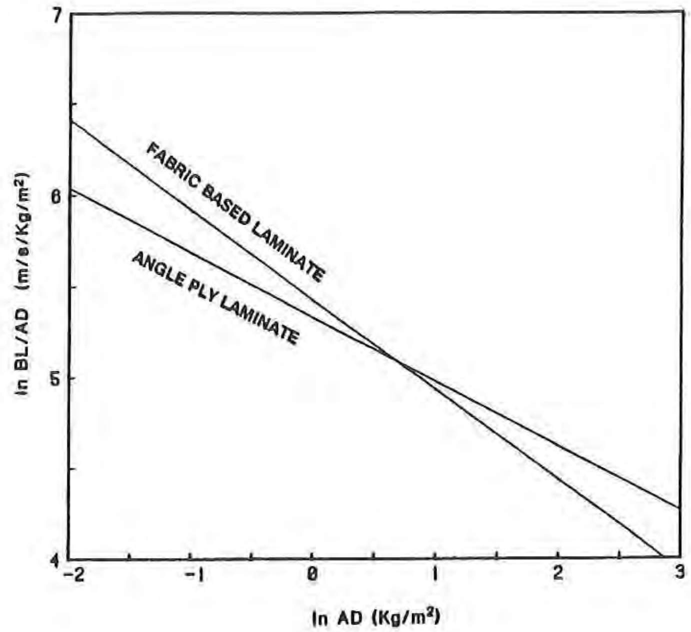

Figure 7. Logarithmic expression of Figure 6. Slopes, which are the reduction rate of ballistic resistance efficiency for angle-plied and fabric-based laminates are (0.35) and (0.49) respectively.

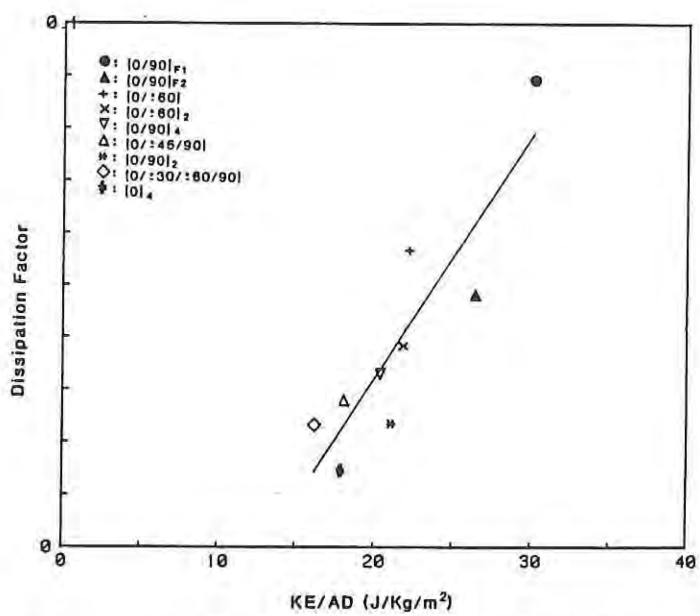

Figure 8. Dissipation factor, η, as a function of KE/AD on various angle-plied and fabric-based laminates.

Spectra® fabric-based composites as well as in the Spectrashield®angle-plied laminates. The Spectra® fabric-based composites show evidence of failure very typical of that reported in other fabric-based composites systems. Specifically observed is delamination in a symmetrical, out-of-plane cone shape around the impact point, with fibers apparently failing due to shear or fiber cutting in the early layers of the composite and in tension at the rear of a completely penetrated panel.[2,17]

The delamination pattern of the Spectrashield® angle-plied laminates appears to be different than that demonstrated in the fabric-based systems. The delamination in the Spectrashield® laminates more closely suggests the generator strip phenomenon reported by Ross et al.[18] That is, upon impact, the projectile pushes a strip of the first layer of the laminate toward the rear of the panel. The length of that strip is considered to be somewhat dependent upon the amount of time required for the projectile to cut through the first layer; the width of the strip usually correlates to the diameter of the projectile. The first strip of the delamination, in turn, applies a transverse load to the second ply and generates delamination successively through the remaining layers of the laminate until penetration occurs or the projectile is stopped. As shown in Figures 9a and b, the delamination failure that occurs in the Spectrashield®angle-plied laminate appears to approximate that phenomenon and each configuration tends to follow the angle of the respective fiber orientation in the panel.

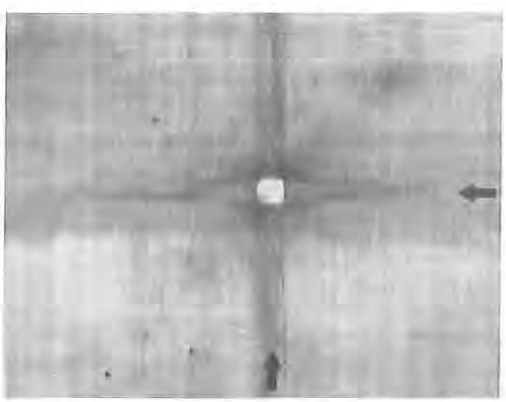

Figure 9a. Delamination pattern of [0/90] Spectrashield®laminate

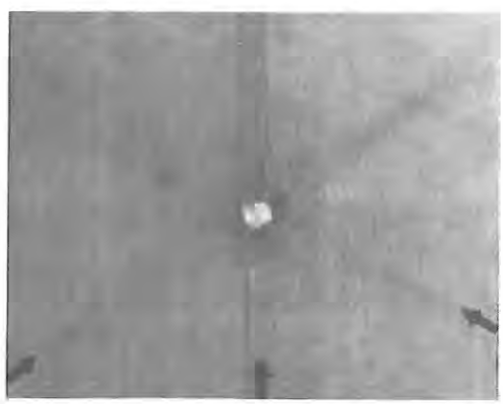

Figure 9b. Delamination pattern of [0/±60] Spectrashield®laminate.

Inspection through scanning electron microscopy of the Spectrashield®composites indicates that fibers experiencing the initial impact in the angle-plied panels fail in shear or from fiber cutting (see Figure 10a, showing the impact area of the [0/±60] sample). In those cases where fiber damage was visible in the back layers of the laminate, such as in the [0/±60] sample, the mode more closely resembled tensile failure (Figure 10b). Many of the laminates appear to allow the test projectile to penetrate by moving fibers laterally or through fiber pull out rather than straining the fibers to break. This was particularly true, as illustrated in Figure 11, of the $[0]_4$ sample, where very little fiber damage is observed, even at the point of impact.

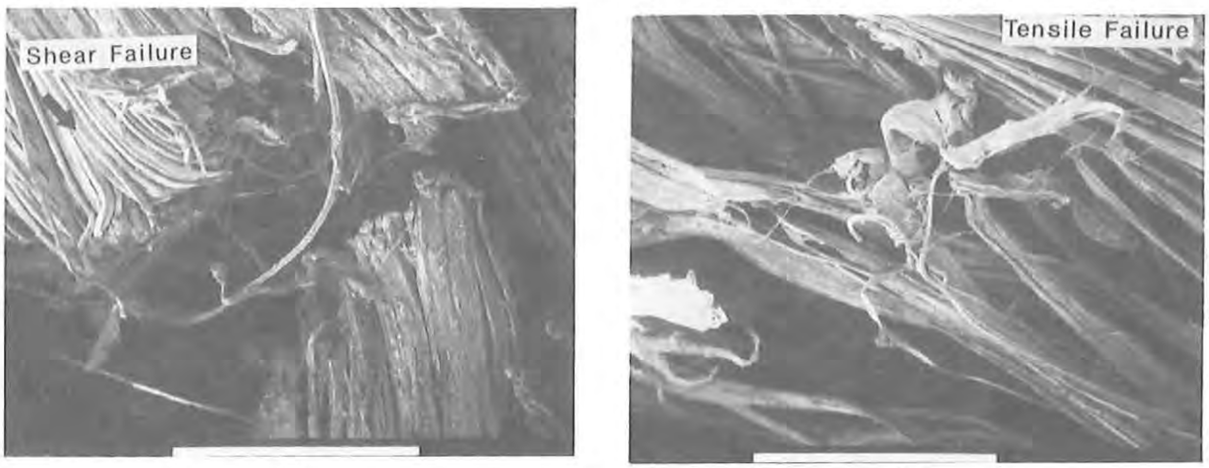

(a) *(b)*

Figure 10. Ballistic failure mode of Spectrashield®[0/±60] laminate at impact point; (a) face of panel - 45X magnification; (b) back of panel - 45X magnification.

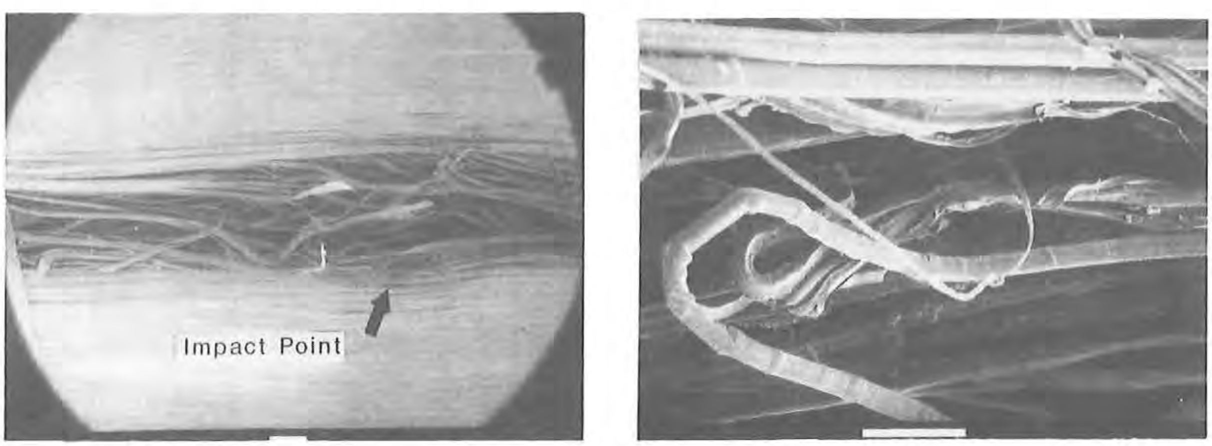

(a) *(b)*

Figure 11. Ballistic failure mode of Spectrashield®$[0]_4$ laminate at impact point; (a) face of panel - 6X magnification; (b) back of panel - 200X magnification.

The lack of significant fiber breakage in the Spectrashield®angle-plied laminates at the low areal densities is likely responsible for the reduced energy absorption efficiencies compared to the woven fabric-based laminates at similar areal densities (see Table 2). Spectrashield® laminates at much higher areal density do demonstrate some of the same failure mechanisms. The generator strip delamination is less observable in thicker samples; however, substantial delamination does occur. Considerable fiber pull out is also evident in panels at areal densities equivalent to helmet weights.

The photomicrographs included in the preceding discussion show some melting at the point of rupture in the Spectra®fibers that underwent ballistic impact. In this study, no attempt is made to determine if the apparent melting occurs as a result of friction generated during the impact event or if it is a post-impact phenomenon. That discussion, alone, could be the topic for several additional papers on the Spectra®-based composites, whether fabric-based or unidirectional-based materials.

CONCLUSIONS

Dynamic mechanical analysis revealed that the effect of fiber orientation within the Spectrashield®composite is significant. Composites with fiber alignment along the test direction show higher stiffness with lower damping than those with fiber orientation away from the test direction. Low temperature transition (T_g of polyethylene) observed at -125 °C is considered to be an important behavior in regard to ballistic impact resistance since the behavior of viscoelastic material at high strain rates, such as ballistic impact, is similar to the behavior at very low temperature.

A generalized average energy dissipation factor, η, was obtained from the relation of flexural storage and flexural loss moduli at the T_g of polyethylene, which was recorded from several testing directions within an angle-plied composite. Relations between the generalized average energy dissipation factor, η, and the kinetic energy absorption efficiency upon ballistic impact show reasonably good agreement. This fact suggests that the damping behavior of polyethylene at the low temperature transition is another important parameter contributing to the excellent ballistic impact resistance of Spectrashield®composites.

At very low areal density, both Spectra®-based composites appeared to demonstrate similar ballistic resistance performance; at higher areal denisty, the Spectrashield®angle-plied composite showed an advantage. Among the angle-ply composites, the [0/±60] laminates gave the highest performance followed closely by $[0/90]_2$, and then the [0/±45/90], $[0]_4$ and 0/±30/±60/90]. As areal density increases, ballistic resistance efficiency dropped rapidly. The rate of decline for the fabric composite was faster than for the angle-ply laminate. Multiple failure mechanisms and delamination modes were observed in the Spectra® composites. In either composite (fabric-based or the Spectrashield®-based), fiber failure appeared to be caused by transverse shear on plies near the impact face and by axial tensile failure or pull out at the exit point. Evidence of extensive strain wave propagation was observed on both the front and back of the laminates as was melting in the impacted fibers.

REFERENCES

1. Harpell, G. A. et al. US. Patent 4,748,064, Ballistic Resistant Composites.
2. Pervorsek, D.C., Kwon, Y.D., Harpell, G.A. and Li, H.L., Proceeding of 34th International SAMPE Symposium, 1780 (1989).
3. Prevorsek, D. and Li, H.L., Development of a Spectra® Helmet Shell, Phase II Interim Report (Contract No. DAAK60-87-C-0097), To Be Published.
4. Ward, I.M., Mechanical Properties of Solid Polymers, 2nd Ed.,Wiley-Interscience, London (1983).
5. Kline, D. E., Sauer, J.A. and Woodward, A.E., J. Polymer Sci. 22, 455 (1956).
6. Takayanagi, M., Proceedings of the Fourth International Congress of Rheology, Part 1, Interscience Publishers, N.Y., 161 (1965).
7. Simmat, K.M., J. Appl. Phys., 37, 3385 (1966).
8. McCrum, N.G. and Morris, E. L., Proc Roy. Soc. A. 292, 506 (1966).
9. Bhatnagar, A., Lin, L.C., Lang, D.C., Chang, H.W., Proceedings of 34th International SAMPE Symposium, Vol.34, 1529 (1989).
10. Prevorsek, D. C. and Chin, H.B., Proceedings of 21st International SAMPE Technical Conference, Vol.4,812 (1989).
11. Song, J.W. and Allen, R., U.S. Army Natick Research, Development and Engineering Center Technical Report, Natick/TR-87/040L (1987).
12. Song, J.W., and Egglestone, G. T., Proceedings of the 19th SAMPE International Technical Conference, Crystal City, VA (1987).

13. Military Standard, MIL-STD-662E, V50 Ballistic Test for Armor, Jan 1987.

14. Prevorsek, D. and Chin, H.B., Lightweight Spectra®Helmet, Phase I Interim Report (Contract No. DAAK60-87-C-0089), To Be Published.

15. Laible, R. C., "Ballistic Materials and Penetration Mechanics", Elsevier Scientific Publishing Company, Amsterdam, Vol.5, 233 (1980).

16. Morrison, C.E., The Mechanical Response of An Aramid Textile Yarn To Ballistic Impact, Thesis for Degree of Doctor of Philosophy, University of Surrey (1984).

17. Song, J.W., Relationships Between Failure Mechanisms and Ballistic Impact Resistance of Composite Helmets, Proceedings of the 1988 Army Science Conference (1988).

18. Ross, C.A. and Sierakowski, R.L., "Delamination Studies of Impacted Composite Plates", Shock and Vibration Bulletin, Bull.46, Part 3 of 5, (August 1976).

ACKNOWLEDGEMENTS

The authors wish to acknowledge and thank T. Gerardi and K. Batton for data collection assistance, M. Goode for the excellent scanning electron photomicrographs, and our technical reviewers, W. Kohlman, R. Laible, P. Cunniff, and M. Hepfinger. The authors also thank Dr. H.W. Chang and Dr. H.L. Li of Allied Signal, Inc. for providing the Spectrashield®materials used in this evaluation.

TITLE: Advances in Shelf Stable Operational Rations

*Daniel Berkowitz, Mr., Gary W. Shults, Mr., and
Edmund M. Powers, Mr.

ABSTRACT:

Thermal processing has long been the principal means of stabilizing low acid, moist foods commercially marketed worldwide and for inclusion in military operational rations. Since the quality attributes of foods are always significantly modified and frequently degraded by the thermal process, heat stabilization is limited to those foods that satisfactorily survive thermostabilization. Recently employed means to develop non-thermoprocessed shelf-stable, items with satisfactory organoleptic qualities include "hurdle" techniques that may utilize moderate heat; preservatives; reduction of: water activity, (Aw), pH and oxygen tension to provide insurmountable obstacles for microbial growth. Acceptable long- shelf-life breads have been developed using this technology. In addition, the "hurdle" technique has been applied to stabilize other prototype items that do not survive thermoprocessing, such as pizzas and burritos. Furthermore, the physical parameters involved in retort processing in flexible containers have been exploited to develop thermostabilized items, such as fried breaded foods heretofore not considered technically achievable.

*BIOGRAPHY OF PRESENTER: Daniel Berkowitz

PRESENT ASSIGNMENT: Mr. Berkowitz is Project Officer of the "New Food Items for Department of Defense" Project. He is tasked with the development and improvement of shelf-stable food items for inclusion in the Meal,Ready-to-Eat (MRE), Tray Rations (TR) and other operational rations.

PAST EXPERIENCE: Since 1979, Mr. Berkowitz has been engaged in the development of new food products and processes for operational ration use. Mr. Berkowitz is the author of 15 technical papers, holder of 5 patents and is the recipient of numerous awards for technical achievement.

DEGREES HELD: Associate in Applied Sciences Degree in Hotel and Restaurant Management, New York City Community College (1956). Completed a Two-Year Army Scholarship In Food Technology, Iowa State University (1960).

Advances in Shelf-Stable Operational Rations

Daniel Berkowitz, Gary W. Shults and Edmund M. Powers

Introduction

Objective

Operational rations must adequately nourish the soldier whose mission may require optimal physical and mental performance under conditions that are extremely stressful. However, regardless of the degree to which rations are nutritionally balanced, adequate nourishment is not obtained if they are not consumed because of dislike or menu boredom. The objective of this work was to exploit formulation, processing and packaging opportunities to develop thermally and combination treatment stabilized foods that provide variety, are nutritious and satisfy the food preferences of today's ethnically and demographically diverse military consumers.

Historical Perspective

Despite a continuum of change in the packaging and menu content of operational rations, thermostabilization of entree items has long been the processing method of choice. The field ration mainstay of World War II and the Korean War was the Combat (C) ration. It contained a limited variety of thermostabilized shelf-stable canned entrees and other items. These were packed three meals per carton and provided about 3600 Kcalories per day. Obtaining food variety was by luck-of-the-draw. Furthermore, lengthy subsistence on this ration lead to menu boredom, diminished food consumption, weight loss and deterioration of physical and mental performance. The C ration was upgraded in time to the Meal-Combat-Individual (MCI), comprising 12 meals of retort-processed canned entrees and baked-in-the-can bread and cake items. Although this ration provided somewhat greater variety, obtaining preferred items and maintenance of weight and optimum performance continued to be problematic. Despite these deficiencies, the MCI served the individual soldier relatively well during the Vietnam conflict era.

The successor of the MCI is the Meal, Ready-To-Eat (MRE), with flexible retort pouch packaging that represents a total departure from rigid cylindrical cans. However, due to the lack of appropriate technology for producing shelf-stable conventional breads and cakes in flexible containers, this ration contained crackers in lieu of bread and also thermoprocessed cakes, which were not well liked. To reduce ration weight, and therefore the soldier's back-pack load, the MRE entrees originally contained an assortment of 10 casserole entree items weighing five ounces each and freeze-dried pork, beef and potato patties (15).

In response to consumer preference, these entrees have been reformulated and resized to contain eight ounces, the number of thermostabilized cakes have been reduced from 6 to 3, and the freeze-dried entrees and starches have been replaced with more desirable items.

However, irrespective of menu changes or container used, thermal processing-related similarities between current and past rations continue to exist (Table 1).

Technical Considerations

Advances in Food Thermostabilization

The retort pouch affords both challenges and opportunities for product improvement and development. Its thin profile permits quality enhancement due to significant process time reduction, as opposed to thermal processing in cylindrical cans. Furthermore, foods not producible in rigid containers may be successfully processed in the flexible retort pouch. Commercially produced canned foods are generally processed in pressurized steam or steam-heated water at temperatures of 240 degrees Fahrenheit or greater. Therefore, cans are generally solidly packed or contain fluids to limit head space, facilitate heat transfer to their contents and support the can's structure during the inevitable pressure changes that occur during thermal processing. Though effective for the purposes intended, this practice has limited thermostabilization in rigid containers, to semimoist or wet-pack foods. Fried breaded items, for example, are not compatible with processing in rigid containers because breadings cook off in fluids, yielding meat particles suspended in gruel. When breaded items are vacuum packaged in retort pouches, the packaging material conforms closely to the contained foods, limiting headspace and assuring satisfactory conductive heat transfer without the need for fluids for container protection. As a result, breadings on foods survive the thermal process, permitting inclusion of a class of items in operational rations heretofore not considered feasible.

Combination Treatment Technology

While thermostabilized, breaded items may enhance operational ration variety and acceptability, and their development indicates a broadening scope for the retort pouch, it is in the realm of nonthermal food stabilization techniques that the greatest changes in food variety and quality are likely to occur. The inclusion of conventionally baked items, for example could not, until recently, be included in the MRE because of physical and residual oxygen constraints associated with nonthermal processing in the flexible pouch. The techniques utilized to develop shelf-stable pouched breads, cakes (16,17,18,19) and other items employ a series of hurdles or obstacles which individually or cumulatively provide insurmountable obstacles for microbial growth or metabolism. These may include preservatives, reduction of oxygen, acidification and reduction in water activity (Aw) to prevent food degradation (Fig 1).

The employment of competing microorganisms, essential in fermentative food preservation, has not in our work been used. Although new opportunities are presented by the "hurdle" technique, the potential for degradative processes and microbial hazards, which are water-content related, must be carefully considered when this technique is used for food stabilization (Fig 2).

Water is generally the largest constituent of foods and frequently determines their stability, acceptability, digestibility, structure, and handleability. It is the principal quality determinant and prime consideration when nonthermal food stabilization methods are employed. Foods such as jams, jellies, preserves, cakes, cookies, candies, dried fruits and vegetables, cheeses, reduced moisture sausage and dried meats have been traditionally stabilized by nonthermal means, such as acidification or reduction of water activity. However, attempts to stabilize foods that traditionally are not sweet, salty, highly acidic, low in moisture or that require high levels of humectants to achieve Aw reduction sufficient to inhibit microbial activity do not generally result in foods that are widely acceptable (4). Nonthermal methods employing a number of mechanisms, which collectively assure food stability, are relatively new techniques. The preservation of canned, subsporadically processed shelf-stable sausage items by means of combination treatment or "hurdle" technique has been previously described (13). However, its application to stabilize a broad range of foods is a relatively recent endeavor (Table 2).

Inhibition of Staling

In addition to prevention of food degradation by judicious application of the above methods, prevention of irreversible staling in baked items is essential to stabilize bread and bread-based, ration items. Starches exist in nature as mixtures of linear and branched molecules of glucose units (Fig 3), the ratios of which are grain-species dependent. Staling is a complex phenomenon related to the retrogradation process that occurs in linear or high amylose starch that typically constitutes twenty seven percent of the carbohydrate component of wheat flour (20,22). Although amylopectin starches that are resistant to retrogradation may be derived from genetically modified waxy maize or from chemically cross-linked starches, wheat flour starch is chemically unmodified as used for bread production. It has been long understood (10,11) that emulsifiers complex with starches to prevent gelation and starch retrogradation, inhibiting the staling process (Fig 4).

Although a variety of emulsifiers such as sodium stearyol$_2$lactylate and other esters of fatty acids are widely used to extend the shelf life of commercially produced breads, their benefit is limited to days of shelf-life extension. However, military shelf-life requirements are measured in years. As a result, an evaluation of emulsifiers used as bread dough conditioners was undertaken to elucidate their long term antistaling effects. Among these, polyglycerol and sucrose stearate fatty acid esters were found to provide enhanced antistaling effects with the latter being superior with respect to: shelf-life extension; blandness; dough mixing times and its post mixing handleability. The structures of sucrose and polyglycerol fatty acid esters are similar, except that since sucrose has eight hydroxyl groups, compounds ranging from sucrose "mono" to "octa" fatty acid esters can be produced having a broad range of hydrophilic, lypophilic and starch complexing characteristics (Fig 5).

Prevention of Mold Growth and Toxin Production

Baked goods, other than custard-filled items, are not generally implicated in food poisoning outbreaks (9,14). Nevertheless, prevention of spoilage due to mold growth is of considerable economic consequence to the baking industry, and is of particular importance in military field rations due to their lengthy shelf-stability requirements. Furthermore, molds are a persistent cause of food spoilage and may produce aflatoxins, ochratoxins, penicillic acid and other toxins of public health concern (1,6,7,21). Although readily destroyed during the baking process, airbourne molds must be presumed to recontaminate baked items shortly after they exit the oven. Sanitary commercial practice and use of inhibitors such as sorbic, benzoic and propionic acids or their salts, prevent or retard postbaking mold growth. In the absence of chemical mold inhibitors, reduction of available oxygen to the range 0.5 percent or below, effectively inhibits outgrowth of mold contaminants.

Since a variety of nonthermally stabilized, flexibly packaged items currently under development depend on inhibition of molds for their stability (Table 2), reduction of intrapackage oxygen tension sufficient to assure mold inhibition is essential. Oxygen scavengers employing ferrous iron as the oxygen depleting substance appeared to have commercial production advantages over other oxygen reductive methods. However, information relative to their mold-inhibiting capability was empirical rather than definitive (2,23,24). Therefore, elucidation of their effectiveness was undertaken.

Residual oxygen levels of 0.5 percent or below are required for mold inhibition in the absence of chemical inhibitors (24). It is important to note therefore, that oxygen scavengers are capable of reducing redox potential sufficiently to inhibit mold growth even under optimal nutrient and water availability (Table 6). Furthermore, sorbic acid and reduced oxygen appear to be synergistic relative to mold inhibition in plate count agar (Table 3). This seems to be more pronounced in a complex substrate, such as bread where molds did not grow at oxygen concentrations of 1.5 percent or below (Table 5). These data indicate that postbaking mold contaminants are capable of outgrowth in the presence of sorbates if sufficient oxygen is available. The inclusion of an oxygen scavenger with the barrier packaged bread provided absolute mold inhibition despite an inoculum of 10^4 mold spores per pouch, demonstrating its effectiveness in prevention of mold growth.

Relationship between Water Activity and Available Oxygen

Water activity and oxygen are interrelated with respect to food degradation. At Aw below 0.95, anaerobic spore forming microorganisms of public health significance such as Clostridium botulinum, and facultative, spore forming, nontoxigenic food spoilage bacilli are inhibited regardless of oxygen concentration. Nonsporogenic food poisoning microorganisms, such as Staphylococcus aureus, will grow and produce toxin at Aw levels of about 0.85 or above in suitable culture media in the presence of adequate oxygen. At low-oxygen tension and in complex food substrates, toxin may not be produced in the range Aw 0.91 or below (8,12,25,26,27,28,29). Furthermore, although xerophilic molds may grow at Aw as low as 0.65 in air, even these low-moisture tolerant molds generally do not grow at low available oxygen (3). Reduction of intrapackage oxygen by means of oxygen scavengers and inclusion of potassium sorbate appears to be synergistic with respect to mold inhibition in vitro (Table 4) and in bread (Table 5). Furthermore, prevention of oxidative rancidity appears to beneficially accrue from oxygen scavenger use. Sensory and chemical analyses indicate that the pouched breads are stable with respect to oxidative effects (Table 4), (Figs 6,7).

Stability Considerations

As indicated above, military operational rations are exposed to a significantly greater range of temperatures stressful to food quality for considerably longer times than that experienced by foods in ordinary commerce. Operational ration items of all types must therefore be formulated to limit stability-diminishing effects, such as nonenzymatic browning. For example, sugar, milk and eggs typically added to commercial breads to enhance acceptability are not contained in MRE breads because their inclusion would exacerbate carbonyl-amine reactions, markedly diminishing their long-term stability and quality. Department of Defense regulations that, until recently, prescribed that developmental items must be acceptable after conditioned storage for at least six months at 37.8^{o}C and three years at 21.2^{o}C respectively, now mandate three years of stability at 26.7^{o}C before they may be considered sufficiently stable for inclusion in operational rations (5). The former requirement has been demonstrated by both acceptability and quality studies. Extrapolation from 18 months of conditioned storage at 21.1^{o}C indicates that MRE pouched breads will probably meet the original and new, more severe, stability requirement (Figs 6,7).

SUMMARY

Techniques including combination or "hurdle" treatments, product formulation and process control to limit browning reactions, control of Aw, reduction of oxygen, adjustment of pH and use of appropriate preservatives together with nonsporicidal heat treatments in retort pouches may result in shelf-stable foods not preservable by conventional means or in rigid containers. This affords significant potential for new product development for enhancement of military operational rations.

REFERENCES

1. Bacon, C. W., Sweeney, V. G., Robbins, J. D. and Burdick, D. 1973. Appl. Microbiol. 26:155.

2. Best, D. 1988. Processors Pursue Natural Preservation. Prepared Foods, P 128, September.

3. Beuchat, L. R. 1987. In: Water Activity: Theory and Application to Food, IFT Basic Symposium Series. Rockland, L. B. and Beuchat, L.R. (ED.) P 101, Marcel Dekker, Inc. New York.

4. Brockman, M. C. 1970. Food Technol. 24: 60

5. Department of Defense Manual 4145.19-R-1.Oct 1988. Storage and Materials Handling

6. Diener, U. L., and Davis, N. D. 1967. J. Am Oil Chem. Soc. 44:259.

7. Diener, U. L., and Davis, N. D. 1970. J. Am Oil Chem. Soc. 47:347

8. Gould, G. W. and Measures, J. C. 1977. Phil. Trans. R. Soc. Lond. B. 278: 151

9. Jay, J. M. 1986. Modern Food Microbiology. (3rd ed), P 242, Van Nostrand Reinhold Company, New York.

10. Krog,N. 1971. Die Starke, 23:206.

11. Langley, R. W. and Miller, B. S. 1971. Cereal Chem., 48: 81.

12. Lee, R. Y., Silverman, G. J. and Munsey, D. T. 1981. J. Food Sci. 46: 1687.

13. Leistner, L. 1985. In: Properties of Water in Foods. Simatos, D. and Multon, J. L. (Ed.), P 309., Martinus Nijhoff Pub. Dordrecht, Netherlands.

14. Longree, K. 1967. "Quantity Food Sanitation"., P 301, John Wiley & Sons, New York.

15. Mason, V. C., Meyer, A. J. and Klicka, M. V. 1982. Technical Report (Natick/TR/821/013) U. S. Army Natick Research Development and Engineering Center, Natick, MA 01760.

16. Military Specification, Mil-B-44360(GL) 1989. Bread, Shelf Stable, For Meal, Ready-To-Eat. Naval Publications and Forms Center (ATTN: NPODS), 5801 Tabor Avenue, Philadelphia, PA 19120-5099.

17. Military Specification, Mil-B-44359(GL) 1989, Bun, Hamburger, Shelf Stable for Tray Ration. Naval Publications and Forms Center, (ATTN: NPODS), 5801 Tabor Avenue, Philadelphia, PA 19120-5099.

18. Military Specification for Cake, Shelf Stable for Meal, Ready-To-Eat, in preparation.

19. Military Specification for Cake, Shelf Stable for Tray Ration, in preparation.

20. Moe, O. A. 1953. In: "Starch, Its Sources, Production and Uses., Brantlecht, C. A. (Ed.) P 354. Reinhold, New York.

21. Northolt, M. D., Van Edmond, H. P. and Paulsch, W. E. 1978. J. Food Prot. 41:885.

22. Radley, J. A. 1953. "Starch and its Derivatives", Vol 2. Chapman & Hall, London.

23. Rice, J. 1988. Oxygen Eliminators. Food Processing, P 58, June.

24. Rice, J. 1989. Modified Atmosphere Packaging. Food Processing, P 60, March.

25. Scott, W. J. 1953. Aust. J. Biol. Sci. 6: 549.

26. Scott, W. J. 1957. In: Adv. Food Res. 7: 83. Academic Press, New York.

27. Silverman, G. J., Munsey, D. T., Lee, C. and Ebert, E. 1983. J. Food Sci. 48: 1783.

28. Troller, J. A. 1987. In: Water Activity: Theory and Application to Food, IFT Basic Symposium Series. Rockland, L. B. and Beuchat, L. R. (ED.) P 101., Marcel Dekker, Inc. New York.

29. Troller, J. A. 1985. In: Properties of Water in Foods. Simatos, D. and Moulton, J. L. (Ed.). Martinus Nijhoff Pub., Dordrecht, Netherlands.

Table 1 - Previous and Current Operational Ration Entree Items

Meal Combat Individual	Original MRE	Current MRE
Beef w/Spiced Sauce[a]	Beef Slice w/BBQ[b]	Pork w/Rice BBQ[c]
Beef Slices and Potatoes w/Gravy	Beef Stew	Beef Stew
Ham Slice w/Juices	Ham Slice[e]	Ham slice[d]
Ham/Eggs Chopped	Ham/Chicken Loaf	Ham/Egg Omelet[d]
Chicken or Turkey Boned	Turkey, Diced w/ Gravy	Chicken Stew
Pork Slices w/Juices	Pork Sausage Patty[e]	Pork W/Rice BBQ
Beans w/Meatballs in Tomato Sauce	Meatballs/BBQ	Meat Balls/BBQ
Beefsteak	Beef, Diced w/Gravy[f]	Corned Beef Hash
Turkey Loaf	Chicken Loaf	Chicken and Rice
Beans w/Frankfurters	Frankfurters[f]	Ham/Scalloped Potatoes
Tuna Fish	Beef Patty[f]	Tuna/Noodles
Spaghetti w/Beef Chunks in Sauce	Chicken ala King	Chicken ala King
		Spaghetti w/Meat Sauce

(a) Twelve-ounce entrees
(b) Five-ounce entrees
(c) Eight-ounce entrees
(d) Potatoes Au Gratin (six ounces) packed separately
(e) Freeze Dried (Approximately two ounces dry weight, five ounces rehydrated)
(f) Beans (five ounces) packed separately

Table 2 - Acceptability of Prototype Items Developed Using Advanced Processing Methods

Item	Acceptability Rating	N	S.D.
Bread[a,d]	7.1	36	1.14
Smokey Frankfurters[b]	6.8	38	1.41
Spice Cake[a]	7.1	37	1.27
Coffee Cake[a]	7.1	37	1.51
Marble Cake[a]	6.7	37	1.73
Fudge Brownie Cake[a]	6.7	37	1.45
Vanilla Pound Cake[a,d]	7.3	20	0.64
Lemon Pound Cake[a,d]	7.3	20	0.62
Chocolate Chip,Mint Cake[a,d]	6.9	20	0.73
Pineapple Pound Cake[a,d]	6.8	20	1.08
Orange Pound Cake[a,d]	6.8	20	0.68
Cheese Pizza[c,d]	5.6	38	1.63
Beef/Cheese Burrito[c,d]	5.5	38	1.95
Fruit Chew Bars[a]	6.4	20	0.77

(a) Aw stabilized
(b) Reduced moisture, thermostabilized
(c) Hurdle technique
(d) Oxygen scavengers

Table 3 - Combined Effect of Oxygen Scavengers and Sorbic Acid on Growth of Molds on Plate Count Agar During 104 Day Incubation

Percent Potassium Sorbate	Mold	Day Showing Growth — Number of Scavengers per Pouch: 0	1	2	3
0.05	Penicillium Sp.	4	10	28	N.G.
	A. niger	5	15	N.G.	N.G.
	A. Versicola	5	15	N.G.	N.G.
0.10	Penicillium Sp.	4	20	N.G.	N.G.
	A. Niger	5	20	N.G.	N.G.
	A. Versicola	5	N.G.	N.G.	N.G.

N.G. - No growth after 104 days at 25°

Table 4 - Effect of Oxygen Scavenger Packets on Residual Oxygen and TBA[a] Levels in MRE Pouched Bread

Months	Percent Oxygen	TBA
0	1.40	0.21
3	1.47	0.20
7	1.50	0.21
15	1.44	0.17

(a) Thiobarbituric acid/Malonaldehyde reaction as an indicator of oxidative rancidity.

Table 5 - Effect of One Oxygen Scavenger Packet (OSP) on Growth of a Mixed Mold Inoculum[a] on MRE Pouched Bread

Months at 25°C	Mold Growth — Inoculated Bread: One OSP	Mold Growth — Inoculated Bread: No OSP
1	-[b]	+[c]
2	-	+
3	-	+
4	-	+
5	-	++
6	-	++
12	-	+++

(a) *Penicillium species*, *Aspergillus niger*, *A. versicola*, at 10^4 spores per loaf.

(b) -, No growth

(c) +, Scant growth; +++, Heavy growth

Residual oxygen in the range 1.4 --1.5 percent

Table 6 - Effect of Oxygen Scavengers on Growth of Molds on Plate Count Agar after 30 Days.

	Number of Oxygen Scavengers per Pouch					
Mold	0	1	2	3	4	5
Penicillium species	4+	4+	1+	0	0	0
Aspergillus niger	4+	2+	0	0	0	0
A. Versicola	4+	0	1+	0	0	0

4+, Heavy Growth

1+, Scant growth

0, No growth

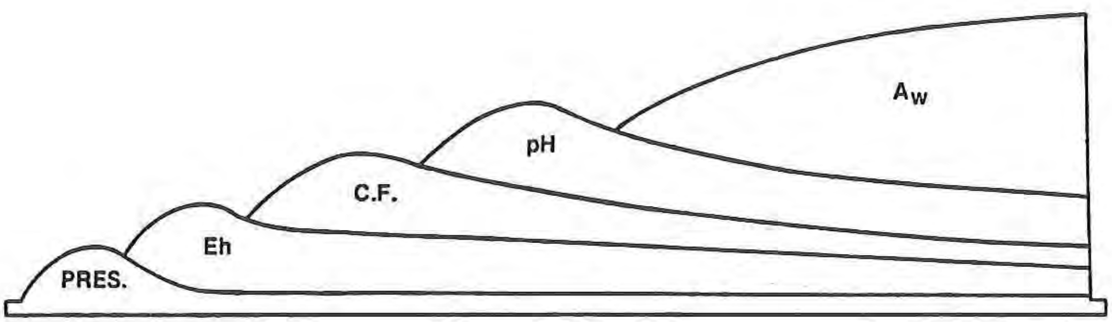

FIG.1 - SEQUENCE OF HURDLES OCCURING DURING RIPENING AND STORAGE OF FERMENTED SAUSAGES (SALAMI). PRES. = NITRITE, E_h = DECREASE OF REDOX POTENTIAL, C.F. = GROWTH OF COMPETITIVE FLORA, pH = ACIDIFICATION, AND A_W = THE DRYING PROCESS. (FROM LEISTNER, 1987)

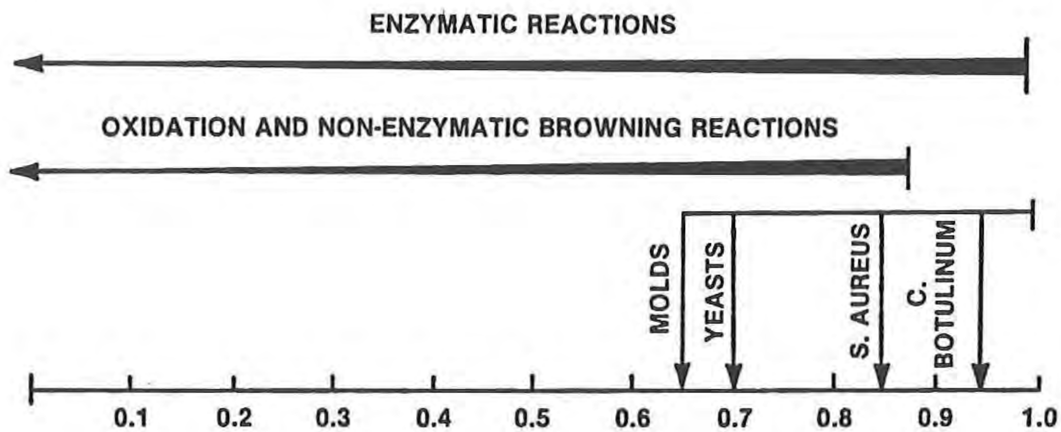

FIG. 2- RANGE OF DETERIORATION IN UNHEATED FOODS AS A FUNCTION OF Aw

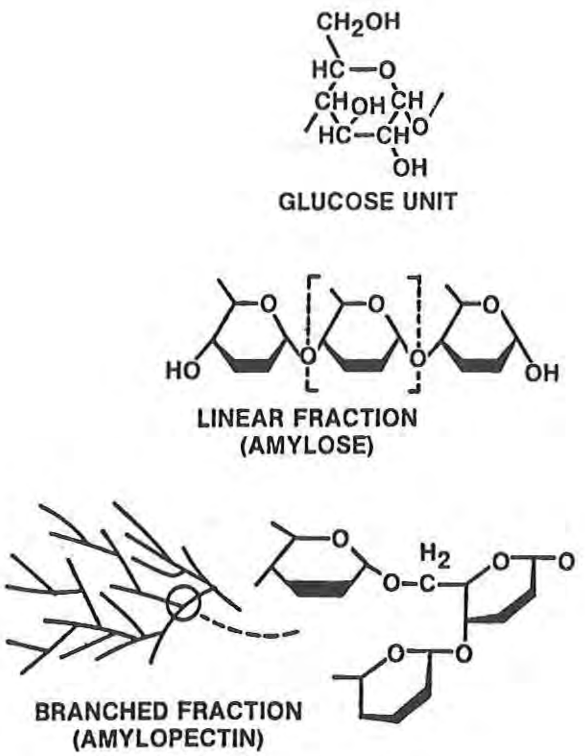

FIG. 3 - STRUCTURE OF STARCH COMPONENTS

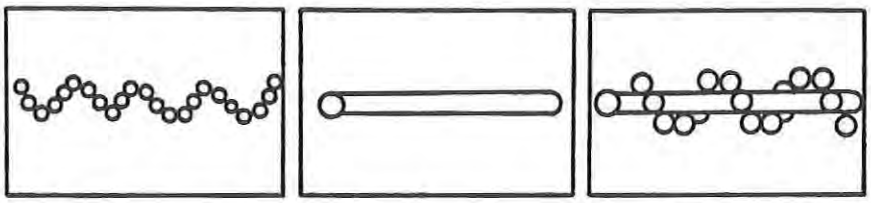

AMYLOSE MOLECULE

STRAIGHT-CHAIN MONOGLYCERIDE MOLECULE

AMYLOSE/MONOGLYCERIDE COMPLEX

FIG. 4- STARCH COMPLEXING

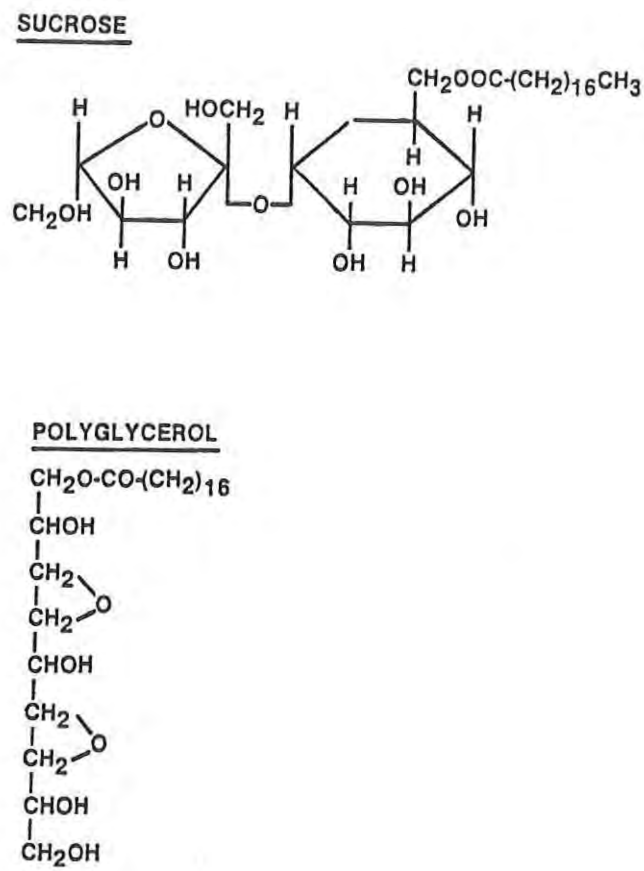

FIG. 5- SUCROSE AND POLYGLYCEROL FATTY ACID ESTER EMULSIFIERS

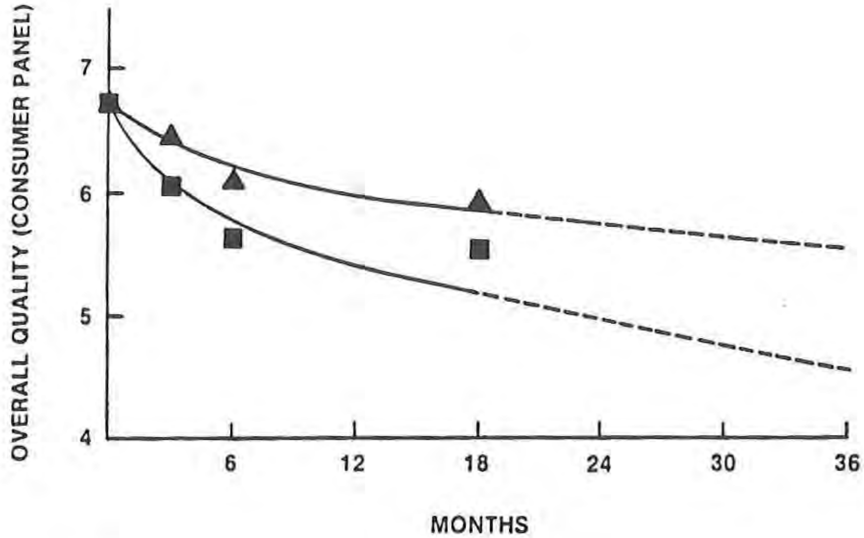

FIG. 6- ACCEPTABILITY OF MRE POUCHED BREAD AT 21.1°C AND 37.8°C

(▲); 21.1°C, (■); 37.8°C

9 = LIKE EXTREMELY, 5 = NEUTRAL, 1 = DISLIKE EXTREMELY

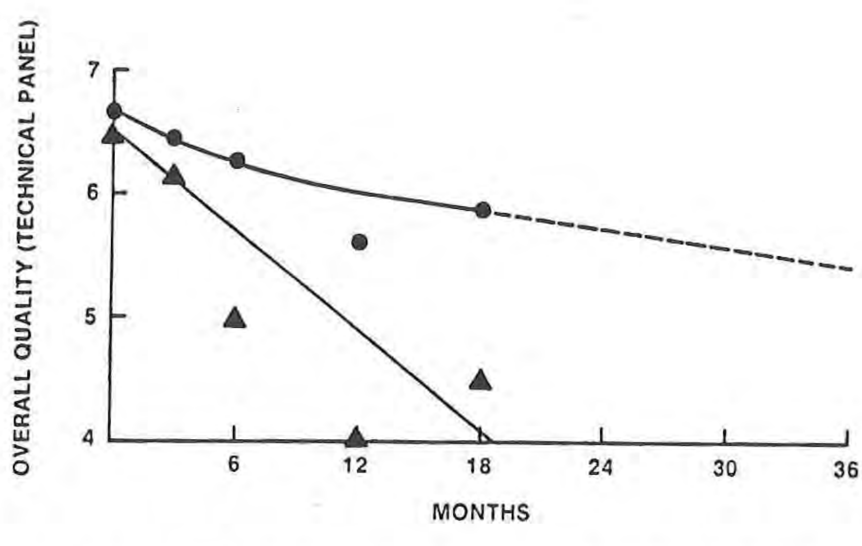

FIG. 7 - EFFECT OF TEMPERATURE ON OVERALL QUALITY OF MRE POUCHED BREAD

(●); 21.1°C, (▲); 37.8°C

9 = EXTREMELY GOOD, 5 = FAIR, 1 = EXTREMELY BAD

TITLE: Intrinsic Chemical Markers for Thermal Processing of Particulate Foods
*Hie-Joon Kim, Dr., and Irwin A. Taub, Dr.

ABSTRACT:

Two thermally produced compounds that could be used as intrinsic chemical markers for high temperature/short time processing of particulate foods were discerned for the first time in foods heated to temperatures associated with aseptic processing. These compounds were detected in aqueous extracts of heated foods using anion exclusion chromatography and an ultraviolet (UV) sensitive photodiode array detector.

One marker compound, M-1, was produced upon heating vegetables, fruits, and meats and showed a characteristic UV absorption maximum at 300 nm. The molecular weight, determined by gel filtration chromatography, was estimated as 280. The compound was shown to be derived by thermal fragmentation of a slightly larger precursor molecule. This compound was undetected in unheated samples and its concentration in heated samples increased steadily with increasing heat treatment. Most importantly, the observed concentration showed a good correlation with the sterility value, F_0, over a wide range. These observations suggest that it could be a useful intrinsic chemical time-temperature integrator.

Another marker, M-2, was discerned in heated meats. The UV maximum was 285 nm and the molecular weight was estimated as 290. This marker was observed from chicken meat aseptically processed at an industrial facility. The concentration of the marker observed from the center of the meat was somewhat lower than that from the surface, but high enough to suggest sufficient heat penetration to the center.

These markers represent a significant breakthrough in providing a non-invasive indicator of thermal treatment, and it is anticipated that they will be used for establishing commercial sterility at the center of a food particulate undergoing aseptic processing and even retort processing.

*BIOGRAPHY: Hie-Joon Kim

PRESENT ASSIGNMENT: Research Chemist, Food Engineering Directorate, 1985-1990.

PAST EXPERIENCE: Research Associate, Harvard Medical School; Postdoctoral Associate, MIT

DEGREES HELD: B.S., Seoul National University, 1970; M.S., University of Chicago, 1974; Ph.D., University of Chicago, 1977.

Intrinsic Chemical Markers for Thermal Processing of Particulate Foods

Hie-Joon Kim, Dr., and Irwin A. Taub, Dr.
Food Engineering Directorate

INTRODUCTION

Since Nicholas Appert invented canning in 1809, industrial thermal processing of foods has remained primarily a batch process. Currently, it is undergoing a revolutionary change through the introduction of aseptic processing, in which fluid foods of uniform consistency are sterilized while flowing through tubes maintained at a high temperature (between 130°C and 150°C) for a short time (HT/ST) and packaged in a sterilized container in a continuous process. Aseptic processing is widely used in drinks and semiliquid foods, but its use has not been approved for foods containing particulates. The Food and Drug Administration (FDA) requires demonstration of sterility at the center of a food particulate based on a definitive microbiological procedure and a conservative mathematical model.[1]

Recently, attempts have been made to use B. stearothermophilus, a thermophilic bacteria, as a bioindicator of aseptic processing of particulate foods.[2,3] Encouraging results have been reported. For example, Hinton et al. placed at the center of meat cubes small alginate beads inoculated with B. stearothermophilus and found no survivors after a short (0.87 min) processing at 131°C.[3] Based on this observation, they estimated the equivalent lethality for C. botulinum at the center of the particulate to be at least 25D (D is time required to destroy 90% of the microorganism), which represents a gross overprocessing compared to the required 12D for commercial sterility. The drawback of the microbiological procedure is that it is tedious and subject to many experimental uncertainties. Moreover, the extent of overprocessing is difficult to assess because, once the entire microbial population is destroyed, only a minimum lethality can be estimated.

The mathematical modeling approach, which involves calculating microbial destruction within the particulate as it flows through the holding tube, is subject to even more uncertainties. Various assumptions and estimates have to be made, because direct temperature measurement at the center of a moving food particulate is extremely difficult. The major uncertainties relate to estimating the convective heat transfer coefficient at the liquid-particulate interface and the residence time distribution of the particulates in the holding tube.[4] Moreover, the conservative estimates used for these parameters, which are difficult to verify experimentally, often lead to unrealistically long processing time requirements.[5]

Monitoring chemical changes within the food, which involves compounds either indigenous to or added to the food, offers an alternative route for assessing the integrated time-temperature exposure at different locations within the food particulate. Published data in the literature are either scarce (for thermal processing in general) or nonexistent (for particulate foods). There are good reasons for this scarcity. A typical chemical reaction in foods is either too fast or too slow for the associated compound to be a useful indicator of sterility. For example, destruction (blanching) of heat-resistant enzymes, such as peroxidase and catalase, is complete in about 2 min at 100°C. On the other hand, destruction at high temperatures of such nutrients as ascorbic acid and thiamin is generally much slower than thermal death of bacterial spores. For example, the use of thiamin added to pea or beef puree in cans was suggested as an indicator of sterility for retorting at 122°C.[6] The z value, i.e., the degrees in F required to increase the destruction rate by 10, is 18 for C. botulinum, but it is 48 for thiamin at 122°C. Therefore, at aseptic processing temperatures, the destruction of thiamin will be too slow to be an adequate indicator of sterility. Incidentally, this higher retention of nutrients is one of the important advantages of aseptic processing.

To date, there is no information available in the literature that would point to a chemical reaction potentially useful for monitoring thermal processing of particulate foods at temperatures above 122°C. However, the desirability of such an approach has been recognized in the past. In 1975, Mulley et al. stated "while the whole area of chemical indicators promises to be a fertile ground for research and patent hunters, its practical application may be just beginning. The authors believe that the use of a chemical index in sterilization processing has the potential of effecting a revolutionary change in the food and pharmaceutical industries."[6] Despite this prophetic statement, not much progress has been made during the past 15 years.

Recently, we undertook a systematic investigation of chemical markers whose changes could effectively represent integrated time-temperature exposure at different locations within a food particulate. The desired features of the chemical markers were considered to be as follows:

(a) The chemical reactions should be intrinsic to the foods, because addition of chemicals to the foods would be tedious and would introduce experimental errors.

(b) The marker should be thermally produced instead of destroyed, because analytical results will be more reliable when the baseline concentration for unheated food is essentially zero.

(c) The marker should be easily detectable, because heating will generate a large number of compounds that when taken together with existing compounds in the foods make analysis more difficult.

(d) The analytical method for the marker should be sensitive, because the marker concentration at the center portion (less than 50 mg sample) of a food particulate (less than 1 inch in diameter) needs to be determined.

(e) The marker or its precursor should be stable toward oxidation or enzymatic reactions, because instability of the marker or the precursor could lead to inconsistent results in the marker concentration.

(f) The marker should be common to many foods to be suitable for broad applications.

(g) The marker should be a time-temperature integrator instead of a maximum temperature indicator, because microbiological lethality, F_o, corresponds to the accumulation of incremental lethalities at different time-temperature exposures.

(h) The reaction rate for the marker should follow first-order kinetics so that the marker reaction could be related to the thermal death of microorganisms, which is a first-order process.

(i) The marker concentration should show a correlation with F_o so that one could in principle verify F_o from the marker concentration.

In this paper we report the detection and isolation of two as yet unreported compounds that, based on the above-mentioned considerations, appear to be promising time-temperature integrators at aseptic processing temperatures.

DETECTION

Many analytical methods are available for determination of food components. Gas or liquid chromatographic techniques are most commonly used. Various chromatographic techniques with different detection methods are useful for detecting a different subset of compounds in foods. Since organic acids and carbohydrates represent an important class of compounds commonly present in most foods, we decided to investigate thermally induced changes in the profile of these compounds. Anion exclusion chromatography (AEC) is a useful high-performance liquid chromatographic (HPLC) technique for determination of organic acids and other carbohydrates such as ascorbic acid and various sugars. Since we were searching for markers without any knowledge of their properties, a general, instead of a specific, detection scheme was desired. Therefore, a photodiode array (PDA) detector, which is sensitive in the UV region and has scanning capability, was used. With it, the UV absorption spectra of compounds eluting from the chromatographic column could be obtained every fraction of a second, stored in a computer, and manipulated for display as a three-dimensional (3-D) representation, a contour map, or a spectrum at a specific time. The 3-D nature of this anion exclusion chromatography-photodiode array (AEC-PDA) system proved extremely useful for discerning new compounds being produced as a result of heating.

Figure 1 shows the contour diagram for the spectrochromatogram (i.e., the absorbance vs. wavelength as a function of retention time) of unheated and heated broccoli. Wescan anion exclusion column (sulfonated polystyrene/divinylbenzene, 7.8x100 mm) and Waters 990 photodiode array detector were used. The eluant was 5 mM sulfuric acid solution and the flow rate was 1 ml/min. Comparison of the contour diagram for unheated (control) and heated broccoli clearly shows production of a new compound (M-1: retention time, 4 min; UV maximum, 300 nm) not present in unheated broccoli. The thermal reaction is intrinsic to the food, i.e., the new compound is produced without adding any compounds prior to processing. It is easily detectable because the compound has a relatively long retention time and a characteristic absorption maximum at 300 nm. No similar absorption peak is present in the wavelength-time domain of the control broccoli. The same peak was observed upon heating other vegetables (e.g., potato, green bean, pea, carrot) and fruits (e.g., apple, orange). The compound was also observed from heated meats (e.g., beef, chicken), even though an interfering peak with slightly shorter retention time and lower peak wavelength presented a potential problem in meats. Fortunately, another compound was discerned in heated meats (M-2: retention time, 6 min; UV maximum, 285 nm). These compounds were observed reproducibly. Unlike destruction of ascorbic acid, the thermal production of these compounds was not observed to be influenced by oxygen. They were also stable, which facilitates analysis and subsequent purification. We further investigated the usefulness as time-temperature integrators of M-1 for vegetables and of M-2 for meats .

CORRELATION WITH F_o

F_o is the time in minutes at 121.1°C required to achieve "commercial sterility" by reducing the population of a tester spore-forming microorganism a specified factor, such as 10^6 for PA3679 or 10^{12} for *C. botulinum*. At temperatures other than 121.1°C, the lethality, F_T, is calculated by

$$F_T = F_o \times 10^{(T-121.1)/z} , \qquad \text{(eq. 1)}$$

where z is the increase in temperature that decreases the thermal death time by a factor of 10 (z=10°C for *C. botulinum*). In a thermal processing experiment under changing temperatures, the recording instrument (Digistrip) is programmed to calculate incremental F_o values

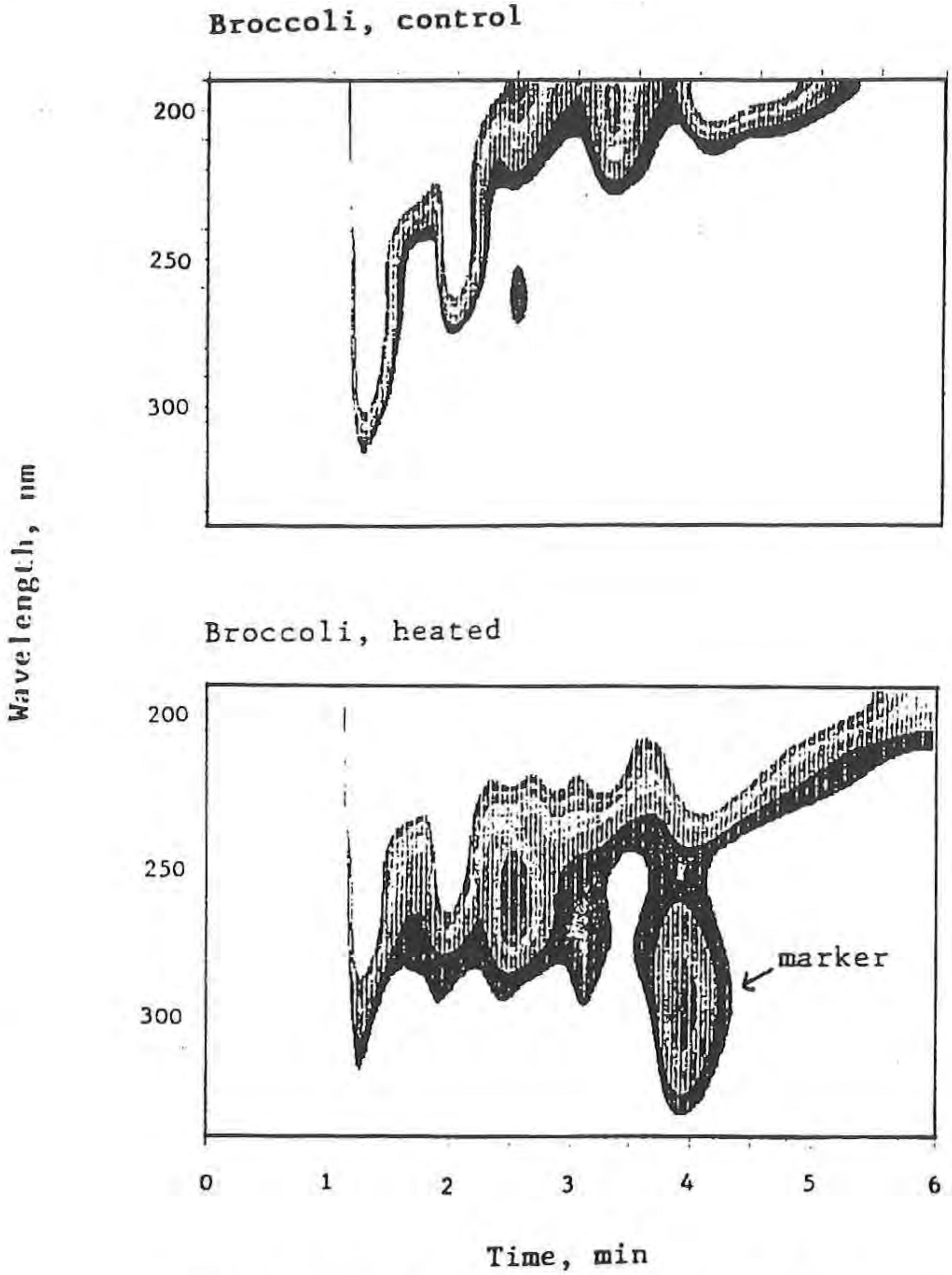

Fig. 1 Contour diagram corresponding to the spectrochromatogram for control broccoli and heated broccoli

according to eq. 1 from the measured temperature and print out accumulated F_o values. The accumulated F_o value is the index of sterility at the site of temperature measurement. F_o for C. botulinum is 2.5 min. A good correlation with F_o is the key to adopting any chemical marker, since the objective is to assess F_o from measurement of the marker concentration.

In order to determine if a correlation exists between the marker concentration and F_o values, experiments were conducted with a puree of potato in brine prepared by blending 160 g cut potatoes with 120 mL hot brine (3.4% sugar, 1.7% salt). Ten 20 mL glass vials were filled with the puree, sealed with rubber septum and aluminum cap, and placed in a laboratory oven preheated to 130°C. Two of these vials were used for temperature measurements. One thermocouple was pushed through the rubber septum and placed at the center of one vial. Another thermocouple was placed in another vial midway between the wall and its center. The temperature and the accumulated F_o were printed out every minute by the recorder. The average of the F_o measurements at two locations was used for interpretation of data. At certain predetermined F_o values, a vial was withdrawn from the oven and quickly cooled with cold water. The content of each vial was homogenized with fivefold excess water and the extract was filtered through a 0.45 µm membrane filter. The marker (M-1) concentration in the filtrate was determined by the AEC-PDA system.

As shown in Figure 2, the average temperature at two locations within the vial increased slowly toward 130°C. As the temperature increased, the accumulated F_o increased rapidly. The marker was undetected in the unheated sample, but its concentration in the heated samples increased as the temperature and accumulated F_o increased. More importantly, the observed marker concentration showed a good overall correlation with F_o values. Although the data need to be supplemented at low F_o values, the results indicate that M-1 has a great potential as a time-temperature integrator of thermal processing.

The fact that the correlation is valid at high F_o is important. Since the attained lethality must exceed a minimum required value (usually F_o of 6 for low acid foods), it is desirable to optimize the processing parameters under slightly overprocessing conditions. In a direct microbiological procedure, it is difficult to recover any survivors from an inoculum of 10^6 spores after F_o of 6 min has been exceeded at the center of a particulate, so the extent of overprocessing cannot be estimated from the postprocess assays. The same is often true even with the more resistant thermophilic spores.[3] In contrast, the extent of overprocessing could be easily estimated using the marker, because the marker concentration increases steadily and maintains a good correlation with accumulated F_o. This observed correlation indicates that the marker is a time-temperature integrator over a wide range of F_o values.

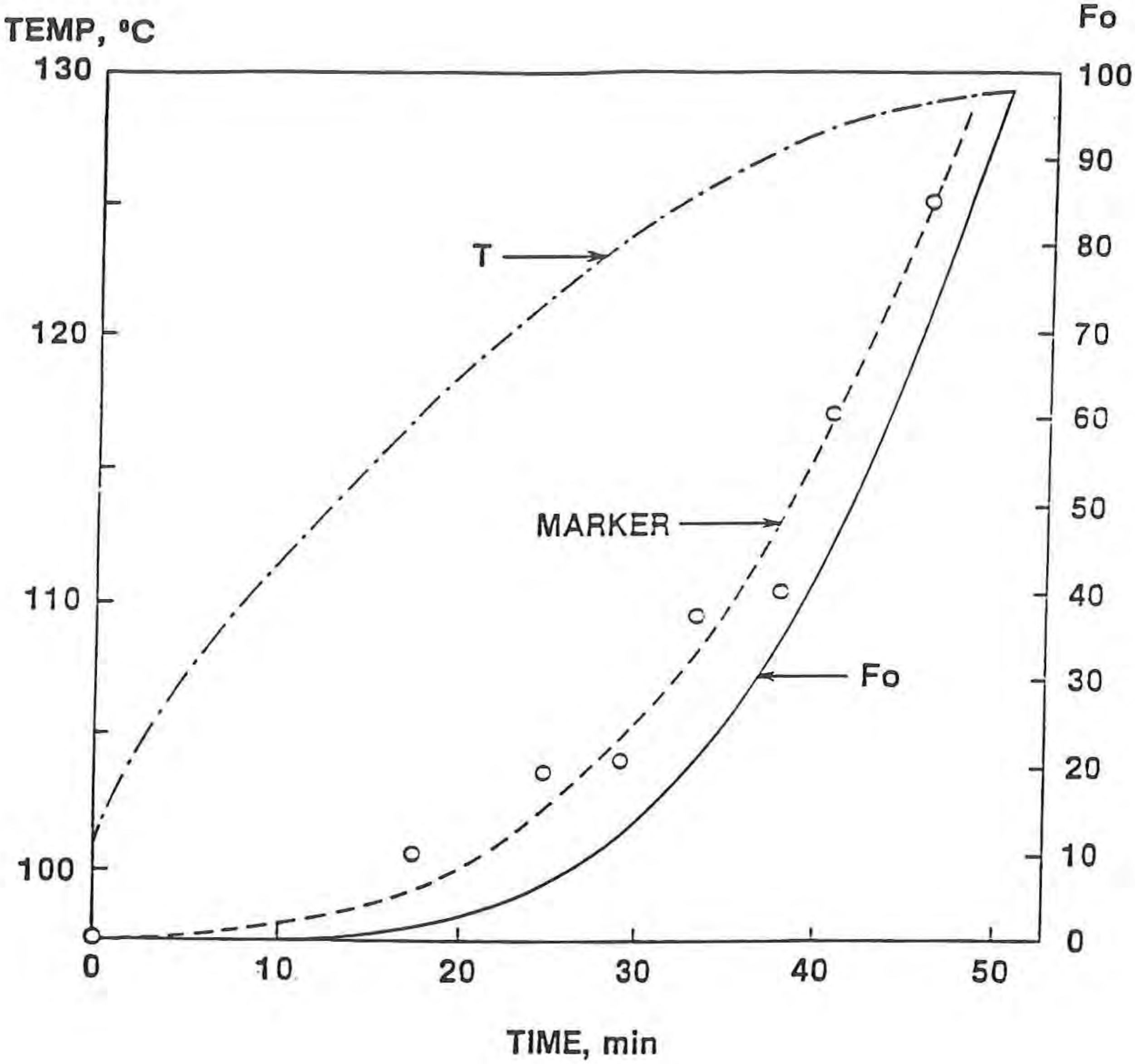

Fig. 2 Correlation of the observed marker concentration with the lethality value, F_o, calculated from the temperature (T). T is the temperature-time profile. The marker concentration is on an arbitrary scale (not shown).

PRELIMINARY MARKER CHARACTERIZATION

The mode of the reaction leading to the marker compound has a significant bearing on the usefulness of the compound as a chemical marker for thermal processing. The thermal death of bacterial spores can be represented as a simple first-order process as follows:

$$\text{LIVE SPORE} \xrightarrow{\text{heat}} \text{DEAD SPORE} \qquad \text{(eq. 2)}$$

A first-order reaction for the production of the marker resembling the thermal death of bacteria could be written as follows:

$$\text{PRECURSOR} \xrightarrow{\text{heat}} \text{MARKER} \qquad \text{(eq. 3)}$$

In order to investigate the possible correspondence of the two processes, the mode of formation of the marker from its precursor was examined.

The aqueous extract from heated broccoli was fractionated on a gel filtration column (1.0 x 42 cm) packed with Bio-Gel P-2 (molecular weight (MW) cut-off: 2,000 daltons) at a flow rate of 10 mL/h. A 1.7 mL volume was collected per fraction. The collected fractions were analyzed for the marker, M-1, by the AEC-PDA system and the marker was found in fraction 24. The gel filtration column was calibrated with riboflavin phosphate (MW=455, fraction 12) and tryptophan (MW=202, fraction 32). The molecular weight of M-1 in fraction 24 was estimated as approximately 280.

In order to investigate the precursor, the aqueous extract from unheated broccoli was fractionated on the same gel filtration column and the collected fractions were heated in sealed glass tubes. When the heated fractions were analyzed for M-1, only fraction 22 (MW$\approx$ 300) yielded the marker. This observation suggests that the net effect on the precursor of the thermally-induced reaction is the removal of a small functional group.

When the aqueous extract was heated in sealed capillary tubes, an exponential increase in the marker concentration up to a limiting value was observed. The limiting concentration presumably reflects depletion of the precursor. When the logarithm of the difference between the limiting value and the observed value was plotted against heating time, a linear relationship was obtained. This first-order behavior is consistent with the proposed reaction in eq. 3 whose rate is solely dependent on the precursor concentration. This mode of reaction resembles thermal death of microorganisms represented by eq. 2 and supports the proposition that the compound is a potential indicator of sterility. Purification of M-1 is in progress, and elucidation of the structure by infrared spectroscopy and mass spectrometry will follow.

TEST APPLICATIONS

Potato Cooked at Low Temperature

The occurrence of the marker, M-1, was investigated in potato cubes (approximately 1 cm cube) in home-cooked beef stew. The stew was simmered for about 30 min, and the potato cubes were frozen for analysis of the marker. Each partially thawed potato cube was sliced with a razor blade. Each surface slice or remaining center portion was placed in a test tube containing fivefold excess water, and the content vigorously mixed using a vortex mixer. The aqueous extract was filtered and injected into the chromatograph for determination of M-1 by the AEC-PDA system. The marker was present at a significant concentration in the surface slice of the potato cube, but it was barely detectable from the center portion. These qualitative results indicate that the temperature gradient within the potato cube established under the cooking conditions is reflected in the concentration differential of the marker, which makes M-1 a useful indicator of thermal processing.

Aseptically Processed Chicken Meat

Chicken meats in chicken stew aseptically processed at an industrial facility (Alfa-Laval, Newburyport, MA; courtesy of Dr. Margaret Driver) were tested for occurrence of the marker, M-2, at different locations within the meat piece. Chicken meats were frozen with ice immediately following aseptic processing at 129^{o}C at two flow rates, 500 lb/h and 1,300 lb/h. The meats, which were of irregular shape (approximate dimension, 1.5x2.5x3 cm), were divided into surface, middle, and center portions of approximately equal thickness with a razor blade, and these portions from several meat pieces were pooled together. Each aqueous extract from these meat portions was concentrated by freeze-drying and then redissolved in a small volume of 5mM sulfuric acid solution. The concentration of M-2 was determined by the AEC-PDA system as described above.

Several important features are evident in the results summarized in Figure 3. First, a definite concentration gradient exists for the marker, decreasing gradually in the direction of heat transfer from the surface to the center. This concentration gradient presumably reflects the temperature gradient within the meats. The concentration gradient was observed at both flow rates. Second, the marker concentration is higher at the lower flow rate, which corresponds to a longer residence time. As a matter of fact, the concentration of M-2 at the surface was inversely proportional to the flow rate (or directly proportional to the residence time), which strongly suggests that the marker is a good indicator of heat exposure. Third, the marker concentration at the center of the meat processed at the lower flow rate (500 lb/h) is higher than that at the surface of the meat processed at the higher flow rate (1,300 lb/h). This observation suggests that lethality at the center of a food particulate will be determined more by external parameters, such

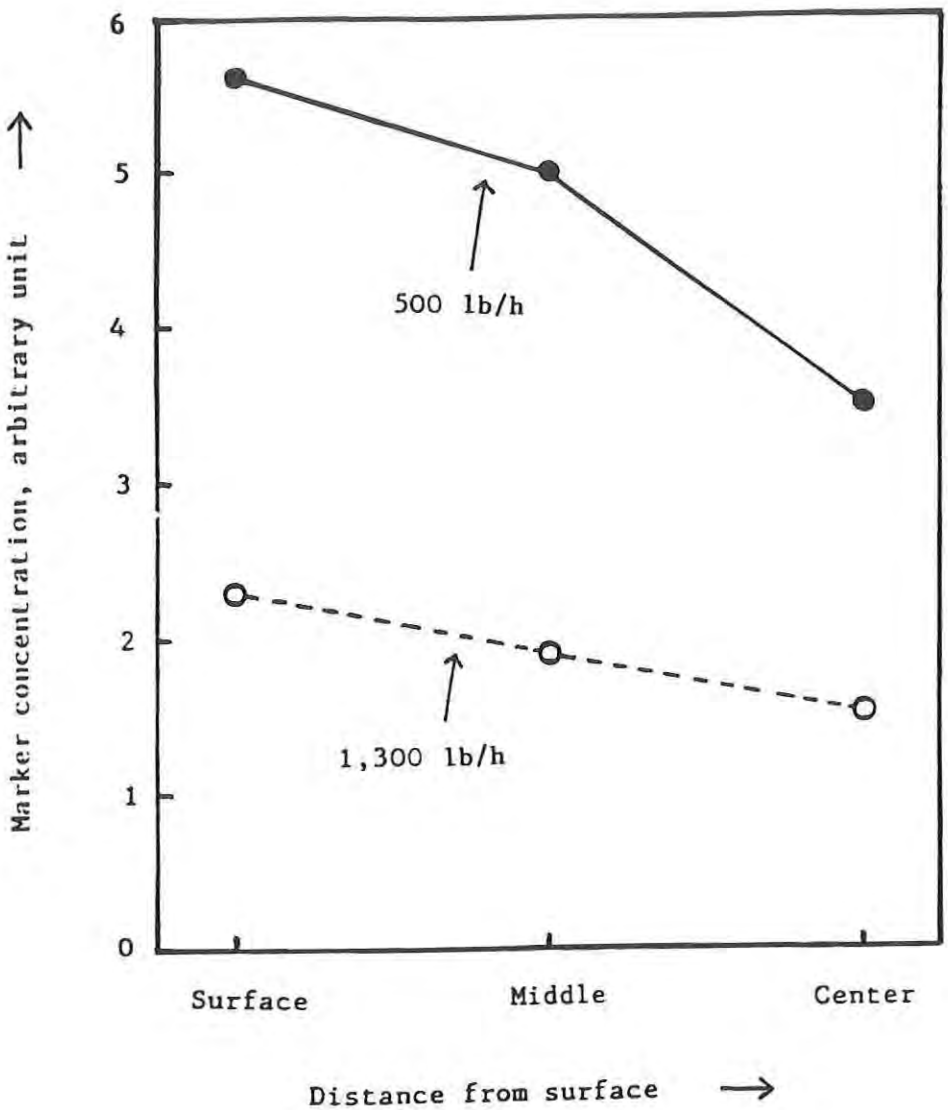

Fig. 3 Concentration of marker, M-2, at surface, middle, and center portion of chicken meat aseptically processed at 129°C

as temperature and flow rate than by heat transfer characteristics, which are inherent in the food system and depend on composition and microstructure.

It should be noted that the marker was observed at a significant concentration at the center even at the higher flow rate. A correlation, such as shown in Figure 2, is needed for M-2 at low F_o values in order to translate this concentration to F_o. The precursor concentration or limiting marker concentration in the meat also needs to be determined for accurate assessment of F_o. Nevertheless, the above observations indicate that the compound, M-2, is a good candidate marker for meats.

CONCLUSION

Two compounds were detected and separated for the first time that appear to be extremely useful chemical indicators of time-temperature exposure at different locations within a food particulate. They are easy to detect with a high sensitivity. Once the precursors are identified and the kinetic parameters are measured, it will be possible to accurately determine the F_o at different locations within a food particulate from the observed marker concentration and limiting marker concentration in heated food.

ACKNOWLEDGMENT

We thank Karen R. Conca and Michelle J. Richardson for technical assistance.

REFERENCES

1. Dignan, D.M., Berry, M.R., Pflug, I.J., and Gardine, T.D., Food Technol., 43(3), 118 (1989).

2. Sastry, S.K., Li, S.F., Patel, P., Konanayakam, M., Bafna, P., Doores, S., and Beelman, R.B., J. Food Sci., 53, 1528 (1988).

3. Hinton, Jr., A., Driver, M.G., Silverman, G.J., and Taub, I.A., Activities Report of the R&D Associates, 41(1), 39 (1989).

4. Heldman, D.R. Food Technol., 43(3), 122 (1989).

5. Chandarana, D.I., Gavin III, A., and Wheaton, F.W., Food Technol., 43(3), 137 (1989).

6. Mulley, E.A., Stumbo, C.R., and Hunting, W.M., J. Food Sci., 40, 993 (1975).

TITLE: Role of Ascorbic Acid and Tin in Maillard Browning of Wet Pack Fruits

*William L. Porter, Dr., D.F. Grant, Mr., E.D. Black, Dr., J.J. Pignatiello, Mr., D. Rosano, Ms., D. Nattress, Mr., and C. P. Dunne, Dr.

ABSTRACT: At the 1988 Natick Science symposium, we reported that non-enzymatic browning occurs in pasteurized fruit that is wet-packed in retort pouches and stored at the high temperatures required for military ration shelf life. We reported that the fluorescence, off-color, cooked odors and mushy texture which result may be effectively inhibited by pre-treatment with cation exchange resin to remove free amino acids. This finding implicated the Maillard reaction between reducing sugars and amino acids as a possible cause of the observed browning. We have recently developed computerized 3-D front-face fluorescence methods which use discriminating multi-wavelength excitation. These improved methods have revealed that ascorbic acid added for protection during processing often becomes oxidized and forms carbonyl groups that combine avidly with amino acids, at the low pH and high temperatures of military testing. The reaction becomes even more predominant at lower pH (≤ 3.5), which was studied in an attempt to minimize the classic sugar-amine browning reaction.

Using these methods, we have also shown, using ascorbate-dipped, individual quick frozen pears stored without further processing 4 days at $50^{\circ}C$, that, at pH 4, tin metal plus tin ions added at 190 ppm, reduce the absorbance change of the clarified juice by 53% over control, increase surface lightness (Hunter L) of the fruit by 48%, and decrease fluorescence emission indicators signifying the presence of reaction precursors by 30-70%.

These findings explain the protection afforded by tin under acid conditions. They also suggest remedies such as minimization of ascorbic acid in pretreatment, careful exclusion of oxygen from both the headspace and pouch contents and addition of reducing agents such as tin or cysteine.

*BIOGRAPHY OF PRESENTER: William L. Porter

PRESENT ASSIGNMENT: Research Chemist at the U.S. Army Natick Research, Development and Engineering Center, Soldier Science Directorate.

PAST EXPERIENCE: Meteorologist/Climatologist with Environmental Protection Research Division, Natick Laboratories from 1953-1962

DEGREES HELD: PhD in Plant Biochemistry, Harvard University, 1962. Meteorologist, U.S. Army Air Force Aviation Cadet School, 1943.

Role of Ascorbic Acid and Tin In Maillard Browning of Wet-Pack Fruits

William L. Porter, Dr., C.P. Dunne, Dr., D. Nattress, Mr., E.D.Black, Dr., J. MacNeill, Ms., D. F. Grant, Mr., J. J. Pignatiello, Mr., and D. Rosano, Ms.

INTRODUCTION

The U.S. military is currently evaluating conversion from freeze-dehydrated fruit in the ration Meal, Ready-to-Eat (MRE) to fruit wet-packed in tri-laminated retort pouches and thermally processed for shelf stability. Wet-packed fruit has shown greater acceptance in field tests and encourages greater water intake. However, in the initial trial accelerated storage tests at 100°F (38°C), fruit wet-packed at Natick in retort pouches was found to fail much faster than the usual experience with similar fruit commercially produced in unlined tin cans. Brown color, baked and caramel odors, and mushy texture were the conspicuous quality losses. Further investigation led to the development of an improved processing procedure for preserving flavor and texture; this process was used by contractors for the peaches used in this investigation. Currently, very few vendors can process fresh fruit and pack it in retort pouches. Use of individually quick frozen fruit (IQF) and fruit repacked from cans increases the number of possible vendors and the time available for processing. There was a need for methods to evaluate these two alternative sources of fruit for the MRE.

At the 1988 Natick Science Symposium, we reported[1] that nonenzymatic browning occurs in pasteurized fruit that is wet-packed in retort pouches and stored at the high temperatures and long times mandated by military storage requirements. We reported that the fluorescence increases, off-color, cooked odors and mushy texture that result may be effectively inhibited by pretreatment with cation exchange resin to remove free amino acids. This finding implicated either phenolic browning or the Maillard reaction between reducing sugars and amino acids as possible causes of the observed browning.[2] In addition, studies of quality loss in peaches and pears that were packed in retort pouches in 1987 [1,3] revealed that prominent quality loss producers were: 1) excess air in the headspace, 2) lowering of pH ($\leq$3.5), and 3) comminution of the fruit.

Color and flavor losses like those we observed in wet-pack, retort pouch fruits stored at elevated temperatures to simulate field storage conditions might result from several causes: enzymatic and autoxidative browning involving phenols, thermal/acid caramelization of sugars, or Maillard browning from reactions of reducing sugars or oxidized ascorbic acid with amino acids or proteins.[2] Lipid oxidation, although theoretically possible, would produce increased fluorescence like that observed but would give yellow colors and rancid odors instead of the red-brown colors and baked odors we found.[4] Most fruits have very low lipid levels and high water activity that minimize lipid oxidation.[5] Phenolic browning quenches fluorescence,[5] does not produce baked odors, and is strongly inhibited by normal heat processing and pretreatment with ascorbic acid like that used on the trial fruit. The fact that cation exchange resins, which sequester amino acids, strongly inhibit the browning largely precludes simple sugar caramelization as a quality loss factor for our pouch-packed fruits. Our search, therefore, concentrated on the Maillard reaction.

To monitor this reaction under various treatments, there was a need for rapid, sensitive, reliable, objective measurement methods, which would permit determination of the causes of quality loss and also allow prescription of preventive measures. We settled on front-face measurement of fluorescence (in contrast to the right angle viewing of solutions). Front-face measurement allows a rapid, sensitive and reproducible gauge of the Maillard reaction.[1,2] Furthermore, using multiwavelength excitation and computer analysis, it promised to give the needed discrimination between sugar-amine and oxidized ascorbic acid-amine browning. Fluorescence has not been widely used in browning studies, because the fluorophore compounds are polymeric and often insoluble. They are usually colloidally dispersed and therefore lost after clarification by filtration prior to studies of solution fluorescence. We have shown[1] that front-face sensing of fluorescence of the moderately turbid supernatants of homogenized, centrifuged fruit suspensions at an angle of 22^{o} to the excitation beam gives good reproducibility, providing that one measures internal ratios of fluorescence emission intensity from two excitation wavelengths. Unlike the absolute emissions in front-face fluorescence, these change little with particulate concentration or sample position, both of which have unpredictable fluctuations in front-face work. Reference 1 gives details of the validation of this method against other Maillard measures. Also discussed are the strong correlations of fluorescence changes with color and degree of polymerization of the Maillard product.

In the present study, this method was used together with high performance liquid chromatographic (HPLC) measurement of sugars, 5-hydroxymethylfurfural (HMF) and furfural (F); colorimetric measurement of ascorbic acid; reflectance; and pH. The fruit studied was peaches wet-packed in retort pouches in 1988 from either fresh, individually quick frozen (IQF), or repacked fruit, the latter having been initially packed in unlined tin cans. Conspicuous among the results after storage for six months at $100^{o}F$ were the pronounced quality loss in the fresh fruit, which had a very high ascorbic acid level from processing, and the much reduced loss in the repacked fruit, which contained about 30 ppm tin ions and very much less ascorbic acid. Also reported herein are two accelerated laboratory storage tests of the effect of tin metal and tin ions and of oxidized ascorbic acid on IQF and fresh pears, respectively.

MATERIALS AND METHODS

Front-face Fluorescence Method of Assessing Maillard Reactions

Details of the method as applied to browned casein slurries and to wet-pack peaches and pears have been described.[1,4] As used on fruit, measurements are made on a SPEX FLUOROLOG 2 Spectrofluorometer, using front-face excitation of solutions or slurries and sensing of emission at an angle of 22^{o} to the exciting beam. The instrument is used in the DC mode, slits 2.0, 1.5, 1.5, 1.0, with 500 volts setting on the photomultiplier. A 390 nm filter is placed in the emission path. Excitations are at 360 nm and 395 nm and emission wavelengths observed, although variable, are typically at about 460 nm and 520 nm in fresh peaches, the latter shifting to below 500 nm as browning progresses. An excitation spectrum is read from an emission setting of 470 nm. (Typical spectra are shown in Figures 14, 15 and 16.)

Thus, at each reading five measurements are normally made: emission intensity at the max from both 360 nm (A) and 395 nm (B) excitation, excitation peak wavelength (C) and excitation intensity at 370 nm (D) and 395 nm (E) with emission set at 470 nm. From these values, two ratios are computed: B/A, emission ratio, and E/D, excitation ratio, both of which have excellent reproducibility. Also of moderate reproducibility and thus reported herein are the two emission intensities (A and B), and the excitation wavelength maximum (C) for 470 nm emission. Emission intensities are standardized with quinine sulphate (QS), 1 ppm in 0.1N sulphuric acid but are reported as u amperes (uA). Under these conditions, 1 ppm QS normally reads 1.25×10^{-2} uA.

Preparation of Fruit Samples for Fluorescence Measurements

Twenty grams of stored fruit previously drained of excess syrup on an aluminum screen are added to 10 mL of the syrup and 10 mL of deionized water. This mixture is blended 2 min at high speed on a Waring blender and the slurry centrifuged 30 min in a clinical centrifuge. The supernatant is used undiluted for front-face fluorescence measurements.

Calculation of Means and Variability of Results

For each stored sample, duplicate preparations are made and, after initial fluorescence readings, these are mixed, recentrifuged and reread, to give a total of four readings per sample. Means and standard deviations of the five above-mentioned parameters are calculated. Reported herein are emission ratio (B/A), emission intensity (B) and maximum emission wavelength from 395 nm excitation, and maximum excitation wavelength from 470 nm excitation (C). In the figures, standard deviations are reported only for B/A and B.

Processing and Packing of Peaches for Simulated Storage Tests*

Clingstone peach samples from three sources were packed and processed in U.S. Army MRE retort pouches: 1) fresh, 2) individually quick frozen (IQF) and 3) repacked from previous unlined tin can packaging. The first two types were packed and processed by a California contractor in August 1988 and the latter were done in-house in January 1989. Sliced fresh peaches, after lye peeling and washing, were held in ascorbic acid dips before pouch filling and syruping. The ascorbic acid dips were designed to yield a postprocess concentration of 500 ppm. IQF peaches, which were bleached and dipped in ascorbate, were used after thawing and draining to remove excess ascorbate. Results reported below, however, indicate that after packing and equilibration there were wide differences between types, the fresh fruit containing over 1100 and the other types between 200 and 250 ppm. After removal from the dip, the slices were packed in a sucrose syrup, which, after processing, was targeted to yield 18-22% Brix for the entire contents. The pH of the syrup was adjusted to 4.0 with a citric acid buffer. Pouches were filled, sealed and thermally processed at 190^{o}F (88^{o}C) for 3-4 minutes, which previous studies showed as optimal.[1,3] Appropriate quality control tests of sample pouches were made for pH, Brix, enzyme (polyphenol oxidase) activity and approximate ascorbate level. Headspace was maintained at less than 10 cc.

---

*Simulated storage denotes controlled storage at two temperatures, 40^{o}F (4^{o}C) and 100^{o}F.

Repacked peaches were prepared in-house from commercial canned peaches initially packed in "ultralite" sucrose syrup. The fruit had been in unlined tin cans for no more than 6 months prior to repacking. Adjustment of Brix, estimated ascorbic acid level, pH and thermal processing were carried out as for the fresh and IQF fruit.

Fresh and IQF fruit were equilibrated approximately 3 months at 40^{o}F, until pH, Brix and sugar content had stabilized. Repacked fruit was held until it had equilibrated with respect to pH and temperature. Then the fruit was placed in controlled temperature storage at 40^{o}F for control and 100^{o}F as simulated high temperature field storage. Analyses were performed at this time, at 3 months and at 6 months.

Ascorbic Acid Analysis

A standard colorimetric method was used, based on 2,6-dichlorophenol-indophenol (DCIP) dye reduction.[6] Standard ascorbic acid solutions are prepared in citric acid buffer and 3% metaphosphoric acid. Ethylene diamine tetraacetic acid (EDTA) is added to prevent interference from ferrous, cuprous, or stannous ions. To prepare a standard curve, 5 mL of standard is added to 5 mL of DCIP and absorbance is read at 520 nm, after 10 seconds, 20 seconds and after the addition of a grain of ascorbic acid. For the fruit sample, the entire pouch contents are blended 20 seconds in an Oster blender. A 5-10 gram sample is diluted in citric and metaphosphoric acid buffer, filtered and read as above. A computer program calculates ascorbic acid concentration in the sample homogenate. However Maillard sugar-amine browning-generated reductones, if present, may interfere in this method.

Sugar Analysis by HPLC

The peach homogenate from the ascorbic acid assay was used after centrifugation for 20 minutes at 10,000 rpm for pH, Brix and HPLC analysis of sugars, 5-hydroxymethylfurfural (HMF) and furfural (F). The sample for HPLC analysis was diluted tenfold with distilled water and filtered using a Millipore Millex-GV 0.22 u filter. Analysis for fructose, glucose and sucrose was done on a Waters HPLC using a Waters Carbohydrate Analysis Column and differential refractometer detection. The solvent used was acetonitrile: water (80:20) and the flow rate was 2 mL/min. Output was handled by a Spectra Physics Integrator which reports concentrations using specific response factors calculated from external standards. Total sugar values are reported as the sum of concentrations of glucose, sucrose, and fructose determined by the integrator.

HMF and F Determinations by HPLC

A modified method [7,8] for HMF and F used dilute sulphuric acid (0.001N) as solvent at a flow rate of 0.5 mL/min., on a Varian Model 8500 HPLC with a Bio-Rad Fast Preservative Analysis column (30 x 4.6 mm). Detection was by a Kratos Spectroflow 783 UV/VIS Absorbance Detector set at 283 nm, outputting to a Waters 745/745B Integrator. Sample concentrations were calculated from a least squares standard curve of fit, of external standards at three different concentrations.

Reflectance

Reflectance measurements on peach homogenates (entire pouch contents) were done on a Hunter Color Difference Meter, Model D-25-9, in 50 x 8 mm Millipore covered plastic petri dishes, flush-filled with the fruit centrifugate after decanting supernatant. Appropriate white and grey plate standardization was carried out for each set of readings, which included Hunter L, a, and b.

Accelerated Laboratory Storage Test of the Tin Effect on Pears

To study the effect on stored pears of tin metal and stannous ions, unblanched IQF diced Bartlett pears were procured from J.R. Wood, Inc., Sanger, California. They contained ca. 1000 ppm ascorbic acid from the original processing. The frozen fruit dice were separated and, without further processing, the samples were prepared as shown in Table I.

Table I. Additives to IQF Bartlett Pears

SAMPLE	Pears (g)	Sucrose 36% (mL)	Deionized Water (mL)	0.02N** NaOH (mL)	$SnCl_2.2H_2O$ (mg)	Sn*** (g)
Control	20	10	2.8	0.0	0.0	0.0
$SnCl_2$*	20	10	0.0	2.8**	12.3	0.0
$SnCl_2$* + Sn	20	10	0.0	2.8**	12.3	0.38

*Stannous ion was present initially at 190 ppm

**NaOH added to counteract the pH lowering by stannous chloride hydrolysis.

***Tin metal was analytical tin foil, ca. 0.1 mm thickness, contained in conventional tea bags, washed 3x in deionized water.

The fruit was stored for 93 hours in screw-top Ball jars of 1/2 pint (225 mL) capacity in a 122°F (50°C) draft oven. The final pH values of the samples before storage were, respectively: 3.63, 3.65, and 3.61. Head space was air.

After 4 days storage, the jars were opened, the tea bag with tin metal was removed, 10 mL deionized water was added, and the standard blending, centrifugation, and fluorescence measurements were carried out. In addition, the supernatants were filtered using a 0.45 u filter and the absorbance at 420 nm carried out on a Cary Model 15 UV/VIS Spectrophotometer. Reflectance measurements were also carried out by techniques mentioned above.

Accelerated Laboratory Storage Test of the Ascorbic Acid Effect on Pears

To study the effect of excess ascorbic acid on fresh pears during high temperature storage, ripe Bartlett pears were purchased at a local market. Twenty grams of the pears were diced into 0.4% citric acid, then rinsed and dropped into boiling water for 5 minutes to inactivate enzymes. The samples, in duplicate, were placed in screw-top Ball jars as in the tin study according to the scheme outlined in Table II.

Table II Additives to Fresh Pears (in 10 g added syrup)

	Pears (g)	Sucrose (%)	Fructose (%)	Ascorbic Acid (%)	pH
Control	20	36	0	0	4.32
Fructose*	20	24	6	0	4.05
Ascorbic Acid	20	24	0	1	4.34

*Total added sugar was iso-osmolar with control.

Duplicate samples of each category were stored for 144 hours (6 days) at 122°F (50°C) in a draft oven. After withdrawal from storage, 11 mL deionized water was added to each sample and the procedures described above for work-up and analysis of the samples were carried out.

RESULTS AND DISCUSSION

Retort Pouch Peach Storage Simulation Study

This part of the study compared quality loss in simulated storage at $40^{o}F$ and $100^{o}F$ of fresh and IQF peaches retort pouch-packed by a commercial contractor and peaches repacked at Natick from previous packing in unlined tin cans into pouches. An analysis of the data follows.

Ascorbic Acid Content

Figure 1 shows ascorbic acid concentration at 0, 3 and 6 months for the total pouch contents. The processed fresh peaches contained about four times the ascorbic acid content of the IQF and repacked peaches. The fresh peach ascorbic acid content declined sharply with a decreasing rate, losing about 600 ppm in three months. The other two peach types experienced declines in the first three months but appeared to stabilize at between 3 and 6 months. Except for the repacked peaches at 6 months, there was little evidence of an increase in reducing power, which might come from Maillard sugar-amine reductones and might not be distinguished in this test from ascorbic acid.

Fluorescence Increase

Figures 2, 3, 4 and 5 show the anomalous changes in fluorescence ratios, absolute emission, and critical wavelengths associated with the fresh fruit during storage. Both fluorescence emission ratio (Fig. 2) and absolute fluorescence emission from excitation, at 395 nm (Fig. 3) show this very clearly. Figure 4, the maximum excitation wavelength from 470 nm emission setting, shows the strong red shift of the processed fresh fruit after $100^{o}F$ storage. Figure 5, the maximum emission wavelength from 395 nm excitation, also shows the processed fresh peaches changing more dramatically with storage, but in addition displays another diagnostic feature. Fluorescence arising from oxidized ascorbic acid-amine browning, when excited at 395 nm, can be sharply distinguished from sugar-amine browning because the emission is in the 460-480 nm range, whereas that from sugar-amine browning is well above this. We have studied this differential both in in vitro model systems and with heat-stressed fruit to which ascorbic acid has been added. The latter will be reported on below.

Reflectance

The results of reflectance studies are shown in Figure 6, which is a plot of Hunter L value, a measure of lightness versus time in storage. Declines in this value are indicative of browning. Again, the processed fresh sample with the very high ascorbic acid shows the greatest darkening, although the IQF fruit also darkened strongly. The repacked sample, containing a measured 30 ppm tin, is conspicuously lighter initially and changes at a lower rate with time in storage than either IQF or fresh processed peaches.

pH

Figure 7 shows the pH values of the total pouch contents. Although the repacked fruit is noticeably higher in pH, the fresh sample differs little from the IQF in this parameter, and the total spread of the values has been magnified for this figure. The fact that, as we found previously, samples with lower pH can experience more browning and fluorescence, is a cogent argument against sugar-amine browning, for which the opposite behavior is expected.

Sugar Content

Changes in content of fructose, glucose, sucrose and total sugars are shown in Figs. 8, 9, 10, and 11. Hydrolytic production of fructose and glucose and loss of sucrose because of the low pH and high temperature of the simulated storage, proceeded at a high but slowly decreasing rate during the period. The rate was noticeably greater for fresh and IQF than for the repacked fruit, and is in agreement with the relative pH values. Noteworthy, however, is the total sugar content, which, except for the IQF fruit, remains nearly constant. Any appreciable sugar-amine browning would have markedly reduced the total sugar.

HMF and F Content

Figures 12 and 13 show the changes in 5-hydroxymethylfurfural and furfural content. The major increment of change in concentration of both HMF and F occurs in the interval from 3 to 6 months, not in the interval from 0 to 3 months in contrast to the changes observed from $100^{o}F$ storage for reflectance, fluorescence or increases in glucose and fructose.

Discussion of Peach Storage Simulation Study

Fortunately, for elucidation of mechanism, the data demonstrated a very large and anomalous initial ascorbic acid content in the fresh peaches compared to the IQF and repacked fruit, and very large commensurate increases in oxidative Maillard browning in the fresh fruit only, as evidenced by fluorescence ratios and absolute emission. Although pronounced acid hydrolysis of sucrose occurred, total sugars changed little, contrary to what would be expected from sugar-amine browning. Furthermore HMF, which is a volatile indicator of sugar-amine browning, was produced in only trace amounts, about 0.01% of the reducing sugars present, which are the most probable precursors. Unless one considers HMF to be a very transient intermediate at a very low steady state concentration, its low level provides little support for much sugar-amine or caramelization loss of sugars, in agreement with the relative constancy of total sugar, above.

As noted above, although the Hunter reflectance lightness factor (L) was most reduced by high temperature storage in the fresh fruit, the IQF fruit also darkened strongly. Because of the relatively low fluorescence levels in the latter, it seems probable that this is residual autoxidative phenolic browning occasioned, in the absence of tin, by the low ascorbic acid.

Accelerated Storage Test of the Tin Effect on Pears

As detailed in Materials and Methods above (Table I), IQF pears containing roughly 1000 ppm ascorbic acid and either tin metal or tin metal plus stannous ions, respectively, were compared with control pears without tin, during 93 hours of storage at 122°F. Results are shown in Tables III and IV.

Table III: Effect of Tin Ions on Maillard Reaction in IQF Pears stored 4 days, 122°F.

	ADDITIVES			
SAMPLE	Sn^{++}	Sn^{o}	APPEARANCE	ODOR
Control	-	-	Very Tan Brown	Baked Apple
Pears-Sn^{++}	190 ppm	-	Pale Yellow	Much Less
Pears-Sn^{++}& Sn	190 ppm	1.15%	Pale Yellow	Much Less

Table IV: Effect of Tin Ions ± Tin on Maillard Reaction in IQF Pears Stored 4 days, 122°F.

SAMPLE	ABSORBANCE 420 nm	REFLECTANCE L	a	b	FLUORESCENCE $\frac{M395X}{M360X}$	M395X ($\mu A \times 10^{-2}$)
CONTROL	0.53	29	-.04	10.2	1.54	1.46
PEARS +Sn^{++}	0.28	43	-.39	16.3	1.25	0.89
PEARS +Sn^{++} & Sn	0.25	43	-1.59	16.0	1.19	0.86

After storage, the tin-containing samples showed much less color and baked odor, were 48% lighter in reflectance, and the filtered juice was 53% lower in absorbance than the controls. The emission ratio was about 30% higher and the absolute emission 70% higher in the control pears. The latter differences would be much greater were it not for an artifact fluorescence produced by tin ions and some compound, as yet unidentified, observed in pear juice but not in peaches. This compound produces a strong brightening effect analogous to that of laundry brightening compounds. In the case reported here, the tin brightener effect was exceeded by the very strong ascorbic acid browning fluorescence, from which it can be clearly separated by wavelength differences.

Accelerated Laboratory Storage Test of the Ascorbic Acid Effect on Pears

As outlined in Materials and Methods above (Table II), fresh Bartlett pears containing 10 g of either 36% sucrose syrup, 24% sucrose plus 6% fructose syrup, or 36% sucrose syrup plus 1% ascorbic acid were stored with air in the headspace for 144 hours at 122°F. Figure 14 shows the fluorescence spectrum of the supernatant from pears with sucrose only after storage; Figure 15, on a twelve times reduced scale, that of the pears containing fructose and sucrose; and Figure 16, on the same twelve times reduced scale, that of the pears with ascorbic acid and sucrose. The profound change occasioned by oxidized ascorbic acid is obvious, both in absolute amplitude and in ratio of 395 nm stimulated emission to that excited by 360 nm. The data are summarized, together with sensory observations and absorbance measurements of the filtered juice, in Table V.

Table V: Effect of Ascorbic Acid on Maillard Reaction in Fresh Bartlett Pears Stored 144 Hours at 122°F.

SAMPLE	APPEARANCE	ODOR	ABSORBANCE 420 nm Mean (n=2)	FLUORESCENCE Emission Ratio	Absolute Emission ($\mu A \times 10^{-3}$)	EXCITATION WAVELENGTH 470 nm Emission (nm)
Fresh Pears 36% Sucrose	Juice Clear Pear Color	Slight Baked	0.14	0.60	0.88	354
Fresh Pears % Fructose 24% Sucrose	Juice Clear Pear Color	Slight Off Odor	0.26	0.73	1.25	354
Fresh Pears 1% Ascorbic Acid 36% Sucrose	Juice Brown	Very Disagreeable Baked	1.81	1.90	22.2	395

The ascorbic acid treated pears, in all of the above indices, show very marked changes when compared to the fructose treated or control pears. The fluorescence spectrum for the heated control pears differs only slightly from that of fresh pears.

Thus, when compared by absolute emission, 1% ascorbic acid, under aerobic conditions, produced 18 times as much Maillard product as 6% fructose. Roughly compared, ascorbic acid was therefore about 100 times as reactive with fruit amino acids at pH 4 as fructose, which is a very active reducing sugar in Maillard browning. Similar results were found with 0.1% ascorbic acid. It should be noted that, in these stored pears as with the fresh peaches in simulated storage, ascorbic acid-amine browning can be sharply distinguished from sugar-amine browning by the relatively low wavelength (460-480 nm) emission excited by 395 nm light.

CONCLUSIONS

As noted above, the occurrence of anomalously high ascorbic acid content in the fresh peaches in simulated storage presented an opportunity to understand the mechanistic role of ascorbate in the browning reactions, as contrasted with that of the IQF and repacked peaches. The concomitant occurrence of very high Maillard indicating fluorescence in the same fresh peaches after storage is strong evidence for the major contribution of oxidized ascorbic acid-amine browning to the color changes at pH 4 in retort pouch-packed fruit. The strong pro-browning effect of air in the headspace and of softening due to low pH, which was found in earlier studies and was noted above, are strong arguments against a dominating role of the sugar-amine type of Maillard reaction as is the approximate constancy of total sugars. The fact that comminution enhances the browning in pasteurized fruit containing high added ascorbic acid, which is therefore presumably immune to enzymic phenolic browning, also is consistent with oxidized ascorbic acid and not sugar-amine browning, since both sugars and amino acids coexist in the vacuole, whereas ascorbic acid in these fruits is largely an additive.

The evidence from the two laboratory model systems in accelerated storage stress indicates that added ascorbic acid in fresh pears with air in the headspace strongly promotes the production of odors, color and Maillard-indicative fluorescence, and stannous ions or tin metal plus stannous ions, in IQF pears containing high levels of ascorbic acid with an aerobic headspace, strongly inhibit the production of these same three factors.

Together with the evidence from the simulated storage of peaches that the repacked peaches containing 30 ppm tin were the most resistant to the quality changes reported here (although they did suffer more softening than the fresh and IQF fruit), one may conclude that sugar-amine browning is not a major problem in the fruit reported here. One important color and flavor loss problem in retort-pouch packing of wet fruit is protection from enzymic or autoxidative phenolic browning during the peeling, dicing, filling and sealing stages prior to pasteurization and even during storage. Ascorbic acid protects the color very well, but both the thermal process and storage generate oxidized ascorbic acid products which, under the heat stresses mandated by military storage conditions, can cause very detrimental color and odor changes, particularly if there is substantial air in the headspace.

Protective measures against ascorbic acid-amine browning are radically different from those for sugar-amine browning. Proposals to reduce sugar-amine browning by exclusion of reducing sugars are not really possible because some fruits (e.g., pears) contain naturally high levels of fructose, a reducing sugar; also, with time in storage, hydrolysis of sucrose invariably produces two reducing sugars, glucose and fructose. The lowering of pH proposed to decrease sugar-amine browning by prevention of the initial attack of the amino group has been shown to be counterproductive when high ascorbate levels are present.[3]

On the basis of the studies reported herein, we propose two effective measures to be taken to prevent oxidized ascorbic acid-amine browning. The first is to keep concentration of ascorbate used to minimize enzymatic browning prior to processing at the minimum required level and the second is to reduce oxygen in headspace as well as total headspace to prevent oxidation of residual ascorbate. Although ascorbate does function as an oxygen scavenger, the subsequent deleterious reactions of oxidized ascorbate are contraindicative of the use of ascorbate as an oxygen scavenger for fruits. Alternative water-compatible oxygen scavengers such as cysteine, which has been used in pear juice concentrate and apples[9,10] may be employed, but the simpler expedient may be to use an effective hot fill with steam or nitrogen flushing or a supplemental mechanical vacuum during the pouch sealing prior to thermal processing. Alternative chemical approaches to find functional alternatives to the protective effects of ascorbate without some of the deleterious side effects of oxidized ascorbate will be the focus of future efforts in our laboratory; these approaches include: 1) chemical reduction of both residual oxidized ascorbic acid and quinones by including cysteine (1.5 mM) in the syrup, 2) inclusion of soft tin metal within a removable porous package within the pouch to serve as a reservoir of reducing power and 3) use of a cation exchange resin -- in bead or film form within the package -- to sequester the reactive amino acids.

ACKNOWLEDGEMENTS

The authors express their gratitude to Michael Di'Nunzio for able technical assistance in measurement of sugars and furfurals. Thanks are also due to Dr. K.A. Narayan and Ms. Bonita Atwood for expert advice and editorial review. The indispensable aid of Ms. Ann Marie Huwe in preparing the manuscript is gratefully acknowledged.

REFERENCES

1. Porter, W.L., E.D. Black, C. Anastasia, and K.A. Narayan, "Reduction of Maillard Browning in Wet-Pack Fruit by Amino Acid Sequestration". Technical Report Natick/TR-88/052. U.S. Army Natick Research, Development and Engineering Center, Natick, MA. p. 175 (1988). (AD-A 200 977)

2. Hodge, J.E. and E. M. Osman, "Carbohydrates". In Food Chemistry, Ed. O.R. Fennema, Marcel Dekker, Inc., N.Y., p. 51 (1976).

3. Kluter, R.A., C.P. Dunne, R. Popper, and D. Nattress, "Optimization and Storage Stability of Fruits Processed in Retort Pouches", *Poster Session Paper presented at the 50th Annual Meeting, Institute of Food Technologists, Chicago, Ill., 27 June 1989.

4. Porter, W.L., E.D. Black, Y.-K. Kim, and L. Hoke, "Development of Rapid Methods to Monitor Oxidative and Maillard (Sugar-amine) Polymerization in Energy-Dense, Encapsulated Model Systems." Technical Report, NATICK/TR-86/063, U.S. Army Natick Research, Development and Engineering Center, Natick, MA, p. 15 (1986) (AD A 179 574)

5. Singleton, V.L. and P. Esau. Phenolic Substances in Grapes and Wine and Their Significance, Acad. Press, NY, pp. 136, 142, 179, 196 (1969).

6. Methods of Vitamin Assay. Ed. J. Augustin, B. Klein, D. Becker, and P. Venugopal, John Wiley and Sons, NY, Chapter 12 (1985).

7. Lee, H.S., R.L. Rouseff and S. Nagy, J. Food Science, 51:1075 (1986).

8. Wucherpfennig, K. and D. Burkardt, Fussiges Obst., 9:416 (1983).

9. Montgomery, M. W., J. Food Science, 48: 951 (1983).

10. Walker, J.R. L. and C.E.S. Reddish, J. Sci. Fd. Agric., 15:902 (1964).

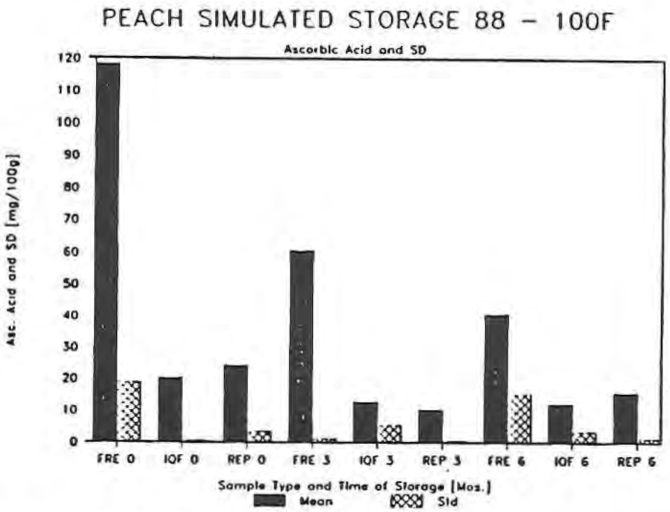

Figure 1. Ascorbic acid concentration.

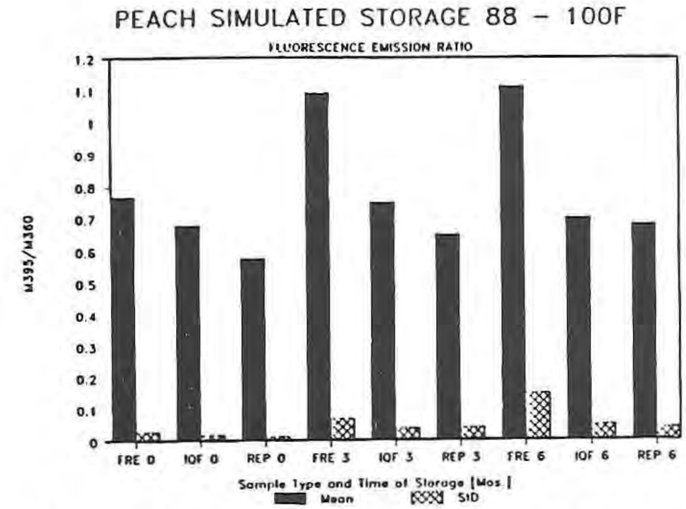

Figure 2. Fluorescence Emission Ratio.

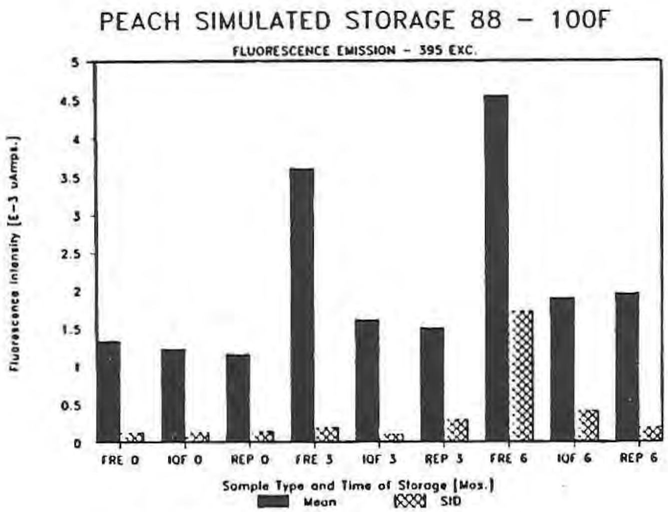

Figure 3. Fluorescence Emission.

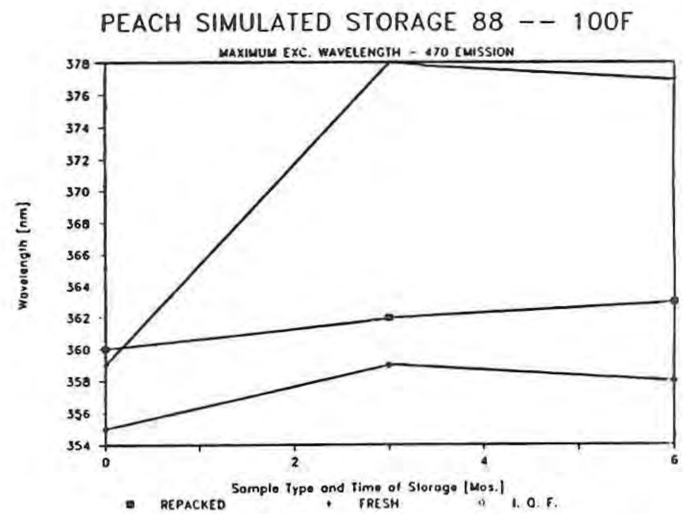

Figure 4. Maximum excitation wavelength.

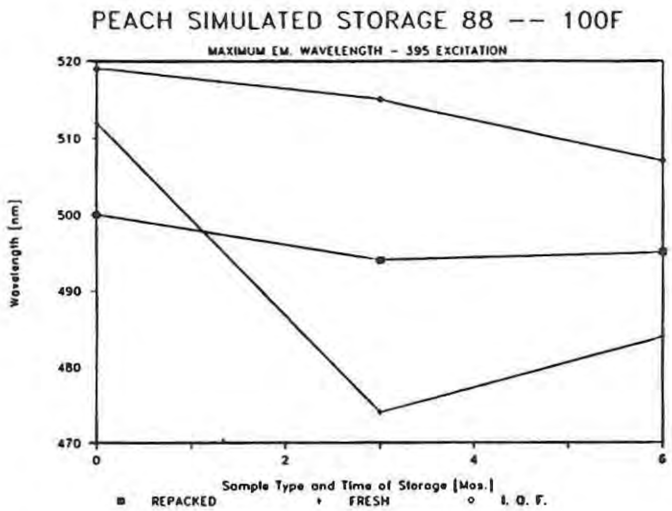

Figure 5. Maximum emission wavelength

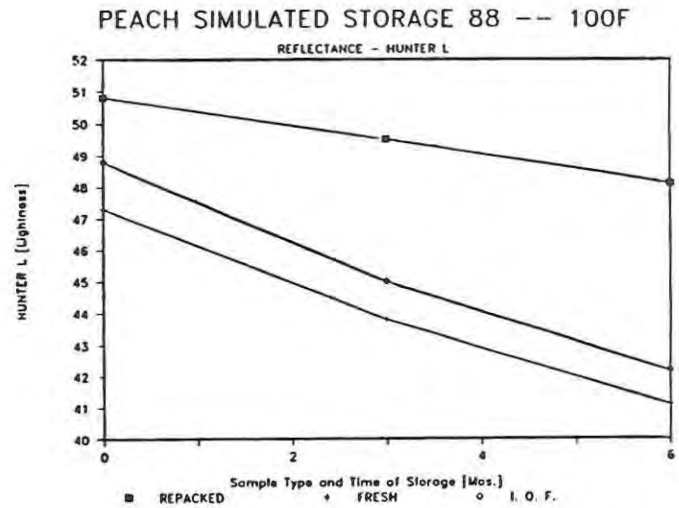

Figure 6. Reflectance - Hunter L Value.

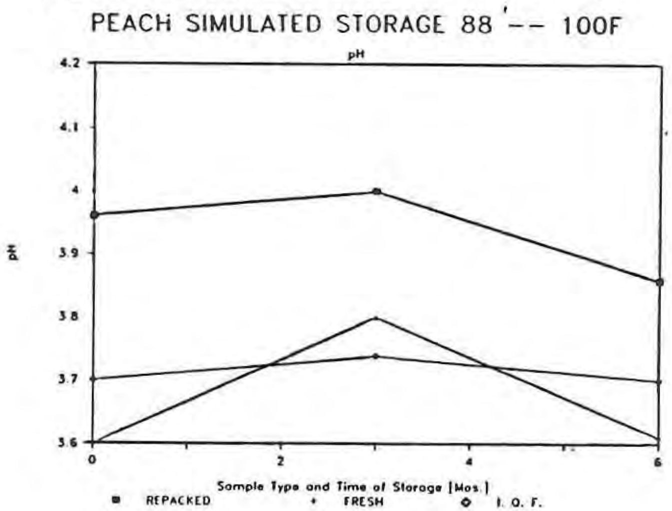

Figure 7. pH of Samples.

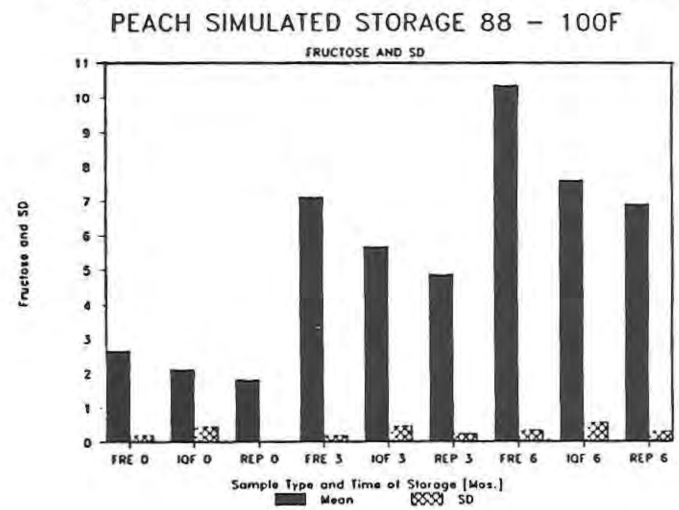

Figure 8. Fructose concentration (g/100g).

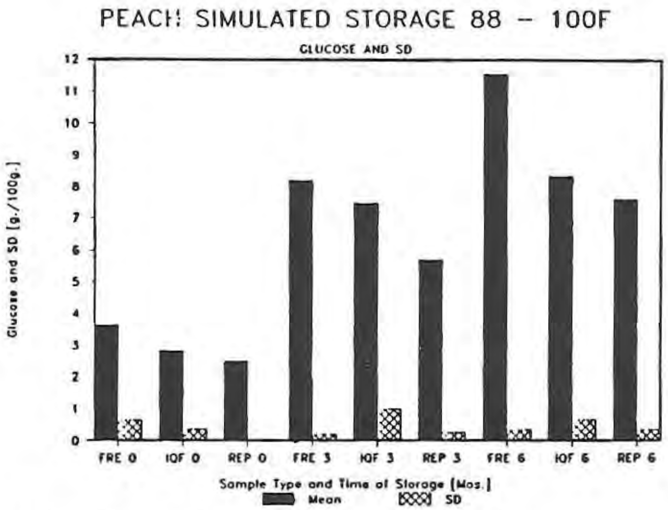

Figure 9. Glucose concentration.

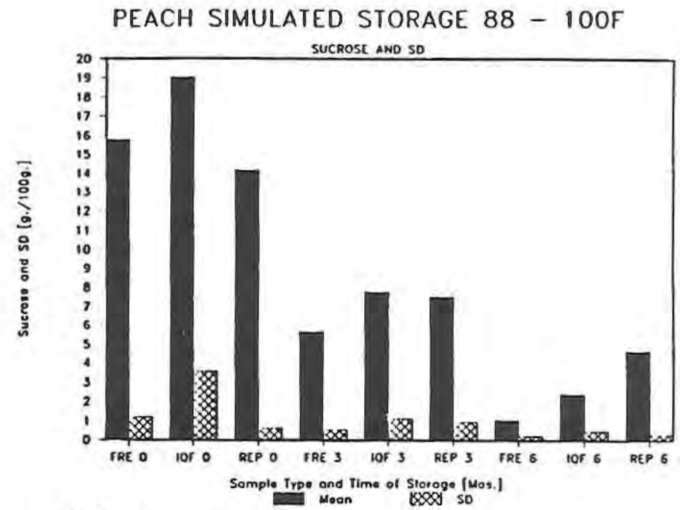

Figure 10. Sucrose concentration.

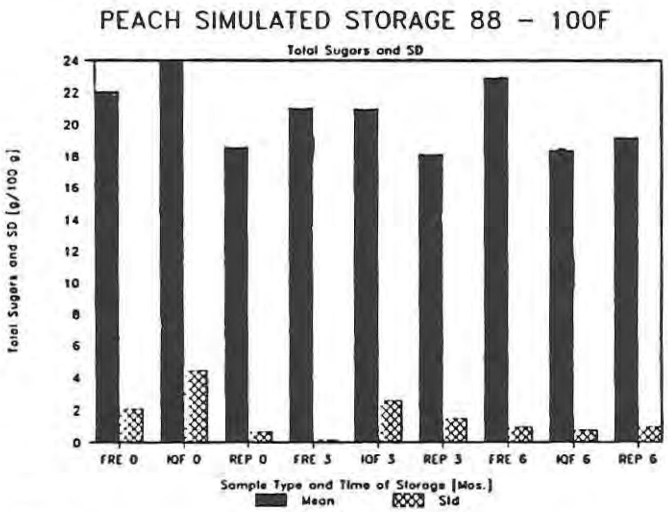

Figure 11. Total sugar concentration.

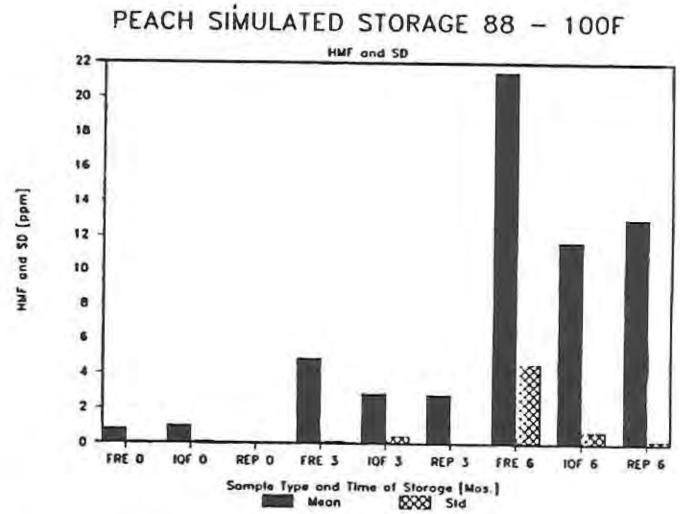

Figure 12. HMF concentration.

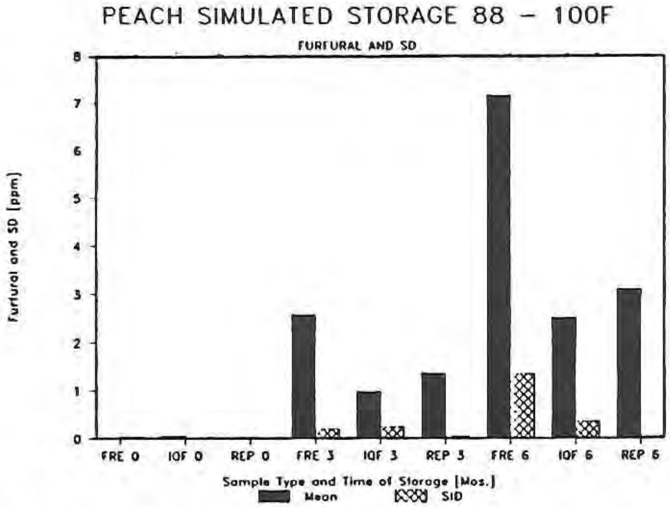

Figure 13. F concentration.

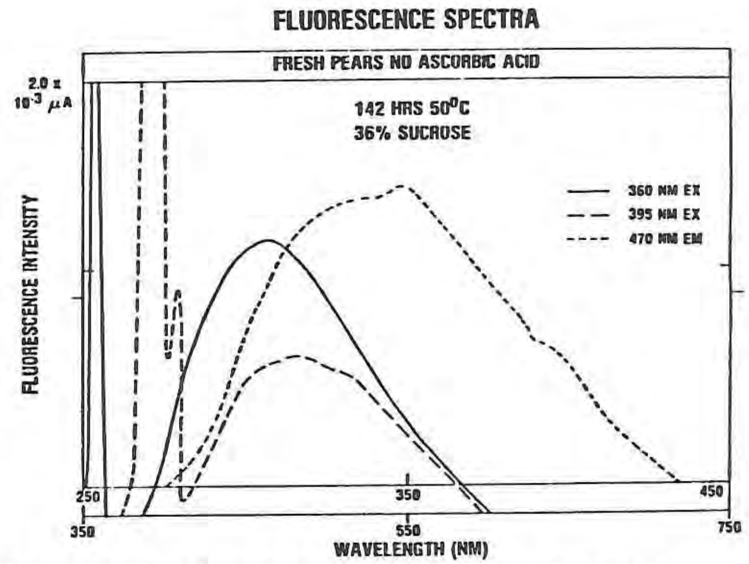

Figure 14. Fluorescence spectra of fresh pears with no ascorbic acid.

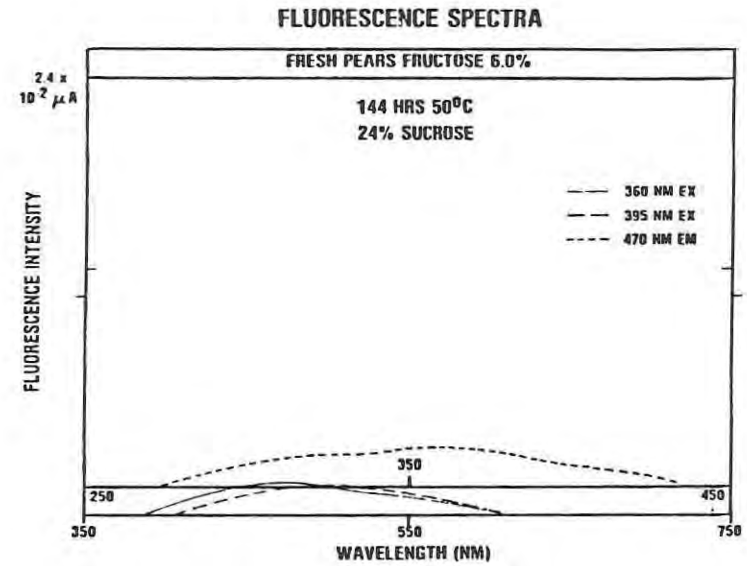

Figure 15. Fluorescence spectra of fresh pears with 6% fructose.

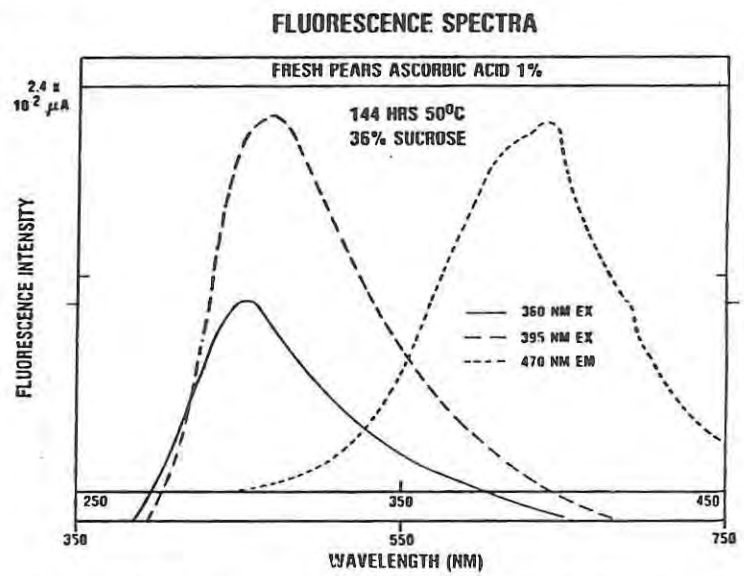

Figure 16. Fluorescence spectra of fresh pears with 1% ascorbic acid.

TITLE: PATHOGENIC LISTERIA IN MILITARY RATIONS: RAPID DETECTION
*Lachica, R. Victor., Dr.

ABSTRACT: Listeria monocytogenes (Listeria) has been recognized recently as a foodborne pathogen. It is presently unknown how infectious it is. It does appear to be widely distributed in the environment. Therefore, keeping the pathogen from contaminating the military food supply is not easy. The risk of listeriosis is especially high from refrigerated, ready-to-eat foods since the pathogen can grow at refrigeration temperatures. To have better control of Listeria in our food supply, it is desirable to have the capability to rapidly screen for its growth in the food. Such a capability has been achieved in our laboratory using a recently developed three-phase procedure that is completed in less than 48 hours. The first phase involves the use of a highly selective plating medium for Listeria cells to emerge as large colonies in 40 hours at 30° C. The second phase is the initial recognition of these colonies using a simplified optical technique. The final stage involves subjecting each representative suspect colony to a battery of tests that can be completed in less than 8 hours, a feat made possible by the use of high concentrations of robust cells.

The Natick Listeria procedure is to date the most rapid method for the quantitative detection of foodborne Listeria, a vast improvement over the standard procedure that often takes weeks to complete.

*BIOGRAPHY OF PRESENTER: R. Victor Lachica

PRESENT ASSIGNMENT: Research Microbiologist in the Biological Sciences Division of the Soldier Science Directorate, U.S. Army Natick Research, Development and Engineering Center, Natick, MA.

PAST EXPERIENCE: Chief, Microbiology Branch, Food Control Division, Institute of Nutrition, Guatemala City, Guatemala.

DEGREES HELD: B.A., Wartburg College. Ph.D., Iowa State University.

PATHOGENIC LISTERIA IN MILITARY RATIONS: RAPID DETECTION

R. VICTOR LACHICA, DR.

INTRODUCTION

The potential for outbreaks of listeriosis from foods contaminated with *Listeria monocytogenes* (Listeria) has been recognized recently and has raised concern regarding the adequacy of methods for the quantitative detection of the cold-tolerant pathogen in foods (24). Consequently, considerable amount of effort has been expended recently in the development and evaluation of selective agar media (3,5,6,14,15,18). A major concern has been the complications associated with enumerating *L. monocytogenes* in foods containing high levels of other microorganisms. Typically, cells of this pathogen emerge as small colonies (< 2.0 mm in diameter) on most plating media after 40 h at 30-35 C. This pattern is certainly true with lithium chloride-phenylethanol-moxalactam agar (LPM, 14), which seems to be the most commonly used plating medium for detection of *L. monocytogenes* in various foods (5,7,15).

Subsequent recognition and identification of suspect *L. monocytogenes* colonies take three to four weeks to complete (16). Datta et al. (7) succeeded in accelerating the identification phase into two days by exploiting a colony hybridization technique. One disadvantage with this approach is the use of a rapidly decaying radioisotope.

The U.S. Air Force became aware of the problem of listeriosis from foods and gave us the task of assessing the risk that military personnel and families may face from consumption of refrigerated ready-to-eat food ration components. An important component of the task is the availability of a convenient and rapid procedure to monitor pathogenic listeriae in foods.

This paper describes the successful development in our laboratory of a three-phase Natick Listeria procedure that can be completed in less than 48 h (11,12,13). The first phase involves the use of a highly selective plating medium for recovery of *Listeria* cells that emerge as large colonies in 40 h at 30°C. The second phase is the initial recognition of these colonies in seconds using a simplified optical technique. The final stage is the definitive identification of pathogenic Listeria in less than eight hours.

PHASE I : RECOVERY

Our laboratory designed the lithium chloride-ceftazidime agar (LCA) to promote the formation of large colonies of *L. monocytogenes* and at the same time suppress the growth of most of the other foodborne microflora (11). The medium provides a nutritious environment; its nutritive agar base (brain heart infusion agar or BHIA, Difco) contains glucose, which is considered the best energy source for growth of *Listeria* species (21,23). Most published formulations of plating media do not contain any added carbohydrate that can be utilized by *Listeria*. Some media do contain esculin as a diagnostic test (6). However, it is not used as efficiently as glucose by *L. monocytogenes*, as pointed out by Swaminathan *et al.* (23). Among the various glucose-containing basal media examined, none could match the ability of BHIA to promote good growth of *L. monocytogenes*.

The choice of selective agents for the LCA was aided immensely by an extensive survey by Smith and Archer (22) on the degree to which selective agents inhibit the recovery of sublethally heat-injured *Listeria* cells. The assumption was made in our laboratory that agents highly inhibitory towards injured cells are also likely to effect a diminution of colony size. Consequently, the choice of selective agents was sharply focused on a few compounds. In combination with 0.5% LiCl and 10% glycine anhydride, ceftazidime (50 µg/mL) and moxalactam (20 µg/mL) were generally comparable in their effectiveness in controlling the background microflora. However, ceftazidime was slightly more permissive towards *L. monocytogenes* and more inhibitory towards the other foodborne bacteria. Use of tellurite reduction as a diagnostic test was abandoned when potassium tellurite levels as low as 0.001% were found inhibitory to heat-injured *Listeria* cells. Moreover, the occasional staphylococci, streptococci, and bacilli that emerged on LCA were also capable of reducing tellurite.

The use of naturally contaminated food samples as test materials provided convincing evidence of the efficacy of LCA for the quantitative detection of foodborne *L. monocytogenes*. Moreover, the results from the artificially contaminated samples further indicated that the presence of an overwhelming level of background microflora is not a problem with either LCA or LPM.

The unique ability of LCA to efficiently recover healthy and sublethally injured *L. monocytogenes* cells is an advantage that can be useful for the recovery and enumeration of injured cells that might be present in certain foods such as pasteurized milk (8). Of greater significance is the ability of LCA to promote the formation of large *Listeria* colonies and still control the growth of the background microflora.

PHASE II : RECOGNITION

For over 40 years, the HOT technique (9) has been used for the initial recognition of *Listeria* colonies that appear with a distinctive bluish cast facilitating their selection in the midst of numerous other colonies (21). It is currently included in two protocols (16,18) devised by the U.S. regulatory agencies for the detection of food-borne listeriae. However, other investigators (1,10) have reported that certain non-*Listeria* organisms, especially the streptococcal colonies, exhibit a similar bluish cast as the listeriae. A likely explanation for this observation is the difficulty in setting a precise angle with which to obliquely illuminate the object with a mirror. Seeliger and Jones (21) have emphasized the importance of the angle of light with the HOT technique. Another disadvantage with the technique is its cumbersome procedure of viewing uncovered agar plates right-side up instead of viewing covered plates bottom side up that would allow scoring for typical colonies with the use of a marking pen. Consequently, investigators have explored alternative diagnostic properties such as tellurite reduction (3) or dark color resulting from the reaction of ammonium ferric citrate with the hydrolytic product of esculin (6). However, these properties lack specificity, a problem especially with streptococci that manage to grow on the various *Listeria* plating media (1,17). Our laboratory recently described the successful modification of the HOT technique (12) that provides for a more precise, convenient and familiar manner with which to read and recognize colonies of listeriae on LCA.

In reassessing the HOT technique as shown in Fig. 1, it became apparent that the focus on the angle of reflected light ($\beta = 45^0$) was misdirected. In essence, the technique consists of viewing the object at point B (the colony) at right angle (90^0) from point A and illuminating it from point C with white light reflected by a mirror at 45^0. Thus, the angle of concern is actually α (designated as the angle of transillumination) whose value (135^0) is the sum of 45^0 and 90^0. It also became apparent that neither a mirror for illumination of the object nor a scanning light microscope was necessary for viewing a colony with oblique lighting. Consequently, a simplified HOT (SHOT) technique was developed, as shown in Fig. 2. For ease of viewing and counting (scoring) of suspect colonies, each agar plate was examined by placing it bottom-side up on a transparent platform that was tilted towards the viewer at 45^0 and illuminated directly from below with a high intensity lamp at right angle (90^0) to the bench top. . Each colony on the agar plate was scanned with a 5x magnifying hand lens attached to a tube that was clamped at 45^0 to the bench with the aid of a set square, thereby attaining the angle of transillumination of 135^0. The agar plates were freed of water condensate to reduce distortion.

All the listeriae on LCA plates that were streak inoculated to obtain well-isolated colonies after 40 h at 30°C exhibited the bluish cast. The large, well-isolated colonies showed the bluish hue primarily on the rim, whereas the bluish hue was uniform among the small colonies on the crowded sections of the agar plates. A distinct bluish hue was readily discerned when the thick, opaque center portion of a large colony was streaked into a thin layer. This distinctive hue was practically obliterated when the listeriae were grown on BHIA containing 4% NaCl or 1.5% LiCl.

Among the nonlisteriae growing on BHIA, only *C. aquaticum, J. denitrificans, A. cloacae, P. aeruginosa* and *S. marcescens* appeared with a bluish hue similar to the listeriae. LCA was completely inhibitory to these strains with the exception of *C. aquaticum,* which grew as pin-point colonies in marked contrast to the large colonies of listeriae.

Colonies with atypical iridescence or morphology were picked during a routine screening for listeriae by direct plating on LCA of retail level foods (brie, camembert, yogurt, sliced chicken luncheon meat and pork sausage). These samples turned out to be negative for listeriae (<100 colony forming units--or CFU--per gram). The colonies consisted of 7 spore-forming *Bacillus,* 5 yeasts, 13 catalase-negative cocci (streptococci) and 11 catalase-positive cocci (staphylococci). The lactic acid bacteria from yogurt that formed tiny colonies on BHIA plates appeared reddish when viewed by the SHOT technique. No colony was encountered that resembled the distinctive bluish cast of *Listeria* colonies.

The efficacy of the SHOT technique was also verified using five frozen retail-level food samples that were naturally contaminated with moderate levels of *L. monocytogenes* (>100 CFU/g) (11). When these samples were again plated onto LCA, all but one (precooked sliced beef) were positive for *L. monocytogenes* at levels similar to a previous report (11). The suspect colonies were easily recognized by their bluish cast when viewed by the SHOT technique. Subsequently, representative colonies were all definitively identified as *L. monocytogenes* in less than 8 h . All the colonies that exhibited the typical bluish cast turned out to be *L. monocytogenes.*

PHASE III : IDENTIFICATION

In the rapid identification of *L. monocytogenes,* each well-isolated, representative large colony that emerges from an LCA plate and appears bluish by the SHOT technique is directly subjected to a battery of tests without the prior purification step required for the conventional procedure. With a sterile inoculation loop, a colony is harvested as a viscid cell mass for inoculation of three diagnostic agar plates that are divided into quadrants.

(i) **Rapid hemolytic activity test.** A sterile disk of β-lysin (Remel) is aseptically placed at the center of a blood agar plate (5% sheep blood in Columbia blood agar base, Difco) to allow the diffusion of the β-lysin through the agar gel. As many as four heavy inocula are smeared as bands no larger than 3 x 4 mm at a distance of 2-3 mm perpendicular to the edge of the lysin disk. Each inoculum is massive enough to be visible to the naked eye. Observation of complete hemolytic reactions is made after 4, 5, 6 and 7 h at 35°C.

(ii) **Rapid sugar acidification.** Acid production from rhamnose and xylose is detected using an agar plate method. Each fermentation test agar plate is prepared by adding an appropriate sample of a filter-sterilized sugar stock solution to an autoclave-sterilized purple agar base (Difco) medium. The final carbohydrate concentration in the agar medium is 1%. The plates are inoculated with the viscid cell mass and incubated in a similar fashion as the rapid hemolytic activity test.

(iii) **Phase microscopy.** The remaining cells on the inoculation loop are suspended in a loopful of distilled water on a microscope slide, covered with a glass slip, and examined by phase contrast microscopy for cell morphology and motility.

(iv) **Catalase test.** After phase microscopy, the cell suspension on the microscope slide is examined for catalase by adding a drop of 3% hydrogen peroxide to one side of the cover slip and observed for an immediate effervescence from one end of the slip to the other.

(v) **KOH viscosity test.** The convenient KOH viscosity test of Ryu is used in place of the Gram stain (20). It involves using a heavy cell mass obtained from one of the diagnostic agar plates described above after an incubation period of 7 h. A heavy suspension in a drop of 3% KOH solution on a glass slide is stirred with an inoculation loop and within a few seconds a sticky slurry is observed with cells of Gram-negative bacteria. Gram-positive bacteria, such as the listeriae, are impervious to the lytic action of alkali.

Well isolated cells of listeriae grew on LCA as white, fine-textured, dense and dome-shaped colonies that attained a diameter of about 2.5 mm. The colonies that appeared bluish at the rim when viewed by the SHOT technique consisted predominantly of distinct short rods whose lengths were about three times their width. Many of these cells were in pairs with a few single cells that were long. Consistent with Lovett (16), tumbling motility was observed among the short rods from cultures that were grown at 30^{0}C. All showed vigorous catalase activity and as expected were negative for the KOH viscosity test. This composite of characteristics was highly efficient in screening for listeriae colonies. Moreover, LCA was observed to be highly selective for the listeriae.

Five hours after transfer from LCA, colonies of *L. monocytogenes* and *L. seeligeri* were observed to be CAMP-positive as indicated by the clearing on the area of the blood agar in proximity to the colony and the β-lysin disk. There was no clearing on the area next to the colony distal to the disk until β-lysin had diffused into the area. *L. ivanovii* colonies exhibited rapid hemolysis (4 h) without the potentiation by the staphylococcal β-lysin disk. As expected, the rest of the *Listeria* species exhibited no hemolytic activity. In 6 h, *L. monocytogenes* colonies turned yellowish on rhamnose purple agar but not on xylose purple agar. The opposite was true with colonies of *L. seeligeri*. Only the colonies of *L. seeligeri*, *L. welshimeri*, and *L. ivanovii* turned yellowish on xylose purple agar. The yellowing of the colonies was best observed by indirect lighting. Table 1 summarizes the differentiation of all but three species of *Listeria* using an abbreviated number of properties that comprise the RAP-ID scheme. Additional tests such as mannitol fermentation and nitrate reduction were required for the differentiation of the rhamnose-negative strains of *L. innocua* from *L. gray, L. murrayi* and *J. denitrificans*.

The non-*Listeria* colonies that emerged on LCA were mostly Gram-positive cocci (streptococci and staphylococci) whose red-blue iridescence was distinct from the bluish hue of Listeria colonies by the SHOT technique. The few large *Bacillus* and small yeast colonies appeared white. Reddish, pinpoint colonies of lactobacilli were also observed.

As a primary plating medium, LCA plays a critical role in the RAP-ID scheme by selectively promoting the growth of listeriae in the form of large colonies of distinctly rod-shaped cells of high catalase activity.

Consequently, the scheme obviates the practice of subculturing to a rich, nonselective medium for the purpose of eliminating the likelihood of mistakenly discarding isolates of listeriae that appear in their coccoid forms and exhibit very poor catalase activity that may be overlooked (21) Therefore, the possibility of confusing colonies of Gram-positive cocci (streptococci and staphylococci) from the listeriae is remote. Moreover, the robustness of the mass of cells, which have also been doubling during this period appears to contribute in the acceleration of the hemolytic and fermentative activities. The determination of these properties within a few hours of incubation indicates that LCA-grown cells may already have the necessary infrastructure to synthesize the hemolysins and to catabolize the sugars.

Although LCA is quite inhibitory towards Gram-negative bacteria, the use of the KOH viscosity test as a substitute for the Gram stain provides a convenient means to ascertain that one is dealing only with Gram-positive isolates. The test was described over 50 years ago (20) and its efficacy has been verified in recent years (2,4,) yet the use of this convenient and cost-effective procedure does not appear to be widespread.

In conclusion, the Natick Listeria procedure is to date the most rapid method for the quantitive detection of foodborne *Listeria*-- a vast improvement over the standard procedure that often takes weeks to complete. Using this procedure in a limited survey of retail refrigerated ready-to-eat foods indicated that consumers are sporadically exposed to elevated levels of *L. monocytogenes*. It is envisioned that the adoption of the Natick Listeria procedure by regulatory agencies and the food industry would significantly reduce the risk of listeriosis from foods.

LITERATURE CITED

1. Bailey, J.S., D.L. Fletcher, and N.A. Cox. 1989. Recovery and serotype distribution of *Listeria monocytogenes* from broiler chickens in the southeastern United States. J. Food Prot. **52:** 148-150.

2. Bourgault, A.-M., and F. Lamothe. 1988. Evaluation of the KOH test and the antibiotic disk test in routine clinical anaerobic bacteriology. J. Clin. Microbiol. **26**: 2144-2146.

3. Buchanan, R.L., H.G. Stahl, and D.L. Archer. 1987. Improved plating media for simplified, quantitative detection of *Listeria monocytogenes* in foods. Food Microbiol. 4: 269-275.

4. Buck, J.D. 1982. Nonstaining (KOH) method for determination of Gram reactions of marine bacteria. Appl. Environ. Microbiol. **44:** 992-993.

5. Cassiday, P.K., and R.E. Brackett. 1989. Methods and media to isolate and enumerate *Listeria monocytogenes:* a review. J. Food Prot. **52**:207-214.

6. Curtis, G.D.W., R.G. Mitchell, A.F. King, and E.J. Griffin. 1989. A selective differential medium for the isolation of *Listeria monocytogenes.* Lett. Appl. Microbiol. **8**:95-98.

7. Datta, A.R., B.A. Wentz, D. Shook, and M.W. Trucksess. 1988. Synthetic oligodeoxyribonucleotide probes for detection of *Listeria monocytogenes*. Appl. Environ. Microbiol. **54:** 2933-2937.

8. Doyle, M.P. 1988. Effect of environment and processing conditions on *Listeria monocytogenes*. Food Technol. **42**:169-171.

9. Gray, M.L. 1957. A rapid method for the detection of colonies of *Listeria monocytogenes*. Zentral. Bakteriol. Hyg. A. **169**: 373-377.

10. Hao, D. Y.-Y., L.R. Beuchat, and R.E. Brackett. 1987. Comparison of media and methods for detecting and enumerating *Listeria monocytogenes* in refrigerated cabbage. Appl. Environ. Microbiol. **53**: 955-957.

11. Lachica, R.V. 1990. Selective plating medium for quantitative recovery of foodborne *Listeria monocytogenes*. Appl. Environ. Microbiol. **56**: 167-169.

12. Lachica, R.V. 1990. Simplified Henry technique for the initial recognition of *Listeria* colonies. Appl. Environ. Microbiol. **56**: 1164-1165.

13. Lachica, R.V. 1990. Same-day identification scheme for colonies of *Listeria monocytogenes*. Appl. Environ. Microbiol. **56**: 1166-1168.

14. Lee, W.H., and D. McClain. 1986. Improved *Listeria monocytogenes* selective agar. Appl. Environ. Microbiol. **52:** 1215-1217.

15. Loessner, M.J., R.H. Bell, J.M. Jay, and L.A. Shelef. 1988. Comparison of seven plating media for enumeration of *Listeria* spp.**4:**3003-3007.

16. Lovett, J. 1988. Isolation and identification of *Listeria monocytogenes* in dairy products. J. Assoc. Off. Anal. Chem. **71**:568-660.

17. Mavrothalassitis, P. 1977. A method for the rapid isolation of *Listeria monocytogenes* from infected material. J. Appl. Bacteriol. **43**: 47-52.

18. McClain, and W.H. Lee. 1988. Development of USDA-FSIS method for isolation of *Listeria monocytogenes* from raw meat and poultry. J. Assoc. Off. Anal. Chem. **71**: 660-664.

19. Rocourt, J., A. Schrettenbrunner, and H. P. R. Seeliger. 1983. Differentiation biochimique des groupes genomiques de *Listeria monocytogenes (sensu lato).* Ann. Inst. Pasteur (Paris). **134**: 65-71.

20. Ryu, E. 1938. On the Gram-differentiation of bacteria by the simplest method. J. Jap. Soc. Vet. Sci. **17**: 31.

21. Seeliger, H.P.R., and D. Jones. 1986. *Listeria*. In: Bergey's manual of systematic bacteriology. Vol. 2. Edited by P.H.A. Sneath, N.S.Mair, M.E. Sharpe and J.G. Holt. Williams and Wilkins, pp. 1235-1245.

22. Smith, J.L., and D.L. Archer. 1988. Heat-induced Injury in *Listeria monocytogenes*. J. Ind. Microbiol. **3**:105-110.

23. Swaminathan, B., A.S. Hayes, and V.A. Przybyszewski. 1988. Evaluation of enrichment and plating media for isolating *Listeria monocytogenes*. J. Assoc. Off. Anal. Chem. **71**:664-668.

24. Wehr, H.M. 1987. *Listeria monocytogenes* - a current dilemma. J. Assoc. Off. Anal. Chem. **70:** 769-772.

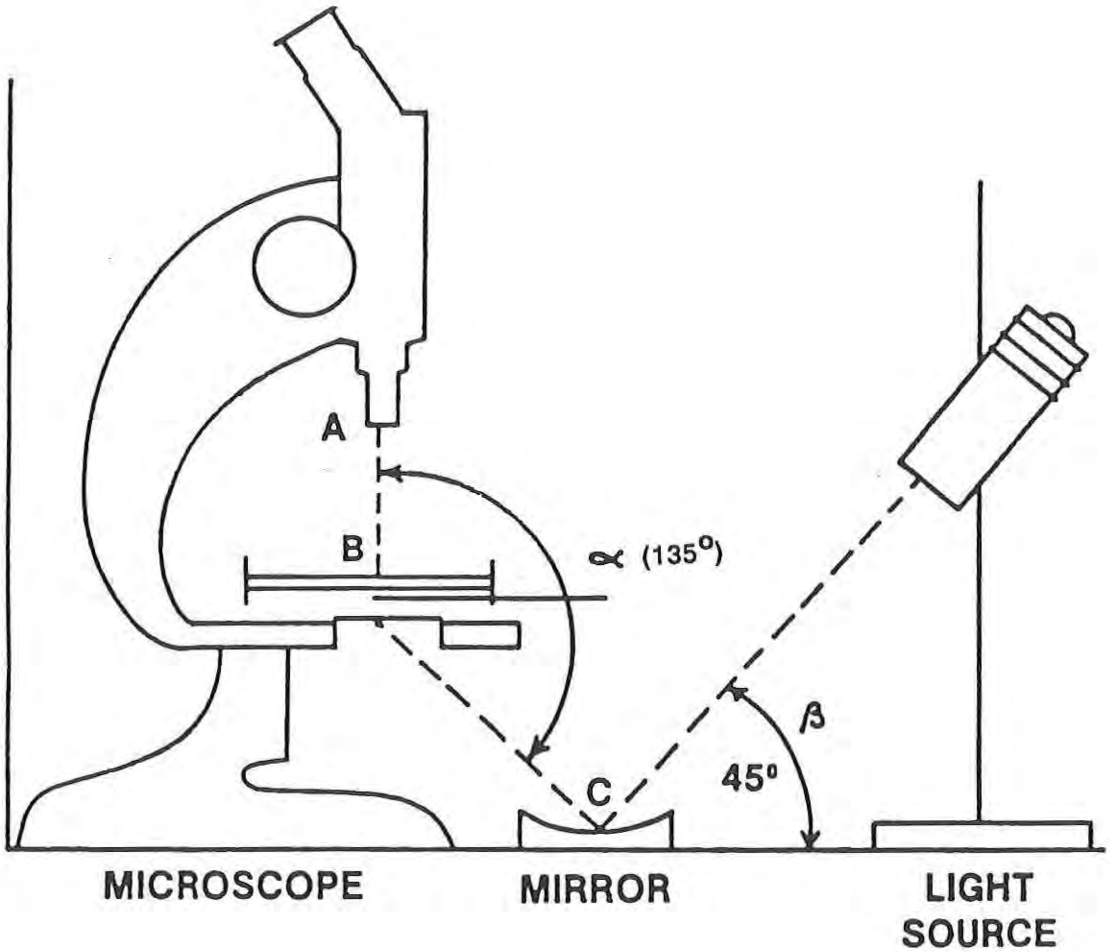

Fig. 1. Graphic illustration of the Henry oblique transmitted light technique (HOT) for the initial recognition of listeriae colonies in which the object at point B is viewed from point A and illuminated from point C.

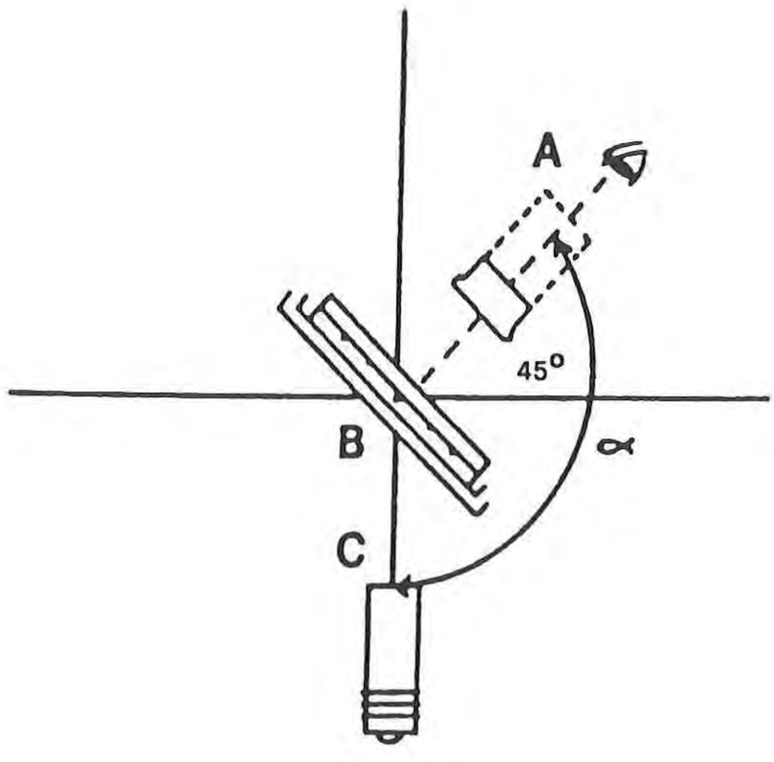

Fig. 2. Graphic illustration of the simplified Henry oblique transillumination (SHOT) technique of viewing colonies for the initial recognition of listeriae colonies that appear with a distinctive bluish cast. Note the attainment of the 135° transillumination angle (α) with direct illumination (C) of the colony (B) and the replacement of the scanning light microscope with a hand lens (A).

TABLE 1. Differentiation of most *Listeria* species by the RAP-ID scheme

Species	Hemolytic Activity		Fermentation of:	
	CAMP[a]	Hemolysis[b]	L-Rhamnose	D-Xylose
Listeria monocytogenes	+	–	+	–
L. seeligeri	+	–	–	+
L. ivanovii	–	+	–	+
L. welshimeri	–	–	±[c]	+
L. innocua[d]	–	–	+	–

[a]Detection of hemolytic activity in six hours with staphylococcal β-lysin potentiation

[b]Detection of hemolytic activity in four hours without potentiation

[c]Positive and negative results

[d]Excluding rhamnose-negative strains of *L. innocua*

TITLE: Stress-Strain Relationships and the Effect of Functional Ingredients on Recoverability of Bread as Related to the Cellular and Molecular Studies

PAVINEE CHINACHOTI, DR., AMOS NUSSINOVITCH, DR.

ABSTRACT:

Recoverability of bread was studied by calculating percent recoverable work of bread after it was compressed to a certain degree of deformation. The influence of added different ingredients on the recoverability of bread was studied. It was found that only a very limited number of ingredients can contribute to the recoverable properties of bread. If it will be possible to postpone the staling of the bread, then these ingredients will be found useful in the baking industry of the future. A three parameter model was used to describe compressive stress-strain relationships of bread. The model's constants were found sensitive to different kinds of bread and to A_w to which the bread was adjusted. Molecular mechanisms of bread staling were investigated by determining the starch retrogradation (using Differential Scanning Calorimetry) and the water mobility (using ^{17}O Nuclear Magnetic Resonance). Surfactants were found to retard the retrogradation process but not found to play a major role in improving the recoverability. The drop in bread recoverability over storage time was found to correspond with the decrease in water mobility. This indicates that the water mobility might have a significant contribution in governing the recoverability of the bread.

BIOGRAPHY OF PRESENTER: Pavinee Chinachoti

PRESENT ASSIGNMENT: Principal Investigator, Contract: Fundamental Mechanisms of Molecular Effects of Bread Components on the Recoverability of Compacted Breads; Assistant Professor, Dept. Food Sci. & Nut., UMass.

PAST EXPERIENCE: Lecturer, Teaching Assistant, Dept. Food Science, U. Illinois.

DEGREE HELD: B.S. Biology, Mahidol University, Thailand; M.S. & Ph.D. Food Science, University of Illinois.

STRESS-STRAIN RELATIONSHIPS AND THE EFFECT OF FUNCTIONAL INGREDIENTS ON RECOVERABILITY OF BREAD AS RELATED TO THE CELLULAR AND MOLECULAR STUDIES

PAVINEE CHINACHOTI, DR., AMOS NUSSINOVITCH, DR.

University of Massachusetts
Department of Food Science
Amherst, MA 01003

INTRODUCTION

There is an increasing need for a shelf-stable bread with good recoverable "resiliency" properties. In order to check bread's mechanical properties it is necessary to get information about stress-strain relationships. Very few attempts have been made to model the stress-strain relationship in the entire deformation range (i.e., from zero to about 70-80% deformation). Therefore, one of the objectives of this work was to test the applicability of a three-parameter empirical exponential model for the compressibility of bread, and to check its sensitivity to changes in bread content.

Much information can be found on bread firmness testing; however, there is still a need for evaluation of other mechanical parameters of bread. Bread crumb is a chewy material that has an aerated cellular nature and generally does not behave as an ideally elastic material. It is, in fact, viscoelastic and the range of stresses over which bread crumb behavior is linearly elastic is low, narrow, and very poorly defined (1).

A sigmoid compressive stress-strain relationship is a familiar characteristic of many spongy baked goods. The three main parts of the stress-strain relationship are the deformability of the intact structure, the region where cell walls collapse as a result of buckling or fracture and densification when the collapsed wall materials are compressed.

The use of several methods to characterize bread crumb texture has been reported by many investigators (2-8). A wide range of instruments have been used to measure the applied force and the deformation of bread crumb samples. A common test is based on the use of the Baker compressimeter, which can be utilized to measure the deformation corresponding to an applied force, or the force which is required to attain a given deformation (9,10).

Since many additive manufacturers claim to improve bread "elastic" properties, the necessity of a simple test, which can give useful information on the "resiliency" of bread, while being uncomplicated to perform is apparent. As a second area of study, this work also investigates the recoverability properties of different kinds of bread over a storage period, using a simple technique, which has been used for other food materials (11). Thirdly, bread recoverability in relation to staling was studied, since the quality loss during storage includes the loss in its resiliency, accompanied by the crumbliness. Much has been speculated and hypothesized about the bread staling process being affected by various molecular interactions that result in quite a dramatic change in the bread functionality (12-14). Regardless of the high interest among food scientists, the molecular changes in bread are still not yet well understood, primarily due to the lack of physico-chemical analytical techniques. For this obvious reason, we believe that, in order to improve the bread functionality (recoverability or resiliency in this case), one needs to understand the system on its molecular and microscopic/macroscopic level.

On the molecular level, three possible contributions were suggested to explain bread staling in terms of textural changes: a) starch retrogradation or recrystallization of the starch polymers that had been melted during baking (15, 16); b) conformational modification of the protein (gluten) structure; and c) a partial redistribution of moisture from the gluten to the starch fraction (12, 17). Addition of an anti-staling agent, such as mono-/di-glycerides, sodium stearoyl lactylate, and sucrose esters, are often applied to soften the bread over a storage period (18-21). This has been speculated to be due to the interaction between the additive and the starch that prevents the starch from retrogradation (recrystallization). In addition, most of these additives are surfactants and they have also been proposed to emulsify the dough, forming a layer or a barrier between hydrophilic and hydrophobic compartments (19). Gluten, once denatured by the baking process, released its water of sorption (due to its denaturation and thus loss in its ability to adsorb water). This water has been thought to diffuse to its close vicinity, the starch. Therefore, once the starch gains moisture, it becomes better plasticized and recrystallizes. With surfactants added, the surfactants could form a moisture barrier as described above and thus help to prevent the moisture from reaching the starch. As a result, less starch recrystallizes.

Another alternative proposed mechanism was that these anti-staling surfactants interact with amylose (14, 22) and possibly with amylopectin (23). Much has been discussed about this amylose-surfactant complex to play an important role during bread staling (e.g., 14). Unfortunately, most of the retrogradation during staling has been believed to be mainly due to amylopectin recrystallization (amylose leaches out from starch granules during baking and has been known to precipitate or crystallize completely within hours after baking (24); thus, the rest of starch crystallization is believed to be due to amylopectin.)

One of the major problems in scientific interpretation of this phenomena is that gluten itself has not been much studied in terms of its conformation and interaction with other bread ingredients. Moreover, physico-chemical study of gluten structure in bread is extremely difficult and has been a great obstacle to this study. With many unproven proposed mechanisms discussed above, controlling bread textural property during storage has been extremely difficult. Therefore, this work was done in order to evaluate the bread mechanical properties, its cellular structure, starch retrogradation and water mobility, as a function of various parameters known to influence the extent of bread staling, such as moisture, sugar, surfactants, flour and storage condition. Results of such coordinated experimentation could lead to a better understanding of the key components and their reactions controlling the mechanical properties of a bread during storage.

MATERIALS AND METHODS

Different kinds of breads used for this study and bread preparation

Commercial sliced bread purchased at a local supermarket as well as bread baked at our laboratory was used for testing. Typical straight dough bread formula (Table 1) was evaluated for the study of recoverable work and for studying the applicability of an empirical mathematical model. After baking the loaves were cooled for one hour, weighed and volumes were measured by rapeseed displacement. The loaves were stored, double wrapped in polyethylene bags until tested, under ambient conditions. Another formula of standard bread was used (Table 2). In this case levels of sucrose, flour types, surfactants, humectants and sources of lipids as well as gluten levels were changed and checked for their influence on recoverability.

Table 1: Straight Dough Formulation*

Ingredients	Formula (by weight)
Flour	100.0
Water	60.0
Active dry yeast	2.0
Salt	1.5
Sugar	4.7
Nonfat dry milk	2.0
Shortening	3.0

*Mix time 12 min (Hobart mixer model D-300), dough temperature 90F; flour time= 15 min; intermediate proof 10 min; proofed for 55 min, baked 20 min at 380F (Gerald Commercial Inc., model 680-z), specific volume 5.42 cm^3/g.
(This commercial process was used for the evaluating of the concept of recoverability and checking the validity of the empirical model.)

Table 2: Standard Bread Formula*

Ingredients	Formula (by weight)
Flour	800.0
Water	480.0
Margarine	42.0
Sugar	37.5
Active dry yeast	14.6
Salt	12.0

*Used for checking the effects of sucrose, %RH, flour types, surfactants, gluten and methocel on recoverability of bread.

Moisture Determination

Moisture loss content determination was measured by drying bread specimens in a vacuum oven at 60°C and 30" Hg for 24 h.

Mechanical Testing

Flat, cylindrical specimens were prepared from the bread slice using a cork borer, avoiding the crust. The bread was sliced using an electric knife (Hobart) and a guide to keep the side perpendicular and the size constant The specimens had a diameter of 25 mm and thickness (height) on the order of 25 mm. (Exact dimensions were taken using a caliper). The specimens were taken from the center of each slice, and were compressed between parallel lubricated plates at a speed of 10 mm/min using an Instron Universal Testing Machine model 1000. The Instron was interfaced with a MacIntosh computer (2MB RAM and 40MB disk) through a Strawberry Tree ACM1-12 interface card. Software was developed for the control of the machine during the data acquisition process and for subsequent data processing. The latter included conversion of the machine's voltage vs real time output to force deformation or stress-strain relationships. The specimens were subjected to compression-decompression tests to various deformation levels (and up to 75% deformation). The results of the compression-decompression tests are given as percent recoverable work from the total work necessary for deformation to any particular deformation level. Percent recoverable work was calculated in accordance to a procedure which was used before (11).

$$\text{\% recoverable work} = \frac{\text{area under the decompression curve}}{\text{area under the compression curve}}$$

Time study for 240 h was done for some bread specimens. Percent recoverable work was calculated in accordance to what was explained before.

The Proposed Model

The characteristics of typical compressive stress-strain relationship of bread can be described by the model (25):

$$\sigma_E = \frac{C_1 * (1-\exp -(C_2 * \varepsilon_H))}{(C_3 - \varepsilon_H)}$$

where σ_E is the engineering stress and ε_H the Hencky's strain described by the following:

$$\varepsilon_H = \ln \left(\frac{H_o}{H_o - \Delta H} \right)$$

while H_o is the original height of the sample and ΔH its total deformation. The engineering stress was used since the area of the bread specimen is not changing significantly during the compression test. The three constants C1, C2 and C3, have the following relationships to the curve's shape: C1 determines the absolute magnitude of the stress and its units. The constants C2 and C3 determine the exact shape of the shoulder of the stress-strain curve. C3 determines the asymptotic value of the stress, in other words, it represents the strain at which the densification of the cell wall material is becoming the dominant deformation mechanism.

Analysis of Starch Retrogradation

The degree of starch retrogradation in the samples was measured by the endothermic energy absorbed upon melting of the starch. This was measured by heating the samples under DSC (Differential Scanning Calorimeter DSC 2, Perkin Elmer) at a rate of 20°C per minute, using an empty hermetic pan as a reference. Approximately 10 mg of sample was used for each test.

Analysis for Water Mobility

The ^{17}O NMR spectra were obtained using a Varian XL-300 spectrometer operated at 40.67 MHz. The acquisition parameters included 15,000 Hz of spectral width, 15 μsec of pulse width 4,000-600,000 number of scans and 15 μsec of recycle time. The T2 relaxation time was measured from the linewidth at half height ($\Delta\nu$) by the equation $T2 = 1/\pi\Delta\nu$.

Results and Discussion

The relationship between the recoverable compressive work and the deformation level for a standard bread (Table 1) six hours and 24 hours after baking is demonstrated in Table 3. It shows that percent recoverable work decreased as the level of compressive deformation increased. At small deformation (10 to 20%) the recoverable work was between 50-70 percent and declined to about 16-23% when deformation levels were about 50-75%. Bread has a structure of closed pores that ruptured in the compression, and cell walls that collapsed or fractured, thus weakening its structure (26). The higher the percent of deformation the more unrecoverable damage occurs and that's the reason for finding low values of recoverability (irreversible damage to the cellular structure) when percentage of compressive deformation was high.

Table 3: Recoverable work of bread crumb (Formula in Table 1) under various degrees of deformation (six hours and one day after baking).

% of deformation	% Recoverable work 6 h after baking	 24 h after baking
10	69.8±0.7	62.1±4.8
20	50.3±4.9	42.7±3.0
30	39.2±4.1	31.7±4.2
40	31.2±1.3	24.2±2.7
50	23.3±0.8	19.0±2.3
60	21.6±0.5	15.0±2.3
75	16.5±0.3	13.8±0.2

*Results are mean of three determination ± standard deviation.

After about 24 hours the bread lost 10-25 percent of its recoverability. This is not surprising when one considers that other mechanical properties are also changed dramatically after 24 hours. For example it was found for bread crumb (1) that the mean value for force measured at 10% deformation changed by a factor of 3.3 after 24 hours.

A time study experiment was done in order to check the influence of time on the recoverability of standard bread (Table 1). The bread specimens were compressed to deformation levels of 10-75 percent. Percent recoverable work was calculated and plotted against storage time as presented in Figure 1.

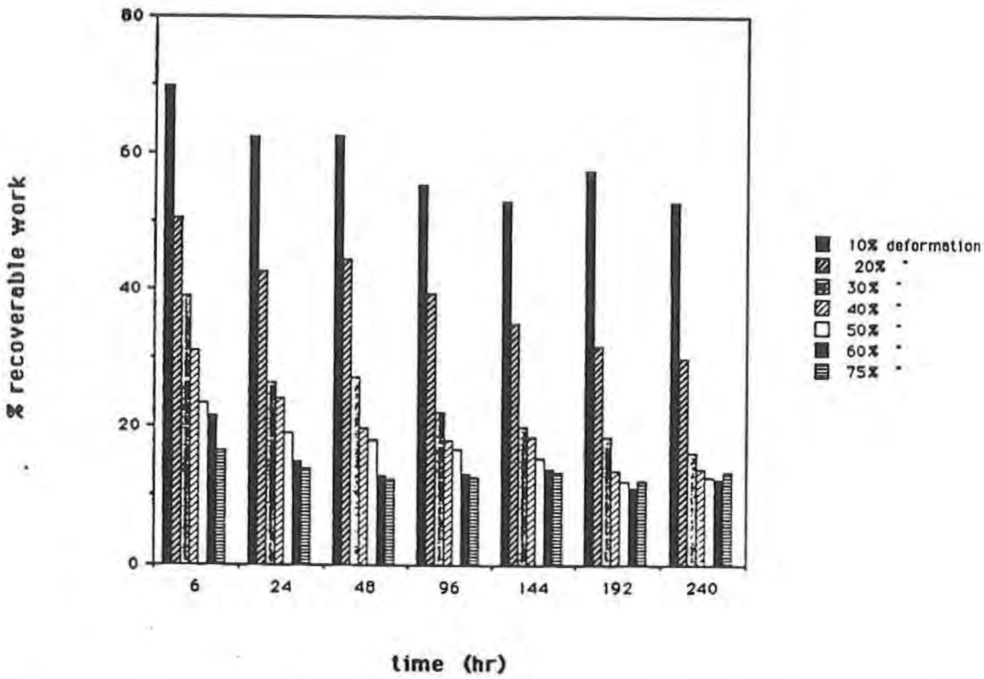

Figure 1. The influence of time on the recoverability of standard bread (Table 1).

From this figure it is evident that bread is losing its recoverability with time. The higher the percent of compressive deformation, the more damage is done to the bread structure, which results in poor recoverability properties. The recoverable work of bread that decreased upon storage could be influenced by the 5% moisture loss (observed over the 10-day storage) and other physico-chemical changes in the structural components that resulted in a dryer texture with less resiliency. This result will be elaborated further in later sections.

Exponential model for the stress strain relationship of bread

A mathematical model describing the stress-strain relationship of bread was suggested and found to be appropriate. The fit of the model to compression data of pumpernickel, dense white, and country oat bread is demonstrated in Fig. 2.

The magnitude of the model's constants and the mean square error (MSE) of the fit are summarized in Table 4. It is clear that the proposed model can represent the stress-strain relationship of these breads reasonably well. In the bread tested, the magnitude of C3 was on the order of 1.27-1.34. This parameter represents the strain level at which

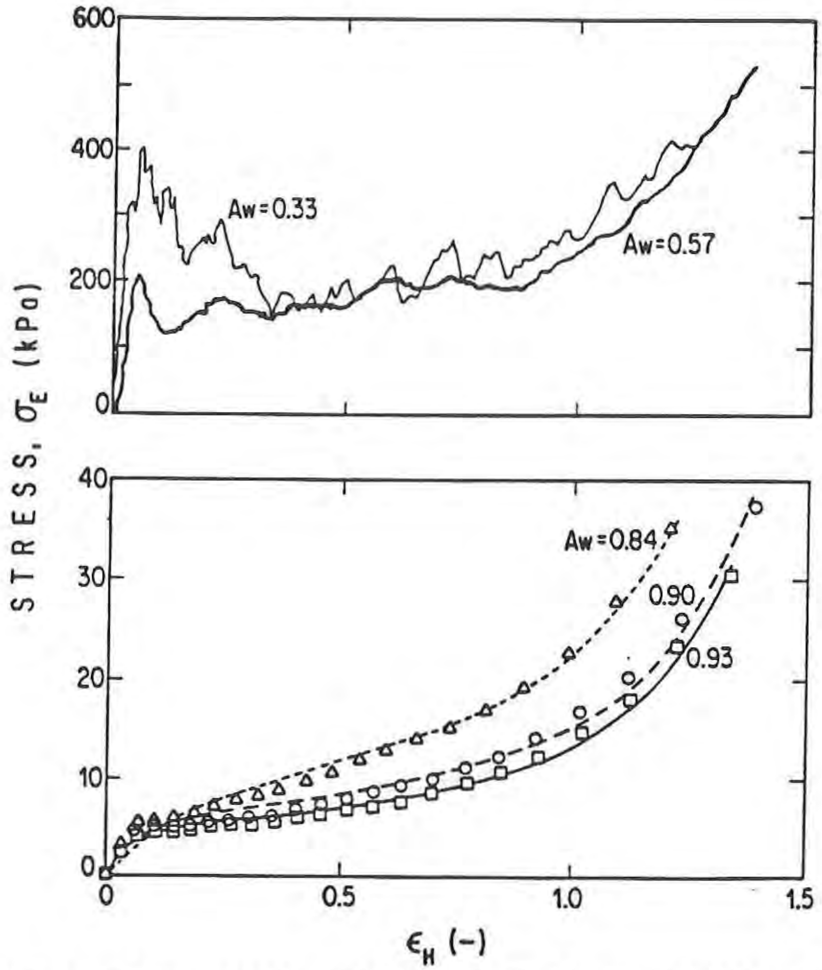

Figure 2. Top: Typical stress-strain curves for compression of standard bread conditioned at 33 and 57% RH. Bottom: Compressive stress-strain relationship of a standard bread conditioned at 84,90 and 93% RH. Dots are experimental values and solid lines are the fit of the model.

densification of the cell wall material becomes the dominant deformation mechanism (parallel to about 75% of deformation). Presenting the strain as Hencky's (or "true") strain has an appreciable effect on the shape of the stress-strain relationship, which is mainly manifested by a less prominent "shoulder". Using Hencky's strain instead of engineering strain (26) has at least one big advantage. It eliminates the possibility of getting C3 values with little or no physical significance as in the case of getting values higher than unity when engineering strain was used (26). The magnitude of C2 was on the order of 5.4-10.6 and that of C1 was 6.8-8.2. Dense white bread was found with the higher

C1 value 8.2 in comparison to pumpernickel bread having the lower C1 value of 6.8. The higher the C1, the higher the magnitude of stress. The model was found sensitive to different breads, which varied in formulation and possibly in history.

Table 4: Regression parameters of the compressive stress-strain relationship of three breads.

Bread	C1 (kPa)	C2 (-)	C3 (-)	MSE*
Pumpernickel	6.8	5.4	1.27	0.99
Dense White Bread	8.2	10.6	1.34	0.43
Country Oat Bread	7.5	7.2	1.27	0.56

*MSE is the mean square error.

The model was found also sensitive to a standard bread baked in our lab that was adjusted to water activity levels of 0.75-0.93 (Table 5) and those in Fig. 2. For the bread samples conditioned to 0.33 and to 0.57 water activity levels, a curve of the form shown in Fig.2 was obtained. The samples conditioned to Aw=0.33 and 0.57 collapsed by brittle fracture. Bread conditioned to Aw higher than 0.75 did not show brittle fracture and appeared to be collapsing by elastic buckling. These results are partially similar to what was found before for a food sponge conditioned to Aw=0.33 (27).

Table 5: Regression parameters of the compressive stress-strain relationship of standard bread conditioned to different water activity levels.

Aw	C1 (kPa)	C2 (-)	C3 (-)	MSE*
0.75	22.6	5.4	1.59	5.53
0.81	16.9	4.6	1.57	2.53
0.84	13.1	6.3	1.59	0.89
0.90	9.7	14.2	1.64	0.78
0.93	7.6	18.0	1.57	0.56

*MSE is the mean square error

The fit of the model to the compression data of the bread conditioned to Aw of 0.75-0.93 is demonstrated in Fig. 2 and in Table 5. C1 and C2 were found to be sensitive to Aw. The magnitude of C1 was on the order of 7.6-22.6. The magnitude of C2 was on the order of 4.6-18. C3 has more or less the same numerical values 1.57-1.64 and demonstrated the asymptotic level of the stress. Thus C1 and C2 can be served as a practical way to give information on changes in the conditions of the bread in accordance to its moisture.

<u>Effects of ingredients on recoverability</u> (Bread obtained from formula in Table 2)

a) <u>Effect of %RH (moisture)</u>

Bread crumb samples of breads made with 5% and 8% additional sucrose (flour basis) were equilibrated against 75 and 85% relative humidity. Each sample was stored for a time study and the percent recoverable work calculated was found to decrease with % deformation as was explained before. Samples with a higher % RH showed a better recoverability.

b) <u>Flour types</u>

Bread baked with hard wheat flour was found to have higher recoverability compared to bread made of soft wheat or all-purpose flour. The soft wheat flour bread showed a decrease of 5-12% in the percent of recoverable work as compared to the hard wheat flour. The difference is most likely because of the different content of gluten in these breads. Hard wheat flour contained the highest level of gluten compared to other flours. The microscopic study for these three different kinds of bread showed cells which are different in size, shape and thickness. The hard wheat flour gives more round-shaped cells with thin cell walls and continuous and unbroken structure. The soft wheat bread had a larger cell size with broken cell walls. The all purpose flour gave a smaller cell size (compared to soft wheat flour) but has also broken cell walls.

The recoverable work for enriched gluten bread was found to be higher than for a standard bread. Time study of bread specimens with 3.3% added gluten showed that if the bread sample is compressed to small deformation like 20 or 30%, the enriched gluten bread will keep its advantage in recoverability only for days but not for weeks. Similar result was found for bread enriched with 0.5% methocel.

c) <u>Surfactants</u>

Breads containing 0.5% (flour basis) of Dimodan^{R}, SSL and sucrose ester were stored and sealed in cans with a minimum head space for 4 days. The recoverability of all the samples decreased with a higher degree of deformation (similar to data discussed above). SSL seemed to give a slight improvement in the recoverability but this improvement decreased with storage time. Sucrose ester, on the other hand, had a slightly negative impact on the recoverability, while Dimodan[R] showed no effect at all.

Only very limited number of ingredients can contribute to the recoverable properties of bread. If it will be possible to postpone the staling of the bread then these ingredients will be found useful in the baking industry of the future for achieving higher recoverability.

Molecular Changes during Bread Staling

Components that gave a higher value of recoverability include moisture, gluten, SSL and Methocel[R]. Unfortunately this effect was small and disappeared with storage time. In addition, result for sucrose ester, which even had a slight negative impact on the bread recoverability, was surprising since it has been claimed to retard bread staling (by retarding starch retrogradation). All of these observations seem to indicate that a time study for starch retrogradation and water mobility should provide a clearer indication of what contributed to such loss in recoverable work. It also may lead to understanding how anti-staling additives work.

First we looked into the extent of starch retrogradation in aged bread. In analogy to aged gravy, the starch crystallization process could cause grainy, nonhomogeneous and rigid product. The DSC results shown in Table 6 indicated that the surfactants did retard the degree of retrogradation in bread (expressed in terms of enthalpy of melting the starch in the samples). All bread samples treated with SSL, Dimodan[R] and sucrose ester were not significantly different in retrogradation.

Table 6: The effect of Surfactants (percent, flour basis) on the Retrogradation of Bread at 22°C after 7 days.

Sample	Enthalpy (cal/g sample) *
Control	0.226 ± 0.012^{a}
+ 0.5% Dimodan[R]	0.180 ± 0.100^{b}
+ 0.5% SSL	0.170 ± 0.222^{b}
+ 0.5% Sucrose ester (HLB = 16)	0.160 ± 0.150^{b}

*Results are mean of at least three determination ± standard deviation. Means within the same column followed by the same superscript are not significantly different (p=0.05).

Although the surfactants retarded the starch retrogradation significantly, the recoverability property did not seem to improve greatly and kept decreasing with the storage time.

Another mechanism for bread staling investigated was water released from the gluten. It has been reported that water mobility (^2H NMR) in a bread sample decreased with storage time and this was explained to be due to the incorporation of the water molecules into the starch crystalline lattice upon retrogradation (recrystallization)(28). This water was hypothesized to be released from the gluten (which was denatured during baking and lost its water sorption ability). If this mechanism was the case, the added surfactants, with their emulsifying properties, could form a film between the hydrophilic regions (mostly starch) and the hydrophobic regions (of the gluten) and this prevents such moisture migration. Thus, less water would be available to plasticize the amorphous starch in order to allow recrystallization.

In order to check this point, an ^{17}O NMR water mobility was measured and expressed in terms of T_2 relaxation time. In Fig. 3, T_2 of various breads decreased with the storage time, as previously observed (28). For the case of bread with added surfactants, T_2 was always lower and decreased at an even faster rate than that of the control. This was contradictory to the proposed hypothesis. If the decreased water mobility was due to the starch recrystallization, slowing down the starch recrystallization process (by surfactants) should have resulted in less decrease in water mobility (T_2). Our result showed the opposite.

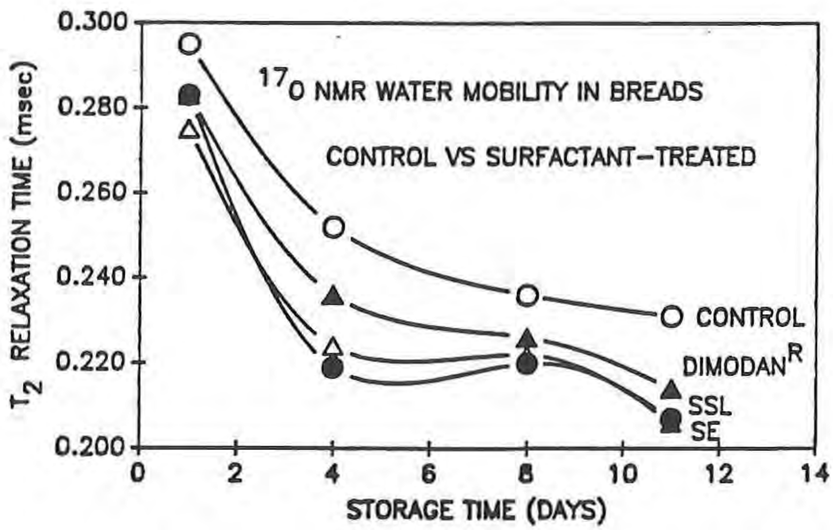

Figure 3. Transverse relaxation time of bread with different surfactants during storage. STD means bread without surfactant and SSL, SE and Dimodan represent the bread sample with the corresponding surfactants.

Therefore, it was concluded that the decreased recoverability was due to other physico-chemical changes in either the gluten and/or noncrystallizing, amorphous starch, rather than due to the crystallizing starch.

From a slightly different perspective, this decreased recoverability could also be explained by looking at the plasticizing ability (mobility) of the water. Surfactants reduced the T_2 of the bread (Fig. 3, day 1) and this decreased water mobility has made the water less able to plasticize and thus less starch retrogradation was observed (Table 6). There was also a possibility for a direct surfactant-amylopectin interaction as well as surfactant-gluten interaction that may complicate this picture. Unfortunately, it was not possible to differentiate how much water was associated with gluten or starch at a given time. Therefore, no further conclusion was made. However, it should be emphasized here that bread recoverability in surfactant-treated bread improved very little, if not at all, despite the lowered degree of starch retrogradation. This seems to lead to a conclusion that either the gluten or the noncrystallizing starch played a more important role in controlling the bread recoverability. One important observation found was that all breads that lost their recoverability over time also showed a decrease in water mobility, indicating that during staling water became less efficient to plasticize and thus resulted in a decreased recoverability. It is speculated here that this effect of water is mainly due to its influence on the gluten and/or the noncrystallizing starch as discussed above.

Much is yet to be desired in understanding the mechanism of bread staling. The relationship between the bread recoverability (resiliency) and water mobility along with physico-chemical changes in the polymers could lead to a better understanding of the staling process. More sophisticated work is needed in the area of gluten conformational changes, water migration, surfactants starch interactions and their effect on the thermo-mechanical properties, etc., have to be measured in comparison with the textural changes during storage. This information is severely lacking in this field.

REFERENCES

1. Lasztity, R. 1980. Rheological studies on bread at the Technical University of Budapest. J. of Texture Studies 11:81.

2. Hibberd, G.E. and Parker, N.S. 1985. Measurements of the compression properties of bread crumbs. J. Texture Studies 16:97.

3. Dahle, L.K. and Sambucci, N. 1987. Application of devised universal testing machine procedures for measuring texture of bread and jam-filled cookies. Cereal Foods World 32: 466.

4. Kamel, B. 1987. Bread firmness measurements with emphasis on baker compressimeter. Cereal Foods World 32:472.

5. Walker, C.E., West, D.I., Pierce, M.M. and Buck, J.S. 1987. Cake firmness measurements by the Universal testing machine. Cereal Foods World 32:477-480.

6. Joensson, T. and Toernaes, H. 1987. The effect of selected surfactants on bread crumb softness and its measurement. Cereal Foods World 32:482.

7. Baker, A.E. and Ponte, J.G. JR 1987. Measurement of bread firmness with the Universal Testing Machine. Cereal Foods World 32:491.

8. Baker, A.E., Walker, C.E., and Kemp, K. 1988. An optimum compression depth for measuring bread crumb firmness. Cereal Chemistry 65:302.

9. Platt, W. and Powers, R. 1940. Compressibility of bread crumb. Cereal Chemistry, 17:601.

10. Crossland, L.B. and Favor, K.H. 1950. A study of the effect of various techniques on the measurement of the firmness of bread by the Baker compressimeter. Cereal Chemistry 27:15.

11. Lee, Y.C., Roseanu, J.R. and Peleg, M. 1983. Rheological characterization of tofu. J. of Texture Studies 14:143.

12. Willhoft, E.M.A. 1973. Mechanism and theory of staling of bread and baked goods, and associated changes in textural properties. J. of Texture Studies 4:292.

13. Maga, J.A. 1975. Bread Staling. CRC Critical Reviews in Food Technology (April):443.

14. Kulp, K. and Ponte, Jr., J.G. 1981. Staling of white pan bread: fundamental causes. CRC Critical Reviews in Food Sci and Nutrition 15:1.

15. Fearn, T. and Russell, P.L. 1982. A kinetic study of bread staling by differential scanning calorimetry. The effect of loaf specific volume. J. Sci. Food Agric. 33:537.

16. Russell, P.L. 1983. A kinetic study of bread staling by DSC. Verlag Chemie. 35:277.

17. D'appalonia, B.L. and Morad, M.M. 1981. Bread Staling. Cereal Chem. 58:186.

18. Dragsdorf, R.D. and varriano-marston, E. 1980. Bread Staling: X-ray diffraction studies on bread supplemented with β-amylases from different sources. Cereal Chem. 57:310.

19. Pisesookbunterng, N. and D'appolonia, B.L. 1983. Bread Staling Studies. I. Effect of surfactants on moisture migration from crumb to crust and firmness values of bread crumb. Cereal Chemistry 60:298.

20. LaBell, F. 1983. Dough conditioner adds to volume of freestanding breads. Food Processing 44:34.

21. Anon, 1981 Crumb softener delays staling of bread. Food Development 15:48

22. Zobel, H.F. 1973. A review of bread staling. Baker's Dig. 47:52.

23. Eliasson, A. -C., Ljunger, G. 1988. Interactions between amylopectin and lipid additives during retrogradation in a model system. J. Sci. Food Agric. 44:353.

24. Lagendijk, J. and Pennings, H.J. 1970. Relation between complex formation of starch with monoglycerides and the firmness of bread. Cereal Science Today 15:354.

25. Swyngedau, S., Nussinovitch, A., Roy, T., Peleg, M. and V. Huang 1990. Comparison of four models for the compressibility of breads and plastic foams J. of Food Science (submitted)

26. Peleg, M. Roy, I., Campanella, O.H. and Normand, M.D. 1989 Mathematical characterization of the compressive stress-strain relationship of spongy baked goods. J. Food Sci. 54:947.

27. Attenburrow, G.E., Goodband, R.M., Taylor, L.J., and Lillford, P.J. 1989. Structure, mechanics and texture of food sponge. J. Cereal Sci. 9:61.

28. Leung, H.K., Magnuson, J.A. and Bruinsma, 1983. Water binding of wheat flour doughs and breads as studied by deuteron relaxation. J. Food Science 48:95.

TITLE: Optimization of Functional Ingredients in a Low Water Activity Bread Using Response Surface Methodology

*LINNEA M. HALLBERG, MS., TOM C.S. YANG, DR., IRWIN A. TAUB, DR.

ABSTRACT:
A long shelf life, low water activity bread was produced with various levels of stabilizing ingredients including sucrose ester, sorbitol, glycerol, and lactic acid. The quality of bread after long term storage at 40^{o}F and 100^{o}F was determined by sensory evaluation and objective measurements such as texture, color, specific volume, and starch retrogradation as determined by differential scanning calorimetry. Combination of these stabilizing ingredients was optimized by a response surface methodology based on the quality attributes. A formula with 1.2% sucrose ester, 4% sorbitol, 2% glycerol, and 0.08% lactic acid provides the most acceptable shelf stable bread.

BIOGRAPHY OF PRESENTER: Linnea M. Hallberg

PRESENT ASSIGNMENT: Food Technologist, Advanced Foods Branch, Technology Acquisition Division, Food Engineering Directorate.

PAST EXPERIENCE: Project officer: modernization of Navy bakeries; packaged shelf stable bread; compact springback bread; support to modernization of M1945 mobile field bakery; evaluation of foreign military field bakeries; thermohydrostabilized canned cake development and development of field bread bases and dough conditioning mixes.

DEGREE HELD: B.S. Food Science, Framingham State College.
M.S. Food Science and Nutrition, Framingham State College.

OPTIMIZATION OF FUNCTIONAL INGREDIENTS IN A LOW WATER ACTIVITY BREAD USING RESPONSE SURFACE METHODOLOGY

*LINNEA M. HALLBERG, MS., TOM C.S. YANG, DR., IRWIN A. TAUB, DR.

Advanced Foods Branch
Technology Acquisition Division
Food Engineering Directorate
U.S. Army Natick RD&E Center
Natick, MA 01760-5018

INTRODUCTION

A bread with low water activity and reduced pH will not support microbial growth and should be ideal for long term storage (Graham, 1980). However, all starch containing foods are prone to staling, and intermediate moisture foods containing sugar tend to discolor (i.e., browning effect), especially after long term storage at high temperatures (Troller and Christian, 1978). Previous shelf life studies on bread had a maximum storage duration of 2 weeks (Russel, 1983), whereas this investigation examined the effects of 24 weeks of controlled storage. The use of several functional ingredients, such as sucrose ester, sorbitol, glycerol, and lactic acid, to prevent or reduce staling (Chung et al., 1981), to prevent microbial spoilage (Harrigan and Breene, 1989; Pierce and Walker, 1987), and to increase acceptance (Leung, 1983), was also investigated. These ingredients are found in various long shelf life bread products developed for military field feeding (Anonymous, 1989). They act and interact in multiple ways, influencing the form and association of the structural components (gluten and starch) and the mobile components (water and lipids). The association of water, when altered by the functional ingredients, is evidenced by changes in the ability of water to migrate, lubricate, and affect reaction rates involving the structural components (Czuchajowska and Pomeranz, 1989; Hoseney, 1983; Krog et al., 1981; Leung, 1983; Lim et al., 1989; Chungcharoen and Lund, 1987; Pomeranz, 1985; Joensson and Toernaes, 1987). For the purpose of this investigation, data will be interpreted in terms of optimization of acceptability of bread during storage. Optimization is defined by both instrumental characterization and subjective sensory analysis.

Sucrose esters, having documented anti-staling and antimicrobial functions, have been used in bread making since 1976 (Chung et al., 1981; Chinachoti, 1988; Chung et al., 1981; Harrigan and Breene, 1989; Pierce and Walker, 1987). A stable complex is achieved by having the fatty acid groups enveloped by the helical structure of the starch amylose

(Mitsubishi-kasei Foods, 1989). It has been shown that the natural flour lipids and the added shortening can be partially replaced with the higher HLB (hydrophilic-lipophilic-balance) sucrose esters (Pomeranz, 1985). These studies showed that the most effective esters for increasing loaf volume and tenderness are the high range HLB esters (>11) with higher monoester content (Breyer and Walker, 1983). The ester used in these studies is a sucrose stearate with a monoester concentration of 75% and an HLB of 16; the same as that currently used in military pouch bread (Anonymous, 1989). The currently used levels are between 0.5-1.0% total weight basis. This study investigated levels between 0 and 2% total weight basis.

Glycerol and sorbitol have been used in previous long shelf life breads to lower water activity to safe levels (Pomeranz, 1985). Both bind approximately equal amounts of water and are classified as humectants. The ratio of glycerol to sorbitol was varied between 0 and 1.0 to balance the bitterness and sweetness. Sorbitol, in addition to being an excellent humectant, is used to reduce the problematic chemical notes (glycerol) or sourness (lactic acid) upon long term storage noticed in previous studies (Morgan, 1986). To optimize the levels of these ingredients singularly or synergistically, a response surface methodology (RSM) was used in conjunction with measurements of such quality parameters as texture, color, water activity, and sensory ratings. Differential Scanning Calorimetry (DSC) was used to provide an objective means to quantify crystallinity (staling) in bread (Czuchajowska and Pomeranz, 1989; Hoseney, 1983; Paton, 1987; Russel, 1983; Zeleznak and Hoseney, 1986).

Response surface methodology allows the simultaneous analysis of many variables with a limited sample size; its theory has been presented elsewhere (Davies, 1954; Cochran and Cox, 1957; Johnson and Leone, 1964; Hill and Hunter, 1966; Myers, 1971; Box et al., 1978; Thompson, 1982), and its adequacy for the optimization design and data analysis of multivariables has been demonstrated by Joglekar and May (1987) and Mudahar et al. (1989). Twenty formulations of bread were produced, packaged, and then stored in controlled temperatures of 40°F and 100°F for 0, 4, 12 and 24 weeks.

The objective of this paper was to determine the best combination of these ingredients and their optimum levels to produce a highly acceptable shelf stable bread formula suitable for long term storage.

MATERIALS AND METHODS

Low water activity bread was baked by the AACC straight dough method (AACC, 1976) using a hard wheat flour (12.5% protein) and a basic formula as listed in Table 1. The doughs were developed in a Hobart 20-qt mixer with a standard dough hook. Various levels of functional ingredients (i.e., sucrose ester, glycerol, sorbitol, and lactic acid) were added

TABLE 1. Basic formula of low water activity bread.

%	Ingredients	Type	Source
100	Flour	(12.5% protein) Hard Wheat Bread	General Mills
47.0	Water		
3.8	Yeast	Instant active dry	Red Star
10.0	Shortening	Cottonseed and palm oil (100h AOM Hydrogenated)	Bunge
3.0	Sugar	Bakers Special Fine, granulated	
1.5	Salt	Iodized, regular grind	Morton
(40ppm)	Ascorbic Acid	USP	Cain
(10ppm)	Potassium Bromate	USP	Cain
0.5	Sodium Stearoyl-2-lactylate	FCC	Grinsted
0.3	Calcium Proprionate	FCC	Mycoban
1.0	Propylene Glycol	FCC	Dow

after the gluten was fully hydrated at room temperature. Ten oz doughs were divided, rounded, machine molded, panned, and proofed at 90^{o}F and 90% relative humidity until 1/2 inch above the pan. Baking was done in a Middleby Marshall Rotary oven at 375^{o}F until an internal temperature (I.T.) of 200^{o}F was obtained. Breads were cooled to 100^{o} F (I.T.) and hermetically packaged in trilaminated pouches (polyester, aluminum foil, polyolefin), under a partial vacuum after nitrogen flush. The breads were immediately placed in 40^{o} and 100^{o}F storage for 4, 12, and 24 weeks. Duplicate samples were withdrawn, tempered to room temperature, and analyzed following the methods in Table 2. A Computer Aided Design of Experiments (CADE; International Qual-Tech, Ltd., Plymouth, MN) was used with an

TABLE 2. Analytical and evaluation methods of low water activity bread.

Test	Method
Specific Volume	Rapeseed displacement (Cathcart & Cole, 1983)
Texture	Voland Stevens Texturometer (Probe #7; Depth: 10 mm; Speed: 2 mm/sec) (Platt and Powers, 1940.)
Color	Pacific Scientific Spectrogard and Color System Hunter Lab (L values)
pH	Orion pH Meter (AACC, 1983)
Aw	Rotronic Hygroskop (AOAC, 1980)
DSC	Perkin Elmer DSC-4 with TADS data analysis
Sensory	Consumer test: 9 point hedonic, overall acceptance; 9 = like extremely; 1= dislike extremely; n=40

optimization module for the design and analysis of this experiment using response surface methodology. Contours were based on a central composite configuration with three variables and four responses, and results of each response (i.e., texture, color, Aw, and sensory) were obtained. According to the CADE design, 20 sets of functional ingredients were added to the basic formula (Table 3).

RESULTS AND DISCUSSION

In determining the optimum formulation, the first consideration was the effect of ingredients on Aw and the second was their effect on acceptance, color, texture, and staling. These effects were considered both in terms of the fresh (i.e., initial, unstored) bread and the breads stored at selected temperatures.

With the limitation of Aw $\leq$ 0.94 as a clear safety margin and using results from the fresh bread compared at five pH's (Leistner and Rodel, 1976; Rodel et al., 1976), we must choose the optimum from among formulations containing less than 1.8% sucrose ester (Fig. 1 for pH = 5.2).

TABLE 3. Set-up of functional ingredients for low water activity bread optimization experiment.

Run #	% Sucrose Ester	Ratio Glycerol/Sorbitol	% Lactic Acid
1	0.41	0.2	0.03
2	1.60	0.2	0.03
3	0.41	0.8	0.03
4	1.60	0.8	0.03
5	0.41	0.2	0.13
6	1.60	0.2	0.13
7	0.41	0.8	0.13
8	1.60	0.8	0.13
9	0.00	0.5	0.08
10	2.00	0.5	0.08
11	1.00	0.0	0.08
12	1.00	1.0	0.08
13	1.00	0.5	0.08
14	1.00	0.5	0.00
15	1.00	0.5	0.16
16	1.00	0.5	0.08
17	1.00	0.5	0.08
18	1.00	0.5	0.08
19	1.00	0.5	0.08
20	1.00	0.5	0.08

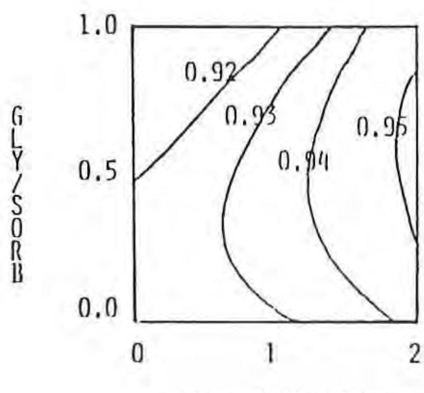

Fig. 1. Contour plots of water activity at different levels of independent variables in bread at pH = 5.2.

The appearance of a clear peak in the response surface for overall acceptance, whose position is essentially unaffected by pH but whose height changes slightly with pH (Fig. 2A, B, C), indicates the optimum

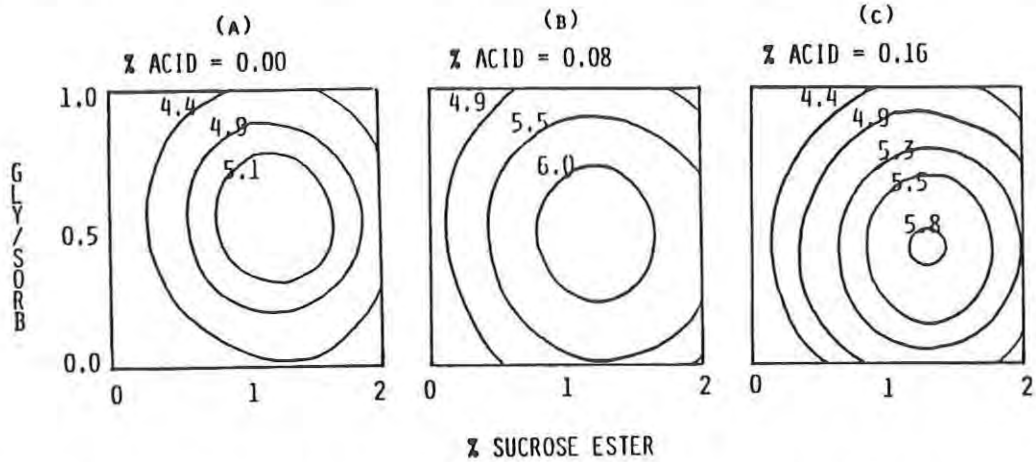

Fig. 2. Contour plots of sensory values at different levels of independent variables in fresh, low water activity breads.

formulation corresponds to 1.2% sucrose ester and ratio of glycerol to sorbitol of 0.5, which amounts to 2% and 4% (total weight basis), respectively, of each humectant; the peak is highest for the breads formulated with 0.08% acid, pH = 4.8 (Fig. 2B). Though the response surfaces tend to show only slopes for the textural and color attributes, they correspond to desirable values in the vicinity of the optimum combination. Textural values are about 400, which can be considered relatively "soft;" color values, which indicate "whiteness" are about 65 (Fig. 3).

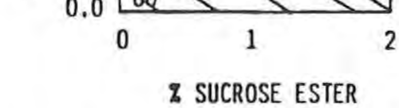

Fig. 3. Contour plots of color (L-value) at different levels of independent variables in fresh, low water activity bread (pH = 4.8).

If it is assumed that the most desirable bread is one that scores highest just after preparation, then the bread formulation as depicted in Fig. 2B is the one to choose. In principle, response surfaces for all three indices of quality should be overlaid to determine the regions where the peaks overlap, which is not appropriate in this case. However, the most desirable bread is also one that retains these desirable qualities despite the stress of long term storage.

STORAGE EFFECTS: SOFTNESS, OVERALL ACCEPTANCE, AND COLOR

The results for breads stored at 40°F and 100°F show that changes do take place, but tend to stabilize eventually. These two temperatures are critical to judging quality retention, because the former promotes staling and should affect texture, whereas the latter promotes darkening of the crumb. Comparison of texture, acceptance, and color changes as a function of time and temperature is instructive.

As Fig 4 shows for 40°F and 100°F, the texture values obtained

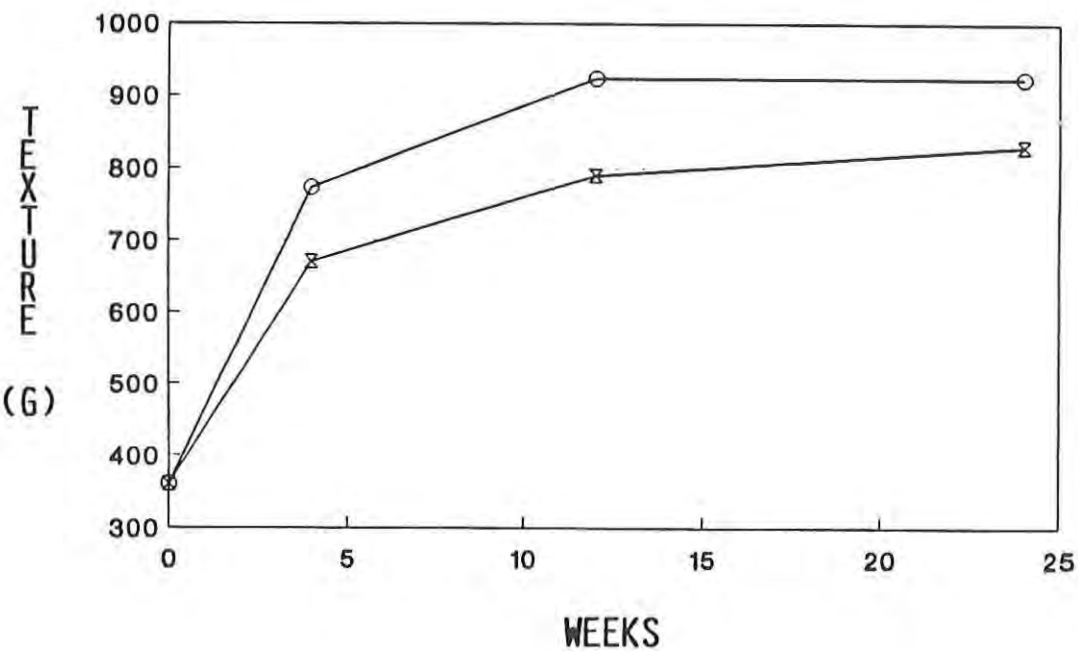

Fig. 4. Texture of optimized low Aw breads stored at 40°F (—⧖—) and 100°F (—⊖—) for up to 24 weeks.

for the optimum formulation by interpolation from the contour diagrams increase rapidly at first and then level off by 12 weeks. The bread becomes harder, but appears to stabilize. Though not shown, the effect is even more pronounced in the breads made with 0.08 and 0.16% lactic acid, the plateau at 40°F being 50% higher for the higher acid bread than for the 0% acid bread. Curiously, the plateau value for the optimum bread is slightly higher when stored at 100°F than at 40°F. Moisture loss from the crumb could be more significant at 100°F and might account for this effect. In principle, reaching a plateau implies that equilibration has taken place and no additional net change in structure is being thermodynamically driven. The 100°F result is particularly relevant, because 24 weeks at this temperature corresponds to three years at 70°F, the shelf life normally required for rations.

Similarly, as Fig. 5 shows for these same two temperatures, the

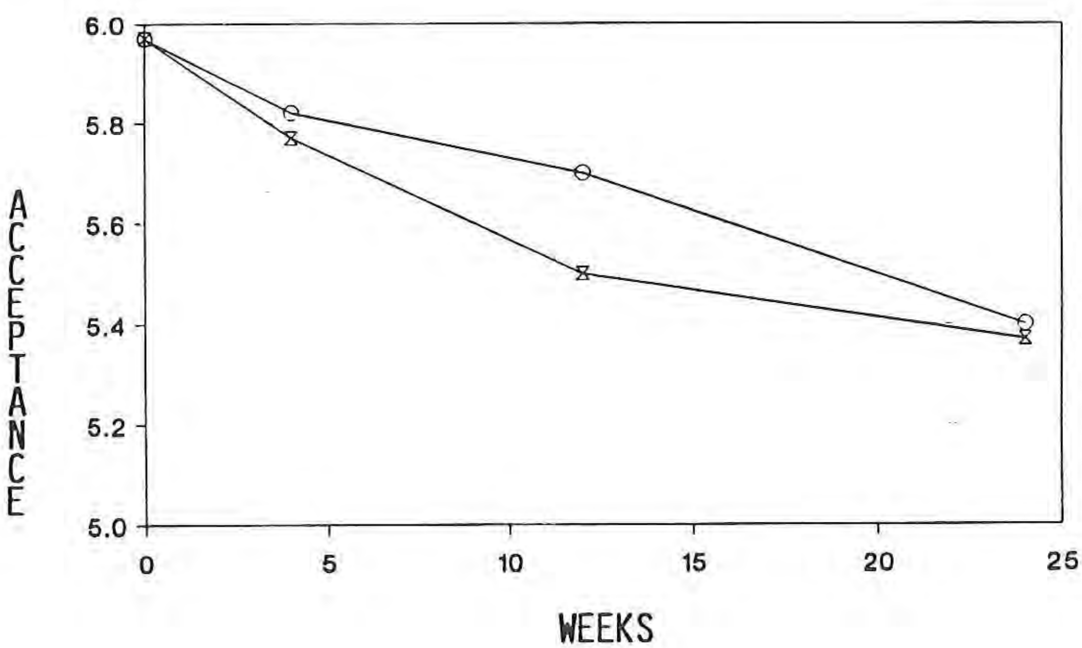

Fig. 5. Sensory evaluation of optimized low Aw breads stored at 40°F (—⧗—) and 100°F (—⊖—) for up to 24 weeks.

overall acceptance of the optimal formulation falls off with time in storage. The response surfaces from which the 100°F values were obtained show generally a flattening, indicating that the proportions of individual ingredients in the formulation do not have a strong influence in the changes taking place that contribute to this falloff.

The lower values perhaps reflect the increase in hardness, and also tend to bottom out as time in storage progresses. Similar trends are seen for the breads stored at 40°F, but the decrease seems to be continuing monotonically.

Results for color change at both temperatures indicate a possible complex set of reactions occurring that affects the lightness value. Figure 6 shows the trends at 100°F. There is an increase in the

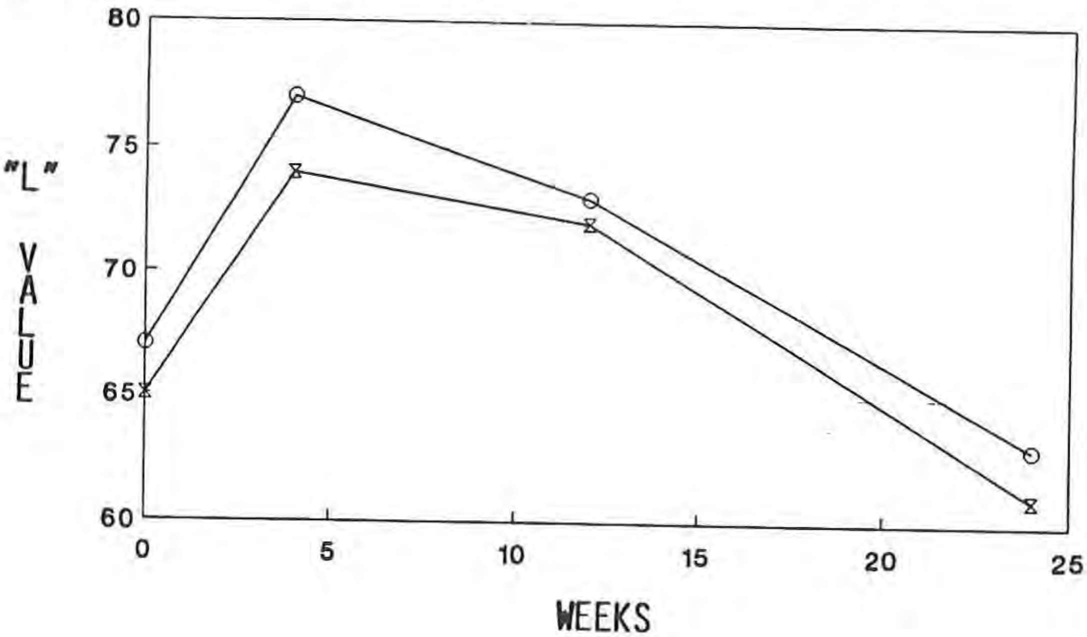

Fig. 6. Color (L-value) of low Aw breads with 0.08% (—⧖—) and 0.16% lactic acid (—⊖—) at 100°F for up to 24 weeks.

lightness (i.e., increasing L-value) at 4 weeks, and then a gradual darkening (i.e., decreasing L-value) thereafter. Acid level has no influence on the color change. Apparently, the compounds responsible for the initial color decompose to less-colored compounds, while other more-colored and less light-reflecting compounds are continually forming and eventually predominate. The increase in lightness can also be explained by the original samples being fresh and the stored samples being vacuum packaged, which causes the compactness of the bread, thus increasing reflectance.

STORAGE EFFECTS: STALING

Though staling would have an influence on texture and consequently on overall acceptance, it can be discerned directly and its influence on the other attributes can be separately ascertained. By using differential scanning calorimetry (DSC), starch that has retrograded (i.e., converted from the amorphous to the crystalline state) will melt at a distinctive temperature and release energy in proportion to the amount of crystalline starch present. Providing that other energy absorbing or releasing processes do not occur in the vicinity of this melting point, the "staling" peak should be discerned and quantified. Even if there is some interference, the staling peak can be distinguished because the melted starch upon cooling reforms the amorphous glass and the peak will not appear when the sample is rescanned.

Thermograms for three differently formulated breads stored for 12 weeks at 40°F depicted in Fig. 7 illustrate the data available and

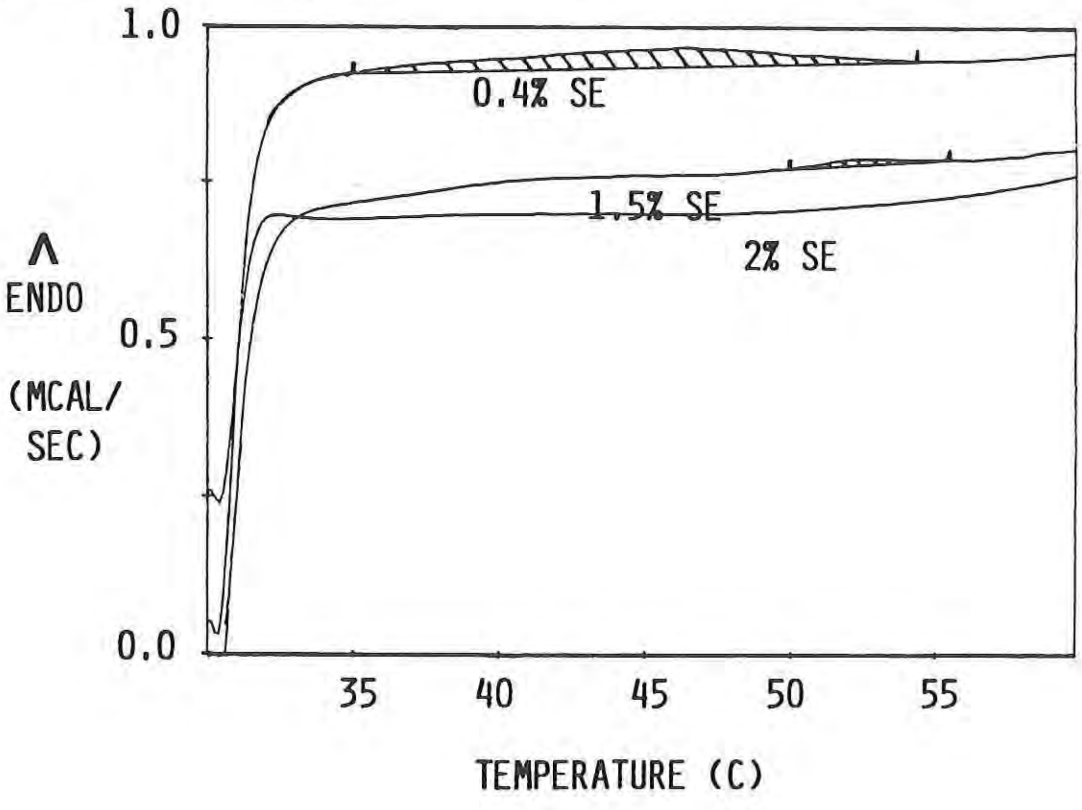

Fig. 7. Differential scanning calorimetry curves for low Aw breads with different amounts of sucrose ester. 0.4% sucrose ester: maximum endothermicity at T = 46.26°C, Δ H = 0.72 cal/g; 1.5% sucrose ester: maximum endothermicity at T = 52.2 C, Δ H = 0.05 cal/g.

indicate the effect of sucrose ester on staling. Since it is well known that the peak in the melting of crystalline starch occurs at a temperature of about 50°C (122°F), the peaks appearing in the middle and upper scans can be associated with staling. The total energy released, which is computed from the area bounded by the peak and the baseline obtained by rescanning, depends on the amount of crystalline starch present and is typically several tenths of a calorie per gram in a staled bread sample. Although the samples used here differ more than just in sucrose ester level, the effectiveness of this ingredient in preventing staling is evident. More crystalline starch is seen at 0.4% sucrose ester than at 1.5%, and none is observed at 2%. Except for the fact that the optimum formulation calls for 1.2% sucrose ester, the sample with 2% almost is identical to the optimum (0.08% lactic acid, 2% glycerol, and 4% sorbitol). The overall trend with time will be determined when results for the 24-week samples are analyzed.

CONCLUSION

The use of RSM is very effective in ascertaining an optimum formulation in an otherwise very complicated system of ingredient influences on bread quality and gives one a clear pictorial representation of these influences (Fig. 8). The optimum determined

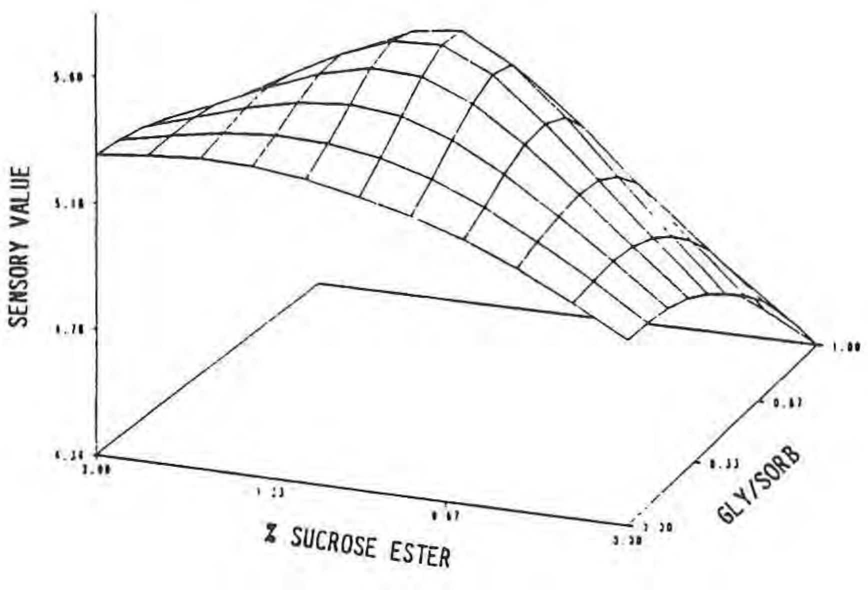

Fig. 8. Response surface methodology representation in 3-D of sensory evaluation of low Aw bread stored at 40°F for 4 weeks.

has a water activity (0.94) and pH (4.8) that ensure microbiological safety. This optimum corresponds to the addition to the basic formulation of 1.2% sucrose ester to minimize staling and the use of two humectants, glycerol and sorbitol, at 2% and 4% levels, respectively, that along with propylene glycol in the basic formulation give the desired Aw. Depending on the conditions and time in storage, the quality attributes of texture, acceptance, and color tend to change, but at rates that over the desired duration of three years at 70^{O}F should not compromise overall acceptability.

ACKNOWLEDGMENTS

The authors wish to thank Ms. Michelle Richardson, Ms. Susan Butler, MSG Hukin White, Mrs. Ruth Ross, Ms. Mary Friel, Mr. Ray Spring, and Mr. Larry Lasher for their outstanding contribution to the evaluation of color, Aw, moisture, specific volume, and sensory ratings and to the RSM analysis. We also thank Dr. Pavinee Chinachoti of the University of Massachusetts for her valuable advice concerning the DSC measurements and their interpretation.

REFERENCES

AACC. 1976. Method 10-10. Approved Methods of the AACC. The Association: St. Paul, MN.

AACC. 1983. Method 02-52. Approved Methods of the AACC. The Association: St. Paul, MN.

Anonymous. 1989. Military Specifications: Pouch Bread #Mil-B-44360 (GL); Canned Bread #Mil-b-1070E.

AOAC. 1980. "Official Methods of Analysis," 13th ed. Assoc. Official Analytical Chemists, Washington, D.C.

Baker, A.E., Dibben, A.R., and Ponte, G.J. 1987. Comparison of bread firmness measurements by four instruments. Cereal Foods World 32(7): 486.

Box, G.E.P., Hunter, W.G., and Hunter, J.S. 1978. "Statistics for Experiments." John Wiley and Sons., Inc., New York.

Breyer, L.M. and Walker, C.E. 1983. Comparative effects of various sucrose-fatty acid esters upon bread and cookies. J. Food Sci. 48: 955.

Chinachoti, P. 1988. The structural and molecular mechanism of the cellular deformation of compacted and stabilized bread. Tech. Report Department of Food Science, University of Massachusetts.

Chung, H., Seib, P.A., Finney, K.F., and Magoffin, C.D. 1981. Sucrose monoesters and diesters in bread making. Cereal Chem. 58(3):164.

Chungcharoen, A. and Lund, D.B. 1987. Influence of solutes and water on rice starch gelatinization. Cereal Chem. 64(4):240.

Cochran, W.G. and Cox, G.M. 1957. "Experimental Designs." John Wiley and Sons, Inc., New York.

Czuchajowska, Z. and Pomeranz, Y. 1989. Differential scanning calorimetry, water activity, and moisture content in crumb center and near-crust zones of bread during storage. Cereal Chem. 66(4): 305.

Davies, O.L. (Ed.) 1954. Design and Analysis of Industrial Experiments. Oliver and Boyd, Edenburgh.

Graham, H.D. 1980. The Safety of Foods. 2nd ed. AVI Publishing Co., Inc., Westport, Conn.

Harrigan, K.A. and Breene, W.M. 1989. Fat substitutes: sucrose esters and simplesse. Cereal Foods World 34(3): 261.

Hill, W.J. and Hunter, W.G. 1966. A review of Response Surface Methodology. A literature survey. Technometrics 8(4): 571.

Hoseney, C.R. 1983. Chemical changes in carbohydrates produced by thermal processing, presented at the American Chemical Society annual meeting, August 30, 1983.

Joensson, T. and Toernaes, H. 1987. The effects of selected surfactants on bread crumb softness and its measurements. Cereal Foods World 32(7): 482.

Joglekar, A.M. and May, A.T. 1986. Product excellence through design of experiments. Cereal Foods World 32(12): 857.

Johnson, N.L. and Leone, F.C. 1964. "Statistics and Experimental Designs in Engineering and the Physical Sciences." Vol. II. John Wiley and Sons, Inc., New York.

Krog, N., Olesen, S.K., Toernaes, H., and Joensson, T. 1981. Retrogradation of the starch fraction in wheat bread. Cereal Foods World 34(3): 281.

Leistner, L. and Rodel, W. 1976. Inhibition of microorganisms in food by water activity. In F.A. Skinner (Ed): Inhibition and Inactivation of Vegetative Microbes. Academic Press, London. p. 219-237.

Leung H. 1983. Low Water Activity Packaged White Bread, Washington State University, Contract No. DAAK 60-83-C-0039.

Lim, H., Sobczynska, D., and Setser, C. 1989. ^{17}O NMR studies on wheat starch-sucrose-water interactions with increasing temperature. Presented at IFT Annual Meeting, Chicago, IL., June 1989.

Mitsubishi-kasei Foods. 1989. Ryoto Sugar Ester Technical Information. Mitsubishi-kasei Foods Corp., Japan. p: 14.

Morgan, H.A. 1986. Problematic chemical notes and sourness in the shelf stable bread. Natick Notebook # 8236. Unpublished data.

Mudahar, G.S., Toledo, R.T., Floros, J.D., and Jen, J.J. 1989. Optimization of carrot dehydration process using response surface methodology. J. Food Sci. 54(3): 714.

Myers, R.H. 1971. "Response Surface Methodology." Allyn and Bacon, Boston.

Paton, D. 1987. Differential scanning calorimetry of oat starch paste. Cereal Chem. 64(6): 394.

Pierce, M.M. and Walker, C.E. 1987. Addition of sucrose fatty acid ester emulsifiers to sponge cakes. Cereal Chem. 64(4): 222.

Platt, W. and Powers, R. 1940. Compressibility of bread crumb. Cereal Chem. 17: 601.

Pomeranz, Y. 1985. Functional Properties of Food Components. Academic Press, Inc., London.

Rodel, W., Ponert, H., and Leistner, L. 1976. Einstufung von fleischerzeugnissen in leicht verderbliche, verderbliche und lagerfahige produkte. Fleischwirtsch. 56: 417-418.

Russel, P.L. 1983. A kinetic study of bread staling by differential scanning calorimetry and compressibility measurements. The effects of added monoglyceride. J. Cereal Sci. 1: 297.

Thompson, D.R. 1982. Response surface experimentation. J. Food Proc. Preser. 6: 155.

Troller, J.A. and Christian, J.H.B. 1978. Water Activity and Food. Academic Press, London.

Zeleznak, K.J. and Hoseney, R.C. 1986. The role of water in the retrogradation of wheat starch gels and bread crumb. Cereal Chem. 63(5): 407.

TITLE: Correlation of Extrudate Infusibility with Bulk Properties Using Image Analysis Techniques

*ANN BARRETT, MS., EDWARD ROSS, DR.

ABSTRACT:
Corn meal extrudates were produced using process parameters designed to obtain various product structures. The extrudates were infused with a particle-containing, high melting point lipid suspension, a process used to produce calorically dense components for military rations. Image analysis was used to estimate the degree of particle penetration into the extruded matrices and to determine cell size distributions. Infusion uniformity was correlated with structural attributes, such as density, expansion, and average cell size.

* BIOGRAPHY: Ann Barrett, Ms.
PRESENT ASSIGNMENT: Project Officer, Analysis of Extrusion; Chemical Engineer, Food Engineering Directorate; Employed at Natick RD&E Center for six years.
PAST EXPERIENCE: Process Engineer, Brady Enterprises, Inc.
DEGREES HELD: B.A., Chemistry, Williams College; M.S. Food Engineering, University of Massachusetts

CORRELATION OF EXTRUDATE INFUSIBILITY WITH BULK PROPERTIES USING IMAGE ANALYSIS TECHNIQUES

ANN BARRETT, MS., EDWARD ROSS, DR.

INTRODUCTION

Vacuum infusion of porous food matrices is a process currently used to produce one type of calorically dense ration component. This technique increases the caloric value of a food by filling the pore volume of the matrix with a calorically rich, usually lipid-based, substance (Briggs et al., 1986). Food matrices typically used in infusion are highly expanded, extruded, grain-based flatbread crackers, which generally have porosities of 90% or higher. The infusing liquid, or "infusate", consists of a high melting point fat blended with a high concentration of food powder, the actual composition of which is determined by the product formulation. Infusion is carried out at elevated temperatures so that the infusate is liquid; the infused product is subsequently cooled to room temperature and the infusate becomes solid.

Since the infusate will largely determine the appearance, flavor, and caloric density of the finished product, maximum penetration of lipid and suspended particles into the matrix is desirable. Vacuum infusion is essentially a reverse filtration process during which a suspension containing a high concentration of particles is forced to permeate a porous structure. If suspended particles are too large to pass through the available fractures and intercellular channels in the extrudate, visible exclusion of the particles from some portions of the matrix will result. Since the suspending lipid is white when it is solid and food powders are frequently colored, separation of particles from the lipid will produce a nonuniform "patchwork" appearance in a cut surface of the product. In these instances some cells are completely infused with the lipid and particles, and thus have the same appearance and color as the original formula; others, however, are virtually impermeable to particles, and contain exclusively the white suspension lipid. Separation of food powders during infusion detracts from the quality, acceptance, and in extreme cases the nutritive value of the infused product.

Efforts to optimize infused products have included decreasing suspended particles size through milling (Barrett, 1986), using of surfactants (Barrett, 1987), and modeling the process using idealized components (Barrett et al., 1989). These authors, using standard filters and well characterized particles, found that particle penetration through a porous interface, prior to particle bridging and filtercake formulation, increases exponentially with the ratio of pore size to particle size; the authors also found that the rate of particle bridging and clogging of pores is accelerated by increasing the concentration of particles in the suspension. Infusion of extruded matrices, however, is a more complex problem than infusion through filters due to the difficulty in determining extrudate permeability--which can vary markedly from cell to cell within the same extruded sample--and in quantitatively assessing the degree of particle penetration into the matrix.

Many investigators have worked in the area of relating process parameters to extrudate attributes, particularly expansion and density. Chinnaswamy and Hanna (1988) documented a negative correlation between the radial expansion of corn starch and moisture content for systems having at least 13% moisture, which they attributed to increased gelatinization at low moisture levels. These authors further suggested that reduced expansion at extremely low moisture contents, below 13%, was due to degradation of the starch into low molecular weight fragments. Fletcher et al. (1985) similarly reported that the radial expansion of extruded maize grits was negatively correlated, and that product density was positively correlated with moisture. Faubion and Hoseney (1982), working with wheat starch, demonstrated a negative relationship between product diameter and moisture levels exceeding 17%.

A negative relationship between radial and longitudinal expansion has been documented by Launay and Lisch (1983), who attributed this correlation to the respective influences of melt elasticity and melt viscosity on the two indices. Alvarez-Martinez et al. (1988) incorporated radial and longitudinal expansion into a generalized model that shows a negative correlation between volumetric expansion and moisture content.

Starch type has also been shown to influence expansion and density. Chinnaswamy and Hanna (1988) demonstrated that the radial expansion of corn starch peaked at a 50:50 ratio between amylose and amylopectin. Bulk density, however, was negatively affected by amylose content throughout the experimental range.

Increased degradation of corn starch at low moisture contents, as indicated by increased extrudate solubility, gelatinization, and susceptibility to enzyme attack, has been documented by Gomez and Aguilera (1983; 1984). These authors (1984) also addressed the issue of cell size, finding that the extrudates were progressively broken down into flaky, thin-walled structures as the widened, distribution of cell sizes and noted the presence of ruptures in wheat starch products extruded at high moisture contents.

The objective of this study was to relate the functional properties--permeability and infusibility--of extrudates to other structural characteristics such as density, expansion, and cell size distribution; such correlation of infusibility with bulk properties would assist the development of infused products by revealing what types of extrudates are acceptable matrices. Experiments were therefore designed to measure the penetration of a standard infusion formula into a series of widely varying extrudate structures. Extrudates were produced under conditions expected to yield a range of bulk properties, primarily through variation of moisture. The products were then infused using identical conditions. New analytical techniques were developed to evaluate the extrudate structures and to determine the efficiency of infusion into the extruded matrices. Image analysis was used to determine cell size distributions and also to measure the uniformity (i.e., extent of visibly separated lipid) of infused products. Data from these determinations were correlated with results from other analysis, including measurements of product density, longitudinal and radial expansion, and solubility.

MATERIALS AND METHODS

Extrusion Parameters

Corn meal obtained from American Maize was processed on a Wenger X20 extruder through a 3 mm by 18 mm flatbread die. The moisture content of the dough was adjusted during extrusion to levels of 16, 18, 20, 22, 24, and 26% at a solids feed rate of 1.8 kg/min. The extruder was operated at 350 RPM with no external heating or cooling. The die temperature varied inversely with moisture content from 155° to 200°C. All extrudates were dried at 115°C to a moisture content between 5% and 7%.

Infusion Parameters

Each extruded product was vacuum infused with the formula consisting of 70% Durkee Kaomel, 15% Dazaan cocoa powder, 14% Domino confectionery sugar, and 1% lecithin. The formula was made by melting the Kaomel and mixing all ingredients together in a high shear blender. Infusion was carried out in small vacuum chambers. The chamber, with the extrudate within, was evacuated to 1.5 kPa pressure and a valve leading to the infusion liquid reservoir opened, allowing the liquid formula to fill the chamber and permeate the extrudate. The valve was closed and the system restored to atmospheric pressure and held for 2 min. The chamber was then drained and the products cooled to 22°C to solidify the lipid. A cocoa-based formula was selected because separation of particles in this system produces a distinct pattern of suspension-filled (dark) cells and exclusively Kaomel-filled (white) cells that lends itself well to image analysis.

Image Analysis Techniques

An Olympus Cue 2 image analyzer was used to characterize the extrudates and infused extrudates. The image analyzer operates by assigning a grey level value (i.e., position between black and white) to each pixel in the image. Threshold levels are then selected to construct a binary (black and white) image in which pixels having grey levels between the thresholds are black and pixels having gray levels below these values are white. Black objects within the binary image can then be counted, measured, and subjected to statistical and morphological analysis.

Extrudates Expansion and Density.

The bulk density of each product was calculated by measuring both linear weight (g/cm), determined by weighing measured length of the extrudate, and cross-sectional area (cm^2) determined by image analysis. Cross-sectional area was measured by tracing the circumference of the extrudate image (cut cross-section) on the video monitor using the computer mouse. The computer program was calibrated to convert number of pixels to square centimeters, giving a measure of the interior area of the image. Linear weight was then divided by radial area in order to determine density. For each sample, three sections were averaged for radial area and four lengths were averaged for linear weight. This method of measuring density is particularly useful for unevenly shaped products, since cross-sectional area is measured directly and not calculated from a geometric formula that assumes a perfectly round, or in the case of flatbread crackers, a perfectly rectangular or oval shape.

Extrudate Cell Size Distribution.

The cell size distributions of the extrudates were measured by cutting cross-sections of the products and then blackening the cut, cell wall surfaces with ink (Fig. 1a), which delineated cells and allowed clear projection of the structure onto the video monitor. The problem of depth, or picking up features lying deeper than the blackened cut surface, was eliminated by adjusting grey level threshold values so that only truly black pixels were incorporated into the image. The result was a black and white image of the cell wall "skeleton" at that particular plane. The computer mouse was used to trace over any slightly broken sections in the structure to ensure that cell walls were continuous, so that the program could measure discrete, separated cells. The image was then inverted--making black pixels white and white pixels black (Fig. 1b) -- because the analyzer only measures black objects. Upon analysis, the number of cells in each section and the area of each cell (larger than the assigned cutoff of 0.5 mm^2, selected to eliminate noise) were measured. Three sections of each extrudate were analyzed and the cell area data combined so that between 60 and 130 cells of each product were measured by this technique. Statistical analysis, including calculation of average and median cell areas and evaluation of area distributions, was performed using a MINITAB (Minitab, Inc., State College, PA)

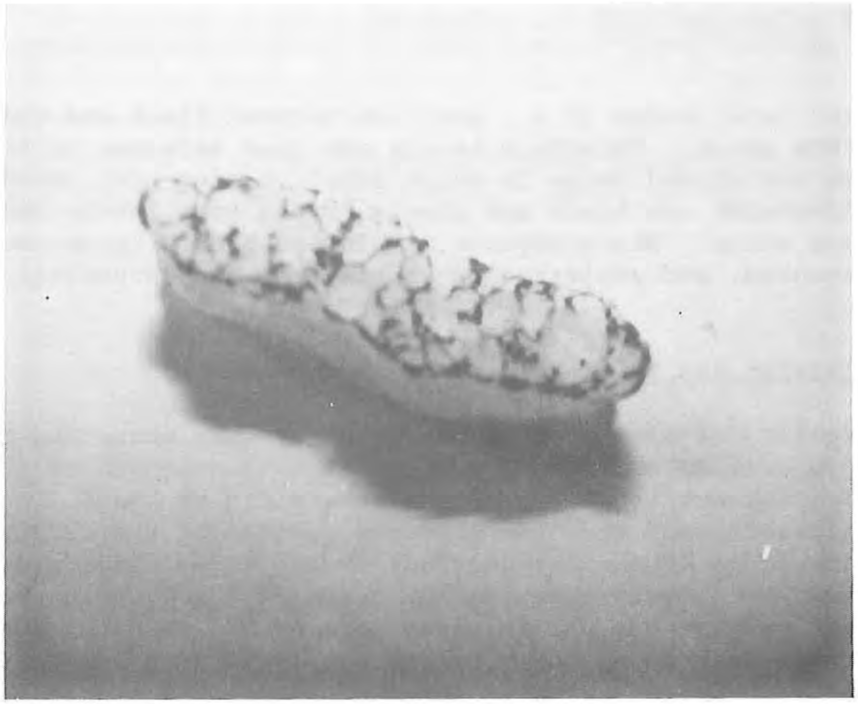

Figure 1a. Photograph of inked extrudate section.

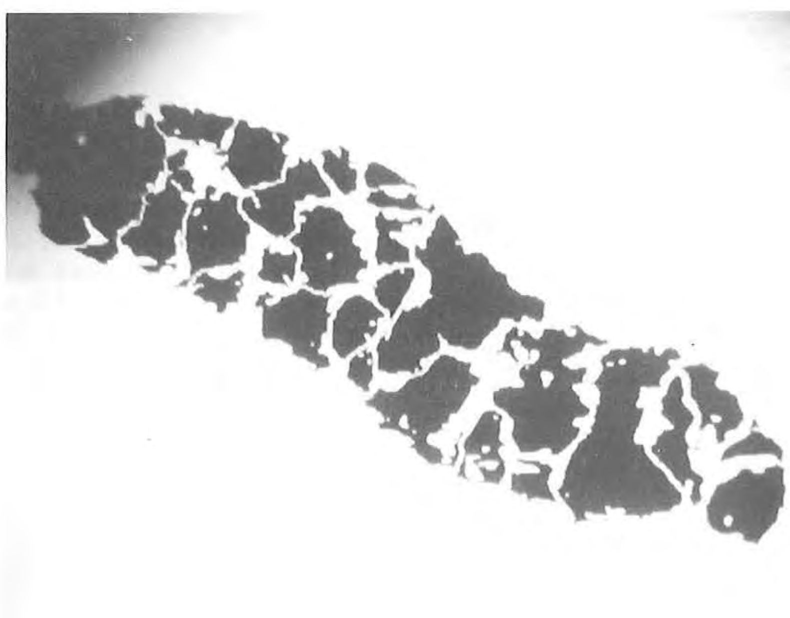

Figure 1b. Video image of inked extrudate section, after thresholds, inversion, and enhancement.

program. The tests were repeated on selected samples cut axially to determine if orientation significantly affects cell size.

Extrudate Solubility.

The water soluble fraction of the uninfused extrudates was measured by pulverizing each product in a coffee grinder and soaking 10 g of the powder in 100 ml water overnight at 22 C. The slurries were then centrifuged at 5700 RPM for 15 minutes and aliquots of the supernatant dried to determine percent solubility.

Infusion Uniformity

The infused products were sectioned into 1 cm slices. No further preparation for image analysis was required. The image of each sample was projected on the video monitor (Fig. 2a), and the largest rectangle that could be inscribed within the sample was constructed using the mouse; a rectangular image is required by the program for this function. Grey level threshold values were then selected so that a black and white image that closely corresponded to the actual sample could be formed (Fig. 2b). These initially selected threshold levels were subsequently used for every sample in the run. The program automatically calculated the percentages of the image containing black and white pixels. The fraction of the image that was black, which corresponded to the parts of the extrudate that were infused with particles, was taken as an index of sample uniformity, and the fraction that was white, which corresponded to sections of the extrudate that contained separated fat and no particles, was taken as a measurements of visible particle separation. Six sections of each infused extrudate were analyzed.

RESULTS

Varying the moisture content in the extrusion dough produced samples having extremely different densities and degrees of expansion, and results are similar to the findings of Chinnaswamy and Hanna (1988a) and Fletcher et al. (1985). Extrudate density followed an approximately linear relationship with moisture (Bulk Density (g/cm^3) = 0.02 + 0.021 x (Moisture (%) - 16); $r^2 = 0.91$) within the range of this experiment (Fig. 3). Cross-sectional area and linear weight, however, showed a more complex dependence on moisture content (Fig. 4). Cross-sectional area had the greatest rate of change at high moisture levels, and was maximum at 20% moisture; linear weight (the reciprocal of axial expansion) had the greatest rate of change at intermediate moisture levels (18%-20%) and was fairly constant above 20% moisture.

Average cell size (i.e., area) roughly followed radial expansion and is maximum at approximately 0.10 g/cm^3 bulk density, or roughly 20%

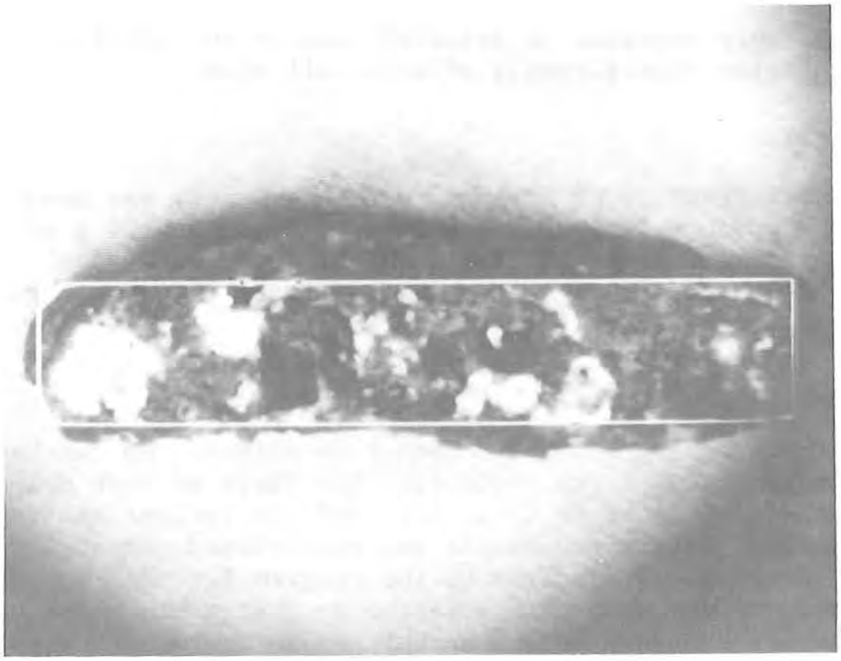

Figure 2a. Video image of an infused extrudate cross section, with inscribed rectangle.

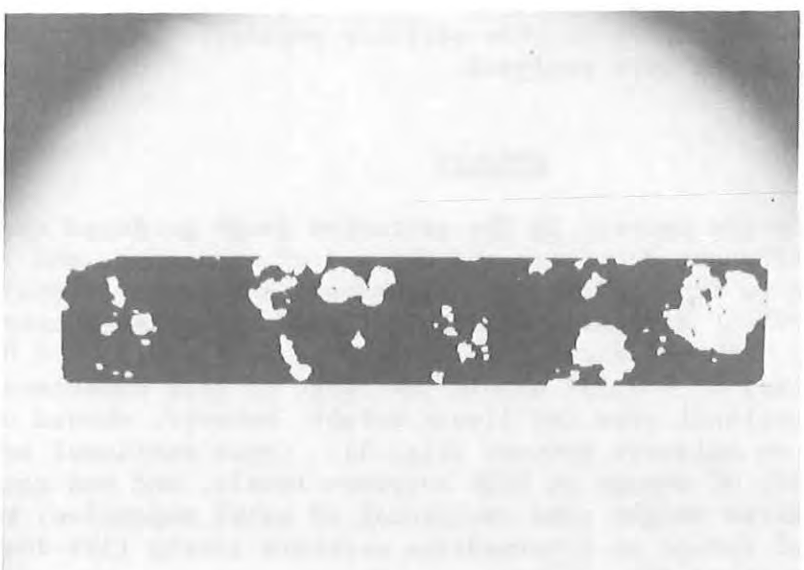

Figure 2b. Binary video image of infused extrudate after thresholds.

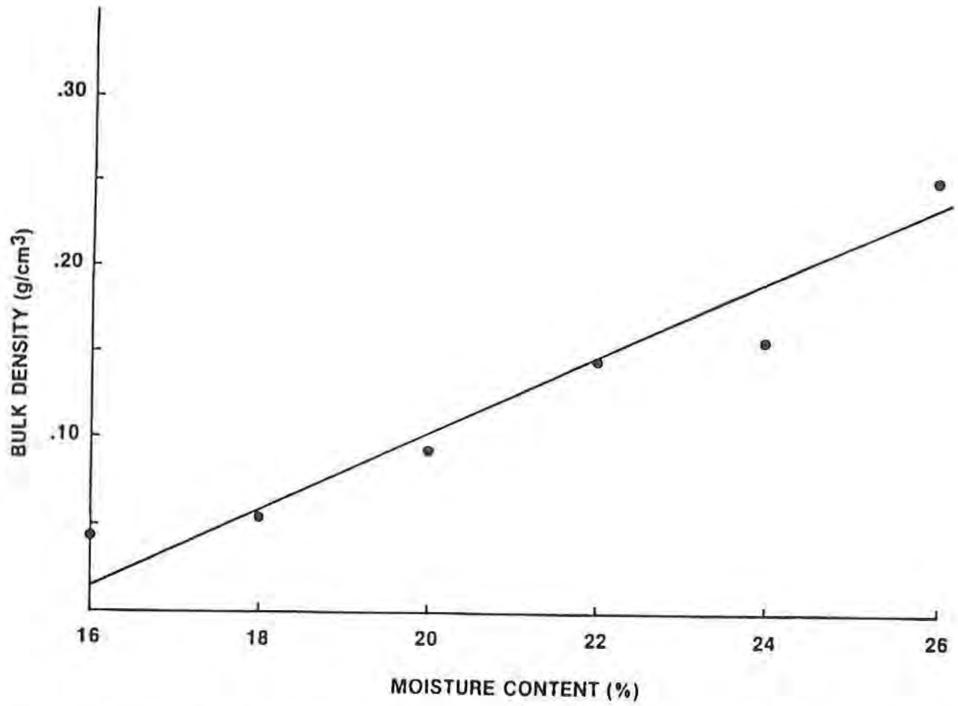

Figure 3. Effect of extrusion moisture on extrudate bulk density.

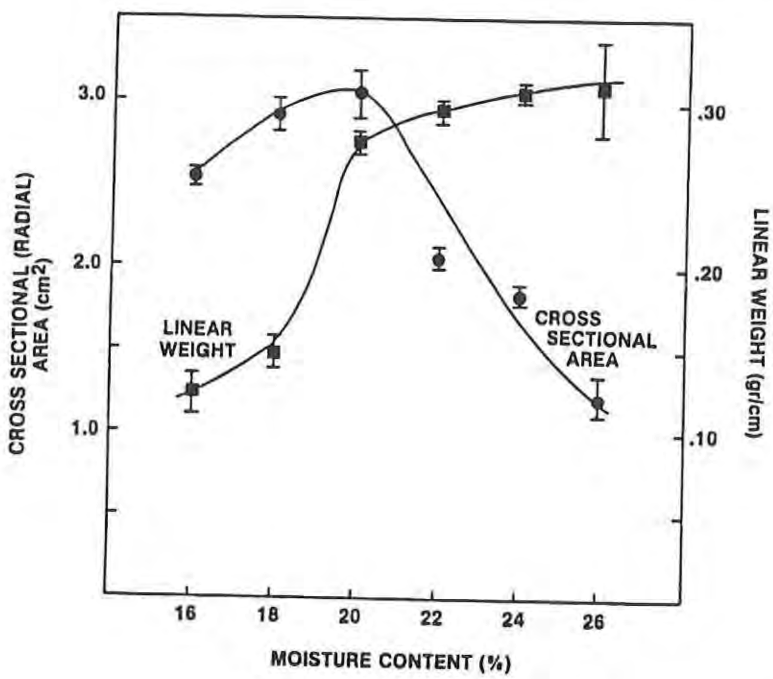

Figure 4: Effect of extrusion moisture on extrudate cross sectional area (●) and linear weight (■).

moisture content (Fig. 5). Cell size for selected samples (24%, 20%, and 16% moisture contents) measured axially was only slightly larger than cell size measured radially. The respective values for radial and axial determinations of average cell area were: 24% moisture content - 5.67 vs 5.74 mm^2; 20% moisture content - 6.24 vs. 6.72 mm^2; 16% moisture content - 3.32 vs. 3.78 mm^2. Cells measured axially also displayed slight orientation, in that many aligned with the direction of extrusion (i.e., a high proportion of cells had their longest dimension within 15 degrees of the axis).

Cell area distributions were in all cases skewed toward small size cells. Two of these distributions, for the 24% and 22% moisture content samples, were distinctly lognormal (log (cell area) normally distributed). The others failed to conform to lognormal distributions in that they had too few extreme values. Comparison of average and median values is shown in Table 1.

Table 1-Average and median cell areas (mm^2) of corn meal extrudates.

	Sample moisture content (%)					
	16	18	20	22	24	26
Average cell area	3.23	4.25	6.24	5.33	5.67	4.35
Median cell area	2.27	2.73	5.04	3.89	3.47	3.53

The number of cells per cross section was also found to be highly dependent on moisture content and density, with low density products having the highest count (Fig. 5). Low density extrudates formed under low moisture processing conditions were generally much more finely subdivided, and had a greater number of small cells than did high density extrudates produced with a higher moisture content.

Infusion uniformity was strongly correlated with extrudate bulk density (Fig. 6). Although there was substantial within-sample variation, which would be anticipated due to the inherent structural variation of extrudates, the average value for particle penetration--percent dark as determined by image analysis--was correlated with bulk density and followed the linear relationship (% Dark = 98.5 - 187 x Extrudate Density (g/cm^3); $r^2 = 0.98$). Including all data points (instead of averages) in the regression gave (% Dark = 98.2 -184 x Extrudate Density (g/cm^3); $r^2 = 0.73$). As is indicated by Fig. 6, most of the scatter occurred in dense, high moisture samples.

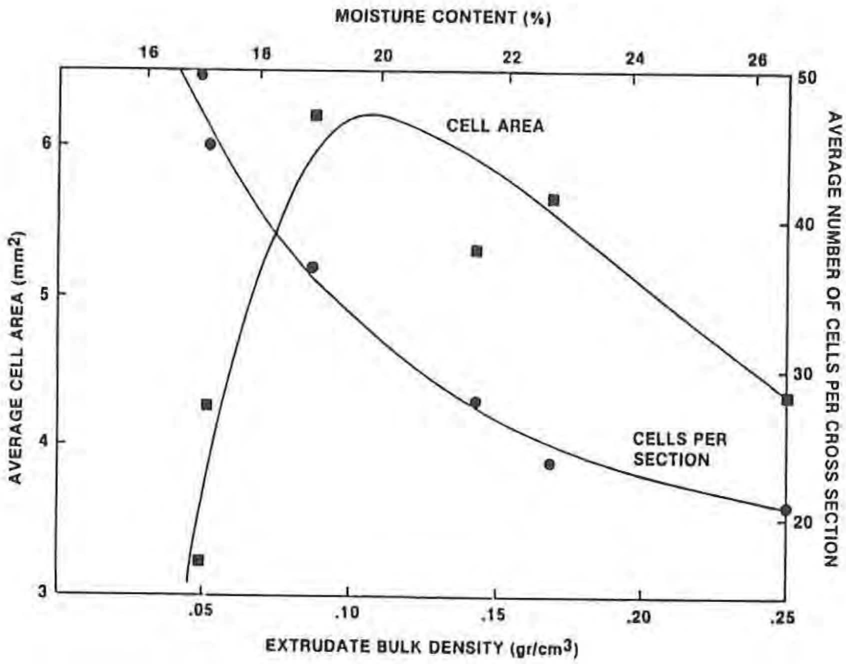

Figure 5: Effect of extrudate bulk density and extrusion moisture on extrudate average cell area (■) and average number of cells per section (●). (% moisture scale calculated from density-moisture function; Fig. 4)

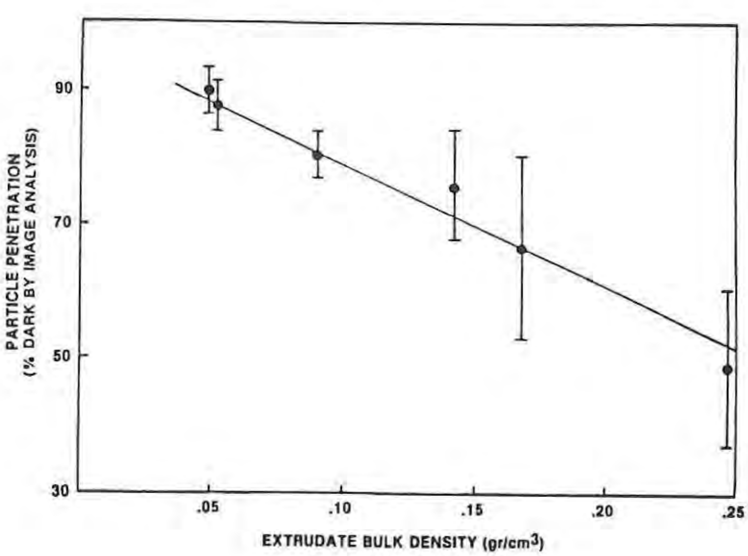

Figure 6: Effect of extrudate bulk density on infusion uniformity (% dark).

Solubility of the extrudates ranged from 30% to 60% (Table 2).

Table 2-Water solubility of pulverized corn meal extrudates.

	Sample moisture content (%)					
	16	18	20	22	24	26
% Soluble fraction	61	58	59	52	37	30
Standard deviation	3.5	3.2	2.9	1.8	2.0	2.3

Low moisture samples were found to have twice as much soluble material as did high moisture samples, indicating greater degradation of the starch into low molecular weight fragments.

DISCUSSION

The suitability of extrudates as infusible matrices, assessed by infusion uniformity, varied widely among the samples. Receptivity to infusion with particles can be thought of as analogous to permeability; in general, we expect that the larger in size and more numerous the openings that allow infusion, the more permeable the product. During high-temperature, short-time extrusion, the starch "melt" undergoes rapid expansion as it exits the extruder die due to abrupt reduction in pressure. The resultant structure is cellular but generally not closed, and the openings, consisting of intercellular channels or fractures in the cell walls, are pathways that allow infusion into the extrudate (Briggs et al., 1986). Such openings, produced during expansion, are failures in the structure and result from overstreching of the cell wall film while the extrudate is still plastic. The number, size, and distribution of these pores that connect cells therefore must be affected by properties of the starch melt; characteristics such as dough extensibility and elasticity should influence the cell wall thickness and in turn the permeability of the extrudate.

It is reasonable that a physical property such as density would be negatively correlated with permeability and infusion uniformity: the more mass in a unit volume, the higher the potential for increased resistance to penetration. Two extrudates having roughly similar cell size distributions but different densities would have different cell wall thicknesses. For example, an increase from 30 microns to 60 microns in cell wall thickness would not cause a noticeable difference in macroscopic measurements of cell size by image analysis; however, this two-fold increase in wall thickness would--all other factors being equal--reduce the likelihood of rupture during stretching. Thick cell walls are inherently less fragile and less likely to rupture than are thin cell walls.

A similar argument can be made for the comparison of two samples of identical bulk density but different cell structure. Extrudates that have small cells are more finely subdivided and contain more cells per unit volume than do extrudates that have large cells. If density is constant, finely subdivided extrudates have relatively thinner cell walls and are more likely to develop pores than are coarsely subdivided extrudates. An interesting correlation existed between density and average cell size in these experiments in that the lowest density extrudates had the smallest average cell size. Cell area, however, went through a maximum and declined beyond a density of about 0.10 g/cm^3, possibly due to shrinkage of the high moisture extrudates after puffing.

Cell size distribution is partly a result of moisture content in that cell walls in high moisture products are relatively more fluid and set more slowly than do cell walls in low moisture products, possibly allowing cells to coalesce. The structure of very high moisture products, however, is soft and subject to partial collapse before cooling. At the other extreme, at very low moisture levels, quick setting cell walls may simply be brittle and highly prone to fracture during expansion.

Another factor in permeability may be the chemical structure of the starch at the time of expansion. It is documented that low moisture extrusion doughs undergo greater degradation or dextrinization of starch than do high moisture doughs (Gomez and Aguilera, 1983; 1984). Our results, which show a two-fold increase in solubility due to reducing extrusion moisture from 26 to 16 percent, corroborate these findings. It is possible that cell wall films that contain a high proportion of low molecular weight starch molecules are physically less extensible than less dextrinized cell wall films, due to decreased water holding capacity or reduced interaction of starch molecules. Further work investigating the effects of starch type, additives, and additional processing conditions on extrudate structural integrity is being undertaken.

CONCLUSION

Structural analysis of extruded products has provided an understanding of factors that render an extrudate permeable and infusible. Data obtained from density, cell size, and solubility measurements have supported trends observed in the relative infusion efficiency of samples. New image analysis techniques have provided useful data by which to characterize extrudate structures.

REFERENCES

1. Alvarez-Martinez, L., Kondury, K.P., and Harper, J.M. 1988. J. Food Sci. 53(2):609.

2. Barrett, A.H., 1986. Activities Report of the R&DA Associates. 38:56.

3. Barrett, A.H., 1987. Activities Report of the R&DA Associates. 39:154.

4. Barrett, A.H., Ross, E.W., and Taub, I.A. 1989. Army Science Conference Proceedings. In print.

5. Briggs, J.L., Dunne, C.P., Graham, M.A., Risvik, E., Cardello, A., Barrett, A.H., and Taub, I.A. 1986. Army Science Conference Proceedings. 1:81.

6. Chinnaswamy, R. and Hanna, M.A. 1988a. J. Food Sci. 53(3):834.

7. Chinnaswamy, R. and Hanna, M.A. 1988b. Cereal Chem. 65(2):138.

8. Faubion, J.M. and Hoseney, R.C. 1982. Cereal Chem. 59(6):529.

9. Fletcher, B.I., Richmond, P., and Smith, A.C. 1985. J. Food Eng. 4:291.

10. Gomez, M.H. and Aguilera, J.M. 1983. J. Food Sci. 48:378

11. Gomez, M.H. and Aguilera, J.M. 1984. J. Food Sci. 49:40

12. Launay, B. and Lisch, J.M. 1983. J. Food Eng. 2:259

An Analysis of the System Effects in Woven Fabrics Under Ballistic Impact

* Philip M. Cunniff

Striking and residual velocity data, collected for single-ply fabric systems of Spectra®, Kevlar® 29, Kevlar®129 and nylon with various different yarn deniers and weave types, are used to establish the response of spaced armor systems. The system effects of assembling fabric plies into body armor systems are determined by comparing the response of spaced armor systems to actual multiple-ply systems. A pronounced decrease in energy absorption capacity was noted for the Spectra® and nylon systems; this deleterious effect is ascribed to increased transverse stresses, and possible interference of the deflection characteristics of fabric plies by subsequent plies.

* BIOGRAPHY: Philip M. Cunniff
PRESENT ASSIGNMENT: Research Mechanical Engineer
Materials Research and Engineering Division
Individual Protection Directorate
U.S. Army Natick Research, Development and Engineering Center
Natick, Massachusetts

PAST EXPERIENCE: Electronics Engineer
U.S. Naval Undersea Warfare Engineering Center
Keyport, Washington

DEGREE HELD: B.S. Mechanical Engineering, University of Portland

An Analysis of the System Effects in Woven Fabrics Under Ballistic Impact

Philip M. Cunniff

INTRODUCTION

Simplifying assumptions are required in the formulation of numerical models to predict the performance of body armor systems under ballistic impact to make these models tractable. One such assumption has been to model a multi-layer body armor panel as a single ply of fabric. The validity of these assumptions must be verified through experiment.

The extent that system effects are significant in body armor materials is reflected in the difference in performance between a system of spaced armor and a more traditional edge-sewn and clamped fabric armor panel. If a system of armor were constructed with sufficient spacing between the layers so that no two layers were in contact during the impact event, the ballistic performance of the system would be exactly equivalent to the sum of the single ply performances. Such a spaced armor system removes all multi-layer system effects. The spaced system response may be determined using the single layer response.

MATERIALS

The fabrics of Table 1 were used in the experimental portion of the work.

Table 1. Construction characteristics of investigated fabrics.

MATERIAL	DENIER	FABRIC WEIGHT (oz/yd^2)	FABRIC WEIGHT (g/cm^2)	ENDS/PICKS PER INCH (in^{-1})	WEAVE
KEVLAR 29	1500	14.0	0.048	34 / 34	2X2 BASKET
KEVLAR 29	1000	8.7	0.029	37 / 37	PLAIN
KEVLAR 29	200	3.2	0.011	64 / 63	PLAIN
KEVLAR 129	1000	8.3	0.028	24 / 28	PLAIN
SPECTRA 1000	650	6.5	0.022	33 / 36	PLAIN
SPECTRA 1000	375	5.2	0.018	50 / 51	PLAIN
SPECTRA 1000	200	3.3	0.011	55 / 56	PLAIN
NYLON	1500	14.0	0.048	34 / 34	2X2 BASKET

EXPERIMENTAL

The striking and residual velocity characteristics of the fabrics listed in Table 1 were determined for an XX-grain chisel-nosed fragment simulator. The samples were clamped between thick aluminum plates with an 8-inch aperture and impacted in the center of the aperture.

Some of the data of the ballistic tests would require a CONFIDENTIAL security classification if the characteristics of the projectile were fully identified. Omitting the projectile mass allows for a free disclosure of the data of the tests and does not significantly affect the discussion of the results. In addition to omitting the projectile mass, the energy absorption curves have been scaled by an undisclosed number to preserve the security classification of this report.

The energy absorption characteristics of the fabrics were determined from the striking and residual velocity data; a typical energy absorption plot is provided in Figure 1. Examination of the plots of Figure 1 indicates that the energy absorbed by the fabrics reached a maximum at the ballistic limit and sharply decreased as projectile velocity was increased. Several of the energy absorption curves indicate a leveling of the energy absorbed by the fabric at high impact velocities, and some of the energy curves suggest a slight increase in fabric energy absorption at velocities much higher than the ballistic limit. The eventual increase is typical of multiple-ply fabric armor systems at velocities well above the ballistic limit.

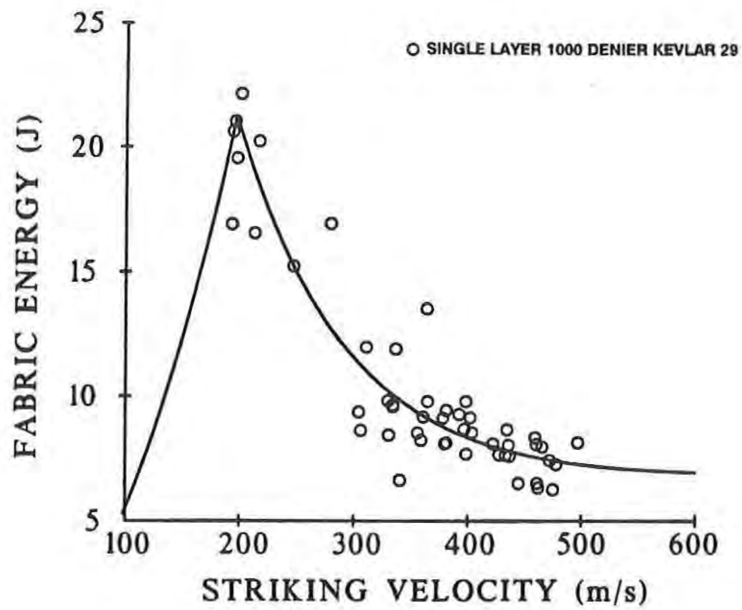

Figure 1. **TYPICAL ENERGY ABSORPTION CHARACTERISTICS FOR SINGLE-PLY FABRICS.** The energy absorption characteristics of the fabrics of Table 1 were determined from the Vs - Vr data. A typical plot is illustrated above. Fabric energy absorption is seen to decrease rapidly as the projectile velocity exceeds the system ballistic limit.

DISCUSSION

The energy absorption curve for each fabric of Table 1 was normalized by fabric areal density and plotted against a common pair of axes in Figure 2. The specific energy absorption curves indicate the potential ballistic performance of the various fabrics. Figure 2 indicates the superior performance of the Spectra® material over the other fabrics. However, the extraordinary performance potential of woven fabric Spectra® suggested by both its single-layer ballistic performance and by its tensile properties has not been fully realized, at least not for military body armor applications.

In a multiple-ply fabric system, the force acting on the projectile is due to the component of tension in the direction of projectile velocity in the principal yarns of each layer of fabric. Each layer transfers the force from the principal yarns through previous layers to the projectile. In such a system, the transverse stress components at the impact point in the first layers are obviously affected by the subsequent layers. Where these stresses are large in comparison to the ultimate compressive or shear strength of the material, the addition of subsequent plies will adversely affect the performance of the system.

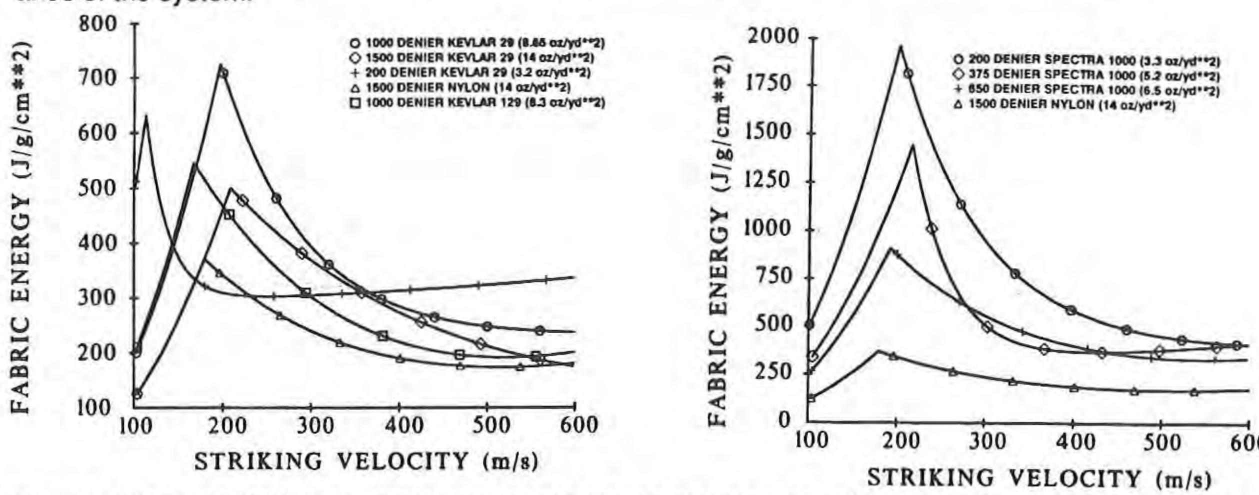

Figure 2 **SPECIFIC ENERGY ABSORPTION CURVES FOR SINGLE-PLY FABRIC SYSTEMS.** Specific energy absorption curves were determined for each fabric system by normalizing the fabric energy absorption curve by fabric areal density. The specific energy absorption curves give an indication of multiple-ply armor system potential. However, due to system effects of combining single plies of the material into body armor panels, the potential may not be fully realized. The legends used in the graphs above refer to various line styles used to draw respective curves.

The performance of spaced armor systems was determined from the single-ply striking and residual velocity data using an iterative procedure. The experimental data of each system was curve-fit to a semiempirical expression derived to express projectile residual velocity as a function of impact conditions and system characteristics. This equation was then used to determine the maximum velocity that would yield a residual velocity exactly equal to the ballistic limit of a single ply for the fabric under consideration. That velocity was then taken to be the ballistic limit of a two-ply system of spaced armor. The iterative procedure was continued for subsequent plies until the striking velocity approached the upper limit of the experimental data. The energy absorption capacity of spaced armor systems (smooth curves) is plotted as a function of areal density along with the performance of edge-sewn and clamped systems (figures) in Figure 3.

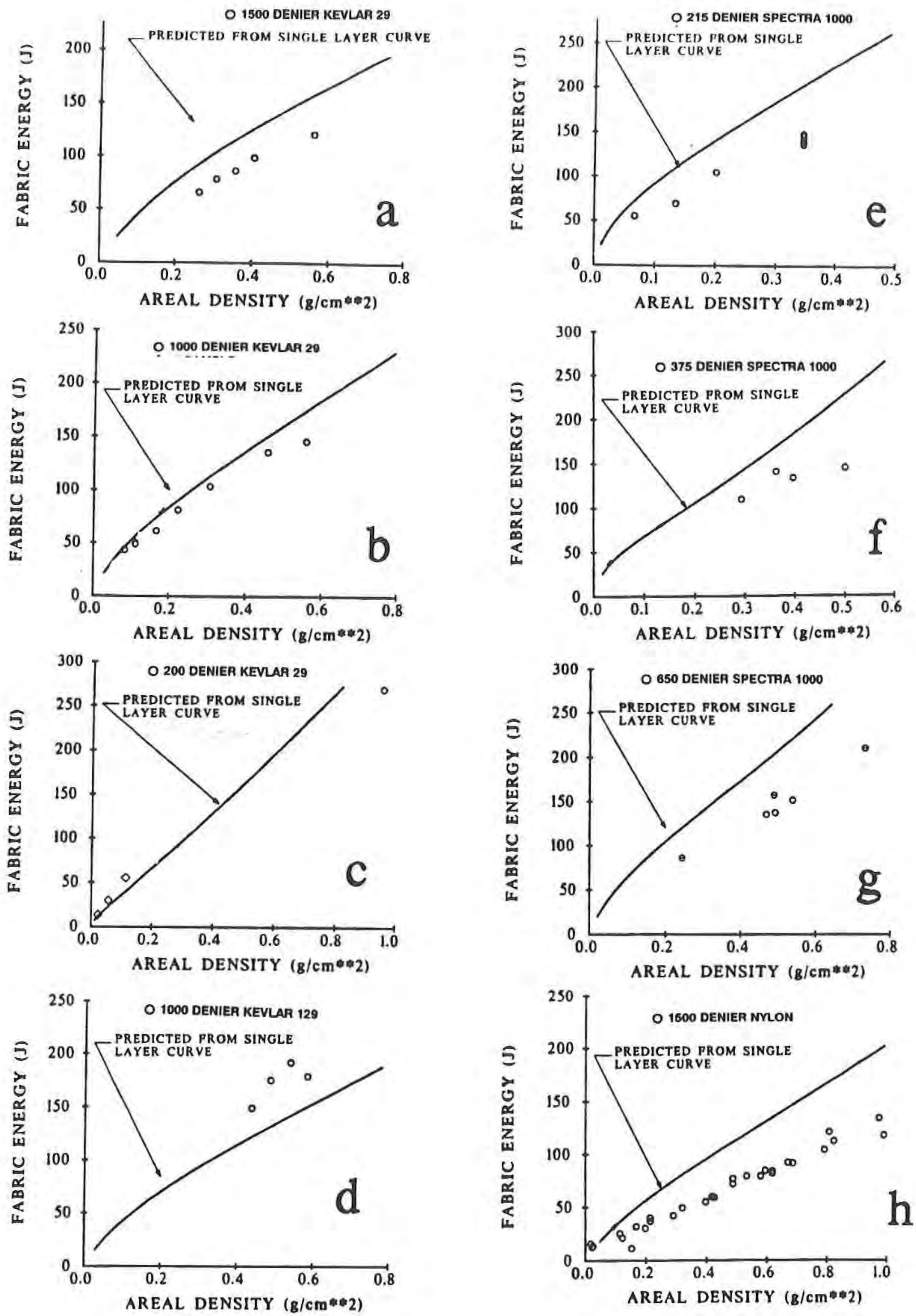

Figure 3. **COMPARISON OF SPACED ARMOR SYSTEMS TO BODY ARMOR PANELS.** The response of a spaced system of armor was determined from the single layer Vs - Vr data and compared to actual multiple-ply system response data. The difference in performance is attributed to system effects.

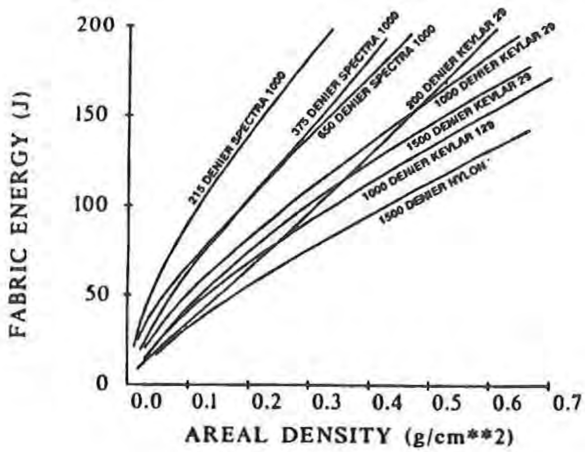

Figure 4. **RESPONSE OF SPACED ARMOR SYSTEMS.** Each of the spaced armor system responses, as predicted from the single layer Vs - Vr data is shown in the plot above.

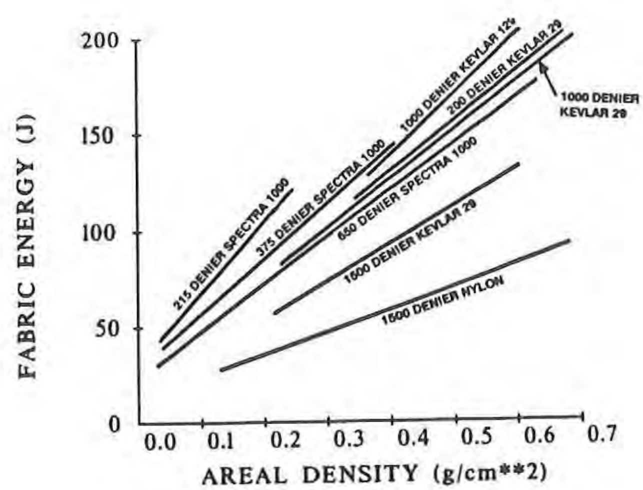

Figure 5. **RESPONSE OF MULTIPLE-PLY SYSTEMS.** Approximate curves, derived from actual ballistic limit data for multiple-ply systems are shown together in the plot above.

The consequence of reducing the denier of the Kevlar®material from 1500 to 1000 (and consequently reducing the fabric weight) increased the specific energy absorption capacity of the single-layer systems at low impact velocities (as illustrated in Figure 2) and reduced the deleterious systems effects observed in the 1500 denier system (as illustrated in Figures 3b and 3c). The consequence of further reducing the denier of the Kevlar® material from 1000 to 200 (with additional reduction in fabric weight) reduced the specific energy absorption capacity of single plies of the fabric at low impact velocities (see Figure 2). However, single plies of the lightweight Kevlar® fabric provide superior specific energy absorption capacity at striking velocities over 400 m/s. Additionally, it appears that a synergistic effect was observed when multiple-ply panels of this fabric were tested at low-impact velocities, as illustrated in Figure 3c. The Kevlar®129 material also showed synergistic effects when tested as a multiple-ply system (Figure 3d). The exact nature of the synergistic effect is not fully understood at this time. However, it appears that shear and compressive failure of the Kevlar® material is no more pronounced in multiple-ply systems than in single-ply systems.

Figures 3e-3h illustrate that the energy absorption capacity of the Spectra® and nylon fabric panels is significantly reduced from the equivalent spaced systems. In the Spectra® systems the consequence of reducing yarn denier (and reducing fabric weight) consistently increased the specific energy absorption of single plies of the fabric (see Figure 2) but also increased deleterious system effects (Figures 3e-3g). It is well known that the transverse properties of the Spectra® material are inferior to the axial properties; such orthotropic material properties exist in most highly crystalline fibers including Kevlar®. However, the torsional shear modulus of the Kevlar®material is over four times as great as the nylon material. It is speculated that the more pronounced system effects in the Spectra®and nylon systems may be attributed to their relatively poor transverse properties.

Comparison of the spaced armor response curves of Figure 4 with the actual ballistic performance curves of Figure 5 illustrates the difficulty of predicting the response of a multiple-ply system response characteristics from single-ply response data. The difference in performance between these two types of systems is seen to be a consequence of system effects (namely additional transverse stresses and additional constraint due to the addition of subsequent plies). Although the effects have been quantified in this report, it has not been possible to relate the deviation of the respective responses to fabric geometry or material properties in an exact sense. Numerical models to predict the performance of fabric body armor systems under ballistic impact are the subject of active research at this Center. Since an exhaustive treatment of the geometry of multiple-ply body armor systems is not feasible; some simplifying assumptions must be used in formulating the models.

CONCLUSIONS

The ballistics data and analysis presented in this report indicate plain-woven, 1000 denier Kevlar® 29 should outperform equivalent areal density 1500 denier basket-woven fabric systems. . Additionally, the ballistics data and analysis indicate the 375 denier Spectra® 1000 material to provide superior performance to the 650 denier Spectra® 1000, and both Spectra® materials to be superior to 1500 denier Kevlar®29 systems.

Spectra® materials show evidence of shear or compressive failure at the impact point in multiple-ply fabric armor systems. The ballistic performance of these systems may be improved by improving the shear properties of the fibers perhaps even at the expense of reducing the materials' axial tensile properties. A synergistic effect was noted for multiple-ply systems of Kevlar®129 fabric armor systems. Multiple-ply systems of this material appear to perform better than spaced armor systems. This synergistic effect is not fully understood and may warrant further investigation.

TITLE: Analytical Modeling of Fragment Penetration of Composite Shelter Laminates (U)

*BLANAS, ANDREAS M., MR.

ABSTRACT: Fiber-reinforced composite laminates are increasingly used in tactical shelters for structural and ballistic resistance purposes to provide survivability in the field. The development of an analytical technique to predict the level of ballistic protection provided by composite laminates would greatly enhance the effective use of new materials and composite design concepts and reduce the need for testing.

The first stage of the effort involves using the computer code DYNA3D to macromechanically model the impact, and possible penetration, of a composite shelter wall by fragments from conventional bomb bursts. The model accommodates fragments of different material, shape, grain size and velocity and composite walls of different material, ply orientation, thickness and volume fractions.

DYNA3D is a finite element analysis computer code for analyzing the large deformations present during fragment penetration. A mesh generator is used to create the input model's geometry. A postprocessor is used to interpret and graphically display results. Input models for fragments and composite material shelter walls, having layup and material configuration similar to existing experimental models, have been run and compared.

Future work, to be discussed in the paper, should be oriented towards a micromechanical approach of the analytical modeling. Efforts should concentrate on developing an analytical model based on a fundamental description of the lamina, its material properties, utilization of impact dynamics, stress wave propagation, consideration of energy absorption and failure interactions between fiber and matrix.

*BIOGRAPHY: Andreas M. Blanas
PRESENT ASSIGNMENT: Mechanical Engineer, Engineering Technology Division, Aeromechanical Engineering Directorate, U.S. Army Natick Research Development and Engineering Center, Natick, MA 01760-5020
PAST EXPERIENCE: Visiting Lecturer and Research Assistant at the Mechanical Engineering Department of University of Lowell.
DEGREES HELD: B.S. (1986) and M.S. (1989) in Mechanical Engineering, University of Lowell.

Analytical Modeling of Fragment Penetration of Composite Shelter Laminates

Andreas M. Blanas

INTRODUCTION

Composite materials have been used as engineering materials for structural support and ballistic protection because of their high strength to weight ratios and effective ballistic performance. Even though analytical techniques for the response of composite materials under static loads have been developed, no comparable analytical methods of modeling the ballistic impact and penetration of composite laminates are available.

Traditionally, work has concentrated on penetration and prediction of ballistic limits for metals, such as steel and aluminum, and the development thereof of hydrocodes to model the penetration process of those materials. Only empirical or semiempirical models using curvefitting techniques have been used to provide design charts for composite structures and their ballistic resistances based on experiment. However, reliance solely on experimental methods could become expensive and certainly limit the possibilities of a near-optimum design if the number of variables involved are taken into consideration.

A general description of the problem considered here is shown in Fig. 1 [1]. A fragment from a conventional bomb burst impacts a composite material target wall at a moderate velocity of 500 to 2000 fps. The size and shape of the fragment and the material, ply orientation and areal density of the target can vary. For modeling purposes, steel fragment simulating projectiles (FSP, MIL-P- 46593A) of three mass levels 5.85 grains, 17 grains and 44 grains are used. Symmetric laminates (glass /epoxy, graphite/epoxy, Kevlar(R)/epoxy) having variable areal densities (1.0 to 2.50 pounds per sq ft) are considered in an effort to reproduce the experiment.

Modeling of fragment penetration will potentially be a valuable tool for the composites design engineer allowing an analytical, systematic and scientific approach of the ballistic penetration into composite laminates problem. This approach will increase optimization and efficiency of the composite shelter design while reducing the high cost and inflexibility of the experiment.

APPROACH

Macromechanics vs. Micromechanics

Composite materials, unlike most common engineering materials (e.g., steel, aluminum), are heterogeneous and anisotropic. A heterogeneous body has nonuniform properties and therefore they are a function of position in the body. An anisotropic body has material properties that are different in all directions or they are a function of orientation at a point in the body. Because of the inherent heterogeneous nature of composite materials, they can be studied from two points of view: micromechanics and macromechanics.

In the context of this paper, we will refer to macromechanics as being the study of composite material laminates behavior wherein each ply is presumed homogeneous and the constituent materials are detected only as averaged apparent properties of the lamina. On the other hand, we will refer to micromechanics as being the study of composite material behavior wherein the interaction of the constituent materials (fibers and resin) is examined on a localized microscopic scale [8].

Experimental Data Acquisition

Experimental investigations were conducted to determine the fragment ballistic resistance and damage tolerance of different composite laminates and to evaluate composite materials that might be useful for armor on tactical shelters. Experimental results, such as ballistic limits (V50) vs. areal densities [2], [3] are used for comparison purposes with analytically obtained results.

Ballistic limit (V50) is the velocity calculated as the average of a maximum of six-test velocities within a spread or velocity interval of 125 feet per second, half of which result in complete penetration of the target and half of which result in incomplete or partial penetration of the target. A complete penetration of the target is defined as an impact that results in a hole in a witness sheet made of 0.020 inches thick aluminum plate parallel to and six inches behind the target [2]. The ballistic performance of a composite target wall is significantly affected by the properties and volume fractions of the constituent materials (fiber, resin), ply orientation, stacking sequence of the layup and the thickness of the wall (areal density).

Preliminary Decisions - Code Search

Even though ballistic penetration is a localized problem around the area of impact, a decision was made to look at the macromechanical method of analysis first. This method is traditionally used for structural analysis of composite laminates. This first stage of the analysis will allow us to qualitatively compare the macromechanically obtained analytical results with experiment. Originally our intention was to develop our own in-house computer code. Nevertheless, a hydrocode search revealed that this development would be an enormous task.

Further research showed that a code using a macromechanical model existed. A three dimensional finite element code, called DYNA3D [4a], was obtained from Lawrence Livermore National Lab (LLNL). This code has a composite damage material model [5]. A graphics package, containing a preprocessor (INGRID [6]) and a postprocessor (TAURUS [7]), was also obtained from LLNL. All of the above software is well documented, runs on our SUN computer microsystem and is free. Source files of all the above codes were obtained, allowing the user to define a new material model and recompile the code.

Structure of Codes

Two dimensional numerical simulations of impact and penetration phenomena have been performed since the early seventies. In recent years interest has arisen in three dimensional codes. These codes were developed to solve impact problems characterized by [1]:

- localized material response as contrasted to global structural response
- shock wave problems characterized by steep stress or high velocity gradients
- time of loading and response in the milli or microsecond regime.

A generic structure of the computational process followed by these codes is shown in Fig. 2 [1]. A preprocessor is used to generate the finite element mesh and define the material properties of the model. Initial and boundary conditions and material interfaces are also defined. The main code uses a finite element technique to discretize the conservation equations as coupled to the material model equations. These equations are then integrated in time. Finally a postprocessor is used to interpret and graphically display results, such as deformation modes, stress and strain fields and velocities.

The most important aspect of the main program is the material model equations. Appropriate use of the constitutive relations, failure criteria and postfailure model are essential to the modeling of the material behavior. Quasistatic failure models may be proven inadequate in situations involving dynamic and high-rate loadings. Development of a micromechanical constitutive and failure model may be necessary, especially when the material modeled is a composite laminate.

DYNA3D

DYNA3D [4c] is an explicit three dimensional finite element code for analyzing the large deformation dynamic response of solids and structures. It is a Langrangian code and it follows the motion of fixed elements of mass. The computational grid is fixed in the material and distorts with it. Equations of motion are integrated in time explicitly using the central difference method. DYNA3D contains 28 material models and eleven equations of state. Spatial discretization is achieved by the use of the following elements: 8 node solid hexahedron, 2 node beam, 4 node shell, 8 node solid shell, triangular shell and rigid bodies.

An artificial viscosity is used to treat shock wave development and propagation. Shocks result from the property that sound speed increases with increasing pressure. A pressure wave gradually steepens until it propagates as a discontinuous disturbance, called shock. Shocks lead to jumps in pressure, density, particle velocity and energy. The artificial viscosity method eliminates shock discontinuities by smearing the shock fronts over a small number of elements.

DYNA3D has an extensive slide-line capability. Sliding interfaces are used where continuity of normal stress and velocity components between two surfaces is required. They are also used to provide movement of interface nodes between two surfaces that are expected to slide on each other (penetration of projectiles into materials).

Langrangian calculations lose accuracy as the mesh distorts. In explicit calculations used by DYNA3D, the time step size will drop resulting in very high cost. A rezoning capability exists. The user can interrupt the calculation, view the calculation including the display of all history variables, decide whether to modify the mesh and do so if necessary; all without stopping the calculation.

Governing Equations

The conservation equations used by DYNA3D [4b] are shown here. Consider the body shown on Fig. 2a.

We are seeking a solution to the momentum equation

$$\sigma_{ij,j} + \rho b_i = \rho \ddot{x}_i \tag{1}$$

satisfying the traction boundary conditions,

$\sigma_{ij} n_j = S_i(t) \quad \text{on } S^1,$

the displacement boundary conditions,

$x_i(X_\alpha, t) = K_i(t) \quad \text{on } S^2,$

and the contact discontinuity

$(\sigma_{ij}^{+} - \sigma_{ij}^{-}) n_j = 0 \quad \text{on } S^0.$

Here σ_{ij} is the Cauchy stress, ρ is the current mass density, b_i is the body force, $\ddot{x}_i$ is the acceleration, the comma denotes covariant differentiation, and n_j is a unit outward normal to a boundary element.

The mass conservation equation is

$$\rho J = \rho_0 \tag{2}$$

where J is the determinate of the deformation gradient matrix, and ρ_0 is the reference density.

The energy equation is stated as

$$\dot{E} = V s_{ij} \dot{e}_{ij} - (p + q)\dot{V} \tag{3}$$

where s_{ij} and p are the deviatory stresses and pressure, $\dot{e}_{ij}$ is the strain rate tensor and V is relative volume.

The equation for total stress is

$$\sigma_{ij} = s_{ij} - (p + q)\delta_{ij} \tag{4}$$

where q is the bulk viscosity and δ_{ij} is the Kronecker delta.

We can write a weak form of the equilibrium equation as [4c]

$$\int (\rho \ddot{x}_i - \sigma_{ij,j} - \rho b_i)\delta x_i dv + \int (\sigma_{ij} n_j - S_i)\delta x_i ds + \int (\sigma_{ij}^{+} - \sigma_{ij}^{-}) n_j \delta x_i ds = 0 \tag{5}$$

Application of the divergence theorem leads to

$$\delta \pi = \int \rho \ddot{x}_i \delta x_i dv + \int \sigma_{ij} \delta x_{i,j} dv - \int \rho b_i \delta x_i dv - \int S_i \delta x_i ds = 0 \tag{6}$$

which is a statement of the principle of virtual work. This last equation can be discretized and solved by using a finite element method as shown in [4c]. The central difference method is used to explicitly integrate in time.

Composite Damage Material Model

Failure criteria proposed by [5] are used here. Chang and Chang use similar equations (equilibrium, total stress) as DYNA3D to do stress analysis. In addition, [5] use classical lamination theory to form the reduced moduli and check for failure in each ply through the thickness. Plane stress condition is assumed and three different inplane failure modes are looked at: matrix cracking, fiber-matrix shearing and fiber breakage. DYNA3D uses the same failure criteria for each element since the one point integration is used for the 8 node hexahedron solid element.

The matrix failure criterion is

$$(\sigma_y / Y_t)^2 + (C_1 / C_2) = e_m^2 \tag{7}$$

where $C_1 = (\sigma_{xy}^2 / 2G_{xy}) + (3/4)\alpha\sigma_{xy}^4$

and $C_2 = (S_c^2 / 2G_{xy}) + (3/4)\alpha S_c^4$

σ_y and σ_{xy} are the transverse and shear stresses in each ply, G_{xy} is the initial ply shear modulus, Y_t is the transverse tensile strength and S_c is the in-situ ply shear strength measured from a cross-ply laminate, $[0/90]_s$, with the same thickness as the laminate considered.

For laminates with linear elastic behavior, $\alpha = 0$, and the criterion reduces to

$$(\sigma_y / Y_t)^2 + (\sigma_{xy} / S_c)^2 = e_m^2 \tag{8}$$

For the above equations, matrix cracking occurs if e_m is greater or equal to 1.

Compressive failure in matrix is predicted by the Hashin failure criterion

$$(\sigma_y / 2S_c)^2 + [(Y_c / 2S_c)^2 - 1](\sigma_y / Y_c) + (C_1 / C_2) = e_d^2 \tag{9}$$

Here C_1 and C_2 are the same as in (7) and Y_c is the transverse compressive strength of a unidirectional ply.

For linear elastic laminates eq. (9) reduces to

$$(\sigma_y / 2S_c)^2 + [(Y_c / 2S_c)^2 - 1](\sigma_y / Y_c) + (\sigma_{xy} / S_c)^2 = e_d^2 \tag{10}$$

Matrix compression failure occurs, in a layer or an element, if e_d is greater or equal to 1.

Both fiber-matrix shearing and fiber breakage are predicted by

$$(\sigma_x / X_t)^2 + (C_1 / C_2) = e_f^2 \tag{11}$$

Here C_1 and C_2 are the same as in (7), σ_x and X_t are the longitudinal tensile stress and strength in each ply.

For linear elastic laminates the criterion reduces to

$$(\sigma_x / X_t)^2 + (\sigma_{xy} / S_c)^2 = e_f^2 \tag{12}$$

The fiber failure criterion states that when, in any one of the plies or elements in a laminate, the combined stresses σ_x and σ_{xy} satisfy the criterion (e_f is greater or equal to 1), that element fails by either fiber breakage or fiber-matrix shearing.

Description of DYNA3D Model Used

The geometry of the 3d axisymmetric model used is shown in Fig. 3. A kinematic/isotropic elastic-plastic material model was used for modeling the fragment simulating projectile. The composite damage material model [5] was used to model the composite wall. An 8 node solid hexahedron element was employed to model both the fragment and the composite target meshes. Quarter symmetry was used to reduce calculation time. Symmetry boundary conditions were set along the x,y planes. A fixed boundary condition was imposed along the outer edge of the target. A coarse geometric mesh was constructed at the outer part of the wall away from the point of impact. A finer mesh is required near the impact zone because of the high rates of stress change and large deformations developed.

The model accommodates fragments with varying shape, grain size, material and initial velocities. The composite wall model could also have varying material and volume fractions, ply orientation and thickness.

Material properties used for a unidirectional ply of GL/EP 3M Scotchply 1002(R) are [10]:

Ex=7.08 Msi, Ey=2.70 Msi, Es=1.00 Msi, nu1=.25, rho=1.8

where Ex, Ey, Es are the longitudinal, transverse, xy shear modulus, nu1 is the major Poisson's ratio and rho is relative density.

also X=154 Ksi, Y=4.53 Ksi, X'=88.5 Ksi, Y'=17.1 Ksi
S=10.5 Ksi, Sc~19.0 Ksi

where X,Y are the tensile longitudinal and transverse strengths
X',Y' are the compressive longitudinal and transverse strengths
S is the xy shear strength of a unidirectional ply
Sc is the shear strength of a cross ply laminate having the same thickness as the total laminate [5].

PRELIMINARY RESULTS AND COMPARISON TO EXPERIMENT

Several cases for crossply (0/90) GL/EP material (Scotchply 1002) were run. Wall thickness of 0.15, 0.2 and 0.26 inches were considered to match the areal density used in the experiment. All cases considered were impacted by a 44 grain fragment simulating projectile. A typical case of a 0.2 inches thick GL/EP crossply wall in the process of penetration by a 44 grain fragment is shown in Fig. 4. Both the undeformed mesh prior to impact and the deformed mesh at a time 20 microsecs after impact are shown. Stress contours and contour values of the fragment and the wall showing Von-mises effective stress are shown in Fig. 5.

A ballistic limit was approximated as the initial velocity of the fragment carrying enough kinetic energy to completely penetrate the wall. Residual velocities of the fragment were very small compared to the striking velocities. Table 1 shows preliminary results as compared to experiment [2]. Graphical representation of these comparisons are also shown in Fig. 6. Runs for Kevlar/Epoxy walls are currently being pursued.

Table 1. 3M Scotchply 1002 impacted by a 44 grain steel fragment.

Areal Density (psf)	Thickness (in)	Ballistic Limit (ft/sec)	
		Experiment	DYNA3D model
1.38	.15	646	~ 600
1.84	.2	966	~ 780
2.40	.26	1149	~ 870

CONCLUSIONS AND FUTURE EFFORTS

Preliminary results and comparisons with experiments show that DYNA3D macromechanical model could be an acceptable analytical method of modeling the penetration phenomena of composite laminates. The ballistic limits for all cases run (Scotchply) were consistently lower than the experimental ones. This finding would lead us to believe that the model does not account for energy absorbed due to certain failure modes observed in experiment. Extensive delamination, fiber pull-out and frictional dissipation of energy may be some of the failure and energy absorption mechanisms that the macromechanical model studied herein does not consider.

Further evaluation of the existing macromechanical model, by reproducing and comparing to experimental cases for other materials, such as Kevlar/epoxy, are being pursued. If results from other materials show the same consistently lower ballistic limit, an improvement of the model should be considered using a micromechanical model.

Development of this micromechanical model requires knowledge of the actual failure modes observed during penetration and therefore an extensive study of fiber to matrix interaction during impact. Constitutive and failure equations need to be developed for situations involving dynamic and high-rate loadings for the fiber-resin system. A property degradation model, updating the local strength and properties of the damaged zone around the failed material, may be considered. Stress wave propagation and deflection in a heterogeneous media, such as a fiber-resin system, should also be addressed. This new micromechanical material model can be incorporated into the existing DYNA3D material models.

REFERENCES

1. J. A. Zukas, T. Nicholas, H. F. Swift, L. B. Greszczuk, D. R. Curran, "Impact Dynamics", John Wiley and Sons, Inc., 1982.

2. F. C. Hodi, "Ballistic Evaluation of Glass-Reinforced Plastic, Kevlar-29 Laminates, and Shelter Wall Combinations", Materials Dynamics Branch, U.S. Army MTL, Watertown, MA., MTL TR 89-60, Sponcored by ETD/AMED, U.S. Army Natick RD&E Center, Natick, MA., July, 1989.

3. S. J. Bless, R. V. Krolak, D. R. Askins, "Evaluation of Lightweight Materials for Shelter Armors", University of Dayton, Dayton, Ohio, Prepared for ETD/AMED, U.S. Army Natick RD&E Center, Natick, MA., Natick/TR-86/046L, July, 1986.

4A. J. O. Hallquist, "DYNA3D User's Manual", LLNL, CA., Rev. April 1988.
4B. J. O. Hallquist, "DYNA3D Course Notes", LLNL, CA., UCID 19899, Rev. 2, November, 1987.
4C. J. O. Hallquist, "Theoretical Manual for DYNA3D", LLNL, CA., UCID 19401, March, 1983.

5. F. K. Chang and K. Y. Chang, "A Progressive Damage Model for Laminated Composites Containing Stress Concentration" and "Post-Failure Analysis of Bolted Composite Joints in Tension or Shear-Out Mode Failure", Journal of Composite Materials, Volume 21, pp. 809-855, 1987.

6. D. W. Stillman and J. O. Hallquist, "INGRID: A 3D Mesh Generator for Modeling Nonlinear Systems", LLNL, CA., UCID 20506, Rev. July, 1985.

7. B. E. Brown and J. O. Hallquist, "TAURUS: An Interactive Post-Processor for the Analysis Codes NIKE3D, DYNA3D, TACO3D, and GEMINI", LLNL, CA., UCID 19392, Rev. 1, May, 1984.

8. R. M. Jones, "Mechanics of Composite Materials", Scripta Book Co., Washington, D.C., 1975.

9. S. W. Tsai and H. T. Hahn, "Introduction to Composite Materials", Technomic Publishing Co., Inc., Westport, CT., 1980.

10. S. W. Tsai, T. N. Massard, I. Susuki, "Composites Design", 4th Ed., Think Composites, Dayton Ohio, 1988.

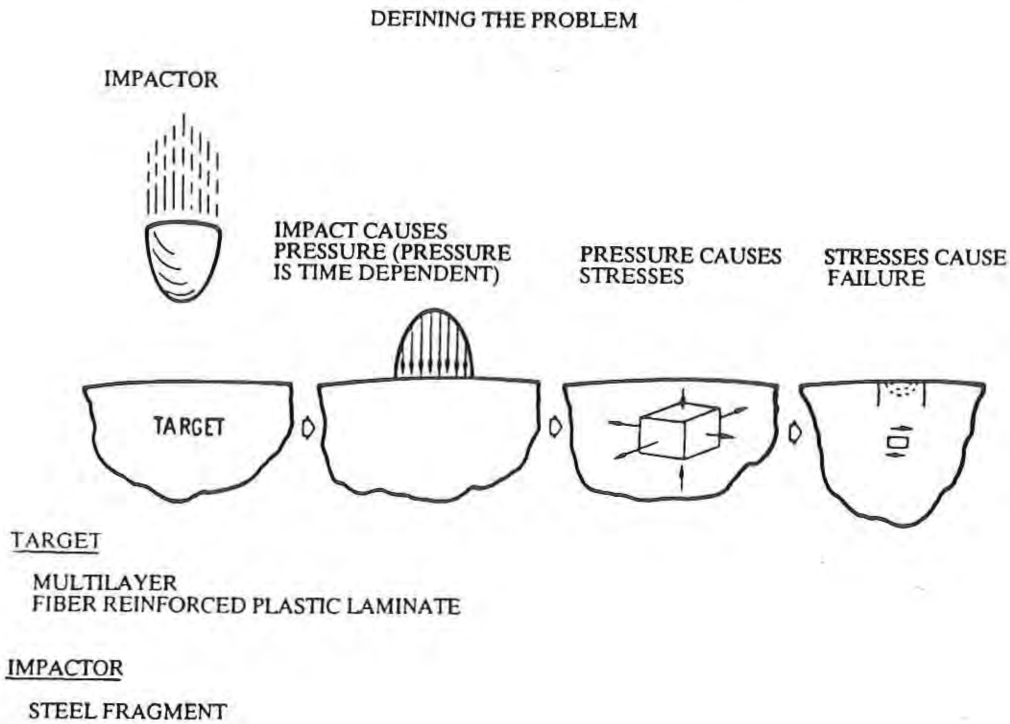

Figure 1. A General Description of the Impact Problem [1].

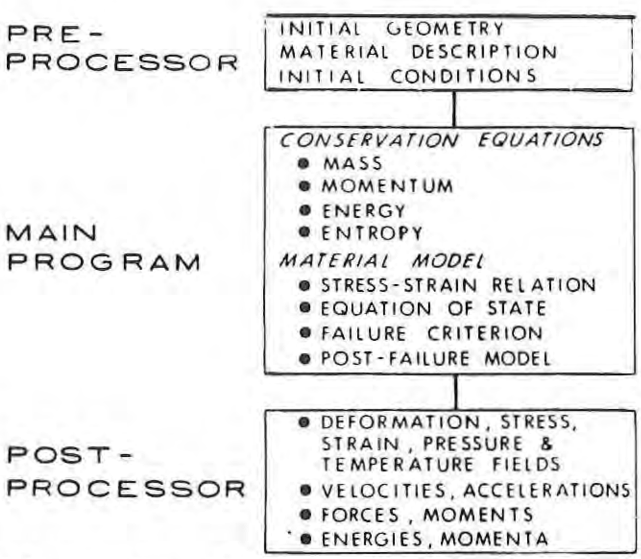

Figure 2. Structure of the Computational Process [1].

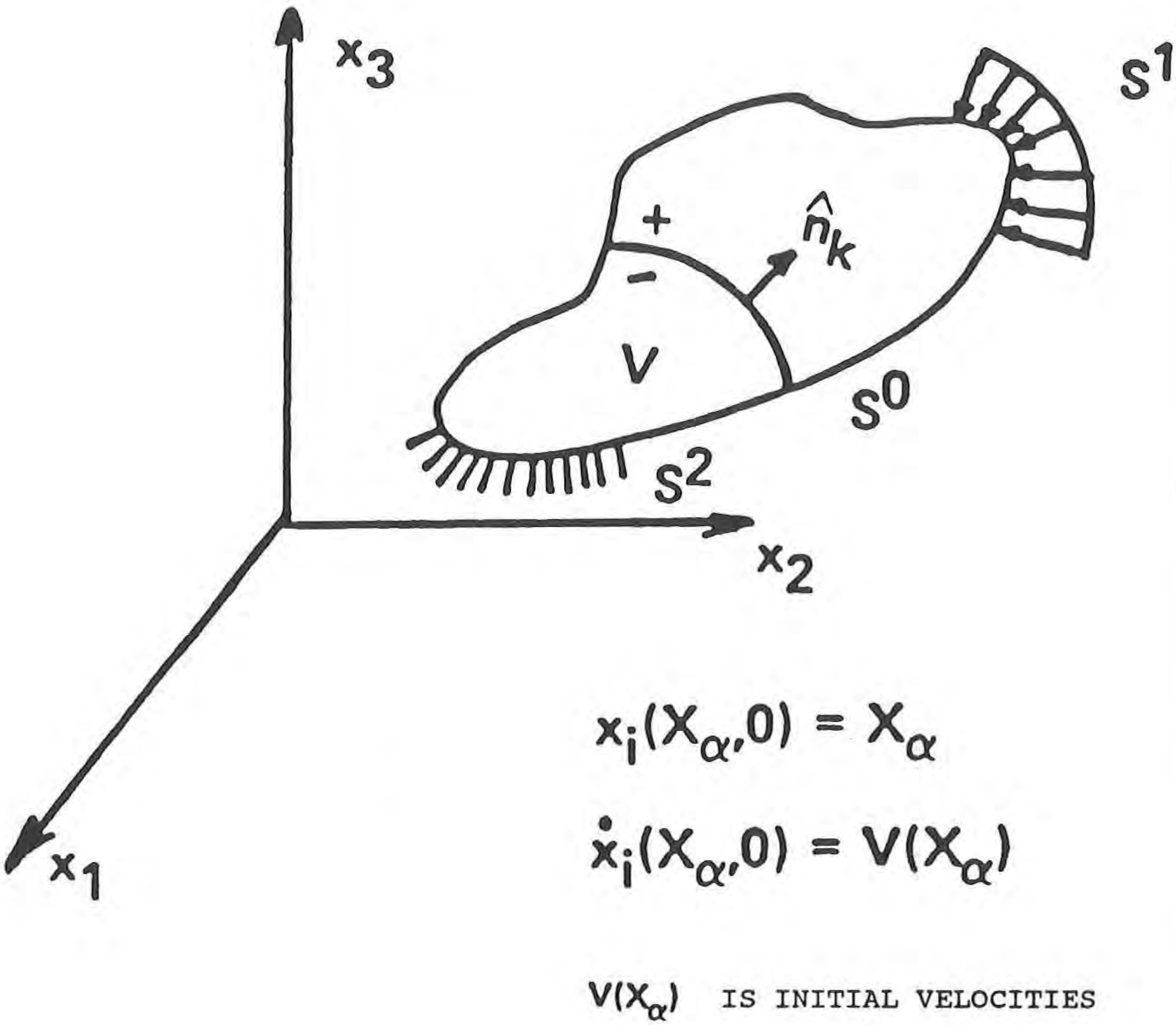

Figure 2a. A Body in a Fixed Rectangular Cartesian Coordinate Syst
Lagrangian Formulation is Considered [4b].

3D Axisymmetric

Quarter Symmetry Used.

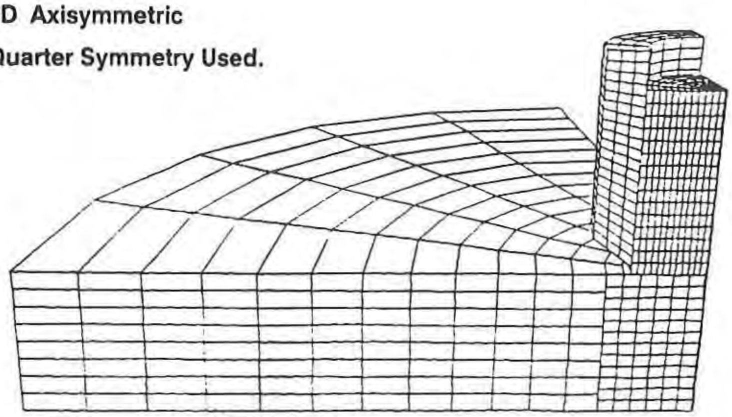

MODEL ACCOMMODATES:

- Fragments With Varying: Shape, Grain Size, Material Properties, Initial Velocity.
- Target Wall With Varying: Material, Ply Orientation, Thickness and Volume Fractions.
- Materials Under Consideration: Glass/Epoxy, Kevlar/Epoxy, Graphite/Epoxy

Figure 3. Geometry Mesh of DYNA3D Model.

.2 INCHES THICK GLASS/EPOXY WALL IN THE PROCESS
OF PENETRATION BY A 44 GRAIN FRAGMENT.

UNDEFORMED MESH
PRIOR TO IMPACT
V = 6000 IN PER SEC

DEFORMED MESH
AT TIME t = 20 MICROSECS

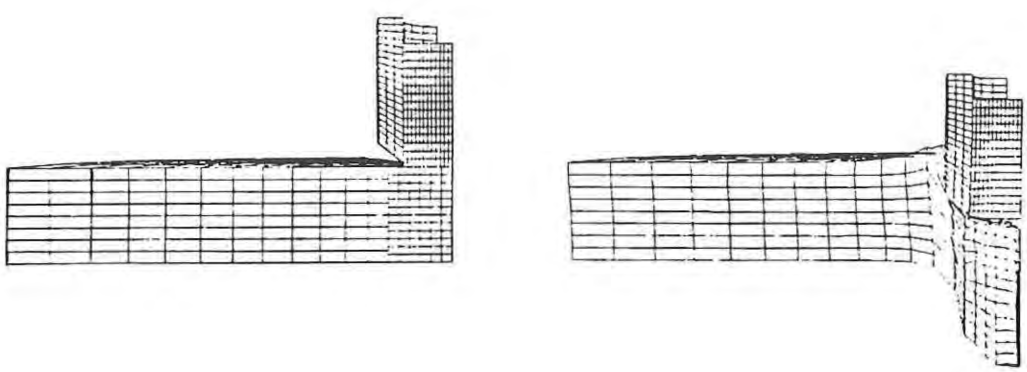

Figure 4. Scotchply Wall (.2 inches) Prior to and During Penetration.

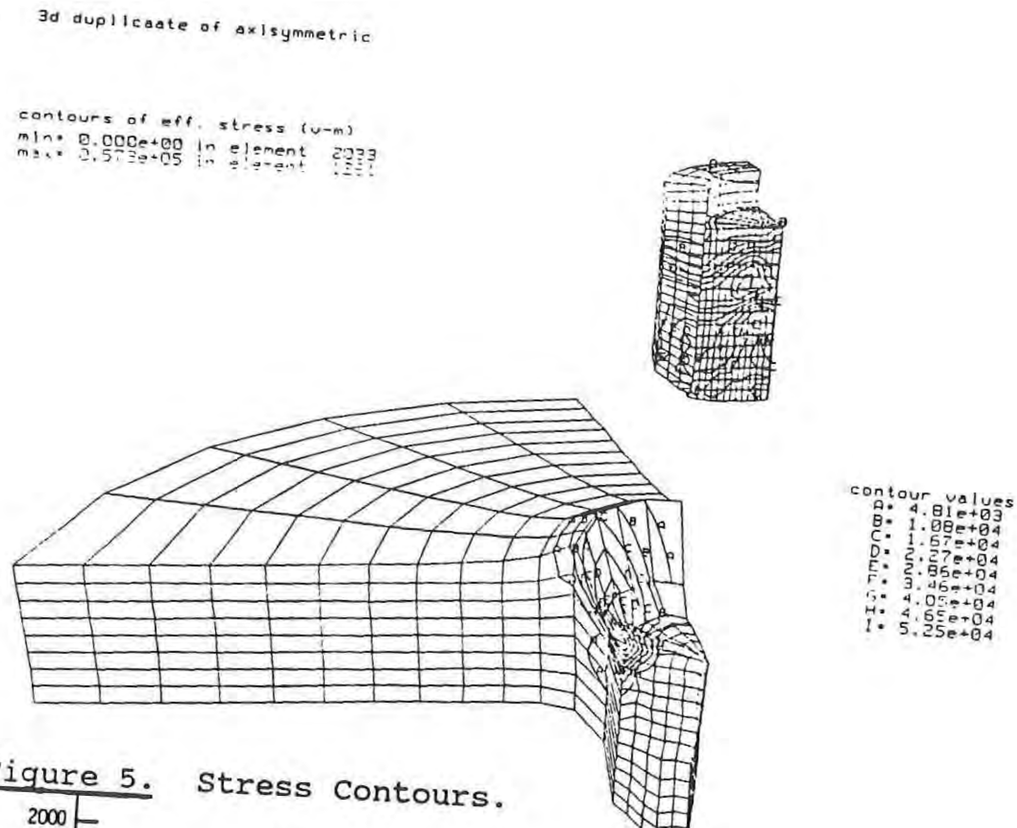

Figure 5. Stress Contours.

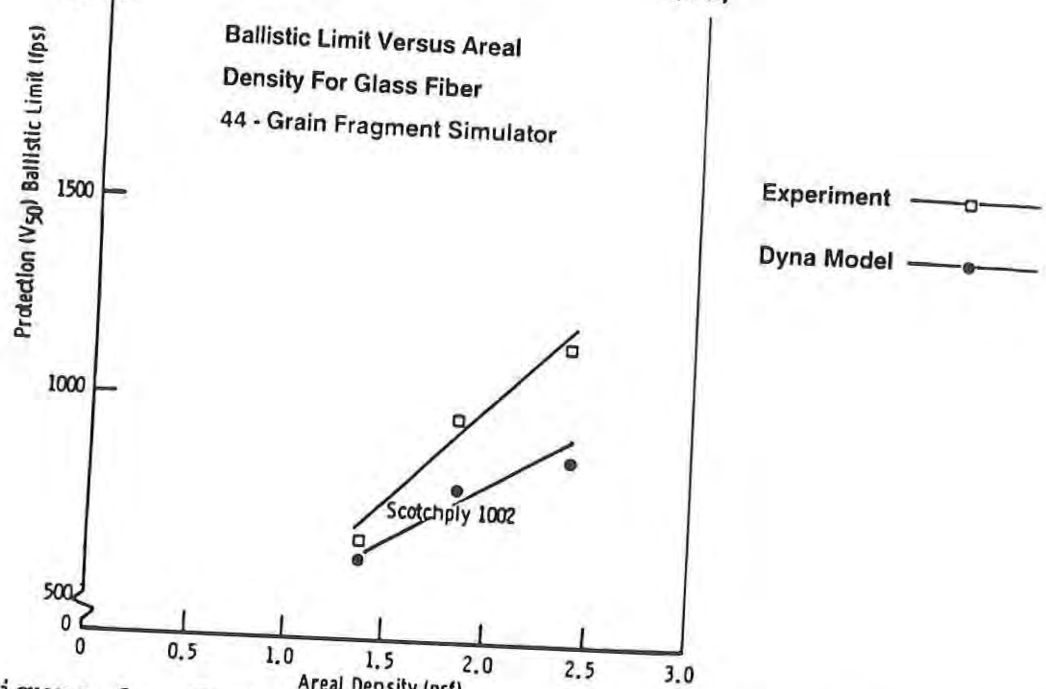

Figure 6. Graphical Comparison to Experiment (Scotchply) [2].

TITLE: Numerical Modeling of the Penetration of Airborne Contaminants into Pressurized, Porous Fabric Structures

*Struan R. Robertson, PhD

ABSTRACT: When an airborne contaminant impinges upon a porous fabric structure it will, in time, infiltrate through the fabric both by diffusion and mass transport and subsequently be distributed throughout the interior. Pressurizing the fabric structure, thus causing a net outflow, can effectively reduce the interior level of contamination. The equations needed to model this process are the Navier-Stokes equations for the flow field and the transport equation for the contaminant. The effect of the fabric on the flow field is modeled using a source term in the Navier-Stokes equations that is analogous to the Ergun equation for flow through packed columns. The diffusion coefficient in the transport equation for the fabric is obtained using results from the mechanics of composite materials.

The numerical model is based on the control volume method and the SIMPLER technique. This approach requires one grid for scalar variables, such as pressure and concentration, and a staggered grid for the velocity components. Since the fabric is very thin relative to the scale of the domain needed to model the external and internal flow fields, numerical experiments were run to determine the advisability of smearing its effect over a larger computational domain. It was found that such smearing was acceptable, thus significantly reducing the complexity of the model.

The effects of external air velocity and internal pressurization on the external and internal distribution of contaminant are presented for two-dimensional flows. It is shown that slight overpressures significantly reduce the contaminant level within the fabric structure.

*BIOGRAPHY OF PRESENTER: Struan R. Robertson

PRESENT ASSIGNMENT: Associate Professor of Mechanical Engineering at the University of Lowell under contract to US Army Natick Research, Development and Engineering Center.

PAST EXPERIENCE: University of Lowell for seven years; prior to which, GTE Research Labs for eight years, the US Army Ballistic Research Labs for two years, the Central Electricity Research Labs (U.K.) for one year and the US Army Watervliet Arsenal, Maggs Research Center for three years.

DEGREES HELD: PhD in Mechanics, Rensselaer Polytechnic Institute; BS and MS in Mechanical Engineering, Clarkson University.

Numerical Modeling of the Penetration of Airborne Contaminants into Pressurized, Porous Fabric Structures

Struan R. Robertson, Ph.D.

INTRODUCTION

When airborne contaminants impinge against a porous fabric structure, the level of contaminant concentration within the structure, in the steady state, will be the same as without. As might be expected, some qualitative experiments [1] have shown that if the structure is pressurized the level within will be lower than without. This paper studies the effect of pressurization on concentration level for a simple structure with porous walls for the case of two-dimensional flow. The governing equations for the problem are the Navier-Stokes equations for the velocity field and the concentration equation for the contaminant. These equations are nonlinear and coupled. The velocity and concentration equations can be put into the same generic form.

The contaminant is transported to the fabric structure by the external flow. It is then diffused and convected through the fabric to the interior of the structure. If the interior is pressurized there will be a net outflow from the structure, which will reduce the infiltration of contaminant. The equations for flow through the fabric are the same as those for the external and internal regions but with the addition of a source term that accounts for the pressure drop across the fabric. The equation for the transport of contaminant by convection and diffusion is the same for the fabric as for the external and internal regions except that the diffusion coefficient for the fabric is different from that for the air. The concentration levels for the contaminant are assumed to be low enough that its presence does not affect the Navier-Stokes equations. Further, the external flow is assumed to be laminar and steady.

The problem is solved numerically using the SIMPLER algorithm [2]. The interesting aspect is the way the flow of air and transport of contaminant through the fabric are modeled. Ergun [3] developed an empirical relation for the steady flow of fluid through a packed column. The equation is the sum of two terms, one linear and one square in the velocity. Armour and Cannon [4], in the spirit of Ergun's work, developed a similar relation for flow through woven screens. The coefficients in their equation depend on the void fraction, surface to volume ratio, effective pore diameter, effective screen thickness and the viscosity and density of the fluid. They give relations for determining the fabric parameters for various weaves such as plain square, full twill, etc.

These relations, of course, are for one-dimensional flow. Stanek and Szekely [5] have given an invariant form for Ergun's relation that is applicable to multi-dimensional problems. Such an expression was used, for example, by Beckerman et al. [6] to study natural convection between a fluid layer and a porous layer. In much the same way, the relation of Armour and Cannon is applied here to model the flow through the fabric.

Results from the theory of composite materials [7] are used to determine the effective diffusion coefficient for the fabric.

GOVERNING EQUATIONS

The governing equations for steady flow can be cast in the generic form,

$$(\rho v_i \phi)_{,i} = (\Gamma \phi_{,i})_{,i} + S \tag{1}$$

where a repeated index implies summation over the range of the index and a comma preceding an index (,i) implies $\partial/\partial x_i$.

For two dimensional problems in Cartesian coordinates the Navier-Stokes (momentum) equations are

$$(\rho uu)_{,x} + (\rho vu)_{,y} = (\mu u_{,x})_{,x} + (\mu u_{,y})_{,y} - p_{,x} + F_x \tag{2}$$

and

$$(\rho uv)_{,x} + (\rho vv)_{,y} = (\mu v_{,x})_{,x} + (\mu v_{,y})_{,y} - p_{,y} + F_y \tag{3}$$

where u in equation (2) and v in equation (3) correspond to ϕ in equation (1).

The equation for agent concentration is

$$(uC)_{,x} + (vC)_{,y} = (\eta C_{,x})_{,x} + (\eta C_{,y})_{,y}. \tag{4}$$

where C corresponds to ϕ in equation (1). Thus, equations (2)-(4) are in the form of the generic equation.

The continuity equation,

$$(\rho u)_{,x} + (\rho v)_{,y} = 0 \tag{5}$$

when substituted into equations (2) and (3) yields the usual equations associated with these problems. However, since the pressure field is not known a priori, it is used in the finite difference formulation to form a pressure correction equation [2].

The source terms F_x and F_y are zero in the gas. For the fabric, F_x and F_y are used to represent the effect of porosity on the pressure drop according to the following relations [5,6],

$$F_x = -(a_1 + a_2 | \bar{u} |)u \tag{6a}$$

$$F_y = -(a_1 + a_2 | \bar{u} |)v \tag{6b}$$

where a_1 and a_2 are given by [3]

$$a_1 = \alpha\mu A^2/\varepsilon^2 \tag{7}$$

$$a_2 = \beta\rho/D\,\varepsilon^2 \tag{8}$$

The viscous flow resistance coefficient $\alpha = 8.61$ and the inertial resistance coefficient $\beta = 0.52$ [3]. D is the pore diameter, A the surface area to volume ratio and ε is the void fraction.

Note that for steady uniform flow (i.e., u = constant and v = constant independent of x and y) equations (2) and (3) reduce to $\nabla p = \bar{F}$ as given in [5].

The diffusion coefficient for the fabric is found by using the Tsai-Halpin equation [7] as follows.

$$\eta_{fabric} = (1+\sigma V_f)\eta_{air}/(1-\sigma V_f) \tag{9}$$

where

$$\sigma = (\eta_{fiber} - \eta_{air})/(\eta_{fiber} + \eta_{air})$$

and $V_f = 1-\varepsilon$ is the volume fraction of fiber.

Noting that equations (2) - (4) are of the same form as the generic equation (1), the following table of analogies can be written. The pressure terms in eqs. (2) and (3) are part of the source term. The code, however, treats these internally so they do not appear in the table.

TABLE 1.
Parameter Analogies

Generic Eq.	Φ	ρ	Γ	S
X-Momentum Eq.	u	ρ	μ	F_x
Y-Momentum Eq.	v	ρ	μ	F_y
Concentration	C	1	η	0

On the boundaries u and v will be either normal or tangential to the boundaries. For the momentum equations, therefore,

u or v = 0 normal to the boundary

or

u or v specified normal to the boundary in case of inflow,

or

u and v not specified in the case of outflow.

For the concentration equation,

C or $\partial C/\partial n$ is specified on the boundary.

MODELING CONSIDERATIONS

The SIMPLER algorithm utilizing a staggared grid [2] is used to solve the equations. The FORTRAN program for the algorithm was provided by McKelliget and Charmchi [8].

When considering fabric structures the thickness of the fabric is significantly less than other dimensions in the problem, thus raising the following question. Is it necessary to have a very fine mesh in the fabric, or is it possible to use a coarse mesh and appropriately modify the source terms so that the physical behavior of the fabric with respect to pressure drop and contaminant diffusion is maintained? In order to answer this question a test problem was modeled for which an analytical solution could be found. The problem was for fully developed unidirectional flow in a tube with fabric placed across the tube near the exit, (see Fig. 1). The velocity distribution was parabolic with a maximum value of 2.032e-3 m/s. This distribution would ensure laminar flow through the fabric so the square term in the pressure drop expression would be small. The problem was modeled using a variety of meshes.

The analytical solution is found by assuming fully developed parabolic flow in the tube. The velocity distribution in the fabric is assumed to be the same as in the tube, which is

$$u = (1.0 - r^2/R^2)u_{\max}$$

where R is the outer radius of the tube. In this case, the equivalent of eq. (2) in cylindrical coordinates when evaluated at the centerline yields

$$\Delta P_{anal}/B = a_1 u_{\max} + a_2 u^2_{\max} + 4\mu u_{\max}/R$$

where B is the effective thickness [4] of the fabric. In this case only the first term will be significant.

Several cases were run in order to study the effect of mesh gradation on the numerical results. In the first case the fabric was was taken to be 2.54e-4 m thick and divided into 10 cells. The fluid was subdivided using a graded mesh that decreased from a cell of 2.54e-2 m to a cell of

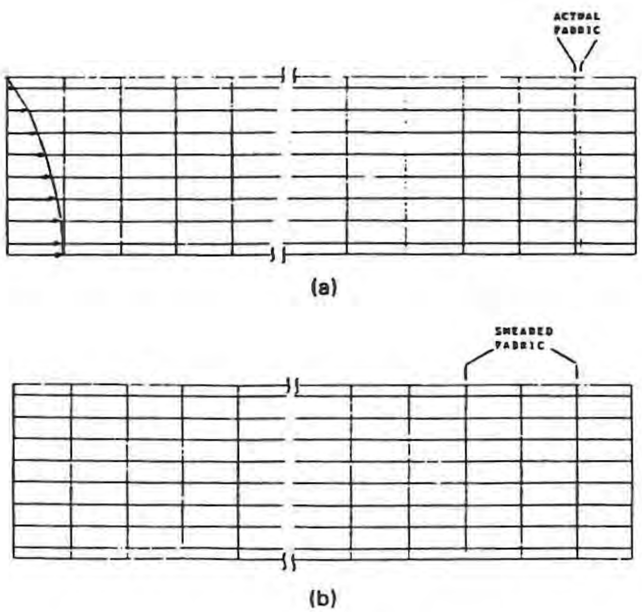

Figure 1. A circular tube with fully developed parabolic air flow to test fabric modeling strategies. The uniform mesh is shown for: (a) using the actual thickness of the fabric; (b) smearing the fabric over two large cells.

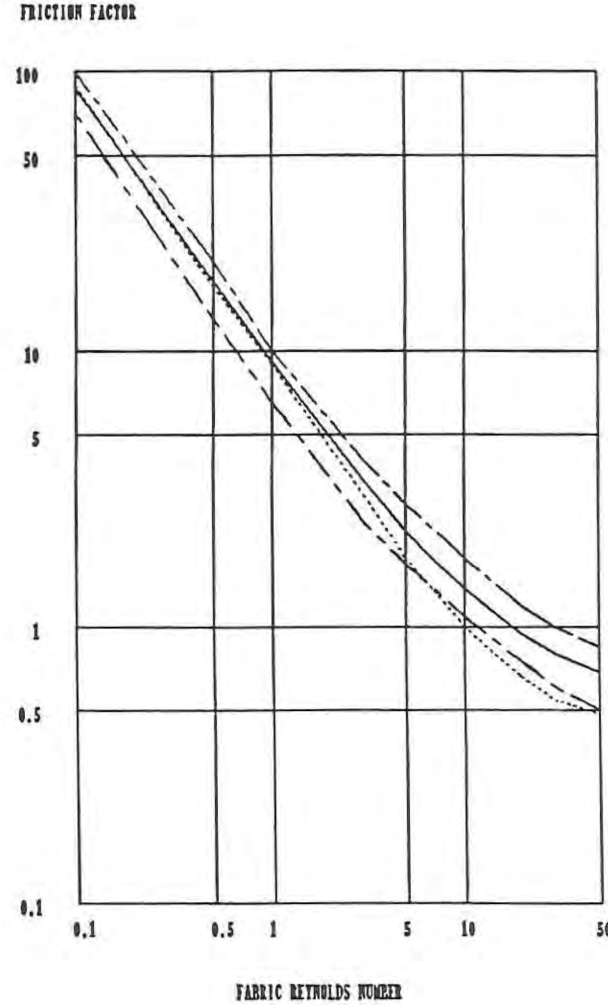

Figure 2. A comparison of pressure drop predictions for the fabric: _ _ _ _ numerical model, ______ empirical model, _ ___ _ experimental scatter bands.

2.54e-5 m where each successive cell was 0.75 times the size of the preceding cell. The second case had a uniform mesh with cells 2.54e-2 m wide in the fluid and ten cells 2.54e-5 m wide in the fabric. The pressure and contaminant drop across the fabric for the second case were the same as predicted in the first case. Then the number of cells in the fabric was reduced to 4 and 3. In the final case, the actual fabric was replaced by 2 cells whose thicknesses were 2.54e-2 m. This, of course, is extreme. In this instance the source term had to be modified as follows,

$$F^* = FB/2C_v \tag{10}$$

where F is defined as in eq. (6a) or (6b) and C_v is the thickness of the each cell. Also, in order that the concentration on the inside and outside of the fabric in the model be the same as that for the actual fabric, the diffusion coefficient is modified as follows,

$$\eta^* = \eta_{fabric}(2C_v/B). \tag{11}$$

It was found that the results for this very crude representation agreed with the previous results. Table 2 compares the results for the pressure drop across the fabric for the cases where the fluid was divided into cells of uniform thickness with the analytical solution. The goodness of the approximation is clear. Similar results were found for the concentration. Because of this, the modeling of the problem of interest here was greatly simplified.

TABLE 2. $(\Delta P_{anal} - \Delta P)/\Delta P_{anal}$		
Thickness	Cells	Result
2.54e-4 m	10	0.000
2.54e-4	4	0.003
2.54e-4	3	0.009
5.08e-2	2	0.012

As a further verification of the model, the case with the smeared mesh was solved completely without assuming a particular form for the velocity distribution except at the inlet. At the inlet a parabolic distribution was used and the solution was performed for average inlet velocities ranging from 0.0254 to 25.4 m/s. Fig. 2 plots the friction factor $f = \Delta P \varepsilon^2 D/B\rho u^2$ versus the fabric Reynolds number $Re_f = \rho u/\mu a^2 D$ for the fabric at the centerline of the tube. Shown are the empirical relation of Armour and Cannon, the results for the model and the envelope for their experimental data. The numerical model is in good agreement with the empirical model up to $Re_f = 1.3$ after which it starts to diverge. This corresponds to a Reynolds number in the tube of nearly 2000, which is the point of transition from laminar to turbulent flow. Since the model assumes only laminar flow, such behavior is to be expected. However, up to $Re_f = 6$ the numerical results are still within the experimental data scatter band. Beyond this value the numerical results are just below the lower scatter band.

For the purpose of preventing infiltration of contaminant into a fabric structure it is necessary to have only a low mass outflow at very low velocities. It is precisely at such low velocities that the numerical model is closest to the empirical relation.

THE MODEL

The problem studied is shown in Fig. 3. The flow is two dimensional with the inflow specified with the profile,

$$u_{in}=6.0*u_{avg}(1.0-y/h)y/h. \tag{12}$$

The outflow condition is zero pressure. The top and bottom are impermeable except for the bottom of the chamber. The inflow velocity, v_{in}, is assumed to be uniform. The velocity is also assumed to be normal to the fabric walls of the chamber. The concentration has a uniform maximum value on the inflow side of $C_{\max} = 1.0$ and a uniform minimum value on the outflow side and on the bottom of the chamber of $C_{\min} = 0.0$.

The mesh is nonuniform starting with a spacing of 0.1016 m down to 0.00508 m for the cell adjacent to the wall. For the chamber the first two and last two cells are fabric. The cell horizontal cell spacing for the chamber is 0.00508 m for the two cells through the fabric and the interior adjacent cells. These increase toward the center where the cell is 0.0127 m wide. The cells increase from the right wall to a width of 0.1016 m at the outlet. In the vertical direction, the cells decrease from 0.0127 m to 0.00508 m for the cells adjacent to and in the two cells through the top of the chamber. These increase to a maximum of 0.0254 m and then decrease to 0.00508 m next to the upper surface in order to accommodate the no-slip condition. There are 83 horizontal and 50 vertical velocity points in the mesh.

Because the concentration of contaminant is low, the concentration equation can be solved separately from the velocity equations. Thus, the velocity field is solved for first. This is then used in the solution of the concentration equation.

The problems considered are for air with $\mu = 1.896e{-5}\ N{-}s/m^2$ and $\rho = 1.135\ kg/m^3$ and a fabric with $\varepsilon = 0.759, A = 3909./m$, and $D = 5.49e{-4}\ m$. The fabric is 5.08e-4 m thick. This corresponds to a plain weave fabric. The dimension "a" in Fig. 3 is 0.254 m. The diffusion coefficients are $\eta_{air}=2.84e{-5}m^2/s$, $\eta_{fiber}=0.0$ and, using eq. (9), $\eta_{fabric}=1.73e{-5}$.

RESULTS

If there is no inflow along the base of the chamber the concentration will have the upstream value of 1.0 everywhere in the steady state. If there is no crossflow, i.e., the left boundary is a wall, and there is inflow along the base, it would be expected that the chamber would be free of contaminant. Fig. 4 shows the velocity field for this case when the inflow along the base of the chamber is 0.0254 m/s. Fig. 5 shows the concentration contours for this case. Note that the chamber is free of contaminant.

In the event of crossflow some contaminant might be expected to infiltrate into the chamber

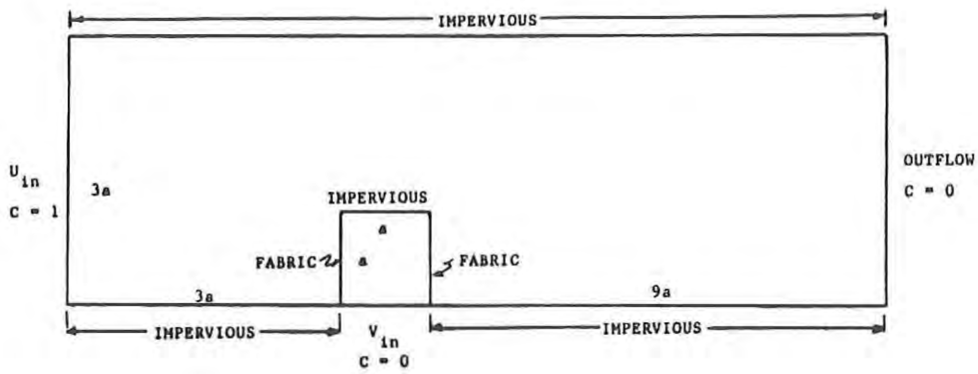

Figure 3. The problem domain with a = 0.254 m.

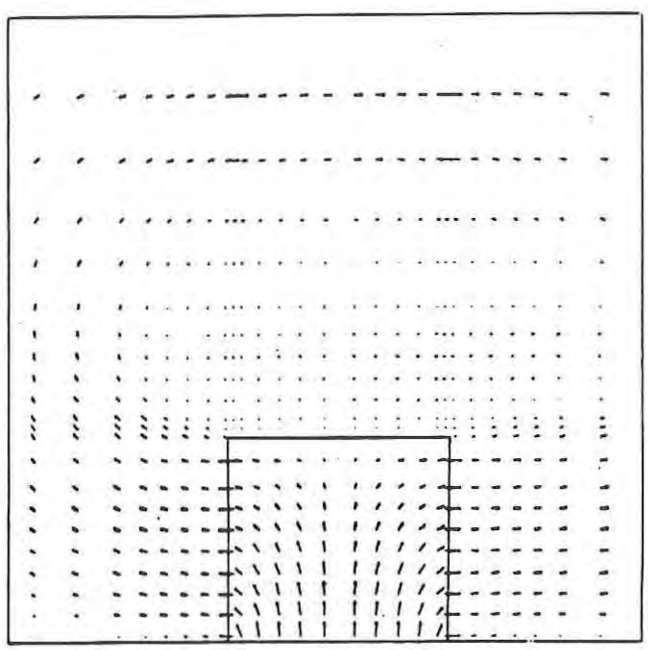

Figure 4. The velocity field in the neighborhood of the chamber when there is no crossflow and the inflow into the chamber is 1.0.

if the inflow is low enough. For all the crossflow cases considered u_{avg} in eq. (12) is 0.0508 m/s. Fig. 6 shows the velocity field for the case when the inflow velocity along the base is $0.5u_{avg}$ and Fig. 7 shows the concentration contours for this case. Figs. 8 and 9 show the velocity field and concentration contours, respectively, when the inflow velocity is $0.2u_{avg}$. When the inflow is $0.5u_{avg}$ there is no significant contamination of the chamber but with the reduced inflow of $0.2u_{avg}$ the contaminant is starting to infiltrate into the chamber. Even so the contamination is slight because of the favorable pressure gradients, as shown by the pressure contour plot in Fig. 10.

TABLE 3.

Mid height pressures ($10^{-3}Pa$) for the exterior left wall and the center of the chamber.

u_{avg}	v_{inflow}	P_{wall}	P_{ctr}	ΔP
0.0	0.0254	0.0689	13.64	13.57
0.0508	0.0254	9.16	16.67	7.51
0.0508	0.0203	9.23	13.37	4.13
0.0508	0.0152	5.10	9.71	4.62
0.0508	0.0102	3.45	6.55	3.10

Table 3. compares the mid-height pressure on the exterior of the left wall to the pressure at the center of the chamber for the cases studied. Clearly the pressure within the chamber is higher than outside but, just as clearly, there is no clear trend in ΔP as inflow velocity is reduced. This lack of trend is due to the changes in the flow field that occur with changing inflow velocity.

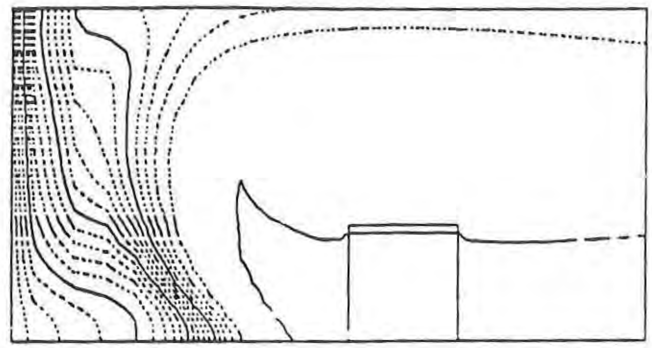

Figure 5. Concentration contours for no crossflow and an inflow of 0.0254m/s.

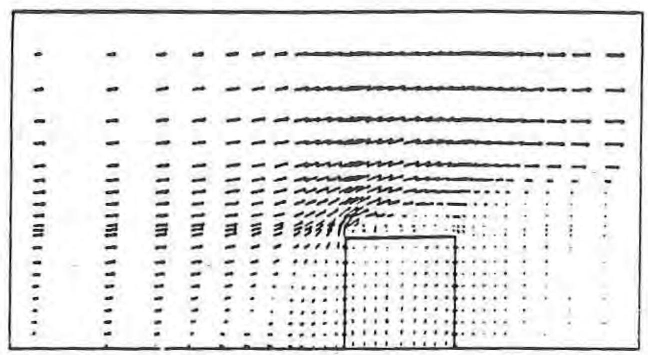

Figure 6. The velocity field for the case with crossflow and an inflow of 0.0254m/s.

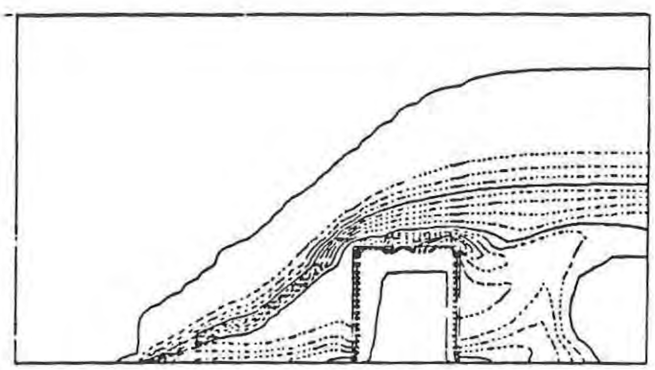

Figure 7. Concentration contours for the case with crossflow and an inflow of 0.0254m/s.

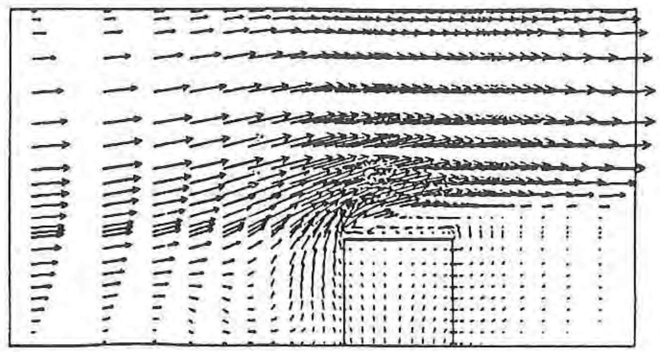

Figure 8. The velocity field for the case with crossflow and an inflow of 0.0102m/s. (The scale is 3 times that of Fig. 6.)

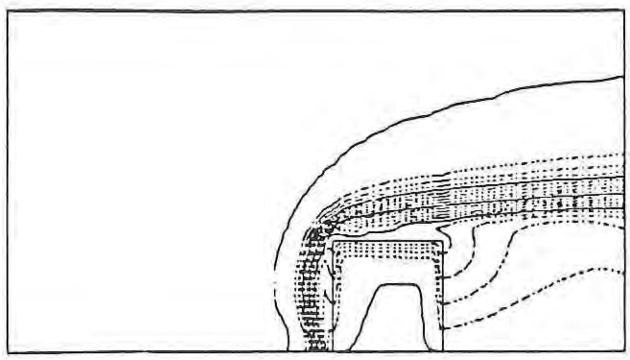

Figure 9. Concentration contours for the case with crossflow and an inflow of 0.0102m/s.

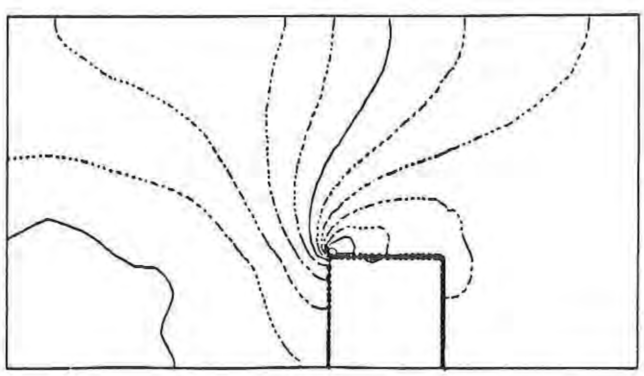

Figure 10. Pressure contours for the case with crossflow and an inflow of 0.0102m/s.

DISCUSSION

It is possible to effectively model the infiltration of airborne contaminant through porous walls into a chamber and to study the effect of pressurization on infiltration. Small positive pressure differences help to maintain a low level of contamination within the chamber. If the velocity through the fabric is small enough only the linear term in eqs. 6a and 6b will be important. Thus, if one were interested in the case where flow through the fabric were slow and the external flow were laminar, a similarity solution could be usefully pursued. Another class of problems that would be interesting to study is where the external flow is turbulent, which is the case of most practical interest. In this case the flow through the fabric might be either slow or fast depending on the pressure differences between the inside and outside. In this situation it is not clear at this time what the important parameters are without further study.

ACKNOWLEDGEMENT

The author wishes to thank the U. S. Army Natick RD&E Center for supporting this study.

NOMENCLATURE

A - surface area to volume ratio

B - effective thickness of the fabric

C - concentration of contaminant

C_v - cell thickness

D - pore diameter

F_x, F_y - source terms in the Navier-Stokes equations

$\mathrm{Re}_f = \rho u / \mu A^2 D$ - fabric Reynolds number

a_1, a_2 - constants in the Armour-Cannon equation

$f = \Delta p\, \varepsilon^2 D / B\, \rho u^2$ - friction factor

p - pressure

$\overline{u}$ - velocity vector

u, v - x and y components of $\overline{u}$

α - viscous flow resistance coefficient

β - inertial resistance coefficient

ε - void fraction

η - contaminant diffusion coefficient

μ - viscosity

ρ - density

REFERENCES

1. Kuntavannish, M., private communication, US Army Natick RD & E Ctr., Natick, MA., June 1987.

2. Patankar, S. V., NUMERICAL HEAT TRANSFER AND FLUID FLOW, Hemisphere, Washington, D. C., 1980.

3. Ergun, S., "Fluid Flow Through Packed Columns", Chemical Engineering Progress, V48, N2, pp 89-93, Feb. 1952.

4. Armour, J. C. and Cannon, J. N., "Fluid Flow Through Woven Screens", AIChE Journal, V14, N3, pp 415-419, May 1968.

5. Stanek, V. and Szekely, J., "Three-Dimensional Flow of Fluids Through Nonuniform Packed Beds", AIChE Journal, V20 N5, pp 974-980, Sept. 1974.

6. Beckermann, C., Ramadhyani, S. and Viskanta, R., "Natural Convection Flow and Heat Transfer Between a Fluid Layer and a Porous Layer Inside a Rectangular Enclosure", Jour. of Heat Transfer, V109, pp 363-370, May 1987.

7. Agarwal, B. D. and Broutman, L. J., ANALYSIS AND PERFORMANCE OF FIBER COMPOSITES, J. Wiley & Sons, New York, 1980.

8. McKelliget, J. and Charmchi, M., private communication, U. Lowell, Lowell, MA., June 1986.

TITLE: A New Production Scheduling Algorithm for Large Volume Multi-Product Bakery Operations Afloat.

*YUHASKI, STEVEN J., JR., DR.

ABSTRACT:

Navy bakery operations afloat are characterized by a highly erratic manpower utilization distribution over any given shift. A number of undesirable consequences can be associated with these erratic work schedules including stress among workers and insufficient time to complete preventative maintenance schedules.

The problem addressed in this project was to develop a new production scheduling algorithm that would result in smoother work schedules while taking into account equipment availability and recipe procedures. It is important to note that the objective of this project involves smoothing the work schedule rather than minimizing costs or labor or maximizing equipment usage.

Equipment, labor, and recipes were converted to build a data base. The principle of the new scheduling algorithm builds upon the familiar Gantt diagram which is compatible with worksheets now prepared manually by shipboard bakers. A combinatorial approach is used to enumerate feasible starting times for each batch of products to be produced during a shift. A sequence of differential starting times is assigned selectively so that the search for the best schedule begins at regions in the solution space that are most likely to contain schedules that result in the smoothest possible labor usage distribution.

With current manual production scheduling methods, labor usage profiles ranged from 100% of the work force productively engaged to 0% so used. The production schedules derived with the new algorithm smoothed out the peaks and valleys significantly. Also, the new algorithm makes it possible to produce production schedules on Zenith personal computers. The algorithm has general applicability for improving any scheduling operation which can be represented by Gantt diagrams.

*BIOGRAPHY: Steven J. Yuhaski, Jr.
PRESENT ASSIGNMENT: Operations Research Analyst, Food Systems Division, Advanced Systems Concepts Directorate, U. S. Army Natick Research, Development and Engineering Center for two years.

DEGREES HELD: B.S. Aerospace Engineering, Univ. of Mass.; M.E. Mechanical Engineering, Univ. of Florida; M.S., Ph.D., Industrial Engineering and Operations Research, Univ. of Mass.

A New Production Scheduling Algorithm for Large Volume Multi-Product Bakery Operations Afloat

Steven J. Yuhaski, Jr., Dr.

INTRODUCTION

As part of an overall effort to modernize shipboard bakeries, an effort to upgrade and enhance production efficiency was made through the development of a scheduling algorithm.

The produce-to-order scheduling methods that are currently in use tend to produce manpower utilization distributions that exhibit periods of considerable worker activity along with periods of complete idleness, in which the equipment is operating while the workers themselves are unoccupied.

Adverse consequences, such as stress among the workers and lack of time to perform maintenance duties, can be the result of these erratic work schedules. In food service operations in general, some studies, such as Lundberg and Armatus (1), reveal that as much as 33% of the available labor is lost due to inefficient scheduling practices. Thus, a more efficient utilization of limited human and equipment resources would occur if schedules that yield smoother manpower utilization distributions could be derived.

The production scheduling algorithm that is presented in this paper generates schedules having smooth manpower utilization distributions very efficiently with a personal computer.

SCHEDULING TECHNIQUES

Many techniques have been developed to solve a wide variety of scheduling problems. Much research has been devoted to the well-known flow-shop and job-shop scheduling problems (2). Each of these kinds of problems involves routing $J_1,\ldots,J_m$ jobs through $M_1,\ldots,M_n$ machines (or processors). Many constructive algorithms have been developed to solve these problems. Constructive algorithms are techniques that determine (i.e., construct) the global optimal solution by following a well-defined set of logical procedures that lead irreversibly (i.e., not by trial and error) to the optimal solution for a given criterion. These constructive algorithms are very efficient, impose very little demand on computer memory, and determine the global optimal solution in polynomial time. Besides constructive algorithmic techniques, there are many other methodologies that employ dynamic programming (3) and integer programming (4) usually to determine the global optimal solution, and methods involving nonlinear programming. Also, there are a myriad of heuristic methodologies (2) that are useful in determining suboptimal solutions to scheduling problems that are not related to the job-shop or flow-shop variety.

The bakery production problem, which will be described in more detail in the following section, is far more complex that either the flow-shop or the job-shop problems, principally because it is resource constrained in terms of both manpower and (bakery) equipment and because it is precedence constrained in terms of a series of distinctly different but connected tasks. Therefore, constructive algorithms that are useful in solving flow-shop and job-shop problems are not useful in dealing with the bakery scheduling problem. Thus, optimization techniques that are enumerative are required to deal with the bakery production scheduling problem.

Dynamic and integer programming techniques require considerable amounts of computer storage capacity to solve their corresponding formulations because of the number of trial solutions that have to be recorded during the enumeration of all possible solutions. Typically, if storage is compromised than speed is also compromised. Therefore, solving a bakery production scheduling problem of even modest size (e.g. 14 to 20 decision variables) on a personal computer is far from viable if the enumerative methods that are characteristic of mathematical programming techniques are applied.

The heuristic (algorithm) that is presented in this paper is enumerative; however, it avoids storage capacity problems since the combinatorics proceed in such a progression that large sections of the potential solution space can be eliminated in an easily defined pattern. The algorithm is also able to identify large regions of infeasibility during its search and to discard these regions as candidates for more thorough examination. Although combinatoric algorithms obtain solutions in exponential time, the manner in which this algorithm proceeds effectively mitigates the severity of the time involved in solving the bakery scheduling problem to such an extent that the casual observer may be led to believe incorrectly that the solutions occur in polynomial time.

Obviously, the algorithm is applicable to many other kinds of scheduling problems. The algorithm can be used to solve a myriad of simpler variations of the structure of the bakery scheduling problem by manipulating the values of the input parameters. This can be done by assigning the parameter values either zero or unity (whichever is appropriate) to reduce and simplify the structure of the problem. Additionally, upper bounds that are unapproachably large can be assigned to eliminate constraints.

PRODUCTION SCHEDULING MODEL FORMULATION

The formulation of the bakery production scheduling model consists of the conceptualization of its structure, along with its definitive terminology, and the mathematical model in terms of an objective function, decision variables, and constraints. The mathematical model defines the functional relationships between the input variables, the decision variables, the objective function, and the constraints.

Model Structure

The structure of the bakery production scheduling model is most easily depicted by a diagram that is similar to a Gantt diagram (2); refer to Figures 1 and 2. Unlike the Gantt diagram, whose horizontal rows each represent a single assignment, the conceptual diagram for the bakery production scheduling model depicts a horizontally connected sequence of homogenous steps, which will be referred to a a batch. Each step is a separate task that requires a designated amount of time to complete. The information from which the steps and batches are derived is the recipe for the batch. Note, from Figure 1, that each of the (nine) steps that represent the batch schematic for 100 pecan pies is divided into equal subsections that represent time increments. For the profiles in the recipes that are depicted in this paper, the increments each represent 10 minutes. A collection of batches of the same recipe are referred to as a product; the terms batch and product may be used interchangeably when the collection consists of only one batch. A shift refers to the interval of time in which all (bakery) products are assigned for initiation and completion.

Note, from Figure 1, that the resource utilization for each batch is defined in terms of worker and equipment profiles. Each step (which is delineated by solid lines) is assigned a constant number of workers as indicated by the worker profiles. The numerical designations in the increments of the equipment profiles will henceforth be referred to as activities, although they usually correspond to a specific kind of

Worker Profiles

4	4	4	1	1	4	4	2	0	0	0	0	2	0	0	0	0	0	0	2

Equipment Profiles

0	0	0	0	4	0	0	3	3	3	3	3	0	0	0	0	0	0	0	0

<u>Equipment Activity Designations</u>

0 - None or other (than 1, 2, 3, or 4 below)

1 - Horizontal Mixer

2 - Proofer

3 - Oven

4 - Vertical Mixer

Figure 1: Worker and Equipment Profiles
for Pecan Pie Recipe (100 Pies)

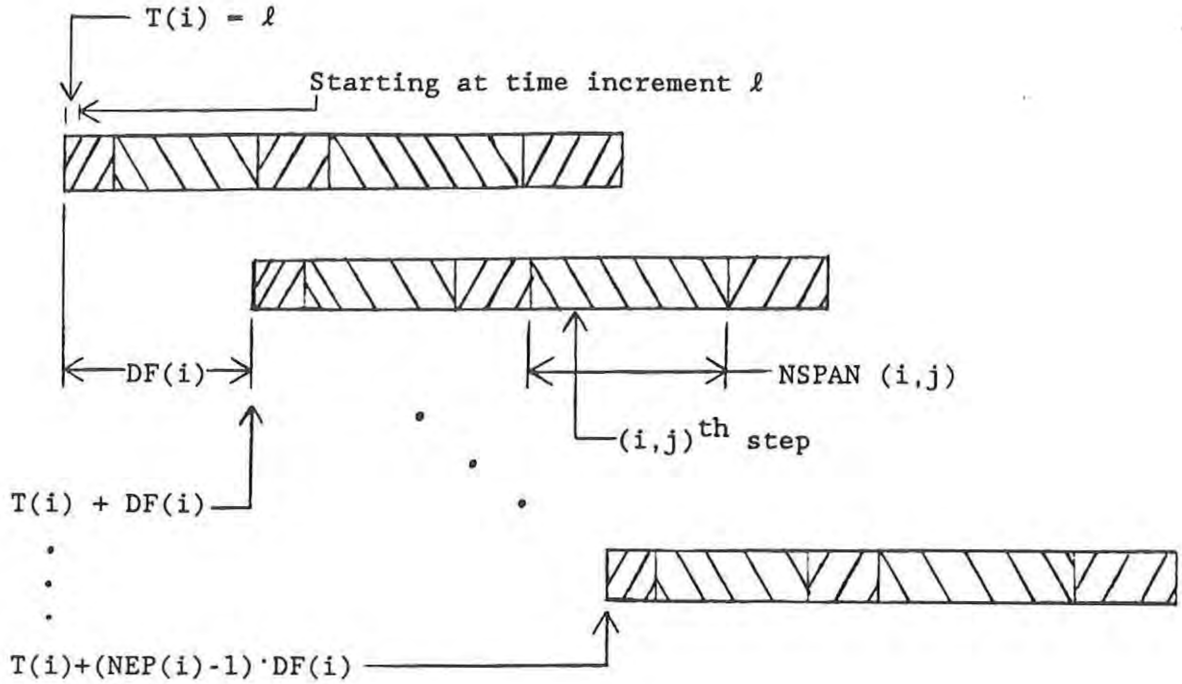

Figure 2: Schematic Representation of a Batch of Products with Starting Times for Each Batch.

equipment. Note that the activities are always the same throughout each step. Thus any activity requires a given number of workers or a particular kind of equipment or both during any given step. It is important to note that some activities require no sustained human effort and, conversely, some human efforts require no equipment that corresponds to a limited or nonportable resource. Baking is an example of the former; rolling dough is an example of the latter. Activities not involving a limited resource are designated by zero since resources that are, for all practical purposes, unbounded within the context of the situation in the bakery do not need to be accounted for quantitatively. Thus, it is possible for a step (e.g., next to the last in Figure 1) to have zero designated in its (time) increments for both the worker and equipment profiles (and still be productive). For example, the eighth step of the recipe for 100 pecan pies consists of refrigerating the pies for 1 hour. Since there is always enough refrigeration space regardless of whatever is being produced in the bakery, the activity number for refrigeration is zero.

Mathematical Model

The objective of the production scheduling problem is to generate schedules having smooth manpower utilization distributions over time and to select the schedule having the smoothest manpower distribution of those generated.

Denote $SW(\ell)$ as the sum of the workers that are occupied during time increment ℓ, for $\ell = 1,\ldots,NINC$. (See list of input variables).Thus, all $W(i,j)$ for all (i,j) during time increment ℓ are summed to obtain $SW(\ell)$. The manpower utilization distribution over time, also referred to as the worker distribution, is defined by the sequence $SW(1),\ldots,SW(\ell),\ldots,SW(NINC)$. The absolute difference in adjacent worker sums gives an indication of the roughness of the worker distribution. The mean of these differences gives an indication of the overall roughness of the worker distribution over the entire shift from $\ell = 1$ to NINC. The mean of the absolute differences squared is an indicator of roughness that is more sensitive to the larger absolute differences since squaring the terms in the summation accentuates the larger absolute differences (relative to the other absolute differences). Thus the mean of the square of the absolute differences is MSAD in equation (1).

$$MSAD = \frac{1}{NINC-1} \sum_{\ell=2}^{NINC} (SW(\ell) - SW(\ell-1))^2 \quad (1)$$

LIST OF INPUT VARIABLES

NINC	= number of time increments in the shift
NP	= number of products, i = 1,...,NP
NA	= number of activities or the highest integer that represents an activity during the shift
NEP(i)	= the number of batches of each product
NSP(i)	= the number of steps (in the recipe) in product i
DL(i),DU(i)	= the lower and upper bounds in the delay in the start of the next batch after the finish of the preceding batch in product i (this designation is optional)
NSPAN(i,j)	= the time (in increments) required by step j of product i, j = 1,...,NSP(i)
AUB(k)	= the limit of the number of times activity k = A(i,j), defined below, can be preformed simultaneously (i.e., during any increment)
AQ(i,j)	= quantity or units of activity A(i,j) used by step j of product i
WUB	= worker upper bound, the number of workers present in the bakery
A(i,j)	= the activity performed during step j of product i
W(i,j)	= the number of workers used to perform step j of product i
TLBC(i),TUBC(i)	= the lower and upper bounds of the starting times of product i,...,NP

LIST OF OUTPUT VARIABLES

T(i)	= the starting time of the first batch of product i (in time increments)
DF(i)	= the differential between the starting times of successive batches in product i (in time increments)
CRWD	= the coefficient of roughness in the distribution of workers over the shift
TSM(i),DFSM(i)	= the values of T(i) and DF(i) corresponding to the smoothest worker distribution, i.e., having the smallest value of CRWD found
CRMIN	= the smallest value of CRWD found

Dividing the sum by the number of absolute differences, NINC - 1, is necessary, but not sufficient, for cross-comparisons between different shifts. In order to make comparisons in smoothness between schedules having significantly different numbers of workers and different amounts of assigned products, it is necessary to scale down MSAD by dividing by indicators of the average number of workers employed throughout the shifts. The average number of workers is shown in equation (2).

$$\mathrm{ASUMW} = \frac{1}{\mathrm{NINC}} \sum_{\ell = 1}^{\mathrm{NINC}} \mathrm{SW}(\ell) \qquad (2)$$

Dividing the mean of the square of the absolute differences by the square of the average number of workers yields a nondimensional term that is an indicator of roughness that can be used to compare schedules. This term is referred to as the coefficient of roughness and is given by equation (3) with respect to equations (1) and (2).

$$\mathrm{CRWD} = \mathrm{MSAD}/(\mathrm{ASUMW}^2) \qquad (3)$$

The figure of merit is the inverse of the coefficient of roughness, this would be an indicator of smoothness of the worker distribution. Therefore, the objective is the minimum (value) of CRWD. Thus, the schedule having the smallest value of CRWD is the schedule that has the smoothest worker distribution.

The decision variables are T(i) and DF(i); they are defined as the starting time (in increments) of the first batch of product i and the (incremental) difference in the starting times between any successive batches of product i respectively. The relationships between the starting times of each batch and the values of the decision variables T(i) and DF(i) for product i are apparent in Figure 2. For instance, the incremental starting time for the n^{th} batch of product i is given as follows:

$$T(i) + (m-1)DF(i)$$

The parameter NEP(i), shown in Figure 2 (see list of input variables), indicates how many batches there are for each product i. NSPAN(i,j), which is the (incremental) time required to complete step j of product i, is also indicted in Figure 2. Therefore if values for T(i), DF(i), NSPAN(i,j) and NEP(i) are given for every step j of product i, then the starting (and ending) time increments for all the steps of all the batches in product i can readily by computed.

The schedules that are generated by the algorithm are subject to resource constraints. The resources, which are the worker and equipment capacities of the bakery, are constrained by their corresponding upper bounds. The sums of the workers occupied during increment ℓ, $SW(\ell)$, is constrained as shown in equation (4). The parameter WUB is the number of workers that are assigned to the bakery.

$$SW(\ell) \leq WUB \qquad (4)$$

The activities are constrained by the limited amount of equipment in the bakery. AUB(k), for k = 1,...,NA (see list of input variables), is the upper bound on activity k, indicates the number of units of equipment that can perform activity k. For example, in reference to Figure 1, AUB(2), would be the number of proofers in the bakery. Referring to the definitions in the list of input variables, note that AQ(i,j) is defined in terms of A(i,j). Thus, the sum of the quantity of activity k that occurs during time interval l, which is denoted by SA(k,l), for l = 1,...,NINC, and k = 1,...,NA, must not exceed AUB(k), as expressed by equation (5).

$$SA(k,\ell) \leq AUB(k) \qquad (5)$$

Another type of constraint that influences the bakery production scheduling problem is referred to as precedence, or technological, constraint. The precedence constraints specify the order of the sequence of connected steps for each product. In the model that is presented in this paper, the order of execution of the steps within any given batch is fixed. The steps are not executed concurrently with any other step within the same batch.

The next section outlines an algorithm that efficiently generates trial values for the decision variables T(i) and DF(i) for i = 1,...,NP (i.e., the number of products to be scheduled) and checks for feasibility, during its search for a schedule having the smoothest worker distribution possible.

PRODUCTION SCHEDULING ALGORITHM

The production scheduling algorithm locates feasible solution points that represent product starting times and batch starting time differentials within each product. The algorithm stops after locating a given number of feasible schedules, and the solution corresponding to the schedule having the smoothest worker distribution is given as output in terms of starting times and batch differentials for each product and the coefficient of roughness.

This section contains a general description of the production scheduling algorithm and a detailed description of the search routine that locates the product starting times, given the batch differential of each product. Refer to the flow charts in Figures 3 and 4.

Production Scheduling Algorithm Synopsis

The algorithm is initiated when the data that define the operating parameters of the bakery and the demands of the production goals for the shift are input to the algorithm.

A preliminary quick check is done for infeasibility that can occur when the magnitude of the production demands is so overwhelming that it is obvious the resources of the bakery are not extensive enough to lead to a feasible production schedule. The quick check is done in terms of worker demands and activity demands on the bakery resources. The man-hours required to produce all the batches of all assigned products is summed; if this sum exceeds the man-hours that would be obtained by multiplying the number of bakers by the length in hours of the shift, then the problem is infeasible. A similar approach is done for each activity (number); that is, the sum of the demands for each activity is taken and compared to what would be the activity-hours if each activity was performed at its bounds throughout the shift.

Next, given that feasibility has not been ruled out, the lower and upper bounds for the differentials are computed for each product that has more than one batch assigned during the shift. Referring to Figure 2, DF(i) = 0 tends to additively concentrate demands of the same kind and magnitude on particular increments of time; resource upper bounds may be exceeded at some of the (time) increments. Values of DF(i) are progressively increased until the first feasible value of DF(i) is found; this is the lower bound for DF(i). To determine the upper bound, it is necessary to realize that any differential is limited because the time difference between the start of the first batch of product i and the completion of the final batch cannot exceed to length of time of the shift. In the algorithm, a preliminary upper bound is set (by default) to the minimum of the previously mentioned bound and the length of time of each batch of product i plus one (increment).

An important concept inherent to the effectiveness of the algorithm is that if schedules that each, by themselves, produce smooth worker

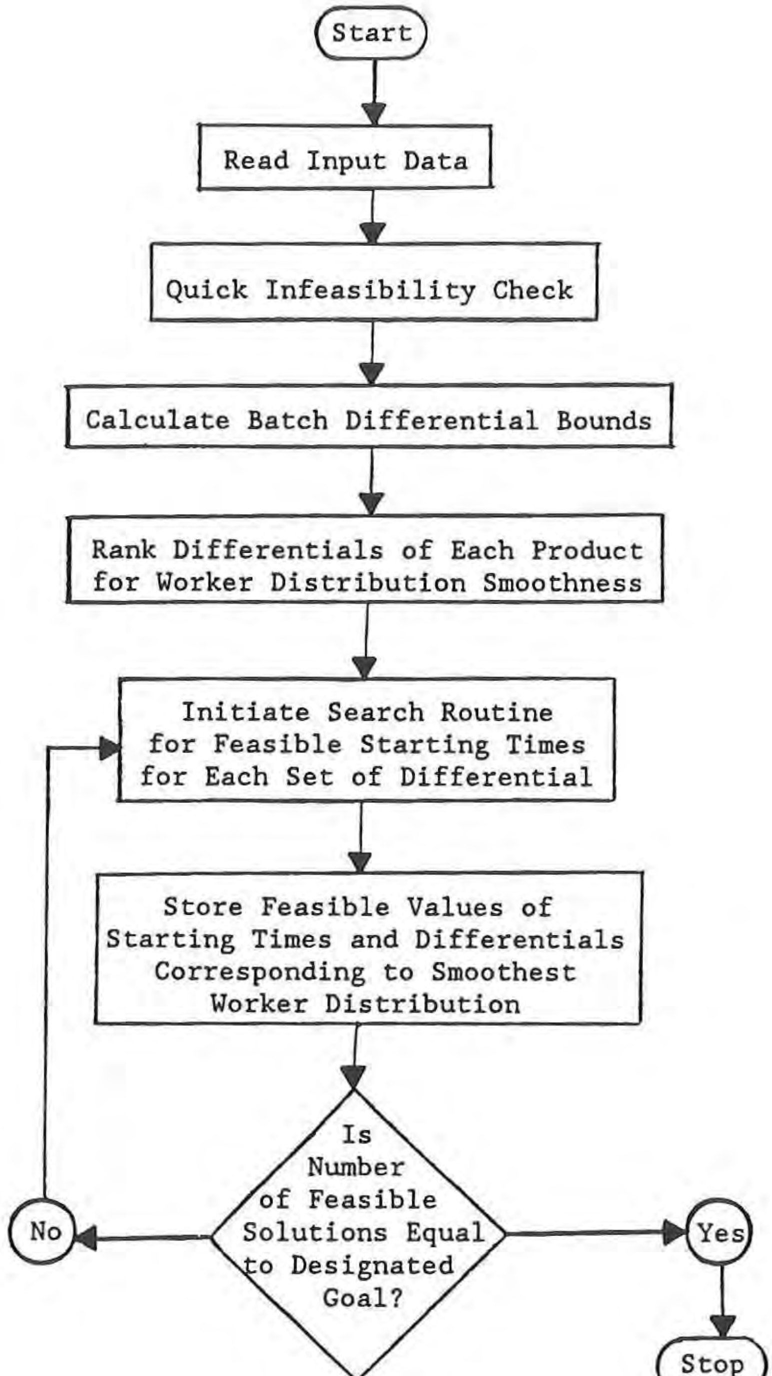

Figure 3: Overview of Production Scheduling Algorithm.

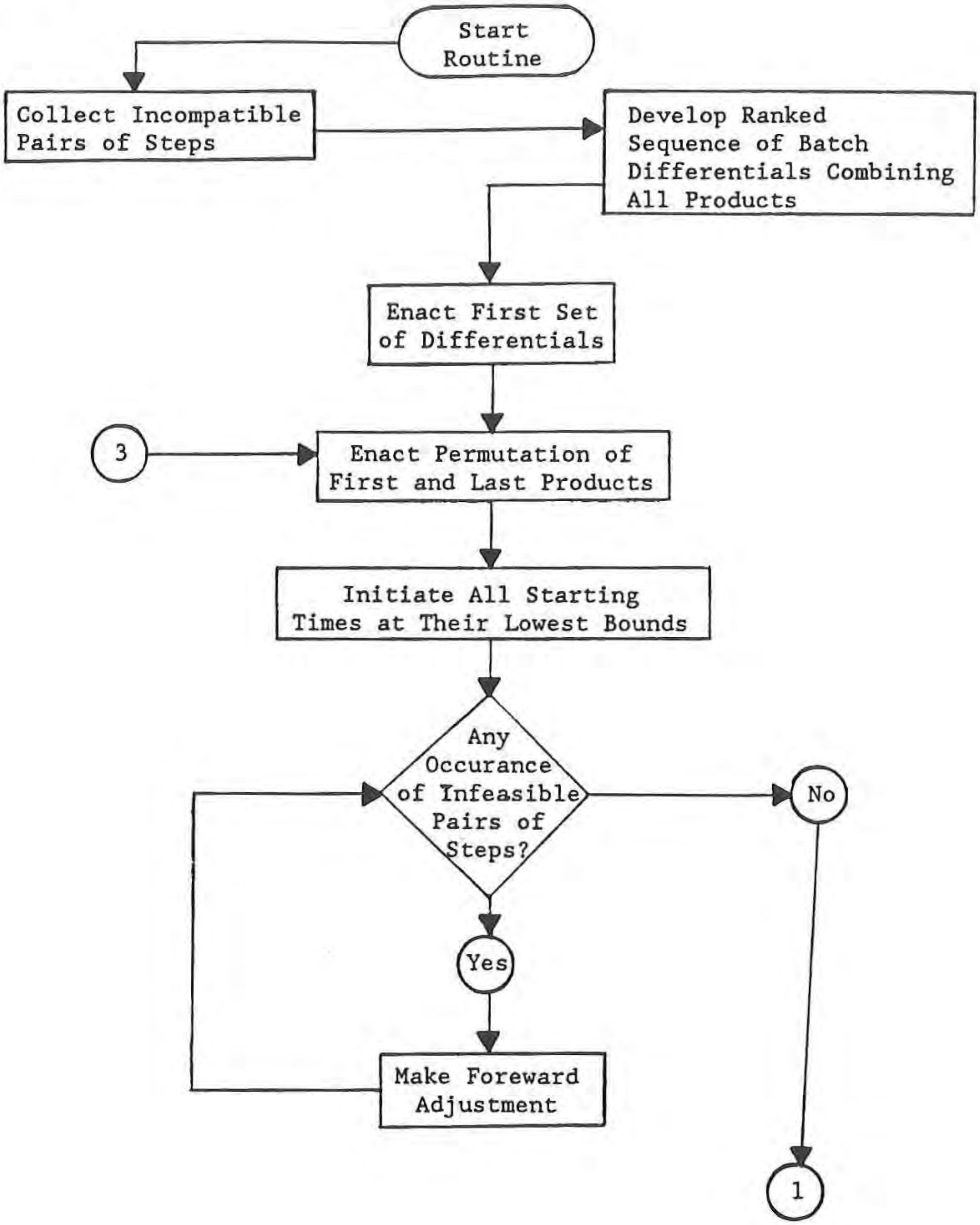

Figure 4: Overview of Starting Time Search Routine.

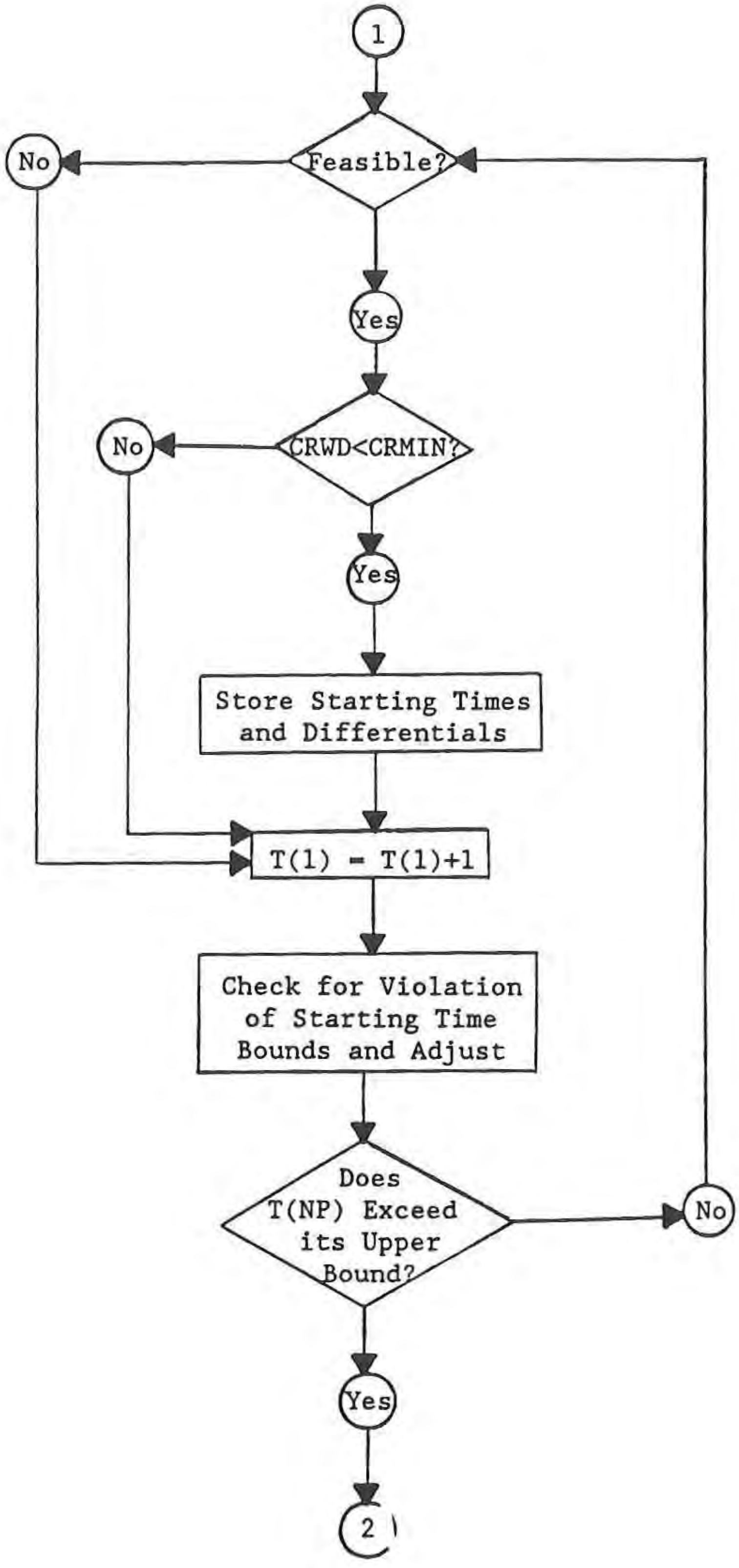

Figure 4: Overview of Starting Time Search Routine (cont'd).

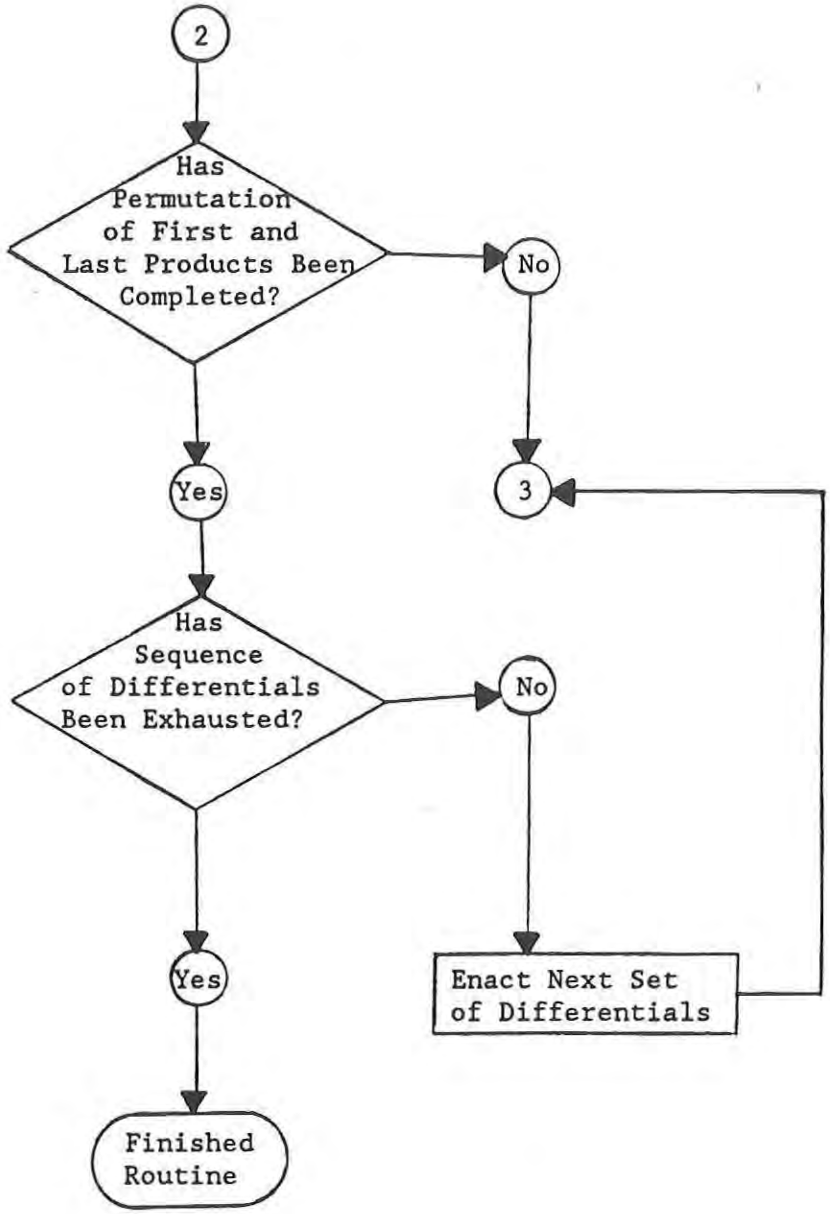

Figure 4: Overview of Starting Time Search Routine (cont'd).

distributions are placed into the same shift simultaneously, then they can be placed in such a way that a smooth composite schedule is produced. Stated much more simply, smoothness upon smoothness will yield smoothness. To exploit this concept of smoothness, successive values of DF(i) that are within their corresponding bounds are used to compute worker sums, SW(ℓ), for each increment within the span of time covered by the product; the beginning of the first batch of each product is set (i.e., pinned) at $\ell = 1$. The coefficients of roughness (described in the previous section) are calculated for each setting of DF(i) and the differentials are ranked according to their corresponding coefficient of roughness. The differentials producing the smoothest worker distributions are ranked first; the differentials responsible for the rougher worker distribution are ranked among the last, for each product i.

The search routine, which determines feasible starting times for all products, is applied. This routine relies upon the differential rankings (for corresponding worker distribution smoothness) of each product to delineate sectors in the (potential) feasible solution space that are most likely to produce the smoothest schedules. The search routine is described in much more detail in the next part of this section.

All feasible solutions for T(i) are used to determine the coefficient of roughness of their corresponding schedules. The solutions for the starting times that correspond to the lowest coefficient of roughness replace previous solutions as the exhaustive search proceeds. The search routine stops when the number of starting time solutions equals a designated number of feasible solutions or when all the sectors that are delineated by the ranked differentials have been thoroughly searched.

The next part of this section is devoted to the detailed description of the search routine for feasible starting times.

Feasible Starting Times Search Routine

Immediately after the ranked differentials for each product, i, are determined, a search routine that locates feasible solutions for the starting times is enacted. The search routine (refer to Figure 4) performs a sequence of directed searches for feasible starting times for all the products collectively. Ranked sets of batch starting time differentials are constructed according to the smoothness of the worker distribution for the individual products (as described in the previous part of this section). The ranked differentials, for each product, are melded to define a sequence of sectors, in the solution space. A trial and error iterative search is directed through the sectors, starting with the sectors most likely to contain feasible solutions that produce schedules having the smoothest worker distributions.

Tentative starting times are tested for feasibility in terms of the constraints that are inherently present in the model (as previously described). The sequence of starting time searches starts by setting the trial starting times at their lower bounds, feasibility is checked, and the next trial set of T(i), for i = 1, ..., NP is produced, in effect, by setting T(i) = T(i) + 1 for i having the lowest indice for which the values for T(i) are not fixed; i.e., the temporary lower bound on T(i) is not set equal to its temporary upper bound. Whenever the value of T(i) exceeds its upper bound, it is set equal to its lower bound and the value of T(i+1) is set by letting T(i+1) = T(i+1) + 1, unless T(i+1) is temporarily fixed (e.g., to its bounds). If T(i+1) is fixed, then set T(i+2) = T(i+2) + 1, unless T(i+2) is fixed, etc. The feasibility is checked again and the procedure is repeated. Note that the sequence of trial values for T(i), for i = 1,..., NP, can be thought of as a metaphorical odometer approach in which some of the digits are (temporarily) fixed and other digits are variable over different bounds.

For example, for some products, T(i) might have a range of values of over 60 values for a 12 hour shift with increments of 10 minutes. Each sector is defined by its corresponding ranked set of batch differentials DF(i), for i = 1,..., NP. When the search has exhausted the set of ranked batch differentials, DF(i), for i = 1,..., NP, the next highest ranked set of DF(i), for i = 1,..., NP, is assigned and a new sector is searched. It is important to note that during any search, two of the trial starting times are fixed. One of the T(i) is fixed at zero, to start production at the beginning of the first increment. Another T(i) is fixed at the highest value such that the final batch of its corresponding product will be produced exactly at the end of the entire shift; that is, at the end of increment NINC, given the value of DF(i) that corresponds to that product. Selecting the products to be fixed in that manner will be referred to as a permutation; i.e., two (products) taken out of the number of products in the schedule, NP.

The preceding description of the algorithm is that of the heuristic in its crude form. In such an unrefined form, the algorithm would take many years searching for a feasible set of starting times for a schedule having several products if, in fact, that particular scheduling problem has no feasible solutions. Refinements have been made to the original heuristic to produce a final version of the algorithm that can search all the sectors in the (potential) solution space at a rate that is estimated to be millions of times faster if very few or no solutions are available in a given production scheduling problem having several products. The refinements are based on the elimination of trial values of T(i) for the highest indice, i, possible within any permutation (of fixed pairs of starting times) within a given set of ranked differentials DF(i),

$i = 1, \ldots, NP$. This elimination of values of $T(i)$ at the higher values of i eliminates a huge number of possible combinations of $T(i)$ among the lower values of i since the trial and error progression is sequentially most active at the lowest indices of i; recall the metaphorical odometer analogy.

The refinements consist of two distinct concepts; namely, the location of incompatible pairs of (recipe) steps when they occur during the same (time) increment, and detection of infeasibilities at the highest indices first by the summing of worker and activity demands in reverse order of the i indices (starting with $i = NP$).

To locate incompatible pairs of product steps, all possible pairs of distinct steps are summed in terms of their worker and activity quantity requirements. All pairs of steps having worker or activity quantity sums that exceed either the number of workers in the bakery, WUB, or the activity upper bounds of any of the $k = 1, \ldots, NA$ activities are detected and listed, i.e., collected. Given a trial set of $T(1), \ldots, T(NP)$, the pair of starting times, say $T(a)$ and $T(b)$ such that $b > a$, having the highest (product) indice a and causes a pair of incompatible of steps to occur simultaneously (i.e., overlap in time) is located. Next, $T(a)$ is increased by the number of increments necessary to eliminate the overlap in the pair of incompatible steps. All starting times with indices, $i < a$ are set equal to their corresponding lowest bounds, and the search proceeds as usual after another feasibility check is made.

Reverse order summing is done to detect the occurrence of an infeasibility at the highest product indice. Instead of summing the workers and activity quantities for each time increment, ℓ, at a time over all the products, a progressive tally of the worker and activity quantity requirements is done by summing the batches of the product having the highest product indice, $i = NP$, first. Next, sum the requirements for batches in product $i = NP-1$ and add to those of $i = NP$ to form cumulative sums, in all the time increments, of the resource requirements. This backward cumulative summing of products $i = NP$, $i = NP-1, \ldots$, etc. proceeds until a cumulative requirement in one of the time increments exceeds either the worker or activity bounds. The first product indice, i, that produces a detectable violation in the constraint due to backward summing is the highest indice such that infeasibility would occur even if every product with lower indices $1, \ldots, i-1$ were removed from the production schedule. Therefore, set $T(i) = T(i) + 1$ and set all $T(1), \ldots, T(i-1)$ to equal their lower bounds and repeat the feasibility check as described.

It is very important to note that the products having the highest indices, ℓ, should correspond to product assignments that require the most work and resources. This ordering is done so that constraints will tend to be violated at higher indices by the starting time search routine; this makes the search proceed much more quickly since a large number of combinations of trial candidates for starting times are ruled out all at once.

The combining of the ranked differentials for each product i into a single list of rankings such that each rank on the list consists of DF(1),..., DF(NP) can be done in many arbitrary ways. The method that is used as part of the algorithm in this paper emphasizes the higher ranking differentials. The number of differential ranks for each product varies. Therefore, the product that produces the greatest number of ranks has its ranks entered only once in the list. The products that produce the fewest ranks have their most highly (i.e, first) ranked differential repeated at the top of the list of ranks as many times as needed to enable the lists of differentials for each product to be as long as the other lists. This process is illustrated best by a simple example. Suppose there are three products to be scheduled such that the differentials corresponding to the lowest coefficient of roughness to the highest are shown as follows:

Product 1: 5, 4, 6, 3, 8, 10
Product 2: 7, 6, 10
Product 3: 2, 3, 7, 5

The list of ranking can be represented as follows:

Rank	DF(1)	DF(2)	DF(3)
1	5	7	2
2	4	7	2
3	6	7	2
4	3	7	3
5	8	6	7
6	10	10	5

Therefore, the search for feasible values of T(1), T(2), and T(3) that would produce the smoothest schedules would start with the batch differentials that delineate a region in the solution space that is most likely to contain the smoothest feasible schedule; these are DF(1) = 5, DF(2) = 7, and DF(3) = 2.

The flow chart that is depicted in Figure 4 illustrates the overall process of the starting time search routine.

EXAMPLE PROBLEM

A production scheduling assignment that is intended to be representative of bakery activities in general is given here as an example problem. The location is the aft bakery on the USS Saratoga CV-60, an aircraft carrier with approximately 6000 military personnel.

The resources in the aft bakery consist of a given number of bakery personnel and the equipment that is used to prepare the food. The number of workers available varies according to the shift and is typically on the order of 10. There are about a dozen different kinds of equipment in the bakery, such as ovens, proofers, work tables, sinks, etc.; however, only four kinds of equipment will be considered as limited resources. The limited resources in this model consist of the following:

1 Horizontal Mixer	---	Activity #1
1 Vertical Mixer	---	Activity #4
1 Proofer (Box)	---	Activity #2
10 Ovens	---	Activity #3

All the other equipment and activities default to an activity number of zero, as if no activity was being performed.

The production scheduling assignment consists of the following products:

Product #1:	Frosting (for 10 cakes); 1 batch
Product #2:	Yellow Cake (10 cakes); 1 batch
Product #3:	Pie Crusts (for 100 pies); 1 batch
Product #4:	Pecan Pie (100 pies); 1 batch
Product #5:	Hamberg Rolls (1000 rolls); 1 batch
Product #6:	Hot Dog Rolls (1000 rolls); 1 batch
Product #7:	Bread (320 loaves); 5 batches

These assignments are to be completed in 12-hour shifts, the equivalent of 72 ten-minute increments. The activity upper bounds, AUB(k), for activity k, for k = 1, 2, 3, and 4 are 1, 1, 10, and 1, respectively, since there are only one each of the horizontal and vertical mixers, and the proofer, and 10 oven (units).

The activity quantity, AQ(i,j), for step j of product i, is zero for all steps where no equipment corresponding to a limited resource is involved. AQ(i,j) = 1 for all activities in which A(k) = 1, namely k = 1, 2, and 4. For steps involving the oven, which corresponds to AUB(3) = 10, the quantity AQ(i,j) is frequently greater than unity.

For example, a batch of 100 pecan pies (product #4) contains 2 steps each requiring the use of 3 oven (units) simultaneously; these steps are numbered 5 and 6. Therefore, AQ(4,5) = 3 and AQ(4,6) = 3.

Attempts were made to produce smooth (feasible) schedules with varying numbers of workers assigned to the bakery. Worker upper bounds, WUB, of 8, 10, 11, and 12 were attempted. (Other values of WUB were executed, but they were found not to be relevant for the purposes of this example.) The assignments that were allocated 8 and 10 workers turned out to be infeasible. The algorithm required 8 min. 4 sec. and 8 min. 26 sec. to search all the sectors for WUB = 8 and WUB = 10 respectively. An IBM-compatible MS-DOS Zenith personal computer having a base memory of 640k bytes and expansion memory of 1024k bytes was used. When WUB = 12 was attempted and the goal was to locate 100 feasible solutions and provide the smoothest of them all. The solution is T(i) = 0, 58, 53, 1, 38, 35, and 0, with DF(i) = 0, 0, 0, 0, 0, 0, and 7 for i = 1,...,7 respectively. The minimum coefficient of roughness, for the 100 solutions CRMIN, was 0.34712. The algorithm search time was 48.1 sec. Since WUB = 10 proved to be infeasible and WUB = 12 was feasible, an attempt was made using WUB = 11. The results were, T(i) = 0, 58, 32, 1, 38, 35, and 0, with DF(i) = 0, 0, 0, 0, 0, 0, and 7 for i = 1,...,7 respectively; CRMIN = 0.35548. The algorithmic search time was 57.3 sec. Note that the batch differential rankings for i = 7 were (in order from smoothest to roughest) DF(7) = 7, 9, and 8. Note, also, that product #2 (i.e., i = 2, the yellow cake), was the last product to be completed; it started out at T(2) = 58 to finish production at the end of time increment ℓ = NINC = 72.

It is significant to note that CRMIN for WUB = 12 is lower than that of WUB = 11. The reason that WUB = 12 yields a lower value of CRMIN is that a greater number of workers provided more latitude in admitting schedules having smoother worker distributions. Also note that the algorithmic search time is less for WUB = 12, since the 100 feasible solutions were more accessible. It is interesting to note that less time is required to show that WUB = 8 leads to infeasibility than to show that WUB = 10 is infeasible (recall 8 min. 4 sec. and 8 min. 26 sec. respectively). This shows that a greater number of constraint violations were detected at higher indices for WUB = 8 than for WUB = 10.

CONCLUSION

The algorithm that is described in this paper is an effective analytical tool for developing schedules for the production of several bakery products during any given work shift. Since the processing times that are required are on the order of 1 minute if 100 feasible solutions are available to several minutes to confirm infeasibility, literally hundreds of production scheduling test runs can be performed in 1 day on 1 personal computer.

Because of the way the model has been formulated, it is possible to include duties and events other than bakery production in the schedule. For instance, if lunch breaks and rest periods for a specified number of workers are to take place at predetermined times, then the upper and lower bounds for the beginning of the break periods, which require a given number of workers, are set equal to each other to fix the starting time of the break period to a given value. The activity numbers of the break period are set equal to zero. Bakery production tasks are then, in effect, scheduled around the break periods.

It is obvious, from the preceding example, that the algorithm can be used to schedule events that are required to occur in other kinds of event-time related systems. Even if the objective is not to obtain a smoothed worker distribution, the algorithm is of practical significance. If the number of workers is not a consideration, for instance, set all values of W(i,j) = 0 or set the worker upper bound, WUB, to a very large number that cannot possibly be reached. Feasibility studies on the (production) system can then be carried out and feasible schedules would be enumerated if feasibility exists within the resource and time constraints that are involved in the constitution of the system that is being modeled.

REFERENCES

1. Lundberg, D. E. and Armatus, J. P.; The Management of People in Hotels, Restaurants, and Clubs, Brown, Dubuque, Iowa (1971).

2. French, Simon; Sequencing and Scheduling, John Wiley and Sons, Chichester, England (1986).

3. Denardo, E. V.; Dynamic Programming, Models and Applications, Prentice-Hall, Inc., Englewood Cliffs, New Jersey (1982).

4. Salkin, H. M.; Integer Programming, Addison-Wesley Publishing Co., Reading, Massachusetts (1975).

TITLE: Diet and Bright Light Countermeasures to Jet Lag: Effects on Recovery from a Simulated Time Zone Shift.

*Laurie S. Lester, Dr., Charles A. Salter, MAJ, MS, Edward Hirsch, Dr., Margaret L. Moline, Dr., Charles P. Pollak, Dr., and Daniel R. Wagner, Dr.

ABSTRACT: Previous research suggested that diet or bright light or both might increase the recovery rate of biological rhythms disrupted by rapid travel across time zones, thereby preventing or alleviating the symptoms commonly referred to as "jet lag". These hypotheses were tested in the present study under the conditions of a highly controlled laboratory environment. Twenty-three Marines lived in individual, time-isolation apartments for 15 consecutive days. A 6-hour easterly time zone shift was simulated by advancing each subject's time of awakening by 6 hours on the 7th night and by maintaining his daily routine on the new time for the remainder of the study. Subjects in the Diet group were put on a popularized "jet lag diet" for 4 days prior to the shift. The diet regime consisted of alternating days of feasting and fasting, consumption of high protein breakfasts, high carbohydrate dinners, and scheduled consumption of caffeinated beverages. Subjects in the Light group were exposed to bright, full-spectrum light on the morning after the shift and on the following 3 mornings. Subjects in the Control group were maintained on a mixed nutrient, balanced diet and were only exposed to the ambient light conditions in their apartments. All of the subjects experienced jet lag as evidenced by varying degrees of disruption in sleep patterns and body temperature rhythms. Decrements in mood, performance, and levels of physical activity were also noted. In this first empirical test of the "jet lag diet", it was found that the diet actually worsened sleep and did not lessen or promote recovery from other jet lag symptoms. The bright light treatment showed the most promise for future use in that, after 2-3 treatments, subjects in the Light group tended to be more alert and happier than before the shift as well as more alert and happier than subjects in the Diet and Control groups. The light regimen used in the present study hindered temperature rhythm resynchronization and sleep. Additional research is needed to determine if these undesirable effects can be reduced or eliminated by modifying the intensity of the bright light and/or timing of the treatment.

*BIOGRAPHY OF PRESENTER: Laurie S. Lester

PRESENT ASSIGNMENT: Research Psychologist, U.S. Army Natick Research, Development, and Engineering Center

DEGREES HELD: A.B. Mount Holyoke College, Ph.D. Dartmouth College

Diet and Bright Light Countermeasures to Jet Lag: Effects on Recovery from a Simulated Time Zone Shift

Laurie S. Lester, Dr., Charles A. Salter, MAJ, MS, Edward Hirsch, Dr., *Margaret L. Moline, Dr., *Charles P. Pollak, Dr., and *Daniel R. Wagner, Dr.

In an age in which high speed air travel has become extremely common, jet lag is a well known and widely experienced malady. The symptoms associated with jet lag may include fatigue, insomnia during the new nighttime, sleepiness during the new daytime, and decrements in both performance and mood. These symptoms are thought to result from the temporary dissociation among biological rhythms (e.g., the daily rhythm of core body temperature) that occurs when time zones are crossed rapidly.

While jet lag can be a debilitating annoyance to the civilian traveler, its effects on the military traveler arriving in a potentially hostile environment can be life threatening. Therefore, any countermeasure to jet lag that could improve the soldier's ability to perform optimally during the early stages of an overseas mission might confer a tremendous operational advantage. Among the many suggested remedies to jet lag, two that appear promising and amenable to use in the military setting are diet and bright light.

A special "jet lag diet" developed by Charles Ehret[1] has received a good deal of popular acclaim but very little empirical testing. The diet is based on research indicating that food constituents can alter brain biochemistry and ultimately, behavior.[2] The diet prescribes consumption of particular foods at

*Institute of Chronobiology, New York Hospital-Cornell Medical Center, White Plains, New York

times that would facilitate appropriate kinds of behavior at the new destination. For example, the diet recommends that the traveler prepare for his trip by consuming high protein breakfasts for a specified number of days prior to departure, during the flight, and upon arrival. Dietary protein has been shown to increase levels of tyrosine found in the brain.[3] Tyrosine is a precursor to the neurotransmitters dopamine, norepinephrine, and epinephrine and has been associated with alertness and increased resistance to stress.[2, 4, 5] The diet also recommends consuming high carbohydrate dinners in preparation for and during the flight. Meals that are high in carbohydrate and low in protein have been shown to elevate brain levels of tryptophan, a precursor to the neurotransmitter serotonin.[6,7] Serotonin has a long history of association with sleep onset.[8,9]

The "jet lag diet" also makes use of the class of substances known as the methylated xanthines that are found in coffee (caffeine) and tea (theophylline). These substances have been shown to phase delay (i.e., reset to an earlier time) the body's biological clock if consumed early in the day and phase advance (i.e., reset to a later time) the biological clock if consumed late in the day.[10] Thus, consumption of coffee or tea at appropriate times and abstinence at inappropriate times could accelerate adjustment of biological rhythms to coincide with the new time zone.

As mentioned above, exposure to bright light has also been suggested as a means of alleviating or promoting recovery from jet lag. Ambient light serves as the major source of time information that keeps all of the physiological and behavioral rhythms of organisms, including humans, synchronized precisely to the 24 hour environment. This is possible since an organism is differentially responsive to light stimuli presented at various times (phases) of the day. For example, light early in the morning advances rhythms, and evening light delays them.[11,12,13,14] As with the scheduled consumption of coffee or tea, scheduled exposure to bright light could accelerate resynchronization of biological rhythms disrupted by rapid travel across time zones.

The research presented here describes the investigation of these two countermeasures, diet and bright light, under the conditions of a highly controlled laboratory setting. A 6-hour easterly shift was simulated, since eastward travel requires greater adjustment of the body's biological clock and thus produces more severe jet lag symptoms[15] than does westward travel.

METHOD

Subjects

Twenty-three male Marines between 18 and 30 years of age participated in this study. All subjects were screened to ensure that they were physically and psychologically healthy. Individuals taking medication on a regular basis, high caffeine users (i.e., more than 2 or 3 caffeinated beverages per day), and individuals who napped frequently or had an unusual sleep schedule (i.e., sleeping more/less than 7-8 hours per night and retiring later than 0100) were not included in this study.

Dependent Measures

Data from a large number of dependent measures were collected in this study. This paper reports representative examples of the measures used and data collected with regard to sleep, core body temperature, cognitive performance, alertness and mood (see Moline et al.[16] for a complete report).

Sleep Efficiency. Polysomnograms (i.e., recordings of the electrical activity occurring in the brain during sleep) were taken for every sleep period. Sleep efficiency was defined as the percentage of time in bed that was actually spent sleeping.

Core Body Temperature. Body temperature was measured every minute from a rectal thermometer worn by each subject. The temperature rhythms obtained by plotting these data were examined with regard to phase and amplitude changes that occurred over the course of the study. Phase refers to the position of the daily minimum/maximum temperature relative to the sleep/wake period. Amplitude refers to the number of degrees between the daily minimum and maximum temperatures.

Verbal Reasoning Task (VRT). The VRT was one of the tasks used to assess cognitive performance. This complex verbal reasoning task is a modified form of the Baddeley Reasoning Test.[17] The task is composed of a set of 32 sentences, each of which is followed by a letter pair consisting of the letters "M" and "C". The subject is required to decide whether or not the sentence accurately describes the letter pair. For example:

M IS NOT PRECEDED BY C - MC   response: true

Latency to respond and accuracy were recorded. The VRT was administered on a computer 5-8 times per day including once upon waking, once before each meal or snack, and once before sleep.

Alertness and Mood. Changes in self-reported alertness and mood were measured by asking the subject to complete nine questions. The subject was asked to indicate how alert, sad, tense, motivated, happy, weary, calm, and sleepy he was feeling at that moment. He was also asked how he was feeling overall. The subject responds by moving the cursor on a computer screen along a line anchored at one end by "very little" and at the other end by "very much" (Visual Analog Scales), or by other appropriate endpoints. Measures of alertness and mood were taken in conjunction with the measures of cognitive performance.

Procedure

The 23 Marines lived in individual, time-isolation apartments for 15 consecutive days. Prior to the shift, subjects slept according to their own routine schedules. A 6-hour easterly time zone shift was simulated by advancing each subject's time of awakening by 6 hours on the 7th night and by maintaining his daily routine on the new time for the remainder of the study. Subjects in the Diet group were put on Ehret's "jet lag diet"[1] for 4 days prior to the shift. The diet regimen consisted of alternating days of feasting and fasting, consumption of high protein breakfasts, high carbohydrate dinners, and scheduled consumption of caffeinated beverages. Subjects in the Light group were exposed to bright, full-spectrum light (2500 lux) on the morning after the shift and on the following 3 mornings. Subjects in the Control group were maintained on a mixed nutrient, balanced diet and were exposed only to the ambient light (200-400 lux) conditions in their apartments.

RESULTS

The data collected on sleep efficiency (i.e., the percentage of time in bed spent sleeping) are summarized in Figure 1. It is clear from Figure 1 that all subjects slept well during baseline with sleep efficiency averaging 92.5% for the Control and Light groups and 93.4% for the Diet group. While all groups slept at least as well as they had during baseline on the night following the shift (sleep period 8), sleep efficiency showed signs of deterioration thereafter. The most striking aspect of Figure 1 is the dramatic decline (>40%) in sleep efficiency by Diet group subjects on the night of the shift (sleep period 7). This decline can be accounted for by an increase in sleep latency, which subjects attributed to the caffeine consumed with dinner.

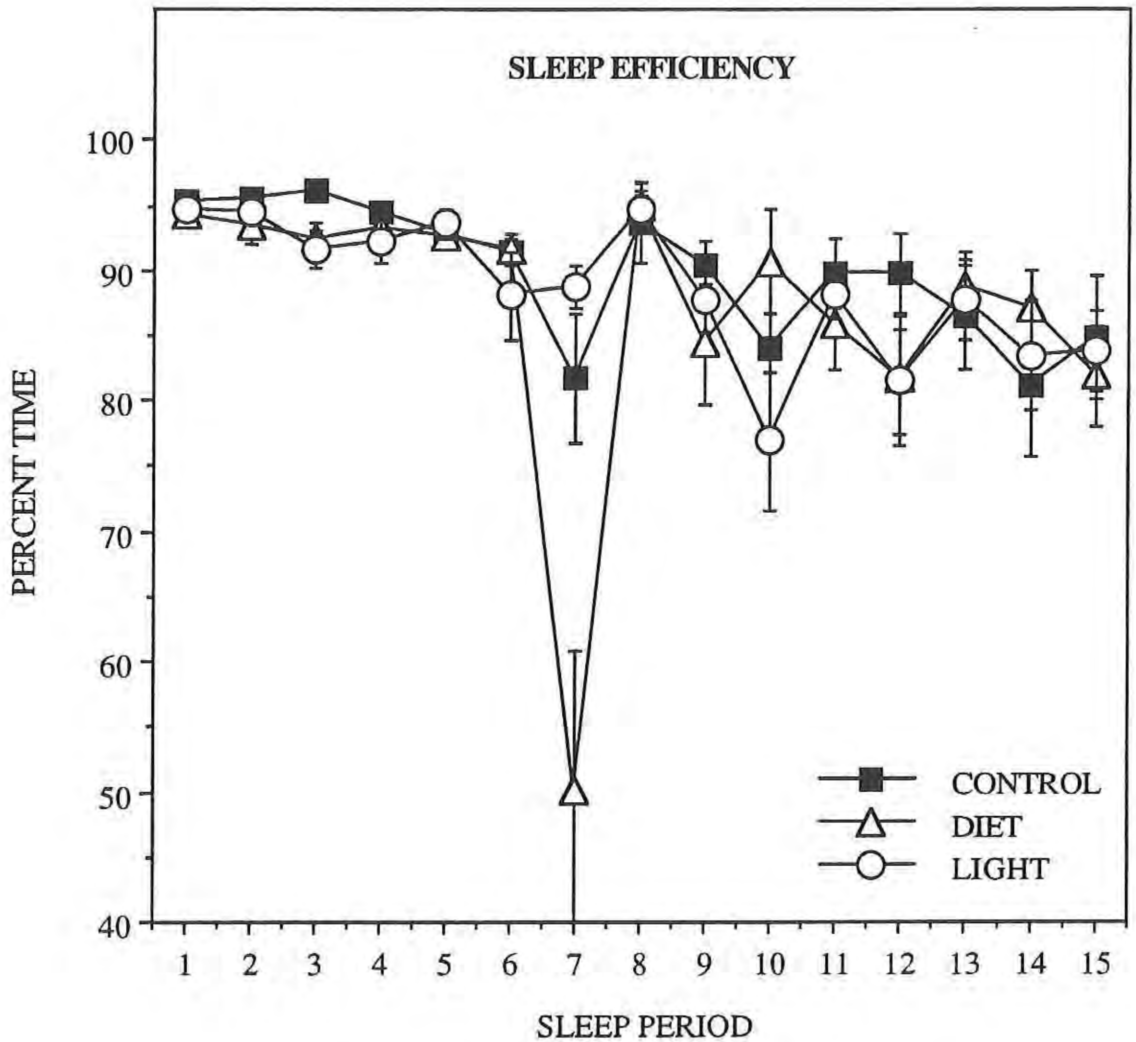

Fig. 1. Mean (± SEM) sleep efficiency for every sleep period of the study. The time zone shift (6 h) was simulated at sleep period 7.

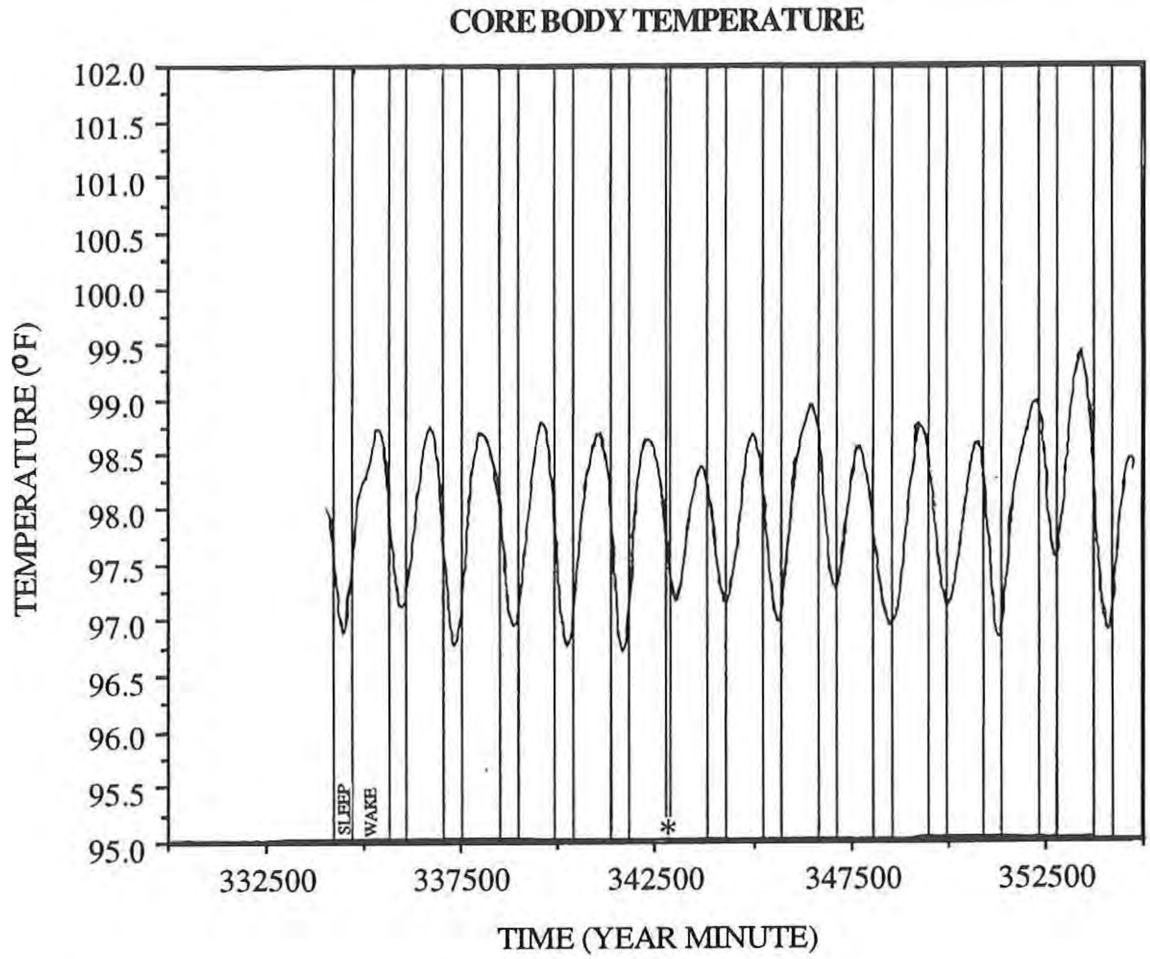

Fig. 2. Core body temperature as a function of time (mins) past midnight of January 1 for Control subject JL42. The * marks the point of the shift.

Figure 2 provides an example of a subject's fluctuations in body temperature during the study period. The effects of the shift (i.e., the shortened sleep period just after 342500) are evident in terms of disruption of both phase and amplitude. Phase disruption is apparent by noting that the daily minimum temperature that occurs just after the midpoint of the sleep period during baseline occurs at the beginning of the wake period following the shift. The minimum does not return to its baseline position until the end of the study. Similarly, the amplitude of the rhythm was decreased following the shift and required several days to readjust. Amplitude decreased most notably for Light group subjects, with the smallest amplitudes appearing on the days following the last light treatment.

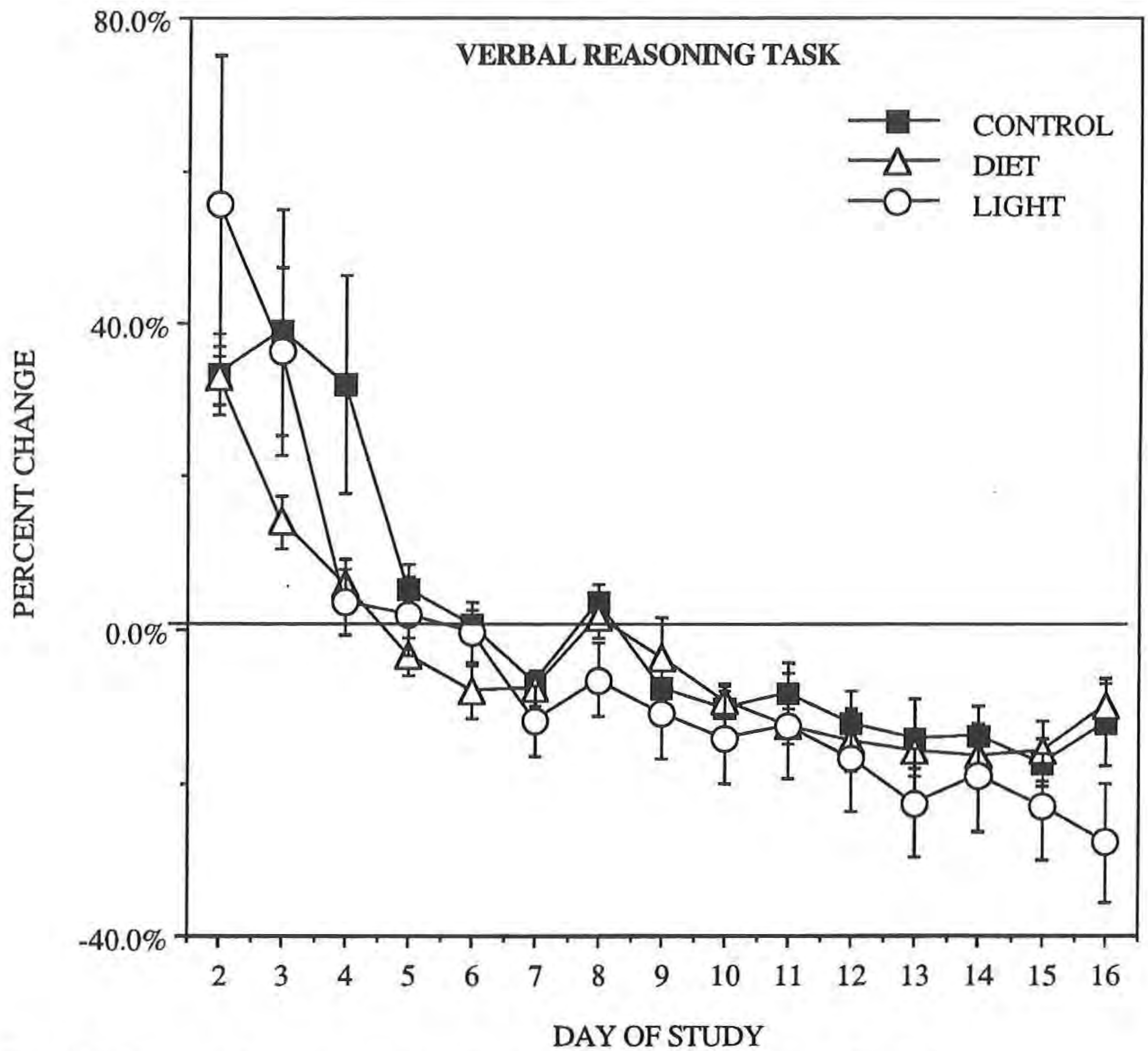

Fig. 3. Percent change from total study mean in time taken for VRT.

The data collected on the VRT are summarized in Figure 3. These data were derived by calculating an individual's mean across all days of the study. This value was used to determine individual percent change scores for every day of the study. The percent change scores were then averaged across subjects in a group. Points above the zero line indicate that it took longer than the mean time to complete the task. Performance on the VRT improved over the study, but all groups tended to show impaired performance on the day after the shift (Day 8). Accuracy was unaffected by the shift.

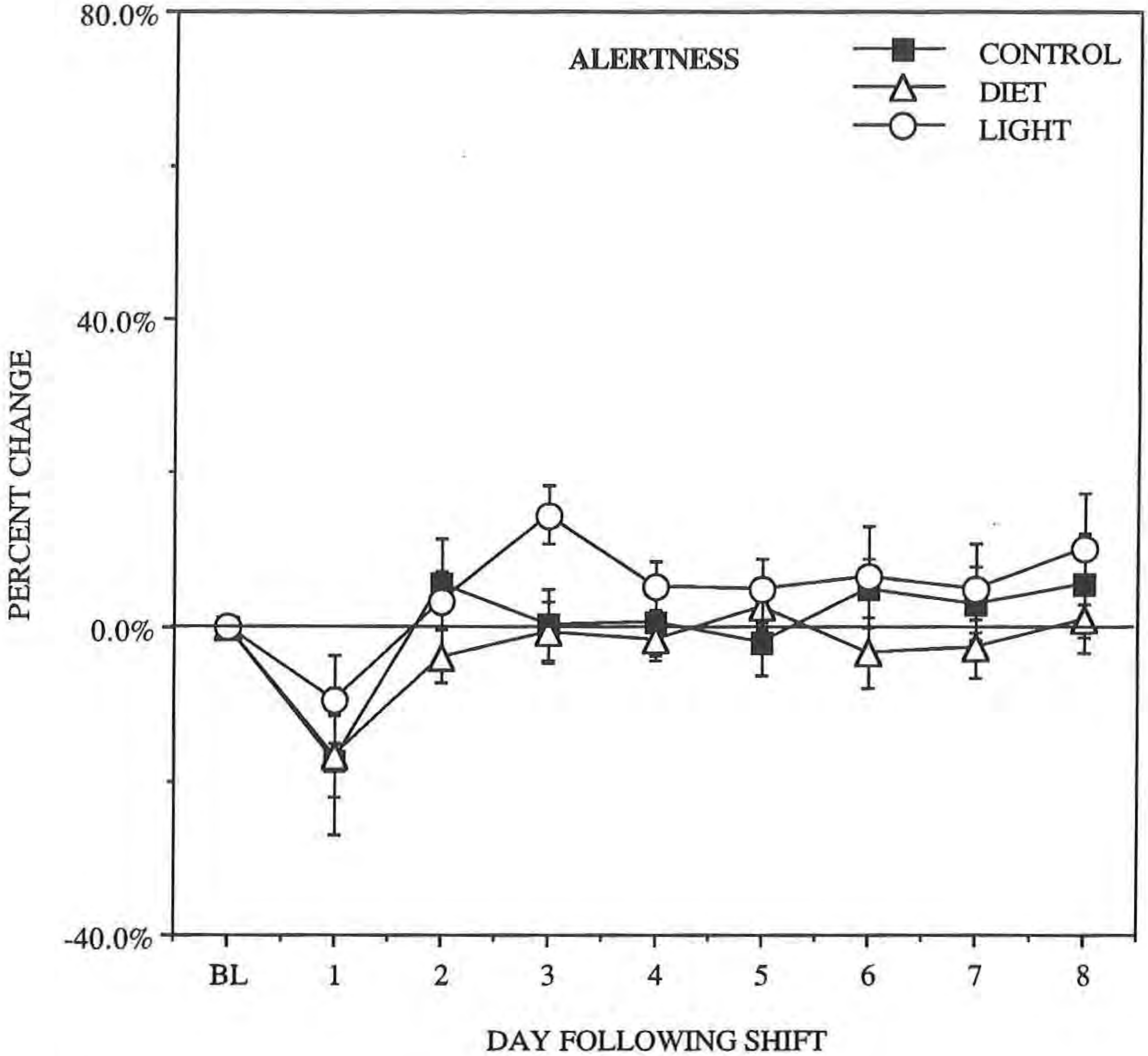

Fig. 4. Percent change in self-reported alertness, relative to baseline (BL).

Changes, with respect to baseline, that occurred in ratings of alertness are shown in Figure 4. The values displayed in Figure 4 were obtained by calculating a mean alertness rating for each subject during baseline. The percent change from the baseline value was calculated on an individual basis for each day after the shift. Group means were then taken. Points above the zero line indicate that the subjects were more alert than they had been, on average, during baseline. All groups reported at least a 10% decrement in alertness on the first day after the shift. The Light group showed an increase in alertness on the third day after the shift, or, after three light treatments.

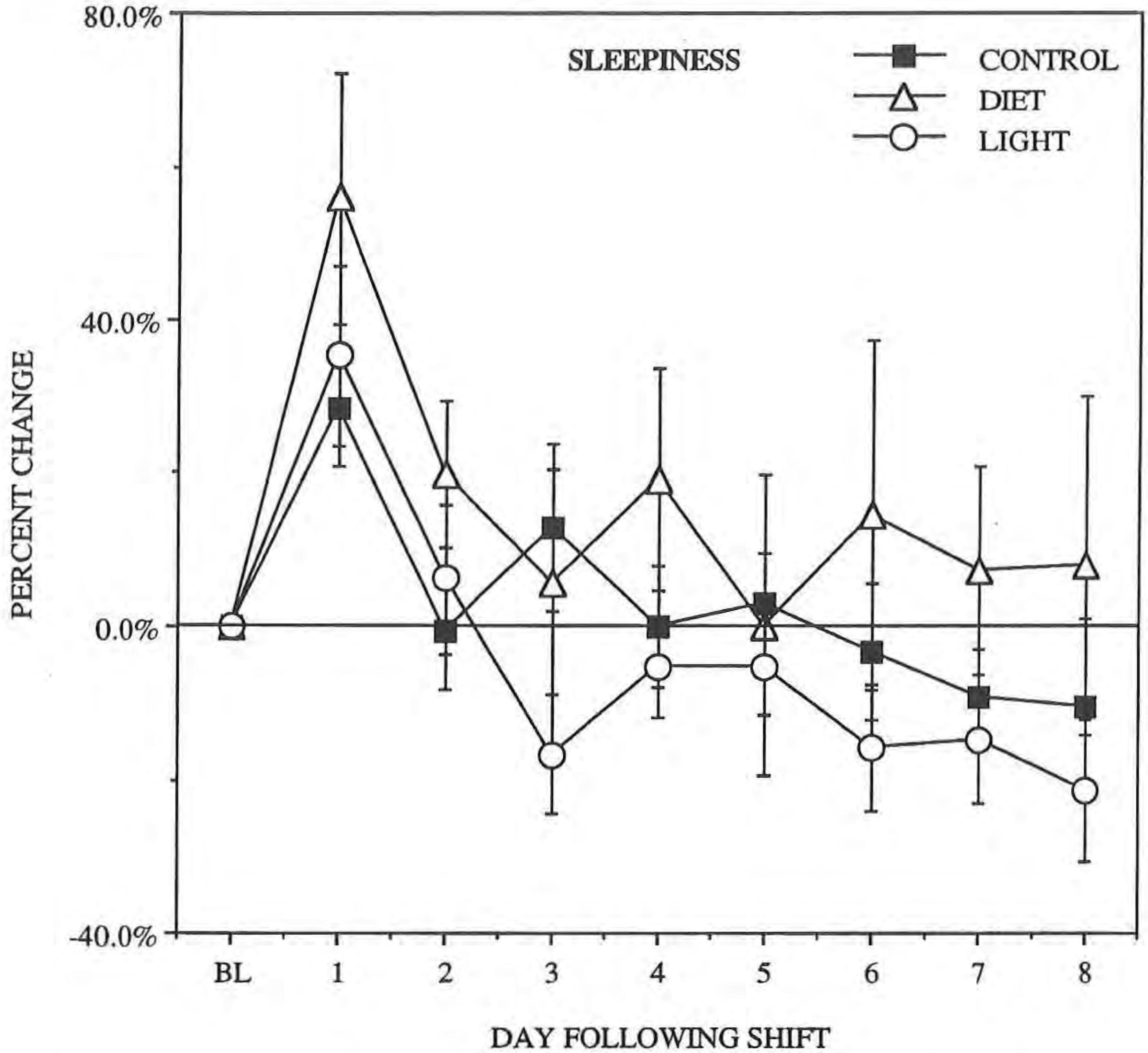

Fig. 5. Percent change in self-reported sleepiness (calculated as in Fig. 4), relative to baseline (BL).

Significant changes, relative to baseline, were noted for several indices of mood. As examples, the changes reported for sleepiness and happiness are shown in Figures 5 and 6, respectively. Points above the zero line in Figure 5 indicate an increase in sleepiness. All groups reported an increase in sleepiness on the first day after the shift. By the third day after the shift, subjects in the Light group tended to rate themselves as the least sleepy.

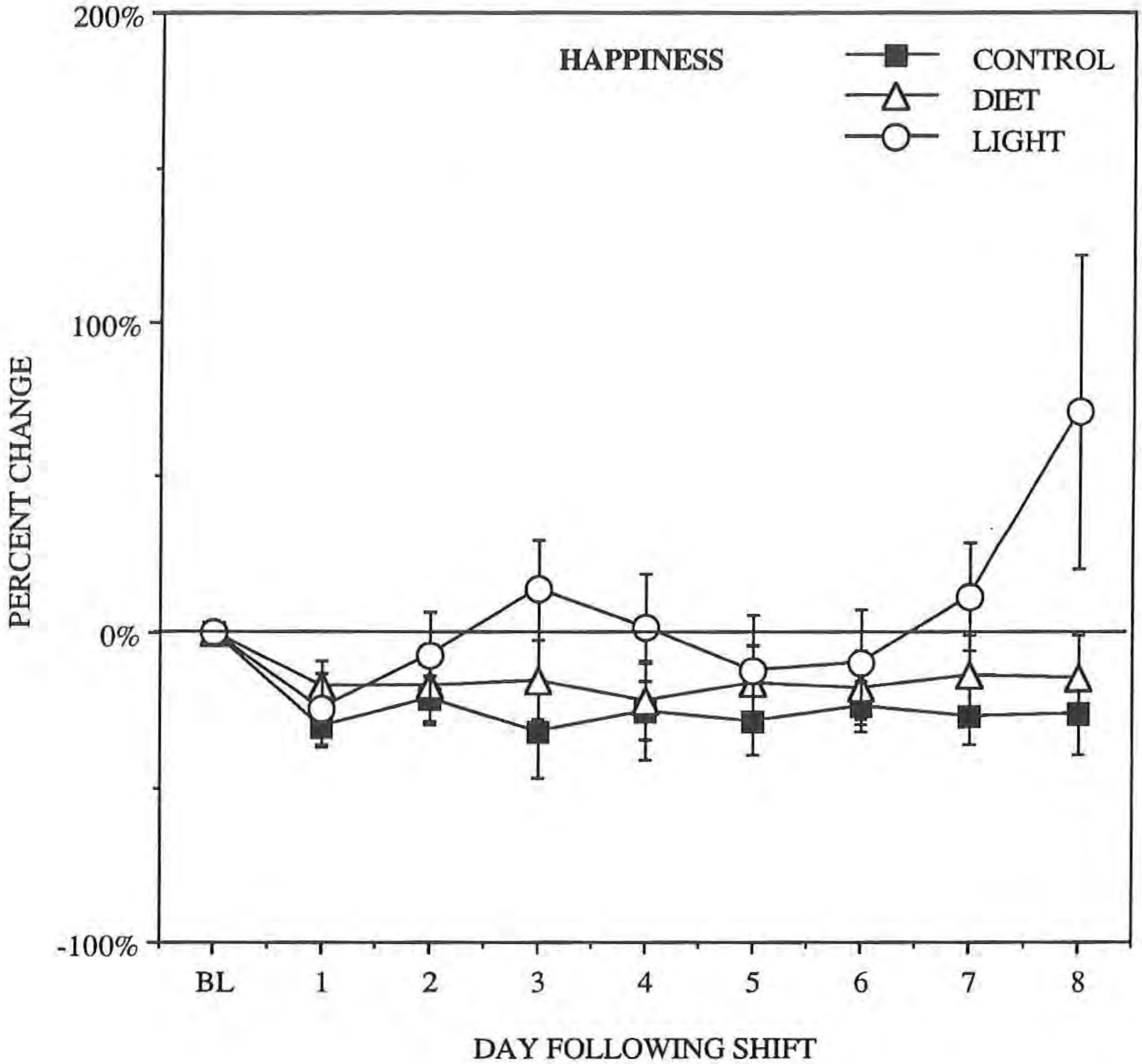

Fig. 6. Percent change in self-reported happiness (calculated as in Fig. 4), relative to baseline (BL).

Points above the zero line in Figure 6 indicate an increase in happiness. Subjects in the Control and Diet groups rated themselves as less happy than during baseline on each day following the shift. Subjects in the Light group also reported a decline in happiness on the first day after the shift, but showed an increase in happiness on the third day after the shift. The timing of this improvement corresponds with the third light treatment and the noted increase in alertness and decrease in sleepiness. The large increase in happiness on day 8 suggests that subjects in the Light group may have anticipated the end of the study.

CONCLUSIONS

Polysomnography and core temperature recordings indicated that all subjects in this study experienced jet lag symptoms. Disruption of sleep patterns and body temperature rhythms persisted for several days following the shift. Sleep patterns were disrupted to a greater extent on the shift night for Diet group subjects. These subjects were required to consume a caffeinated beverage with dinner on the night before the shift. Light treatment led to poorer sleep after several days of treatment and hindered amplitude and phase readjustment of the temperature rhythm.

The performance measures presented here and others included in this study (Memory and Search Task, modified Purdue Pegboard Task) did not reveal large or long-lasting decrements following the shift. Small decrements in performance were noted on the first day after the shift. These were probably the result of sleep deprivation rather than jet lag per se. Performance on the Verbal Reasoning Task and the Visual Search Task was not affected by diet or bright light treatments.

Several of the self-reported measures of alertness and mood indicated that subjects were affected adversely by the simulated time zone change. Subjects in all groups reported feeling less alert, less happy, more sleepy, and more weary than they had prior to the shift. Subjects in all groups also reported that more effort was required to perform routine activities and in general, they didn't feel as well after the shift as they had during baseline. Feelings of sadness, tension, and calmness were relatively unaffected by the shift. Only the light treatment appeared to affect recovery. Subjects in the Light group reported improvements in alertness and mood by the third day after the shift. This finding is consistent with the observation that three days of bright light treatment are usually required to elicit a mood elevation in seasonally depressed patients.[12]

In this first empirical test of Ehret's "Jet Lag Diet" we found that the diet did not improve mood or performance and actually impaired sleep on the night of the shift. While additional studies need to be conducted with other subject populations, our findings based on data collected from physically fit, young males indicate that the "Jet Lag Diet" is not a useful countermeasure.

The bright light treatment showed the most promise for future use in that, after 2-3 treatments, subjects in the Light group reported increased alertness and improvements in mood. However, the light regimen used in the present study hindered temperature rhythm resynchronization and sleep. Additional research is needed to determine if these undesirable effects can be reduced or eliminated by modifying the intensity of the bright light and/or the timing of the treatment.

REFERENCES

1. Ehret, E.F. & Scanlon, L.W. (1983). Overcoming Jet Lag. New York: Berkeley Publishing Group.

2. Spring, B. (1986). Effects of foods and nutrients on the behavior of normal individuals. In R.J. Wurtman & J.J. Wurtman (Eds.), Nutrition and the Brain (pp. 47). New York: Raven Press.

3. Glaeser, B.S., Maher, T.J., & Wurtman, R.J. (1983). Changes in brain levels of acidic, basic, and neutral amino acids after consumption of single meals containing various proportions of protein. Journal of Neurochemistry, 41,1016-1021.

4. Lehnert, H., Reinstein, D.K., Strowbridge, B.W., & Wurtman, R.J. (1984). Neurochemical and behavioral consequences of acute, uncontrollable stress: Effects of dietary tyrosine. Brain Research, 303, 215-223.

5. Salter, C.A. (1989). Dietary tyrosine as an aid to stress resistance among troops. Military Medicine, 154, 144-146.

6. Fernstrom, J.D. & Wurtman, R.J. (1971a). Effect of chronic corn consumption on serotonin content of rat brain. Nature New Biology, 234, 62-64.

7. Fernstrom, J.D. & Wurtman, R.J. (1971b). Brain serotonin content: Increase following ingestion of carbohydrate diet. Science, 174, 1023-1025.

8. Spinweber, C.L., Ursin, R., Hilbert, R.P., & Hilderbrand, R.L. (1983). L-tryptophan: Effects on daytime sleep latency and on the waking EEG. Electroencephalography and Clinical Neurophysiology, 55, 652-661.

9. Spring, B., Chiodo, J. & Bowen, D.J. (1987). Carbohydrates, tryptophan, and behavior: A methodological review. Psychological Bulletin, 102, 234-256.

10. Ehret, C.F., Potter, V.R., & Dobra, K.W. (1975). Chronotypic action of theophylline and of pentobarbital as circadian zeitgebers in the rat. Science, 188, 1212-1215.

11. Czeisler, C.A., Allen, J.S., Strogatz, S.H., Ronda, J.M., Sanchez, R., Rios, C.D., Freitag, W.O., Richardson, G.S., & Kronauer, R.E. (1986). Bright light resets the human circadian pacemaker independent of the timing of the sleep-wake cycle. Science, 223, 667-671.

12. Lewy, A.J., Sack, R.L., Miller, L.S. & Hoban, T.M. (1987). Antidepressant and circadian phase-shifting effects of light. Science, 235, 352-354.

13. Lewy, A.J., Sack, R.L., & Singer, C.M. (1985). Immediate and delayed effects of bright light on human melatonin production: Shifting "dawn" and "dusk" shifts the dim light melatonin onset (DLMO). Annals of the New York Academy of Sciences, 453, 253-259.

14. Czeisler, C.A., Kronaurer, R.E., Allan, J.S., Duffy, J.F., Jewett, J.E., Brown, E.N., & Ronda, J.M. (1989). Science, 244, 1328-1333.

15. Weitzman E.D., Moline, M.L., Czeisler, C.A., & Zimmerman, J.C. (1982). Chronobiology of aging: Temperature, sleep-wake rhythms and entrainment. Neurobiology of Aging, 3, 299-309.

16. Moline, M.L., Pollak, C.P.,& Zendell, S. and Lester, L.S., Salter, C.A., & Hirsch, E. A laboratory study of the effects of diet and bright light countermeasures to jet lag. Technical Report NATICK/TR-90/024, March, 1990.

17. Baddeley, A.D. (1968). A three-minute test based on grammatical transformation. Psychonomic Science, 10, 341-342.